DOE/ER-0313/1

Fusion Reactor Materials

Semiannual Progress Report
for Period Ending
September 30, 1986

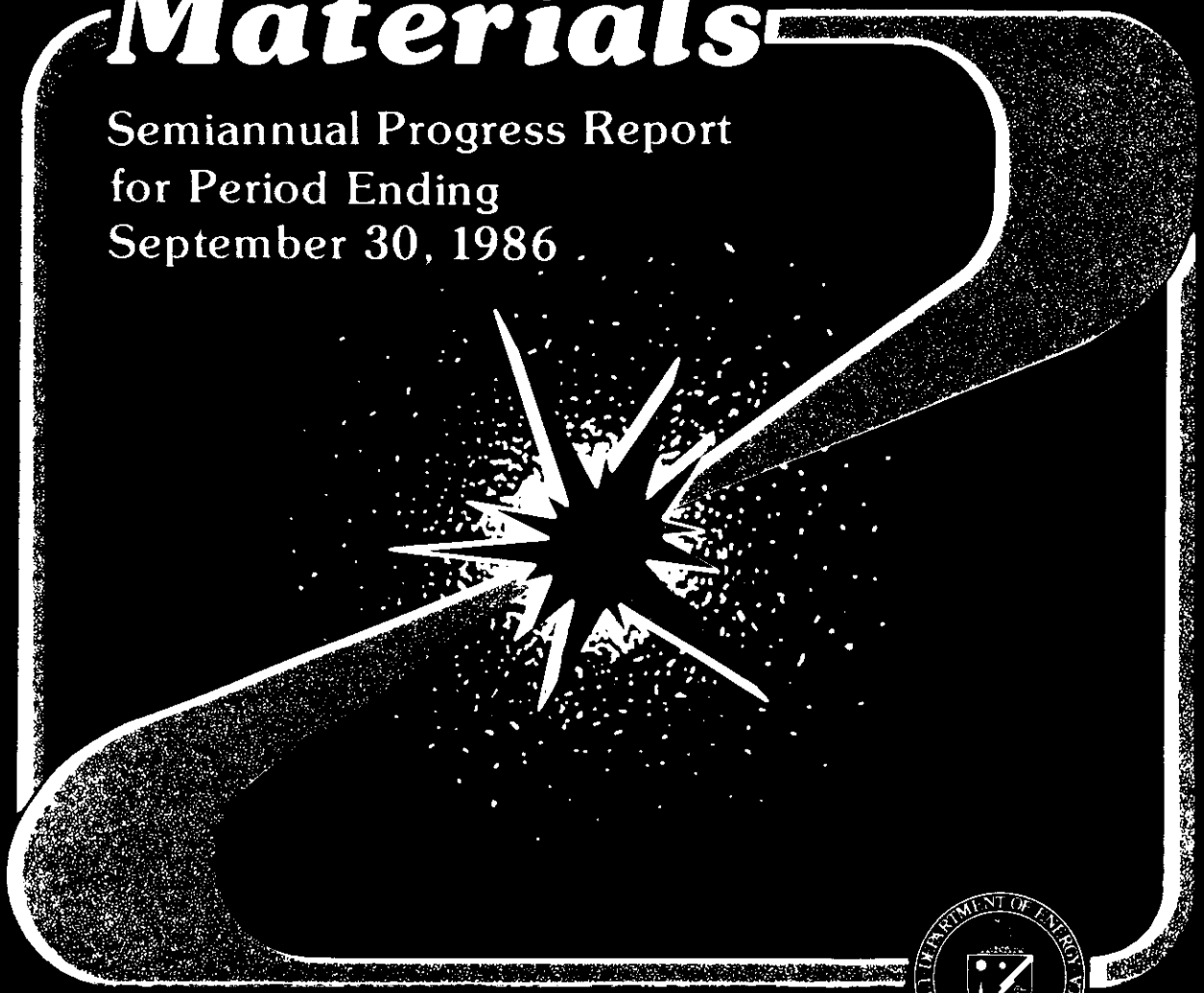

U. S. Department of Energy
Office of Fusion Energy

Printed in the United States of America. Available from
National Technical Information Service
U.S. Department of Commerce
5285 Port Royal Road, Springfield, Virginia 22161
NTIS price codes—Printed Copy: A19 Microfiche A01

DOE/ER-0313/1
Distribution
Categories
UC20, 20c

FUSION REACTOR MATERIALS SEMIANNUAL PROGRESS REPORT FOR THE PERIOD ENDING SEPTEMBER 30, 1986

Date Published: September 1987

Prepared for
DOE Office of Fusion Energy

Prepared by
OAK RIDGE NATIONAL LABORATORY
Oak Ridge, Tennessee 37831
operated by
MARTIN MARIETTA ENERGY SYSTEMS, INC.
for the
U.S. DEPARTMENT OF ENERGY
under Contract DE-AC05-840R21400

FOREWORD

This is the first in a series of semiannual technical progress reports on fusion reactor materials. This report combines research and development activities which were previously reported separately in the following technical progress reports:

- Alloy Development for Irradiation Performance
- Damage Analysis and Fundamental Studies
- Special Purpose Materials

These activities are concerned principally with the effects of the neutronic and chemical environment on the properties and performance of reactor materials; together they form one element of the overall materials program being conducted in support of the Magnetic Fusion Energy Program of the U.S. Department of Energy. The other major element of the program is concerned with the interactions between reactor materials and the plasma and is reported separately.

The Fusion Reactor Materials Program is a national effort involving several national laboratories, universities, and industries. The purpose of this series of reports is to provide a working technical record for the use of the program participants, and to provide a means of communicating the efforts of materials scientists to the rest of the fusion community, both nationally and worldwide.

This report has been compiled and edited under the guidance of A. F. Rowcliffe, Oak Ridge National Laboratory, and D. G. Doran, Battelle-Pacific Northwest Laboratory. Their efforts, the work of the publications staff in the Metals and Ceramics Division at ORNL, and the many persons who made technical contributions are gratefully acknowledged. T. C. Reuther, Reactor Technologies Branch, has responsibility within DOE for the programs reported on in this document.

G. M. Haas, Chief
Reactor Technologies Branch
Office of Fusion Energy

CONTENTS

1. IRRADIATON FACILITIES, TEST MATRICES, AND EXPERIMENTAL METHODS

RTNS-II IRRADIATIONS AND OPERATIONS - D. W. Short and D. W. Heikkinen (Lawrence Livermore National Laboratory)

OBJECTIVE

The objectives of this work are operation of RTNS-II (a 14-MeV neutron source facility), machine development, and support of the experimental program that utilizes this facility. Experimenter services include dosimetry, handling, scheduling, coordination, and reporting. RTNS-II is supported jointly by the U.S. and Japan and is dedicated to materials research for the fusion power program. Its primary use is to aid in the development of models of high-energy neutron effects. Such models are needed in interpreting and projecting to the fusion environment, engineering data obtained in other spectra.

SUMMARY

Irradiations were performed on eleven different experiments during this period.

PROGRAM

Title: RTNS-II Operations (WZJ-16)
Principal Investigator: D. W. Short
Affiliation: Lawrence Livermore National Laboratory

RELEVANT DAF'S PROGRAM PLAN TASK/SUBTASK

TASK II.A.2,3,4.
TASK II.B.3,4
TASK II.C.1,2,6,11,18.

IRRADIATION

During this quarter, irradiations (both dedicated and add-on) were done for the following people.

Experimenter	P or A*	Sample Irradiated
T. Yoshiie (Hokkaido/ H. Kawanishi (Tokyo) K. Miyahara (Tokyo) M. Kiritani (Hokkaido) A. Kohyama (Tokyo) R. Oshima (Osaka) H. Yoshida (Kyoto) K. Abe (Tohoku) H. Matsui (Tohoku) H. Kayano (Tohoku) Y. Shimomura (Hiroshima) N. Yoshida (Kyushu) S. Ishino (Tokyo) H. Takahashi (Hokkaido) C. Kinoshita (Kyushu) K. Okamura (Tohoku) K. Kamata (Nagoya) K. Saka (Nagoya) M. Iseki (Nagoya) K. Hirata (Osaka) T. Kino (Hiroshima) H. Heinisch (HEDL) F. Clinard (LANL)	P	Metals - displacement damage & mechanical properties. Ceramics - neutron damage - irradiated at 200°C and 450°C
R. Borg (LLNL)	A	NiZr, NiNb & NiHf - TEM, phase transformation
Y. Shimomura (Hiroshima) Y. Kitano (Hiroshima) H. Matsui (Tohoku) M. Kiritani (Hokkaido) N. Yoshida (Kyoto) H. Abe (Kyushu) A. Ohshima (Osaka) M. Guinan (LLNL)	P	Au, Cu, Ag, V, Ni, Al, Si, Mo, Ge, Nb_3,Sn, Fe, Mn-Al, Fe-Mo and Fe-Si displacement cascade damage, size & structure analyzed with TEM. Irradiated at 20°K.

Experimenter	P or A*	Sample Irradiated
Y. Shimomura (Hiroshima) contd. P. Hahn (LLNL) J. Huang (LLNL)	P	Au, Cu, Ag, V, Ni, Al, Si, Mo, Ge, Nb_3,Sn, Fe, Mn-Al, Fe-Mo and Fe-Si displacement cascade damage, size & structure analyzed with TEM. Irradiated at 20°K.
M. Kiritani/T. Yoshiie (Hokkaido)	A	Ni, Cu, Fe, Au & Mo - Study of migrating free point defects under neutron irradiation.
R. Borg (LLNL)/ K. Rao (RIT, Stockholm)	A	Amorphous Alloys - Mossbauer effect, Hall effect, TEM, magnetic susceptibility and magneto-resistance.
H. Moriyama (Kyoto)	P	Li, Pb, Be, F, Cl, Br & I - Tritium recovery.
R. Borg (LLNL)	A	Au-Fe - a.c. & d.c. magnetic susceptibility
D. Kneff (Rockwell) L. Greenwood (ANL)	P	Li, O, F, N, Al_2O_3,MgO, Si_3N_4 & SiC dosimetry & cross sections.
F. Clinard (LANL)/ H. Frost (LANL)/ N. Iwamoto (Osaka)	P	SiC & Al_2O_3 - Loss tangent & dielectric constant.
T. Iida (Osaka)	A/P	Fiber optics & photomultiplier tubes - neutron damage.
M. Singh/C. Wang (LLNL)	A	Semiconductors - neutron damage

* P = primary, A = add-on

RTNS-II STATUS - D. W. SHORT AND D. W. HEIKKINEN

No major modifications were made on the facility during this period. Scheduled operations were reduced to 16 hours a day using primarily one neutron source due to loss of personnel.

FUTURE WORK

Irradiations will be continued for F. Clinard (LANL), R. Borg (LLNL), H. Moriyama (Kyoto), T. Iida (Osaka) and M. Singh (LLNL). Also during this period, irradiations for H. Abe (Kyushu), T. Terai (Tokyo), Y. Shimomura (Hiroshima) et al., M. Guinan (LLNL), M. Kiritani (Hokkaido) and E. Franco (Aracor) will be carried out. Some 24-hours-per-day operation will be involved.

DESIGN OF THE HFIR SPECTRAL TAILORING EXPERIMENTS IN THE HFIR RB* CAPSULE IRRADIATION FACILITY —
A. W. Longest, J. E. Corum,† and K. R. Thoms (Oak Ridge National Laboratory)

OBJECTIVE

The objective of this work is to design and build irradiation capsules for use in the HFIR RB* positions. Japanese and U.S. specimens are to be transferred to RB* positions following irradiation to ~5 dpa at temperatures of 60, 200, 330, and 400°C in ORR experiments ORR-MFE-6J and -7J.

SUMMARY

Design of a universal HFIR RB* capsule irradiation facility and four HFIR-MFE-RB* capsules to accommodate specimens preirradiated in a spectrally tailored experiment in the ORR is proceeding satisfactorily. The capsule designs are being standardized as much as possible and the construction drawings are being prepared on a computer-aided design (CAD) system to minimize overall long-term costs. Preparation of construction drawings for the instrumented 330°C capsule is approximately 30% complete; drawings for the first two capsules (330 and 60°C) are scheduled to be completed in November and December 1986, respectively. Operation of the first two capsules is scheduled to begin in June 1987, and the other two (200 and 400°C) in January 1988. A conventional temperature control gas gap, although relatively small, was selected for the 330°C capsule design. Development efforts are in progress to test a larger particle-filled gap concept for possible use for temperature control in the 200°C capsule. In this concept, temperature would be controlled primarily by varying the inert gas pressure in an annular bed of coarse/fine microspheres to change its thermal conductance.

PROGRESS AND STATUS

Introduction

Design of a universal capsule irradiation facility to accommodate the HFIR-MFE spectral tailoring specimens[1] that are being preirradiated in the ORR experiments ORR-MFE-6J and -7J is in progress. The capsules are being designed for insertion into any of the eight large-diameter holes (46 mm) of the new removable beryllium (RB*) facility that is scheduled to be installed in the HFIR in June 1987. The first series of experiments will irradiate the Japanese and U.S. material specimens at temperatures of 60, 200, 330, and 400°C to match their irradiation temperatures in the ORR. Operation of the first two capsules (60 and 330°C) is scheduled to begin in June 1987, and the other two capsules (200 and 400°C) in January 1988. Provisions are being made for removal, examination, and reencapsulation of the MFE specimens at intermediate exposure levels of 10 and 20 dpa en route to the target exposure level of 30 dpa.

Facility

The HFIR RB* capsule irradiation facility will provide for spectral tailoring of the neutron flux by placement of appropriate neutron absorber shields around the in-core section of the capsule. Hafnium sleeves 3.0- and 4.2-mm thick have been selected for spectral tailoring shields for the MFE specimens from the ORR; the 3.0-mm-thick hafnium sleeve will be used while the specimens are irradiated from approximately 5 to 10 dpa, and the 4.2-mm-thick hafnium sleeve will be used while the specimens are irradiated from 10 to 30 dpa. These shields are designed to tailor the neutron flux to closely match (within ±20%) the helium production/atom displacement ratio (14 ppm He/dpa) expected in a fusion reactor first wall. Other features of the new RB* capsule irradiation facility include (1) straight access into any of the eight 46-mm-diam positions, (2) peak unperturbed thermal and fast neutron flux levels of approximately 1.5×10^{15} and 5.0×10^{14} (> 0.1 MeV) neutrons/cm^2·s, respectively, (3) peak unperturbed gamma heating rate of approximately 18 W/g, (4) standard capsule diameter (38 mm) and lead tube design, (5) containment tube design parameters of 6.9 MPa (1000 psi) external pressure differential at 93°C (200°F), and (6) 180° capsule rotation at the end of each reactor cycle to provide uniform exposure to all specimens at a given elevation.

330°C Capsule

Preparation of construction drawings for the 330°C capsule, now approximately 30% complete, is scheduled for completion by mid-November 1986. This capsule, designated HFIR-MFE-330J-1, will be instrumented with 24 thermocouples. The temperature will be controlled by varying the gas mixture (He/Ne/Ar) and hence the thermal conductance, in a small (0.085 mm "hot") gas gap between the specimen holder and the containment tube. At the same time, the MFE specimens will be maintained under a helium sweep. Sintered aluminum product (SAP) alloy (Al-7 wt % Al_2O_3) was selected for the specimen holder to provide adequate strength and dimensional stability under the planned irradiation conditions. SAP also meets requirements of high thermal conductivity (close to that of aluminum) and reasonably low density (2.74 g/cm^3). The capsule containment tube consists of 6061-T6 aluminum in the in-core region and 304L stainless steel in the upper region. The upper and lower sections of the containment tube will be joined by a special aluminum-to-stainless steel

† Midwest Technical, Inc., under Subcontract No. 85B-73978C

transition tube. Because this is the first of a series of RB* irradiation capsules, the capsule (and irradiation facility) designs are being standardized as much as possible, and construction drawings are being prepared on a computer-aided design (CAD) system to minimize overall long-term cost.

60°C Capsule

Preparation of construction drawings for the 60°C capsule, designated HFIR-MFE-60J-1, is scheduled to start in November and be completed by the end of December 1986. This capsule will be uninstrumented with the test specimen in contact with the reactor cooling water.

400°C Capsule

Design of the 400°C capsule, designated HFIR-MFE-400J-1, is not firm at this time, but it will be an instrumented capsule similar in most respects to the 330°C capsule.

200°C Capsule

Design of the 200°C capsule, designated HFIR-MFE-200J-1, will depend on the outcome of development efforts currently under way. This capsule presents a special design problem because it is difficult to remove the large amount of gamma heat generated in the capsule while, at the same time, controlling the operating temperature at 200°C. An aluminum alloy specimen holder with a conventional temperature control gas gap would be a risky design for this capsule because the required gas gap would be too small to predict its operating thermal conductance with sufficient accuracy. Various other possible designs have been considered, one of which is the use of very low density material for the specimen holder, such as 10% dense Duocel aluminum, which would generate less heat and permit use of a larger gas gap. Duocel aluminum may have adequate thermal conductance, but it needs to be tested to determine its dimensional stability under the planned irradiation conditions.

Also under investigation as a possible design concept for the 200°C capsule is the use of a relatively large temperature control gas gap (~0.76 mm) filled with a binary (coarse/fine) mixture of SiC coated carbon microspheres. In this concept, temperature would be controlled primarily by varying the inert gas pressure (and hence the mean free path of the gas molecules) in the particle bed to change its thermal conductance. An apparatus for development testing of this design concept is being prepared, and first results are expected by December 1986.

A backup design concept for the 200°C capsule is to utilize electrical heaters for temperature control. In this approach, gas gap thicknesses would be reduced to the minimum needed for assembly in the hot cell so that the capsule would operate below 200°C under the condition of no heater power. Disadvantages of this design concept, in addition to the added cost of heaters, are the additional temperature gradients induced electrical heaters and the possibility that high heater power may be required because of the uncertainties in small-gap thermal conductances and in the gamma heating rate in the new facility.

FUTURE WORK

Design and preparation of construction drawings for the first four HFIR-MFE RB* capsules are scheduled to be completed by June 1, 1987. Preparation of construction drawings for reencapsulation of the MFE specimens will be an ongoing but relatively small effort because the drawings will all be on the CAD system and only minor changes are expected to be required in going from each capsule to its successor.

REFERENCE

1. J. L. Scott, L. K. Mansur, M. L. Grossbeck, E. H. Lee, K. Farrell, L. L. Horton, A. F. Rowcliffe, and M. P. Tanaka, "Description of the U.S./Japan Spectral Tailoring Experiment in ORR," pp. 12-20 in ADIP Semiannu. Prog. Rep., March 31, 1985, DOE/ER-0045/14, U.S. DOE, Office of Fusion Energy.

DESIGN AND OPERATION OF THE HFIR INSTRUMENTED (JP TYPE) TARGET TEMPERATURE TEST (TTT) CAPSULE -
I. I. Siman-Tov (Oak Ridge National Laboratory)

OBJECTIVE

The primary objective of this experiment is to determine the temperatures in the JP series capsules by placing an instrumented JP mockup experiment in the modified HFIR instrumented target facility. A secondary objective is to determine the nuclear heating rate in stainless steel as a function of axial core position and time in a HFIR cycle.

SUMMARY

The JP-TTT capsule assembly was completed, and irradiation started on August 17, 1986, as planned. First results indicate that temperatures at the beginning of the experiments are within 15% of predicted values except in the G-1 position (Fig. 1). The specimens accumulated a total irradiation time of 42.51 full power days (FPD) at 100 MW through September 30, 1986.

PROGRESS AND STATUS

Earlier details concerning the TTT experiment have been previously described.[1-5] The design, fabrication, and assembly of the TTT capsule were completed by the end of July and the capsule was ready for the August insertion, as planned. The capsule was first inserted in the Instrumented Target Facility Mockup and was adjusted to be positioned correctly in the facility. The capsule was inserted on August 15 and started operation on August 17.

The capsule completed two irradiation cycles by September 30, 1986, for a total irradiation time of 42.51 FPD at 100 MW. Figure 1 shows the specimen and thermocouple (TE) final configuration. Table 1 presents the temperature history for the two cycles. The thermocouple positions given are at the center of the specimens.

The temperatures in all positions except for G-1 are within 15% of the predicted values. Figures 2 and 3 present the temperature distribution during cycles I and II, respectively. It should be noted that the time-dependence of the nuclear heating rate in the target position is steadier than previously anticipated. Positions 1 and 9 show little change when compared to the changes observed in the RB experiments. Figure 4 compares the two symmetric fatigue specimen temperatures; the nuclear heating rates in these positions are symmetric about the core HMP and show the same time development. Figure 5 compares the experimental and design temperatures for the gamma susceptors for both cycles. The measured temperature in position G-1 does not agree very well with the design temperature. At the symmetric position (T-11) there is no thermocouple. Therefore, there is no direct confirmation (or contradiction) of the implied lower heating rates. A thermal analysis using "as-built" dimensions for all positions is under way. This analysis should provide

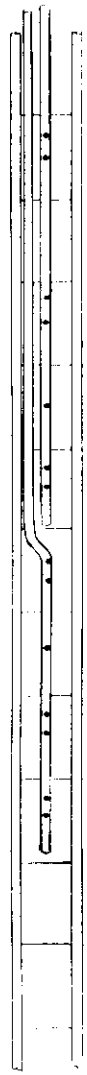

ORNL-DWG 87-3717 ETD

REGION DESIGNATION (SPECIMEN)	AXIAL POSITION (ABOVE HMP) (mm)	CENTRAL TE #	TEMP. (°C)	NUCLEAR HEATING RATE IN S.STEEL (W/G)	IN ALUMINUM (W/G)
G-1 GAMMA SUSCEPTOR	233.60	TE102	300	32.6	20.5
T-2 TENSILE	189.05		400	39.1	24.6
G-3 GAMMA SUSCEPTOR	144.45	TE104	500	41.6	26.2
F-4 FATIGUE	96.98	TE105	430	46.9	29.5
G-5 GAMMA SUSCEPTOR	46.36	TE107	430	51.7	32.4
TEM	0	TE202	400	54.6	34.4
F-7 FATIGUE	-45.90	TE203	430	51.8	32.5
F-8 FATIGUE	-96.01	TE205	430	47.0	29.6
T-9 TENSILE	-35.26	TE207	500	41.7	26.3
JPT-10 JAPANESE TENSILE	-187.73		400		
JPT-11 JAPANESE TENSILE	-232.18		300		

Fig. 1. Design configuration and parameter description.

Table 1. Temperature History of the TTT Specimens for Cycles I and II

Specimen	G-1 TE102 (°C)	G-3 TE104 (°C)	F-4 TE105 (°C)	G-5 TE107 (°C)	TEM TE202 (°C)	F-7 TE204 (°C)	F-8 TE205 (°C)	T-9 TE207 (°C)
Design	300	500	430	430	400	430	430	500
Cycle 1								
Average	205.3	500.4	433.5	448.9	356.3	469.8	419.0	444.8
Minimum	204	495	416	429	340	451	405	438
Maximum	207	509	441	456	363	477	426	450
Cycle 2								
Average	203.8	482.9	430.6	441.4	357.9	466.5	418.0	440
Minimum	199	475	424	434	349	456	406	427
Maximum	206	488	436	447	362	472	422	446

ORNL-DWG 87-1911

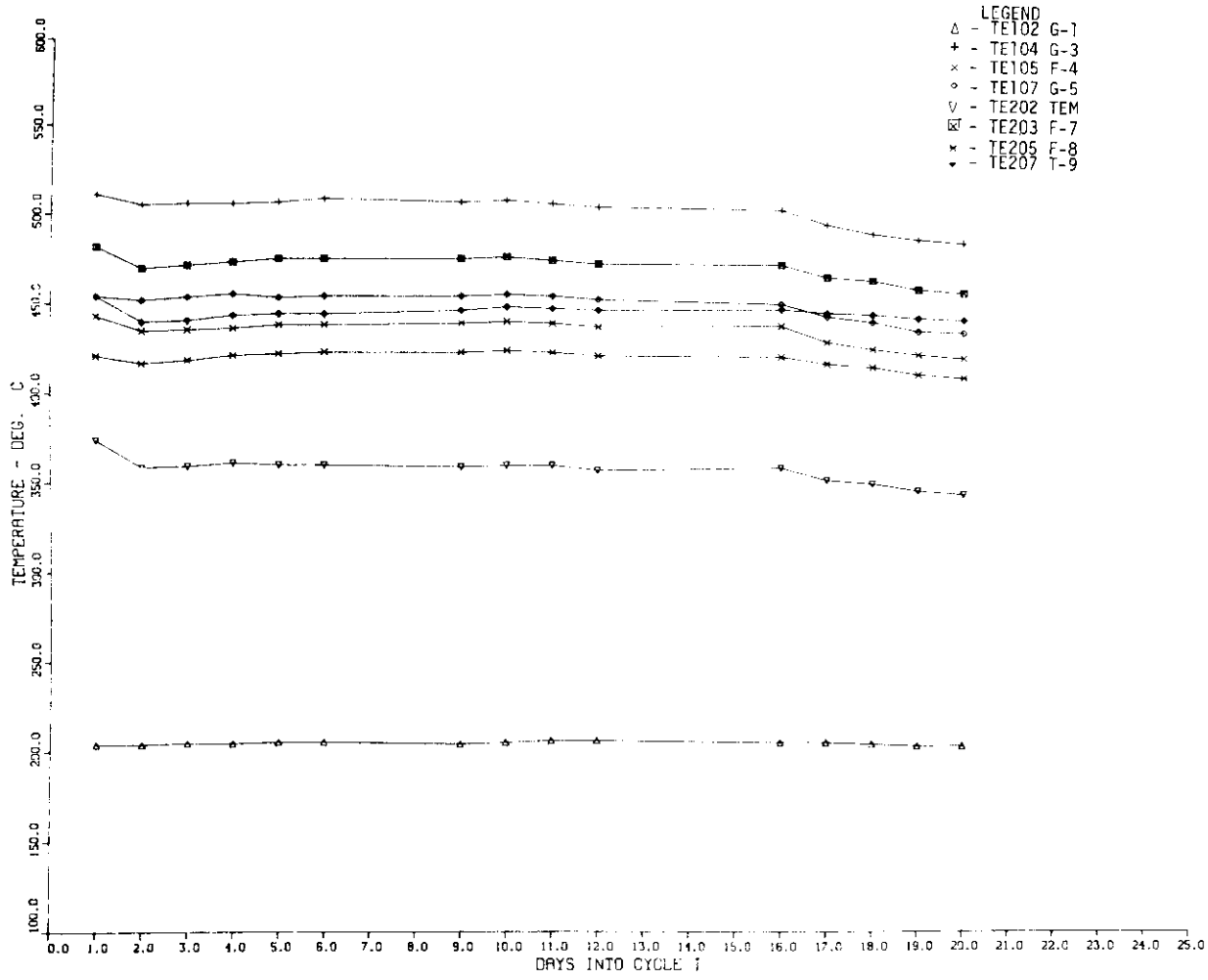

Fig. 2. Temperature distribution in the TTT capsule — Cycle I.

ORNL-DWG 86-18209

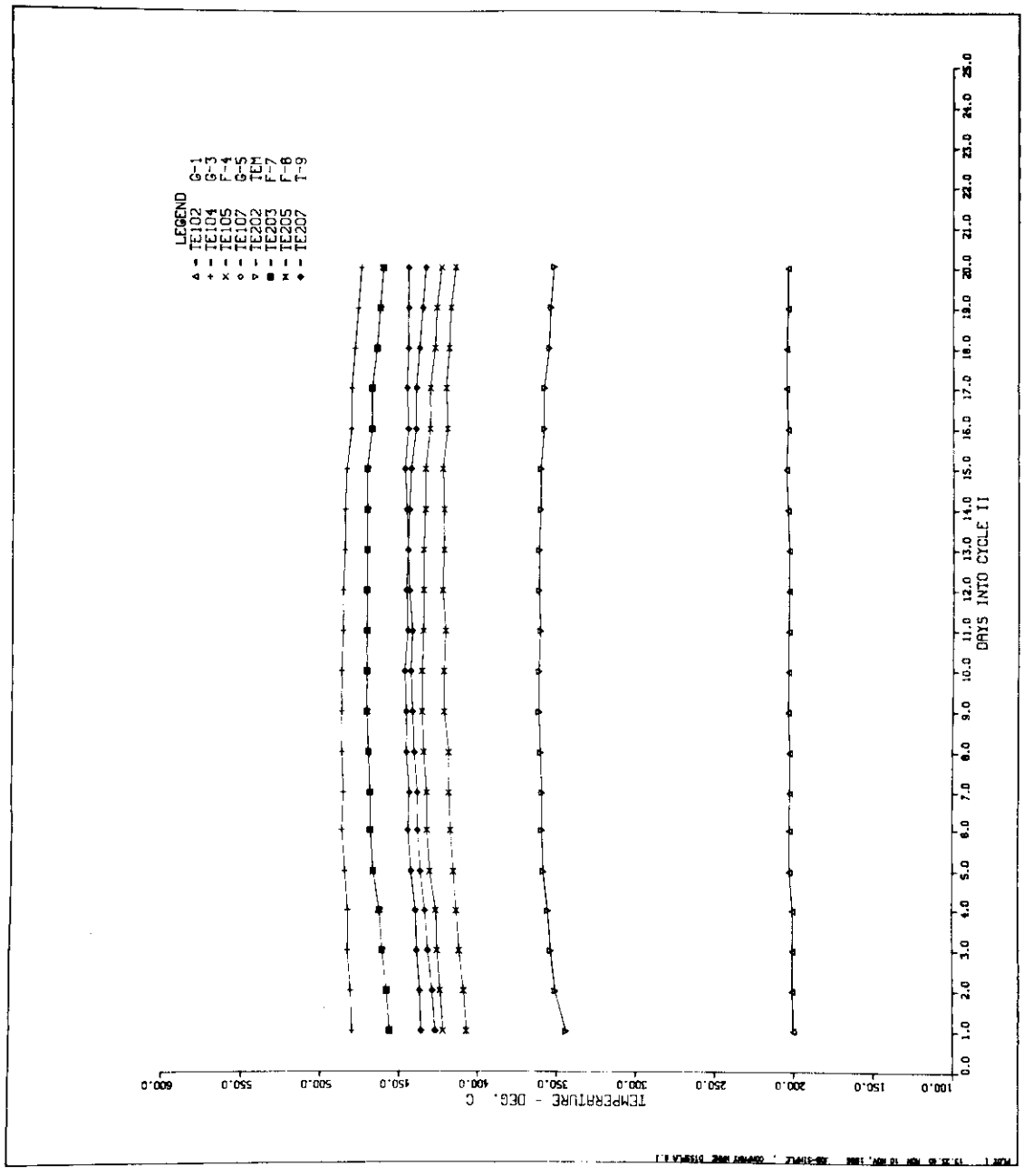

Fig. 3. Temperature distribution in the TTT capsule — Cycle II.

ORNL-DWG 86-18211

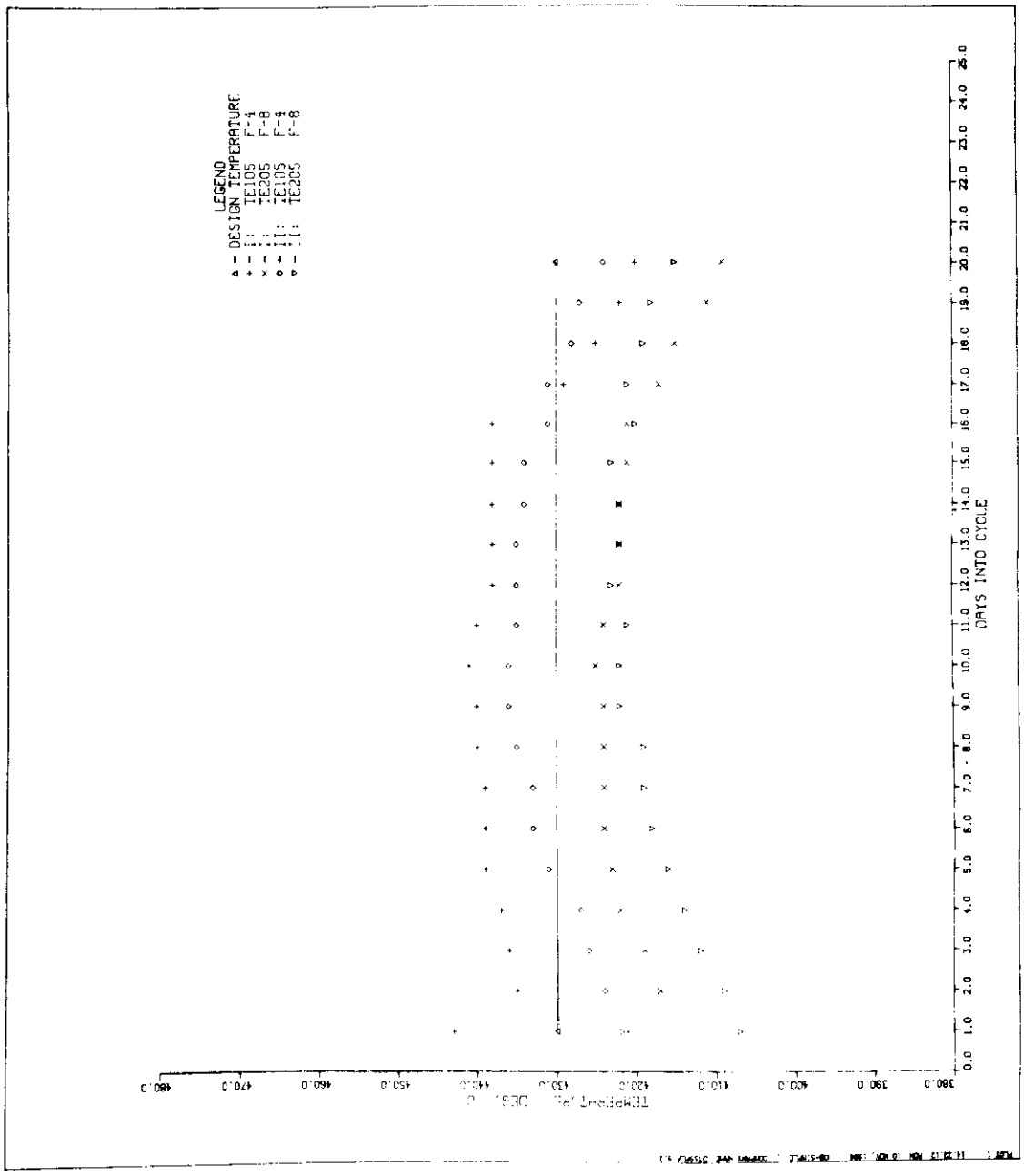

Fig. 4. Temperature comparison — symmetric fatigue specimens.

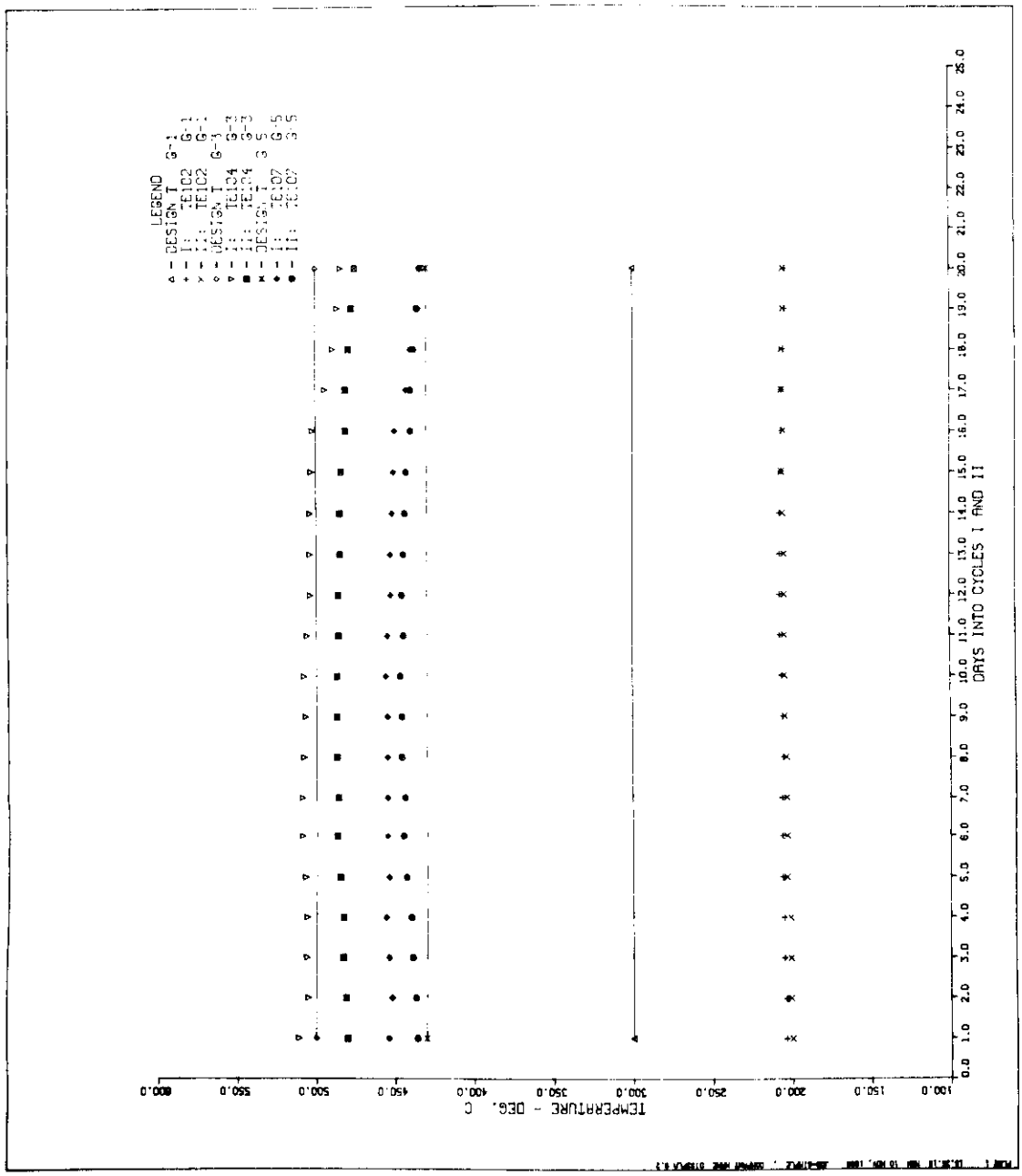

Fig. 5. Measured versus computed temperature in the gamma heaters.

bounds for the nuclear heating rates as a function of axial position in the capsule. The capsule is scheduled for a five-cycle irradiation and will provide valuable information on the stability of the thermal conditions as a function of accumulated irradiation time. A major factor may be the change in the control gap dimensions due to swelling. The thermocouples underwent extensive electrical testing at the end of cycle II, and we hope to learn how constant these readings remain by the end of the irradiation.

FUTURE WORK

The thermal analysis with "as built" dimensions will be completed. We hope to determine bounds on the gamma heating rate in stainless steel as a function of axial position in the instrumented target facility.

REFERENCES

1. A. F. Rowcliffe, M. L. Grossbeck, and S. Jitsukawa, "The U.S./Japan Collaborative Testing Program in HFIR and ORR," pp. 38-43 in ADIP Semiannu. Prog. Rep., March 31, 1984, DOE/ER-0045/12, U.S. DOE, Office of Fusion Energy.

2. A. F. Rowcliffe et al., "The U.S./Japan Collaborative Testing Program in HFIR and ORR: Specimen Matrices for HFIR Irradiation," pp. 61-62 in ADIP Semiannu. Prog. Rep., Sept. 30, 1984, DOE/ER-0045/13, U.S. DOE, Office of Fusion Energy.

3. J. L. Scott and M. P. Tanaka, "Preparation for Postirradiation Examination of U.S./Japan HFIR Capsules," pp. 10-11 in ADIP Semiannu. Prog. Rep. March 31, 1985, DOE/ER-0045/14, U.S. DOE, Office of Fusion Energy.

4. J. L. Scott, M. L. Grossbeck, and M. P. Tanaka, "Phase I HFIR Capsules - Irradiation and Postirradiation Examination," pp. 18-21 in ADIP Semiannu. Prog. Rep., Sept. 30, 1985, DOE/ER-0045-15, U.S. DOE, Office of Fusion Energy.

5. I. I. Siman-Tov, "Design of the HFIR (JP Type) Instrumented Target Capsule," pp. 9-10 in ADIP Semiannu. Prog. Rep. for March 31, 1986, U.S. DOE, Office of Fusion Energy.

CHARACTERIZATION OF THE NLTNIF FACILITY IN THE BSR - L. R. Greenwood (Argonne National Laboratory)

OBJECTIVE

To characterize neutron irradiation facilities in terms of neutron fluence and spectra as well as displacement damage, gas production, and other transmutation.

SUMMARY

Dosimetry measurements and damage calculations have been completed for the National Low-Temperature Neutron Irradiation Facility in the Bulk Shielding Reactor at Oak Ridge National Laboratory. This facility will permit neutron irradiation at $4^{o}K$. Results show that the fast flux for materials studies is about $1.4x10^{13}$ n/cm^2-s producing about 0.3 dpa and 1.7 appm He in 316 stainless steel in one year.

PROGRESS AND STATUS

Introduction

Neutron spectral measurements have been conducted in the new National Low-Temperature Neutron Irradiation Facility (NLTNIF) in the Bulk Shielding Reactor (BSR) at Oak Ridge National Laboratory. This facility permits irradiation of materials in the core of the BSR at liquid helium temperatures ($4^{o}K$). Dosimetry materials were irradiated for 6 hours on May 23, 1986 at full reactor power (2 MW). The following report describes the activity measurements, neutron spectral analyses, flux gradients, and damage calculations needed to characterize the facility for future materials experiments.

Activity Measurements

Dosimetry materials were placed at various locations in the cryostat in order to measure the neutron spectrum and flux gradients. An aluminum tube was mounted on the axis of the cryostat. This tube was about 10 in. long by 1/8 in. OD and contained six dosimetry packets. One of the packets was covered with 1 mil Gd foil in order to separate the thermal and epithermal flux components. The spectral set of materials included the following wires: Fe, Ni, 0.1% Co-Al, Cu, 0.1% Au-Al, 2.2% Lu-Al, Ti, Nb, 80% Mn-Cu, and ^{237}Np. Twelve smaller aluminum dosimetry packets were located at 8 radial and 4 vertical locations in order to measure the flux gradients. These packets contained Fe, Ni, and 0.1% Co-Al wires.

Following the irradiation the samples were returned to Argonne for gamma counting using our Ge spectrometer systems. The measured activities were then corrected for sample weight, gamma self-absorption, and decay during and after irradiation. The results are listed in Tables I-II. All of the nuclear data used in the analysis (eg - half-lives and gamma intensities) were taken from a recent compilation by D. C. Kocher (Radioactive Decay Data Tables, DOE/TIC-11026, 1981). Neutron self-shielding corrections were applied to the cross sections prior to the spectral analysis since these corrections are spectral-dependent. However, these corrections are small (<2%) except for Lu(20%) and Np(80%).

Spectral Analysis

The STAY'SL spectral adjustment computer code was used to determine the neutron flux spectrum. This code performs a least squares adjustment considering our activity measurements, neutronics calculations by Dick Lillie (ORNL), and activation cross sections taken from the ENDF/B-V dosimetry file. Uncertainties and covariances are assigned to all of these quantities. The activities generally have uncorrelated uncertainties of about 2-3%. Cross section uncertainties were adopted from ENDF. Since no information was available concerning the uncertainties in the calculated flux spectrum, we assumed values of 30% except for the thermal flux which had to be raised about a factor of two to fit the data. A gaussian covariance function was used to describe the correlations between fluxes and cross sections at different energies. This function assumes a strong correlation between nearby groups which declines to a very low value for widely separated groups.

The adjusted flux spectrum is shown in Fig. 1 where it is compared to the calculated spectrum. As can be seen, the adjusted spectrum is considerably softer than the calculation. The integral fluxes are summarized in Table III. The fast flux is about 30% lower than calculated while the thermal flux is about 80% higher. The reasons for this difference are not understood and are now being investigated. The adjusted spectrum (Fig. 1) shows some structure in the energy region from 10-1000 eV. The dip near 50 eV is due to our capture data for Fe, Co, and Cu. Such a structure could be caused by absorption in reactor or cryostat structural materials such as Fe, Al, or Zr which may not be adequately accounted for in the neutronics calculations. However, the nature of spectral adjustments precludes any precise statement concerning the width or depth of such structures and may in fact be caused by the interaction of deficiencies in other spectral regions. In any case, these variations from a 1/E dependence are not very significant and have little effect on the integral fluxes. The structures seen in the spectrum near 1 MeV are present in the neutronics calculations at all locations near the center of the cryostat.

Flux Gradients

Table II lists activity measurements at 8 radial and 10 vertical locations in the cryostat. The vertical flux gradients are shown in Fig. 2 and the radial gradients in Fig. 3. As can be seen, the maximum vertical flux location is about 4 in. from the bottom of the cryostat. The flux variation is less than 10% for a vertical height of about 7 in. and then drops steadily outside of the central region. The thermal flux has nearly the same dependence as the fast flux indicating no significant spectral differences until we get to 10 in. above the bottom of the cryostat at which point the thermal flux begins to decline much more slowly than the fast flux. The radial gradients (Fig. 3) indicate a rapid fall in fast flux of about 20% in the East-West direction as we go away from the core center. In the North-South direction the gradients are less than 3%, with a small preference for the North direction. The thermal flux declines more slowly than the fast flux in the East-West direction indicating a spectral change across the cryostat. The change in the fast flux is about twice that in the thermal flux. These gradients appear to be in satisfactory agreement with the neutronics calculations.

Damage Calculations

The adjusted neutron spectrum was used to calculate damage parameters for various fusion materials assuming a run time of 1 year (365 full power days). The calculations were done with our SPECTER computer code. Gas production cross sections are taken from ENDF/B-V. The results are summarized in Table IV.

FUTURE WORK

Analysis is in progress for the MFE4A/4B spectral tailoring experiment in ORR, fission-fusion correlations (HEDL) in the Omega West Reactor (LANL), and US/Japanese experiments JP2, JP6, and JP7 in HFIR.

PUBLICATIONS

Two papers were presented at the 13th International Symposium on the Effects of Radiation in Materials in Seattle, June 23-25, 1986.

L. R. Greenwood
Recent Research in Neutron Dosimetry and Damage Analysis for Materials Irradiations

D. R. Davidson, R. C. Reedy, L. R. Greenwood, W. F. Sommer, and M. S. Wechsler
Additional Measurements of the Radiation Environment at the Los Alamos Spallation Radiation Effects Facility at LAMPF

Abstracts have also been submitted to the Sixth ASTM-Euratom Symposium on Reactor Dosimetry in Jackson Hole, WY., on May 31-June 5, 1987. They are entitled:

L. R. Greenwood and D. L. Bowers
Measurement of Long-Lived Isotopes in Fusion Materials

L. R. Greenwood
SPECOMP Calculations of Radiation Damage in Compounds

D. L. Smith, J. W. Meadows, P. T. Guenther, and L. R. Greenwood
Development of the Be (d,n) Neutron Source for Cross-Section Investigations in the Few-Mev Energy Range

D. W. Kneff, L. R. Greenwood, B. M. Oliver, and R. P. Skowronski
Helium Production in Mixed-Spectrum Fission Reactors

Table I
Activity Measurements for NLTNIF
(Activity in atom/atom-s, ±2%)
(Values near cryostat center, 2 MW)

Reaction		Bare	Gd Cover
$^{58}Fe(n,\gamma)^{59}Fe$	(10^{-11})	2.37	0.279
$^{59}Co(n,\gamma)^{60}Co$	(10^{-9})	1.11	0.171
$^{63}Cu(n,\gamma)^{64}Cu$	(10^{-11})	8.44	0.947
$^{176}Lu(n,\gamma)^{177}Lu$	(10^{-8})	7.46	1.61
$^{197}Au(n,\gamma)^{198}Au$	(10^{-9})	3.14	1.56
$^{237}Np(n,\gamma)^{238}Np$	(10^{-10})		9.09
$^{237}Np(n,fission)$	(10^{-11})		1.49
$^{54}Fe(n,p)^{54}Mn$	(10^{-13})	7.70	7.50
$^{58}Ni(n,p)^{58}Co$	(10^{-13})	9.12	
$Ti(n,x)^{46}Sc$	(10^{-13})	1.01	1.04
$Ti(n,x)^{47}Sc$	(10^{-13})	1.62	1.66
$^{48}Ti(n,p)^{48}Sc$	(10^{-15})	2.68	2.77
$^{27}Al(n,\alpha)^{24}Na$	(10^{-15})	6.58[a]	6.46[a]
$^{55}Mn(n,2n)^{54}Mn$	(10^{-15})	2.30	2.30
$^{93}Nb(n,2n)^{92m}Nb$	(10^{-15})	4.08	4.24

[a]Accuracy ±5%

Table II
Activity Gradients for NLTNIF Facility
(Activity in atom/atom-s, ±2%, 2 MW)

Height (inches)	$^{54}Fe(n,p)$ 10^{-13}	$^{58}Ni(n,p)$ 10^{-13}	$^{58}Fe(n,\gamma)$ 10^{-11}	$^{59}Co(n,\gamma)$ 10^{-9}	$^{63}Cu(n,\gamma)$ 10^{-11}
Horizontal:					
0.56	7.14	9.68	2.41	1.13	8.70
2.69	7.41	9.97	2.48	1.15	8.76
4.22	7.50		Gd	Gd	Gd
5.75	7.07	9.12	2.37	1.11	8.44
7.53	6.40		2.23	1.04	8.02
9.56	5.72	7.46	2.04	0.93	7.24
11.5	4.76	6.43	1.78	0.83	
13.5	3.76	5.11	1.50	0.71	
16.5	2.24	2.93	1.07	0.50	
19.5	0.87	1.12	0.69	0.35	
Radial:					
E 0.726	7.41	9.92	2.54	1.19	
E 0.363	7.22	9.90	2.46	1.16	
W 0.363	6.40	8.75	2.34	1.08	
W 0.726	6.05	8.28	2.31	1.08	
S 0.726	7.05	9.38	2.35	1.10	
S 0.363	7.07	9.49	2.38	1.11	
N 0.363	7.29	9.36	2.41	1.12	
N 0.726	7.22	9.41	2.37	1.09	

Table III
Integral Neutron Fluxes for NLTNIF
(Flux x10^{13} n/cm^2-s normalized to 2 MW)

Energy	Calculated[a]	Adjusted[b]	Ratio (A/C)
Total	5.33	5.62	1.05
Thermal ($\prec$0.5 eV)	1.59	2.84	1.79
0.5 eV - 0.15 MeV	1.79	1.39	0.78
$\succ$ 0.15 MeV	1.95	1.39	0.71
$\succ$ 1.1 MeV	0.83	0.63	0.76

[a]Calculation by R. Lillie, ORNL
[b]Adjustment using STAY'SL

Table IV
Damage Parameters for NLTNIF
(Calculation for 1 year, 365 FPD)

Element	He,appm	DPA
Al	0.21	0.58
Ti	0.18	0.36
V	0.007	0.41
Cr	0.054	0.36
Mn[a]	0.044	0.40
Fe	0.093	0.32
Co[a]	0.044	0.42
Ni[b]	12.4	0.37
Cu	0.079	0.31
Zr	0.008	0.34
Nb	0.017	0.31
316SS[c]	1.69	0.33

[a]Self-shielding important for thermal capture
[b]Thermal helium production included
[c]316SS: Fe(.645),Ni(.13),Cr(.18),Mn(.019),Mo(.026)

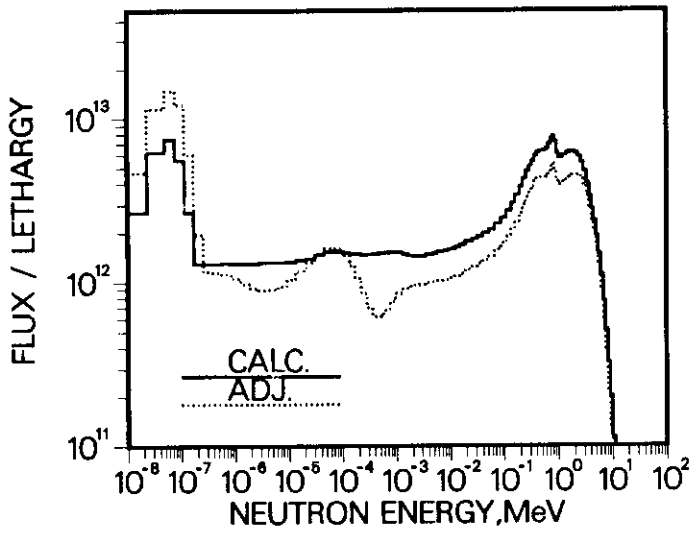

Fig. 1 Calculated and adjusted BSR flux spectrum

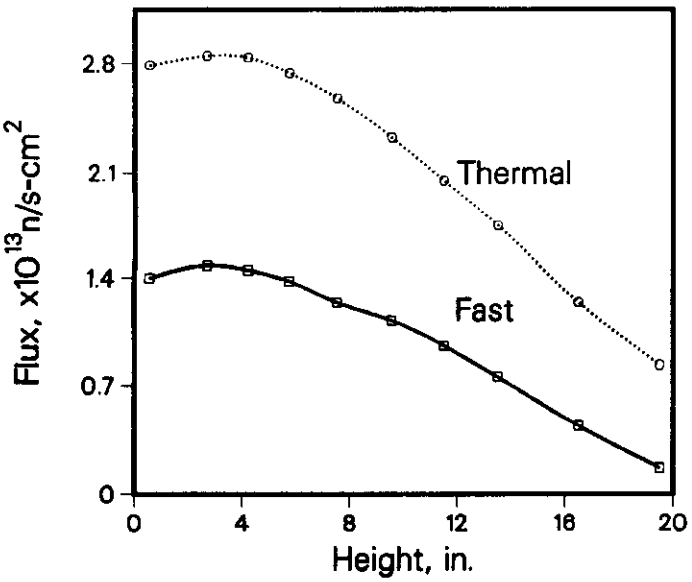

Fig. 2 Vertical flux gradients in the BSR.

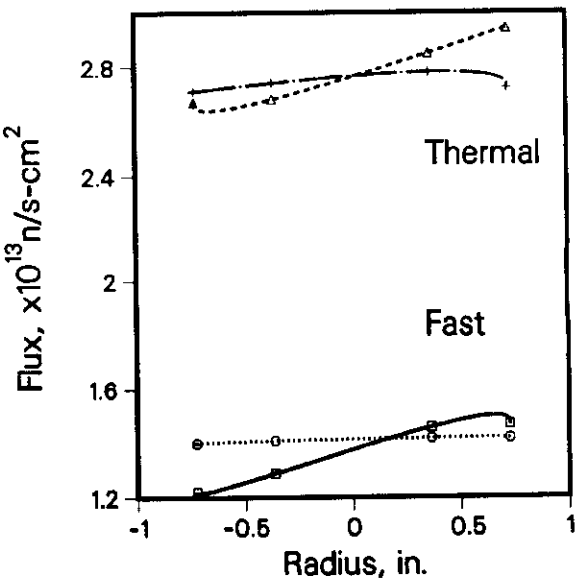

Fig. 3 Radial flux gradients in the BSR

CAPABILITY FOR MEASURING MILLIMETER-WAVE DIELECTRIC PROPERTIES IN FREE SPACE AND AT ELEVATED TEMPERATURES - H. M. Frost (Los Alamos National Laboratory)

OBJECTIVE

To provide a basis of comparison with the in-waveguide method for measuring dielectric constant "k" and loss tangent "tanδ" of fusion ceramics, and to extend measurement temperatures into the regime of first-wall temperatures in a magnetic fusion energy (MFE) reactor.

SUMMARY

The swept-frequency, in-waveguide, scalar network analyser system (SNAS) of a previous progress report on measuring millimeter-wave (MMW) dielectric properties of materials for rf windows (90-100GHz) has been extended to operation in free space via antenna techniques and to elevated temperatures of over 1000°C. The 'matchstick' specimen-cum-waveguide configuration is replaced with a larger disc specimen sandwiched by a pair of collimating antennas that provide a 'parallel' beam for transmission through the specimen. The specimen is mounted in a special 1700°C furnace with doors on opposite walls to permit passage of the MMW beam. During the brief period available for data collection, computer software allows the use of efficient signal averaging of the low-level MMW's that make it through very hot -- and thus highly lossy --ceramic specimens. Dielectric losses measured as a function of temperature allow a closer simulation of the MFE environment. Free-space measurements at room temperature are also important as a comparison standard with data taken by the more difficult waveguide technique compatible with fission-reactor irradiation studies, as problems are much less pronounced in free space with specimen-to-holder clearances, specimen preparation, and spurious standing wave effects. Preliminary room-temperature data are presented.

PROGRESS AND STATUS

Introduction

In the field of MMW measurements, there are a number of competing techniques, each with its own set of pro's and con's. The swept-frequency in-waveguide scalar approach[1] is no exception, though it does have the special and compelling advantage of small specimen volumes and masses compatible with the small capsule-space and low-Curie requirements most experimenters must deal with in fission-reactor irradiations and subsequent non-remote measurements of the activated materials. Some of the other room-temperature techniques, as recently reviewed briefly,[2] include Fourier transform spectroscopy (FTS) and dispersive FTS (DFTS); extremely far infrared spectroscopy; Raman techniques; automated vector network analysis; cavity perturbation; Fabry-Perot, Michelson, and other interferometric approaches; and swept-frequency scalar measurements in free space. ("Vector" refers to measurement of both amplitude and phase, "scalar" to amplitude only -- and thus power.) Some of these approaches were also reviewed by the present writer.[3] When, however, the requirement of elevated-temperature capability is added to the need for an affordable standard of comparison with the in-waveguide (SNAS) approach, the last-mentioned technique of free-space scalar measurements looks the most attractive. This is partly because the use of antennas with adjustable separations of the order of a meter facilitates the thermal isolation of the specimen heater (furnace) from the temperature-sensitive MMW components.[3,4] Such isolation seems to be presently impracticable for some of the preceding approaches such as DFTS. Focusing on the in-waveguide vs. free-space approaches with swept-frequency scalar measurements, Table 1 summarizes the relative advantages of these two methods:

Table 1. Advantages of complementary MMW measurement methods

Method	Advantages (relative to the other method)
FREE SPACE	1. High specimen temperatures, excellent thermal isolation from MMW components. 2. Measured insertion loss closely equaled by desired transmission loss. 3. Spurious standing wave effects easily minimizable. 4. Specimen preparation not critical. 5. No waveguide-wall-loss or specimen-wall-clearance corrections required. 6. Self-consistency cross-checks possible.
WAVEGUIDE	1. Small-volume specimens easily accommodated. 2. Long specimen lengths accommodated (important for very low loss specimens). 3. Propagation mode well defined (if critical specimen dimensions achieved). 4. 'Simple' experimental setup (especially for reflection measurements).

Concerning advantage no. 2 for free space, calculations performed indicate that the error in assuming the measured insertion loss (IL) is equal to the desired transmission loss (TL) can equal 0.2 to 0.3 dB -- a potentially large error compared to the lowest IL values measured of about 1 dB. While this error can be minimized or circumvented, as by empirical calibration data on specimens of different lengths, an independent check is still needed. This is partly because the thermo-mechanical stresses arising in an rf window are proportional to the dielectric loss factor ktanδ and in turn, then, the times-to-failure, related to ktanδ raised to some exponent much greater than one, are quite sensitive to experimental uncertainties in tanδ.[5] These in turn are linked to the uncertainties in TL. (The relation between TL and tanδ is nonlinear,[6] but when tanδ is small linearity is a good approximation.)

Concerning advantage no.6 for free space, there are various ways, such as

*Selection of the alignment between the polarization ("S" or "P") of the incident MMW and the plane of incidence (POI), or,

*For the case of S-polarization (polarization normal to POI), variation of the angle between beam direction and specimen normal,

by which changes in the optical configuration can be used to test for systematic bias in the mathematical algorithms by which the raw data for a particular specimen are reduced to k and tanδ.

The rest of this progress report describes the free-space setup,[5] plus data reduction and some initial data. The electronics portion of the SNAS has already been described.[5]

Experimental setup

The in-waveguide SNAS itself, shown in Fig. 2.2.2 of Ref. 5, is a computer-operated reflectometer (manufactured by Hughes Aircraft Co.) which permits room-temperature measurement of k and tanδ of ceramic specimens (rectangular parallelepipeds or "matchsticks" for short) inserted into WR-10 rectangular waveguide. At 90-100GHz and power levels below 1mW, MMW's are reflected from and transmitted through these matchsticks. From the quasi-periodic power spectra resulting (Fig. 2 in Ref. 1) can be calculated k and tanδ and thus the complex dielectric constant k*=k(1-jtanδ).

The mechanical layout for free-space measurements becomes much more complex than for the matchstick-inside-a-waveguide assembly represented at the bottom of Fig. 2.2.2 in Ref. 5. See Fig. 1 here for the addition of a special furnace and MMW antennas, and Fig. 2 for the corresponding control system.

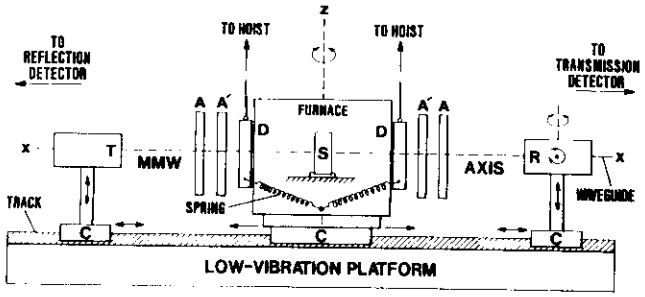

Fig. 1. Simplified mechanical layout for free-space, high-temperature MMW-reflectometer.

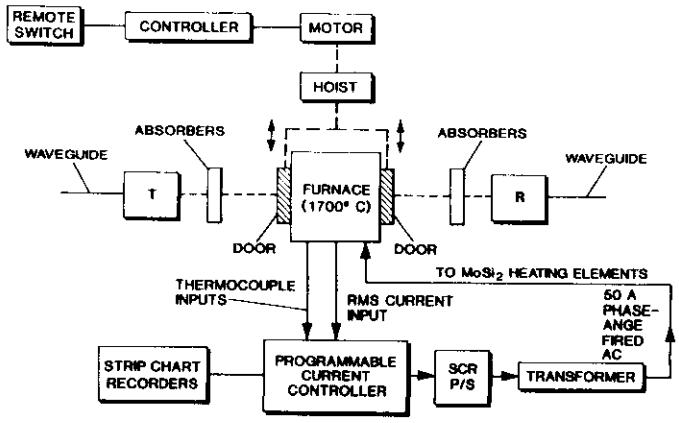

Fig. 2. MMW-furnace control system.

The furnace (1700°C) is mounted on a track via a dovetailed carriage "C". Doors "D" can be raised or lowered electrically to allow the 7.5 cm diameter MMW beam to pass momentarily through the ceramic specimen "S", a 10cm diameter disc. The beam link is formed via a waveguide-fed transmitter antenna "T" and a waveguide-feeding receiver antenna "R". (Manufactured by Alpha Industries, both antennas have a center frequency of 95GHz.) Various absorbers (A,A') are placed in-beam to minimize spurious standing wave effects and transient thermal heating of the plastic lenses in the antennas. Various degrees of freedom in positioning T, S, and R as indicated in the figure are required for optical alignment. The furnace is also mounted on a cross-track ("y" direction; not shown), partly to enable room-temperature data to be collected with "S" instead on a separate, rotatable stand for convenience. A platform, consisting of a 10-cm thick honeycomb table mounted on top of a 3.75-cm (1.5-in.) steel plate, provides vibration damping and

isolation. Control of the door hoists and furnace temperature is represented in Fig.2. Various ramp-and-soak profiles for multi-setpoint operation can be stored in the programmable current controller for different specimen materials and recalled at will.

For either in-waveguide or free-space measurements, calibrations include amplitude normalization, digital frequency correction, and system linearity checks. For example, each 401-point power spectrum digitally measured for a specimen in place is divided point-by-point by the spectrum corresponding to 100% reflection (via a copper 'short') or 100% transmission (no specimen) in order to subtract out the frequency dependence of the MMW electronics, antennas, etc. Because the microwave source is an IMPATT diode with nonlinear, temperature-dependent frequency-vs.-drive-current characteristics, digital corrections are required for a specific diode operating temperature. These are based on measurements of true frequency by a frequency counter to which the IMPATT diode is pseudo-phase-locked. Further, the detector diodes yield nonlinear relations between detected MMW power and output dc voltage if the input levels are outside the linear ('square-law') ranges of these diodes. Variable attenuators "1" and/or "2" in Fig. 2.2.2 of Ref. 5 set to various known values of insertion loss at constant source level enable a check on any 'tracking' error present in the detectors. (These calibrations were also used for the in-waveguide data featured in Table 2 in Ref. 1.)

All these calibration techniques are critical for elevated temperatures at which, for example, thermally-induced opaqueness in the specimen can severely reduce signal levels to below the square-law region and at which the simpler manual measurement of true frequency via a frequency meter (Fig. 2.2.2, Ref. 5) is impracticable because of time constraints on data collection not present at room temperature. On this second point, to minimize uncertainty in the specimen temperature and to speed up the measurement process, the furnace doors are opened for brief periods (e.g., 10 sec) only, during which the IMPATT source is repetitively swept many times from 90 to 100GHz. Simultaneous arithmetic averaging of the resulting power spectra is performed by computer as opposed to the slower "exponential" averaging algorithm available within the network analyzer. This maximizes the number of statistical samples taken and thus the signal-to-noise level obtained. At elevated temperatures, computer operation of the MMW electronics is also important for coordinating the optimal sequence of furnace opening followed by swept measurements by prompting the operator when to activate the electric hoist.

Amplitude normalization is also more critical for elevated temperatures because slight heating of the plastic plano-convex lenses in the antennas 'sandwiching' the furnace can yield calibration spectra differing from those normally obtained at room temperature. Lens heating of only a few degrees centigrade has reduced measurement sensitivity in a prior vector free-space technique involving focussing antennas and high-intensity incadescent lamps.[7] Steps taken here to minimize lens-heating problems include the use of thin, low-density alumina sheets which are essentially transparent to MMW's while blocking the transient heat arising from the momentarily opened furnace doors. Of course, the furnace enclosure itself also provides thermal isolation.

Data reduction

For the case of reflection from and transmission through a plane sheet of dielectric material, the values of k and tanδ generally cannot be obtained from the values, respectively, of the power reflection and transmission coefficients (R^2 and T^2). Generally, the simultaneous equations for R^2 and T^2 are transcendental and must be iteratively solved for k and tanδ.[8] For tanδ <0.1, however, k can be found to a good approximation from R^2or T^2, and tanδ from k and T^2. For S-polarization, k is given by

$$k = (a/L)^2 \, (1/\delta f)^2 + p, \qquad \text{Eq.(1)}$$

where "a" is a constant, L is the specimen length, δf is taken as the frequency difference between successive peaks in T^2 (bottom, Fig. 2, Ref. 1) or nulls in R^2 (top of figure), and p is a constant depending on the angle of incidence. (The use of "δ" here as an incremental operator is not to be confused with the same symbol in the loss tangent, tan(δ).) The amplitude transmission coefficient T (0<T<1) is

$$T = A \, T_o \, / \, (B - C \, T_o^2), \qquad \text{Eq.(2)}$$

where A, B, and C are constants depending nonlinearly on k and p, and $T_o = \exp(-\alpha L)$, where the absorption coefficient $\alpha = b \, f \tan\delta$. Here, b is a constant depending on k and p as well, and f is the frequency. Some of the other assumptions implicit in the preceding equations include no dispersion in k over the measurement band and equality of L to an integral number of MMW half-wavelengths in the material represented by k and tanδ. Measured is the transmission loss TL = -20log(T). Knowing k from Eq.(1) and T from TL permits solution for tanδ from Eq.(2).

Free-space measurements

Free-space data taken on a 10-cm diameter, 2.5-cm thick disc of 96% alumina (1% MgO and 3% silica) of density 3.67 g/cm^3 yielded a dielectric constant of 9.2 and a loss tangent of 0.0032 averaged for the 10°

and 20° orientations employed between specimen normal and beam axis. As expected, this k is lower than the 9.86 found for 99.5% alumina of higher density (3.78 g/cm^3), and the tanδ value is about an order of magnitude higher,[1] not surprising in light of the 8:1 increase in impurity concentration. (This disc was sintered at Los Alamos to a temperature of 1600°C.) Data were also taken on 7.5-cm diameter, 0.635-cm (¼ inch) thick discs of 99.5% alumina (Alcoa) of density 3.90 g/cm^3. Stacked together to form a composite thickness, k was found to be 10.1 and tanδ of the order of 0.001 for the material in the 'as-is' condition. When an apparent SiC residue left on the polished faces from prior surface grinding is removed with hand grinding on a diamond wheel, the dielectric properties will be remeasured. A lower tanδ is expected.

One consequence of the advantages of the free-space approach is the relative ease of measuring weak frequency dispersion over even the relatively small band of 10 GHz (90-100 GHz) pertinent to this report, which enables some extrapolation to dielectric loss values out of band. An approximate expression was developed for relating measured quantities to δ(tanδ)/δf. The critical input quantity is the slope of TL with frequency, as defined by a 'best-fit' straight line connecting the TL peaks. A probable upper limit for δ(tanδ)/δf of 9 x 10^{-6}/GHz was found for the 96% alumina of a preceding paragraph, compared to 1.5 x 10^{-6}/GHz inferred from a linear regression analysis performed by this writer on published data on tanδ over a much larger frequency range (30-140GHz) for Coors AD-995 alumina.[9] The corresponding ratio of six is not surprising in terms of the eight times higher impurity content in the 96% version.

CONCLUSIONS

The free-space scalar network analyzer system is expected to become a valuable adjunct to the in-waveguide approach previously reported, partly for developing the latter into a more accurate room-temperature tool, partly to more realistically simulate the in situ thermal environment of fusion materials. Peak first-wall temperatures expected in an MFE reactor are at least 500-700K.[10,11] Plasma disruptions can increase these values, and rf window temperatures may also increase by window-surface metallization produced by sputtering of a first-wall alloy, then by ohmic heating by the powerful MMW beams.

FUTURE WORK

Disc ceramic specimens of adequate diameter and thickness will continue to be acquired and then measured in free space at room and also at elevated temperatures, and comparisons will be made as appropriate with in-waveguide results and, in the case of elevated temperatures, with the room temperature values.

REFERENCES

1. H. M. Frost and C. D. Kise, "In-Waveguide Measurements of MMW Dielectric Properties of Candidate Fusion Ceramics," this PROGRESS REPORT.

2. F. J. Rachford and D. W. Forester, "Characterization of Magnetic/Dielectric Materials at Millimeter-Wave Frequencies," IEEE TRANS. MAG. 19, 1883-1888 (1983).

3. H. M. Frost, "Facility for Measuring Microwave Properties of Radiation-Damaged Ceramics for RF Windows and Other Fusion Applications," pp. 29-32 in SEVENTH ANNUAL PROGRESS REPORT ON SPECIAL PURPOSE MATERIALS FOR MAGNETICALLY CONFINED FUSION REACTORS, DOE/ER-0113/4, U.S. Department of Energy, Washington, D.C., May 1985.

4. M. N. Afsar, private communication (1985).

5. H. M. Frost, "Millimeter-Wave Properties of Neutron-Irradiated Ceramics for RF-Window MFE Applications," pp. 11-16 in EIGHTH ANNUAL PROGRESS REPORT ON SPECIAL PURPOSE MATERIALS FOR MAGNETICALLY CONFINED FUSION REACTORS, DOE/ER-0113/5, U. S. Department of Energy, Washington, D.C., March 1986.

6. T. S. Benedict, "High Frequency Effects in Semiconductors," pp. 110-114 in METHODS OF EXPERIMENTAL PHYSICS, Vol. 6B: SOLID STATE PHYSICS, ed. by K. Lark-Horovitz and V. A. Johnson, Academic Press, New York, 1959.

7. D. R. Gagnon and D. J. White, " A Millimeter Wave Apparatus for Free-Space Measurement of Dielectric Constants at High Temperature," pp. 99-104 in PROCEEDINGS OF THE SEVENTEENTH SYMPOSIUM ON ELECTROMAGNETIC WINDOWS, (JULY 25-27, 1984, Georgia Institute of Technology), ed. by H. L. Bassett, Georgia Institute of Technology, Atlanta, GA, 1984.

8. J. A. Stratton, ELECTROMAGNETIC THEORY, McGraw-Hill Book Co., New York, NY, 1941, pp. 511-516.

9. W. W. Ho, "Millimeter Wave Dielectric Property Measurement of Gyrotron Window Materials," TECHNICAL REPORT FOR PERIOD JANUARY 1983 - FEBRUARY 1984 [sic], ORNL/SUB/83-51926/2, Rockwell International Science Center, Thousand Oaks, CA, April 1985.

10. C. Copenhaver, et al., "Compact Reversed-Field Pinch Reactors (CRFPR): Fusion-Power-Core Integration Study," LA-10500-MS, Los Alamos National Laboratory, August 1985, pp. 61; 77-79.

11. W. Dienst and R. Heidinger, "Ceramic Insulator Materials for RF Windows," presented at the IAEA Consultants' Meeting on Insulators for Fusion Applications, Karlsruhe, Federal Republic of Germany, June 25-27, 1986.

OPERATION OF THE U.S./JAPAN ORR SPECTRAL TAILORING EXPERIMENTS - I. I. Siman-Tov (Oak Ridge National Laboratory)

OBJECTIVE

The experiments in the U.S./Japan collaborative testing program in the ORR contain austenitic stainless steel alloys for possible use as first-wall and blanket structural materials in fusion reactors. These alloys will be irradiated with mixed-spectrum neutrons and with spectral tailoring to achieve the helium-to-displacement-per-atom (He/dpa) ratios predicted for fusion service.

SUMMARY

The ORR-MFE-6J and -7J experiments continued irradiation during this reporting period ending on September 30, 1986. The total accumulated irradiation time is 330 full power days (FPD) at 30 MW.

PROGRESS AND STATUS

The details of the U.S./Japan collaborative irradiation program have been described previously.[1-5]

ORR-MFE-6J: The experiment continued routine operation with typical temperatures ranging between 175 and 200°C in the 200°C region. The total accumulated irradiation time through September 30, 1986, is 330 FPD at 30 MW.

ORR-MFE-7J: The experiment continued routine operation with a maximum temperature of 330°C in the top region and an average of 400°C (at thermocouple No. TE5) in the bottom region. In August, the control gas mixture was changed from helium-neon to helium-argon because it became impossible to reach 400°C toward the end of a fuel cycle. The total irradiation time through September 30, 1986, is 330 FPD at 30 MW.

FUTURE WORK

Both experiments will have accumulated 5 dpa by October 1986. It has been decided to remove both capsules during the first shutdown in December 1986.

REFERENCES

1. J. A. Conlin and J. W. Woods, "Irradiation Experiments for the U.S./Japan Collaborative Testing Program in HFIR and ORR," p. 37 in ADIP Semiannu. Prog. Rep., Mar. 31, 1984, DOE/ER-0045/12, U.S. DOE, Office of Fusion Energy.

2. J. A. Conlin and J. W. Woods, "Irradiation Experiments for the U.S./Japan Collaborative Testing Program in HFIR and ORR," pp. 66-67 in ADIP Semiannu. Prog. Rep., Sept. 30, 1984, DOE/ER-0045-13, U.S. DOE, Office of Fusion Energy.

3. I. I. Siman-Tov, J. A. Conlin, and J. W. Woods, "Irradiation Experiments for the U.S./Japan Collaborative Testing Program in HFIR and ORR," p. 6 in ADIP Semiannu. Prog. Rep., Mar. 31, 1985, DOE/ER-0045/14, U.S. DOE, Office of Fusion Energy.

4. I. I. Siman-Tov, "Assembly and Operation of the U.S./Japan Spectral Tailoring Experiments," p. 41 in ADIP Semiannu. Rep. Sept. 30, 1985, DOE/ER-0045/15, U.S. DOE, Office of Fusion Energy.

5. I. I. Siman-Tov, "Operation of the U.S./Japan ORR Spectral Tailoring Experiments," p. 8 in ADIP Semiannu. Prog. Rep. Mar. 31, 1986, DOE/ER-0045/16, U.S. DOE, Office of Fusion Energy.

STATUS OF U.S./JAPAN COLLABORATIVE TESTING IN HFIR AND ORR - J. L. Scott (Oak Ridge National Laboratory) and M. P. Tanaka (Japan Atomic Energy Research Institute assigned to ORNL)

OBJECTIVE

The objective of this program is to determine the response of U.S. and Japanese austenitic stainless steels to the combined effects of displacement damage and helium generation at temperatures in the range of 65 to 600°C. Since a basic understanding is sought in addition to an engineering data base, many advanced alloys and model alloys are included in the program.

SUMMARY

All eight Phase-1 Target Capsules have completed irradiation. Postirradiation examination is nearing completion on five of the eight capsules. Construction of the Instrumented Target Capsule was completed and the experiment was installed in the High Flux Isotope Reactor (HFIR). Results of the first cycle of irradiation showed that the measured temperatures were near the predicted values except for the end region. The two Oak Ridge Research Reactor (ORR) spectral-tailoring capsules operated well throughout the reporting period. Removal of the two capsules from ORR for interim examination and reinsertion in the RB* positions in HFIR is scheduled for early FY 1987.

PROGRESS AND STATUS

The program of U.S./Japan collaborative testing in HFIR and ORR consists of eight Phase-1 HFIR target capsules to be irradiated to peak damage levels of about 30 and 50 dpa and two ORR spectrally tailored capsules to be irradiated to 30 dpa with incremental removal and testing at 5, 10, and 20 dpa. During the 5-dpa incremental testing period, the spectrally tailored capsules will be transferred to RB* positions in HFIR. As a result, the damage rate will increase from about 4 dpa per year to about 10 dpa per year. The collaborative test matrix and initial results have been described previously.[1-6]

HFIR Irradiation Experiments and Postirradiation Examination

All eight HFIR target capsules have completed irradiation; final damage levels at the reactor centerline positions are given in Table 1. More detailed information on individual specimens contained in capsules JP4, JP5, and JP8 is given in Tables 2 to 4. Capsules JP7 and JP2 were disassembled in April without incident.

Measurements of length changes and immersion densities of the tensile specimens from JP6, JP7, and JP2 are given in Table 5. With the exception of one U.S. PCA specimen in capsule JP2, measured density changes were small.

Table 1. Status of U.S./Japan High Flux Isotope Reactor (HFIR) Capsules

Capsule	Date irradiation completed	Reactor exposure[a] (MWd)	Damage level[b] (dpa)
JP1	02-01-85	33,644	33.03
JP2	12-17-85	57,507	56.55
JP3	05-28-85	34,019	33.41
JP4	04-18-86	57,909	56.94
JP5	08-12-86	58,217	57.24
JP6	11-14-85	36,677	36.05
JP7	12-17-85	34,652	34.04
JP8	09-07-86	58,214	57.24

[a]Reactor power, 100 MW.

[b]Peak displacement-per-atom (dpa) level in type J316 stainless steel (13.5 wt % Ni).

The results of tensile tests of specimens from capsules JP2, JP3, JP6, and JP7 are given in Table 6. These results have not been analyzed in detail, but total elongations of all specimens are acceptably high. Scanning-electron-microscopy (SEM) analyses of the specimens showed all fractures to be ductile.

Fatigue tests were run on many of the specimens from the JP capsules and on companion specimens from capsule HFIR-CTR-36. Measured data are given in Table 7. These data have not yet been analyzed in detail.

Transmission-electron-microscopy (TEM) disks from capsules JP6, JP7, and J2 were sorted. Twenty U.S. disks from position 2 in capsule JP6 were sent to Hanford Engineering Development Laboratory (HEDL) for reirradiation in the Materials Open Test Assembly (MOTA). These specimens, now with about 23 dpa and 1600 appm He, will be reirradiated at 520°C to about 60 and 100 dpa with little additional helium generation, so that end-point He/dpa ratios will approximate those in a fusion reactor. A listing of the disks transferred to MOTA is given in Table 8.

Table 2. Damage levels and helium contents in JP4 specimens irradiated at 55°C

Level	Specimen Type	Alloy	Condition	Identity	Nickel (at. %)	Boron (wt ppm)	Helium Content (appm)	Distance from HFIR Centerline (m)	Displacements per atom (dpa)
1	SS-1	Ref. 316	20% CW	AB-41,-42,-45	11.71	4	1647	0.227	28.14
	SS-1	EP 838	20% CW	EP-05	4.28	5	683	0.227	26.44
2	SS-1	EP 838	20% CW	EP-06,-10	4.28	5	956	0.181	36.02
	SS-1	PCA	B3	EL-0, -2	15.41	10	3004	0.181	39.62
3	SS-1	PCA	A3	EC-284	15.41	10	3640	0.136	47.82
	SS-1	PCA-20	25% CW	HV01	15.30	10	3616	0.136	47.77
	SS-1	PCA-13	25% CW	HA1	15.14	0	3570	0.136	47.71
	SS-1	PCA-19	25% CW	HT01	18.95	0	4418	0.136	49.21
4	SS-1	T9 Mod/2Ni	NT4	TB-01,-02	2.05	0	734	0.909	47.75
	SS-1	HT-9	NT1	SB-2,-3	0.40	0	323	0.909	49.02
5	SS-1	HT-9/2Ni	NT2	SD-01,-02	2.14	0	804	0.0455	50.88
	SS-1	T9 Mod	NT3	TA-01,-04	0.10	0	264	0.0455	49.92
6	TEM Strips	JPCA	PA-2	PA-2	14.81	31	4262	0	57.89
	TEM Strips	JPCA	PC-1	PC-1	14.81	31	4262	0	57.89
	TEM Strips	C	CS-1	CS-1	14.84	0	4239	0	57.91
	TEM Strips	JPCA	PC-3	PC-3	14.81	31	4262	0	57.89
	TEM Strips	K	KS-1	KS-1	16.70	0	4739	0	58.79
	TEM Strips	JPCA	PS-2	PS-2	14.81	31	4262	0	57.89
	TEM Strips	J316	SC-1	SC-1	12.81	0	3692	0	56.94
	TEM Strips	J316	SS-1	SS-1	12.81	0	3692	0	56.94
	TEM Strips	PCA	A-1	ED	15.41	10	4329	0	58.05
	TEM Strips	PCA	B-3	EL	15.41	10	4329	0	58.05
	TEM Strips	PCA-13	25% CW	HA	15.41	0	4319	0	58.05
	TEM Strips	PCA-19	25% CW	HT	18.96	0	5348	0	59.86
	TEM Strips	PCA-20	25% CW	HV	15.30	0	4363	0	58.12
	TEM Strips	PCA-22	25% CW	HX	15.11	0	4311	0	58.03
7	SS-1	J316	15% CW Weld	D-46,-47,-48	12.81	0	3625	0.0455	55.85
	SS-1	J316	SA Weld	D-16	12.81	0	3625	0.0455	55.85
8	SS-1	J316	SA Weld	D-17,-18	12.81	0	3415	0.0909	52.48
	SS-1	JPCA	SA Weld	CLW-1,-2	14.81	31	3944	0.0909	53.35
9	SS-1	JPCA	SA Weld	CLW-3	14.81	31	3528	0.136	47.58
	SS-1	JPCA	CW Weld	DLW-1,-2,-3	14.81	31	3529	0.136	47.58
10	SS-1	J316	SA	D-1,-2	12.81	0	2517	0.181	38.78
	SS-1	J316	CW	D-31,-32	12.81	0	2517	0.181	38.78
11	SS-1	JPCA	SA	CL-1,-2	14.81	31	2077	0.227	28.85
	SS-1	JPCA	CW	DL-1,-2	14.81	31	2077	0.227	28.85

Table 3. Displacements per atom and helium contents in the High Flux Isotope Reactor (HFIR) JP5 capsule[a]

Position	Distance from HFIR Centerline	Specimen			Specimen No.	Displacements per atom (dpa)	Helium Content (appm)
		Type	Temperature (°C)	Alloy			
1	23.20	Tensile	300	PCA-A3	EC34	27.91	2043
2	18.76	Tensile	400	PCA-A3	EC31	38.63	2923
3	14.31	Tensile	500	PCA-A3	EC32	47.01	3577
4	9.59	Fatigue	430	PCA-A3	EC153	53.38	4053
5	4.58	Fatigue	430	Ref. 316	AA27	55.89	3512
6	0.00	TEM[b]	400	J316	c	57.24	3708
7	4.58	Fatigue	430	JPCA	FE10	57.11	4229
8	9.59	Fatigue	430	JPCA	FE11	53.16	3950
9	14.31	Tensile	500	JPCA	TE7	46.82	3489
10	18.76	Tensile	400	JPCA	TE8	38.47	2854
11	23.20	Tensile	300	JPCA	TE9	27.80	2002

[a]MWd: 58,217. [b]Transmission-electron-microscopy.
[c]This holder contained several alloys.

Table 4. Displacements per atom and helium contents in the High Flux Isotope Reactor (HFIR) JP8 capsule[a]

Position	Distance from HFIR Centerline (cm)	Specimen			Specimen No.	Displacements per atom (dpa)	Helium Content (appm)
		Type	Temperature (°C)	Alloy			
1	23.20	Tensile	600	PCA-B3	EL26	27.91	2043
2	18.76	Tensile	600	PCA-B3	EL35	38.62	2923
3	14.31	Tensile	500	PCA-B3	EL25	47.01	3577
4	9.59	Fatigue	430	PCA-A3	EC163	53.38	4053
5	4.58	Fatigue	430	316	AA53	55.89	3512
6	0.00	TEM[b]	500	J316	c	57.24	3708
7	4.58	Tensile	600	JPCA	TE21	57.11	4229
8	9.59	Tensile	500	JPCA	TE22	53.16	3950
9	14.31	Tensile	430	JPCA	TB12	46.81	3488
10	18.76	Tensile	400	JPCA	TE23	38.47	2854
11	23.20	Tensile	300	JPCA	TE24	27.80	2001

[a]MWd: 58,214.

[b]Transmission-electron-microscopy.

[c]This holder contained several alloys.

Table 5. Length and density changes of submini tensile specimens in HFIR JP6, JP7, and JP2 capsules

Capsule	Specimen No.	Alloy	Condition[a]	Irradiation Temperature (°C)	Length, mm		Increase (%)	Density Change, %	
					Initial	Final		$3\ \Delta L/L_o$	$\Delta V/V_o$
JP6	TE12	JPCA	PC2	300	39.40	39.43	0.08	0.24	0.16
	TE11	JPCA	PC2	400	39.39	39.44	0.13	0.39	0.09
	TE10	JPCA	PC2	500	39.40	34.43	0.08	0.24	0.10
	EL24	PCA	B3	600	39.34	39.36	0.05	0.15	0.05
	AA42	316	20% CW	500	39.31	39.36	0.13	0.39	0.08
JP7	TE20	JPCA	PC2	300	39.39	39.46	0.18	0.54	0.03
	TE19	JPCA	PC2	400	39.40	39.46	0.15	0.45	0.08
	TE18	JPCA	PC2	500	39.40	39.48	0.20	0.60	0.09
	TE17	JPCA	PC2	600	39.40	39.45	0.13	0.39	0.19
	TE16	JPCA	PC2	600	39.41	39.45	0.10	0.30	0.13
	EC36	PCA	A3	600	39.35	39.41	0.15	0.45	0.02
	EL29	PCA	B3	600	39.34	39.39	0.13	0.39	0.22
	EL31	PCA	B3	500	39.34	39.40	0.15	0.45	0.22
JP2	TB6	JPCA	PS2	300	39.38	39.47	0.23	0.69	0.06
	TB5	JPCA	PS2	400	39.39	39.54	0.38	1.14	0.08
	TB4	JPCA	PS2	500	39.39	39.58	0.48	1.44	0.08
	EL36	PCA	PS2	300	39.34	39.44	0.25	0.75	0.05
	EL37	PCA	B3	400	39.34	39.39	0.13	0.39	0.13
	EL39	PCA	B3	500	39.34	39.70	0.92	2.76	2.08

[a]A3 — SA at 1100°C + 25% CW. B3 — SA at 1100°C + 8 h at 800°C + 25% CW.

PS2 — SA at 1100°C. PC2 — PS2 + 15% CW.

Table 6. Results of tensile tests for JP capsules

Capsule	Specimen No.	Alloy	Temperature, °C		Damage Level (dpa)	Strength, MPa		Elongation, %	
			Irradiation	Test		Yield	Ultimate	Uniform	Total
JP3	TB9	JPCA	300	300	15	876	889	0.39	8.6
	TB8	JPCA	400	400	22	896	910	0.44	6.0
	TB7	JPCA	500	500	27	631	724	7.2	11.7
	EL30	PCA	300	300	16	945	947	0.19	5.3
	EL34	PCA	400	500	22	931	931	0.21	3.6
	EC29	PCA	500	400	27	793	895	5.1	7.1
JP6	TE12	JPCA	300	300	16	889	903	0.63	7.2
	TE11	JPCA	400	400	23	952	972	0.42	5.5
	TE10	JPCA	500	500	28	678	765	7.1	11.4
	AA42	316	500	500	27	681	807	8.7	10.6
	EL24	PCA	600	600	16	567	643	4.2	6.0
JP7	EC36	PCA	600	600	16	585	643	3.06	3.81
	EL29	PCA	600	600	23	417	528	5.87	7.37
	EL31	PCA	500	500	28	658	756	5.45	8.40
	TE16	JPCA	600	600	34	519	582	3.68	5.18
JP2	EL36	PCA	300	300	28	933	947	0.69	4.53
	EL37	PCA	400	400	38	976	979	0.41	3.95
	EL39	PCA	500	500	46	706	769	4.4	6.57
	TB4	JPCA	500	500	46	620	682	5.76	7.79
	TB5	JPCA	400	400	38	857	871	0.55	5.69
	TB6	JPCA	300	300	27	770	789	2.43	9.93

Table 7. Results of fatigue tests

Specimen	Irradiation Capsule	Alloy	Temperature (°C)	Exposure (dpa)	Total Strain Range (%)	Number of Cycles to Failure
FE14		PCA, PC2	430	0	1.0	32,305
FE1	JP1	PCA, PC2	430	33	1.0	9,000
FE15		PCA, PC2	430	0	0.5	1,330,161
FE2	JP1	PCA, PC2	430	31	0.5	31,596
FE36		PCA, PC2	430	0	2.0	7,904
FE5	JP3	PCA, PC2	430	33	2.0	594
FE12	JP6	JPCA	430	34	0.35	657,179
EF5	JP7	PCA B2	550	34	1.0	6,129
EF20		PCA B2	550	0	1.0	37,015
EF2	HFIR-CTR-36	PCA B2	550	30	0.5	65,453
EF7		PCA B2	550	0	0.5	344,077
EC145	HFIR-CTR-36	PCA, A3	550	30	1.0	4,270
EC149	HFIR-CTR-36	PCA, A3	550	30	0.5	120,006
EC155		PCA, A3	550	0	1.0	24,443
AA5	HFIR-CTR-36	316	550	30	0.5	61,748
AA54	JP7	316	550	30	1.0	7,030
AA3	JP2	316	430	55	1.0	4,323

Table 8. Transmission-Electron-Microscopy (TEM) Disks from Capsule JP6 to be Irradiated in the Materials Open Test Assembly (MOTA)

Disk No.	Alloy	Identification
41	PCA B3	EL84
42	DO 316 CW	AL72
43	EP 838	EP52
44	CW PCA1	FC40
45	CW PCA3	FG99
46	CW PCA6	FN85
47	CW PCA8	FS77
48	CW PCA9	FV98
49	CW PCA00	HH04
50	CW PCA10	FX76
51	CW PCA11	FY69
52	CW PCA12	FZ40
53	CW PCA13	HA66
54	CW PCA16	HD80
55	CW PCA17	HE67
56	CW PCA18	HF60
57	CW PCA19	HT13
58	CW PCA20	HV25
59	CW PCA21	HW38
60	CW PCA22	HX04
61	CW D9 J697	GH12

Results of microstructural analysis of specimens from the JP capsules are reported by M. P. Tanaka and P. J. Maziasz in other sections of this report.

HFIR Temperature Experiment

An important task in the overall U.S./Japan collaboration is the measurement of temperatures of specimens in HFIR target capsules. During the present reporting period, the capsule assembly was completed and the capsule was inserted in HFIR on August 15. All 21 thermocouples were operational and the measured temperatures were generally within 15% of the predicted temperatures in all but the top region. The details of the experiment are reported in the section of this report by I. I. Siman-Tov. It is planned to irradiate the capsule for multiple cycles to determine the reproducibility of the HFIR target region.

Spectral-Tailoring Experiments

The two ORR spectral-tailoring experiments, ORR-MFE-6J and ORR-MFE-7J, operated satisfactorily at the design temperatures of 60, 200, 330, and 400°C throughout the reporting period. As of September 30, 1986, the specimens accumulated a total of 330 full power days at 30-MW reactor power. This is equivalent to approximately 5 dpa. During FY 1987 an interim examination will be performed on selected specimens from these capsules. The specimens will then be re-encapsulated into RB* capsules and irradiated in HFIR to 10 dpa and beyond. Details of the spectral-tailoring capsules are given in another section of this report authored by I. I. Siman-Tov.

CONCLUSIONS

The U.S./Japan Collaborative Program of Testing of First Wall and Blanket Structural Materials with Mixed Spectrum Fission Reactors is proceeding very well. Data are being obtained on the changes in mechanical properties and microstructural evolution at high dpa levels and with high helium contents. Detailed analyses of the data will be made when testing has been completed.

FUTURE WORK

Preparations are being made for eight Phase-2 HFIR target capsules. In the United States the primary interest is in experiments which explore the performance of materials exposed to high levels of displacement damage combined with fusion levels of helium. By varying the concentrations of the isotopes ^{60}Ni, ^{59}Ni, and ^{58}Ni, helium-generation rates can be adjusted to any desired value in austenitic and ferritic steels. This technique is restricted to small (30-g) experimental heats and TEM disk specimens in the case of austenitic steels. In ferritic steels heats up to 1 kg and the use of miniature tensile specimens and creep tubes are possible. The United States will utilize the Phase-2 capsules primarily for isotopic-tailoring experiments and mechanical-property measurements on ferritic steels.

On the Japanese side there is a strong need to add to the extensive data base obtained from the Phase-1 capsules, especially for welded structures. Fusion reactor blankets necessarily must be welded and the interactions among the weld metal, the heat-affected zone, and the matrix are unknown. There is special concern about welded cold-worked structures, since the weld metal itself would be expected to swell quite differently from the base metal. For the studies of interest to the Japanese, irradiation data at 30 and 50 dpa are most important.

Since the objectives of the two sides are different, it was not desirable to have equal numbers and types of specimens as in Phase 1. There is a desire, however, to have equally shared costs. The method selected for equal sharing was to have unequal numbers of capsules and numbers of specimens per capsule for the two sides. Those capsules being irradiated to 30 and 50 dpa will contain mostly Japanese specimens and those being irradiated to 100 dpa will contain mostly U.S. specimens. In addition, credit is given for the cosine distribution of neutron flux along the length of a capsule. That is, the end positions are less expensive than the center ones. Using the above constraints we developed the test plan shown in Table 9. The kinds of specimens to be tested are shown in Table 10. Detailed planning of the experiments will be done in early FY 1987.

Table 9. U. S./Japan Phase-2 High Flux Isotope Reactor Test Matrix

Capsule	dpa	Space Allocation		Cost (Thousands of Dollars)[a]		
				Build	Irradiate	Test
JP9	100	J	1.5	30	500	100
		U.S.	9.5			
JP10	33	J	10.5	30	170	160
		U.S.	0.5			
JP11	33	J	10.5	30	170	160
		U.S.	0.5			
JP12	100	J	1.5	30	500	100
		U.S.	9.5			
JP13	33	J	10.5	30	170	120
		U.S.	0.5			
JP14	55	J	10.5	30	280	160
		U.S.	0.5			
JP15	100	J	1.5	30	500	100
		U.S.	9.5			
JP16	33	J	10.5	30	170	120
		U.S.	0.5			

[a]Fiscal year 1986 dollars.

REFERENCES

1. A. F. Rowcliffe, M. L. Grossbeck, and S. Jitsukawa, "The U.S./Japan Collaborative Testing Program in HFIR and ORR: Irradiation Matrices for HFIR Irradiation," pp. 38–43 in ADIP Semiannu. Prog. Rep. Mar. 31, 1984, DOE/ER-0045/12, U.S. DOE, Office of Fusion Energy.

2. A. F. Rowcliffe, M. L. Grossbeck, M. Tanaka, and S. Jitsukawa, "The U.S./Japan Collaborative Testing Program in HFIR and ORR: Specimen Matrices for HFIR Irradiation," pp. 61–62 in ADIP Semiannu. Prog. Rep. Sept. 30, 1984, DOE/ER-0045/13, U.S. DOE, Office of Fusion Energy.

3. J. L. Scott and M. P. Tanaka, "Preparation for Postirradiation Examination of U.S./Japan HFIR Capsules," pp. 10–11 in ADIP Semiannu. Prog. Rep., March 31, 1985, DOE/ER-0045/14, U.S. DOE, Office of Fusion Energy.

4. J. L. Scott, M. L. Grossbeck, and M. P. Tanaka, "Phase I HFIR Capsules — Irradiation and Post-irradiation Examination," pp. 18–21 in ADIP Semiannu. Prog. Rep., Sept. 30, 1985, DOE/ER-0045/15, U.S. DOE, Office of Fusion Energy.

5. J. L. Scott et al., "Description of the U.S./Japan Spectral-Tailoring Experiment in ORR," pp. 22–40 in ADIP Semiannu. Prog. Rep. Sept. 30, 1985, DOE/ER-0045/15, U.S. DOE, Office of Fusion Energy.

6. J. L. Scott and M. P. Tanaka, "Status of U.S./Japan Collaborative Testing in HFIR and ORR," pp. 4–7 in ADIP Semiannu. Prog. Rep. Mar. 31, 1986, DOE/ER-0045/16, U.S. DOE, Office of Fusion Energy.

Table 10. Detailed Test Matrix for Phase-2 HFIR Capsules

Position	U.S. JP9 (100 dpa)	J JP10 (33 dpa)	J JP11 (33 dpa)	U.S. JP12 (100 dpa)	J JP13 (33 dpa)	J JP14 (55 dpa)	U.S. JP15 (100 dpa)	J JP16 (33 dpa)
1	500°C 316, PCA TEM	500°C 316 TIG T	600°C 316 EB T	400°C 316, PCA TEM	500°C 316 EB T	600°C Mo, V TEM	300°C 316, PCA TEM	500°C PCA, TIG T
2	300°C HT-9 T(B)	400°C 316 TIG T	500°C 316 EB T	300°C 9Cr T(B)	400°C 316 EB T	500°C Mo, V TEM	300°C 2.25 Cr T(B)	400°C PCA TIG T
3	400°C HT-9 T(B)	430°C 316 EB F	430°C 316 EB F	400°C 9Cr T(B)	430°C 316 EB F	500°C Sheet	400°C 2.25Cr T(B)	430°C 316 EB T(B)
4	500°C HT-9 T(B)	300°C 316 EB T	400°C 316 EB T	500°C 9Cr T(B)	400°C PCA CW T	400°C 316 EB T	500°C 2.25Cr T(B)	300°C PCA EB T
5	500°C HT-9 T(B)	400°C 316 EB T	500°C 316 EB T	500°C 9Cr T(B)	400°C 316 PCA T	400°C PCA EB T	500°C 2.25Cr T(B)	400°C PCA EB T
6	500°C TEM	400°C TEM	500°C TEM	400°C TEM	500°C TEM	500°C TEM	300°C TEM	500°C TEM
7	500°C HT-9 T(B)	400°C 316 EB TEM	500°C 316 EB TEM	500°C 9Cr T(B)	500°C 316 EB T	500°C PCA EB T	500°C 2.25 Cr T(B)	500°C PCA EB T
8	500°C HT-9 T(B)	300°C 316 EB TEM	400°C PCA TEM	400°C 9Cr T(B)	500°C PCA CW T	500°C 316 EB T	400°C 2.25Cr T(B)	400°C 316 EB CW T
9	400°C HT-9 T(B)	430°C 316 EB F	430°C 316 EB F	400°C 9Cr T(B)	430°C 316 EB F	500°C Ferrite TEM	400°C 2.25Cr T(B)	430°C 316 EB T(B)
10	300°C HT-9 T(B)	400°C Ferrite TEM	500°C Mo, V TEM	300°C 9Cr T(B)	500°C 316 CW T	400°C Ferrite TEM	300°C 2.25Cr T(B)	500°C PCA EB T
11	300°C HT-9 T(B)	500°C Ferrite TEM	600°C 316 PCA TEM	300°C 9Cr T(B)	400°C PCA EB T	300°C Mo, V TEM	300°C 2.25Cr T(B)	600°C PCA EB T

Legend:
U.S.: United States.
J: Japan.
316: 316 stainless steel.
PCA: Prime candidate alloy.
TIG: Tungsten inert-gas welding.
EB: Electron beam welding.
T: Tensile.
T(B): Tensile (bar).
F: Hourglass fatigue.
CW: Cold worked.

FUSION PROGRAM RESEARCH MATERIALS INVENTORY — T. K. Roche (Oak Ridge National Laboratory) and J. W. Davis (McDonnell Douglas Astronautics Company — St. Louis Division)

OBJECTIVE

Oak Ridge National Laboratory maintains a central inventory of research materials to provide a common supply of materials for the Fusion Reactor Materials program. This minimizes unintended material variations and provides for economy in procurement and for centralized record-keeping. Initially, this inventory is to focus on materials related to first-wall and structural applications and related research, but various special-purpose materials may be added in the future.

The use of materials from this inventory that is coordinated with or otherwise related technically to the Fusion Reactor Materials program of the Department of Energy is encouraged.

PROGRESS AND STATUS

Materials requests shall be directed to the Fusion Program Research Materials Inventory at ORNL (Attention: T. K. Roche). Materials will be released directly if (a) the material is to be used for programs funded by the Office of Fusion Energy, with goals consistent with the approved Materials Program Plans of the Materials and Radiation Effects Branch, and (b) the requested amount of material is available without compromising other intended uses.

Materials requests that do not satisfy both (a) and (b) will be discussed with the staff of the Reactor Technologies Branch, Office of Fusion Energy, for agreement on action.

Records

Chemistry and materials preparation records are maintained for all inventory materials. All materials supplied to program users will be accompanied by summary characterization information.

Summary of Current Inventory and Material Movement During Period April 1, 1986, through September 30, 1986

A condensed, qualitative description of the content of materials in the Fusion Program Research Materials Inventory is given in Table 1. This table indicates the nominal diameter of rod or thickness of sheet for product forms of each alloy and also indicates by weight the amount of each alloy in larger sizes available for fabrication to produce other product forms as needed by the program. No material was added to the inventory during this reporting period. Table 2 gives the materials distributed from the Inventory.

Alloy compositions and more detail on the alloys and their procurement and/or fabrication are given in this and earlier ADIP progress reports.

Table 1. Summary status of materials available in the Fusion Program Research Materials Inventory

Alloy	Product Form: Ingot or bar[a] weight (kg)	Rod diameter (mm)	Thickness, mm: Sheet	Thickness, mm: Thin-wall tubing wall
Path A Alloys				
Type 316 SS	900	16, 7.2	13, 7.9	0.25
Path A PCA[b]	490	12	13	0.25
USSR Cr-Mn steel[c]		10.5	2.6	
NONMAGNE 30[d]		18.5	10	
Path B Alloys				
PE-16	140	16, 7.1	13, 1.6	0.25
B-1	180			
B-2	180			
B-3	180			
B-4	180			
B-6	180			
Path C Alloys				
Ti-64			2.5, 0.76	
Ti-6242S		63	6.3, 3.2, 0.76	
Ti-5621S			2.5, 0.76	
Ti-38644			0.76, 0.25	
Nb–1%Zr		6.3	2.5, 1.5, 0.76	
Nb–5%Mo–1%Zr		6.3	2.5, 1.5, 0.76	
V–20%Ti		6.3	2.5, 1.5, 0.76	
V–15%Cr–5%Ti		6.3	2.5, 1.5, 0.76	
VANSTAR-7		6.3	2.5, 1.5, 0.76	

Table 1 (contd.)

Alloy	Product Form: Ingot or bar[a] weight (kg)	Rod diameter (mm)	Thickness, mm: Sheet	Thickness, mm: Thin-wall tubing wall
Path D Alloys				
LRO-37[e]			3.3, 1.6, 0.8	

Path E Alloys

Alloy	Ingot or bar[a] weight (kg)	Rod diameter (mm)	Thickness, mm: Sheet	Thickness, mm: Thin-wall tubing wall thickness
HT9 (AOD fusion heat)[f]	3400		28.5, 15.8, 9.5, 3.1	
HT9 (AOD/ESR fusion heat)	7000	25, 50, 75	28.5, 15.8, 9.5, 3.1	
HT9			3.1	
HT9 + 1% Ni			4.5, 18	
HT9 + 2% Ni			4.5, 18	
HT9 + 2% Ni + Cr adjusted			4.5, 18	
T-9 modified[g]			4.5, 18	
T-9 modified + 2% Ni			4.5, 18	
T-9 modified + 2% Ni + Cr adjusted			4.5, 18	
2.25Cr-1Mo			[h]	

[a]Greater than 25 mm, minimum dimension.

[b]Prime candidate alloy.

[c]Rod and sheet of a USSR stainless steel supplied under the U.S./USSR Fusion Reactor Materials Exchange Program.

[d]NONMAGNE 30 is an austenitic steel with base composition Fe–14%Mn–2%Ni–2%Cr. It was supplied to the inventory by the Japanese Atomic Energy Research Institute.

[e]LRO-37 is the ordered alloy $(Fe,Ni)_3(V,Ti)$ with composition Fe–39.4%Ni–22.4%V–0.43%Ti.

[f]Alloy 12Cr-1MoVW with composition equivalent to Sandvik alloy HT9.

[g]T-9 modified is the alloy 9Cr-1MoVNb.

[h]Material is thick-wall pipe, rerolled as necessary to produce sheet or rod.

Table 2. Fusion Program Research Materials Inventory Disbursements
April 1, 1986, through September 30, 1986

Alloy	Heat	Product form	Dimension[a] (mm)	Quantity (m^2)	Sent to
Path C Alloys — Reactive and Refractory Alloys					
V–15%Cr–5%Ti	CAM835A	Sheet	1.52	0.008	Radiation Effects Group, M&C Division, ORNL

[a]Characteristic dimensions: Thickness for plate and sheet, diameter for rod and tubing.

IRRADIATION OF Fe-Cr-Ni AUSTENITIC ALLOYS AT 400-750°C IN THE MOTA-1E EXPERIMENT - F. A. Garner (Westinghouse Hanford Company)

OBJECTIVE

The object of this effort is to provide irradiated specimens for the exploration of the compositional dependence of microstructural evolution, particularly that of the spinodal-like decomposition and various order-disorder transformations observed after irradiation of austenitic Fe-Ni-Cr alloys with high nickel levels.

SUMMARY

Seven nominally identical packets, each with 79 TEM disks prepared from 29 Fe-Cr-Ni alloys have been inserted into the MOTA-1E experiment for irradiation in Cycle 9 of FFTF. Two packets each have been included in each of the 420, 520 and 600°C canisters, one each to be withdrawn after Cycles 9 and 10. One additional packet has been included in the 750°C canister.

PROGRESS AND STATUS

Introduction

Recently a correlation has been found between the void swelling of Fe-Cr-Ni austenitic alloys at high nickel levels and a spinodal-like decomposition that develops during irradiation.[1-4] The spinodal-like process in the Invar regime (30-45% Ni) produces at high irradiation temperatures relatively large volumes with reduced nickel and increased chromium levels, both conditions known to favor void nucleation. There is some hope that swelling could be delayed in this alloy system if the onset of the decomposition process could be delayed by compositional or thermal-mechanical modification. It also appears that the onset of long or short range ordering might also delay swelling, particularly at nickel levels in the 50-75% range.

Each of the insights cited above were developed from examination of specimens which were originally prepared and irradiated for some other purpose. Frequently the available specimens exist only as single TEM disks which were not always ideally suited to maximize the microstructural record of the various processes of current interest.

In this experiment the alloys of interest exist as multiple specimens (3 to 4 disks in each disk packet) which will allow the parallel examination by more than one method of each alloy condition and set of irradiation conditions. Some of the examination methods under consideration include destructive techniques such as electron microscopy and martensitic transformations induced by freezing, as well as non-destructive techniques such as small angle neutron scattering and perturbed angular correlation analysis.

The major variables under consideration are the influence of nickel (30-75 wt.%) and chromium (0-15%), cold-working (0 and 40%), and neutron fluence. The latter is being studied via the use of two reactor cycles (9 and 10) with reincapsulation of some specimens for higher fluence if such appears to be desirable based on the results of the lower fluence experiments. Temperature is also a variable, with two capsules included in each of the 420, 520 and 600°C levels. These are considered to be fusion-relevant temperatures.

There are several reasons to explore temperatures in excess of that anticipated in fusion devices, however. First, analysis of 5 MeV Ni^+ ion-induced decomposition of Fe-35Ni has shown that the spinodal-like process occurs in the range 625-725°C.[2,4] (No data are available at higher temperatures). This decomposition is signaled by the formation of cellular martensite in the nickel-poor regions upon cooling. This fortuitous formation allows a visualization of the compositional fluctuations, but the observation is complicated at the higher temperatures by a local loss of nickel, which migrates down the point defect gradients produced by the bombarding ion. This also predisposes the alloy to form martensite in the nickel depleted region. It would be best to explore the spinodal-like decomposition in the absence of displacement gradients, however, using neutron irradiation of bulk specimens at comparable temperatures.

Second, it would also be advantageous to explore the decomposition at even higher temperatures in order to determine whether the spinodal-like process persists to the 900-1000°C level proposed by Tanji and coworkers to develop in Invar alloys in the absence of radiation.[5] The knowledge gained at these higher temperatures would assist in the modeling of this phenomena and impact the choice of metallurgical techniques proposed to delay the onset of decomposition. Since there was only space for one disk packet available in the 750°C canister of MOTA-1E, only one dose level can be attained in the first phase of this experiment. No higher temperatures are currently available but the opportunity for temperatures above 750°C may arise in MOTA-1F.

Experimental details

Table 1 lists the annealed (1040°C, 1 hr, air cool) alloys included in this experiment and Table 2 contains a description of the smaller number of alloys which have 40% cold-work.

Table 1. Annealed alloys included in MOTA-1E packets 3A, 3B, 3E 3F, 3H, 3K and 3L

Alloy Code*	Composition	Alloy Code*	Composition
R-59 (4V)	Fe-30Ni	R-4 (BR)	Fe-45Ni-7.5Cr
G-22 (BA)	Fe-30Ni-7Cr	G-11 (BT)	Fe-45Ni-15Cr
E-21 (3T)	Fe-30Ni-15Cr	R-63 (41)	Fe-50Ni
G-5 (BB)	Fe-35Ni	R-9 (BU)	Fe-50Ni-5Cr
R-8 (BE)	Fe-35Ni-5Cr	R-3 (BV)	Fe-50Ni-11Cr
G-6 (3U)	Fe-35Ni-7Cr	R-10 (BX)	Fe-55Ni-7.5Cr
E-37 (4U)	Fe-35Ni-7.5Cr	G-26 (3V)	Fe-60Ni
R-7 (BK)	Fe-35Ni-11Cr	R-11 (30)	Fe-60Ni-5Cr
G-7 (BL)	Fe-35Ni-15Cr	R-12 (29)	Fe-60Ni-11Cr
R-61 (4X)	Fe-40Ni	G-13 (3X)	Fe-60Ni-15Cr
R-6 (BM)	Fe-40Ni-5Cr	R-13 (3R)	Fe-65Ni-75Cr
R-14 (BN)	Fe-40Ni-7.5Cr	G-29 (3Z)	Fe-75Ni
R-5 (BO)	Fe-40Ni-11Cr	G-71 (31)	Fe-75Ni-7Cr
R-62 (4Z)	Fe-45Ni	G-14 (33)	Fe-75Ni-15Cr

*The first number is the alloy code specifying the composition. The number in the parentheses is the specimen identifier engraved on the disk and specifies both the composition and heat treatment.

Table 2. Cold-worked alloys included in MOTA-1E

Alloy Code	Composition
G-5 (43)	Fe-35Ni
E-37 (44)	Fe-35Ni-7.5Cr
R-61 (Blank)*	Fe-40Ni
R-62 (Blank)*	Fe-45Ni

*R-61 was placed only in packets 3A (420°C), 3B (520°C), 3E (600°C), and 3L (750°C). R-62 was included only in packets 3F (420°C), 3H (520°C) and 3K (600°C). The other two alloys were included in all seven packets.

FUTURE WORK

Examination of specimens irradiated earlier in EBR-II as well as in MOTA-1B and 1C are in progress to determine whether solute modification affects the development of spinodal-like decomposition. If such an approach appears to be feasible, additional specimens will be prepared for insertion in MOTA-1F.

REFERENCES

1. H. R. Brager and F. A. Garner, p. 141 in Optimizing Materials For Nuclear Applications, F. A. Garner, D. S. Gelles and F. W. Wiffin, Eds.; TMS-AIME, Warrendale, PA, (1985).

2. F. A. Garner, H. R. Brager, R. A. Dodd and T. Lauritzen, Nuclear Instruments and Methods in Physics Research, B16, 244 (1986).

3. F. A. Garner, H. R. Brager and J. M. McCarthy, to be published in the Proceedings of the 13th International Symposium on Effects of Radiation on Materials, Seattle, WA, June 23-25, 1986.

4. R. A. Dodd, F. A. Garner, J.-J. Kai, T. Lauritzen and W. G. Johnston, ibid.

5. Y. Tanji, Y. Nakagawa, Y. Saito, K. Nishimura and K. Nakatsuka, Phys. Stat. Sol. A, 513 (1979).

2. DOSIMETRY, DAMAGE PARAMETERS AND ACTIVATION CALCULATIONS

PRODUCTION OF LONG-LIVED ACTIVITIES IN FUSION REACTORS - L. R. Greenwood and D. L. Bowers (Argonne National Laboratory)

OBJECTIVE

To measure 14 MeV neutron production rates of long-lived isotopes in fusion materials for waste disposal, maintenance, and dosimetry applications.

SUMMARY

Experiments are in progress to measure the 14 MeV production rates of several long-lived radioisotopes in fusion materials. Samples of separated isotopes of ^{56}Fe, ^{60}Ni, ^{64}Ni, and ^{94}Zr were irradiated at the RTNS II in July. Radio-chemical separations, liquid scintillation counting, and gamma spectroscopy have successfully been used to measure cross sections for the $^{56}Fe(n,2n)^{55}Fe$, $^{60}Ni(n,2n)^{59}Ni$, $^{64}Ni(n,2n)^{63}Ni$, and $^{63}Cu(n,p)^{63}Ni$ reactions.

PROGRESS AND STATUS

The production of long-lived radionuclides is of concern in the waste disposal of fusion materials. Unfortunately, the production cross sections are generally not well-known for many of the isotopes of interest. Consequently, we have initiated an effort to measure selected reactions near 14 MeV using long irradiations at the Rotating Target Neutron Source (RTNS II) at Lawrence Livermore National Laboratory. Previously we have reported on measurements of the $^{27}Al(n,2n)^{26}Al$ ($7.2x10^5y$)[1], $^{54}Fe(n,2n)^{53}Fe(_2)^{53}Mn$[2] ($3.7x10^6y$), $^{94}Mo(n,p)^{94}Nb$ ($2.03x10^4y$), and $^{92}Mo(n,x)^{91}Nb$ (700y)[3] reactions.

New irradiations were conducted at the RTNS II on July 7-12, 1986. This was a joint experiment with D. Kneff (Rockwell International) who is measuring helium production in numerous isotopes at 14 MeV. By combining radiometric dosimetry and helium spectrometry we are able to determine helium production cross sections. Data for 26 elements, 22 separated isotopes, and 3 alloys were recently published.[4]

In order to study long-lived isotopes we irradiated separated isotopes of ^{56}Fe, ^{60}Ni, ^{64}Ni, ^{94}Zr, and TiN along with numerous dosimetry samples to determine the neutron fluence. The dosimetry measurements will be used to construct a neutron fluence map near the RTNS II target so that the fluence can be determined at the location of each specimen.

The reactions which we plan to study include $^{14}N(n,p)^{14}C(5700y)$, $^{56}Fe(n,2n)^{55}Fe(2.7y)$, $^{64}Ni(n,2n)^{63}Ni(100y)$, $^{60}Ni(n,2n)^{59}Ni(7.6x10^4y)$, and $^{94}Zr(n,2n)^{93}Zr(1.5x10^6y)$. Samples from previous RTNS II irradiations will also be analyzed for $^{63}Cu(n,p)^{63}Ni(100y)$, $^{94}Mo(n,2n)^{93}Mo(3500y)$, and $^{93}Nb(n,n')^{93m}Nb(13.6y)$. Many of these products can be detected by liquid scintillation counting. All of the samples contain other isotopes which could interfere with the counting of the desired products. However, most of these can be readily separated by ion exchange. Our new liquid scintillation counter has spectral analysis capabilities so that we can compare the energy spectrum to standard spectra of the same or similar isotope. Further, we can gamma count samples from each phase of the separation to check for the presence of unwanted isotopes.

Preliminary results look very encouraging for several of the reactions. Analysis of several samples for each reaction gives consistent cross sections near 14.8 MeV of about 440 mb for $^{56}Fe(n,2n)^{55}Fe$, 54 mb for $^{63}Cu(n,p)^{63}Ni$, and 950 mb for $^{64}Ni(n,2n)^{63}Ni$. These production rates can be used to determine the residual activities in various fusion reactor designs such as STARFIRE or MARS.

FUTURE WORK

Analyses of other reactions is in progress. For the longest-lived products we plan to use the relatively new technique of accelerator mass spectrometry at the Argonne ATLAS facility.

REFERENCES

1. R. K. Smither and L. R. Greenwood, Jour. Nucl. Mater. 122, 1071-1077 (1984).

2. R. K. Smither and L. R. Greenwood, Damage Analysis and Fundamental Studies Quarterly Progress Report, DOE/ER-0046/17, May 1984.

3. L. R. Greenwood, D. G. Doran, and H. L. Heinisch, Production of ^{94}Nb, ^{94}Nb, and ^{95}Nb from Mo by 14.5-14.8 MeV Neutrons, to be published in Phys. Rev. C.

4. D. W. Kneff, B. M. Oliver, H. Farrar, and L. R. Greenwood, Nucl. Sci. Eng. 92, 491-524 (1986).

NEUTRONICS ANALYSIS IN SUPPORT OF THE U.S.-JAPAN SPECTRAL TAILORING CAPSULES — R. A. Lillie (Oak Ridge National Laboratory)

OBJECTIVE

The objective of this work is to provide the neutronic design for materials irradiation experiments in both the Oak Ridge Research Reactor (ORR) and High Flux Isotope Reactor (HFIR). Spectral tailoring to control the fast and thermal fluxes is required to provide the desired displacement and helium production rates in alloys containing nickel.

SUMMARY

The neutron fluxes for the ORR-MFE-6J dosimetry capsule have been recalculated and compared with the previously[1] measured fluxes. Scale factors obtained from this new comparison are being used to scale the neutron fluences obtained from three-dimensional neutronics calculations. As of September 30, 1986, this procedure yields 32.6 appm He (not including 2.0 appm He from ^{10}B) and 4.79 dpa for type 316 stainless steel in ORR-MFE-6J and 56.5 appm He and 5.32 dpa in ORR-MFE-7J.

PROGRESS AND STATUS

A comparison of the measured and calculated fluxes for the ORR-MFE-6J dosimetry capsule is presented in Table 1. The neutron fluxes were recalculated because an increase in flux levels between the ORR-MFE-6J dosimetry capsule and the currently operating experimental capsule was predicted by the neutronics calculations, whereas gamma heating data did not indicate any increase in flux levels between the two capsules. The increase in flux levels between the old and new calculations is due to the use of an improved geometric model of the hafnium shield employed in the ORR-MFE-4A and -4B capsules. The improved model caused a shift in reactor power from the fuel positions surrounding the ORR-MFE-4A and -4B capsules to the fuel positions surrounding the ORR-MFE-6J capsule, which in turn caused an increase in the calculated flux in the 6J dosimetry capsule. The end result of these new calculations is that the thermal and total fluxes obtained from the ongoing neutronics calculations will be reduced by approximately 7.4 and 22.5%, respectively, whereas the previous comparison predicted corresponding reductions of only 2.0 and 13.8%.

Table 1. Comparison of measured and calculated data for the ORR-MFE-6J dosimetry capsule

	Measured[a] Flux ($n/m^2/s$)	Calculated, $n/m^2/s$			
		Old	C/E	New	C/E
E > 0.1 MeV	2.03 + 18[b]	2.40 + 18	1.18	2.76 + 18	1.36
Total	5.99 + 18	6.93 + 18	1.16	7.73 + 18	1.29
Thermal	1.97 + 18	2.01 + 18	1.02	2.13 + 18	1.08

[a]See ref. 1.

[b]2.03 + 18, read as 2.03×10^{18}.

In addition to recalculating the fluxes in the ORR-MFE-6J dosimetry capsules, fluxes for the ORR-MFE-6J and -7J experimental capsules were recalculated for a number of ORR cycles. These new calculations were performed using a slightly different representation of the radioisotope production capsules since many of the ORR cycles containing the ORR-MFE-6J and -7J capsules also contained up to six of the radioisotope capsules. Average total and thermal flux reductions of 3 and 5%, respectively, were obtained for the ORR-MFE-6J capsule. For the ORR-MFE-7J capsule, the new calculations resulted in a 6% decrease in the average total flux and an 8% increase in the average thermal flux. After applying the new scaling factors to the new fluxes obtained from the ongoing neutronics calculations, the calculated average total fluxes in the ORR-MFE-6J and -7J experimental capsules are approximately 1% lower and 17% higher, respectively, than the fluxes measured in the ORR-MFE-6J dosimetry capsule.

The operating and current calculated data based on the new scaling factors are summarized in Table 2 for the ORR-MFE-6J and -7J experiments. Both experimental capsules have been exposed to 236,924.1 MWh as of September 30, 1986. At the present time, the dpa rate based on the scaled total fluences is 5.32 and 5.91 dpa per full power year for the ORR-MFE-6J and -7J experiments, respectively. Because the ORR-MFE-7J experiment is similar to the ORR-MFE-4A and -4B experiments (i.e., it contains more water in its aluminum corepiece), the thermal fluence in the ORR-MFE-7J experiment is approximately 38% greater than the thermal fluence in the ORR-MFE-6J experiment.

The real-time projections of the helium-to-displacement ratios based on current calculated data as of September 30, 1986, are presented in Figs. 1 and 2 for the ORR-MFE-6J and -7J experiments, respectively. The projected dates were obtained assuming an ORR duty factor of 0.86. The solid aluminum corepiece should be inserted in the ORR-MFE-6J experiment on or before September 30, 1987. Because of the increased thermal fluence in the ORR-MFE-7J experiment, its solid aluminum corepiece should be inserted on or before October 28, 1986.

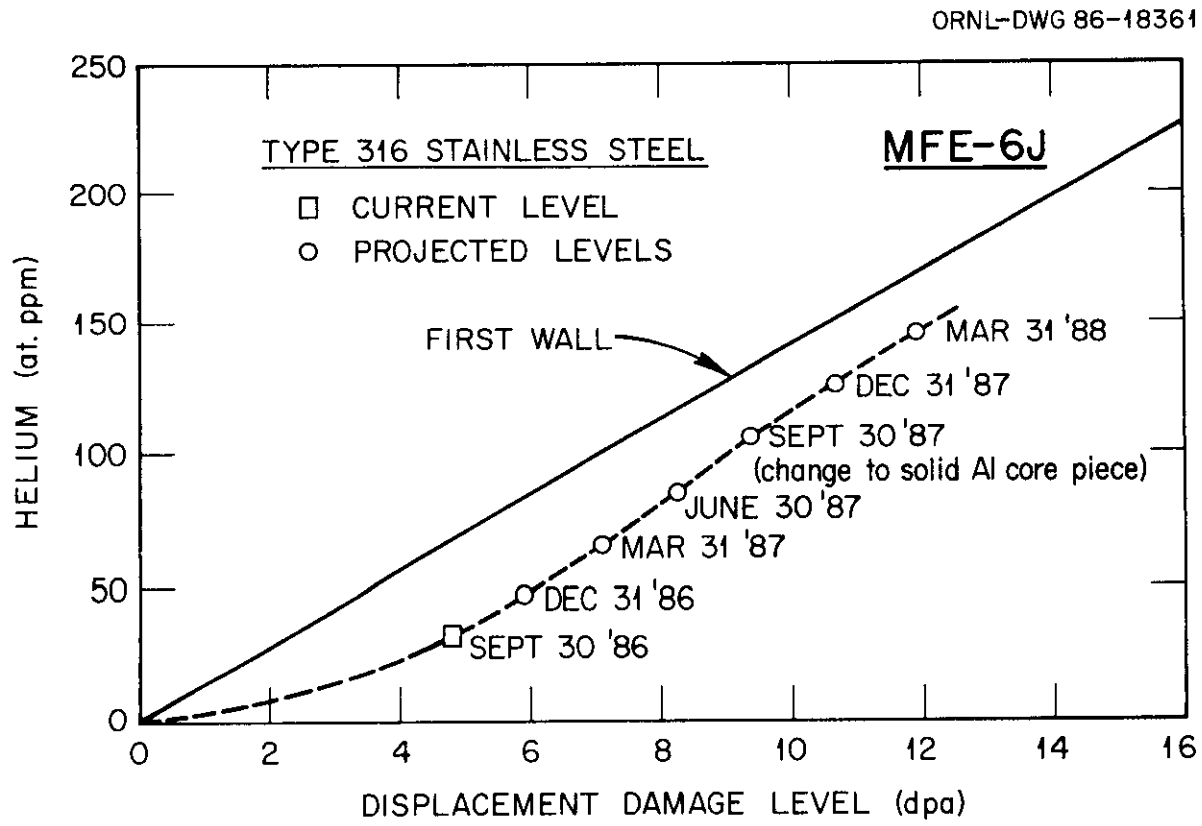

Fig. 1. Current and projected helium and displacement damage levels in the ORR-MFE-6J experiment.

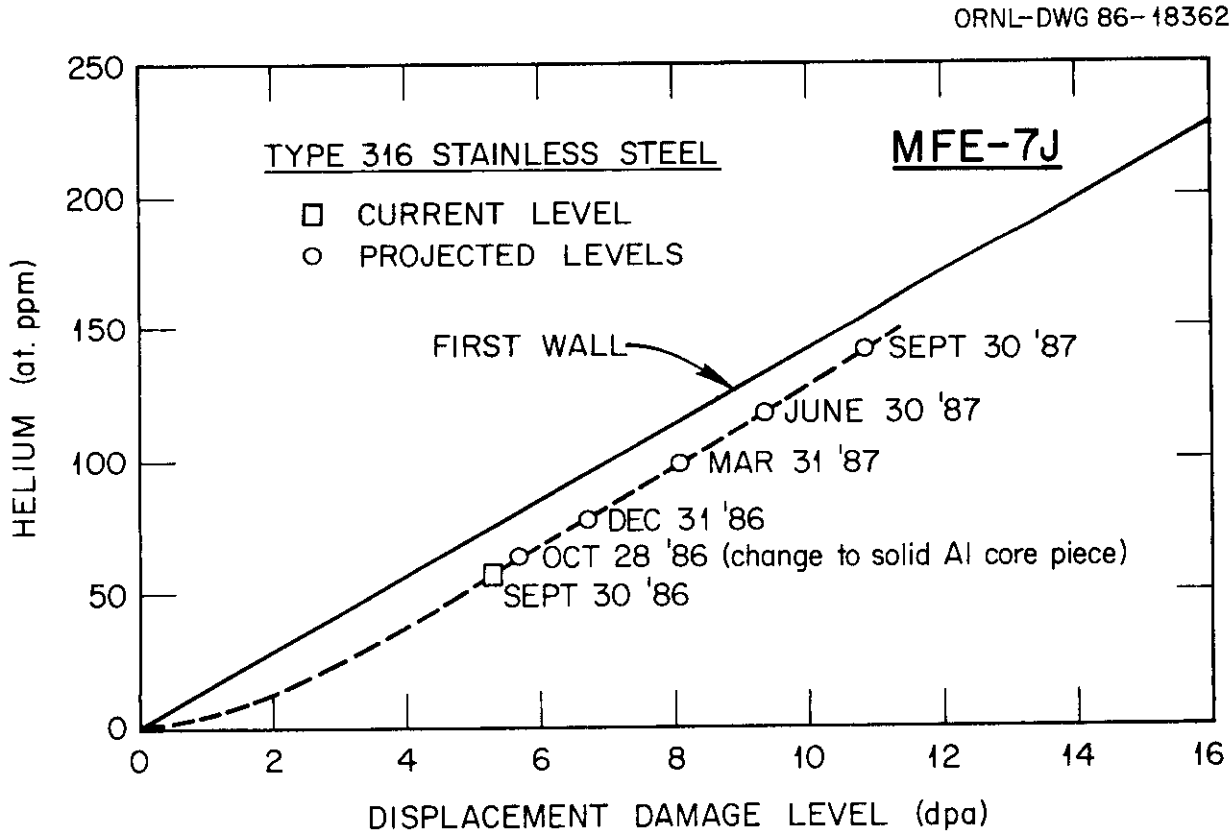

Fig. 2. Current and projected helium and displacement damage levels in the ORR-MFE-7J experiment.

Table 2. Operating and calculated data for the ORR-MFE-6J and -7J experimental capsules as of September 30, 1986

	ORR-MFE-6J	ORR-MFE-7J
Insertion date	6-28-85	6-28-85
Exposure, MWh	236,924.1	236,924.1
Equivalent full power days[a]	329.1	329.1
Thermal fluence, n/m^2	5.08 + 25[b]	7.00 + 25
Total fluence, n/m^2	1.70 + 26	2.00 + 26
dpa[c]	4.79	5.32
Direct helium,[c] appm	3.77	4.16
Two-step helium,[c] appm	28.8	52.3
Total helium,[c] appm	32.6	56.5

[a]Full power for the ORR is 30 MW.

[b]5.08 + 25 is read as 5.08×10^{25}.

[c]Helium and dpa values are for type 316 stainless steel.

FUTURE WORK

The three-dimensional neutronics calculations that monitor the radiation environment of the ORR-MFE-6J and -7J experiments will continue with each ORR cycle. The scale factors used to scale the calculated fluences will be updated as new experimental data become available.

REFERENCE

1. L. R. Greenwood, "Neutron Dosimetry and Damage Calculations for the ORR-6J Test, HFIR-RB-Hafnium Test, and the HFIR-RB1 and RB2 Experiments," pp. 4–14 in ADIP Semiannual Progr. Rep. Sept. 30, 1985, DOE/ER-0045/15 (February 1986).

INTERNATIONAL DOSIMETRY STANDARDIZATION ACTIVITIES - L. R. Greenwood (Argonne National Laboratory)

OBJECTIVE

To standardize neutron dosimetry measurements and radiation damage calculations to facilitate the comparison of materials effects under irradiation.

SUMMARY

Results of the REAL84 exercise to compare spectral unfolding and damage calculations between ten different laboratories in the U.S., Europe, and Japan were reviewed at an IAEA Consultants' Meeting at the Technical University in Budapest, Hungary, on September 8-10, 1986. A formal report on the project will be issued by the IAEA.

PROGRESS AND STATUS

This report concerns an international program (REAL84) to compare dosimetry techniques, nuclear data, and damage calculations. This effort was organized by the Nuclear Data Section of the International Atomic Energy Agency in Vienna, Austria. The purpose of the exercise was to compare spectral unfolding results and damage calculations provided by different laboratories. Ten laboratories participated from the U.S., Europe, and Japan. Seven different data sets were distributed including two related to fusion provided by Argonne from the 14 MeV neutron spectrum at the Rotating Target Neutron Source at Lawrence Livermore National Laboratory and a Be(d,n) spectrum measured at the tandem accelerator in Physics Division at ANL. Other spectra included pressure vessel surveillance at the Oak Ridge Research Reactor, the Arkansas Power and Light Reactor #1, a ^{235}U fission spectrum (National Bureau of Standards), and the Coupled Fast Reactivity Measurement Facility at Idaho National Engineering Laboratory.

Results of the exercise were reviewed at an IAEA Consultants' meeting at the Technical University in Budapest, Hungary, on September 8-10, 1986. Attendees included E. Zsolnay and E. Szondi (BME, Budapest), W. Zijp and H. Nolthenius (ECN, Petten, the Netherlands), W. Matzke (PTB, Braunschweig, West Germany), L. Greenwood (ANL), and V. Piksaikin (IAEA, Vienna).

A draft report was prepared by the project evaluators in Budapest and Petten for review at the meeting.[1,2] A number of problems were discussed including ambiguities in the spectral information, transfers of flux and uncertainty data between different energy group structures, singulaties in matrix procedures, nuclear data discrepancies, spectral weighting procedures, and uncertainty analyses. Detailed recommendations were formulated in each of these areas and a formal report will be issued by the IAEA. This report will also be presented at the Sixth ASTM-EURATOM Symposium on Reactor Dosimetry in Jackson Hole, WY., May 31-June 5, 1987.

Two basic conclusions were agreed to at the meeting. Although there were a number of irregularities in the spectral analyses, nuclear data, and uncertainties, integral fluences and damage rates generally showed a relatively small spread (~5-10%) which is considered adequate for many applications. However, considering the nature of this exercise, the spread was expected to be lower (~2-5%). Hence, it was agreed that further work was needed to resolve these differences. The goal is to produce several standardized data sets which can be processed in a specified manner and which will produce a very low spread in values between the participants. We will continue to participate in this effort. Ultimately, the goal is to develop standardized data and procedures for neutron dosimetry and damage analysis.

REFERENCES

1. W. L. Zijp, E. M. Zsolnay, H. J. Nolthenius, and E. J. Szondi, First Progress Report on the REAL-84 Exercise, ECN-86-021, Petten, February 1986.

2. E. M. Zsolnay, H. J. Nolthenius, and W. L. Zijp, Third Progress Report on the REAL-84 Exercise, ECN-86-102, Petten, July 1986.

HELIUM PRODUCTION CROSS SECTIONS FOR FUSION-ENERGY NEUTRONS - D. W. Kneff, R. P. Skowronski, and B. M. Oliver (Rockwell International)

OBJECTIVE

The objective of this work is to measure the total helium production cross sections of materials for fusion-energy neutrons.

SUMMARY

Two major fast-neutron irradiations were conducted for the measurement of the total helium production cross sections of several pure elements and separated isotopes. The first was a Rotating Target Neutron Source-II (RTNS-II) irradiation conducted to expand the 14.8-MeV cross section data base developed from earlier RTNS experiments.[1,2] The second was a 10-MeV neutron irradiation at the Los Alamos National Laboratory (LANL) using the $^1H(t,n)$ source reaction, to provide cross section information in a lower neutron energy region. Two RTNS-II add-on experiments were also initiated, to examine the 14- to 15-MeV energy dependence of selected pure-element cross sections.

PROGRESS AND STATUS

Collaborative research programs at Rockwell International and Argonne National Laboratory (ANL) are investigating the measurement and prediction of helium production in candidate fusion reactor materials in neutron test environments. Monoenergetic fast neutron measurements, conducted in part in collaboration with other laboratories, have included the determination of the total helium production cross sections for 26 pure elements, 33 separated isotopes, and 3 alloy steels for 14.8-MeV T(d,n) neutrons.[1-3] Two new neutron irradiations have now been performed to extend this cross section data base in the 8- to 15-MeV neutron energy region. Various aspects of this new work were supported by the Office of Fusion Energy and the Office of Basic Energy Sciences of the U.S. Department of Energy.

The first of these two experiments was a primary-volume irradiation at the Rotating Target Neutron Source-II (RTNS-II) at the Lawrence Livermore National Laboratory (LLNL). This irradiation was a joint experiment with L. R. Greenwood of ANL. The primary objective of this irradiation is to measure the cross sections of some additional materials at 14.8 MeV, including N [irradiated in the form of the compounds TiN and ZrN], Mg, S [irradiated as PbS], Ge, W, and four W isotopes. Several other materials were included to obtain additional basic helium production data for previously examined materials, and a number of ANL separated isotopes were included for fundamental studies of long-lived radionuclides. The irradiation lasted one week, producing an average total neutron fluence of about 6×10^{17} n/cm^2 on the front (upstream) face of the sample assembly.

The other helium-generation materials irradiated in this experiment, whose previous cross section measurements had relatively large uncertainties, included O [irradiated as Nb_2O_5, Al_2O_3, GeO_2], F [PbF_2, MgF_2, NdF_3 + pure-element Nd, CaF_2 + pure-element Ca], Ta, and eleven separated isotopes of Sn and Pb. The multiple compounds included in this irradiation for the N, O, and F measurements provide additional data to reduce the analysis uncertainties associated with unfolding the pure-element cross sections from those of the measured compounds. Selected materials, including Be, C, N, O, and F, were also included at several source angles up to 60° to examine the energy dependence of their total helium production cross sections in the 14- to 15-MeV energy region. The carbon cross section, for example, rises steeply between 14 and 15 MeV, and there are discrepancies in some of the published cross sections.[1] The compounds, plus the carbon (diamond and graphite) and beryllium samples, were vacuum-encapsulated in platinum for irradiation and analysis.

Radiometric counting of the dosimetry foils from this irradiation has been completed at ANL. Subsequent work will include the mapping of the dosimetry data to determine the neutron fluence distribution for the irradiation volume, and the analysis of the helium generation samples by isotope-dilution gas mass spectrometry for total helium production.[4] The results will be combined to deduce total helium generation cross sections.

An add-on RTNS-II experiment has also been prepared, to extend the cross section data on energy/angle effects to be derived from the primary-volume irradiation. This experiment includes, for example, Be, C, and O samples to be irradiated at a source angle of 110° (13.8-MeV neutrons). A second add-on experiment to irradiate several pure element metals is also in preparation.

The second major irradiation performed was a joint experiment with R. C. Haight at LANL. The objective of this experiment is the measurement of the cross sections of several pure elements and separated isotopes for ~10-MeV neutrons, an energy region for which few helium production data exist. The neutrons were produced by the $^1H(t,n)$ reaction, using a rotating hydrogen gas target developed by Haight. The one-week

experiment accumulated a total neutron fluence of about 3 x 10^{14} n/cm^2, with samples including Cu, Ni, Fe, Cr, Al, C, Mn, V, Ti, Si, Be, and the separated isotopes of Ni and Be.

Counting of the radiometric dosimetry foils and activated helium-generation samples from this irradiation is also near completion at ANL. Neutron fluence and energy spectrum mapping will be more complex for this experiment, due to steep energy gradients with neutron source angle, and scattering and triton energy-degradation effects produced by the thick gas target and its molybdenum entrance window. Helium analyses for these samples, with their lower helium concentration levels, will be performed using the recently developed constant-temperature furnace at Rockwell.[3] This furnace provides a lower, more constant helium measurement background than our conventional furnaces, and allows the analysis of larger samples with lower helium concentrations.

FUTURE WORK

The analysis of these irradiation experiments has been initiated with the radiometric dosimetry measurements at ANL. Helium analyses and the mapping of the dosimetry information will follow, and the results will be used to determine total helium production cross sections.

REFERENCES

1. D. W. Kneff, B. M. Oliver, H. Farrar IV, and L. R. Greenwood, "Helium Production in Pure Elements, Isotopes, and Alloy Steels by 14.8-MeV Neutrons," Nucl. Sci. Eng. 92, 491-524 (1986).

2. D. W. Kneff, B. M. Oliver, E. Goldberg, and R. C. Haight, "Helium Production Cross Sections for 15-MeV Neutrons on ^{6}Li and ^{7}Li," Nucl. Sci. Eng. 94, 136-144 (1986).

3. B. M. Oliver, D. W. Kneff, R. P. Skowronski, and H. Farrar IV, "Helium Production Cross Sections for 14.8-MeV Neutrons," pp. 34-6 in Damage Analysis and Fundamental Studies, Quarterly Progress Report January-March 1985, DOE/ER-0046/21, U.S. Department of Energy, May 1985.

4. B. M. Oliver, J. G. Bradley, and H. Farrar IV, "Helium Concentration in the Earth's Lower Atmosphere," Geochim. Cosmochim. Acta 48, 1759-67 (1984).

FULL DERIVATION OF AN APPROXIMATE SOLUTION TO THE SCATTERING INTEGRAL FOR GENERAL INTERATOMIC POTENTIALS - J.P. Blanchard, N.M. Ghoniem and S.P. Chou (University of California, Los Angeles)

OBJECTIVE

The objective of this work is to develop a new analytical approximation for the calculation of the scattering integral in atomic collisions. The method can be applied to any arbitrary interatomic potential.

SUMMARY

An approximation to the scattering integral is derived by expanding the potential about the distance of closest approach and truncating the expansion so that the integral can be performed analytically. The results are improved by using the approximate integrand only in the region near the closest approach and assuming zero potential for large distances. The analytical solution, which requires little computation time relative to other solution methods, is shown to yield sufficient accuracy for a wide range of particle energies and impact parameters, using both the Moliere and "Universal" potentials.

PROGRESS AND STATUS

Introduction

The Monte Carlo method is now widely used to predict the transport of energetic ions in solids.[1,2] This numerical simulation method requires repeated calculations of the scattering angle of an ion in a collision with the lattice. If these evaluations are simplified, computer time is saved and more particle histories can be simulated. Numerical evaluation of the scattering integral can be time consuming and inaccurate because the integrand is weakly singular at the distance of closest approach, so accurate analytical approximations for scattering in a general potential field are desirable. In this report, an approximate method for obtaining an analytical representation of the scattering integral is presented and its region of validity is discussed.

The scattering integral

In a two-body collision influenced by a central potential field V(r), the scattering angle is given by:[3]

$$\Theta = \Pi - \int_{\rho}^{\infty} \frac{2\,p\,dr}{r^2\,(1 - V(r)/E_o - p^2/r^2)^{1/2}} \quad ,$$

where Θ is the scattering angle, p is the impact parameter, ρ is the distance of closest approach, and E_o is the particle energy, which is measured in center of mass coordinates, i.e.

$$E_o = \frac{M_1}{M_1 + M_2}\, E_1 \quad ,$$

where M_1 and M_2 are the masses of the projectile and target particles, respectively, and E_1 is the projectile energy in lab coordinates. The geometry of the collision is shown in Fig. 1.

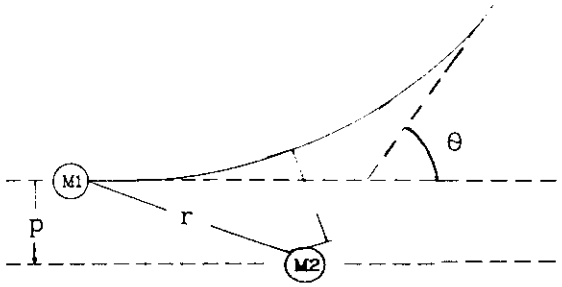

Fig. 1. Geometry for scattering model.

The distance of closest approach, which is the point at which the projectile's radial velocity is zero, is determined from the following equation:

$$1 - \frac{V(\rho)}{E_o} - \frac{p^2}{\rho^2} = 0 \quad .$$

To non-dimensionalize the integral, the following substitutions are made:

$$x = \frac{r}{a} \quad , \qquad \eta = \frac{\rho}{a} \quad , \qquad \beta = \frac{p}{a} \quad , \qquad \epsilon = \frac{aE_o}{Z_1 Z_2 e^2} \quad , \qquad V(ax) = \frac{Z_1 Z_2 e^2}{ax}\,\phi(x) \quad ,$$

where $\phi(x)$ is the screening function and a is the screening length, which depends on the Bohr radius and the atomic numbers of the two particles. Two forms commonly used for the screening length are given by Lindhard:[4]

$$a = 0.8853\, a_o (Z_1^{2/3} + Z_2^{2/3})^{-1/2} \quad ,$$

and Firsov:[5]

$$a = 0.8853\, a_o (Z_1^{1/2} + Z_2^{1/2})^{2/3} \quad ,$$

where a_o is the Bohr radius ($a_o = 0.529$ Å). The resulting integral is

$$\Theta = \Pi - \int_{\eta}^{\infty} \frac{2\,\beta\,dx}{x^2\,(1 - \phi(x)/\epsilon x - \beta^2/x^2)^{1/2}} \quad , \tag{1}$$

and the non-dimensional distance of closest approach η is found from

$$1 - \frac{\phi(\eta)}{\epsilon\eta} - \frac{\beta^2}{\eta^2} = 0 \quad . \tag{2}$$

As seen from Eq. (2), the integrand in Eq. (1) is singular at $x = \rho$, so the choice of numerical integration scheme is limited and requires many quadrature points. Hence, an analytical approach is desirable. In the discussions that follow, both the Moliere and Universal screening functions will be used to demonstrate the usefulness of analytical approximations. The Moliere screening function[6] is defined by

$$\phi(x) = 0.35\, e^{-0.3x} + 0.55\, e^{-1.2x} + 0.1\, e^{-6x} \quad ,$$

and the Universal screening function, which was recently developed by Ziegler et al.[7] and is given by

$$\phi(x) = 0.1818\, e^{-3.2x} + 0.5099\, e^{-0.9423x} + 0.2802\, e^{-0.4028x} + 0.02817\, e^{-0.2016x} \quad ,$$

where the screening radius is modified to yield:

$$a = 0.8854\, a_o (Z_1^{0.23} + Z_2^{0.23})^{-1/2} \quad .$$

An analytical approximation

In general, analytical solutions for the integration of Eq. (1) are not available, so approximations are necessary to obtain analytical formulas for the scattering angle. The solution approach used here expands the screening function about the distance of closest approach (where the integrand is singular) and truncates the series to obtain an analytically integrable function. To facilitate this approach, an additional substitution is introduced:

$$w = \frac{1}{\eta} - \frac{1}{x} \quad ,$$

which leads to

$$\Theta = \Pi - 2\beta I \quad , \qquad I = \int_0^{1/\eta} h(w)\, dw \quad ,$$

and $$h(w) = \left[1 - \frac{\eta^2}{\beta^2} - \frac{\phi(x)}{\epsilon\eta} + \frac{\phi(x)w}{\epsilon} + \frac{2\beta^2 w}{\eta} - \beta^2 w^2\right]^{-1/2} ,$$

or, using Eq. (2),

$$h(w) = \left[\frac{\phi(\eta) - \phi(x)}{\epsilon\eta} + \frac{\phi(x)w}{\epsilon} + \frac{2\beta^2 w}{\eta} - \beta^2 w^2\right]^{-1/2} ,$$

The screening function is expanded about $w = 0$ to yield

$$\phi(x) = \phi(\eta) + w\eta^2 \left.\frac{d\phi(x)}{dx}\right|_{x=\eta} + w^2\eta^3 \left[\left.\frac{d\phi(x)}{dx}\right|_{x=\eta} + \frac{\eta}{2}\left.\frac{d^2\phi(x)}{d^2x}\right|_{x=\eta}\right] + O(w^3) ,$$

where $w \to 0$, and the integrand becomes

where
$$\left.\begin{aligned} h(w) &\simeq g(w) , \\ g(w) &= (Kw - Qw^2)^{-1/2} . \end{aligned}\right\} \quad (3)$$

The constants K and Q are given by

and
$$\left.\begin{aligned} K &= \eta + \frac{\beta^2}{\eta} - \frac{\eta}{\epsilon}\left.\frac{d\phi(x)}{dx}\right|_{x=\eta} \\ Q &= \beta^2 + \frac{\eta^3}{2\epsilon}\left.\frac{d^2\phi(x)}{d^2x}\right|_{x=\eta} . \end{aligned}\right\} \quad (4)$$

Integrating this approximate function yields the scattering angle:

$$\Theta \simeq \pi - \frac{2\beta}{\sqrt{Q}} \cos^{-1}\left[1 - \frac{2Q}{K\eta}\right] . \quad (5)$$

In order to find the scattering angle for given values of energy and impact parameter, we first find the distance of closest approach from Eq. (2), then determine K and Q from Eq. (4) and plug into Eq. (5) to find the angle. This procedure is much quicker than numerical integration, especially after the distance of closest approach, which must be determined in either case, is calculated.

The primary error in Eq. (5) comes from the behavior of the series expansion of the screening function near the point $w = 1/\eta$. Since $\phi(x)$ is expanded about $w = 0$, the error increases for large w. As w approaches $1/\eta$ the potential should be zero (because this point corresponds to $r = \infty$), but the approximation clearly has a non-zero value at this point, i.e.

$$\phi(w = 1/\eta) = \phi(x \to \infty) \simeq \phi(\eta) + 2\eta \left.\frac{d\phi(x)}{dx}\right|_{x=\eta} + 0.5\eta^2 \left.\frac{d^2\phi(x)}{d^2x}\right|_{x=\eta} .$$

The difficulty caused by this error is evident when the exact integrand h(w) is compared to the approximation g(w) at $w = 1/\eta$, where one finds

$$h(1/\eta) = 1 ,$$

$$g(1/\eta) = \left[1 - \frac{1}{\epsilon}\left.\frac{d\phi(x)}{dx}\right|_{x=\eta} - \frac{\eta^2}{2}\left.\frac{d^2\phi(x)}{dx}\right|_{x=\eta}\right]^{-1/2} .$$

From this one can see that the approximation breaks down for small ϵ. This can also be seen in Fig. 2, which compares the exact and approximate integrands for different values of ϵ and β. In Fig. 2(a), ϵ and β are unity and the two functions are almost indistinguishable, so one would expect Eq. (5) to yield an accurate representation for the scattering angle. In contrast, Fig. 2(b) shows a large discrepancy in the two functions at one endpoint and the results cannot be relied upon. Modifications are required if accuracy is desired over a wide range of impact parameter and particle energy.

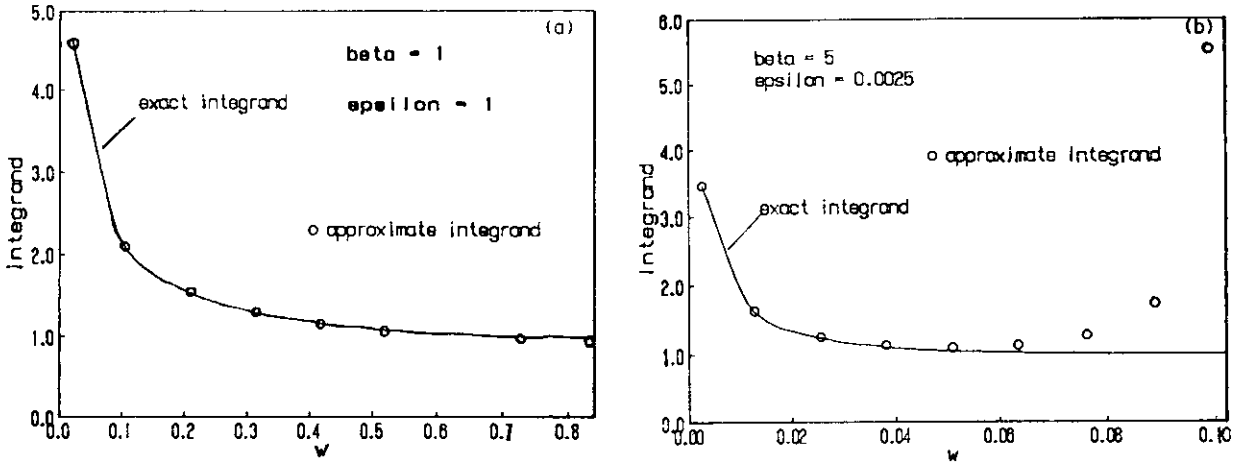

Fig. 2. Comparison of exact and approximate integrands for (a) small beta and large epsilon and (b) large beta and small epsilon.

An improved approximation

In order to improve the analytical approximation to the scattering angle, another representation for $\phi(x)$ is needed for large x (w near $1/\eta$). An expansion is inadvisable here because the most interatomic potentials are not analytic at $x = \infty$. Therefore, the potential will be assumed to be zero for all x greater than some value and the scattering integral will be divided into two intervals. Hence

$$\left.\begin{aligned} I &= \int_0^c h(w)\ dw + \int_c^{1/\eta} h(w)\ dw \\ \text{or} \\ I &\simeq \int_0^c g(w)\ dw + \int_c^{1/\eta} f(w)\ dw \end{aligned}\right] , \tag{6}$$

where g(w) is given by Eq. (3) and

$$f(w) = \left[1 - \frac{\beta^2}{\eta^2} + \frac{2\beta^2 w}{\eta} - \beta^2 w^2\right] .$$

The choice for c, the point at which the integral is divided, is somewhat arbitrary. Ideally the choice would depend on the impact parameter and the particle energy, but this complication is avoided initially by assuming that c depends only on the distance of closest approach. By comparing the two approximations for the integrand in the interior of the interval $0 < w < 1/\eta$, it seems that they intersect very near $w = 1/(2\eta)$ for a wide range of energy and impact parameter. This can be seen in Fig. 3, which plots the two approximate integrands, f(w) and g(w), against the exact integrand h(w) for different values of ϵ and β. In Fig. 3(a) the two approximations are indistinguishable on the interval $1/(2\eta) < w < 1/\eta$ and there is little difference between the scattering angle calculated using a single approximation over the whole interval and the angle from the two-interval approach of Eq. (6). In Fig. 3(b), however, ϵ is small so neither approximation is useful over the whole interval and two separate integration intervals are required. The two approximations intersect near the center $[w = 1/(2\eta)]$, so c has been chosen such that the interval is split into two equal parts and Eq. (6) becomes

$$I \simeq \int_0^{1/2\eta} g(w)\ dw + \int_{1/2\eta}^{1/\eta} f(w)\ dw \quad . \tag{7}$$

The advantage of this approach is seen in Fig. 4, which shows the two-interval approximate integrand for $\beta = 5$ and $\epsilon = 0.0025$. The improvement over the single interval approximation is

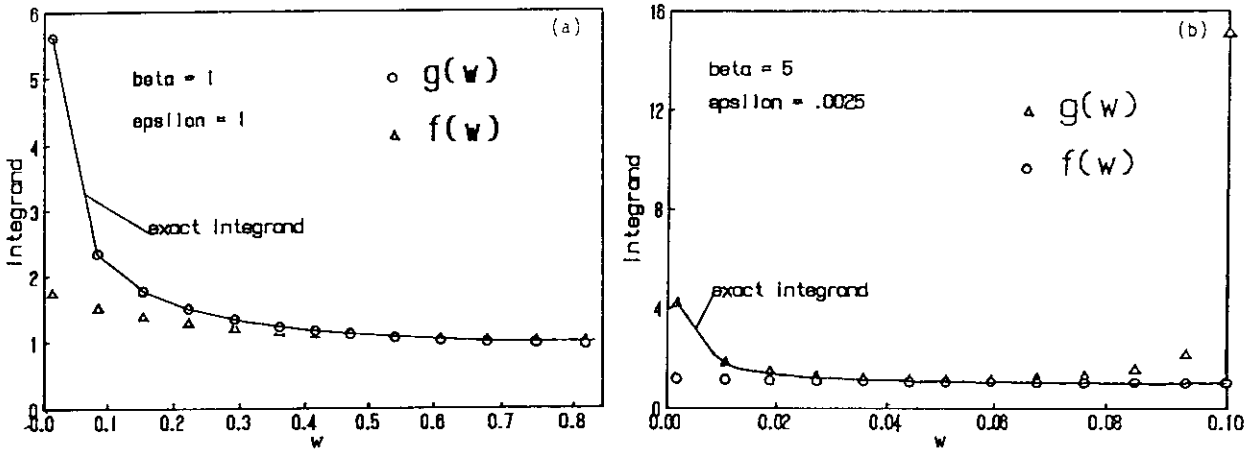

Fig. 3. Accuracy of small x and large x approximations for (a) small beta and large epsilon and (b) large beta and small epsilon.

evident when Figs. 4 and 2(b) are compared, so the integration of Eq. (7) should yield more accurate results even for small ϵ. Performing the integration, the resulting scattering angle is

$$\Theta \simeq 2 \cos^{-1}\left[\frac{\beta}{2\eta}\right] - \frac{2\beta}{\sqrt{Q}} \cos^{-1}\left[1 - \frac{Q}{K\eta}\right] \tag{8}$$

The maximum error in this result comes from the behavior of the two approximations at the center of the integration interval, so these functions are compared to the exact integrand h(w) at $w = 1/(2\eta)$:

$$h(1/2\eta) = \left[1 - \frac{\beta^2}{4\eta^2} - \frac{\phi(2\eta)}{2\epsilon\eta}\right]^{-1/2} ,$$

$$g(1/2\eta) = \left[1 - \frac{\beta^2}{4\eta^2} - \frac{\phi(\eta)}{2\epsilon\eta} - \frac{1}{2\epsilon}\frac{d\phi(x)}{dx}\bigg|_{x=\eta} - \frac{\eta}{8\epsilon}\frac{d^2\phi(x)}{dx}\bigg|_{x=\eta}\right]^{-1/2} ,$$

and

$$f(1/2\eta) = \left[1 - \frac{\beta^2}{4\eta^2}\right]^{-1/2} .$$

As before, the error increases as ϵ decreases, but the dependence on η is less clear.

One of the difficulties with the approximate result for the scattering angle [Eq.(8)] is that it is undefined for certain values of ϵ and β. For a fixed impact parameter, decreasing the reduced energy reduces the quantity $1-Q/K\eta$. When this quantity is less than -1, the inverse cosine is undefined and the approximation is no longer valid. Figure 5 shows the region in ϵ-β space where Eq.(8) is valid for both the Moliere and Universal screening functions. In either case, the approximation for the scattering angle is valid for $\epsilon > 1.7 \times 10^{-4}$ for all impact parameters and ϵ can be even lower for larger values of β.

Comparison with numerical results

The validity of the approximate expression for the scattering angle, given by Eq. (8) can be judged by comparison with numerical calculations. This indicates the usefulness of the approximation as compared to the more time-consuming numerical calculations, but does not address the validity of the screening function as a model for the actual potential. With this in mind, Table 1 gives the scattering angle for different values of ϵ and β using both the Moliere and Universal screening functions. The angles are also plotted in Fig. 6, using the Universal screening function. (In all cases, the numerical calculations were performed using

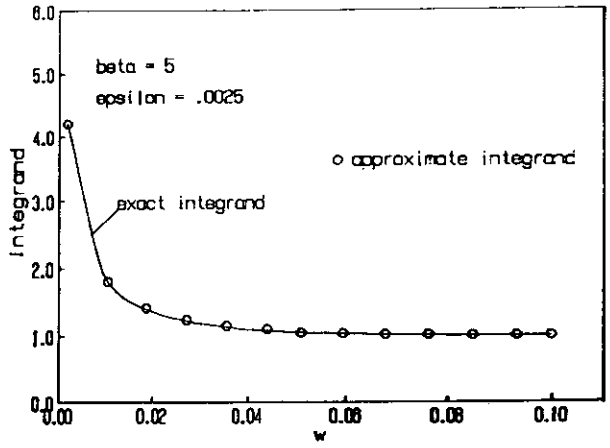

Fig. 4. Comparison of exact and two-interval approximate integrands.

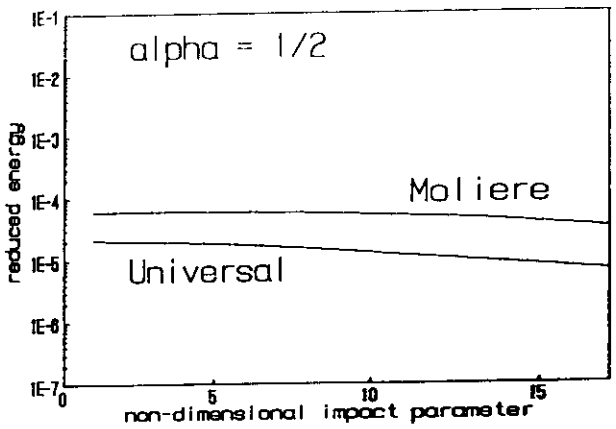

Fig. 5. Region of validity for different potentials using constant alpha.

Table 1. Scattering Angle (radians), $\alpha = 1/2$

β	ϵ	MOLIERE Numerical	MOLIERE Analytical	UNIVERSAL Numerical	UNIVERSAL Analytical
1	0.0002	2.99	3.07	2.96	3.03
7	0.0002	2.07	2.60	1.90	2.34
17	0.0002	0.690	1.50	0.517	0.720
1	0.0006	2.95	3.00	2.91	2.97
7	0.0006	1.80	2.19	1.58	1.93
17	0.0006	0.383	0.561	0.248	0.225
1	0.002	2.87	2.89	2.82	2.85
7	0.002	1.40	1.49	1.13	1.19
17	0.002	0.157	0.139	0.0896	0.0814
1	0.006	2.76	2.76	2.69	2.69
7	0.006	0.934	0.934	0.681	0.673
17	0.006	0.0591	0.0525	0.0319	0.0290
1	0.02	2.52	2.52	2.45	2.45
7	0.02	0.457	0.460	0.301	0.299
17	0.02	0.0186	0.0166	0.00982	0.00890
1	0.2	1.44	1.46	1.43	1.44
7	0.2	0.0621	0.0627	0.0377	0.0374
17	0.2	0.00193	0.00169	0.001020	0.000899
1	2.0	0.277	0.288	0.277	0.286
7	2.0	0.00646	0.00651	0.00388	0.00384
17	2.0	0.000219	0.000169	0.0001310	0.0000900

the IMSL quadrature routines.[8]) The approximations are very accurate for small β, but for a reduced energy of 0.0002, the two solutions differ by a factor of two. If ϵ is restricted to be above 0.002, the agreement between the analytical and numerical results is much better, with a maximum error of about 23%. Because there are errors in the numerical results and in the representations of the potentials themselves, the accuracy of the analytical formula in this restricted energy range is sufficient for most calculations.

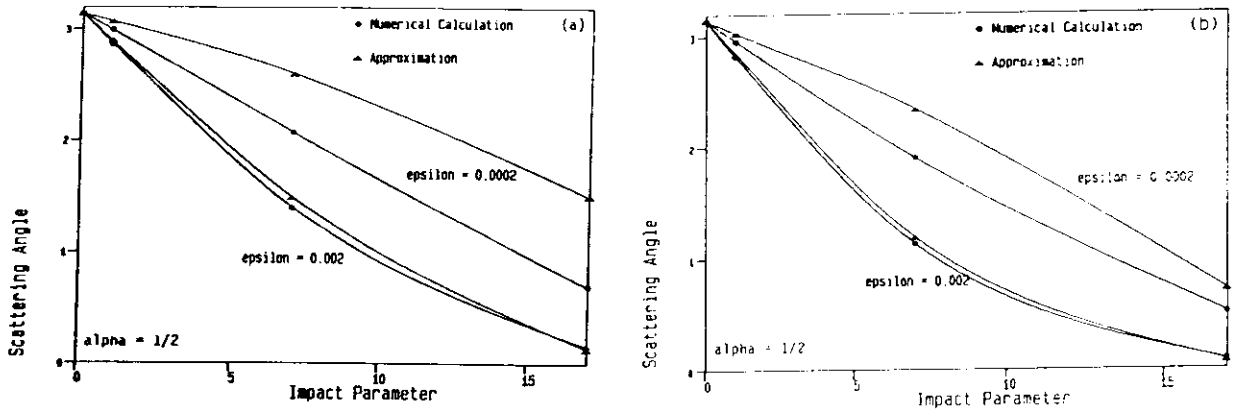

Fig. 6. Comparison of scattering angles for numerical and analytical solution methods using (a) Moliere and constant alpha and (b) Universal potentials.

Adjusting the integration interval

As mentioned previously, the accuracy of the analytical approximation represented by Eq. (6) can be improved by adjusting c, the point at which the integration interval is split. By varying this point and comparing the results to the numerical calculations of the scattering angle, the optimal split was found to depend only on the impact parameter and the distance of closest approach:

$$c = \frac{\alpha}{\eta} \quad , \qquad \alpha = 0.42 - \frac{\beta}{80} \quad .$$

The scattering angle is now given by:

$$\theta \simeq 2\cos^{-1}\left[\frac{\beta}{\eta}(1-\alpha)\right] - \frac{2\beta}{\sqrt{Q}}\cos^{-1}\left[1 - \frac{2\alpha Q}{K\eta}\right] \quad . \tag{9}$$

The results for this new approximation are shown in Table 2 and plotted in Fig. 7. The accuracy is greatly improved, with errors of less than 10% for $\epsilon = 0.0002$ and a maximum error of about 23% (β=17, ϵ=2, Universal screening function). Considering the wide range of impact parameters and energies shown in Table 2, Eq. (9) gives a reasonably accurate representation for the scattering angle over the entire practical range of impact parameter and reduced energy. An added benefit is that the region of validity is extended, so the approximate result for the scattering angle (using the Universal screening function) is now valid for $\epsilon > 7.3 \times 10^{-6}$, as compared to 5.0×10^{-5} previously. This advantage improves as the impact parameter increases, as can be seen by comparing Fig. 5 to Fig. 8, which show the valid regions of the old [Eq. (8)] and new approximations [Eq. (9)], respectively.

Conclusions

The scattering integral can be approximated by expanding the potential about the distance of closest approach before integrating the resulting integrand over a portion of the interval, and assuming that there is zero potential over the rest of the interval. This is successful because the integral is dominated by the influence of the potential in the neighborhood of the distance of closest approach, unless the particle energy is extremely small. This analytical approach yields accurate results at a significant savings in computation time as compared to numerical quadrature methods. The results are good for a fixed split in the integration interval, and much improved when the split depends on the impact parameter. The final result yields excellent accuracy over a wide range of energies and impact parameters.

Table 2, Scattering Angle (radians), $\alpha = 0.42 - (\beta/80)$

β	ϵ	MOLIERE Numerical	MOLIERE Analytical	UNIVERSAL Numerical	UNIVERSAL Analytical
1	0.00002	3.04	not valid	3.03	3.07
7	0.00002	2.41	2.67	2.35	2.49
17	0.00002	1.34	1.41	1.26	1.26
1	0.00006	3.02	3.07	3.00	3.04
7	0.00006	2.27	2.49	2.17	2.29
17	0.00006	1.05	1.04	0.905	0.912
1	0.0002	2.99	3.03	2.96	3.00
7	0.0002	2.07	2.21	1.90	1.96
17	0.0002	0.690	0.689	0.517	0.524
1	0.0006	2.95	2.97	2.91	2.93
7	0.0006	1.80	1.80	1.58	1.57
17	0.0006	0.383	0.385	0.248	0.252
1	0.002	2.87	2.87	2.82	2.82
7	0.002	1.40	1.40	1.13	1.13
17	0.002	0.157	0.158	0.0896	0.0916
1	0.006	2.76	2.76	2.69	2.69
7	0.006	0.934	0.942	0.681	0.687
17	0.006	0.0591	0.0596	0.0319	0.0326
1	0.02	2.52	2.52	2.45	2.46
7	0.02	0.457	0.465	0.301	0.305
17	0.02	0.0186	0.0188	0.00982	0.01000
1	0.2	1.44	1.47	1.43	1.45
7	0.2	0.0621	0.0637	0.0377	0.0383
17	0.2	0.00193	0.00191	0.00102	0.00100
1	2.0	0.277	0.295	0.277	0.293
7	2.0	0.00646	0.00662	0.00388	0.00394
17	2.0	0.000219	0.000192	0.000131	0.000101

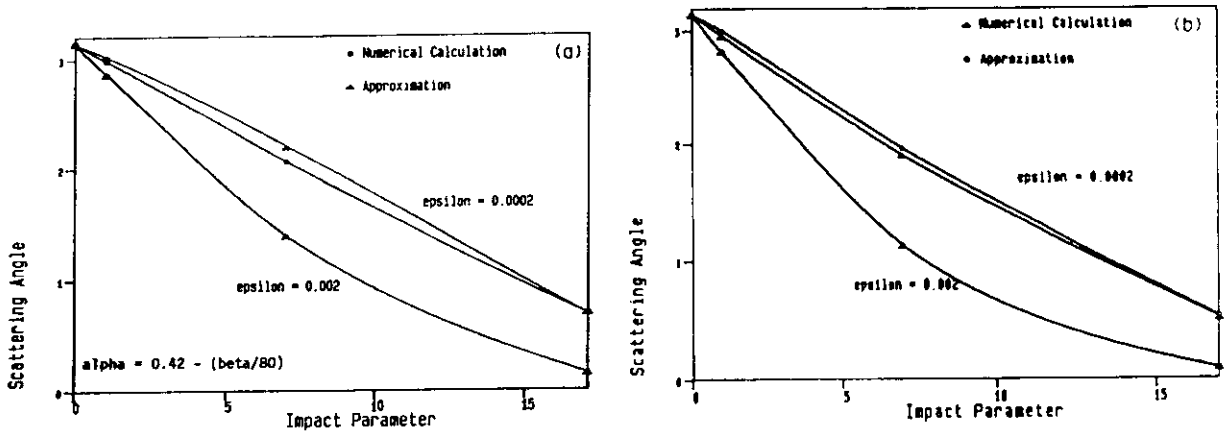

Fig. 7. Comparison of scattering angles for numerical and analytical solution methods and variable alpha using (a) Moliere and (b) Universal potentials.

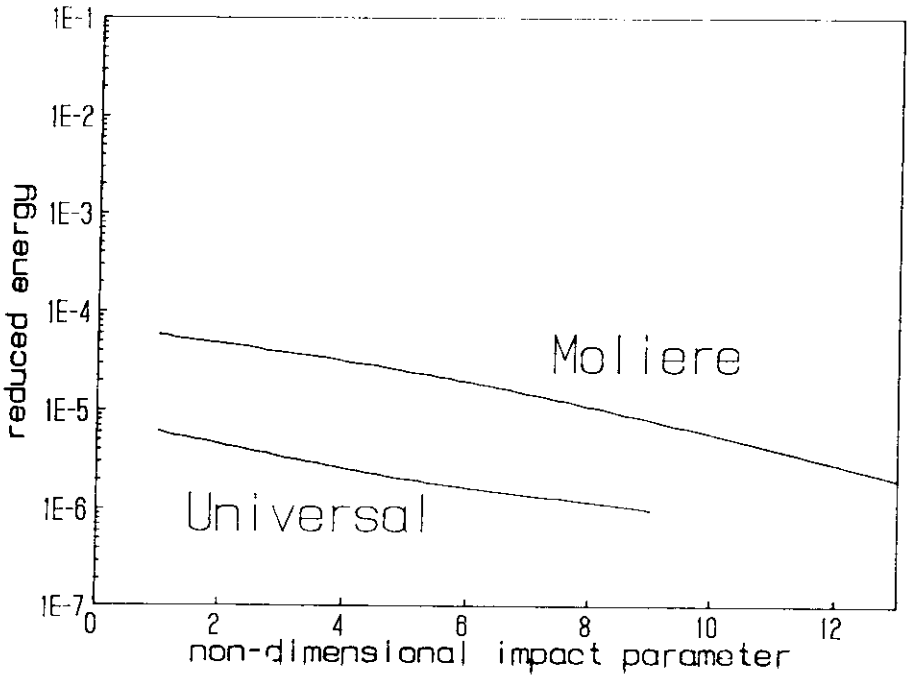

Fig. 8. Regions of validity for different potentials using variable alpha.

Acknowledgements

This research was performed under appointment to the Magnetic Fusion Energy Technology Fellowship Program administered at Oak Ridge Associated Universities for the U.S. Department of Energy. Additional support was provided by the U.S. Department of Energy, Office of Fusion Energy, Grant #DE-FG03-84ER52110, and the State of California through the MICRO Project, Grant #UC-85-151, and by TRW Corporation, Grant #TRW-A57678AB5S, with UCLA.

References

1. J. P. Biersack and L. G. Haggmark, Nucl. Instr. and Meth., 174, 257 (1980).
2. S. P. Chou and N. M. Ghoniem, J. Nucl. Mater., 117, 55 (1983).
3. J. F. Ziegler, J. P. Biersack and U. Littmark, The Stopping and Range of Ions in Solids, Vol. I, Pergamon Press, New York, 1985, p. 23.
4. J. Lindhard, M. Scharff and H. E. Schiott, Mat. Fys. Medd. Dan. Vid. Selsk., 36 (1968).
5. O. B. Firsov, Soviet Phys. JETP, 7, 308 (1958).
6. G. Moliere, Z. Naturforschung, A2, 133 (1947).
7. J. F. Ziegler, J. P. Biersack and U. Littmark, op. cit., p. 41.
8. The IMSL Library Reference Manual, Vol. 1, LIB-0009 (IMSL, Inc.), Houston, Rev. June, 1982.

FUTURE WORK

The analytical approximations will be used in the TRIPOS Monte Carlo Code for the analysis of charged particle transport in solids.

TRIPOS: A DYNAMIC MONTE CARLO CODE FOR THE TRANSPORT OF IONS IN POLYATOMIC SOLIDS - P. S. Chou and N. M. Ghoniem (University of California, Los Angeles)

OBJECTIVE

The objective of this work is to develop a new Monte Carlo code, TRIPOS, for the TRansport of Ions in POlyatomic Solids. The computer code is capable of simulating a large variety of ion/solid interaction phenomena for both bulk and surface applications.

SUMMARY

A general dynamic Monte Carlo ion transport code, TRIPOS, TRansport of Ions in POlyatomic Solids, is presented. TRIPOS uses both power-law cross sections and a newly developed solution to the scattering integral for treatment of nuclear collisions. Applications of TRIPOS to surface, bulk, and deep penetration problems in multi-layer polyatomic media are given. The dynamic nature of surface evolution caused by energetic ion-surface collisional events are also simulated by TRIPOS.

PROGRESS AND STATUS

Introduction and background

A sound understanding of the physical phenomena associated with ion transport in solids is critical to advancing new and emerging technologies. For example, the first wall and divertor or limiter components of fusion energy devices experience high fluxes of charged particles and neutrons, which lead to a variety of effects (i.e., sputtering, blistering, and bulk damage). The production of primary knock-on atoms (PKAs) in fission nuclear reactor materials leads eventually to the degradation of design and safety related material properties. New material processing technologies using ion beams or plasmas rely on a detailed knowledge of ion transport physics. Understanding of the physics of radiation damage on structural solids and microelectronic materials is critical to the development of space and defense related technologies.

Ion slowing-down processes can be attributed to ion energy losses through different interactions (e.g., excitation and ionization of electrons, inelastic nuclear collisions, elastic nuclear interactions, and bremsstrahlung photon emissions). There are two general classes of approaches for the analysis of ion transport phenomena, the deterministic and probabilistic methods. Deterministic approaches are based on either analytical or numerical solutions to the ion transport equation. On the other hand, probabilistic solutions rely on using the Monte Carlo method, where an ensemble of particles is used to simulate the ion interaction processes following physical laws.

The ion transport equation is derived based on particle and energy conservation principles. A generalized form of the ion transport equation is given as,[1-6]

$$\frac{1}{v}\frac{\partial\phi(\vec{r},E,\vec{\Omega},t)}{\partial t} + \Omega\cdot\nabla\phi(\vec{r},E,\vec{\Omega},t) + \Sigma_t(\vec{r},E,t)\phi(\vec{r},T,\vec{\Omega},t)$$

$$= Q(\vec{r},E,\vec{\Omega},t) + \frac{\partial}{\partial E}\left[S(\vec{r},E,t)\phi(\vec{r},E,\vec{\Omega},t)\right]$$

$$+ \int_0^\infty dE' \int_{-1}^{1} d\vec{\Omega}'\ \Sigma_s\ (E'\to E,\Omega'\to\Omega)\phi(\vec{r},E',\vec{\Omega}',t) \quad , \tag{1}$$

where $\vec{r}$ is spatial vector, E is energy, $\vec{\Omega}$ is the direction vector, t is time, ϕ is particle flux, Σ_t is total cross section, Σ_s is differential scattering cross section, Q is particle source rate, and S is electronic stopping cross section. It is not possible to solve Eq. (1) for general conditions. However, its solution can always be obtained with simplifications and assumptions. Also, for polyatomic solids, coupled transport equations are required[5-6] which further increase the complexity of the problem. If only a few ion parameters are desired, simpler forms of the ion transport equation can be used. Lindhard, Scharff, and Schiott[7] used the moment method by assuming continuous slowing-down processes to calculate the range distribution and associated parameters. Lindhard et al.[8] developed an integral equation

relating radiation damage to deposited energy and atomic displacement. Parkin and Coulter[9] extended the treatment for the atomic displacement calculation in polyatomic solids. However, these calculations neglect the spatial distribution of radiation damage.

Sanders[10] derived a vector range distribution function. For one-dimensional geometry, Sigmund[11] expanded the vector range distribution in Legendre polynomials in moment solutions. Brice[12] developed an integral equation describing the energy deposition profiles using a similar approach. All of the above methods, however, use simplified forms of the ion transport equation where detailed particle phase-space are not included. Hoffman et al.[5] used the discrete-ordinate multi-energy-group method used in neutronics[13,14] for the analysis of surface sputtering problems. Using approximate coupled diffusion equations, Chou and Ghoniem[6] developed an analytical method for the slowing down of ion-induced cascades in precipitate dissolution problems. The diffusion equations were de-coupled using the Neumann series expansion technique.

A complete treatment of ion transport using deterministic methods is complex. The degree of difficulty increases quickly when less assumptions and higher degrees of freedom are used, and limiting simplifications are usually required. For example, the requirements of multigroup cross sections, coupled transport equations for polyatomic media, recoil multiplication, and higher order angular expansions can make the computational burden prohibitive in the detailed discrete-ordinate multi-energy-group method.

The Monte Carlo method can accurately simulate particle behavior in solids, with modest increments in computational difficulties for each added degree of freedom. This method is particularly suitable to the fast development of computer technology. In the Monte Carlo method, sampling is conducted from probability distribution functions according to relevant physical laws. Monte Carlo techniques developed for ion transport can be categorized into two groups. In the first group, dynamic many-body calculations are performed. The other category is known as the binary collision approximation method where only two interacting particles are considered at a given time.

To describe the many-body interaction of N atoms in the crystal, 3N Newtonian equations of motion are required for the description of the crystal. A PKA event can be initiated by giving an atom a kinetic energy E with the momentum gained in a specified direction. Numercial procedure is then used to integrate these equations of motion until equilibrium is reached. These calculations are fully dynamic since all degrees of freedom are allowed to vary simultaneously to satisfy the requirements of interaction forces and the Newtonian laws of dynamics. This many-body integration method is very useful in demonstrating directional effects such as focusing and channeling. The major limitations lie with the maximum available memory capacity and computation speed of a computer. Consequently, only a small number of low energy PKAs can be simulated in this type of analysis.[15]

Beeler[16,17] applied the assumption that the atomic collision cascade can be described as a branching sequence of binary collision events to ion transport calculations. Yoshida,[18] Oen and Robinson,[19,20] Ishitani et al.,[21] Robinson and Agamy,[22] Biersack and Haggmark,[23] Ziegler et al.,[24] Attaya,[25] and Chou and Ghoniem[26] developed Monte Carlo codes based on the binary collision approximation. Roush et al.[27] as well as Moeller and Eckstein[28] used the same concept to develop time-dependent Monte Carlo codes. In this work, a dynamic binary collision Monte Carlo ion transport code, TRIPOS, is presented. It is a general purpose code for the efficient calculation of ion transport and effects in a multi-layered structure composed of polyatomic solids. TRIPOS can be applied to the analysis of bulk or surface time- and fluence-dependent problems. Thus, complex surface evolution problems can be analyzed. Importance sampling techniques are incorporated in order to enhance the computation speed and reduce the variance in the results.

The validity of the results from ion transport simulations depends heavily on the ability to reproduce the actual interatomic collisional behavior during the analysis. In order to correctly predict the ion collisional behavior in solids, the interatomic potential has to be known with great accuracy. However, the overlapping and shielding effects of the electron clouds during the atomic collision process make a complete description of the interatomic potential difficult. Various interatomic potential models were proposed such as Thomas-Fermi,[29,30] Bohr,[31] Born-Mayer,[32] Moliere,[33] and Ziegler[24] potentials. However, these complex potentials result in difficulties for analytical solutions of the scattering integral. Biersack et al.[23,24] used a fitting function to the numerical results from the scattering integral to approximate the atomic scattering. In the present work, two methods of calculating scattering properties are used. The first is based on approximate power-law fits to the

Thomas-Fermi potential. In the second method developed by Blanchard, Ghoniem, and Chou (BGC),[34] a second order Taylor expansion about the distance of closest approach is used for the integrand of the scattering integral. Accurate analytic approximate solutions are developed in this method.

Theoretical background for the TRIPOS code

Lindhard et al.[7] used the momentum approximation to solve for the scattering integral based on the power-law potentials. The solutions from the power potentials are applied for the derivation of the so-called power-law cross sections. This technique bypasses the slow and costly process of numerically solving the scattering integral in Monte Carlo ion transport analysis. In this section, we present our application of the power-law approximation and discuss its range of validity. We will then present a brief description of our new method for calculating the scattering integral. The scattering integral has the form

$$\Theta = \Pi - 2\int_{\rho}^{\infty} \frac{pdr}{r^2\left[1 - \frac{V(r)}{E_c} - \frac{p^2}{r^2}\right]^{1/2}} , \tag{2}$$

where Θ is the deflection angle in the center of mass system, p the impact parameter and ρ the distance of closest approach, E_c the center of mass kinetic energy, and V(r) the interatomic potential. Lindhard et al.[7] used the momentum approximation to simplify the scattering integral. Their approximation for the new scattering integral has the form

$$\Theta = -\frac{1}{Edp}\frac{d}{dp}\int_0^{\infty} V[(x^2 + p^2)^{1/2}]dx \tag{3}$$

Using the power-law potentials, analytical results are obtained as

$$\Theta = \frac{k_s \gamma_s}{\epsilon \eta^s} , \tag{4}$$

where s is the power-law index, k_s the constant for the power-law screening constant, and γ_s a constant equals to $0.5\beta[0.5,(s+1)/2]$. The power-law potential has the form

$$V(r) = \frac{Z_1 Z_2 e^2}{r}\frac{k_s}{s}\left(\frac{a}{r}\right)^{s-1} , \tag{5}$$

where a is the Lindhard screening function. It is to be noted that for s = 1 (pure Coulombic) and s = 2, the exact scattering integral, Eq. (2), can be analytically solved. The results, Eq. (4) from the momentum approximation, agree well with those from the exact scattering integral for small scattering angles. However, for near head-on collisions, the momentum approximation yields larger scattering angles.

The power-law representations of interatomic potentials are derived from appropriate fits to the Thomas-Fermi potential. Moliere[33] and Ziegler et al.[24] have attempted various forms of exponential screening functions to fit interatomic potentials. The Moliere screening function is given by

$$\phi = 0.35e^{-0.3r/a} + 0.55e^{-1.2r/a} + 0.10e^{-6.0r/a} \tag{6}$$

and

$$a = 0.8853a_o/(Z_1^{2/3} + Z_2^{2/3})^{1/2} ,$$

where Z_1 and Z_2 are atomic numbers for colliding particles, a_o is the Bohr radius. On the other hand, the Ziegler universal screening function has the form

$$\phi = 0.1818e^{-3.2r/b} + 0.5099e^{-0.9423r/b} + 0.2802e^{-0.04028r/b} + 0.02817e^{-0.2016r/b} . \tag{7}$$

where b is the Ziegler screening length defined as

$$b = 0.8854a_o/(Z_1^{0.23} + Z_2^{0.23}) .$$

Fig. 1 shows a comparison between the scattering angle results from the power-law approximation, the BGC analytical solution,[34] and exact numerical calculations using Ziegler's universal screening function with dimensionless energies, ϵ, of 10^{-5}, 3×10^{-4}, 3×10^{-3}, 10^{-2}, and 3. The dimensionless energy is defined as

$$\epsilon = \frac{EM_2}{(M_1 + M_2)} \frac{a}{Z_1 Z_2 e^2} \qquad (8)$$

Other calculations were made using the Moliere potential.[34] The results of this analysis indicate the following.

1. The "exact" form of the screening function has the most significant effects on the solution of scattering integral. This is clear when we compare Moliere potential results to calculations with Ziegler's universal potential.

2. The power law is a reasonable approximation to the scattering process. Its major advantage lies in its simplicity within the context of the Monte Carlo method.

3. The BGC analytical solution is accurate and within a few percent of the numerical results with impact parameter up to 25 screening lengths for both Moliere and Ziegler potentials.

Because of the relative simplicity of the power-law potential results and the fact that collisions are near-coulombic at high energies, the majority of the calculations in TRIPOS are performed in this mode. However, for verification, an option using the BGC method is provided. In the following, we describe the details of the power-law approximation.

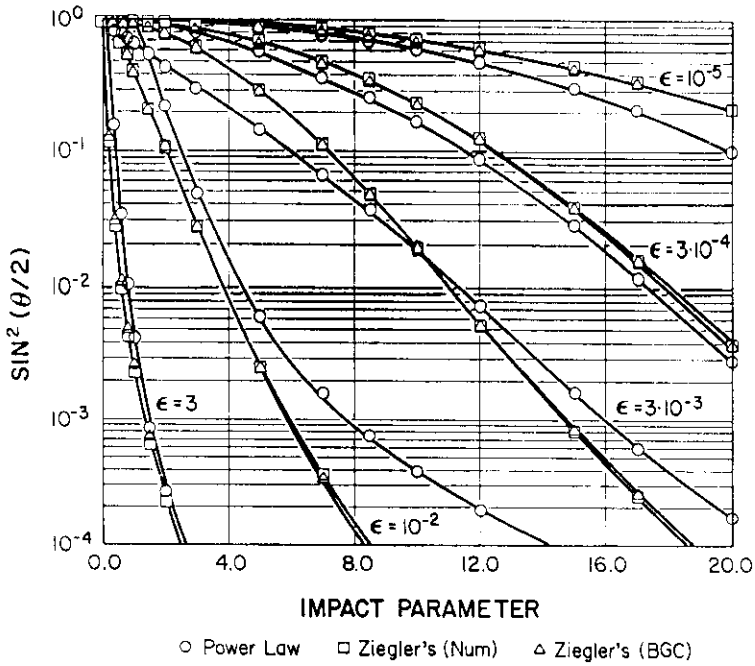

Fig. 1. The scattering angle as a function of impact parameter using power-law and Ziegler's universal potentials at dimensionless energy [Eq. (8)] of 10^{-5}, 3×10^{-4}, 3×10^{-3}, 10^{-2}, and 3. The scattering integrals are numerically integrated for both power-law and Ziegler's universal potentials. The approximate integral method by BGC [34] is also used to solve for Ziegler's universal potentials.

Mean-free path between collisions. In the power-law approximation, the differential cross section is given by[35]

$$d\sigma(E,T) = C_m E^{-m} T^{-1-m} dT \quad , \qquad (9)$$

where $$C_m = \frac{\pi}{2} \lambda_m a_{12}^2 \frac{1}{M_2} \left(\frac{M_1}{M_2} \frac{2Z Z e^2}{a_{12}}\right)^{2m} ,$$

and M_1, Z_1 = mass and charge of incident particle,

M_2, Z_2 = mass and charge of recoil particle,

E = incident particle energy,

T = recoil energy.

$$a_{12} = 0.4683 \left(Z_1^{2/3} + Z_2^{2/3}\right)^{-1/2} \text{ Å} , \tag{10}$$

$$m = 1/s ,$$

$$(m, \lambda_m) = \begin{cases} (\tfrac{1}{3}, 1.309) , & \text{for } E_A \le E \le E_B \\ (\tfrac{1}{2}, 0.327) , & \text{for } E_B \le E \le E_C \\ (1, 0.5) , & \text{for } E \le E_C \end{cases} \tag{11}$$

For energies below E_A, the differential cross section for Born-Mayer interaction is represented by a power approximation of $(m, \lambda_m) = (0, 24)$, and $a_{12} = 0.219$ Å.[34]

A major problem with the use of the power-law approximation is the determination of the transition energies E_A, E_B, and E_C, such that the calculation of energy transfers are accurate. Based upon range considerations, Winterbon[35] determined these transition energies. In the present work, we determine transition energies by requiring the continuity of the **total** nuclear stopping power $S_n(E)$. The quantity $S_n(E)$ is therefore continuous across an energy boundary.

$$S_n(E) = \int_{T_s}^{\Lambda E} T d\sigma(E,T) , \tag{12}$$

$$= \frac{C_m}{1 - m} \Lambda^{1-m} E^{1-2m} , \qquad m \neq 1 , \tag{13}$$

$$= \frac{C_1}{E} \ln\left(\frac{\Lambda E}{T_s}\right) , \qquad m = 1 , \tag{14}$$

where $$\Lambda = 4M_1M_2/(M_1 + M_2)^2 . \tag{15}$$

Λ is the maximum fractional energy transferred in a collision, and T_s is the smallest value of transferred energy. Equating the nuclear stopping power at the energy boundaries results in a unique set of equations which determine E_A, E_B, and E_C. This ensures that the ion mean-free path during nuclear stopping is independent of the power, s, at the transition energies E_A, E_B, and E_C. The value of T_s is chosen as the energy transferred for an impact parameter equal to one half the interatomic spacing.

The total nuclear scattering cross section for charged particle interaction in a binary collision can be expressed in the form:

$$\sigma(E) = \frac{C_m}{m} E^{-m} \left[T_s^{-m} - (\Lambda E)^{-m}\right] , \qquad m \neq 0 , \tag{16}$$

$$= C_o \ln(\Lambda E/T_s) , \qquad m = 0 , \tag{17}$$

where C_m is a constant used in the power-law approximation [Eq. (8)]. In our treatment of energy loss, energy transfers below T_s are treated in a continuous way and added to the electronic energy loss, as will be shown later.

The probability of a particle undergoing a binary collision after moving a distance $\Delta\ell$ in the solid is given by

$$P = 1 - \exp[-N\sigma(E)\Delta\ell] \quad , \tag{18}$$

where N is the atomic density of the solid. This assumes a decoupling of electronic and nuclear energy losses. A random number R_1 is generated for an even distribution of P between 0 and 1. The distance between collisions is therefore determined by

$$\Delta\ell = \frac{1}{N\sigma(E)} \ell n\left(\frac{1}{1 - R_i}\right) = \frac{1}{N\sigma(E)} \ell n\left(\frac{1}{R_1}\right) \quad , \tag{19}$$

where R_1 and R_i have the same probability distribution.

Type of recoil. In the binary collision approximation, a moving atom can interact with only one medium atom at a time. If the moving atom is in a polyatomic medium, it is necessary to determine the interaction probabilities with each of the components of the polyatomic medium. To implement this, we first calculate the total cross section for the interaction $\Sigma_T(E)$ which is defined as

$$\Sigma_T(E) = \sum_{i=1}^{NM} \Sigma_i(E) \quad , \tag{20}$$

where NM is the total number of species in the polyatomic medium. $\Sigma_i(E)$ is the total cross section for species i at energy E. We also define a partial total cross section $\Sigma_{TP}(E)$ as follows:

$$\Sigma_{TP}(E) = \sum_{i=1}^{NP} \Sigma_i(E) \quad , \qquad 1 \le NP \le NM \quad . \tag{21}$$

Therefore, the cummulative distribution function is $\xi_{NP} = \Sigma_{TP}(E)/\Sigma_T(E)$, which is bounded between 0 and 1. A random number R_2 is then generated; if $\xi_{NP-1} < R_2 \le \xi_{NP}$, a type-NP atom is chosen for the collision of interest.

Scattering angle. The scattering angle in a collision is determined here from cross-section information. The energy to the recoil is proportional to the differential cross section. From the CDF, a random number R_3 is related to the transferred energy T and the incident energy E by

$$R_3 = \frac{T_s^{-m} - T^{-m}}{T_s^{-m} - (\Lambda E)^{-m}} \quad , \qquad m \neq 0 \quad , \tag{22}$$

$$= \frac{\ell n(T/T_s)}{\ell n(\Lambda E/T_s)} \quad , \qquad m = 0 \quad . \tag{23}$$

Equation (21) is easily solved for the transferred energy, which leads to

$$T = [T_s^{-m}(1 - R_3) + R_3(\Lambda E)^{-m}]^{-1/m} \quad , \qquad m \neq 0 \quad , \tag{24}$$

$$= (\Lambda E)^{R_2} T_s^{(1 - R_3)} \quad , \qquad m = 0 \quad . \tag{25}$$

The determination of the scattering angle θ, in the CMS, is achieved by using the well-known kinematic relation

$$\theta = 2 \sin^{-1}(T/\Delta E)^{1/2} \quad . \tag{26}$$

In the laboratory system, the scattering angle Ψ is given by

$$\Psi = \tan^{-1}\left[\frac{\sin\theta}{\cos\theta + (M_1/M_2)}\right] \quad . \tag{27}$$

The azimuthal scattering angle is finally selected using the relation

$$\phi = 2\pi R_4 \quad , \tag{28}$$

where R_4 is a random number uniformly distributed between 0 and 1. The angles for recoils are given by

$$\psi_r = \tan^{-1}[\sin\theta/(1 - \cos\theta)] \quad , \tag{29}$$

$$\phi_R = 2\pi R_4 - \pi \quad . \tag{30}$$

Particle position. The scattering angles described in the previous section are determined with reference to the incident particle direction. In a fixed frame of reference however, the direction cosines of the particle velocity vector must be calculated after each collision. Let $(\alpha_i, \beta_i, \gamma_i)$ be the direction cosines of the particle after the ith collision. It can be easily shown that

$$\alpha_i = \frac{\alpha_{i-1}\cos\psi + \sin\psi(\gamma_{i-1}\alpha_{i-1}\cos\phi - \beta_{i-1}\sin\phi)}{(1 - \gamma_{i-1}^2)^{1/2}} \quad , \tag{31}$$

$$\beta_i = \frac{\beta_{i-1}\cos\psi + \sin\psi(\gamma_{i-1}\beta_{i-1}\cos\phi + \alpha_{i-1}\sin\phi)}{(1 - \gamma_{i-1}^2)^{1/2}} \quad , \tag{32}$$

$$\gamma_i = \gamma_{i-1}\cos\psi + (1 - \gamma_{i-1}^2)^{1/2} \sin\psi \cos\phi \quad . \tag{33}$$

The position of the particle at the point of collision i is given by

$$X_i = X_{i-1} + \alpha_{i-1}\Delta\ell \quad , \tag{34}$$

$$Y_i = Y_{i-1} + \beta_{i-1}\Delta\ell \quad , \tag{35}$$

$$Z_i = Z_{i-1} + \gamma_{i-1}\Delta\ell \quad . \tag{36}$$

The position of the particle is checked in relationship to the surface boundary. This information is used for the determination of sputtering events and particle history termination.

Electronic and small angle nuclear energy losses. The energy transferred between electrons and a moving atom is very small and much more frequent than atom-atom collisions. Also, for large impact parameters the nuclear scattering energy loss is small and has been neglected in many previous treatments. It is possible, therefore, to treat both the electronic and low-angle nuclear scattering energy losses in a continuous way. We will first describe the treatment of electronic energy loss and then show how we include nuclear collisions that result in an energy transfer below T_s.

For ion velocities $v < v_0 Z_1^{2/3}$, where $v_0 = e^2/h \approx c/137$ and c is the speed of light, the electronic stopping is represented by the Lindhard-Scharff formula,

$$[S_c(E)]_{LS} = \frac{1.212\ Z_1^{7/6}\ Z_2}{(Z_1^{2/3} + Z_2^{2/3})^{3/2}\ M_1^{1/2}}\ E^{1/2}\ \text{eV Å} \quad . \tag{37}$$

At higher particle velocities, $v > v_0 Z_1^{2/3}$, the Bethe-Bloch formula is used. This has the form[24]

$$[S_c(E)]_{BB} = \frac{8\pi Z_1^2 e^4}{I_0 \epsilon_B}\left[\ell n(\epsilon_B) + \ell n(1 - \frac{v^2}{c^2}) - \frac{v^2}{c^2} - \frac{C}{Z} - \frac{\delta}{2}\right] \quad , \tag{38}$$

where v is the incident particle velocity, C/Z is low energy shell correction term, δ is high energy density correction term, and

$$\epsilon_B = 4\ \frac{m_c}{M_1}\ \frac{E}{Z_2 I_0} \quad , \tag{39}$$

where $(Z_2 I_0)$ is the mean excitation energy, I_0 is the Bloch constant given by[23]

$$\begin{aligned} I_0 &= 12.0 + 7.0\ Z_2^{-1}\ \text{eV} \quad , \quad Z_2 < 13 \quad , \\ &= 9.76 + 58.5\ Z_2^{-1.19}\ \text{eV} \quad , \quad Z_2 \geq 13 \quad . \end{aligned} \tag{40}$$

In the intermediate regime, there is no simple analytical formula for S_c. In order to bridge this gap, where $v \sim v_0 Z_1^{2/3}$, an interpolation scheme proposed by Biersack et al.[23,24] is used:

$$[S_c]^{-1} \simeq [S_c]_{LS}^{-1} + [S_c]_{BB}^{-1} \quad . \tag{41}$$

Now we turn our attention to small-angle nuclear energy loss. In order to render the total nuclear scattering cross section finite, the lower limit on energy transfers is set to a small value T_s. This value corresponds to an impact parameter of half the interatomic spacing. Below T_s small amounts of energy are transferred in collisions, yet they contribute to total energy loss because of the high probability of their occurrence. It is necessary to keep good energy accounting in this energy range. The following quantity is therefore evaluated and added to the electronic energy loss:

$$S_{ns}(E) = \int_{T_c}^{T_s} T d\sigma \quad ,$$

$$= \frac{C_m}{(1 - m)}\ \Lambda^{1-m} E^{-m} (T_s^{1-m} - T_c^{1-m}) \quad , \quad m \neq 1 \quad , \tag{42}$$

$$= \frac{C_1}{E}\ \ell n(\frac{T_s}{T_c}) \quad , \quad m = 1 \quad , \tag{43}$$

where T_c is of the order of a few eVs. The total "continuous" energy loss is therefore

$$\Delta E_{cn} = [S_c(E) + S_{ns}(E)] N \Delta \ell \quad . \tag{44}$$

Particle history termination and sputtering. A particle history is terminated in two cases: (1) if its energy falls below a minimum value, which is the displacement threshold energy (E_d) in the bulk, or the surface binding energy near the surface; or (2) if it physically leaves the boundary of interest.

Calculations of sputtering into vacuum are sensitive to the surface binding energy. In our work, the planar potential barrier to the surface binding energy is used for slab geometry.

The binding energy U at an ejection direction cosine with plane normal μ as in the planar model is given by[27]

$$U(\mu) = U_0/\mu^2 \quad , \tag{45}$$

where U_0 is the minimum energy for particle history termination. For spherical geometry or the isotropic model,[11,27]

$$U(\mu) = U_0 \quad . \tag{46}$$

In order to take account of all the sputtered particles, all ions with energy greater than U_0 have to be simulated. However, it is known that recoils with energy less than the displacement threshold energy are not displaced from their original lattice positions. Cascade simulations by Heinish[37] using the MARLOWE code[19,20] indicated that a displaced atom has to be at least a distance of 6.5 lattice constants away from the vacancy site to be permanently displaced. Based on this conclusion, we define an equivalent surface binding energy, U_{0e}, as follows:

$$\begin{aligned} U_{0e} &= U_0 + x(E_d - U_0)/\lambda \quad , \qquad \text{for } x < \lambda \quad , \\ &= E_d \quad , \qquad \text{for } x > \lambda \quad , \end{aligned} \tag{47}$$

where E_d is the displacement energy, x is the depth of recoil generation, and λ is a distance of 6.5 lattice constants. The use of this equivalent surface binding energy can terminate all of the bulk recoils with energy less than E_d and hence reduce the number of recoils simulated without affecting the displacement damage results.

Dynamic surface evolution. The evolution of an alloy surface is both time and flux dependent because of the ion beam induced changes in surface compositions. In the TRIPOS code, the surface regions are divided into many layers, with the thickness of each being a small fraction of the incident ion projected ranges. For each layer, a good accounting of its composition is required for tracing its time and fluence dependence. During the simulation, pseudo particle histories are used with each history representing a fluence of W, which is on the order of 10^{12} cm^{-2}. Each layer is generally represented by N pseudo particles. Conservation requires that

$$N = n\Delta t/W \tag{48}$$

for each layer where n is the atomic density and Δt is the thickness of the layer. A good particle balance is performed for each layer in the events of sputtering, dissolution, and implantation. Such balance yields information on the local layer composition. Also, other phenomena in dynamic surface evolution processes require additional modeling. For example, the recoil implantation and mixing can cause the formation of local super-dense material which eventually leads to local relaxation and expansion. This process is related to the phenomenon of recoil mixing. The super-dense solid is modeled to expand homogeneously until the theoretical density is reached. Because light ions are implanted deeper, such a process can lead to the de-enrichment of heavier atoms in the bulk in a fusion environment.

Variance reduction and importance sampling. The standard deviation, which is the square root of the variance, is used as a measure of the statistical uncertainty in the Monte Carlo results. The variance decreases with the number of simulated histories. The uncertainty in simulated average results decreases with the square root of the number of particle histories used. Since the cost of computation can be approximately regarded as a linear function of the number of histories, estimates of average values improve moderately with an increase in the number of histories.

Variance reduction techniques can serve as the means to reduce the variance by using complex and biased sampling schemes.[38-41] In the meantime, the extra computational efforts which arise because of more complex schemes are counter-balanced by the faster reduction in variance. As a result, the overall cost of computation is reduced, or stays at the same level, while the variance is reduced.

One of the most widely used schemes in variance reduction is called "importance sampling." As implied in its name, importance sampling refers to recording more samples from the more important regions in a given problem. In other words, the regions which are likely to contribute to the final results are well sampled.

In this work, importance sampling is performed using particle splitting technique. It is desirable to increase the number of histories in important regions to reduce error in the results. The particle splitting technique splits one particle into several particles with conservation of the total weight (importance) in the important region. This technique artificially increases the number of particles in the important regions. Let there be an important region where, once a particle enters, it is split into n particles. The importance of the incoming particle is I_o. Then, the importance for the newly formed particles, I_n, is given by

$$I_n = I_o/n \quad . \tag{49}$$

Through this scheme, the importance of the entire system is conserved. Now, when those split particles leave the important region, it is necessary to reduce the number of particle histories to decrease the computation overhead. The Russian roulette scheme is used to reduce the number of particle histories in the less important regions. Let I_o be the current particle importance and I_n be the desired importance in the less important region, where $I_o < I_n$. A random number r is called. If $r \leq I_o/I_n$, then the particle survives and its importance is increased from I_o to I_n. On the other hand, for $r > I_o/I_n$, the particle is eliminated and discarded from further consideration. Statistically, this technique also conserves the importance of the entire system.

Results

Several applications of TRIPOS have been previously reported.[26,42] These include particle and energy reflection,[26] precipitate dissolution,[26] cascade simulations,[42] and low energy particle range calculations.[26] In the following, we present applications of TRIPOS to sputtering, dynamic surface evolution, and high energy deep penetration. A number of examples demonstrate the versatility and capability of the TRIPOS code. We first discuss four examples of surface sputtering. This is followed by an example of deep penetration by high energy protons, and finally surface evolution simulations using the dynamic version of TRIPOS.

Surface sputtering can be classified into physical and chemical sputtering. Physical sputtering is caused by the collisional mechanism of ion-solid interaction, where recoils are energetic enough to reach the surface and overcome the surface binding potentials. On the other hand, chemical sputtering results from the chemical interaction of incident ions with the solids such that new compounds are formed in the surface regions. These newly formed compounds may experience lower surface binding potential barriers. Since TRIPOS is based on the physics of atomic collisions, its applications are limited to the physical sputtering phenomenon.

Sputtering mechanisms are very complex and can be categorized into three regimes: the single knock-on regime, the linear cascade regime, and the spike regime. For the single knock-on regime, the incident ion transfers its energy to target atoms which are ejected through the surface after having undergone a small number of collisions. In the linear cascade regime, recoil atoms are energetic enough to produce higher order recoils with some of them sputtered. The spike regime has a very high density of recoils where non-linear effects, such as cascade overlapping, play a major role in enhancing the sputtering rate. Light ion sputtering always falls in the single knock-on and linear cascade regimes.

Sputtering erosion rate is measured using the sputtering yield which is defined as the ratio of the sputtered ion flux to the incident ion flux. The simulations have been performed on four different MFECC (Magnetic Fusion Energy Computer Center) supercomputers, namely, CDC 7600, Cray-1, Cray-1s and Cray-XMP with relative computing speed factors of 0.55, 1.0, 1.0, and 1.3, respectively.[43] In this work, all the CPU time results are normalized with respect to Cray-1.

^{4}He on gold and copper. The direction of incidence is normal to the surface. Both the TRIM[23] and TRIPOS codes are used. Four-thousand particle histories are simulated for each code. The surface binding energies are 3.5 and 3.8 eV for copper and gold surfaces, respectively. Fig. 2 shows a comparison of sputtering yield results from TRIM and TRIPOS as a function of incident ion energy on gold surface. Also included for comparison are the experimental data of Bay et al.[44] Fig. 3 shows theoretical sputtering yield data from TRIM and TRIPOS compared to experimental data by Rosenberg et al.[45] and Yonts[46] on copper surface. TRIPOS is shown to agree well with experiments. Fig. 4 shows the projected ranges in gold and copper from both TRIM and TRIPOS which are in good agreement. Fig. 5 presents the normalized CPU times for TRIM and TRIPOS, which shows that TRIPOS is 3-10 times faster than TRIM.

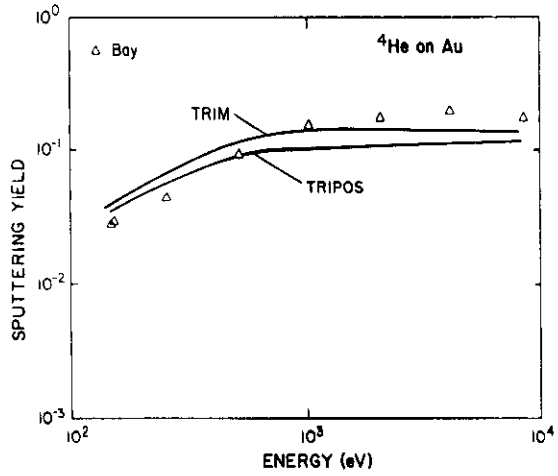

Fig. 2. The sputtering yield as a function of incident ion energies from TRIM, TRIPOS, and experimental results by Bay et al. [44] for α-particles on Au.

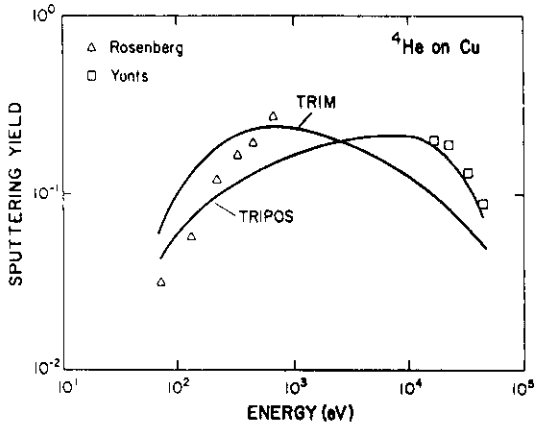

Fig. 3. The sputtering yield as a function of incident ion energies from TRIM, TRIPOS, and experimental results by Rosenberg et al. [45] and Yonts [46] for α-particles on Cu.

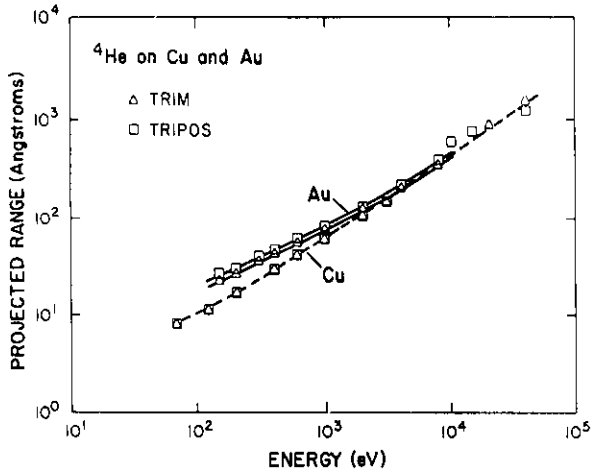

Fig. 4. The projected range predicted by TRIM and TRIPOS as a function of incident ion energies for α-particles on Au and Cu.

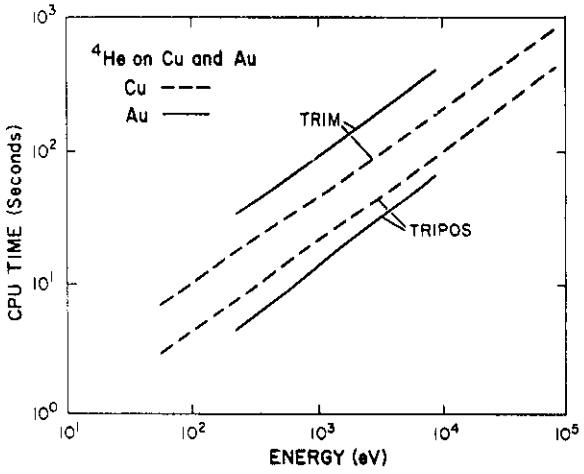

Fig. 5. The normalized CPU time used by TRIM and TRIPOS as a function of incident ion energies for α-particles on Au and Cu. TRIPOS is shown to be 3 and 10 times faster than TRIM for Cu and Au, respectively.

D on gold. The surface binding energy used is 3.8 eV for gold. Fig. 6 shows good agreement between TRIM and TRIPOS on sputtering yield. Also presented are the exprimental data of Bay et al.[44] and Fur et al.[47] The theoretical results also agree with these experimental data. A comparison of the CPU time in Fig. 7 shows that TRIPOS is a factor of 10 faster than TRIM.

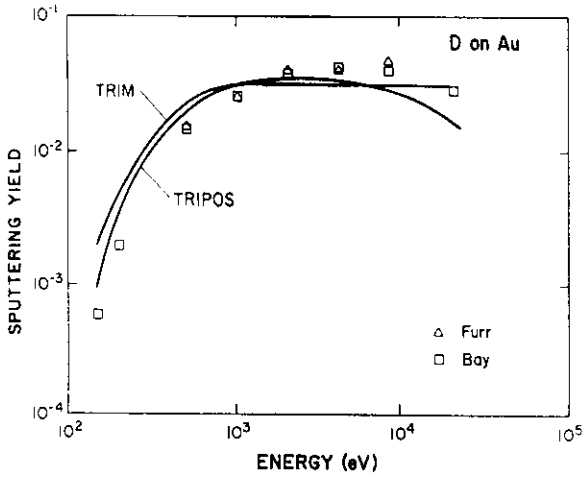

Fig. 6. The sputtering yield as a function of incident ion energies from TRIM, TRIPOS, and experimental results by Bay et al. [44] and Furr et al. [47] for D on Au.

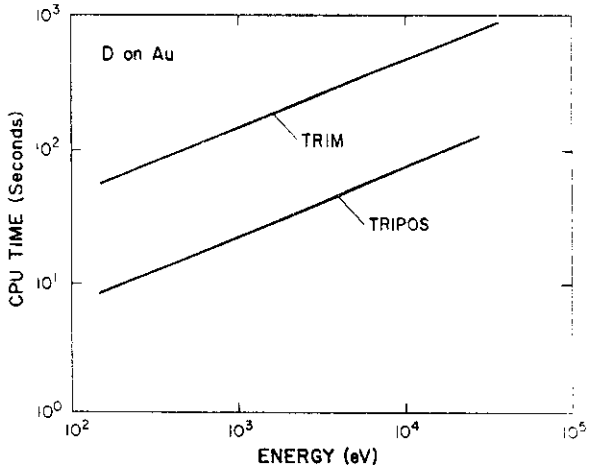

Fig. 7. The CPU time used by TRIM and TRIPOS as a function of incident ion energies for D on Au. TRIPOS is shown to be about 10 times faster than TRIM.

^{4}He on titanium. The surface binding energy for titanium is 4.9 eV.[48] Based on this binding energy, sputtering yield results from TRIM, TRIPOS, and TRIPOS with the Russian roulette technique of 4 for 1 kill ratio are obtained. It is observed that the application of Russian roulette in the TRIPOS code yields similar results as compared to analog TRIPOS. Fig. 8 shows a comparison of CPU times among TRIM, analog TRIPOS, and TRIPOS with the Russian roulette technique. At higher energies, analog TRIPOS is 10 times faster and Russian roulette TRIPOS 30 times faster compared to TRIM. At low energy, however, the efficiency of the Russian roulette technique decreases because of the fact that the importance zone thickness is on the order of the ion projected range.

A comparison of TRIM and TRIPOS sputtering yield results to the experimental data of Rosenberg et al.,[45] Yonts,[46] Roth et al.,[49] Hofer et al.,[50] and Bohdansky et al.[51] shows that both TRIM and TRIPOS overestimate the sputtering yield, using a surface binding energy of 4.9 eV. By increasing the surface binding energy to 7.5 eV, the predictions from the TRIPOS code fall between all the experimental data as shown in Fig. 9.

^{4}He on carbon (graphite). The measured surface binding energy for graphite is 7.4 eV.[48] Predictions of sputtering yield from both TRIM and TRIPOS show an underestimation of the experimental results by Rosenberg et al.,[45] Bohdansky et al.[52] and Roth et al.[53] based on this surface binding energy. A selection of a surface binding energy of 5.0 eV shows a good fit of both TRIM and TRIPOS to the experimental results as shown in Fig. 10. However, the analog TRIPOS simulations were found to be about 6 times faster compared to TRIM in the same figure.

Deep penetration of protons. In a number of space applications, information is needed on the deep penetration of charged particles. A mono-energetic beam of 200 MeV is considered to be incident on an aluminum slab of 9.78 cm thick. The emerging protons immediately enter a slab of an organic material with the following composition: 27.96% hydrogen, 15.29% carbon, 27.06% nitrogen, and 27.96% oxygen. The projected range calculated by TRIPOS is 13.1 cm. The ion energy deposition along the ion track is shown in Fig. 11. The small spikes are caused by high energy PKAs and the dip at 9.78 cm is caused by the discontinuity in material compositions. The range stragglings along the depth (Z-) direction and the X-direction are shown in Fig. 12.

Dynamic surface evolution. Applications of TRIPOS to dynamic surface evolution problems have been performed on AuPt, LuFe, CuAu, and TiC alloys.[59] TRIPOS showed good agreement with the experimental measurements for 150 eV deuterium ions by Bastasz and Nelson[54] on CuAu for up to a fluence of 5.0×10^{15} particles/cm^2 where gold atom enrichment is observed. TRIPOS results qualitatively agree with the experimental results[55-57] for deuterium and tritium ions on TiC where titanium atom enrichment is observed. Our work shows that the dynamic evolution results depend heavily on the modeling. For a more detailed discussion, the reader is referred to refs. 58 and 59.

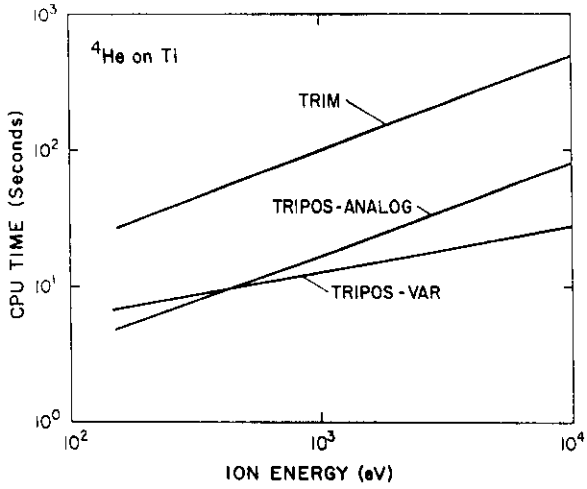

Fig. 8. The CPU time used as a function of incident ion energies by TRIM, TRIPOS (analog version), and TRIPOS (variance reduction version) for α-particles on Ti. It is shown that the variance reduction technique can be advantageous at higher ion energies. However, the simple scheme of analog Monte Carlo is advantageous at low ion energies.

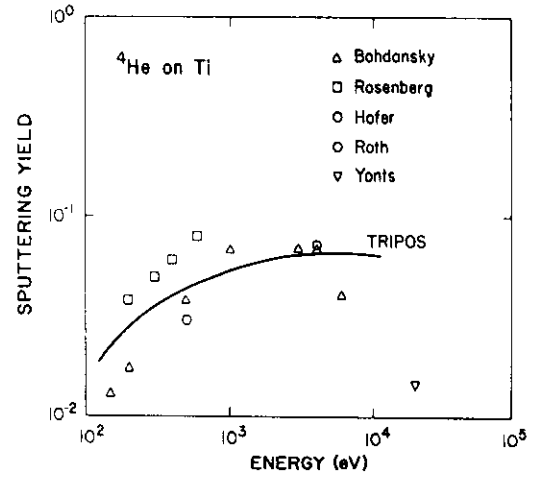

Fig. 9. The sputtering yield from TRIPOS compared to experimental data by Rosenberg et al. [45], Yonts [46], Roth et al. [49], Hofer et al. [50] , Bohdansky et al. [51] as a function of incident ion energy for α-particles on Ti.

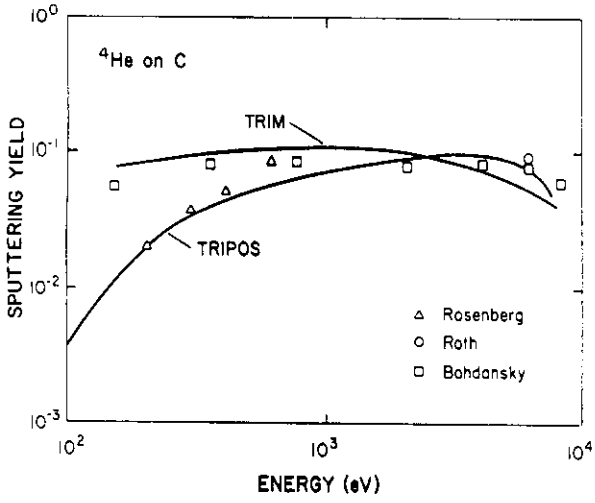

Fig. 10. The sputtering yield from TRIM and TRIPOS compared to experimental results by Rosenberg et al. [45], Bohdansky et al. [52], and Roth et al. [53] as a function of incident ion energy for α-particles on C.

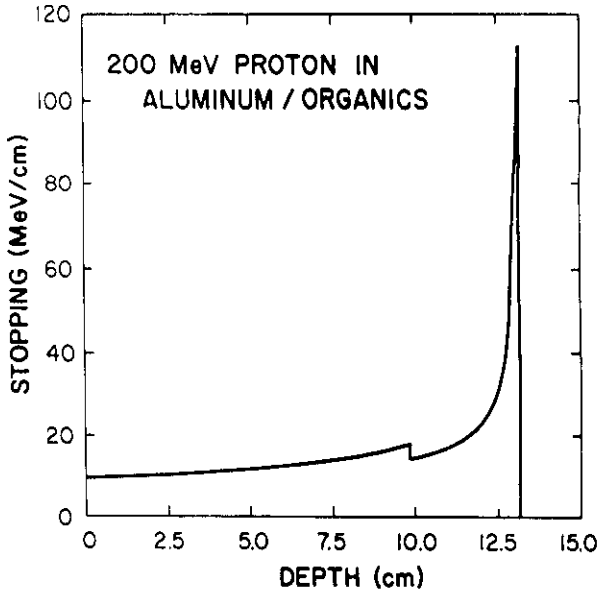

Fig. 11. The stopping of 200 MeV protons as a function of penetration depth in a 9.78-cm-thick aluminum/organic medium. The depth where a discontinuity in the stopping occurs is the boundary for aluminum and the organic materials.

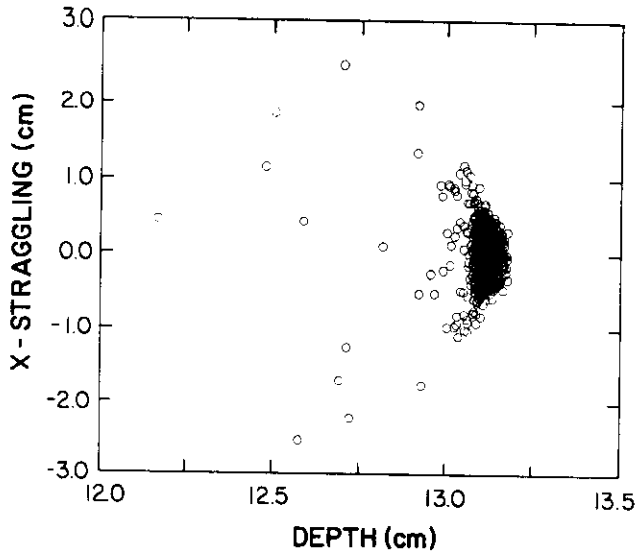

Fig. 12. The straggling of 200 MeV protons along the depth (Z-) direction and the X-direction.

Conclusions

In this work, a dynamic Monte Carlo ion transport code, TRIPOS, is developed. The power-law potential approximation to the Thomas-Fermi potentials at high energies and to the Born-Mayer potentials at low energies are used for describing nuclear collisions. Options of using Moliere or Ziegler universal potentials are also provided using the integration technique developed by Blanchard, Ghoniem, and Chou.[34] Our study shows that the power-law and Born-Mayer potential results agree well with the results from Moliere or Ziegler potentials with the exception that the momentum approximation yields harder collisions at low impact parameters.

TRIPOS simulates ion behavior in materials with multiple layers and different compositions. It treats both surface and bulk ion transport problems where importance sampling techniques are employed. For surface sputtering by light ions, TRIPOS results yield good agreements with the results from the experiments and the TRIM calculations. Our study shows that analog TRIPOS is a factor of 3 to 10 faster compared to TRIM. With the Russian roulette technique, TRIPOS can be 3 times faster than its analog version. Also, TRIPOS simulations of the dynamic surface evolution problems show good agreement with experimental work. However, detailed modeling is still required for surface evolution phenomena. One interesting application of TRIPOS is the treatment of deep penetration by energetic ions. This application is useful in the study of single event upset (SEU) phenomena in microelectronic components used in space explorations. A new version of TRIPOS has been developed where coupled ion-electron transport is simulated for semiconductor applications.[60]

Acknowledgements

This work is supported by the National Science Foundation, Grant #CPE-81-11581; the U. S. Department of Energy, Office of Fusion Energy, Grant #DE-FG03-84ER52110 with UCLA; and the State of California through the MICRO Project, Grant #UC-85-151 with matching funds from the TRW Corporation, Grant #TRW-A576778AB5S.

The authors thank the Magnetic Fusion Energy Center under the U. S. Department of Energy for supplying the major part of the computing time for this work. Thanks are also extended to the National Science Foundation and the San Diego Supercomputer Center for allocation of computer time through the University of California, Los Angeles.

REFERENCES

1. D. E. Bartine, R. G. Alsmiller, F. R. Mynatt, W. W. Engle, Jr. and J. Barish, Nucl. Sci. Eng. 48, 159 (1972).
2. M. M. R. Willianms, J. Phys. A9, 771 (1976).
3. M. M. R. Williams, Radiat. Eff. 37, 131 (1978).
4. M. M. R. Williams, Progress Nucl. Energy 3, 1 (1978).
5. J. J. Hoffman, H. L. Dodds and D. K. Holmes, Nucl. Sci. Eng. 68, 55 (1978).
6. P. S. Chou and N. M. Ghoniem, Nucl. Instr. Meth. Phys. Res. B9, 209 (1985).
7. J. Lindhard, M. Scharff and H. E. Schiott, K. Dan. Vidensk. Selsk. Mat. Fys. Medd. 33, 14 (1963).
8. J. Lindhard, V. Nielsen, M. Scharff and P. V. Thomson, K. Dan. Vidensk. Selsk. Mat. Fys. Medd. 33, 10 (1963).
9. D. M. Parkin and C. A. Coulter, J. Nucl. Mater. 85/86, 611 (1979); ibid. 88, 249 (1980); ibid. 95, 193 (1980); ibid. 101, 261 (1981); ibid. 103/104, 1315 (1983); ibid. 117, 340 (1983).
10. J. B. Sanders, Can. J. Phys. 46, 455 (1968).
11. P. Sigmund, Phys. Rev. 184, 383 (1969).
12. D. K. Brice, Appl. Phys. Lett. 16, 1034 (1970); J. Appl. Phys. 46, 3385 (1975).
13. W. W. Engel, Jr., Radiation Shielding Information Center, Oak Ridge National Laboratory Report CCC-254 (1973).
14. W. A. Rhoades, D. B. Simpson, R. L. Childs and W. W. Engel, Jr., Radiation Shielding Information Center, Oak Ridge National Laboratory Report CCC-320 (1978).
15. J. B. Gibson, A. N. Goland, M. Milgram and G. H. Vineyard, Phys. Rev. 120, 1229 (1960).
16. J. R. Beeler and D. G. Besco, J. Appl. Phys. 34, 2873 (1963).
17. J. R. Beeler, Phys. Rev. 150, 470 (1966).
18. M. Yoshida, J. Phys. Soc. Jpn. 16, 44 (1961).
19. O. Oen and M. T. Robinson, J. Appl. Phys. 35, 2515 (1964).
20. O. Oen and M. T. Robinson, Nucl. Instr. Meth. 132, 647 (1976).
21. T. Ishitani, R. Shimizu and K. Murata, Jpn. J. Appl. Phys. 11, 125 (1972).
22. J. E. Robinson and S. Agamy, Atomic Collisions in Solids, eds., S. Datz, B. R. Appleton and C. D. Moak, Plenum Press, New York, 1975, p. 215.
23. J. P. Biersack and L. H. Haggmark, Nucl. Instr. Meth. 174, 257 (1980).
24. J. F. Ziegler, J. P. Biersack and U. Littmark, The Stopping and Range of Ions in Solids, Pergamon Press, New York, 1985.
25. H. Attaya, Ph.D. thesis, University of Wisconsin Report UWFDM-420 (1980).
26. S. P. Chou and N. M. Ghoniem, J. Nucl. Mater. 117, 55 (1983).
27. M. L. Roush, T. D. Andreadis and O. F. Goktepe, Radiat. Eff. 55, 119 (1981).
28. W. Moeller and W. Eckstein, Nucl. Instr. Meth. Phys. Res. B2, 814 (1984).
29. L. R. Thomas, Proc. Cambridge Philos. Soc. 23, 1 (1927).
30. E. Fermi, Z. Phys. 48, 73 (1929).
31. N. Bohr, K. Dan. Vidensk. Selsk. Mat. Fys. Medd. 18, 8 (1948).
32. M. Born and J. E. Mayer, Z. Phys. 75, 1 (1932).
33. G. Moliere, Z. Naturforsch A2, 133 (1947).
34. J. Blanchard, N. M. Ghoniem and S. P. Chou, University of California Los Angeles Report ENG-86-41/PPG-1014 (1986).
35. K. B. Winterbon, P. Sigmund and J. B. Sanders, K. Dan. Vidensk. Selsk. Mat. Fys. Medd. 37, 14 (1970).
36. M. T. Robinson, Sputtering by Particle Bombardment I, ed., R. Behrisch, Springer-Verlag, New York, 1981, p. 73.
37. H. L. Heinisch, J. Nucl. Mater. 103/104, 1325 (1981).
38. L. L. Carter and E. D. Cashwell, "Particle Transport Simulation with the Monte Carlo Method," TID-26607, ERDA Tech. Info. Center, Oak Ridge, TN, October 1975.
39. J. S. Spanier and E. M. Gelbard, Monte Carlo Principles and Tranport Problems, Addison-Wesley, Reading, MA, 1969.
40. J. M. Hammersley and D. C. Handscomb, Monte Carlo Methods, Wiley and Sons, New York, 1964.
41. W. E. Selph and C. W. Garrett, "Reactor Shielding for Nuclear Engineers," ed., N. M. Schaffer, TID-25951, Nat. Tech. Info. Serv., Springfield, VA, 1983, p. 207.
42. S. P. Chou and N. M. Ghoniem, J. Nucl. Mater. 137, 63 (1985).
43. K. Fong, MFECC consultant, Private Communication (1984).
44. H. L. Bay, J. Roth and J. Bohdansky, J. Appl. Phys. 48, 4722 (1977).
45. D. Rosenberg and G.K. Wehner, J. Appl. Phys. 33, 1842 (1962).
46. O. C. Yonts, Proc. Nucl. Fusion Reactor Conf., British Nuclear Society, Culham, 1969, p. 424.

47. A. K. Furr and C. R. Fingeld, J. Appl. Phys. 41, 1739 (1970).
48. K. A. Gschneider, Solid State Phys. 16, 275 (1964).
49. J. Roth, J. Bohdansky and W. Ottenberger, Garching Institute of Plasma Physics Report IPP 9/26 (1979).
50. W. O. Hofer, H. L. Bay and P. J. Martin, J. Nucl. Mater. 76, 56 (1978).
51. J. Bohdansky, J. Roth and M. K. Sihha, Proc. 9th Symp. on Fusion Technology, Garmisch (FRG), June 1976, Pergamon Press, Oxford, 1976, p. 541.
52. J. Bohdansky, J. Roth and W. Ottenberger, J. Nucl. Mater. 76, 163 (1978).
53. J. Roth, J. Bohdansky and W. Poschenrieder, J. Nucl. Mater. 63, 222 (1976).
54. G. L. Nelson and R. Bastasz, J. Vac. Sci. Technol. 20, 498 (1982).
55. C. Ferro, E. Franconi, A. Neri and F. Brossa, J. Nucl. Mater. 101, 224 (1981).
56. E. Franconi and C. Ferro, J. Nucl. Mater. 128/129, 929 (1984).
57. K. Oishi, Y. Kumushiko, A. Fujimore and S. Usami, J. Nucl. Mater. 128/129, 934 (1984).
58. S. P. Chou, Ph.D. thesis, University of California Los Angeles Report ENG-86-13/PPG-939 (1986).
59. S. P. Chou and N. M. Ghoniem, J. Nucl. Mater. 141/143, to be published.
60. R. Martin and N. M. Ghoniem, University of California Los Angeles Report ENG-86-46/PPG-1024, to be published.

FUTURE WORK

The TRIPOS Code will be applied to problems of cascade structure and interaction with microstructural features in first wall alloys.

CALCULATIONS FOR ISOTOPICALLY-TAILORED CERAMICS IN FISSION AND FUSION REACTORS -R. J. LaBauve, R. J. Livak, and F. W. Clinard, Jr. (Los Alamos National Laboratory)

OBJECTIVE

This work was done to calculate the isotopic compositions of sialon and alumina required to simulate the radiation response of these ceramics in the first wall of the STARFIRE fusion reactor by exposure in the HFIR reactor at Oak Ridge National Laboratory.

SUMMARY

To aid in the design of an isotopically-tailored ceramic experiment in HFIR, calculations have been made to determine the amount of ^{15}N and ^{17}O needed in $Si_3Al_3O_3N_5$ and ^{17}O needed in Al_2O_3 to simulate the 14 MeV fusion neutron response of these ceramics when irradiated with fission neutrons. The calculations were performed using the REAC computer code developed at Hanford Engineering Development Laboratory, and the gas production and damage nuclear data needed were produced with a Los Alamos code. Although the damage data are more appropriate for metals, it is assumed that the comparison of the gas-to-damage ratios in the two reactors is valid. Calculations indicate that 57% ^{17}O and 90.6% ^{15}Ni in sialon and 17.9% ^{17}O in alumina would be adequate for the simulation.

PROGRESS AND STATUS

Introduction

Development of improved ceramics for fusion applications is limited by the lack of high-flux, 14 MeV fusion neutron sources for the irradiation of candidate materials. Fission reactors with lower-energy neutron spectra are used to determine materials' response to neutron damage. Studies modelling the damage response of ionic solids [1] have shown that the relative damage to the anion and cation sublattices can be dependent on the incident neutron energy. Other consequences of the differences in neutron energies have been discussed by Clinard. [2] These may be summarized by noting that fusion neutron damage will induce:

(a) a higher ratio of ionizing to displacive energy deposition,
(b) altered displacement damage events in the cascades,
(c) much greater production of transmutation-induced impurities (most importantly, H and He).

The last effect is expected to be the most significant, and Table 1 gives some calculated results for transmutation products generated in two ceramics at the first wall of a fusion device. [3] The gas production of He and H are orders of magnitude higher in the fusion neutron spectrum relative to fission neutrons. Various mechanisms can be postulated by which transmutation-induced gases worsen (or alternatively, alleviate) damage effects. For example, self-damage of PuO_2 produces He leading to the formation of lenticular grain boundary bubbles that may degrade the mechanical properties. [4] In addition, the transmutation-induced metallic impurities (e.g., carbon) may degrade the electrical and thermal properties of the irradiated ceramics. Thus final evaluation of a ceramic's usefulness for a given fusion reactor application must await results of either high-dose fusion neutron irradiation tests or tests on isotopically-tailored ceramics in which transmutation effects can be simulated. [2]

Table 1: Transmutation products in the first wall of a fusion device (appm at 2 MW-yr/m²)

	Si_3N_4	Al_2O_3
Hydrogen	1,334	912
Carbon	656	1,248
Nitrogen	--	68
Helium	1,516	1,574
Aluminum	142	4
Magnesium	910	868

Procedure

The calculations reported here were done to identify the appropriate isotope enrichment levels needed to reproduce in a mixed thermal-and-fast fission neutron spectrum the characteristic gas-production to displacements-per-atom (dpa) ratio typical for the first wall of a fusion device. In the approach taken here, the thermal neutron reactions ^{17}O (n,α) ^{14}C and ^{14}N (n,p) ^{14}C are exploited to produce controlled amounts of He and H. In the latter case, since ^{14}N transmutes too readily, ^{15}N must be used partially to suppress the reaction. Alumina (Al_2O_3) and sialon ($Si_3Al_3O_3N_5$) were selected as representative ceramics for an irradiation experiment in the High Flux Isotope Reactor (HFIR) at Oak Ridge National Laboratory. The calculations were done to determine the fractional contents of the ^{15}N and ^{17}O isotopes needed to simulate the gas-to-damage ratios expected in normal sialon and alumina when used at the first wall of the STARFIRE fusion reactor design. The fission neutron irradiation experiment will be done in the PTP (peripheral test position) zone near the central plane of HFIR.

The REAC computer code system was used to do these reported calculations. This code was designed to calculate activation rates, dose rates, delayed photon production yields, transmutation yields, and reaction rates for specific reactions for a variety of materials in many different environments and for various residence and cooling times. This system was chosen for its "user-friendly" input, availability of HFIR PTP and STARFIRE first wall spectra in the flux library, availability of damage and gas production data in the cross-section library, and ease with which the material library could be changed for running problems with different isotopic fractions.

The isotopic contents of normal sialon and alumina are given in Table 2. Note, in particular, that the atomic weights of the constituents differ by no more than a factor of two. This is important, as it is the opinion of other scientists [1] that, for this condition, the averaging over the constituents for dpa, as performed by the REAC code, is approximately valid for ceramics even though the underlying theory [5] is more appropriate for metals. Furthermore, inaccuracies due to approximations tend to cancel in the ratio comparisons used in this work.

Table 2. Isotope fractions in normal $Si_3Al_3O_3N_5$ and Al_2O_3

Isotope	Sialon fractions	Alumina fractions
^{14}N	3.558×10^{-1}	----
^{15}N	1.320×10^{-3}	----
Total N	0.3571	----
^{16}O	2.138×10^{-1}	5.986×10^{-1}
^{17}O	8.000×10^{-5}	2.000×10^{-4}
^{18}O	4.300×10^{-4}	1.200×10^{-3}
Total O	0.2144	0.6000
^{27}Al	2.143×10^{-1}	4.000×10^{-1}
Total Al	0.2143	0.4000
^{28}Si	1.976×10^{-1}	----
^{29}Si	1.001×10^{-2}	----
^{30}Si	6.640×10^{-3}	----
Total Si	0.2142	----

Results and discussion

The nuclear cross section data for nitrogen and oxygen isotopic reactions contributing to hydrogen and helium production were taken from the REAC library CROSS. These data were generated by the NJOY code system using ENDF/B-V [6] basic nuclear data as input. Comparison of the threshold energies of the cross sections indicate that the H-production can be most easily adjusted with the $^{15}N/N$ ratio; whereas, both the $^{15}N/N$ and $^{17}O/O$ ratios can be used to adjust the He-production.

REAC calculational results are shown in Tables 3 and 4. As indicated in these tables, iterative calculations were done with various isotope contents in order to match the calculated gas/damage ratios with the corresponding ratios at the first wall of the STARFIRE device. The last line of each table gives the

required isotope content needed to achieve the desired gas/damage ratios. The units of the calculated values for the gas/damage ratios are relative but comparable for all cases. Exposure times and power levels cancel out in the ratios, and the conversion of displacement damage-energy to displacement damage (dpa) is ignored because the conversion factors for the several constituents in the two ceramics are about the same. As given in ref. 5, this factor is $0.8/2E_d$ where E_d is the Lindhard cutoff energy required to displace the atom. The assumed values for E_d are 25, 27, 30, and 30 eV for Si, Al, O, and N, respectively. [5]

Table 3. Gas/damage ratio calculations for $Si_3Al_3O_3N_5$

Reactor/region	$^{15}N/N$	$^{17}O/O$	H/damage	He/damage
STARFIRE/1st wall	Normal	Normal	94.9	61.8
HFIR/PTP	Normal	Normal	998.5	25.7
HFIR/PTP	0.87	0.55	131.7	60.5
HFIR/PTP	0.92	0.55	81.7	59.3
HFIR/PTP	0.91	0.55	91.5	59.4
HFIR/PTP	0.908	0.55	93.7	59.5
HFIR/PTP	0.92	0.50	70.4	55.6
HFIR/PTP	0.908	0.50	93.7	54.6
HFIR/PTP	0.906	0.57	95.7	61.8

Table 4. Gas/damage ratio calculations for Al_2O_3

Reactor/region	$^{15}N/N$	$^{17}O/O$	H/damage	He/damage
STARFIRE/1st wall	---	Normal	28.6	58.0
HFIR/PTP	---	Normal	1.4	4.7
HFIR/PTP	---	0.55	1.4	171.4
HFIR/PTP	---	0.17	1.4	55.5
HFIR/PTP	---	0.26	1.4	83.3
HFIR/PTP	---	0.179	1.4	58.8

As indicated in Table 3, the ^{15}N content of the sialon was mainly adjusted by the H/damage ratio; whereas, the ^{17}O content was adjusted with the He/damage ratio. The final isotopic percentages for simulation of the sialon's response to fusion neutron effects are 90.6% ^{15}N and 57.0% ^{17}O.

The results for alumina are given in Table 4. Only the He/damage ratio can be matched since, as indicated above, the H/damage ration is practically impossible to adjust with ^{17}O. Note that the fusion neutron simulation is achieved with 17.9% ^{17}O.

CONCLUSIONS

Computer calculations were done using the REAC code system to design an irradiation experiment in HFIR to simulate the gas-to-damage ratios expected for two ceramics located at the first wall of a fusion reactor. The results of these calculations indicate the isotopic composition of sialon is to be 90.6% ^{15}N and 57.0% ^{15}O, and for alumina the composition is to be 17.9% ^{17}O.

FUTURE WORK

An experimental program is being planned to irradiate isotopically-tailored Al_2O_3, AlN, and AlON samples in HFIR at ORNL. The post-irradiation examination will include microstructural characterization and measurement of physical and mechanical properties.

REFERENCES

1. D. M. Parkin and C.A. Coulter, "Displacement Functions for Diatomic Materials," J. Nucl. Mater. 85 & 86, 611-615 (1979).

2. F. W. Clinard, Jr., "Ceramics for Applications in Fusion Systems," J. Nucl. Mater. 85 & 86, 393-404 (1979).

3. L. H. Rovner and G. R. Hopkins, "Ceramic Materials for Fusion," Nucl. Tech. 29(6), 274-302 (1976).

4. B. A. Mueller, D. D. Rohr and R. N. R. Mulford, "Helium Release and Microstructural Changes in $^{238}PuO_2$", Report LA-5524, Los Alamos National Laboratory, Los Alamos, NM, April 1974.

5. R. E. MacFarlane, D. W. Muir, and F. M. Mann, "Radiation Damage Calculations with NJOY," J. Nucl. Mater. 122 & 123, 1041-1046 (1984).

6. R. Kinsey, Comp., "ENDF-201: ENDF/B Summary Documentation," Report BNL-NCS-17541 (ENDF-201), 3rd Ed. (ENDF/B-V), Brookhaven National Laboratory, Stony Brook, NY, 1979.

REAC2 ACTIVATION AND TRANSMUTATION COMPUTER CODE SYSTEM - F. M. Mann (Westinghouse Hanford Company)

OBJECTIVE

The objective of this work is to develop a computer code system which can quickly and easily calculate the transmutation and activation of materials in nuclear environments.

SUMMARY

The initial release of the REAC2 transmutation and activation code system is now available for use at the Magnetic Fusion Energy (MFE) Computer Center. REAC2 is over an order of magnitude faster than its predecessor and is easier to use.

PROGRESS AND STATUS

Introduction

With the increased interest in reducing the long term activation of materials exposed to neutrons from fusion of d+t, better codes and nuclear data are needed. Similarly, the added interest of the effect of the transmutation of elements on material properties points in the same direction.

For many years, Hanford Engineering Development Laboratory (HEDL) and other laboratories have used the REAC code[1] and its libraries for such transmutation and activation calculations. When the cross section and decay data libraries were expanded, the limitations of REAC became too evident. Therefore a new code system, REAC2, is being developed.

Discussion

A series of computer codes have been written to form the nucleus of the REAC2 computer code system. The main code calculates the transmutation of isotopes as a function of time and writes the results to a computer file. A second code reads the file and user instructions on formatting, on unit selection, and on sorting order and produces activation and/or element transmutation as desired. Other codes transform the needed libraries from people readable format into a format which the computer can access much faster. Other codes will be written in the future which will generate plots and determine major reaction paths.

Each of the new programs has been written in structured and modular FORTRAN-77 to allow easier maintenance and improvement. Instead of the sequential access of REAC, REAC2 uses direct access input and output whenever possible. The input no longer is required to be in fixed field format and practically all information can be inferred from default values. Many more input checks are in the code to insure consistent input. The methodology of REAC2 is nearly the same as REAC with the only major changes being that more decay generations can be followed (6 versus 2) in a time step and that round off and truncation problems have been lessened.

The information in the data libraries is the same as the latest version of REAC. Thus test runs of REAC2 were directly compared with REAC with excellent agreement found. The major difference was that the REAC2 ran over a factor of ten faster.

CONCLUSIONS

The initial release of the REAC2 system is now operational at the Magnetic Energy Fusion Computing Center. Input instructions, codes, and libraries are available through the mass storage system.

FUTURE WORK

The system will be expanded to allow the determination of reaction paths and the generations of plots. The data libraries will be improved to allow direct calculation of limits for near surface burial as well as heat deposition.

REFERENCES

1. F. M. Mann "Transmutation of Alloys in MFE Facilities as Calculated by REAC (A Computer Code System for Activation and Transmutation)", HEDL-TME 81-37, Westinghouse Hanford Company, Richland, WA, 1981.

2. F. M. Mann "Cross Sections for Reduced Activation Studies", p. 18 in Damage Analysis and Fundamental Studies Quarterly Progress Report, February 1985, DOE/ER-0046/20, U. S. Department of Energy, Office of Fusion Energy.

ACTIVATION OF STRUCTURAL ALLOYS IN FUSION REACTOR MAGNETS - F. M. Mann and D. G. Doran (Westinghouse Hanford Company)

OBJECTIVE

The objective of the work is to calculate the short and long term activation of elements likely to be in the magnet region of a Tokomak reactor.

SUMMARY

Using the STARFIRE conceptual design, niobium is the only element likely to cause problems in meeting Class C near surface burial criteria. Although the materials in the outboard magnet will not cause dose concerns for maintenance purposes in the STARFIRE design, the radiation dose from the inboard magnet position is quite high.

PROGRESS AND STATUS

Introduction

Although activation problems are usually associated with the first wall and blanket of a fusion device, the regions experiencing the highest neutron flux, activation of materials in all regions in a fusion device must be investigated. The REAC2 code system[1] was used to calculate the activation of structural and magnet materials experiencing 30 full power year exposure at the shield-magnet interface of the STARFIRE conceptual fusion device.

Methods and Results

The STARFIRE conceptual tokamak design[2] was chosen because of the extensive analyses performed on that device and because fluxes for the magnet region are available. Of the conceptual reactor designs studied with the REAC code system, STARFIRE produces the highest activation in wall/blanket materials per unit fluence. Two points were taken for analysis: the inboard interface between the shield and magnet (the leg of the toroidal magnet nearest the centerpost of the toroidal machine--in the hole of the donut) and the outboard interface between the shield and magnet (the leg of the magnet on the outside of the donut); both points are on the machine's midplane. Although the flux may be higher at points off the midplane, it should not be significantly more so. The flux drops rapidly as one progresses through the magnet and also become softer. The accuracy of the flux calculation at the deep penetrations of interest here may not be high. All things considered, the activation calculated in this exercise can be taken as an approximate upper bound for both inboard and outboard magnet components.

The shield thickness at the inboard position is the minimum required to protect the superconducting magnet. The shield at the outboard position was designed to provide biological shielding as well. This results in a flux at the inboard position that is a factor of 50 larger than at the corresponding outboard position.

The REAC2 code system is an outgrowth of the earlier REAC code system. The latter has been used for fusion first wall and blanket activation studies, for studies of transmutation in facilities used to test fusion materials, and for studies of shielding for accelerators and for transportation of radioactive substances. Cross sections are based on the evaluated nuclear data files, ENDF/B-V[3], wherever possible, and extended with other evaluations such as the ACTL[4] library or with systematics elsewhere. Because of the soft spectrum in this problem, activation uncertainties arising from cross section uncertainties should be less than 50%. Decay data were taken from ENDF/B-V and the Table of Isotopes[5].

The calculations were performed for each of 20 elements (aluminum, boron, carbon, chromium, cobalt, copper, iron, manganese, molybdenum, nickel, niobium, nitrogen, phosphorus, silicon, sulfur, tantalum, tin, titanium, tungsten, and vanadium) and the results added to obtain values for the complex structural alloys. The 30 full power year lifetime of STARFIRE was assumed, implying a total fluence of 1.9e18 n/cm**2 (1.1e18 n/cm**2 with energy above 0.1 MeV) at the inboard magnet position and a total fluence of 3.4e16 n/cm**2 (a fast fluence of 1.4e16 n/cm**2) at the outboard position. To include the effect of multi-step reactions (a very minor effect in this case), the 30 year exposure was broken into six 5 year segments. Results for cooling times of zero, one, and ten hours were calculated as were results for one day, one week, one year, and ten years. The values for one day cooling are shown in Table 1, while the results for ten years are shown in Table 2.

Discussion

For the short cooling time of one day, where the main concern is radiation dose due to maintenance, the values are very low for all materials for the outer magnet position. If a 2.5 mrem/hr limit is

assumed, then amounts of structural materials on the order of hundreds of kilograms can be tolerated.

This calculation assumes a point source and no attenuation of the photons due to the material itself. Thus the results are very conservative for a person standing one meter away from a large magnet. Only with tantalum and cobalt (which have a dose rate four orders of magnitude greater than the steels) would one be concerned. It should be noted that the type of steel is relatively unimportant. For the cases studied here, the results vary by less than factor of five. These conclusions also are true for shorter cooling times, although the allowable mass does decrease especially for high manganese steels (by a factor of about 300), due to the production of Mn-56 which has a 150 minute half-life. These results are consistent with the STARFIRE study. One criterion for the outboard shield design was that the radiation level in the reactor hall after 24 hours would be less than 2.5 mrem/hr.

For the inboard position, however, dose rates are very much higher. In fact, only about 2 grams of tantalum or cobalt or 2.5 kilograms of the various steels would give doses above NRC limits if a person one meter away were exposed 40 hours/week. That is why all components of STARFIRE are designed so that maintenance can be done remotely.

The large difference between the inner and outer positions results not only from the greater neutron flux at the inner position but also from the neutron spectrum being more energetic, causing a greater number of radioactive isotopes per neutron. For example, for high manganese steels the major reaction of interest is Mn-55(n,2n)Mn-54, while for high nickel steels the major reaction is Ni-58(n,p)Co-58, both of which are high energy reactions. Thus the dose rate increases by a factor of about 150 although the flux is only 50 times higher.

Limitations on waste disposal and recycling are due to the long-lived radioactive isotopes. Using NRC regulations for radioactive waste disposal, supplemented by some other work[6], only niobium is found to be a concern for either spatial position. Pure niobium subjected to a 30 year exposure at the inboard position would have to be diluted by a factor of 16 to meet 10 CFR 61 regulations for near surface burial, due to the Nb-93(n,gamma) reaction. For the outboard position, pure niobium would fall just below the limit.

It should be stressed that no other likely material (except for molybdenum which is a factor of three below the limit at the high flux inboard magnet position) is even close to the NRC limit for near-surface disposal even at the higher flux inboard magnet position. Thus, current waste disposal criteria do not place any restrictions on structural magnet materials in STARFIRE.

CONCLUSIONS

In summary, activation of materials in the outboard magnet region of STARFIRE seems unimportant in terms of personnel radiation dose or waste disposal, with the possible exception of the disposal of niobium. For the magnet inside the core of the torus, however, near-surface waste disposal could be difficult for components containing niobium as a major constituent, such as candidate superconducting materials. Perhaps more importantly, any recycling of such material would require remote operations.

Thus there may be a tradeoff to consider between increased capital costs for thicker shielding at the inboard position in order to facilitate disposition of the niobium-containing material at decommissioning.

FUTURE WORK

Calculations for different conceptual designs will be performed with particular emphasis on designs which use different criteria for the determination of the maximum flux at the shield magnet interface.

Table 1. Thirty year STARFIRE magnet calculations, one day cooling

	Outboard Magnet		Inboard Magnet	
Element	Decay Rate (Curie/g)	Dose Rates at 1 m (rem/g-hr)	Decay Rate (Curie/g)	Dose Rates at 1 m (rem/g-hr)
Aluminum	1.51e-9	2.89e-9	7.93e-7	1.52e-6
Boron	4.15e-9	0.	1.50e-5	0.
Carbon	1.81e-13	0.	1.03e-11	0.
Chromium	1.28e-7	2.12e-8	4.47e-6	7.58e-7
Cobalt	5.07e-5	6.89e-5	1.74e-3	2.36e-3
Copper	3.45e-7	4.72e-8	1.46e-5	2.94e-6
Iron	9.91e-8	1.37e-9	5.05e-6	2.69e-7
Manganese	1.65e-8	1.17e-8	4.56e-6	2.43e-6
Molybdenum	6.71e-7	8.96e-8	2.78e-5	3.76e-6

Table 1 (continued)

Element	Outboard Magnet Decay Rate (Curie/g)	Outboard Magnet Dose Rates at 1 m (rem/g-hr)	Inboard Magnet Decay Rate (Curie/g)	Inboard Magnet Dose Rates at 1 m (rem/g-hr)
Nickel	4.52e-8	1.29e-8	1.53e-5	7.00e-6
Niobium	4.32e-8	1.13e-8	8.96e-6	1.70e-6
Nitrogen	6.62e-9	0.	1.27e-6	0.
Phosphorus	1.42e-7	7.36e-15	7.41e-6	3.97e-12
Silicon	1.09e-10	7.85e-13	5.41e-8	9.23e-10
Sulfur	2.87e-8	5.17e-16	1.00e-5	2.68e-13
Tantalum	5.95e-5	4.65e-5	1.68e-3	1.29e-3
Tin	1.03e-6	9.00e-8	5.46e-5	4.35e-6
Titanium	2.09e-9	1.88e-9	1.11e-6	1.00e-6
Tungsten	9.17e-6	2.16e-8	2.88e-4	1.28e-4
Vanadium	2.27e-10	3.12e-10	1.18e-7	1.62e-7

Material	Outboard Magnet Decay Rate (Curie/g)	Outboard Magnet Dose Rates at 1 m (rem/g-hr)	Inboard Magnet Decay Rate (Curie/g)	Inboard Magnet Dose Rates at 1 m (rem/g-hr)
57.7Fe-25Mn-1Ni-15Cr-0.2N-0.1Nb-1Cu				
Iron	5.72e-8	7.91e-10	2.92e-6	1.55e-7
Manganese	4.13e-9	2.93e-9	1.14e-6	6.08e-7
Nickel	4.52e-10	1.29e-10	1.53e-7	7.00e-8
Chromium	1.92e-8	3.18e-9	6.71e-7	1.14e-7
Nitrogen	1.32e-11	0.	2.54e-9	0.
Niobium	4.32e-11	1.13e-11	8.96e-9	1.70e-9
Copper	3.45e-9	4.72e-10	1.46e-7	2.94e-8
Total	8.40e-8	7.51e-9	5.03e-6	9.78e-7
Fe-22Mn-5Ni-13Cr-0.2N-0.3Si				
Iron	5.90e-8	8.15e-10	2.02e-7	4.28e-8
Manganese	3.63e-9	2.57e-9	1.00e-6	5.35e-7
Nickel	2.26e-9	6.45e-10	7.65e-7	3.50e-7
Chromium	1.66e-8	2.76e-9	5.81e-7	9.85e-8
Nitrogen	1.32e-11	0.	2.54e-9	0.
Silicon	3.27e-13	2.36e-15	1.62e-10	2.77e-12
Total	8.15e-8	6.79e-9	2.55e-6	1.03e-6
60.8Fe-10Mn-12Ni-12Cr-5Mo-0.2N				
Iron	6.03e-8	8.33e-10	3.07e-6	1.64e-7
Manganese	1.65e-9	1.17e-9	4.56e-7	2.43e-7
Nickel	5.42e-9	1.55e-9	1.84e-6	8.40e-7
Chromium	1.54e-8	2.54e-9	5.36e-7	9.10e-8
Molybdenum	3.36e-8	4.48e-9	1.39e-6	1.88e-7
Nitrogen	1.32e-11	0.	2.54e-9	0.
Total	1.16e-7	1.06e-8	7.29e-6	1.36e-6
60.4Fe-1Mn-13Ni-25Cr-0.3N-0.3Si				
Iron	5.99e-8	8.27e-10	3.05e-6	1.62e-7
Manganese	1.65e-10	1.17e-10	4.56e-8	2.43e-8
Nickel	5.88e-9	1.68e-9	1.99e-6	9.10e-7
Chromium	3.20e-8	5.30e-9	1.12e-6	1.90e-7
Nitrogen	1.99e-11	0.	3.81e-9	0.
Silicon	3.27e-13	2.36e-15	1.62e-10	2.77e-12
Total	9.79e-8	7.92e-9	6.21e-6	1.29e-6

Table 2. Thirty year STARFIRE magnet calculations ten year cooling

Element	Outboard Magnet		Inboard Magnet	
	Decay Rate (Curie/g)	Fraction of Class C Waste Disposal Limit	Decay Rate (Curie/g)	Fraction of Class C Waste Disposal Limit
Aluminum	1.10e-12	2.7e-7	5.78e-10	1.4e-6
Boron	2.36e-9	3.9e-11	8.54e-6	2.0e-8
Carbon	1.81e-13	4.1e-10	1.03e-11	2.3e-8
Chromium	1.93e-10	*	1.01e-7	*
Cobalt	1.36e-4	*	4.66e-3	2.5e-11
Copper	8.87e-10	*	4.39e-7	1.8e-4
Iron	7.29e-9	3.3e-9	3.40e-7	7.2e-8
Manganese	2.50e-12	*	1.29e-9	*
Molybdenum	6.80e-9	1.4e-3	2.87e-7	3.4e-1
Nickel	1.71e-8	2.8e-5	7.65e-7	5.5e-4
Niobium	2.70e-8	3.7e-1	4.20e-6	1.6e+1
Nitrogen	5.75e-9	4.6e-6	8.03e-7	1.8e-4
Phosphorus	2.29e-9	*	1.18e-6	*
Silicon	5.79e-11	*	3.01e-8	*
Sulfur	1.81e-11	5.2e-10	9.37e-9	2.6e-7
Tantalum	2.82e-12	*	1.47e-9	*
Tin	1.05e-7	*	4.53e-6	*
Titanium	1.82e-11	*	9.45e-9	*
Tungsten	1.90e-12	*	9.84e-10	*
Vanadium	4.63e-12	*	2.41e-9	*

Material	Outboard Magnet		Inboard Magnet	
	Decay Rate (Curie/g)	Fraction of Class C Waste Disposal Limit	Decay Rate (Curie/g)	Fraction of Class C Waste Disposal Limit
57.7Fe-25Mn-1Ni-15Cr-0.2N-0.1Nb-1Cu				
Iron	4.21e-9	2.0e-9	1.96e-7	4.1e-8
Manganese	6.25e-13	*	3.00e-10	*
Nickel	1.71e-10	2.8e-7	7.65e-9	5.5e-6
Chromium	2.90e-11	*	1.52e-8	*
Nitrogen	1.15e-11	9.2e-9	1.61e-9	*
Niobium	2.70e-9	3.7e-4	4.20e-9	1.6e-2
Copper	8.87e-12	*	4.39e-9	1.8e-6
Total	7.12e-9	3.7e-4	2.29e-7	1.6e-2
Fe-22Mn-5Ni-13Cr-0.2N-0.3Si				
Iron	4.34e-9	2.0e-9	2.02e-7	4.3e-8
Manganese	5.50e-13	*	2.84e-10	*
Nickel	8.55e-10	1.4e-6	3.82e-8	2.8e-5
Chromium	2.51e-11	*	1.31e-8	*
Nitrogen	1.15e-11	9.2e-9	1.61e-9	*
Silicon	1.74e-13	*	9.03e-11	*
Total	5.23e-9	1.4e-6	2.55e-7	2.8e-5
60.8Fe-10Mn-12Ni-12Cr-5Mo-0.2N				
Iron	4.43e-9	2.0e-9	2.07e-7	4.4e-8
Manganese	2.50e-13	*	1.29e-10	*
Nickel	2.05e-9	3.4e-6	9.18e-8	6.6e-5
Chromium	2.32e-11	*	1.21e-8	*
Molybdenum	3.40e-10	7.0e-5	1.44e-8	1.7e-2
Nitrogen	1.15e-11	9.2e-9	1.61e-9	*
Total	6.85e-9	7.3e-5	3.27e-7	1.7e-2
60.4Fe-1Mn-13Ni-25Cr-0.3N-0.3Si				
Iron	1.10e-9	2.0e-9	2.05e-7	4.3e-8
Manganese	2.50e-14	*	1.29e-10	*
Nickel	2.22e-9	3.6e-6	9.95e-8	7.2e-5
Chromium	4.83e-11	*	2.53e-8	*
Nitrogen	1.73e-11	1.4e-8	2.41e-9	5.4e-7

Table 2 (continued)

Material	Outboard Magnet		Inboard Magnet	
	Decay Rate (Curie/g)	Fraction of Class C Waste Disposal Limit	Decay Rate (Curie/g)	Fraction of Class C Waste Disposal Limit
Silicon	1.74e-13	*	9.03e-11	*
Total	3.37e-9	3.6e-6	3.32e-7	7.2e-5

REFERENCES

1. REAC2 is an outgrowth of REAC, which is documented in F. M. Mann, "Transmutation of Alloys in MFE Facilities as Calculated by REAC (A Computer Code System for Activation and Transmutation)," HEDL-TME 81-37, Westinghouse Hanford Company, Richland, WA, 1982.

2. F. M. Mann "Cross Sections for Reduced Activation Studies" p. 18 in Damage Analysis and Fundamental Studies, A Quarterly Progress Report, October-December, 1984, DOE/ER-0046/20, p. 18, U.S. Department of Energy, Office of Fusion Energy, 1985.

3. "STARFIRE- A Commercial Tokamak Fusion Power Plant Study", ANL/FPP-80-1, Argonne National Laboratory, Argonne, IL, 1980.

3. R. Kinsey, Compiler, "ENDF/B Summary Documentation (ENDF-201)", Third Edition (ENDF/B-V), BNL-NCS-17541, Brookhaven National Laboratory, Upton, New York, (1979). Version V.2 was released in 1982-3.

4. M. A. Gardner and R. J. Howerton, "ACTL: Evaluated Nuclear Activation Cross Section Library - Evaluation Techniques and Reaction Index", UCRL-50400, Vol. 18, Lawrence Livermore National Laboratory, Livermore, CA., 1978.

5. C. M. Lederer and V.S. Shirley (editors), "Table of Isotopes; Seventh Edition", John Wiley and Sons, New York, 1978.

6. W. E. Kennedy, Jr. and R. A. Peloquin, "Potential Low Level Waste Disposal Limits for Activation Production from Fusion", PNL-4844, Pacific Northwest Laboratories, Richland, WA (1983).

3. MATERIALS ENGINEERING AND DESIGN REQUIREMENTS

MATERIALS HANDBOOK FOR FUSION ENERGY SYSTEMS - J. W. Davis (McDonnell Douglas Astronautics Company-St. Louis Division)

OBJECTIVE

To provide a consistent and authoritative source of material property data for use by the fusion community in concept evaluation, design, and performance/verification studies of the various fusion energy systems. A second objective is the early identification of areas in the materials data base where insufficient information or voids exist.

SUMMARY

The effort during this reporting period has been directed towards developing the supporting documentation data sheets in preparation for distribution to current handbook holders. These pages are planned for distribution early in 1987. With the release of these pages will constitute the first step towards establishing a data base of fusion developed experimental data.

PROGRESS AND STATUS

The materials handbook has now been expanded to two volumes. Volume 1 contains the basic engineering information, while Volume 2 contains the supporting documentation that was used to develop the data pages found in Volume 1. When the handbook was originally issued it was decided that only the engineering volume (Volume 1) should be issued, since the primary interest was on engineering data. The supporting documentation was held by the Handbook Coordinator and released to those handbook holders who requested the information in order to revise existing data pages. However, with the increasing interest in data bases it was decided to release the supporting documentation to all handbook holders so that they would be aware of the extent of the current data base along with the gaps in the data. It is hoped that this information will help to coordinate some of the experimental effort. In addition these data sets could also be useful in the development of an international materials properties data base.

Volume 2 has been mailed to all qualified handbook holders. Any handbook holders who have not received this volume should contact the Handbook coordinator with their current address and a copy will be sent to them. Current effort has been directed to typing and preparing the supporting data sheets for inclusion in this volume. It is estimated that these pages will be distributed in the first quarter of 1987. In addition, a 12th publication package is currently being prepared for Volume 1. Contained in this package will be data pages on PCA stainless steel, copper alloys, and HT-9.

4. FUNDAMENTAL MECHANICAL BEHAVIOR

MECHANICAL PROPERTIES OF FUSION REACTOR MATERIALS

A Workshop Held on April 18, 1986
in Conjunction with the
Second International Conference
on Fusion Reactor Materials
Chicago, Illinois

Organized by:

Russell H. Jones
Pacific Northwest Laboratory
Richland, Washington.

and:

G. E. Lucas
University of California
Santa Barbara, California.

TABLE OF CONTENTS

PREFACE

The workshop on Mechanical Properties of Fusion Reactor Materials was held in conjunction with the Second International Conference on Fusion Reactor Materials to encourage international representation in this workshop series[a]. The meeting was held in Chicago, Illinois in April 1986, with participants from Japan, Europe and the United States. The topics covered were: 1) Flow processes, 2) Time dependent crack growth, 3) Time independent crack growth/brittle fracture, and 4) Environment assisted crack growth. The background, status, and recommended research are summarized in this report for each of the workshop topics.

The objectives of the workshop were to: 1) identify critical issues, 2) evaluate the status of the data and knowledge base for these issues, and 3) identify potential US/Japan/European collaboration in this area. Item number 1 was covered the most thoroughly, item number 2 was covered only partially, and there was insufficient time to address item number 3. Critical issues in materials behavior, structure-property relationships, and modeling were discussed and identified. Small specimen techniques were discussed as they pertained to a particular topic, but were not discussed as a separate topic.

Interest in convening a similar workshop at the Third International Conference on Fusion Reactor Materials to be held in the Fall of 1987 was expressed. Dr. B. N. Singh agreed to present this idea to the organizing committee for this meeting.

(a) "Fusion Environment Sensitive Flow and Fracture Processes", organized and edited by R. H. Jones. Report of workshop held August 1980 for the Fundamental Mechanical Behavior Sub-Task of the Damage Analysis and Fundamental Studies Task Group, DOE/ER-0046/4, Vol. 2, Feb. 1981, 49 pages.

"Fusion Environment Sensitive Flow and Fracture Processes", organized and edited by R. H. Jones. Report of workshop held August 1982 for the Fundamental Mechanical Behavior Sub-Task of the Damage Analysis and Fundamental Studies Task Group, Quarterly Report, Jan.-March 1983, 53 pages.

I. WORKSHOP AGENDA

Friday, April 18:

8:30 a.m. Flow Processes: - Creep - Hardening	Leader - R. L. Simons Westinghouse Hanford Co.
10:30 a.m. Time Dependent Crack Growth: - Creep-Rupture - Fatigue - Creep-Fatigue	Leader - G. E. Lucas University of California, Santa Barbara
12:30 p.m. Lunch	
2:00 p.m. Time Independent Fracture: - Cleavage - Ductile Fracture	Leader - G. E. Lucas
4:00 p.m. Environment Assisted Crack Growth: - Stress Corrosion - Corrosion Fatigue - Hydrogen Embrittlement	Leader - R. H. Jones Battelle-Northwest

II. TITLES OF SHORT PRESENTATIONS

1. Hardening and/or Creep of Fusion Reactor Materials Naohiro Igata, Professor Materials Science, University of Tokyo, Metals and Material Science, Japan.

2. High Temperature Tensile Properties of Copper-Chromium-Zirconium Alloys, G. Piatti, ISPRA, Materials Science Division, Italy.

3. Effect of Helium on Mechanical Properties, H. Schroeder, Inst. fur Festkorperforschung der Kernforschungsanlage Julich, Federal Republic of Germany.

4. Creep Behavior of Fusion Reactor Materials, R. Puigh, Westinghouse, HEDL, Richland, WA.

5. Creep-Fatigue of Fusion Reactor Components, B. N. Singh, Riso National Laboratory, Denmark.

6. Helium Transport in Fusion Reactor Materials, N. M. Ghoniem, University of California at Los Angeles, School of Engineering and Applied Science, CA.

7. Radiation Anneal Embrittlement in Molybdenum Single Crystals, Katsunori Abe, Research Institute for Iron, Steel and Other Metals, Tohoku University, Sendai, Japan.

8. Size Effect on the Ductile-Brittle Transition of Notched Specimen, K. Kitajima, Research Institute for Applied Mechanics, Kyushu University, Japan.

9. Fracture Behavior of Manganese and Ferritic Steels Studied by the Instrumented Charpy Impact Tests and Mechanical Properties of High Manganese Austenitic Steels, Dr. Hiroyuki Yoshida, Research Reactor Institute, Kyoto University, Osaka, Japan.

10. Deformation and Fracture of Hydrides in Vanadium, H. Matsui, Tohoku University, Research Institute for Iron, Steel and Other Metals, Japan.

11. Hydrogen Embrittlement of Ferritic Steels, K. Kitajima, Kyushu University, Research Institute for Applied Mechanics, Japan.

III. WORKSHOP PARTICIPANTS

Prof. K. Abe
Res. Inst. for Iron Steel
and Other Metals
Tohoku University
Sendai 980
Japan

Dr. J. Boutard
CEN/Saclay
91191 Gif Sur Yvette
Saclay
France

Dr. D. Diercks
Argonne National Lab.
9700 South Cass Avenue
Argonne, IL 60439

Dr. D. G. Doran
Westinghouse Hanford Co.
WHC-A57
P.O. Box 1970
Richland, WA 99352

Dr. F. A. Garner
Westinghouse Hanford Co.
WHC-A58
P.O. Box 1970
Richland, WA 99352

Prof. N. M. Ghoniem
University of California
School Eng. & Applied Sci.
Boelter Hall
Los Angeles, CA 90024

Dr. Akinichi Hishinuma
Japan Atomic Energy Res. Inst.
Tokai Research Establishment
Tokai-mura, Naka-gun
Ibaraki-ken 319-11
Japan

Prof. Naohira Igata
University of Tokyo
Metals & Materials Science
3-1, Hongo 7-chome
Bunkyo-ku 113
Japan

Dr. Russell H. Jones
Pacific Northwest Laboratory
Materials & Sciences Dept.
P.O. Box 999
Richland, WA 99352

Prof. Michio Kiritani
Hokkaido University
Facility of Engineering
Kita-hu, Sapporo 060
Japan

Prof. Kazunori Kitajima
Kyushu University
Res. Inst. Applied Mechanics
6 Kasuga-Koen, Kasuga-shi
Fukuoka 816
Japan

Prof. G. E. Lucas
University of California
Dept. Chem. & Nucl. Engineer.
Santa Barbara, CA 93106

Prof. Hildeki Matsui
Research Institute Iron, Steel
and Other Metals
Tohoku University
2-1-1 Katahira
Sendai, 980
Japan

Dr. Masatoshi Okada
National Res. Inst. of Metals
Tsukuba Laboratories
1-2-1, Sengen, Sakura-Mura
Niihari-Gun, Ibaraki 305
Japan

Prof. G. Piatti
Commission European Communities
Joint Res. Centre - ISPRA
Materials Science DIvision
21020 Ispra
Italy

Dr. R. Puigh
Westinghouse Hanford Co.
WHC-A58
P.O. Box 1970
Richland, WA 99352

Dr. Herbert Schroeder
Inst. fur Festkorperforschung
de Kernforschungsanlage Julich
Postfach 1913
D-5170 Julich
Federal Republic Germany

Dr. R. L. Simons
Westinghouse Hanford Co.
WHC-A65
P.O. Box 1970
Richland, WA 99352

Dr. B. N. Singh
Riso National Laboratory
Postfach 49
DK-4000 Roskilde
Denmark

Prof. H. Yoshida
Research Reactor Institute
Kyoto University
Kumatori-cho, Senman-gun
Osaka, 590-04, Japan
Japan

IV. WORKSHOP SUMMARIES AND RECOMMENDATIONS

1. FLOW PROCESSES: R. L. Simons

A. Summary

Flow processes of fusion reactor materials will affect dimensional stability, stress, and fracture of reactor components. Included in this discussion was creep and hardening processes. Discussion focused on data base development, mechanism modeling, key experiments, and small specimen issues.

1. Data Bases

Austenitic stainless steels have received considerable attention in the last fifteen years, and consequently, have accumulated a substantial data base for material design life predictions. The ferritic and vanadium alloys have had less time to accumulate neutron exposures, and consequently, the neutron exposure and irradiation temperature data base is small. The irradiation temperature regime lacking data for all alloy classes is between 100 and 350°C. This temperature regime is below minimum liquid metal reactor temperature, and consequently, this portion of the irradiation temperature and neutron exposure data base will have to be filled in by water reactor irradiations, such as in HFIR. A near term damage fluence goal is in the range of 100-200 dpa which can be obtained in four to six years in high flux reactors such as FFTF and HFIR.

Two additional alloy classes were pointed out as needing data base development. These included beryllium for neutron multiplier materials and various copper alloys for coils, superconducting magnets, diverters, and limiters. The data base for these classes of alloys is even sparser than for the structural and first wall materials.

2. Mechanisms of Hardening and Creep

Several hardening or creep mechanisms have been observed and were recommended for further study. The first mechanism was solute hardening. This effect could arise from added solute or impurities and was found to be variable enough in both ferritic and copper alloys that undesirable scatter in hardening data could result. The second mechanism, dislocation arrangement (cell structures versus homogeneous structures), was found to impact hardening differently for the same material with similar prior thermal mechanical treatment and irradiation history. The parameter affecting the evolution of cell and homogeneous dislocation structures is of interest. The size, spacing, location and movement of helium bubbles to grain boundaries received considerable discussion as to their impact or creep and hardening. There appears much to be resolved in this area. Finally, it has been observed that at high fluences, creep may cease. Cessation of creep may lead to a substantial design problem because creep in reactor components is necessary to accommodate swelling. The driving forces that cause cessation of creep needed to be understood.

3. Key Experiments

Two key experiments were encouraged for the purpose of understanding hardening and creep mechanisms. These included a comparison of FFTF and HFIR irradiated specimens which have been irradiated in parallel and/or in series in the two reactors. A second set of experiments were encouraged, involving isotopic tailoring to enhance or suppress helium production, to be carried out in order to understand helium effects on hardening and creep.

4. Small Specimens

Small irradiating volumes available for fusion reactor materials studies dictate the need for small specimen development and use. Since the properties obtained with small specimens do not exactly duplicate the properties obtained with bulk specimens, two issues on small specimens were discussed. These included the need to continue the development of property- property correlations. Also, it was proposed that the differences could be accounted for by using effective stress in the evaluation of small specimens. This method could improve the utility of small specimens.

B. Recommendations

1. Assess the data base for irradiation creep and hardening in berylium neutron multiplier materials and copper alloys, for coils, superconducting magnets, diverters and limiters. Help develop the needed data base.

2. Evaluate mechanisms of helium bubble migration and the effect of helium bubble populations and migration on creep and hardening of fusion reactor materials.

3. Study and model the mechanisms of irradiation creep saturation at high fluences.

4. Model the effects of impurities, solutes and dislocation structure on hardening processes.

5. Perform isotopic tailoring experiments to determine the role of helium in hardening and creep.

2. TIME DEPENDENT FRACTURE: G. E. Lucas

A. Summary

The time dependent fracture mechanisms -- creep rupture, fatigue and creep-fatigue interaction -- generally appear to be life limiting for the major structural components in the designs of high temperature fusion reactor systems. A considerable data base has evolved, largely for the austenitic stainless steels, to describe out-of-reactor, in-reactor, and post-irradiation creep rupture and fatigue behavior. Nonetheless, there are still important issues to be resolved for the austenitics, and the data bases for other candidate alloys are only just beginning to emerge.

James [1] has provided an extensive review of fatigue crack propagation data for austenitic stainless steels. The data largely suggest that irradiation has little effect on stage-II crack growth rates. Moreover, most specimen size/geometry differences are eliminated by considering crack growth rates da/dN as a function of stress intensity range ΔK. The effects of R, where R is the ratio of minimum to maximum applied stress, appear to be largely the result of near-threshold behavior differences at high frequencies and creep-fatigue interaction at low frequencies. Hence, these latter phenomena must be considered if data from one test type are being applied to a different situation. For instance, B. N. Singh made the point at the Workshop that most data relevant to the fusion materials program, especially on irradiated materials, are being generated in tension-tension ($R>0$) tests, whereas for most fusion reactor designs a significant compression cycle is included ($R<0$).

The mechanisms of fatigue crack growth and near-threshold phenomena have been reviewed comprehensively by Ritchie [2], and Lucas and Odette [3] have discussed several potential effects of radiation on fatigue crack growth for both long and short cracks. Unlike stage II growth, near-threshold crack growth can be strongly influenced by microstructure and slip distribution. For instance, localized plastic flow can lead to fatigue crack surface mismatch which can increase the threshold intensity level. Near-threshold behavior is also strongly affected by environment, particularly when corrosion products effectively created early closure of a fatigue crack. Jones and Wolfe [4] have discussed the importance of considering chemical environment effects (particularly H) on both near-threshold and stage II fatigue crack growth in steels of interest to the fusion program. However, there are no experimental data to verify whether irradiation effects or irradiation-environment synergisms are important in the systems of interest. Consequently, it remains an important research area to empirically investigate the effects of irradiation on near-threshold fatigue crack growth behavior.

Finally, recent work by Stubbins and co-workers [5] has demonstrated the importance of considering cyclic softening in bainitic steels in predicting component lifetimes under complex loading histories. This could have important implications for the tempered martensitic steels which also derive much of their strength from a lath-type microstructure.

Much of the fusion-relevant work on creep rupture has focused on understanding the failure mechanisms and evaluating the effects of He and in-reactor creep on these mechanisms. Odette [6] and Trinkhaus and co-workers [7] have developed modeling approaches based on a critical bubble size; that is, He-generation leads to gas-filled grain boundary bubbles, and those above a critical size grow rapidly under a tensile hydrostatic stress leading to intergranular fracture. However, alternate models have been suggested, and in general advances in understanding in-reactor creep-rupture will require critical experiments, especially experiments at stresses and temperatures prototypic of anticipated operating conditions. In addition, it will be necessary to produce prototypic He concentrations during testing. Critical bubble models suggest that both the level and generation rate of He can be important factors. Since the models indicate an important role of microstructure and microstructure evolution, it will also be important that critical experiments include a significant microstructural analysis component.

There is also recent work [8,9] which suggests a correlation between the onset of Laves phase formation in austenitics and creep rupture. There may be a causal relationship if the positive misfit of Laves phase leads to cavity nucleation at the precipitate grain boundary interface during the precipitation process [10]. If such is the case, phase-stability and control could be important approaches to extending creep rupture life in the austenitics. Similar behavior might also occur in other alloys. Further work appears to be warranted.

In both cases experiments based on pressurized tube data would be quite useful. This approach has been successfully used in the Breeder reactor materials development program, and hence, the technology is certainly in place. Prototypic helium generation could be achieved by using various pressurized tube designs. This has been suggested at previous Workshops, but alternate designs have never been pursued vigorously. Finally, the need to correlate microstructural evolution with creep rupture behavior would require a periodic examination of unfailed tubes.

Creek crack growth and creep fatigue interaction are both important failure mechanisms which have not received a great deal of attention in the fusion reactor materials program. Much of the pertinent work in creep fatigue interaction has been performed at Julich (cf. ref. 7). Again helium inventories might play a significant role in affecting fatigue life when the stress cycle frequency is low. More attention needs to be focussed on this phenomena for the high temperature devices. Experimental work should be performed with as large a specimen as possible to permit a range of stress cycles to be considered. In particular, it will be desirable to vary R over a range of both positive and negative values, as the work at Julich suggests that bubble growth during tension is not entirely compensated by shrinkage during compression.

B. Recommendations

Based on the discussion summarized above, the following recommendations were made:

1. The effects of both irradiation and fusion-relevant chemical environments on near-threshold fatigue crack growth should be investigated.

2. The questions of how the nature of cyclic stress application affects the fatigue behavior of irradiated material needs to be addressed. This includes the following subissues:

   (a) Does cyclic softening occur in irradiated ferritic/martensitic steels at elevated temperatures of interest?

   (b) What are the appropriate ways to interpret and compare the various methods of generating fatigue data (e.g., rotating bend, push-pull, tension-tension, etc.)?

3. The issue of short cracks and fatigue crack initiation vs. propagation in irradiated fusion reactor structures should be addressed. Critical tests should be identified and performed.

4. Critical experiments should be initiated in support of helium embrittlement/creep rupture modeling. The most useful experiments appear to be pressurized tube tests using isotope tailoring or inter-reactor exchanges (e.g. HFIR/FFTF) to obtain pertinent He/dpa levels. Interim examination of microstructures and alternate pressurized tube designs to examine different stress states would also be very useful.

5. Existing creep-fatigue interaction modeling suggests the importance of helium. Further modeling would be greatly assisted by testing specimens large enough to examine tension-compression cycling, and examination of materials with microstructures typical of neutron irradiated material. Isotopically tailored specimens irradiated in mixed spectrum reactors or specimens irradiated in reactor exchange experiments are recommended. While in situ experiments are ultimately desirable and necessary, post-irradiation testing would be of greatest assistance in the near term.

3. TIME-INDEPENDENT FRACTURE: G. E. Lucas

A. Summary

Historically, there has been continuing interest and concern over time-independent, catastrophic failure mechanisms in candidate structural materials for fusion reactors. Early work has largely focused on characterizing the (ductile) fracture toughness of austenitic stainless steels, and it has now been well-demonstrated (mostly through work in the Breeder reactor program) that irradiation can significantly degrade the fracture toughness of these steels. This is largely attributed to a loss of ductility due to irradiation-induced flow localization processes. Predictive methodologies for assessing the degree of degradation, however, have suffered from both the lack of an adequate data base and incomplete understanding of the exact mechanisms of failure at the microscopic level. Physically-based models have been considered for relating fracture toughness to microstructure and tensile property changes. For instance, the critical strain model for ductile fracture has been applied with some success to the cold-worked 316 stainless steel (cf ref. 3 for review). In addition, the effect of irradiation-induced flow localization on ductile fracture has been considered on this basis [11]. However, there are several material parameters in these models which are not well known or easily characterized, and they often end up being adjustable fit parameters. Additional advances in understanding and predicting changes in ductile fracture toughness will require a combination of critical experiments and more detailed analysis of the stress and strain fields in characteristic irradiated microstructures.

More recently, the emphasis in the fusion materials program has shifted from ductile fracture to brittle, cleavage fracture. This is largely due to the increasing emphasis on ferritic, tempered martensitic, and duplex stainless steels. While these steels may also exhibit a loss of ductile fracture toughness when irradiated, the more immediate concern is their tendency to change fracture modes from ductile to brittle cleavage below a transition temperature (or range of temperatures), and for this transition temperature (range) to increase with irradiation.

Historically, irradiation-induced shifts in transition temperature in structural steels (such as nuclear reactor pressure vessel steels) have been indexed to shifts in Charpy impact energy curves, and consequently the Charpy test has been used in the fusion materials program to-date as an indicator of the susceptibility of candidate steels to irradiation-induced shifts. A ductile-brittle transition temperature (DBTT) is specified at a certain absorbed energy level (usually 41J), and changes in this temperature with irradiation (ΔDBTT) have been used as the indicator. In addition there have been several attempts to scale the Charpy specimen size down to permit greater irradiation volume utilization [12]. Simple phenomenological models suggest that ΔDBTT can be influenced by changes in both the yield strength and the cleavage fracture strength of a material [13], and this approach has been utilized to rationalize data in ferritic steels as well as other body- centered cubic systems (e.g., Mo [14] and V). Because there are considerable data showing that yield strength change saturates with fluence in irradiated steels, initial studies on high Cr steels have been directed at determining whether a saturation in ΔDBTT occurs, and at developing correlations between changes in yield strength, DBTT, and hardness (pre-

vious Workshop recommendations). Recent data suggest that ΔDBTT may saturate at 25 dpa in HT-9 at high temperatures (500°C), but the data do not show such a saturation at lower temperatures or in 9Cr-1Mo steels [15]. Furthermore, there have been observations of an increase in DBTT without a commensurate change in yield strength. Hence, the issues are still unresolved.

It has also been pointed out that ΔDBTT may be irrelevant if: 1) lower shelf fracture toughness is sufficiently large and radiation insensitive, and 2) if the structure is sufficiently thin [13]. When (cleavage initiated) fracture toughness is high, plastic collapse can compete with crack propagation as a failure mode in thin, partially-cracked structures, and various interpolation schemes have been proposed to describe failure conditions when such a competition occurs. Recent experiments have demonstrated the validity of a two-parameter interpolation scheme for unirradiated HT-9, and the results suggest plastic collapse may predominate in fusion structure, even in irradiated HT-9 [16]. The results look even more promising if the cleavage initiated fracture toughness can be raised, but such an improvement requires understanding the appropriate microstructure-property relations and adjusting the microstructure (and/or composition) accordingly. Early work [17] has focussed on evaluating the validity of the Ritchie-Knott-Rice model [18] in HT-9, and more recent work has been directed at evaluating alternate models. Preliminary results suggest that large carbides at prior austenite grain boundaries serve as cleavage microcrack precursors, and that unstable crack propagation requires a sufficiently high stress to propagate the microcracks through high angle boundaries [19]. Considerably more work is needed to understand the processes and identify the appropriate structure-property relations.

Since V-based alloys and low activation ferritics will also be susceptible to fracture mode transitions, the same issues will apply to these alloy systems. An approach similar to the one taken for the high Cr steel should certainly be applicable, and should therefore be pursued. There may however, be differences among alloy systems (e.g., impurity effects in V-based alloys) which require special attention. In addition, work on HT-9 suggests that load limits may be precluded by ductility limits [17], and hence ductility limits should be considered for both the ferritic and V-based systems.

B. Recommendations

Based on the content of the discussion described above, the following recommendations are made:

1. Failure criteria appropriate to irradiated, thin walled, ferritic/martensitic structures need to be further developed. This includes the following subissues:

   (a) Further rigorous testing of interpolation procedures for ferritic systems of interest needs to be conducted.

   (b) The issue of ductility and ductility limits in irradiated ferritics needs to be addressed both theoretically and experimentally.

   (c) Expansion of interpolation techniques into an integrated structural analysis/failure analysis should be considered.

2. Modeling of cleavage fracture mechanisms should continue. This also includes the following subissues.

   (a) Demonstration that cleavage fracture is stress-controlled in ferritic systems of interest should be made.

   (b) Determination of appropriate microstructure-fracture parameter relations should be pursued.

   (c) The effects of irradiation (and particularly He) on cleavage fracture and lower shelf toughness should be evaluated; this may require isotopically tailored specimen and/or reactor exchange experiments.

   (d) A data base should be developed for part through crack stability in ferritics of interest; this should be done in conjunction with developing a sound theoretical basis.

   (e) The dependence of DBTT on irradiation and metallurgical variables should be compared to cleavage fracture models to benchmark applicability of these models.

3. Specimen size effects need to be further addressed in fracture-pertinent testing of ferritics. This includes:

   (a) Size effects of CVN specimens for evaluating changes in cleavage fractue behavior.

   (b) Size effects in specimens used to evaluate lower shelf and near lower shelf fracture behavior.

4. The effects of He on ductile fracture of austenitic stainless steels should be addressed in experiments using isotopically- tailored, miniature compact tension specimens.

5. Consideration should be given to the following issues regarding modeling of ductile fracture in highly irradiated materials containing a significant void fraction:

   (a) What are the mechanics of plastic instability in dilating volumes, especially under complex stress states and field gradients?

   (b) What are the deformation-microstructure relations that control the constitutive behavior under conditions in (a)?

   (c) How can (plasticity induced) void evolution be modeled when the structure contains a high density of radiation-induced pre-existing voids and possibly void nuclei?

   (d) What is the appropriate way to link (a) - (c) in self-consistent fracture model?

4. ENVIRONMENT ASSISTED CRACK GROWTH: R. H. Jones

A. Summary

Material-environment interactions can produce time-dependent subcritical crack growth of materials. Time independent, critical crack growth can also occur but these effects are generally identified in materials evaluation testing and eliminated as a possibility in design. Time dependent subcritical crack growth processes are frequently not easily identified in materials evaluation testing because the crack growth rates are slow relative to laboratory testing times. Therefore, it is imperative in fusion reactor materials development that all prevailing knowledge about environmental effects on subcritical crack growth be evaluated relative to their potential applicability to the fusion reactor environment.

Material-environment interactions will occur between all materials and coolants including liquid lithium, helium and water. However, the extent and nature of these interactions will vary with each environment. In particular, the effects of these interactions on subcritical crack growth are expected to be limited to water and hydrogen environments. Liquid lithium has the potential to cause localized corrosion and if the corrosion rate is sufficiently fast it could affect crack growth; however, there is no evidence at this time that liquid lithium will induce subcritical crack growth. Therefore, the emphasis of the following summary on environment assisted crack growth is on water coolants and hydrogen from the plasma, (n,p) reactions, corrosion processes and tritium breeding.

1. Stress Corrosion and Corrosion Fatigue in Water Environments

Subcritical crack growth occurs in materials in water environments when the stress intensity exceeds a critical value and when a specific localized corrosion process occurs. In austenitic stainless steels, localized corrosion occurs along chromium depleted grain boundaries when chromium carbide precipitation has occurred at the grain boundaries. In ferritic steels, localized corrosion may occur at sulfide inclusions or along impurity segregated grain boundaries. There is sufficient information available from the use of these materials in light water reactors, steam generators, steam turbines, etc. for fusion reactor designers to select materials and water chemistry limits.

The effects of radiation on stress corrosion is a process for which there is insufficient data for design considerations. Irradiation assisted stress-corrosion cracking (IASCC) of in-core components was recognized as a concern for austenitic stainless steel cladding in the 1960's. Recently it has become a concern for several in-core light water reactor components such as the upper guide structure, control blade tubes, and fuel assembly handles in BWR's and bolts and control rod tubes in PWR's. Both austenitic stainless steels and nickel based alloys have shown susceptibility to IASCC. As these materials are not currently of high priority for fusion applications, a key question is whether there are processes which are common to materials such as ferritic steels, high manganese austenitic stainless steels, copper alloys and vanadium alloys which are of concern.

Some of the pertinent observations of IASCC in austenitic stainless steels are: 1) it occurs in non-sensitized material, 2) the cracks appear intergranular, 3) some form of radiation damage is necessary, 4) gamma radiation accelerates cracking, and cracking will occur in irradiated material in high oxygen water at 288°C without a gamma radiation source other than the irradiated sample, 5) cracking is stress assisted, but will occur without applied loads, and 6) data on the effect of hydrogen are contradictory. The radiation damage process associated with IASCC has a fluence threshold of about 10^{21} n/cm^2 and tests on unirradiated material or material irradiated to lower fluences in the presence of gamma radiation did not produce cracking. However, gamma radiation does accelerate cracking of thermally sensitized stainless steel which is thought to result from a shift in electrochemical potential or passive film stability. Cracking has been observed in the absence of an applied load which must have resulted from residual stresses within the material. However, as a crack grows in a material with residual stresses the stress intensity decreases because the internal stress relaxes. Since these cracks propagated through the component thickness, the stress intensity threshold for IASCC must be very small.

The potential radiation damage processes causing IASCC are: 1) radiation enhanced impurity segregation to grain boundaries, 2) radiation hardening resulting in a decrease in toughness, 3) radiation enhanced creep, 4) radiation enhanced segregation altering the chromium profile around grain boundaries, 5) radiation enhanced precipitation at grain boundaries, 6) phase instabilities, 7) radiation damage to the passive film, and 8) transmutations altering the chemistry of the material.

An evaluation of the effect of radiation-enhanced corrosion, creep, and segregation on IASCC has been conducted and supports the conclusion that RES is probably the dominant process in IASCC while radiation-enhanced creep could increase the crack nucleation rate and growth rate of short cracks in components at low stresses. Radiation-enhanced corrosion may increase the crack growth rate by a factor of two to three, but is not expected to be a major contributor to IASCC. These conclusions were based on an assessment utilizing a combination of experimental data and crack growth rate models.

There are several outstanding issues with regard to IASCC in austenitic stainless steels and nickel based alloys. These are: 1) What is the dominant SCC mechanism?, 2) Is there a relationship between radiation hardening/ toughness of these materials and their SCC behavior?, and 3) Are there unusual crack tip strain distributions in these materials which cause SCC? With regard to the first question, much of the data points to the radiation enhanced segregation of impurities to grain boundaries. A key question is whether there is a limiting bulk concentration below which IASCC is eliminated. Also, is cracking related to the corrosion of the impurity enriched grain boundary and if so, is the crack growth rate controlled by a film rupture process and what is the stress dependence? Radiolysis of water increases the hydrogen activity and could therefore contribute to the hydrogen embrittlement of these materials. Radiation hardening and segregation would make the materials more susceptible to hydrogen induced subcritical crack growth. However, the data on hydrogen effects is contradictory with IASCC either being enhanced or eliminated with increased hydrogen overpressure. Another possible radiation effect might be the localized corrosion along shear bands which occur in radiation hardened material. This process would produce flat transgranular fracture surfaces which look very similar to intergranular features. For this process to be viable the planar slip in radiation hardened materials must differ markedly from that which occurs in annealed 304SS and gamma prime hardened nickel based alloys since these materials do not exhibit IASCC without radiation damage.

b. Hydrogen Induced Subcritical Crack Growth

Hydrogen induced crack growth of materials can result from both external gaseous or cathodic hydrogen and from internal dissolved hydrogen. In a fusion reactor there are several potential sources of hydrogen or hydrogen isotopes including direct injection from the plasma, tritium gas in the breeding blanket, nuclear (n,p) reactions within the material or, for water-cooled systems, cathodic reduction from an electrochemical corrosion reaction.

Hydrogen has been shown to induce cracking in a wide variety of materials, including ferritic steels, austenitic stainless steels, nickel-based alloys, and aluminum alloys. The mechanism by which hydrogen causes cracking is generally thought to result from the collection of hydrogen at particle-matrix interfaces, grain boundaries or other defects ahead of the crack tip. The distance that the hydrogen concentrates ahead of the crack tip is not well established, but for external hydrogen it may be anywhere from a few hundred angstroms to a few micrometers [20]. Earlier work by Williams and Nelson [21] and recent analysis by Pasco, Sieradzki and Ficalora [22] considered the hydrogen effect to be primarily a surface chemistry controlled process.

Temperature and hydrogen activity are two parameters on which the crack growth rate is strongly dependent. Material parameters such as yield strength, hydrogen diffusivity, hydrogen trap densities and strength and grain boundary chemistry are also important.

Hydrogen induced crack growth rates of HT-9 have been estimated for three sources of hydrogen: the plasma, nuclear reaction and aqueous corrosion. Estimates of crack growth rates were derived using hydrogen embrittlement models which describe the temperature and hydrogen activity dependence of cracking. A crack growth rate of 10^{-3} cm/s at a reactor operating temperature of 400°C was obtained for a steady-state hydrogen concentration of 0.5 appm resulting from (n,p) reactions, while a much slower crack growth rate was predicted for the same steady-state hydrogen concentration with an alternate model. These calculations have shown the need for further research to assess the effect of temperature on crack growth. Other sources of hydrogen give very slow hydrogen induced crack growth rates at reactor operating temperatures while significant hydrogen induced crack growth rates are possible at lower temperatures. For instance, hydrogen from a cathodic corrosion reaction could produce a crack growth rate of 10^{-7} cm/s at 25°C which could be significant during extended downtime. Also, a non-equilibrium hydrogen uptake from the plasma could occur from surface reaction controlled effects, and a crack growth rate of 10^{-1} cm/s was estimated for this condition at a temperature of 75°C.

Some specific hydrogen embrittlement issues which should be addressed are an improved description of the temperature dependence of crack growth for internal hydrogen, the contribution of tritium and hydrogen from radiolysis to crack growth and the effect of cyclic loading on hydrogen induced subcritical crack growth. Also, of concern is the temperature dependence of hydrogen induced cracking in vanadium alloys. The temperature at which the maximum crack growth rate occurs in iron is around 25°C which results from the solubility and diffusivity of hydrogen in iron. Since these parameters are different in vanadium alloys, it is possible that the temperature of maximum crack growth rate is above room temperature. Vanadium is also a strong hydride former so hydrogen embrittlement by a hydride formation

mechanism is also possible in vanadium at high hydrogen fugacities. H. Matsui of Tohoku University presented results which showed a ductile to brittle transition temperature for vanadium hydride of 250°C. Therefore, vanadium alloys may not be embrittled by vanadium hydride at temperatures above 250°C. The question remains however, as to whether vanadium is embrittled by atomic hydrogen similarly to ferritic steels and, if so, the temperature at which the maximum crack growth rate occurs.

2. Recommendations

1) Determine the irradiation enhanced segregation of P and Si in FeCrMn alloys for the purpose of evaluating the potential for IASCC in these low activation alloys.

2) Evaluate the effect of P and Si segregation to grain boundaries on their stress corrosion cracking behavior if there is evidence of radiation enhanced segregation.

3) Evaluate the effect of thermally and radiation enhanced segregation on the fracture and stress corrosion of copper and vanadium based alloys. There is evidence for intergranular fracture at 350°C in Cu-Cr-Zr alloys tested in air as shown by the results of G. Piatti given in Figure 1.

4) Evaluate the effect of the fusion environment on IASCC. There are a number of processes which differ in magnitude and which are not present in LWR environments. Examples include the helium generation rate with fusion energy neutrons, radiation induced microstructures, irradiation creep, radiolysis and cyclic loading.

5) Evaluate the temperature dependence of crack growth in HT-9 with internal hydrogen concentrations ranging from 0.0005 to 0.5 appm.

6) Assess the contribution of hydrogen from radiolysis and tritium breeding on crack growth of ferritic steels.

7) Determine if hydrogen in atomic solution causes cracking of vanadium alloys, and if so, determine the temperature dependence of cracking.

8) Evaluate the effect of hydrogen on the fatigue crack growth of HT-9. Include vanadium alloys in this assessment if hydrogen is shown to induce subcritical crack growth with static loads.

5. References

1. L. James, Atom. Energy Res. 14(1976):37.
2. R. O. Ritchie, Encyclopedia of Materials Science and Engineering, M. G. Beaves (ed.), Pergamon Press, New York. (1983).
3. G. E. Lucas and G. R. Odette, Nucl. Eng. Des./Fusion 2(1985):145.
4. R. H. Jones and W. Wolfer, J. Nucl. Matls. 122/123(1984):379.
5. J. Stubbins, et al., J. Nucl. Matls. (in press).
6. G. R. Odette, J. Nucl. Matls. 122/123 (1984):435.
7. H. Trinkaus, J. Nucl. Matls. 133/134(1985):105.
8. R. J. Puigh, A. J. Lovell, and F. A. Garner, J. Nucl. Matls. 122/123(1984):242.
9. G. E. Lucas, P. Brashear, and P. Maziasz, DOE/ER-0046/14(1983):96.
10. G. R. Odette, G. E. Lucas, and P. Brashear, unpublished research.
11. W. Wolfer and R. H. Jones, J. Nucl. Matls. 103/104(1981):1305.
12. W. Corwin and G. Lucas (eds.), ASTM-STP-888, American Society for Testing and Materials (1986).
13. G. R. Odette and G. E. Lucas, J. Nucl. Matls., Parts 1 and 2, 117(1983):264.
14. K. Abe -- presentation, this workshop.
15. D. Gelles, J. Nucl. Matls. (in press).
16. G. R. Odette, G. E. Lucas, R. Maiti, and J. W. Sheckherd, J. Nucl. Matls. 133/134(1985):849.
17. G. R. Odette, G. E. Lucas, R. Maiti, and J. W. Sheckherd, J. Nucl. Matls. 123/124(1984):442.
18. R. O. Ritchie, J. Knott, and J. Rice, J. Mech. Phys. Sol. 21(1973):395.
19. G. R. Odette, G. E. Lucas, and R. Maiti, J. Nucl. Matls. (in press).
20. W. W. Gerberich, T. Livne and X. Chen, in: Proceedings of a Symposium on Modeling Environmental Effects on Crack Initiation and Propagation, Toronto, Canada, 1985, eds. R. H. Jones and W. W. Gerberich (TMS-AIME, Warrendale, PA).
21. D. P. Williams and H. G. Nelson, Metall. Trans. 1(1970):63.
22. R. W. Pasco, K. Sieradzki and P. J. Ficalora, Scripta Met. 16(1982):881.

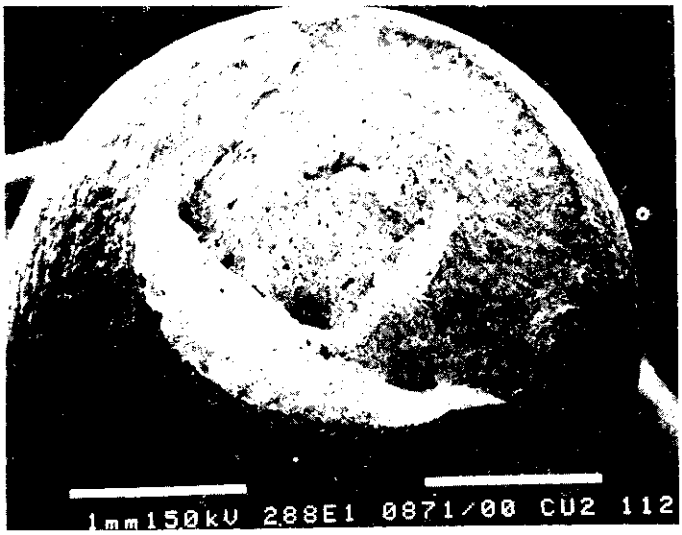

Fracture Surface, 25°C Test

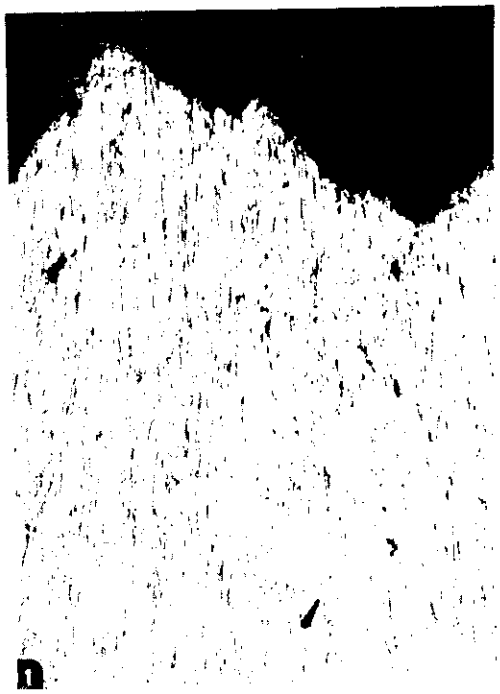

Longitudinal Cross-Section, 25°C Test

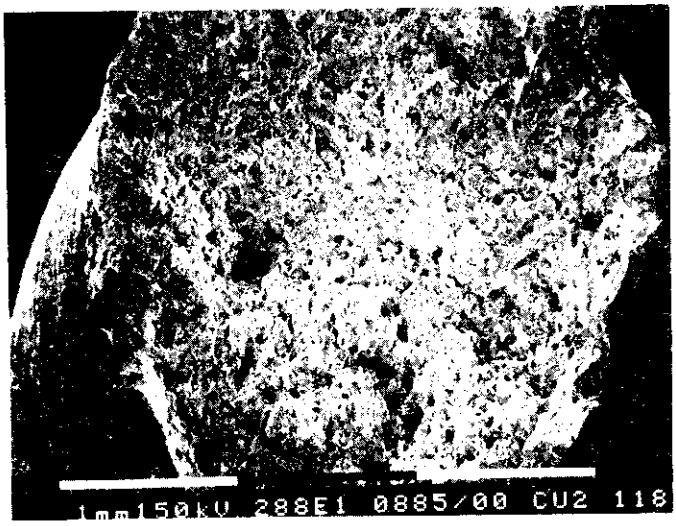

Fracture Surface, 350°C Test

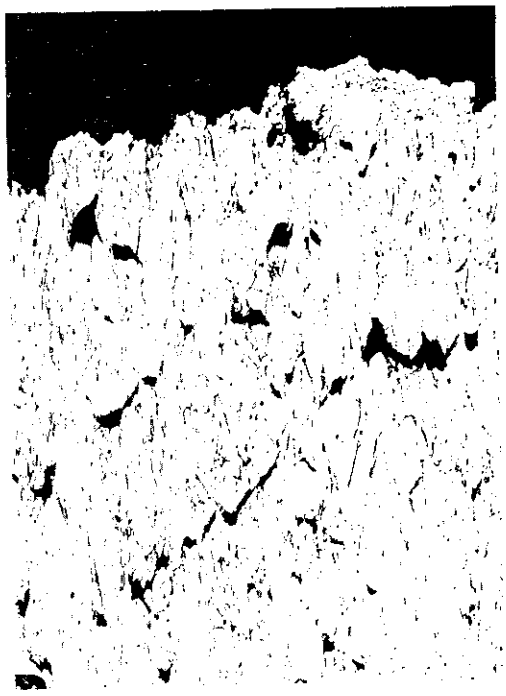

Longitudinal Cross-Section, 350°C Test

APPENDIX A

High Temperature Tensile Properties of Copper-Chromium-Zirconium Alloys, G, PiaHi

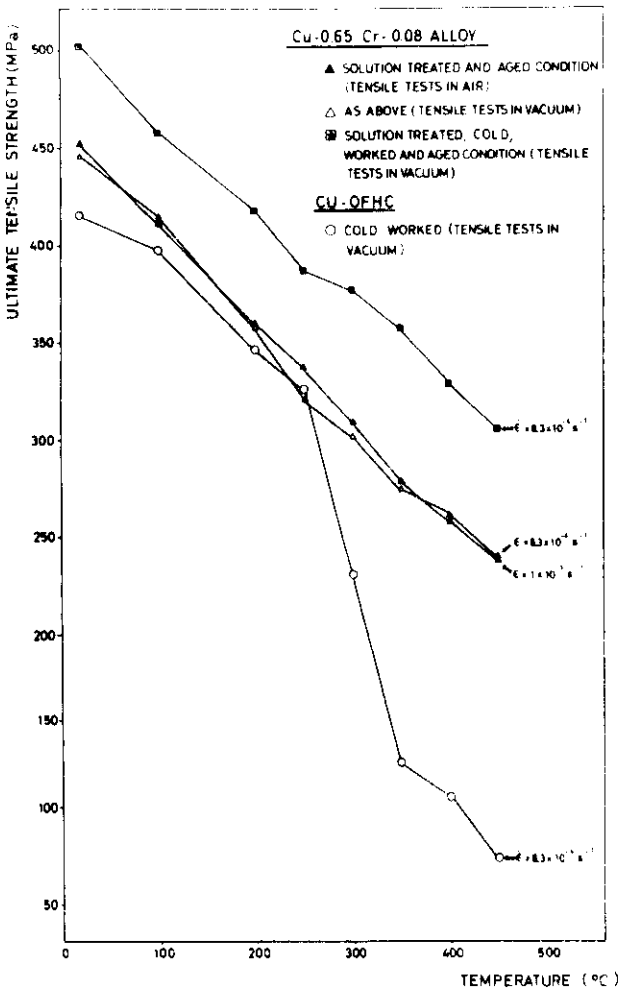

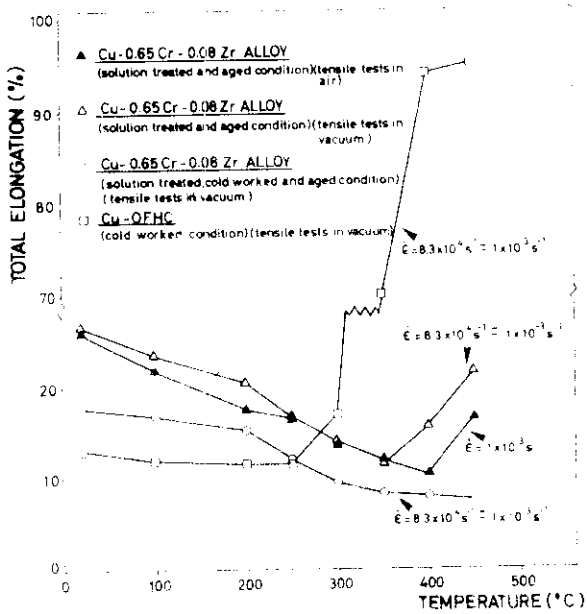

EFFECT OF INTERNAL HYDROGEN ON THE FATIGUE CRACK GROWTH OF HT-9 - G. F. Rodkey and R. H. Jones (Pacific Northwest Laboratory)

OBJECTIVE

A previous (1) evaluation indicated that under certain circumstances hydrogen could cause subcritical crack growth of HT-9 in a fusion reactor environment. This previous evaluation only examined static load conditions and it was noted that there is a lack of data on hydrogen effects on fatigue crack growth of HT-9; however, the fatigue crack growth properties of steels are sensitive to hydrogen. Therefore, the objective of this study was to determine the effects of hydrogen on the fatigue crack growth of HT-9 and to develop a data base which could be used for modeling these effects.

SUMMARY

Internal hydrogen concentrations of 4 appm were found to have a significant effect on the fatigue crack growth rate of HT-9 tested at room temperature. This effect was most pronounced at ΔK's less than about 15 MPa-$m^{\frac{1}{2}}$ for tests conducted at a load ratio of 0.5. At a load ratio of 0.05 internal hydrogen had very little effect on the fatigue crack growth rate. Hydrogen induced an intergranular fracture mode which increased in percentage of the total fracture with decreasing crack velocities at decreasing ΔK's. Hydrogen has been shown to induce intergranular fracture of HT-9 in precharged and dynamic tensile tests and subcritical crack growth tests at cathodic potentials. The fatigue crack growth rate of both the hydrogen charged and uncharged material was a function of the cyclic frequency between frequencies of 0.5 and 5 Hz with the fatigue crack growth rate increasing with decreasing frequency or increasing period. There is some evidence that the as-received hydrogen concentration of 1 ppm affected the crack growth rate. The crack velocity was also dependent on the load ratio with hydrogen having a large effect on the fatigue crack growth rate at a load ratio of 0.5 and a small effect at a load ratio of 0.05. The observed results could have significance to fusion reactor design if they are shown to persist to reactor temperatures. A combination of modeling and experiment will be used to help answer this question.

PROGRESS AND STATUS

Introduction

Hydrogen induced crack growth of materials can result from both external gaseous or cathodic hydrogen and from internal dissolved hydrogen. In a fusion reactor there are several potential sources of hydrogen or hydrogen isotopes including direct injection from the plasma, tritium gas in the breeding blanket, nuclear (n,p) reactions within the material or, for water-cooled systems, cathodic reduction from an aqueous corrosion reaction.

Hydrogen has been shown to induce cracking in a wide variety of materials, including ferritic steels, austenitic stainless steels, nickel-based alloys and aluminum alloys. The mechanism by which hydrogen causes cracking is generally thought to be the collection of hydrogen at particle-matrix interfaces, grain boundaries ahead of the crack tip or other defects. The distance that the hydrogen concentrates ahead of the crack tip is not well established, but for external hydrogen it may be anywhere from a few hundred angstroms to a few micrometers (2). Earlier work by Williams and Nelson (3) and recent analysis by Pasco, Sieradzki and Ficalora (4) considered the hydrogen effect to be primarily a surface chemistry controlled process.

Temperature, hydrogen activity, and fatigue loading conditions are parameters on which the crack growth rate is strongly dependent. Material parameters such as yield strength, hydrogen diffusivity, hydrogen trap densities and strength, and grain boundary chemistry are also important. Esaklul and Gerberich (5) and Pao, Wei, and Wei (6) have observed that hydrogen can have a significant effect on the fatigue crack growth threshold and stage I and stage II crack growth regimes of ferritic steels. Because Tokamak fusion reactor structural materials will be subjected to cyclic loads, it is important to know the environmental effects on the fatigue crack growth of fusion reactor structural materials.

Material Description and Experimental Procedures

Material

Compact-tension (0.4T) specimens were machined in the transverse-longitudinal orientation from 13-mm-thick plate of heat 9607 from the fusion reactor materials stockpile. The specimen dimensions shown in Figure 1 are as follows: width (measured from the load line), W = 25.6 mm, thickness, B = 10.2 mm, machined crack a(n) = 7.7 mm, and the hole radius, r = 2.5 mm. This material had been austenitized at 1040° C for 30 minutes, air-cooled, tempered at 760°C for 2½ hours, air cooled, and then held at 540°C for 240 hours to induce grain boundary segregation. Previous work (7) on this alloy found grain boundary sulfur and phosphorus concentrations to be 0.01 and 0.04 monolayers, respectively. The overall composition,

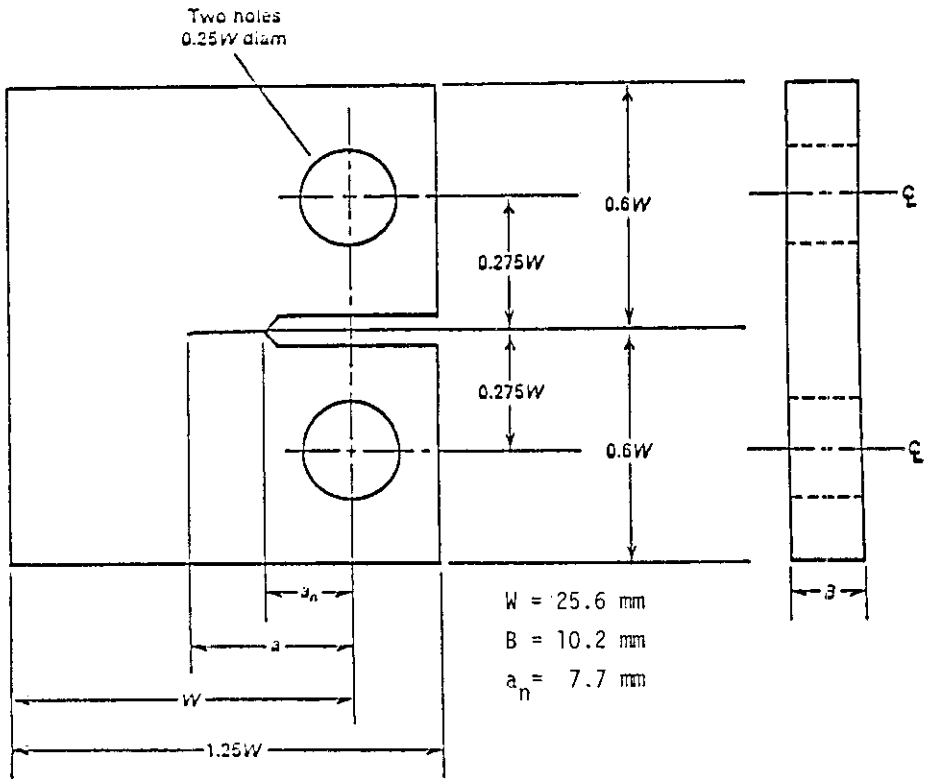

Fig. 1. Standard compact-type specimen for fatigue crack propagation testing.

the grain boundary composition after heat treatment, and the tensile properties at room temperature are listed in Tables I, II and III, respectively.

Previous work (7) was done to characterize the microstructure by optical and transmission electron microscopy (TEM). Techniques used for specimen preparation are described in previous work (7). The prior austenite grain size was approximately 100 μm. Transmission microscopy revealed a carbide-stabilized subgrain structure with carbides and dislocations concentrated at the lath and prior austenite grain boundaries. The microstructure was characterized by a high dislocation density. The average chemistry of the carbides is 64 wt% Cr, 35 wt% Fe, 3 wt% Mo, and 1 wt% W (7).

Experimental Procedure

All tests were performed on a closed-loop Instron servo-hydraulic machine interfaced to a Digital PDP 11/23 computer. Software supplied by Instron was employed to precrack the specimens using a simple fatigue program (SFP) and also to run the test using a fatigue crack propagation (FCP) program. Precracking of the specimens was monitored visually by a video camera set up for ease of crack observation. Precracking was performed until the crack length, measured at the outer surface, was approximately 1 mm, as shown in Figure 2. Due to the difference in stress states between the center and sides of the specimens the crack front was curved after the specimen was pulled apart following fatigue testing, as seen in Figure 3. Therefore, the precrack length used in a program to correct the data based on the crack length was taken as the average of five points equidistant from each other. After precracking, photographs were taken at a low magnification to more accurately measure the crack, as shown in Figure 3. After precracking the specimens were sealed in a vacuum dessicator for storage until fatigue testing.

An Instron Model 1323 with a 25 kN dynamic testing capacity was used with an MTS strain gauge extensometer for specimens tested at 5 Hz and 1 Hz, while an Instron Model 1321 with a 10 kN dynamic testing capacity was used with an Instron strain gauge extensometer for specimens tested at 0.2 Hz. Specimens were tested in the as-received condition at each frequency and load condition to establish baseline conditions. The load ratios, or R-ratios, defined as P(min)/P(max), where P is the load, were chosen at R = 0.5 and R = 0.05. While most tests were performed at R = 0.5, several specimens were tested at R = 0.05 in order to determine if there was a crack closure effect. All tests were run under sinusoidally varying axial loads.

Table I. Chemical composition of fusion AOD-processed HT-9 (heat #9607), weight percent

C	Si	Mn	P	S	Cr	Mo	Ni	V	W	Fe
0.20	0.24	0.57	0.018	0.007	11.64	1.01	0.52	0.30	0.57	bal.

Table II. Grain boundary composition of HT-9, monolayers

P	S	Mo	Cr	C	O
0.04	0.01	0.03	0.73	0.14	0.10

Table III. Mechanical properties of HT-9 in air, 25°C

0.2% Yield Strength, MPa (ksi)	Ultimate Tensile Strength, MPa (ksi)	Reduction of Area, %
540 (78.3)	775 (112.3)	56

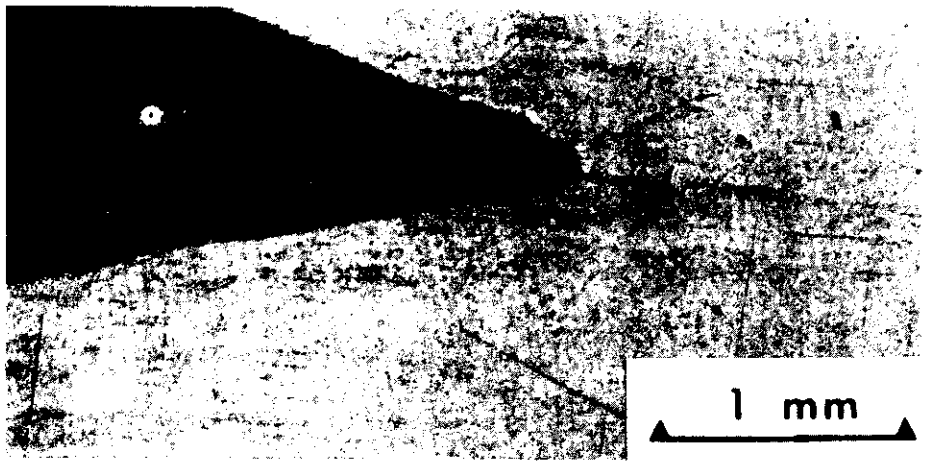

Fig. 2. Photograph of specimen surface used for determining precrack length.

The FCP program ran a load-shedding test according to:

$$\Delta K = \Delta K(i) \exp[C(a-a(i))]$$

where ΔK and $\Delta K(i)$ are the current and initial stress intensity factor range values, respectively, C is the stress intensity factor gradient constant, and a and a(i) are the current and initial crack lengths, respectively, measured from the load line. Values for $\Delta K(i)$ were chosen by the equation:

$$\Delta K = (1-R)\ K(max)$$

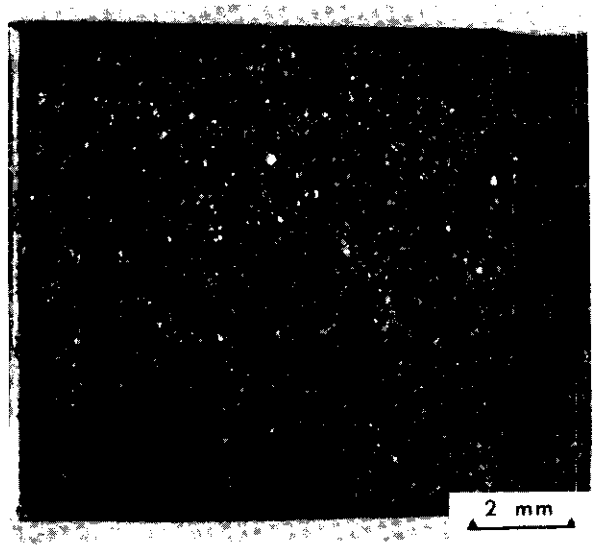

Fig. 3. Photograph of fracture surface. Note slight curve designating precracking.

K(max) was chosen as 40 MPa-$m^{\frac{1}{2}}$, yielding 38 MPa-$m^{\frac{1}{2}}$ as $\Delta K(i)$ for R = 0.05 and 20 MPa-$m^{\frac{1}{2}}$ for R = 0.5. In order for ΔK to fall below 10 MPa-$m^{\frac{1}{2}}$, the stress intensity gradient factor constant was chosen as C = -0.15 for R = 0.05 and C = -0.11 for R = 0.5. This constant allowed ΔK to decrement as the crack length increased. The equation by which ΔK was determined follows the solution for standard compact-type specimens (ASTM E-647) and is given by:

$$\Delta K = \frac{\Delta P(2 + \alpha)}{BW^{\frac{1}{2}}(1-\alpha)^{3/2}} (0.886 + 4.64\alpha - 13.32\alpha^2 + 14.72\alpha^3 - 5.6\alpha^4)$$

where ΔP is the change in applied load, B is the specimen thickness, W is the width of the specimen as defined above, and α is the a/W ratio. This expression is valid for $a/W \geq 0.2$. The specimens were fatigue tested until the crack reached an a/W ratio of 0.6.

Specimens were charged with hydrogen cathodically in 1N H_2SO_4 to which 200 mg/liter of As_2O_3 had been added to act as a hydrogen recombination poison. Specimens were charged at a current density of 2 mA/cm^2 based on previous work by others (8) using an EG&G Princeton Applied Research Model 173 potentiostat/galvanostat over a 48-hour period at 20°C. After charging, a Buehler Edgemet kit was used to nickel-plate the specimens by an electroless plating method to prevent hydrogen effusion. The specimens were then placed into an oven and heated to 150°C for one hour to promote a homogeneous distribution of hydrogen. After cooling, the specimens were fatigue tested by the aforementioned procedure.

To determine the hydrogen concentration in the specimens, samples 4 mm x 4 mm x 10 mm were cut from uncharged material and charged using the same procedure and current density as with the fatigue specimens. Inert gas fusion using a Leco analyzer was employed in performing a hydrogen analysis of the samples. This method involves dissolving the samples in a Sn flux in which the hydrogen solubility is very low. The gas is displaced and analyzed as it is released from the mixture.

Hydrogen analysis done on the specimen material revealed a hydrogen content of 0.77 appm in the uncharged specimens and of 4.5 appm in the charged specimens. The hydrogen content of the individual samples as determined by the inert gas fusion method are listed in Table IV. Based on the diffusion

Table IV. Inert gas fusion analysis of hydrogen content in charged and as-received HT-9.

Sample Condition	Hydrogen Content, appm
Charged	4.5 ± 0.3
As-Received	0.77 ± 0.1

distance equation, $x = (4Dt)^{\frac{1}{2}}$, a time, t = 3600 s (1 hr), and a diffusivity of $D = 5 \times 10^{-5}$ cm²/s (at 150°C) a diffusion distance of about 1 cm results. Since hydrogen charging occurred from both sides of the sample and some diffusion occurred during the 48-hr hydrogen charging process (x ~ 0.4 cm) it is reasonable to assume that the hydrogen concentration was uniform through the 1-cm-thick samples.

After fatigue crack growth testing, a section of the specimen in front of and parallel to the crack plane was cut, leaving a ligament of material. The specimens were then reinserted into the servo-hydraulic machine and pulled to fracture. Photographs were taken of the fracture surfaces at a low magnification in order to measure the crack more accurately. From these photographs, as shown in Figure 3, the actual precrack and crack lengths could be measured and compared against the lengths calculated by the computer, which used the compliance method of crack length determination. The compliance method determines the crack length by using the change in slope of consecutive load-displacement curves.

Scanning electron microscopy (SEM) was used to observe the fracture surfaces and determine the mode of fracture. Photomicrographs were taken along the centerline in the crack direction of several specimens in order to determine the percentage of intergranular fracture and any change in fracture mode as the crack progressed. In addition, photomicrographs were taken at predetermined ΔK's across the thickness of several specimens to check for a connection between ΔK and the percentage of intergranular fracture. The percentage of intergranular fracture was determined using the line intercept method.

Results and Analysis

R = 0.5, f = 5 Hz

The data points from specimens 1, 2, and 3 tested in the as-received condition at a R-ratio of 0.5 and frequency of 5 Hz were contained in a narrow scatter band throughout the stage II region of the crack growth rate versus ΔK curve, as shown in Figure 4. A comparison of the rates at the mid-stage II region taken at approximately ΔK = 14 MPa-m$^{\frac{1}{2}}$ revealed that the crack growth rate of all three specimens was 2 x 10^{-8} m/cycle, demonstrating fairly uniform behavior among the specimens. The threshold ΔK values, established for all specimens at da/dN = 8 x 10^{-9} m/cycle, ranged from 10.6 to 11.48 MPa-m$^{\frac{1}{2}}$. The threshold values for ΔK and the crack growth rates at a common ΔK approximately equal to 14 MPa-m$^{\frac{1}{2}}$ are listed in Table V for all of the specimens tested at R = 0.5. This information is also listed at R = 0.05 with a threshold ΔK of 14 MPa-m$^{\frac{1}{2}}$, and a crack growth rate of 5 x 10^{-8} m/cycle at a ΔK of 22 MPa-m$^{\frac{1}{2}}$. Slopes of da/dN versus ΔK curves determined from log-log plots are also listed in Table V. For uncharged specimens, n is defined as the Paris slope.

Fracture surface observations revealed a transgranular quasi-cleavage mode exhibiting a river-like fracture pattern in the direction of crack growth. No intergranular fracture surfaces were observed for uncharged specimens tested at R = 0.5 and 0.05. Secondary cracking was observed as shown in Figure 5. Evidence of slip bands is shown in Figure 6. Analysis of the stage II region yielded slopes in the range of n = 3.34 to n = 3.98 which is in good agreement with values reported by others (15) in which n = 2-4.

Specimens 4 and 6, tested at R = 0.5 and f = 5 Hz in the hydrogen-charged condition, exhibited more scatter in da/dN at a given ΔK than the uncharged material. There was a 40% spread in the da/dN between specimens 4 and 6 at a ΔK of 11 MPa-m$^{\frac{1}{2}}$ while the baseline data had a spread of only about 10%. The average crack growth rate values taken at ΔK = 14 MPa-m$^{\frac{1}{2}}$ ranged from 2 to 3 x 10^{-8} m/cycle while threshold values of ΔK ranged from 8.8 to 9.8 MPa-m$^{\frac{1}{2}}$. Specimen 5 was charged with hydrogen and then given an outgassing treatment of 180°C. Its crack growth behavior is similar to the baseline data suggesting the hydrogen was totally removed; however, some intergranular fracture was observed. Fatigue crack growth behavior for these specimens is shown in Figure 7.

SEM micrographs revealed intergranular fracture in addition to transgranular quasi-cleavage, secondary cracking and inclusions such as stringers. As shown in Figure 8a, 8b, and 8c taken at ΔK = 17.8, 14.1, and 8.4 MPa-m$^{\frac{1}{2}}$ from specimen 4, respectively the percentage of intergranular fracture increased as the crack growth rate and ΔK decreased. The greatest amount of intergranular fracture occurred in the center regions of the specimens. Two explanations are thought to be possible for this behavior. First, it is possible that hydrogen is lost from the regions of the specimen close to the surface, leaving only the center with hydrogen contributing to intergranular behavior. Second, and more probable, is the explanation due to stress state changes throughout the specimen. Plane stress controls behavior in the outer regions of the specimen, changing to plane strain in the center region. It was reported in other work (4) that a plane strain condition promoted intergranular fracture. The behavior observed could be combination of these two effects.

The most noticeable deviation in behavior of the charged specimens was the appearance of a shoulder at which the slope of the stage II data decreased. The slopes in this region ranged from n = 1.24 to n = 2.89. The slope of the curve of the specimen outgassed at 180°C was n = 4.05 in agreement with that of the uncharged specimens.

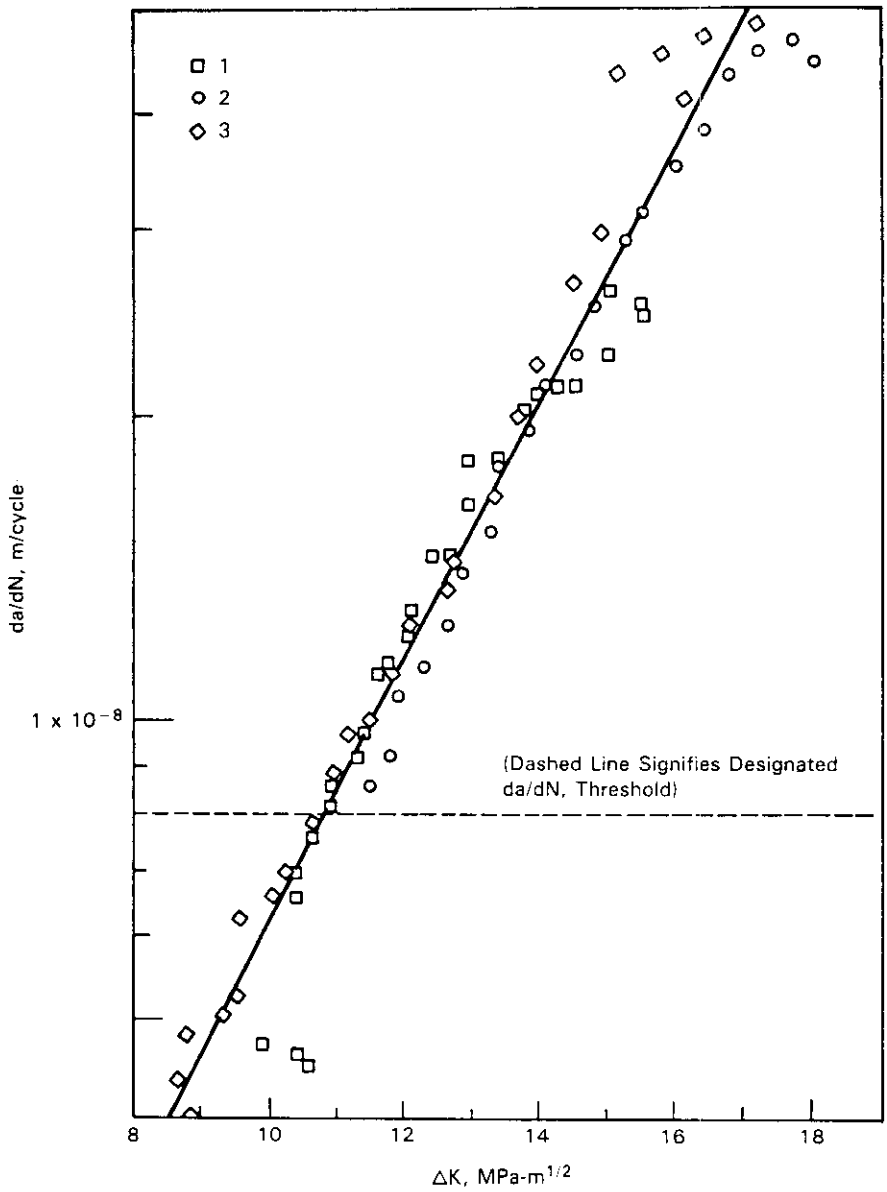

Fig. 4. Fatigue crack growth (FCG) behavior of as-received specimens tested at R = 0.5, f = 5 Hz.

TABLE V. Test conditions, threshold ΔK values (taken at da/dN = 8×10^{-9}m/cycle), stage II slopes, and crack growth rates at common stage II ΔK values (ΔK = 14 MPa-$m^{\frac{1}{2}}$ for R = 0.5 and ΔK = 22 MPa-$m^{\frac{1}{2}}$ for R = 0.05).

R - Ratio, $\frac{P,min}{P,max}$	Specimen	Frequency, Hz	Hydrogen Charged	Threshold ΔK, MPa-$m^{1/2}$	Common Crack Growth Rate, m/cycle	Stage II Slope, n
R = 0.5	1	5	No	10.90	2×10^{-8}	3.34
	2	5	No	11.48	2×10^{-8}	3.98
	3	5	No	10.60	2×10^{-8}	3.78
	4	5	Yes	9.84	3×10^{-8}	1.24
	5	5	*Yes	10.88	2×10^{-8}	4.05
	6	5	Yes	8.81	2×10^{-8}	2.89
	7	1	No	9.65	4×10^{-8}	4.46
	8	1	Yes	--	1×10^{-7}	1.23
	9	1	Yes	7.98	4×10^{-8}	2.90
	10	0.2	No	11.60	2×10^{-8}	4.22
	11	0.2	Yes	9.42	1×10^{-7}	5.31
R = 0.05	12	5	No	14.00	5×10^{-8}	4.21
	13 +	5	Yes	14.80	5×10^{-8}	3.91
	14	5	Yes	13.30	8×10^{-8}	4.13
	15	5	Yes	--	--	--
	16	5	Yes	--	1×10^{-7}	2.84
	17	5	Yes	--	4×10^{-7}	10.85

+ Pin broke during testing
* Charging was interupted twice. Sample was heated at 180°C, 2 hr. to allow hydrogen effusion.

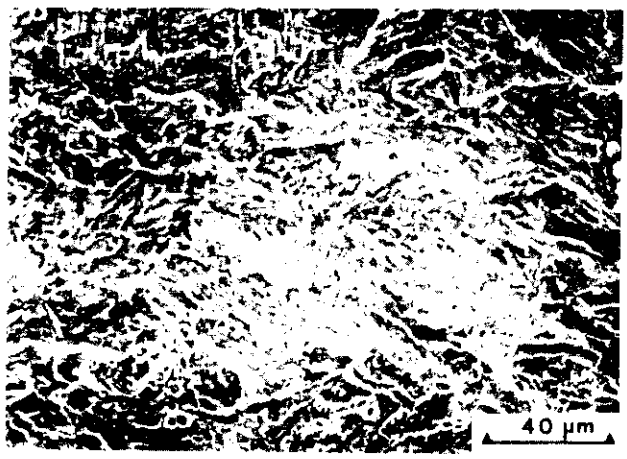

Fig. 5. Scanning electron micrograph showing transgranular quasi-cleavage and secondary cracking.

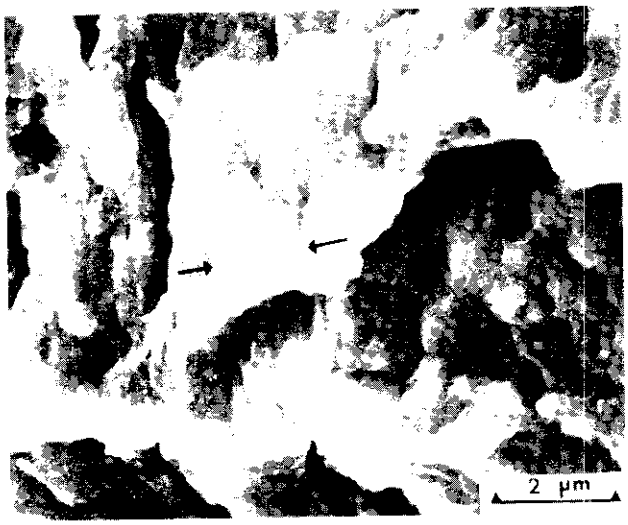

Fig. 6. Scanning electron micrograph showing evidence of slip (between arrows) and microvoid coalescence.

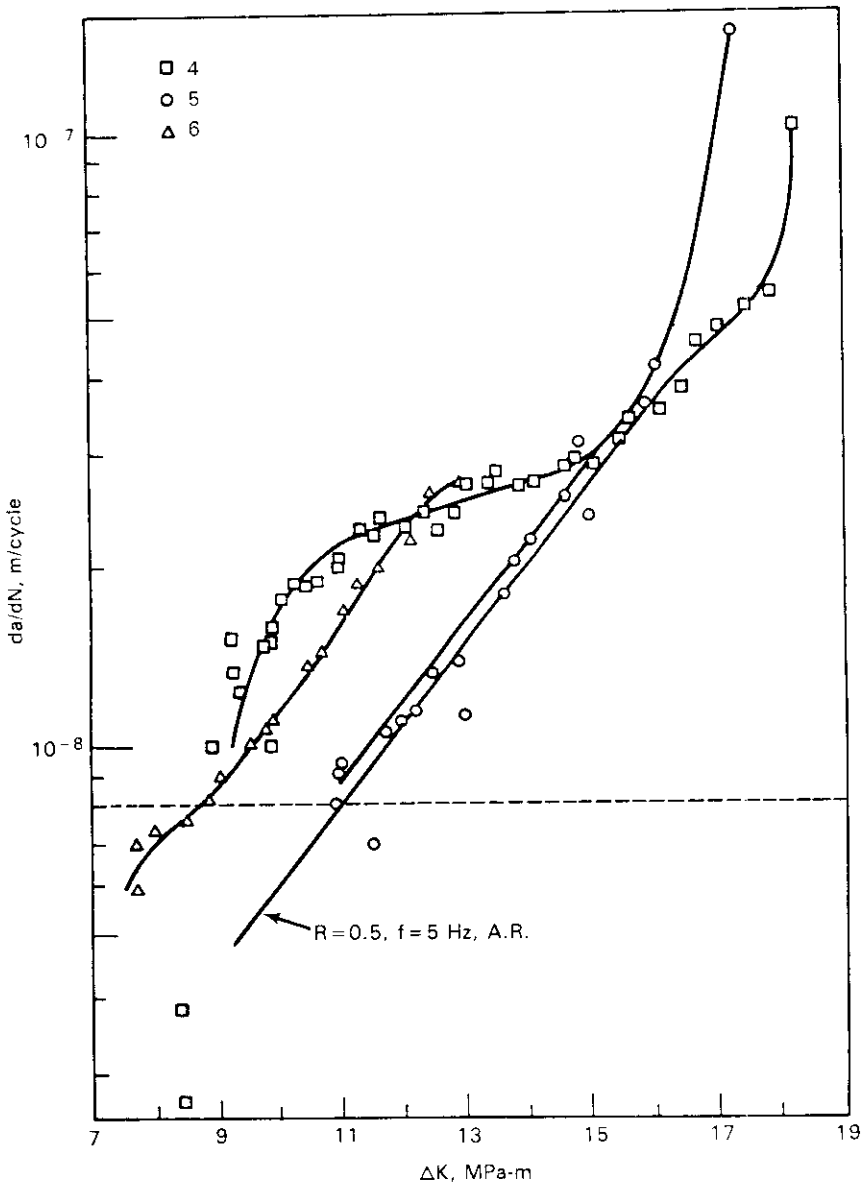

Fig. 7. FCG behavior of hydrogen-charged specimens tested at R = 0.5, f = 5 Hz (Hydrogen was baked from specimen 5).

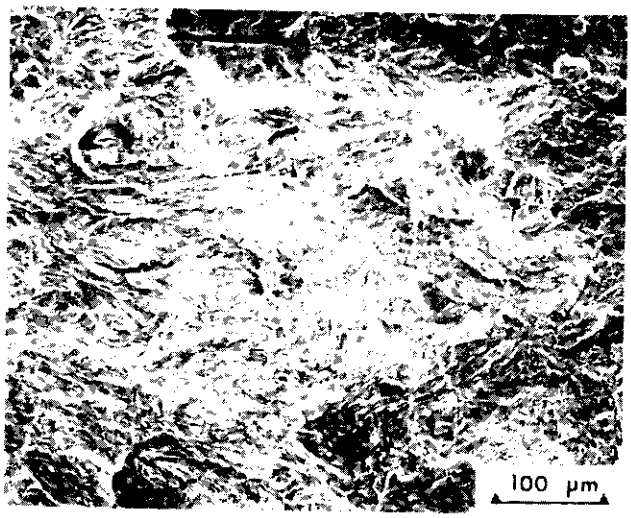

Fig. 8a. SEM micrographs depicting progression of intergranular fracture with decreasing ΔK and da/dN in charged specimen, (a) ΔK = 17.8 MPa-$m^{\frac{1}{2}}$, da/dN = 6 x 10^{-8} m/cycle, % intergranular fracture = 4%.

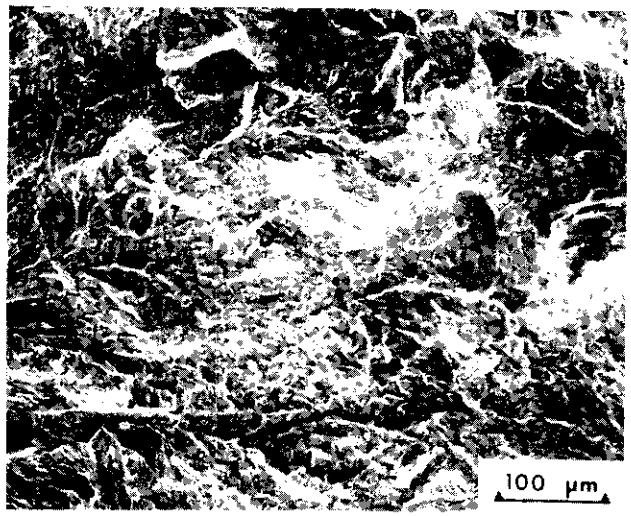

Fig. 8b. SEM micrographs depicting progression of intergranular fracture with decreasing ΔK and da/dN in charged specimen, (b) ΔK = 14.1 MPa-$m^{\frac{1}{2}}$, da/dN = 3 x 10^{-8} m/cycle, % intergranular fracture = 4%. 10^{-8} m/cycle, % intergranular fracture = 4%.

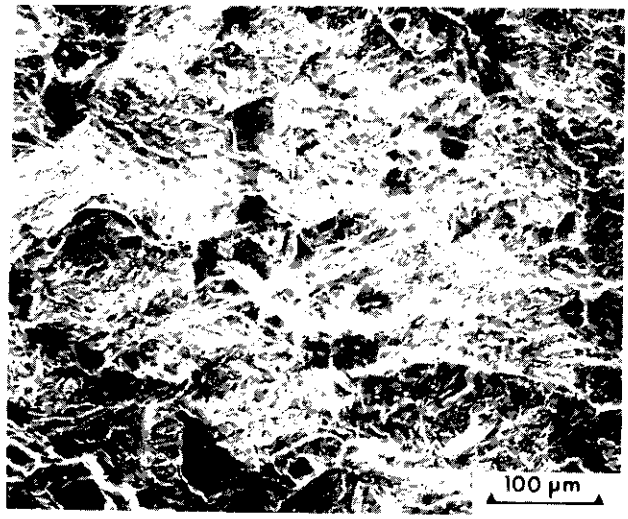

Fig. 8c. SEM micrographs depicting progression of intergranular fracture with decreasing ΔK and da/dN in charged specimen, (c) ΔK = 8.4 MPa-$m^{\frac{1}{2}}$, da/dN = 4 x 10^{-9} m/cycle, % intergranular fracture = 4%. 10^{-8} m/cycle, % intergranular fracture = 8%.

R = 0.5, f = 1 Hz

Specimen 7, tested in the as-received condition at R = 0.5 and f = 1 Hz, exhibited faster crack growth, ranging from two to ten times faster over the total range of ΔK than the specimens tested in the same condition at f = 5 Hz, as shown in Figure 9. The threshold was reached at ΔK = 9.65 MPa-$m^{\frac{1}{2}}$. Fractography revealed no change in fracture behavior from the uncharged specimens tested at f = 5 Hz, again being characterized by quasi-cleavage, inclusions, and microvoid coalescence. The slope of the stage II region, n = 4.46, was also in close agreement with the previous specimens. The crack growth rate at ΔK = 13.4 was 4 x 10^{-8} m/cycle, twice the rate of the uncharged specimens tested at 5 Hz.

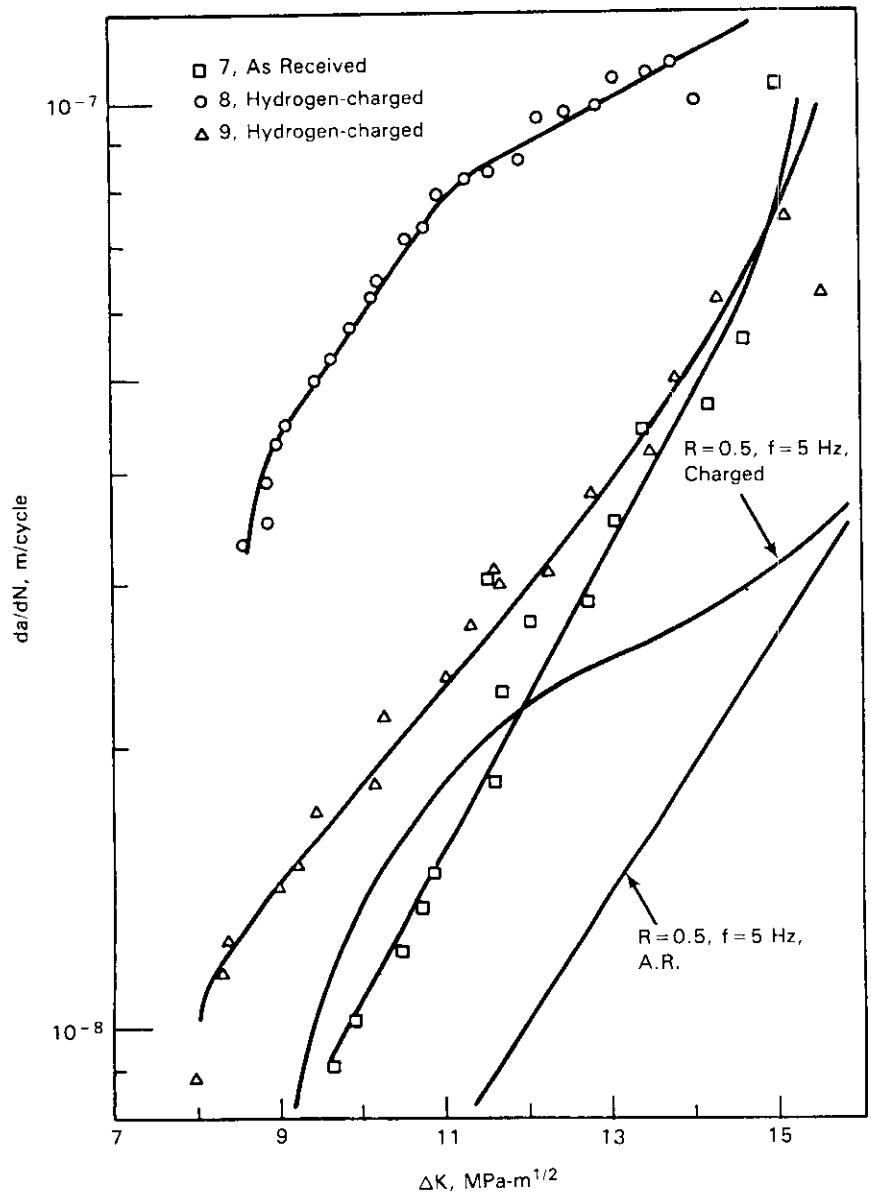

Fig. 9. FCG behavior of charged and as-received specimens tested at R = 0.5, f = 1 Hz.

Specimens 8 and 9, tested at f = 1 Hz and R = 0.5 in the charged condition, displayed two types of behavior. The curve followed by the crack growth in specimen 9 resembled that of specimens 4 and 6 (R = 0.5, f = 5 Hz, charged) in that the curve separates from the curve of the as-received specimen and exhibits a shoulder in the stage II region. The effect is not strong and, at the most, differs from the as-received specimen's growth rates by a factor of two. Specimen 8, however, exhibits the same type of shoulder, converging with the as-received specimen curve at a higher ΔK value, but the crack growth rates

are up to 5 times faster than the as-received specimen's rates. Growth rates taken at around ΔK = 13.4 MPa-$m^{\frac{1}{2}}$ were 1 x 10^{-7} and 4 x 10^{-8} m/cycle for specimens 8 and 9, respectively. Fractography revealed about 12% intergranular fracture at ΔK = 9 MPa-$m^{\frac{1}{2}}$ for both specimens. The other fracture characteristics listed for the as-received specimens were also present.

The ΔK threshold value for specimen 9 was 7.98 MPa-$m^{\frac{1}{2}}$, while specimen 8 did not reach the threshold da/dN value. This value was slightly lower than that of the as-received specimen. The slopes in the stage II region were n = 1.23 and n = 2.90 for specimens 8 and 9, respectively.

R = 0.5, f = 0.2 Hz

Specimen 10, tested in the as-received condition at R = 0.5 and f = 0.2 Hz, yielded a crack growth rate slightly lower than that of specimen 2, tested at 5 Hz. The crack growth rate at ΔK = 13.8 MPa-$m^{\frac{1}{2}}$ was 2 x 10^{-8} m/cycle, or approximately 25% lower than the rate of specimen 2 at a similar ΔK value. The threshold value was higher, at 11.6 MPa-$m^{\frac{1}{2}}$. SEM micrographs indicated a dominance of quasi-cleavage mode with secondary cracking and a small amount of microvoid coalescence. Stringers were evident throughout the specimen and a negligible amount (<1%) of intergranular fracture was observed. The stage II slope was n = 4.22.

Specimen 11, hydrogen-charged and tested at the same conditions as specimen 6, displayed behavior different from that of previous specimens, based upon the slopes of the crack growth curve and the amount of intergranular fracture at the various stages of crack growth. The curve at the upper portion of the stage II regime had a slope similar to that of the uncharged specimen, although the growth rates were about an order of magnitude higher. However, toward the middle range of this region the slope increased markedly, whereas the slopes for other charged specimens had decreased. The overall stage II slope was n = 5.31. The crack growth rate at ΔK = 13.76 MPa-$m^{\frac{1}{2}}$ was 1 x 10^{-7} m/cycle which, as noted earlier, was an order of magnitude faster than the rate of the uncharged specimen at a similar value of ΔK. A comparison of behavior may be made by observation of Figure 10.

SEM micrographs revealed that the mode of fracture was intergranular upon commencement of the test. The trend followed by the fracture mode was opposite to the trend seen in previous charged specimens. The greatest amount of intergranular fracture was seen at the beginning of the test, 19.8% at ΔK = 17.5 MPa-$m^{\frac{1}{2}}$, decreasing as the test proceeded to 10.57% at ΔK = 9.54 MPa-$m^{\frac{1}{2}}$. The large percentage of intergranular fracture at the beginning of the test could be due to the time that hydrogen has to diffuse to the crack tip, and the decrease in the intergranular fracture as the crack propagated could be due to the loss of hydrogen. The total test required about 1½ weeks at a frequency of 0.2.

R = 0.05, f = 5 Hz

Specimen 12, in the as-received condition, tested at R = 0.05 and f = 5 Hz exhibited a crack growth rate of 5 x 10^{-8} m/cycle at a ΔK of 22 MPa-$m^{\frac{1}{2}}$. This ΔK is roughly equivalent to a ΔK of 14 MPa-$m^{\frac{1}{2}}$ at R = 0.5. The observed crack growth rate was 2.5 times faster than that observed at R = 0.5 and 5 Hz as shown in Figure 11. The Paris slope was determined as n = 4.21. SEM again revealed quasi-cleavage, secondary cracking and inclusions in addition to a negligible (<1%) amount of intergranular fracture.

Of the five charged specimens tested at R = 0.05, the cracks of specimens 14, 16, and 17 grew without complications. One of the grip pins broke during the specimen 13 test, resulting in an asymmetrical crack front. The crack growth rate curve coincided with and was slightly lower than those of tests that ran properly. The growth rate at ΔK = 22.7 MPa-$m^{\frac{1}{2}}$ was 5 x 10^{-8} m/cycle. The stage II slope was n = 3.91. SEM revealed the same features seen in uncharged specimens with no intergranular fracture.

Specimen 15 was started three separate times due to a problem in maintaining the ΔK level. All data points were contained in a range from ΔK = 19 to 21 MPa-$m^{\frac{1}{2}}$ and da/dN = 2 to 6 x 10^{-8} m/cycle. A stage II slope could not be taken because these data formed a cluster. Macroscopic examination of the fracture surface revealed that the crack had jumped approximately 3 mm during the first two starts of the test. This area was highly uneven and pits and stringers could be seen clearly on low magnification (20X). Once the crack front passed this area the surface began to exhibit mixed quasi-cleavage and intergranular fracture.

Specimen 14 exhibited behavior similar to the charged specimens tested at R = 0.5 in that the crack growth rate curve was higher than that of the uncharged condition, although the effect was slight, and the percentage of intergranular fracture increased to about 16% at ΔK = 14.3 MPa-$m^{\frac{1}{2}}$ (K_{max} = 15.1) from less than 2% at ΔK = 27.5 MPa-$m^{\frac{1}{2}}$ (K_{max} = 28.9). At an intermediate value, ΔK = 20.4 MPa-$m^{\frac{1}{2}}$ (K_{max} = 21.5), there was approximately 7% intergranular fracture. The threshold was ΔK= 13.3 MPa-$m^{\frac{1}{2}}$ and the crack growth rate at ΔK = 22.6 MPa-$m^{\frac{1}{2}}$ was 9 x 10^{-8} m/cycle, less than 70% faster than the uncharged specimen. The stage II slope was n = 4.13, implying that the hydrogen did not change the shape of the ΔK-da/dN curve.

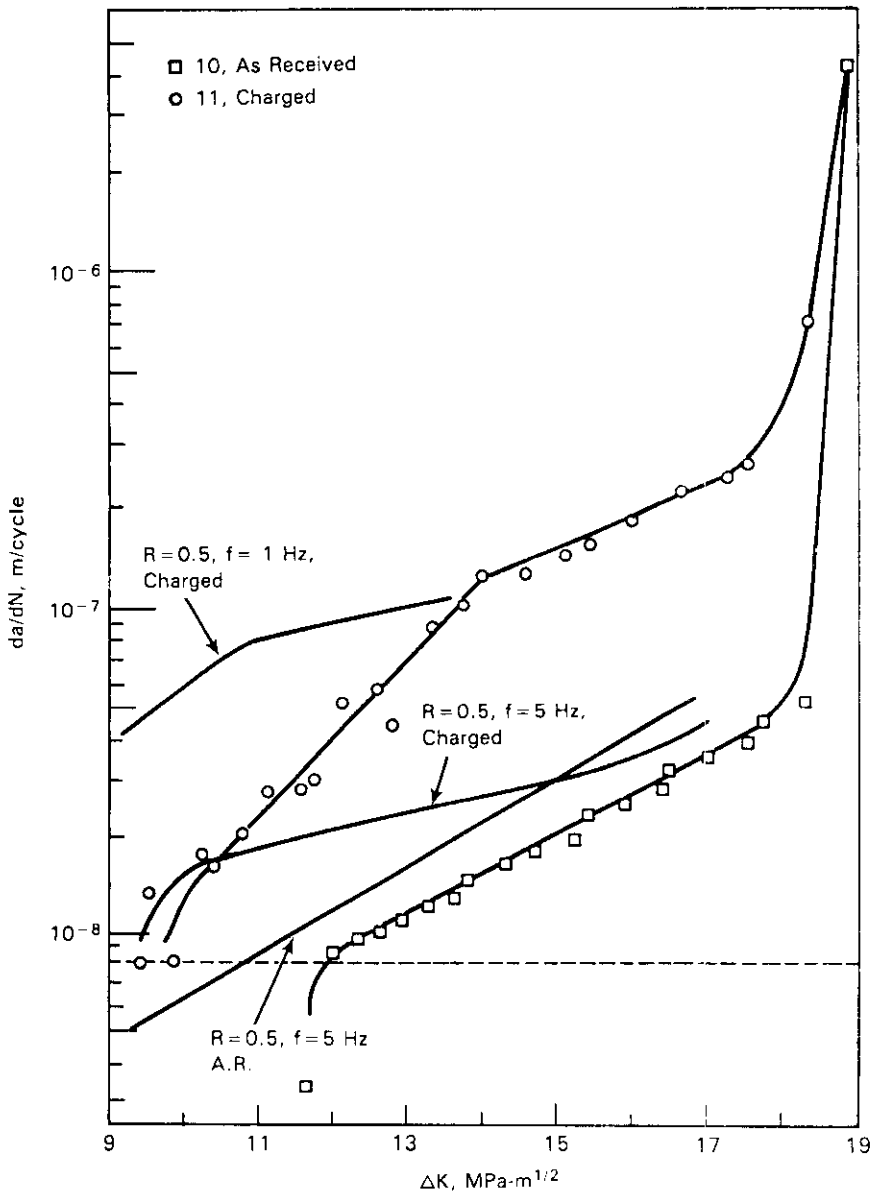

Fig. 10. FCG behavior of charged and as-received specimens tested at R = 0.5, f = 0.2 Hz.

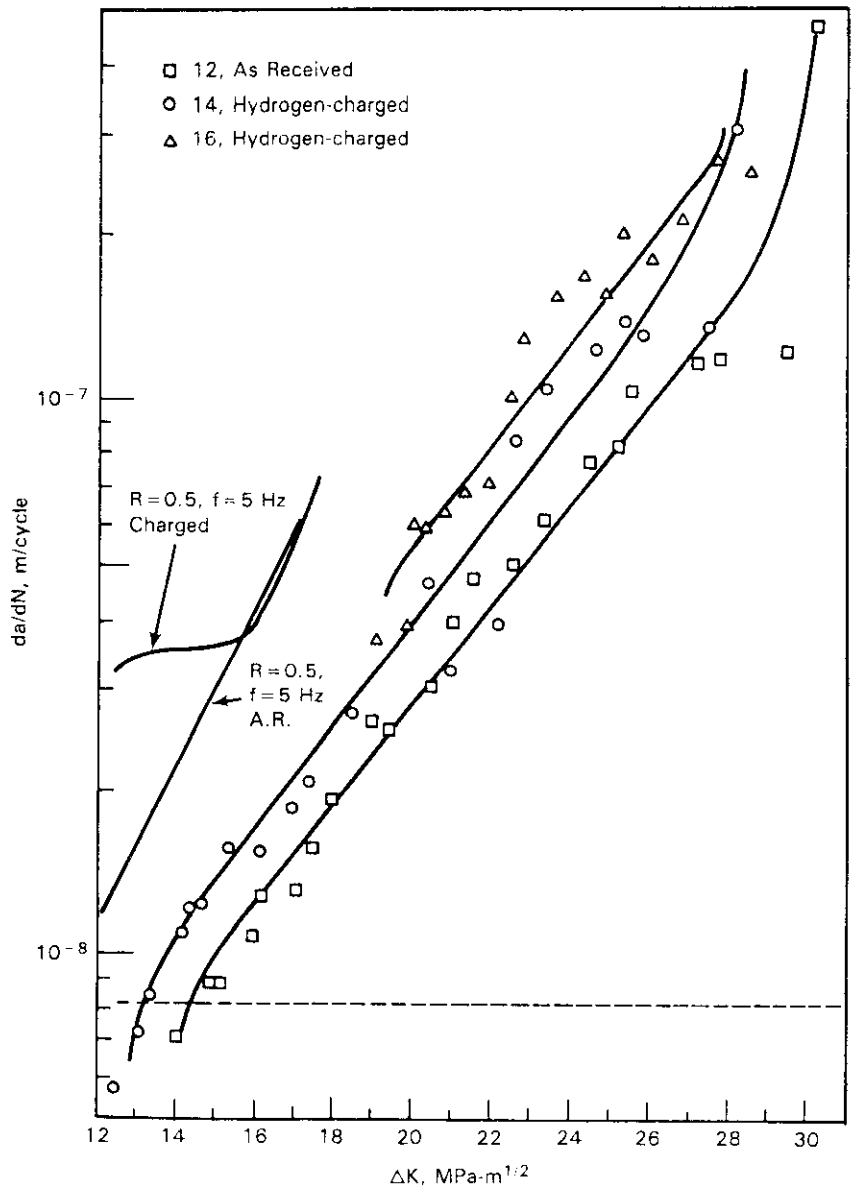

Fig. 11. FCG behavior of charged and as-received specimens tested at R = 0.05, f = 5 Hz.

Specimen 16 exhibited a higher growth rate than the previous specimen, with da/dN = 1 x 10^{-7} m/cycle at ΔK = 22.5 MPa-$m^{\frac{1}{2}}$, or approximately twice the rate of the uncharged specimen. The slope of the stage II region, n, was equal to 2.89. SEM results at ΔK = 27.8 MPa-$m^{\frac{1}{2}}$ (K_{max} = 29.3) indicated a fracture mode of shear ridges, shown in Figure 12, in addition to the secondary cracking, quasi-cleavage, and stringers. Less than 2% of the fracture surface was intergranular at ΔK = 20.8 MPa-$m^{\frac{1}{2}}$ (K, max = 21.9), the slower crack growth region.

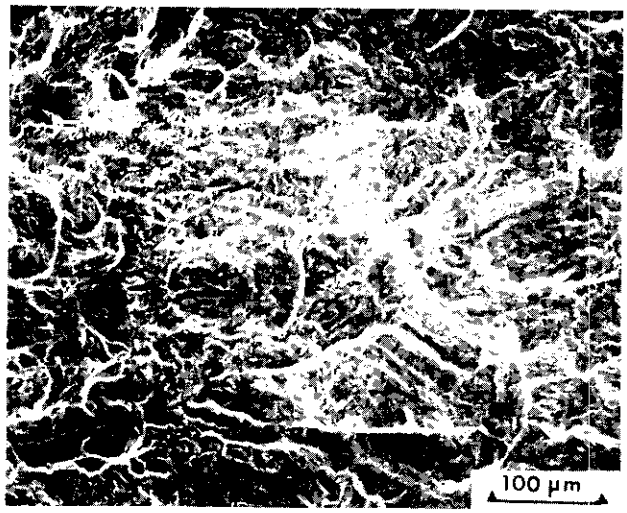

Fig. 12. SEM micrograph showing dimple rupture, quasi-cleavage and stringers in specimen 16 tested at R = 0.05, f = 5 Hz.

Specimen 17 demonstrated a higher crack growth rate than the other specimens but grew only from ΔK = 22 (K, max = 23.2) to 18 MPa-$m^{\frac{1}{2}}$ (K, max = 18.9). At ΔK = 21.4 MPa-$m^{\frac{1}{2}}$ (K, max = 22.5) the crack growth rate was 4 x 10^{-7} m/cycle, almost an order of magnitude faster than the uncharged specimen. The percentage of intergranular fracture was negligible. The stage II slope was n = 10.85 while SEM revealed quasi-cleavage, inclusions, and secondary cracking but no intergranular fracture. A comparison of the crack growth rate curves for specimens tested at R = 0.5 with f = 5, 1, and 0.2 Hz and for R = 0.05 at f = 5 Hz in the uncharged and H charged conditions, respectively, is given in Figures 13 and 14.

Evaluation for Crack Closure

Auger electron spectroscopy was performed on specimens 6, 12, 14, 15, and 16 based on the suspicion of oxide-induced crack closure effects. Specimen 6, tested at R = 0.5, was analyzed in order to compare against specimens tested at R = 0.05. Results of the analysis indicated an oxide thickness from 150-250°A on the fracture surface, but no trends were observed which indicated oxide-induced crack closure.

DISCUSSION

Fracture Mode

The presence of internal hydrogen in the specimens had a definite impact on the mode of fracture. In uncharged specimens, independent of the test frequency and load ratio, no significant amount of intergranular fracture was present. Charged specimens exhibited up to 20% intergranular fracture, indicating that hydrogen played a key role in determining the fracture mode. Impurities such as phosphorus in the presence of hydrogen will also decrease the cohesive strength at the grain boundaries resulting in increased intergranular fracture (11,12). Work performed on this alloy by Jones (7) confirmed this effect in static tests (external hydrogen), revealing a concentration of phosphorus at the grain boundaries in the same heat treated condition as in the present testing.

Traps such as dislocations, carbides, grain boundaries, and other interfaces found in the material may be detrimental or beneficial. Hydrogen is attracted preferentially to these traps (13) and may assist in the fracture process by decreasing the cohesive strength of the trap to the level of local stress, allowing fracture to occur. Other traps may be beneficial by attracting enough hydrogen to prevent critical concentrations from reaching the detrimental traps.

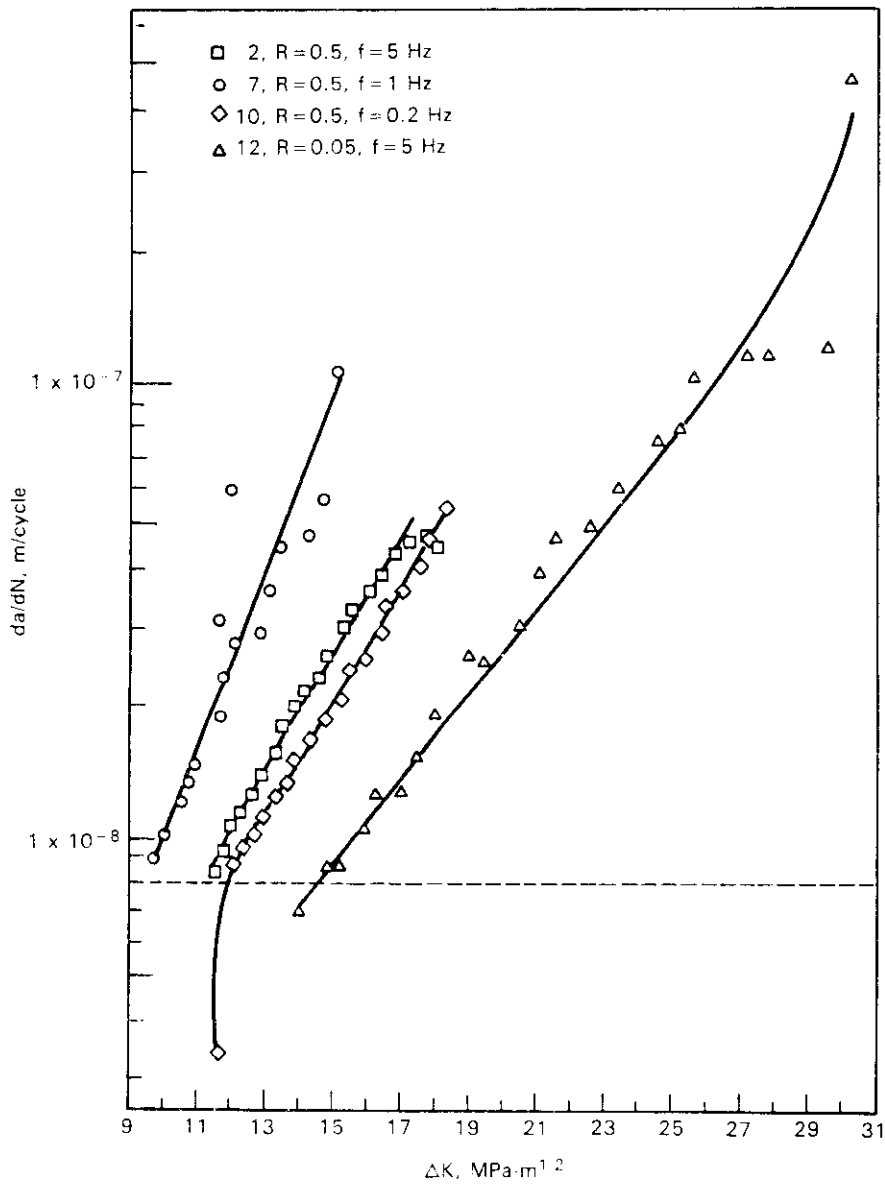

Fig. 13. FCG behavior comparison of representative specimens in the as-received condition.

Another factor to be considered in the mode of fracture is the stress state at the crack tip. As noted earlier, the stress state changes from a plane stress to a plane strain condition from the surface to the center of the specimen. According to Beevers (10), the occurrence of intergranular separation is dependent upon the stress state at the crack tip; i.e., the occurrence of intergranular fatigue fracture is enhanced by plane strain conditions. The high principal stresses maintained at the crack tip by these conditions, combined with the presence of internal hydrogen, encourage an intergranular mode of fracture.

The percentage of intergranular fracture generally increased with decreasing crack growth rates as shown in Figure 15. This effect results from the greater time available at slower crack growth rates for hydrogen to diffuse to the crack tip and to traps such as grain boundaries ahead of crack tip. An opposite trend in the relationship of crack growth rate to percentage of intergranular fracture is demonstrated by specimen 11 tested at a frequency of 0.2 Hz.

Fractography of specimen 5, which was outgassed at 180°C, revealed that intergranular fracture was present even though the crack growth behavior was almost identical to the uncharged specimens tested at the same conditions. Some of the reversible damage was eliminated by heating the specimen and allowing hydrogen to effuse from traps with low binding energies and from the lattice, while enough hydrogen was retained at the grain boundaries to cause intergranular fracture. It is possible that higher baking tem-

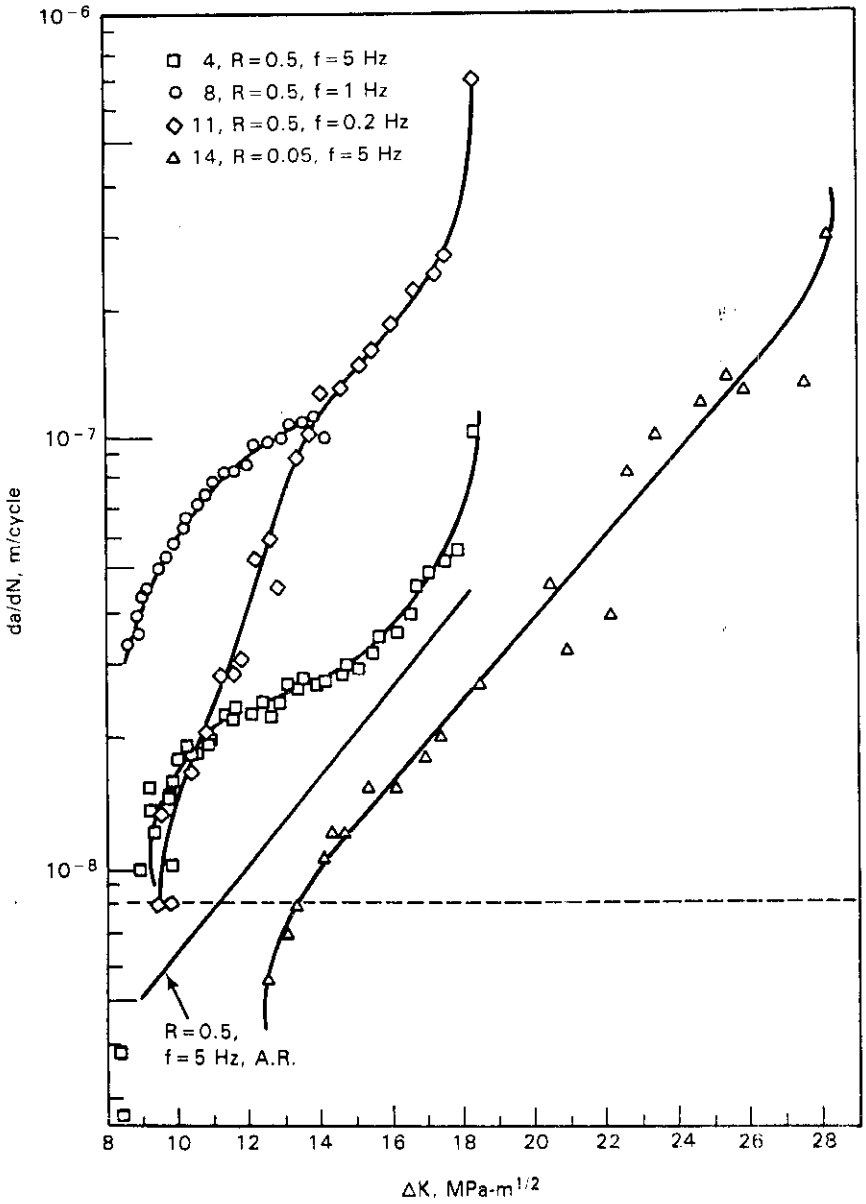

Fig. 14. FCG behavior comparison of representative specimens in the hydrogen-charged condition.

peratures could have reduced the percentage of intergranular fracture further. Similar results were found by Esaklul and Gerberich (14) when a charged sample was baked at 150°C resulting in behavior not unlike that of the uncharged samples.

In the case for R = 0.05 there is an inconsistent trend of increasing percentage of intergranular fracture with decreasing crack growth rates. The trend is followed by specimen 14 but not by any of the others tested in this group as shown in Figure 16.

Crack Growth Rate

As seen in Figures 7, 9, 10, and 11, the presence of internal hydrogen accelerated crack growth rates over the rates of specimens which were uncharged. This effect is mainly evident from the divergence of crack growth rate curves at ΔK values below the upper stage II region. In this study the crack growth rates of the charged specimens ranged from 2-10 times those of the uncharged specimens. This corresponds with work performed on HSLA steel in which crack propagation rates in specimens with internal hydrogen increased 4-10 times over those of uncharged specimens (14). These increased growth rates were generally accompanied by a decrease in the stage II slope, indicating a more gradual change in crack growth rates of the charged versus uncharged specimens. This is in contrast to work performed on HSLA steel in which the

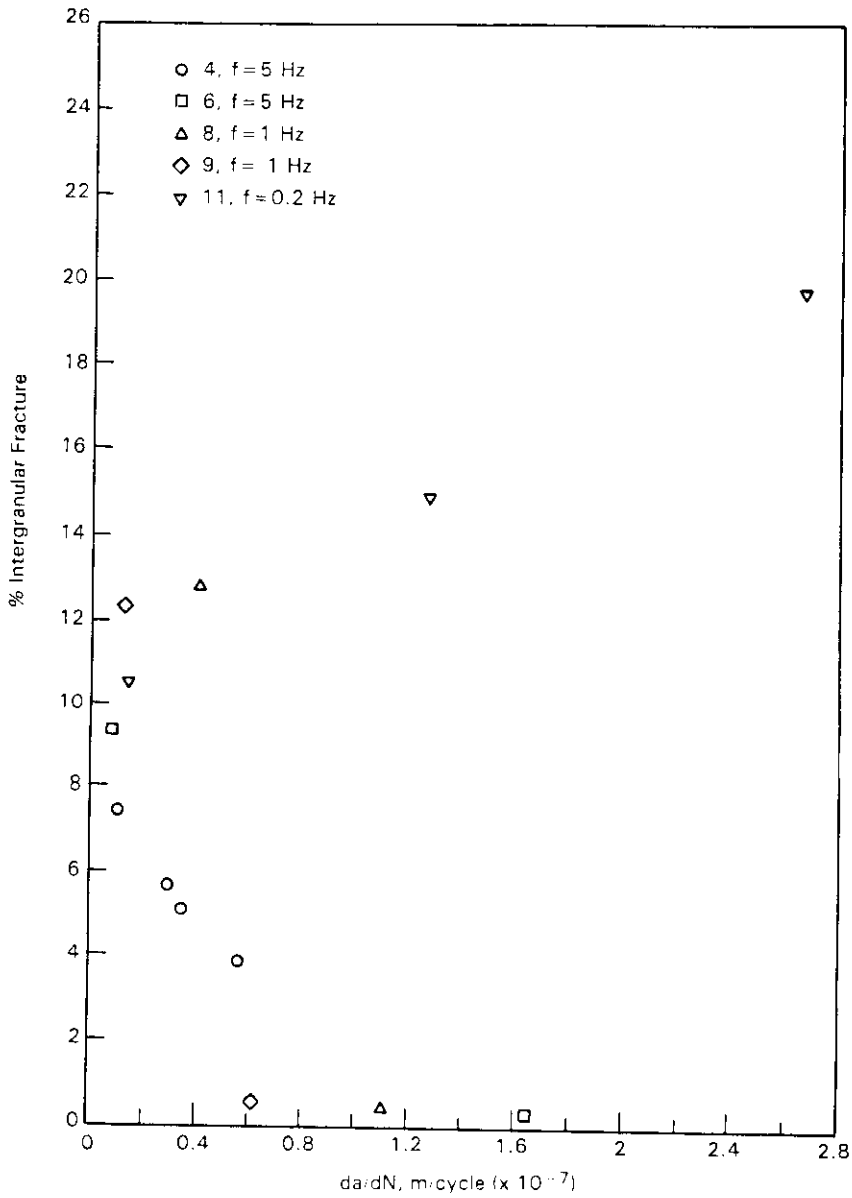

Fig. 15. Relationship of da/dN to percentage of intergranular fracture for five specimens tested at R = 0.5.

Paris slope increased approximately 25% with internal hydrogen (14).

The convergence of the curves for the charged and uncharged cases indicates that there exists a crack growth rate, above which the hydrogen effect is overcome by the mechanical behavior. It is at this point that intergranular fracture begins to appear with decreasing ΔK. The point at which these curves merged varied with test frequency and R-ratio.

Comparing this study to previous work on the same alloy revealed that as the crack growth rate curve reached its threshold values the crack growth rates were 5-10 times greater than those of static tests (7).

Frequency Effect

Decreasing the frequency from 5 Hz to 1 Hz resulted in an increase in the crack growth rates both in the charged and uncharged conditions. The increase in crack growth rate was greater by a factor of 3-6 times over the ΔK range tested. Corrosion fatigue work performed on AISI 4340 resulted in the same type of behavior, with an increase in crack growth rates with decreasing frequency (6).

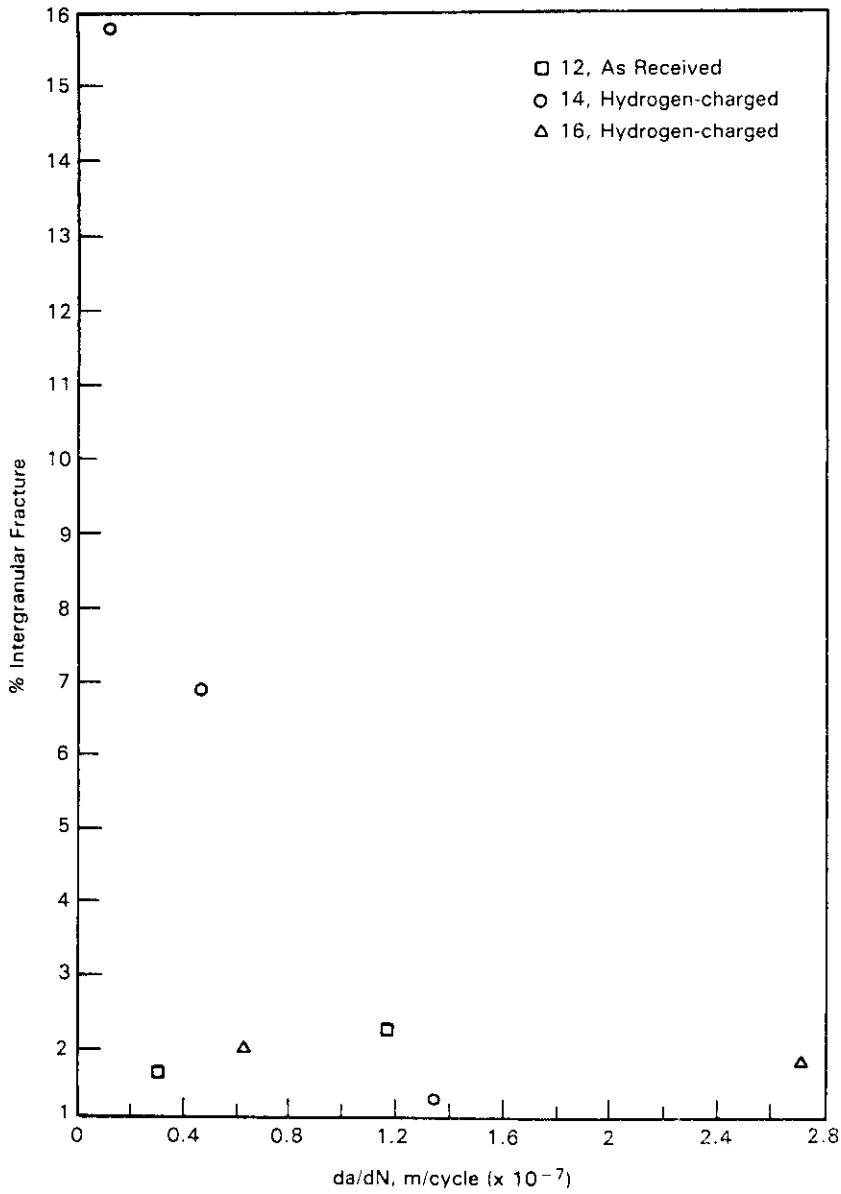

Fig. 16. Relationship at da/dN to percentage of intergranular fracture for five specimens tested at R = 0.05.

The increase in the crack growth rate with decreasing frequency is illustrated in Figure 15 where the increase in crack growth rate at a ΔK of 14 MPa-$m^{\frac{1}{2}}$ for the hydrogen charged condition relative to the uncharged condition tested at the same frequency is plotted as a function of inverse frequency. It is clear from these results that the crack growth rate increases with increasing time between cycles; however, the rate of increase appears to decrease at longer times. The increase in crack growth rate with time can be related to the time available for hydrogen to accumulate in the high stress region ahead of the crack tip.

CONCLUSIONS

Internal hydrogen was found to have a significant effect on the fatigue crack growth rate of HT-9 tested at room temperature. The effect of internal hydrogen was most pronounced at ΔK's below 15 MPa-$m^{\frac{1}{2}}$ for tests at a load ratio of 0.5. At a load ratio of 0.05 internal hydrogen had very little effect. The effect of internal hydrogen on the fatigue crack growth of HT-9 can be summarized as follows:

1. Internal hydrogen affects the stage I and II crack growth regime of HT-9 causing an increase in the crack growth rate and decrease in the threshold stress intensity.

2. Hydrogen induces intergranular crack growth in HT-9 during fatigue crack growth with the percentage of intergranular fracture increasing with decreasing crack velocities. The observation that hydrogen induces intergranular fracture during the fatigue crack growth of HT-9 is consistent with observations of hydrogen induced intergranular fracture of this steel for both precharged and dynamic tensile tests and for subcritical crack growth in cathodic hydrogen.

3. The effect of hydrogen on the fatigue crack growth rate can be partially correlated with the extent of the intergranular fracture; however, there is some evidence that suggests that the hydrogen effect may also be related to its effect on transgranular crack growth.

4. The fatigue crack growth rate of HT-9 of both the uncharged and hydrogen charged material was a function of the cyclic frequency. The difference in the fatigue crack growth rate of the uncharged and charged material showed an increase with increasing time per cycle. This effect indicates that the hydrogen effect may be of concern at Tokamak cycle frequencies if the effect persists to reactor temperatures. There is some evidence that a hydrogen concentration of less than 1 appm affects the fatigue crack growth rate of HT-9.

5. The hydrogen effect was more pronounced at a load ratio of 0.5 than at 0.05 where there was only a small increase in the crack growth rate with hydrogen charging.

FUTURE WORK

Evaluation of the effect of hydrogen on the subcritical crack growth rate of HT-9 at reactor temperatures will be evaluated. Both static and cyclic loading effects will be considered using a combination of experiment and modeling.

REFERENCES

1. R. H. Jones, "Application of Hydrogen Embrittlement Models to the Crack Growth Behavior of Fusion Reactor Materials," in Proceedings of the Second International Conference on Fusion Reactor Materials, April 1986.
2. W. W. Gerberich, T. Livne and X. Chen, in Proceedings of Symposium on Modeling Environmental Effects of Crack Initiation and Propagation, eds. R. H. Jones and W. W. Gerberich, held in Toronto, Canada, published by TMS-AIME, Warrendale, PA, 1985.
3. D. P. Williams and H. G. Nelson, Metall. Trans. 1, 63 (1970).
4. R. W. Pasco, K. Sieradzki and P. J. Ficalora, Scripta Met. 16, 881 (1982).
5. K. A. Esaklul and W. W. Gerberich, "Near-Threshold Fatigue Behavior of HSLA Steels," in International Conference on Technical Applications of HSLA, ASM Metals Congress, 1983.
6. P. S. Pao, W. Wei and R. P. Wei, "Effect of Frequency on Fatigue Crack Growth Response of AISI 4340 Steel in Water Vapor," pp. 565-580 in Environ-Sensitive Fracture of Engineering Materials, TMS-AIME, Warrendale, PA, 1979.
7. R. H. Jones, "Hydrogen-Induced Subcritical Crack Growth of a 12Cr-1Mo Ferritic Stainless Steel," Metall. Trans. A. 17A:1229-1240 (1986).
8. J. M. Hyzak and R. E. Stoltz, "The Effect of Internal Hydrogen on the Mechanical Properties of HT-9: Room Temperature," pp. 180-190 in Alloy Development for Irradiation Performance Quarterly Progress Report, DOE/ER-0045/6, U.S. Department of Energy, Washington, D.C., 1981.
9. R. W. Hertzberg. 1983. Deformation and Fracture of Engineering Materials, 2nd edition, John Wiley and Sons, New York, NY, 1975.
10. C. J. Beevers, "Micromechanisms of Fatigue Crack Growth at Low Stress Intensities," Metal Science (August-September 1980).
11. C. G. Interrante, "Basic Aspects of the Problem of Hydrogen in Steels," ASM, Metals Park, Ohio, 1982.
12. A. R. Troiano, "The Role of Hydrogen and Other Interstitials in the Mechanical Behavior of Metals," Trans. ASM 52:54-80 (1960).
13. R. Gibala and D. S. DeMiglio, "Hydrogen in Iron and Steels: Interactions, Traps, and Crack Paths," pp. 113-122 in Hydrogen Effects in Metals, TMS-AIME Proceedings, Warrendale, PA, 1981.
14. K. A. Esaklul and W. W. Gerberich, "Internal Hydrogen Degradation of Fatigue Thresholds in HSLA Steel," ASTM 16th Fracture Mechanics Conference held August 1983 at Battelle Memorial Institute, Columbus, Ohio, 1983.

5. RADIATION EFFECTS: MECHANISTIC STUDIES, THEORY AND MODELING

MICROSTRUCTURE OF COPPER ALLOYS FOLLOWING 14-MeV NEUTRON IRRADIATION — S. J. Zinkle (Oak Ridge National Laboratory)

OBJECTIVE

The objective of this study is to gain a better understanding of the evolution of the microstructure of fcc metals during 14-MeV neutron irradiation. Results from this study may be utilized to develop fission/fusion neutron correlations and to guide the development of theoretical models of the damage process.

SUMMARY

The microstructure of copper and three single-phase copper alloys (Cu—5%Al, Cu—5%Mn, Cu—5%Ni) has been examined following a room-temperature 14-MeV neutron irradiation up to a maximum fluence of 2×10^{21} n/m^2 ($\sim 10^{-3}$ dpa). The irradiation produced small defect clusters, many of which were resolvable as stacking fault tetrahedra (SFT) or triangle loops. Alloying did not affect the overall cluster density or size distribution, but it did cause a significant reduction in the density of SFT and triangle loops. The overall defect cluster size was independent of fluence with a mean and most probable diameter of ~2.7 and ~1.7 nm, respectively. There was no evidence of cascade overlap in this study. Cascade overlap effects are estimated to become significant for fluences $\sim 10^{23}$ n/m^2. The overall defect cluster density was found to vary as $N \sim \sqrt{\phi t}$ with a short incubation period for all four metals. Reexamination of published data indicates that this relationship may be broadly applicable over the irradiation temperature range 80 to 400 K. Logarithmic plots of the cluster density versus fluence produced anomalous curvature due to the influence of the incubation period.

PROGRESS AND STATUS

Introduction

An extensive radiation effects data base has been established based on fission reactor irradiation of structural materials. However, successful prediction of radiation damage effects in D-T fusion reactors requires that the differences and similarities between fission and fusion neutron damage microstructures be fully understood. The present study is a continuation of a fission-fusion correlation program utilizing the Rotating Target Neutron Source (RTNS-II) 14-MeV neutron source at Lawrence Livermore National Laboratory that was initiated[1] in 1979. Copper was chosen for this program as a representative fcc metal with a relatively low stacking fault energy. Three solid solution copper alloys were included in the irradiation program in order to study solute effects.

Initial results from this program were reported by Brager et al.[2] Several questions remain unanswered following this initial study, so a followup investigation utilizing electrical resistivity, microhardness, and electron microscopy measurements was performed. The resistivity and Vickers microhardness results from this later study are described elsewhere.[3,4] The present report concentrates on the microstructural changes observed in copper and the copper alloys as a result of irradiation.

Experimental Procedure

Foils of pure copper (99.99+%) and copper alloyed with 5 at. % of either aluminum, nickel, or manganese were used in this irradiation study. As shown in Table 1, this produces single-phase alloys containing either undersized (Ni) or oversized solutes.[5,6] The addition of 5 at. % Al reduces the stacking fault energy of copper by a factor of 2 (ref. 7). These three alloys remain single phase at room temperature for solute concentrations up to at least 15 at. %, although there are some indications of short-range ordering at lower solute levels.

Foils of 250 μm thickness were obtained from Westinghouse Hanford Company,[2] and were subsequently cold rolled to a thickness of 25 μm. Transmission electron microscopy (TEM) disks were punched from the rolled foils. The disks were then recrystallized by annealing in high-purity argon and allowed to air cool. The four metals were irradiated at room temperature (25°C) with 14-MeV neutrons from the RTNS-II facility. The TEM disks of each metal were positioned away from the neutron source along four different isoflux contours. This produced four fluence levels of 1×10^{20}, 4×10^{20}, 1×10^{21}, and 2×10^{21} n/m^2 at the end of the irradiation. Earlier studies had determined that variation in the 14-MeV neutron dose rate over three orders of magnitude did not affect the details of cluster formation in copper irradiated at room temperature.[2,8] Further details of the specimen preparation and irradiation are described elsewhere.[4,9]

The TEM specimens were electropolished in a Tenupol twin-jet polishing unit using a solution of 33% HNO_3/67% CH_3OH cooled to −25°C with 100 mA current (6-V dc potential). The foils were examined in a JEOL 2000FX electron microscope. Foil thicknesses were determined using either thickness fringes or convergent

Table 1. Effect of solute additions on the properties of copper

Property	Copper	Cu–5 at.% Al	Cu–5 at. % Mn	Cu–5 at. % Ni	ref.
Lattice parameter, nm	0.36150	0.36290	0.3339	0.36096	5
(Volume size factor of solute)	--	(+19.99%)	(+34.19%)	(–8.45%)	6
Stacking fault energy, mJ/m^2	50	25	50	52	7

beam techniques. Characterization of the microstructure was performed on foils with thicknesses of 50 to 120 nm using a combination of bright-field and weak beam dark-field techniques. The defect cluster size and density measurements were made using a Zeiss particle analyzer on micrographs with a total print magnification of about 1×10^6. A total of 1000 to 4000 defect clusters from at least two different foil regions were counted for each irradiation condition.

Results

The neutron irradiation produced a high density of small defect clusters in copper and the copper alloys. All of the visible defect clusters were less than 10 nm in diameter. There was no evidence of void formation in any of the irradiated foils. Figure 1 shows the general microstructure of copper following irradiation to a fluence of 2×10^{21} n/m^2 ($\sim 7 \times 10^{-4}$ dpa). The irradiated microstructure of the three copper alloys was very similar to that of pure copper. Figure 2 shows typical damage microstructures for each of the four metals.

The mean free path between scattering events for a 14-MeV neutron in copper is 4 cm. Therefore, at low fluences, defect clusters formed as a result of a displacement cascade are well separated from other cascades. The 14-MeV neutron is sufficiently energetic to allow the cascade to develop into distinct subcascade lobes.[10] The subcascade regions may then evolve into defect clusters which are visible by TEM. Figure 3 shows an example of these closely spaced subcascade clusters in a low-fluence specimen. The number of visible defect clusters associated with each cascade region ranges from 1 to 7. The average spacing between clusters in a given cascade is about 5 nm. The relation between the number of visible clusters and the number of subcascade lobes per cascade event is rather uncertain.[11] Vacancy clusters can form directly from the collapse of the vacancy-rich core of the subcascade, whereas interstitial clusters are presumably formed by classical nucleation and growth and may involve cooperative effects from adjacent subcascade lobes.

At sufficiently high fluences (high defect cluster density), the newly created cascades begin to interact with existing defect clusters and the cluster density approaches a saturation value. There is no evidence of cascade overlap at the maximum fluence studied in this investigation, 2×10^{21} n/m^2. Figure 4 shows that the cascade regions are still well isolated from each other at this fluence level. (The actual inter-cascade spacings are even larger than is apparent in Fig. 4 due to foil thickness effects.) This conclusion is important for determining the fluence dependence of the defect cluster density. Brager et al.[2] have similarly determined that there are no cascade overlap effects in these alloys for 14-MeV neutron fluences approaching 10^{22} n/m^2

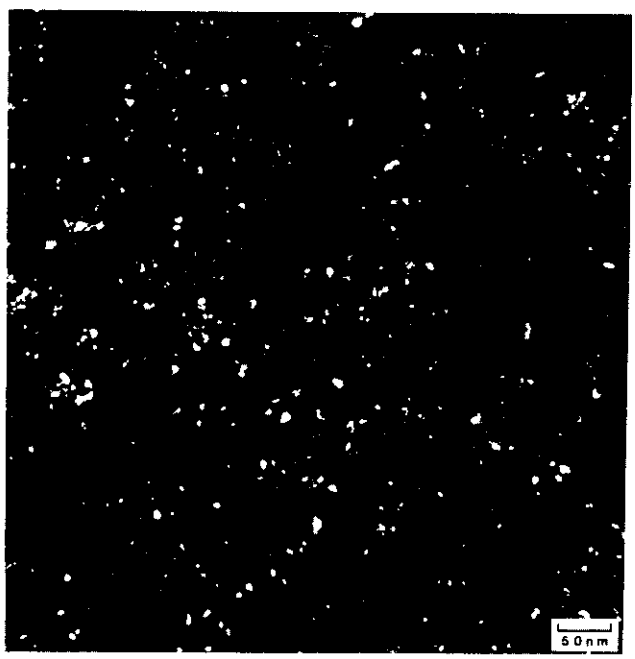

Fig. 1. Weak beam (g, 3g) microstructure of copper irradiated to a fluence of 2×10^{21} n/m^2. The foil normal is near [110]; g = 002 and s = 0.

Figure 5 shows a high magnification example of the bright-field microstructure of copper following irradiation to 2×10^{21} n/m^2. Triangle-shaped defect clusters, which are either stacking fault tetrahedra (SFT) or triangular loops, are clearly visible in this orientation (B = [110]). The use of other orientations such as B = [001] has shown that SFT and triangle loops occur in roughly equal numbers over the fluence range investigated. According to the Silcox and Hirsch model,[12] the SFT is formed from the dissociation of a triangular vacancy loop.

Figure 6 shows one of the largest SFT that was observed in this study. The defect cluster, which has an edge length of 6.5 nm, appears as a square for the beam orientation that was used (B = [001]). This SFT was present in a foil that was irradiated to the lowest fluence studied in this investigation – 1×10^{21} n/m^2. It is possible that the SFT may have formed directly from the vacancy-rich core of the displacement cascade

ORNL-PHOTO 3254-86

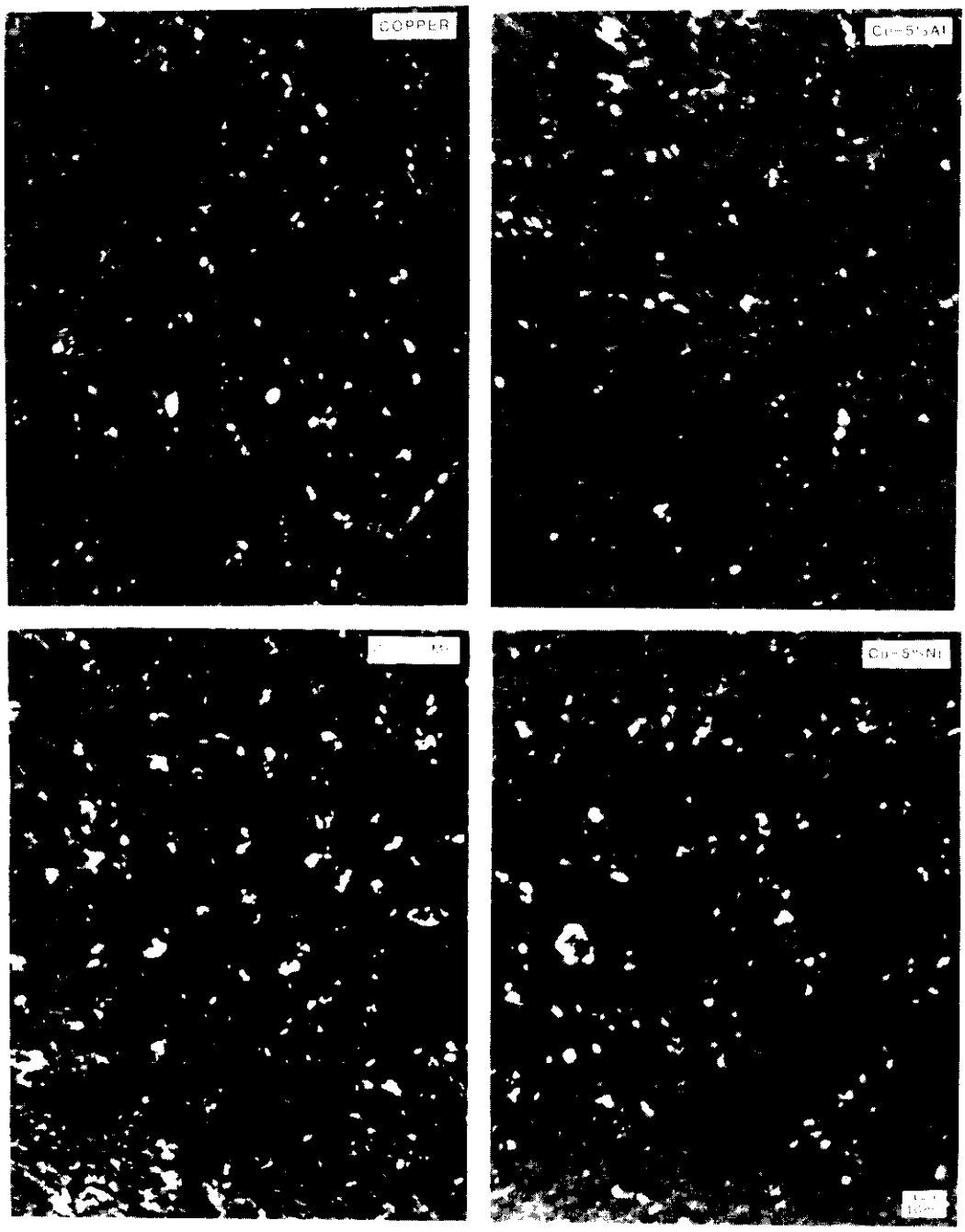

Fig. 2. Weak beam (g, 3g), g = 002, microstructures of copper and copper alloys irradiated to a fluence of 2×10^{21} n/m^2. The foil normal is near [110] for the top two pictures, and B ≈ [001] in the bottom two pictures.

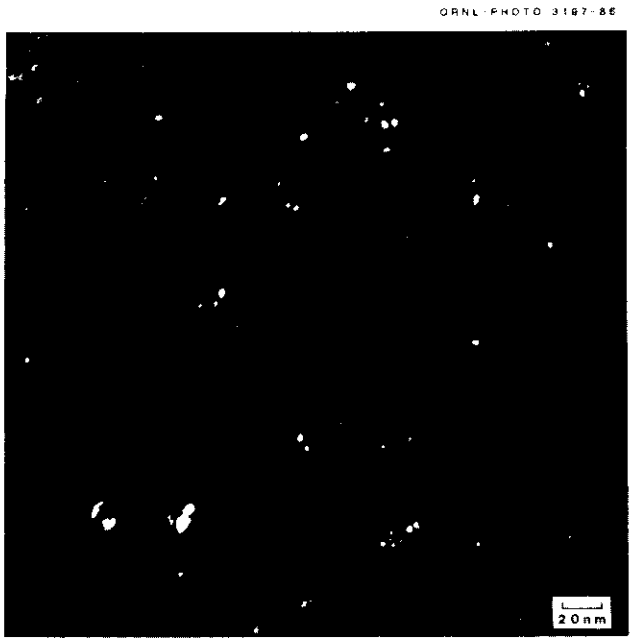

Fig. 3. Isolated groups of defect clusters observed in Cu–5% Al after irradiation to 4×10^{20} n/m^2.

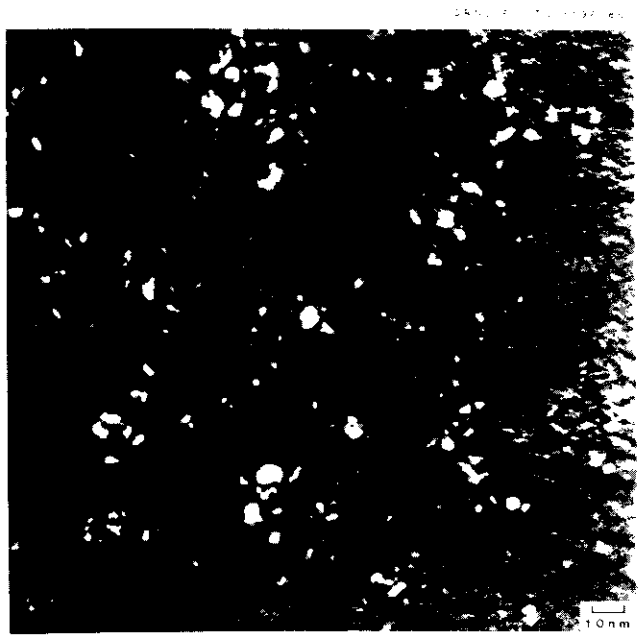

Fig. 4. Groups of defect clusters observed in Cu–5% Mn after irradiation to 2×10^{21} n/m^2. The foil thickness is about 110 nm.

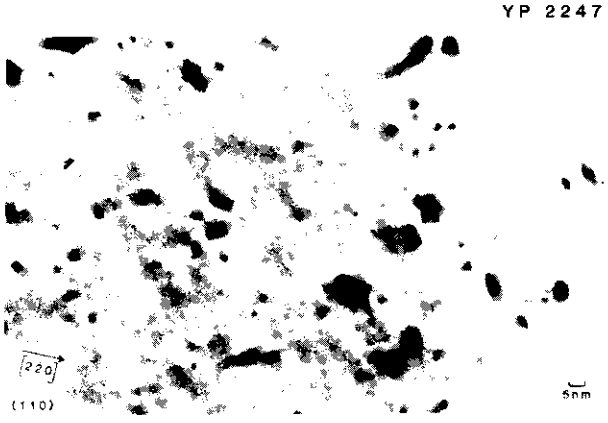

Fig. 5. Bright-field (g = 004) microstructure of copper irradiated to a fluence of 2×10^{21} n/m^2.

region, as proposed by Matthai and Bacon.[13] The observations made in this study do not allow a determination to be made of whether SFT formation occurs directly (Matthai and Bacon) as opposed to dissociation of a Frank vacancy loop (Silcox and Hirch).

The effect of fluence on the damage microstructure is shown in Fig. 7. The average defect cluster size was found to be constant over the fluence range investigated. The only microstructural effect associated with increasing fluence was an increase in the defect cluster density.

Fig. 6. Large stacking fault tetrahedron observed in copper following irradiation to a fluence of 1×10^{20} n/m^2.

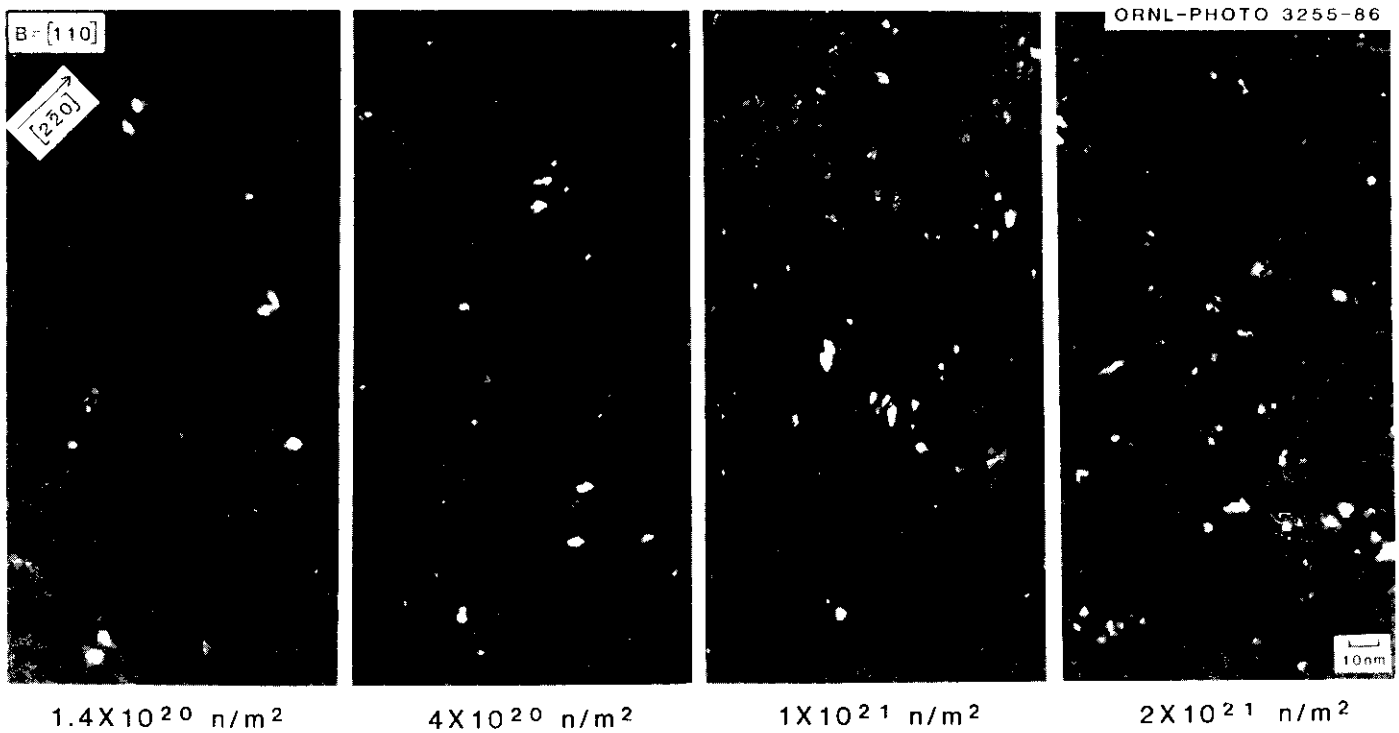

Fig. 7. Weak-beam (g, 3g), g = 002, microstructure of Cu–5% Al at various fluence levels.

The size distribution of defect clusters in the four metals following irradiation to 2×10^{21} n/m^2 is given in Fig. 8. The "total" size distribution includes all visible clusters. The "PDL + SFT" distribution includes only partially dissociated loops and triangle loops and SFT. The total size distributions for the four materials are very similar, with a most probable cluster size of $d_{mp} \approx 1.7$ nm and a mean size of $\bar{d} \sim 2.7$ nm. The size distributions are closely approximated by log-normal curves, as proposed elsewhere.[3] Pure copper contains a larger fraction of defect clusters that are resolvable as triangle loops or SFT compared to the copper alloys (25 versus 12%). The peak in the size distribution of triangle loops and tetrahedra ranges from $d_{mp} \sim 1.6$ to 2.0 nm for copper, Cu–5% Mn, and Cu–5% Ni. The corresponding peak in the SFT size distribution for the low stacking fault energy alloy Cu–5% Al is $d_{mp} \sim 2.3$ nm.

The total cluster density is plotted as a function of fluence in Fig. 9. Following an incubation fluence of $\sim 1 \times 10^{20}$ n/m^2, the data for all four materials is linear with the square root of neutron fluence. There is no significant difference in cluster density between the four metals over the fluence range studied in this investigation. This implies that solute additions to copper do not have a measurable effect on the total number of point defects surviving a room-temperature 14-MeV neutron irradiation.

The density of SFT and triangle loops in the irradiated foils is plotted as a function of fluence in Fig. 10. Uncertainties associated with resolving distinct defect cluster shapes at sizes on the order of 2 nm do not allow the fluence dependence of the cluster density (ϕt vs. $\sqrt{\phi t}$) to be accurately determined. Unlike the total cluster density, the density of SFT and triangle loops is significantly different for the alloys compared to pure copper. The density of these types of clusters in the alloys is less than 40% of the copper value at a fluence of 2×10^{21} n/m^2. The SFT (and triangle loops) are expected to be vacancy-type defect clusters for the irradiation conditions that were employed. If this assumption is correct, then it is clear that substitutional solute additions (both oversized and undersized) greatly reduce the fraction of vacancy clusters that survive the displacement cascade event and subsequent cooldown. This may be due to preferential trapping of vacancies at solute atoms.

Electrical resistivity foils were irradiated along with the TEM disks in this study. It was found[3] that the resistivity change of pure copper was proportional to the square root of neutron fluence with an incubation fluence of about 1×10^{20} n/m^2, in agreement with the TEM measurements of Fig. 9. The resistivity changes of the three copper alloys showed a fluence-dependent behavior that was attributed to short-range ordering effects.[4] This behavior is consistent with the observed low density of vacancy-type defect clusters (SFT) in the alloys compared to copper (Fig. 10), since the short-range ordering process will most likely reduce the free vacancy concentration in the cascade due to vacancy-solute interactions.

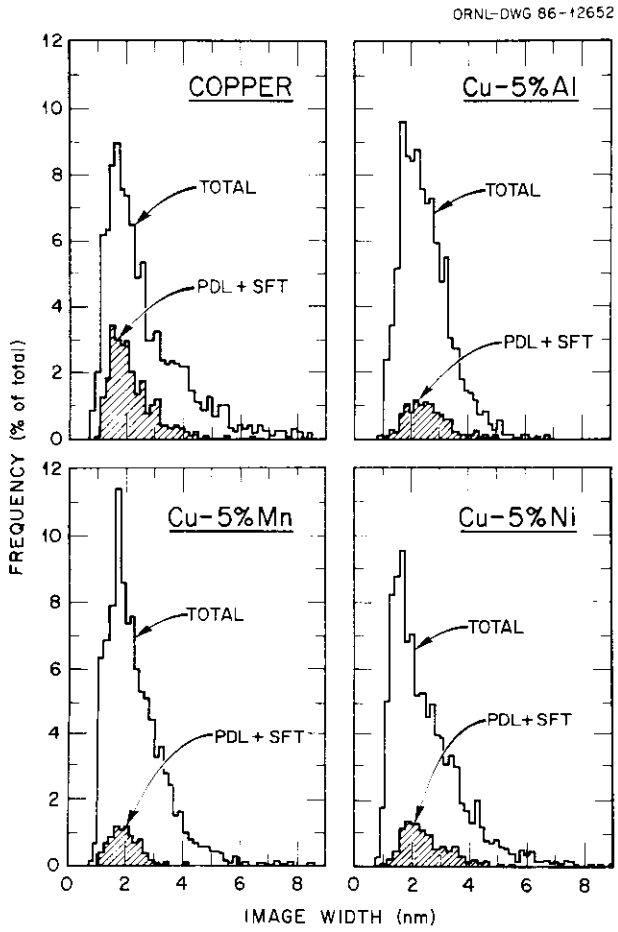

Fig. 8. Size distribution of defect clusters in copper and copper alloys following irradiation to 2×10^{21} n/m^2. The curve marked "Total" includes all visible clusters. The curve marked "PDL + SFT" includes only triangle loops, SFT, and loops that are partially dissociated towards SFT formation.

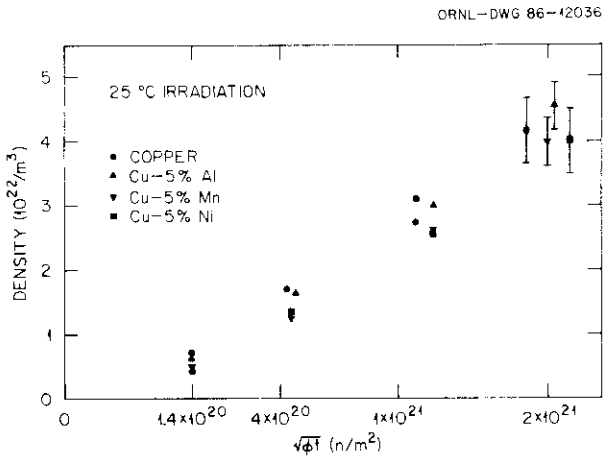

Fig. 9. Overall defect cluster density of copper and copper alloys plotted versus the square root of fluence.

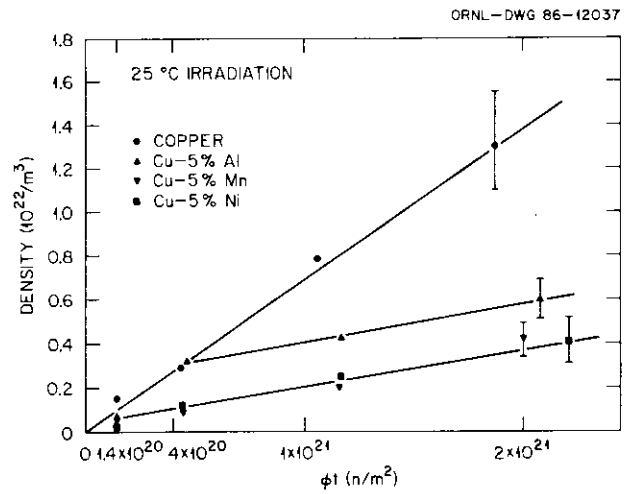

Fig. 10. Density of SFT and triangle loops versus fluence.

Careful examination of the electron diffraction patterns of the irradiated alloys did not reveal any indication of extra spots associated with the proposed short-range ordering (SRO). The only fine structure that was visible in the diffraction patterns obtained at exact zone axes was faint streaks through the diffraction spots and, in some intances, spot splitting. This behavior was also observed in pure copper diffraction patterns and is probably due to the presence of stacking fault tetrahedra and small faulted loops in the foil.[14,15] The absence of additional diffraction spots in the irradiated alloys indicates that appreciable clustering has not occurred. The observed results might be explained by assuming that dispersed SRO[16,17] which does not require homogeneous ordering, has occurred.

Discussion

There have been several recent high resolution TEM studies of copper and copper alloys following neutron irradiation near room temperature.[2,18-20] Muncie et al.[18] found that only about 8% of the defect clusters were in the form of SFT following a fission reactor irradiation to 1.3×10^{21} n/m^2 ($E > 1$ MeV). On the other hand, Yoshida et al.[19] reported that more than one half of the visible defect clusters were SFT following 14-MeV neutron irradiation to fluences between 8×10^{19} and 8.5×10^{21} n/m^2. We have found in this study that 10 to 15% of the defect clusters are resolvable as SFT for 14-MeV fluences between 1×10^{20} and 2×10^{21} n/m^2, in agreement with Muncie et al.[18] An additional 10 to 15% of the defect clusters are visible as triangle loops with their edges along <110> directions. Brager et al. and Shimomura et al.[20] did not report any details regarding SFT formation.

Yoshida et al.[19] has reported that the average size of defect clusters in copper decreased slightly with increasing fluence, whereas Shimomura et al.[20] reported that the defect size increased with fluence. Brager et al.[2] stated that the cluster size in copper and three copper alloys was independent of fluence up to $\phi t = 7 \times 10^{21}$ n/m^2. This last observation is in agreement with the present results, where the mean defect cluster density for each of the four materials was determined to be constant over the fluence range of 1×10^{20} to 2×10^{21} n/m^2. A theoretical model developed by Ghoniem et al.[21] predicts that the mean size of clusters in copper should be essentially constant for fluences between 10^{19} and 10^{22} n/m^2. It is interesting to note that the cluster size may be independent of fluence up to very high damage levels. A recent high-energy ion irradiation study of copper[22] at 10 dpa reported SFT and total cluster size distributions that were essentially identical to those given in Fig. 8, which is for copper irradiated to $<10^{-3}$ dpa. Of course, this direct comparison is not strictly valid since damage rate and primary recoil spectrum effects may be playing a role in the development of the microstructure. Similar size distributions have also been reported by English[23] for copper irradiated with fission neutrons and 30 keV ions. In all cases,[2,19,20,22,23] the cluster size distribution appears to be well described by a log-normal[3] distribution function.

It appears that stacking fault energy by itself does not have a strong effect on the probability of 14-MeV neutron displacement cascades producing visible defect clusters in copper alloys. This conclusion is based on the observation (Figs. 8 and 9) that the overall density and size distribution of defect clusters in Cu–5% Al (γ = 25 mJ/m^2) was the same as for Cu–5% Mn and Cu–5% Ni ($\gamma \simeq 50$ mJ/m^2). The Cu–5% Al alloy did contain a slightly larger density of SFT and triangle loops compared to the other two alloys (Fig. 10), indicating that there may be an effect of stacking fault energy on the formation of these types of clusters. Low-energy (30 keV) ion irradiations of copper alloys have found that SFT formation is strongly influenced by the stacking fault energy.[24] The data from the present study and other researchers on the influence of stacking fault energy,[24] irradiation temperature,[18,24] and knock-on energy[18,19,24] on SFT formation in copper may be summarized as follows: low-energy primary knock-on atoms (PKAs) do not produce SFT in copper at room temperature. Under these conditions, SFT formation occurs only in low-stacking-fault energy alloys ($\gamma \sim 10$ mJ/m^2). The probability of SFT formation in copper increases with increasing irradiation temperature up to 330°C. The formation of SFT at room temperature is enhanced when the mean knock-on energy is increased. At comparable doses ($<10^{-3}$ dpa), the fraction of defect clusters resolvable as SFT varies with knock-on energy in the following way: 0% (30 keV Cu ion), 8% (fission neutron), 10% (14-MeV neutron). There is a complex interdependence between knock-on energy and stacking fault energy (alloying). For example, Stathopoulos et al.[24] found that copper did not form SFT while 26% of the defect clusters in Cu–10 at. % Al were SFT following 30 KeV Cu ion irradiation. On the other hand, we have found significantly (factor of 2.0) more SFT in copper compared to Cu-5 at. % Al following 14-MeV neutron irradiation. The mean PKA energies for these two irradiation conditions are ~1 keV and ~170 keV, respectively.

There is interest in determining at what fluence cascade overlap effects become significant for both fundamental and practical reasons, particularly in relation to damage-rate experiments.[25-28] Ghoniem et al.[21] have predicted that significant cascade overlap should occur in copper during room-temperature irradiation for 14-MeV fluences greater than ~10^{23} n/m^2. We have not observed any significant amount of cascade overlapping for fluences up to 2×10^{21} n/m^2. Brager et al.[2] reported that no cascade overlap effects were observed in copper alloys for 14-MeV fluences approaching 10^{22} n/m^2. A simple estimate of the maximum possible cluster density may be made by assuming that the cluster spacing at saturation cannot be less than the spacing between visible clusters associated with a single cascade. The mean projection of this spacing has been measured in low-fluence specimens (e.g., Fig. 3) to be ~5 nm. The true distance between clusters is $4/\pi$ times the projected spacing, assuming a random orientation between clusters. The maximum possible cluster density (cubic close packing) is therefore $N \sim 7 \times 10^{24}$/m^3. Appreciable cascade overlap effects should be evident when the cluster density is 10% of the maximum value, $N \sim 7 \times 10^{23}$/m^3. A corresponding 14-MeV neutron fluence can be estimated by extrapolating data for pure copper given by Yoshida et al.[19] and Fig. 9 to give $(\phi t)_{sat} \simeq 7 \times 10^{23}$ n/m^2 (0.25 dpa).

There are conflicting results in the literature regarding the fluence dependence of defect cluster formation in fcc metals such as copper. Low-temperature (<20 K) irradiation studies[25-27,29] have shown that the production rate of point defects and defect clusters is directly proportional to the fluence for doses up to 10^{-3} dpa (~10^{22} n/m^2). Saturation effects due to cascade overlap become evident at higher fluences. Electrical resistivity investigations[30,31] have conclusively demonstrated that electron irradiation of copper at temperatures where the interstitial is mobile (>60 K) results in a square root dependence between the surviving defect density and fluence, $N \sim \sqrt{\phi t}$. The nonlinear behavior is due to recombination of the Frenkel defects shortly after they are produced. The results from the present study, using both TEM (Fig. 9) and electrical resistivity[3] methods, and those of Ipohorski and Brown[32] strongly indicate that the surviving point defect density continues to be proportional to $\sqrt{\phi t}$ for irradiation temperatures as high as 40°C and doses >10^{22} n/m^2 (E > 1 MeV). Most TEM studies of copper irradiated near room temperature have reported a "nearly linear" dependence between the visible cluster concentration and the fluence.[2,19,33] Konstantinov et al.[34] described their defect cluster data using a fluence exponent of n = 0.7. Deviation from linear behavior was often observed at moderate fluences; this was attributed to cascade overlap effects.[19] Examination of the published data (e.g., ref. 33) often indicates that it would better be described by a square root dependence. Chaplin and Coltman[35] have recently reported high-dose damage resistivity data for copper irradiated with fast neutrons at 60°C. When their data are replotted versus the square root of fluence, a linear relationship exists up to $\phi t \sim 10^{23}$ n/m^2 (E > 1 MeV). Concave curvature in the N versus $\sqrt{\phi t}$ plot becomes evident at higher fluences, presumably because of cascade overlap effects.

Figure 11 shows the combined data on defect cluster density from Yoshida et al.[19] and the present study as a function of fluence. When presented as a double logarithmic plot, the data are not linear but instead exhibit an apparent change of slope from $n = 1$ to $n = 1/2$ for fluence levels around 10^{20} to 10^{21} n/m^2. This nonlinear behavior cannot easily be attributed to cascade overlap since these effects are not expected to be large for fluences less than 10^{23} n/m^2 (see earlier discussion).

On the other hand, it can be easily shown that an incubation fluence would produce a nonlinear curve in the plot of log N versus log (ϕt). As an example, consider the following expression:

$$N = A[\sqrt{1 + B\phi t} - 1] \ . \tag{1}$$

This equation gives a good description of the observed fluence dependence of the visible cluster density (Fig. 9) and resistivity[3] results (i.e., an incubation period followed by a square root dependence). For small fluences ($B\phi t \ll 1$), the logarithm of this expression reduces to

$$\log N \simeq C + \log (\phi t) \ , \tag{2}$$

where C is a constant. At large fluences ($B\phi t \gg 1$), the corresponding equation is

$$\log N \simeq D + 1/2 \log (\phi t) \ , \tag{3}$$

where D is another constant. The limiting slopes given by Eqs. (2) and (3) are in good agreement with the behavior observed in Fig. 11.

Equation (1) is based on the unsaturable trap model,[30,36] which has been successfully used to describe defect concentrations in copper for electron irradiation in the recovery Stage II temperature range (70 to 220 K). This model is probably a poor description of the actual physical processes that occur during fast neutron (cascade-producing) irradiation at Stage III temperatures (~300 K), where vacancies are mobile along with interstitials. Recombination, nucleation, and spontaneous in-cascade clustering effects occur simultaneously under these conditions, and the overall process may not be described by such a simple analytical expression. Nevertheless, the fluence dependence of the cluster data in all cases investigated[3,19,32-35] is functionally well described by an expression similar in form to Eq. (1) — namely, an incubation period followed by a regime that is nearly proportional to the square root of fluence. Although this agreement is probably coincidental, it allows a simple empirical description of the cluster density to be obtained as a function of fluence. Cascade overlap effects do not appear to become large until the dose approaches 10^{23} n/m^2 ($E > 1$ MeV). A logarithmic presentation of the cluster density data introduces confusion due to the effect of the incubation dose. In summary, logarithmic plots should be used with caution since they may give misleading results with regard to the functional dependence of measured quantities.

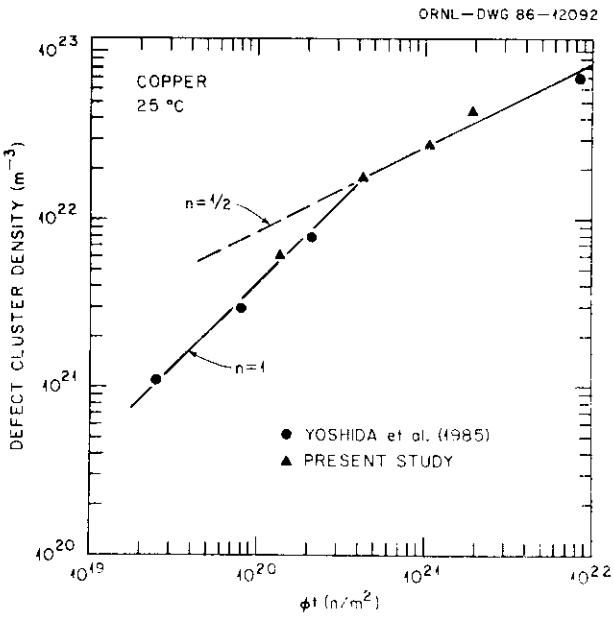

Fig. 11. Total visible cluster density of pure copper as a function of fluence, including data from Yoshida et al.[19] Note the anomalous change in slope that occurs around 5×10^{20} n/m^2.

A considerable amount of uncertainty exists in the literature regarding the fluence dependence of radiation hardening in fcc metals for irradiation temperatures of 80 to 400 K. The fluence exponent for hardening was originally measured as $n = 1/3$ by Blewitt and coworkers,[37] and later reported to be $n = 1/2$ by Diehl and coworkers.[38] Subsequent studies have generally used either $n = 1/3$ or $n = 1/2$ to describe the fluence dependence of the measured hardening (see refs. 39-41 for reviews). It has also been recently proposed that $n \simeq 1/4$ is the appropriate fluence exponent for radiation hardening.[3,4,42]

Several experimental[34,43] and theoretical[21,44] studies have established that the increase in strength of copper due to neutron irradiation near room temperature is given by $\Delta\sigma \sim \sqrt{Nd}$, where N is the cluster density and d is the mean defect size. The assumption $N \sim \phi t$ has commonly been invoked to explain that the yield strength increase should be proportional to the square root of fluence with no incubation period.[38-41,45] However, plots of $\Delta\sigma$ versus $\sqrt{\phi t}$ begin to show curvature at doses well below that where cascade overlap should be important. Since the cluster size is essentially independent of fluence, this implies that the fluence exponent for hardening is less than 0.5. The previous discussion on the fluence dependence of the visible cluster density [$N \sim (\phi t)^{1/2}$] suggests that $n \simeq 1/4$ will give the

correct dependence. A reanalysis by this author of the hardening data given in refs. 2, 38, 39, 44–52 has shown that the change in strength is consistently described by an incubation fluence followed by a one-fourth root dependence on fluence. (The data in the original papers had generally been fit to n = 1/2 or n = 1/3 fluence exponents with varying success.) Deviation from the n = 1/4 curve occurs at relatively high doses (3×10^{22} to $>1 \times 10^{23}$ n/m^2, E > 1 MeV) and is presumably due to cascade overlap effects.

In addition to ambient temperature (20 to 80°C) neutron irradiation data on copper, the analyzed hardening data included results from electron[47] and low-temperature (77 K) irradiations,[49] and fcc metals other than copper.[50,52] Heinisch et al.[42] have recently found that yield strength changes in copper and stainless steel following neutron irradiation near room temperature (25 and 90°C) were best fit by a curve proportional to the fourth root of fluence. It therefore appears that the relationships $N \sim \sqrt{\phi t}$ and $\Delta\sigma \sim (\phi t)^{1/4}$ may be generally applicable to many fcc metals over the irradiation temperature range of 100 to 400 K.

CONCLUSIONS

Room-temperature irradiation of copper and the single-phase alloys Cu–5% Al, Cu–5% Mn, Cu–5% Ni with 14-MeV neutrons produces defect clusters that are less than 10 nm in size. There is no noticeable effect of alloying on the overall cluster density or size distribution. However, the alloys contain a significantly lower density of stacking fault tetrahedra and triangle dislocation loops compared to pure copper. The lower density of these two types of defect clusters on the alloys may be due to preferential binding of vacancies to solute atoms. There was no TEM evidence of short-range ordering in the irradiated alloys, in contrast to previously reported electrical resistivity and microhardness results.

The overall defect cluster size was found to be constant over the fluence range of this investigation, 1×10^{20} to 2×10^{21} n/m^2. The overall size distribution for all four metals was similar to a log-normal distribution, with a peak at a diameter of ~1.7 nm. Comparison with high-dose neutron and ion-irradiation size distributions indicates that the mean cluster size may be essentially constant for any damage level.

There was no visible evidence of cascade overlap occurring for 14-MeV fluences up to 2×10^{21} n/m^2. A simple calculation predicts that cascade overlap effects should start to become significant for damage levels on the order of 10^{23} n/m^2.

The visible defect cluster density of all four metals was found to be proportional to the square root of fluence following an incubation period ~1×10^{20} n/m^2. Examination of published TEM and yield strength data for copper irradiated between 80 and 400 K indicates that this square root dependence between cluster density and fluence is valid over a wide range of experimental conditions. Logarithmic plots should not be used to determine the fluence dependence of processes which may have an incubation dose.

ACKNOWLEDGMENTS

The author would like to thank M. W. Guinan for his assistance with designing and performing the irradiations, and F. Scarboro for manuscript preparation. The helpful assistance of F. A. Garner, C. Rowe, B. Borman, C. Logan, and the RTNS-II staff is also acknowledged. The foils for this study were provided by H. R. Brager of the Westinghouse-Hanford Laboratory. The irradiations were performed while the author was under appointment to the Magnetic Fusion Energy Technology Fellowship Program.

REFERENCES

1. R. W. Powell, N. F. Panayotou, G. R. Odette, and G. E. Lucas, p. 105 in DAFS Quart. Prog. Rep., DOE/ET-0065/5 (Jan.–Mar. 1979).

2. H. R. Brager, F. A. Garner, and N. F. Panayotou, J. Nucl. Mater. 103&104 (1981) 995.

3. S. J. Zinkle and G. L. Kulcinski, J. Nucl. Mater. 122&123 (1984) 449–454.

4. S. J. Zinkle and G. L. Kulcinski, p. 141 in The Use of Small-Scale Specimens for Testing Irradiated Material, eds., W. R. Corwin and G. E. Lucas, Albuquerque, NM, Sept. 1983, ASTM-STP 888 (1986).

5. W. B. Pearson, Handbook of Lattice Spacings and Structures of Metals, Vol. I (1958) and Vol. II (1967), Pergamon Press.

6. H. W. King, J. Mater. Sci. 1 (1966) 79–90.

7. P.C.J. Gallagher, Met. Trans. 1 (1970) 2429; C. B. Carter and I.L.F. Ray, Phil. Mag. 35 (1977) 189.

8. R. H. Howell, Phys. Rev. B 22 (1980) 1722.

9. S. J. Zinkle and G. L. Kulcinski, p. 48 in DAFS Quart. Prog. Rep. Oct.–Dec. 1981, DOE/ER-0046/8.

10. T. Muroga, K. Kitajima, and S. Ishino, J. Nucl. Mater. 133&134 (1985) 378.

11. H. L. Heinisch, J. Nucl. Mater. 117 (1983) 46.

12. J. Silcox and P. B. Hirsch, Phil. Mag. 4 (1959) 72.

13. C. C. Mathai and D. J. Bacon J. Nucl. Mater. 135 (1985) 173.

14. M. J. Whelan and P. B. Hirsch, Phil. Mag. 2 (1958) 1303.

15. G. Thomas, W. L. Bell, and H. M. Otte, Phys. Stat. Sol. 12 (1965) 353.

16. L. Trieb and G. Veith, Acta. Met. 26 (19781) 185.

17. A. Varschavsky and E. Donoso, Met. Trans. A 15 (1984) 1999.

18. J. W. Muncie, B. L. Eyre, and C. A. English, Phil. Mag. A 52 (1985) 309.

19. N. Yoshida, Y. Akashi, K. Kitajima, and M. Kiritani, J. Nucl. Mater. 133&134 (1985) 405.

20. Y. Shimomura, H. Yoshida, M. Kiritani, K. Kitagawa, and K. Yamakawa, J. Nucl. Mater. 133&134 (1985) 385.

21. N. M. Ghoniem, J. Alhajji, and F. A. Garner, p. 1054 in Effects of Radiation on Materials: 11th Conference, ASTM STP 782, eds., H. R. Brager and J. S. Perrin (ASTM 1982).

22. S. J. Zinkle, G. L. Kulcinski, and R. W. Knoll, J. Nucl. Mater. 138 (1986) 46.

23. C. A. English, J. Nucl. Mater. 108&109 (1982) 104.

24. A. Y. Stathopoulos, C. A. English, B. L. Eyre, and P. B. Hirsch, Phil. Mag. A 44 (1981) 309.

25. J. A. Horak and T. H. Blewitt, Phys. Stat. Sol. (a) 9 (1972) 721.

26. R. S. Averback, K. L. Merkle, and L. J. Thompson, Radiation Effects 51 (1980) 91.

27. M. Nakagawa et al., Phys. Rev. B 16 (1977) 5285.

28. C. Abromeit and S. R. MacEwen, Nucl. Instr. Meth. Phys. Res B 15 (1986) 770.

29. J. B. Roberto et al., Appl. Phys. Lett. 30 (1977) 509.

30. R. M. Walker, p. 594 in Radiation Damage in Solids, Proc. Intern. School of Physics (Enrico Fermi) Course XVIII, ed., D. S. Billington (Academic Press, 1962).

31. H. J. Wollenberger, pp. 215–253 in Vacancies and Interstitials in Metals, eds. A. Seeger, D. Schumacher, W. Schilling, and J. Diehl (North-Holland, 1970).

32. M. Ipohorski and L. M. Brown, Phil. Mag. 22 (1970) 931.

33. M. J. Makin, A. D. Whapham, and F. J. Minter, Phil. Mag. 7 (1962) 285.

34. I. O. Konstantinov, V. S. Kharbarov, and V. I. Shcherbak, Fiz. Khim Obrab Mater. (Phys. and Chem. of Materials Processing) No. 3 (1982) 135–138.

35. R. L. Chaplin and R. R. Coltman, Jr. J. Nucl. Mater. 108&109 (1982) 175.

36. L. Thompson, G. Youngblood, and A. Sosin, Rad. Effects 20 (1973) 111.

37. T. H. Blewitt, p. 630 in Radiation Damage in Solids, Proc. Intern. School of Physics (Enrico Fermi) Course XVIII, ed., D. S. Billington (Academic Press, 1962).

38. J. Diehl and W. Schilling, p. 72 in Proc. 3rd Int. Conf. on Peaceful Uses of Atomic Energy, Vol. 9, "Reactor Materials" (United Nations, 1965).

39. M. J. Makin, p. 627 in Radiation Effects, Vol. 37, TMS-AIME Conference, Asheville, N.C., 1965, ed., W. F. Sheely (Gordon & Breach, 1967).

40. T. J. Koppenaal and R. J. Arsenault, Met. Rev. (J. Inst. Metals) 16 (1971) 175.

41. B. L. Eyre, Int. Metallurgical Rev. 19 (1974) 240.

42. H. L. Heinisch, S. D. Atkin, and C. Martinez, p. 76 in DAFS Quart. Prog. Rep. Jan.-Mar. 1986, DOE/ER-0046/25.

43. M. J. Makin, F. J. Minter, and S. A. Manthorpe, Phil. Mag. 13 (1966) 729.

44. J. Diehl and G. P. Seidel, p. 187 in Radiation Damage in Reactor Materials, Vol. I (IAEA, Vienna, 1969).

45. H. G. Mohamed, A. M. Hammad, and F. H. Hammad, Trans. Indian Inst. Metals, 35 (3) (1982) 258.

46. I. A. El-Shanshoury, J. Nucl. Mater. 45 (1972/73) 245.

47. I. Yoshizawa, N. Naramoto, and K. Kamada, J. Phys. Soc. Japan 36 (1974) 202; K. Kamada et al., Phys. Stat. Sol.(a) 18 (1973) 377.

48. J. B. Mitchell, R. A. Van Konynenburg, C. J. Echer, and D. M. Parkin, p. 172 in Radiation Effects and Tritium Technology for Fusion Reactors, Vol. II, eds., J. S. Watson and F. W. Wiffen, Gatlinburg, TN (1975); also see J. B. Mitchell, Lawrence Livermore Laboratory report UCRL-52388 (January 1978).

49. H. C. Gonzalez and E. A. Bisogni, Phys. Stat. Sol. (a) 62 (1980) 351.

50. E. R. Bradley and R. H. Jones, p. 186 in The Use of Small-Scale Specimens for Testing Irradiated Material, ASTM STP 888, eds., W. R. Corwin and G. E. Lucas (ASTM, Philadelphia, 1986).

51. K. Shinohara and S. Kitajima, J. Nucl. Mater. 133&134 (1985) 690.

52. A. Okada, T. Yoshiie, S. Kojima, and M. Kiritani, Mechanical Property Change and Its Correlation with Defect Structure Evolution in D-T Neutron Irradiated Metals, 2nd Int. Conf. on Fusion Reactor Materials, Chicago (April 1986); to be published in Journal of Nuclear Materials.

OWR/RTNS-II LOW EXPOSURE SPECTRAL EFFECTS EXPERIMENT: EFFECTS OF IRRADIATION TEMPERATURE - H. L. Heinisch (Westinghouse Hanford Company)

OBJECTIVE

The objective of this experiment is to determine the effect of the neutron spectrum on radiation-induced changes in mechanical properties for metals irradiated with fusion and fission neutrons.

SUMMARY

The status of the OWR/RTNS-II Low Exposure Spectral Effects Experiment is reviewed. The originally planned irradiations in RTNS-II and the Omega West Reactor at 90°C and 290°C have been completed, and additional irradiations in RTNS-II at 200°C and 450°C have also been carried out. Tensile specimens from each of the irradiations have been tested. The effects of irradiation temperature on the change in yield stress as a function of 14 MeV neutron fluence are reported here for annealed pure copper, annealed 316 stainless steel and HT9 ferritic steel. In copper the effect of increasing the irradiation temperature is to increase the minimum fluence at which a measurable change in mechanical properties takes place. The temperature effects are somewhat smaller in 316 stainless steel, and the incubation effects are less obvious than in copper. In HT9 the 14 MeV irradiation effects are relatively small, and there is no effect of temperature for fluences up to 2.5 x 10^{18} n/cm^2.

PROGRESS AND STATUS

Introduction

The purpose of the RTNS-II/OWR Low Exposure Spectral Effects Experiment is to determine any differences in the effects of 14 MeV neutrons and fission reactor neutrons on the changes in tensile properties and microstructure of metals irradiated to exposures of < 0.1 displacements per atom (dpa). The irradiations at 90°C and 290°C originally planned for RTNS-II and OWR have been carried out, and the results of tensile tests were reported at the Second International Conference on Fusion Reactor Materials[1]. Additional specimens from the same materials matrix have also been irradiated in the Japanese/US long-term RTNS-II irradiation, performed with the Japanese dual-temperature furnace at 200°C and 450°C. The test results for these specimens now make it possible to investigate the temperature dependence of mechanical properties changes over a wide range of irradiation temperatures in RTNS-II.

Experimental procedure

As in previous irradiations, flat miniature tensile specimens of AISI 316 stainless steel, A302B pressure vessel steel, Marz-grade copper, and Marz-grade iron were irradiated to a range of fluences in RTNS-II. Irradiations were performed in the Japanese dual-temperature, vacuum-insulated furnace at temperatures of 200°C and 450°C. The peak fluence obtained was 8 x 10^{18} n/cm^2; the maximum fluence obtained by a US specimen was 6 x 10^{18} n/cm^2.

Specimens of copper and 316 stainless steel irradiated at 200°C were tested at room temperature in a tensile frame made specifically for miniature specimens, which is described in earlier reports[1]. Tensile tests were also performed on specimens of HT9 ferritic alloy that were irradiated at 90°C and 290°C.

Results

Figure 1 shows the change in yield stress of annealed copper as a function of displacements per atom (dpa) for irradiations in RTNS-II. Each point is the result of a single test. The bars on selected points indicate the estimated precision in the measurement of the absolute yield stress of the irradiated specimen.

Specimens at 90°C, 200°C and 290°C were all exposed in long-term irradiations; thus, all specimens at a given dose were irradiated at about the same damage rate. The few specimens irradiated at room temperature were exposed at a damage rate about six times higher at each dose.

The fluence dependence of the yield stress change is qualitatively the same at each irradiation temperature. The effect of increasing temperature is to delay the onset of significant strengthening. To illustrate the fluence dependence in a systematic way, the following expression was fitted to the copper data at each temperature, except for 290°C:

$$\Delta YS = B\,(d - A)^n \qquad (1)$$

where ΔYS is the yield stress change in MPa, d is the dose in dpa, and A, B and n are constants. The resulting curves are plotted in Fig. 1. Only the data at higher doses were used in the fitting. The value of the exponent n was taken to be 1/4 for copper. No attempt was made to fit other curves to data at or below the threshold regions. A rough measure of the threshold or incubation dose at each temperature is

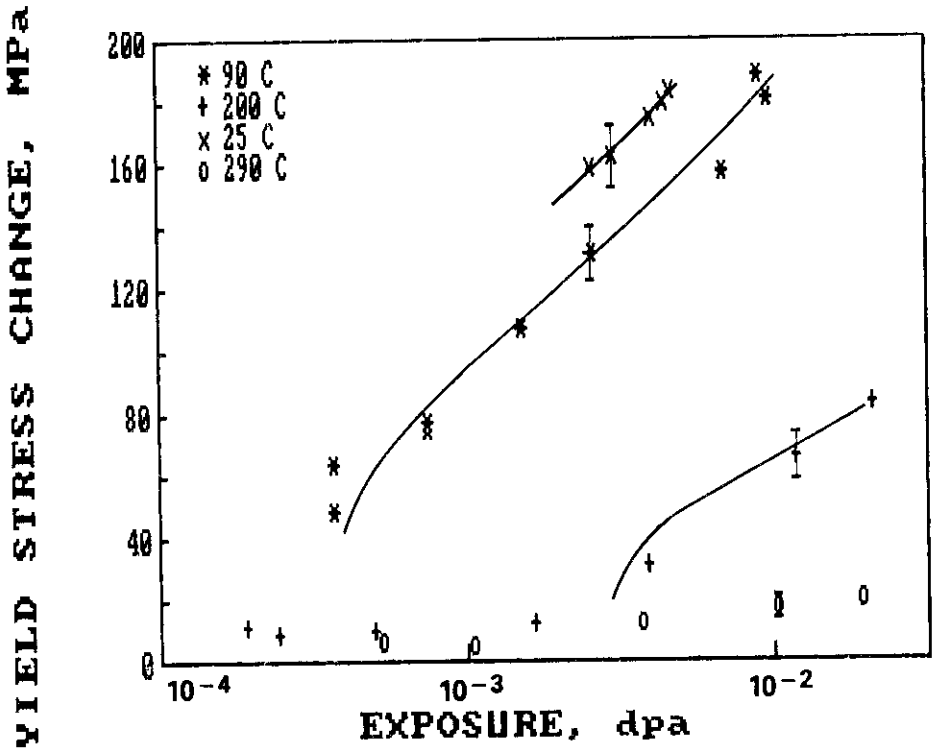

Fig. 1. Yield stress changes as a function of dpa for annealed copper irradiated at several temperatures in RTNS-II. The curves are fits of Eq. 1 to the data. The bars on selected data points represent the estimated precision of the measurement of the individual absolute yield stress measurements.

given by the value of the constant A in expression 1. Table 1 gives the values of A and B obtained in the fitting. The specimens irradiated at 290°C did not reach a discernable threshold fluence, but the threshold is probably on the order of 5.3 x 10^{18} n/cm^2 (0.02 dpa), which is the highest fluence obtained at that temperature.

Table 1. Parameter values obtained from fitting Eq. 1 to yield stress data.

Material	Temperature (°C)	A (n/cm2)	A (dpa)	B (MPa)
Copper	25	2.7 x 10^{16}	1.2 x 10^{-5}	70
	90	1.1 x 10^{17}	3.9 x 10^{-4}	59
	200	7.8 x 10^{17}	2.9 x 10^{-3}	22

Figure 2 shows yield stress changes for solution annealed AISI 316 stainless steel irradiated under the same conditions as the copper above. The estimated precision in the measurements is also indicated on selected data points. The 316 stainless steel is less affected by temperature than copper in this range of temperatures. The room temperature data cannot be distinguished from the 90°C data, and the 290°C data show significant radiation-induced strengthening. As a result, the temperature-dependent incubation-type behavior is less apparent in 316 stainless steel. Another interesting feature is that the data at 200°C show especially large yield stress changes at the low fluences. As with copper, expression 1 was fitted to the higher fluence data at each temperature. For stainless steel a better fit was obtained with the value of n = 1/2. However, the resulting values of A are small or negative, indicating that an incubation model may not be appropriate for stainless steel.

Figure 3 shows the yields stress change as a function of neutron fluence for HT9 irradiated in RTNS-II at 90°C and 290°C to fluences up to 2.5 x 10^{18} n/cm^2. The estimated precision of the measurements is indicated by a bar on one of the data points. There is no apparent effect of irradiation temperature in this fluence and temperature range.

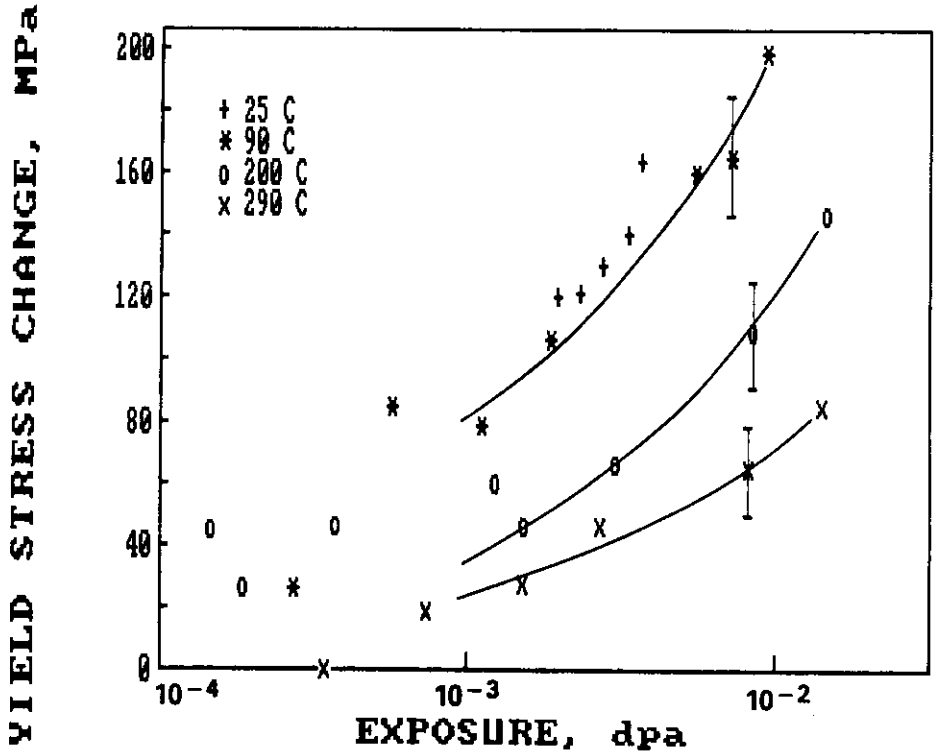

Fig. 2. Yield stress changes as a function of dpa for annealed 316 stainless steel irradiated at several temperatures in RTNS-II. The curves are fits of Eq. 1 to the data. The bars on selected data points represent the estimated precision of the measurement of the individual absolute yield stress measurements.

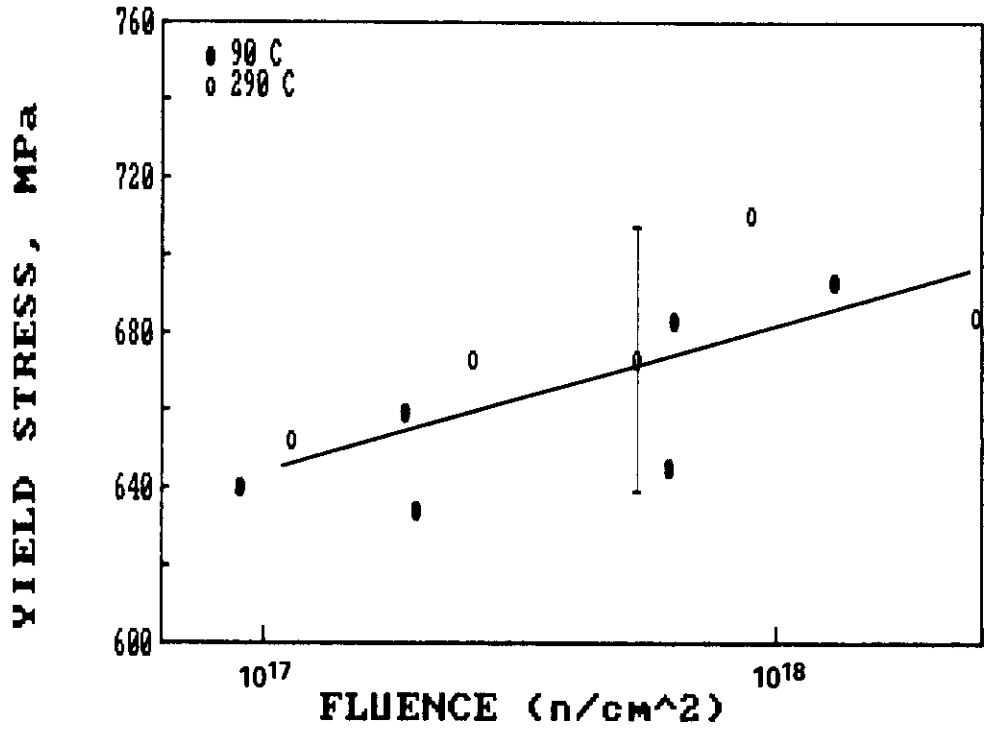

Fig. 3. Yield stress as a function of 14 MeV neutron fluence for HT9 ferritic alloy irradiated in RTNS-II at 90°C and 290°C. The bar on one data point represents the estimated precision of the individual absolute yield stress measurements.

Discussion

Equation 1 is a simple empirical expression; the only attempt at physical basis is the power law behavior. According to theoretical models[2], strengthening is proportional to the factor $(Nd)^{1/2}$, where N is the number density of strengthening obstacles of size d. Depending on the mechanisms involved (clusters, loops, voids, etc.) and how they are affected by increasing dose (direct production, nucleation, growth, etc.) the theoretical models predict power law dose dependence having values of n ranging from 1/2 to 1/4. For example, if the distribution of obstacle sizes remains fixed, and the number density increases directly with increasing fluence, then n = 1/2. Strengthening models are being developed that have functional forms explicitly reflecting the physics of temperature and rate effects[2]. How well such models fit the present data is being explored.

Copper clearly displays threshold or incubation type behavior. The best fit of Equation 1 to the data is obtained with n = 1/4. Such behavior is consistent with a model in which strengthening centers nucleate, reach a critical size, and then grow. The effect of increasing irradiation temperature is to delay the development of critical-size strengthening centers. Hardness measurements by Zinkle and Kulcinski[3] on copper and copper alloys irradiated in RTNS-II also display incubation behavior, and the fluence dependence is also well-fit by a 1/4 power law. Alloying tends to shorten the incubation fluence, perhaps because solute atoms act as nucleation sites.

There is considerable disagreement as to the details of the microstructure of irradiated copper observed by electron microscopy. A review by Zinkle and Knoll[4] points out that both clusters and loops of both interstitial and vacancy types have been reported for copper irradiated by both 14 MeV neutrons and fission neutrons, with vacancy/interstitial ratios varying widely among the investigators. So far this tangle of data has not been sorted out to form a comprehensive description of the microstructure. Thus, it would be difficult at this time to try to relate the tensile behavior observed in the present work with the observed microstructures.

Annealed 316 stainless steel displays temperature dependence in the effects of 14 MeV neutrons on the tensile properties, however, the temperature effects are not as strong as in copper. This may be due to the solute elements of the alloy acting as nucleation sites, as in copper alloys. Also, at higher temperatures loops formed in stainless steel are less likely to shrink or dissolve by emission of defects than loops in copper. The dose dependence of the yield stress changes in 316 stainless steel is better fit by a 1/2 power law than the 1/4 power law found for copper. This may indicate a fundamental difference in the nature of the strengthening mechanisms for the two materials in this fluence and temperature range. However, the differences in fit between n = 1/2 and n = 1/4 were not definitively large for either material.

When the specimen matrix for the original spectral effects experiment was determined, there was a desire to include ferritic alloys such as HT9. However, it was felt that at the low doses obtainable in RTNS-II, it might be difficult to see measurable effects in the tensile properties of HT9. Some specimens of HT9 were later included at intermediate fluence positions in the US/Japan long term irradiation (R-2 of Ref. 1). There is some strengthening observed in HT9 (Fig. 3), but the maximum change in yield stress observed in this irradiation is only 16% of the unirradiated yield stress. Since there is no temperature dependence in the 90-290°C range, it may have been of interest to irradiate HT9 in the 450°C Japan/US irradiation. However, the change in tensile properties would probably be even less than at the lower temperatures.

CONCLUSIONS

Tensile data has been obtained for copper and stainless steel irradiated at four temperatures in RTNS-II. In copper the effect of increasing irradiation temperature is to increase the incubation dose for strengthening as a function of dose. In annealed 316 stainless steel increased irradiation temperature results in less strengthening at a given dose, but whether this results from effects on incubation is not clear from the data.

The small amount of strengthening and the absence of temperature effects in HT9 irradiated at 90°C and 290°C in RTNS-II justify its being omitted from the original low-dose spectral effects experiment matrix.

REFERENCES

1. H. L. Heinisch, S. D. Atkin, and C. Martinez, "Spectral Effects in Low-dose Fission and Fusion Neutron Irradiated Metals and Alloys," Proceedings of the Second International Conference on Fusion Reactor Materials, Chicago, April 13-17, 1986, to be published in J. Nucl. Mat.

2. R. L. Simons, "Damage Rate and Spectrum Effects in Ferritic Steel NDTT Data," Proceedings of ASTM Thirteenth International Symposium on Effects of Radiation on Materials, Seattle, June 23-25, 1986.

3. S. J. Zinkle and G. C. Kulcinski, "14 MeV Neutron Irradiation of Copper Alloys," J. Nucl. Mat., 122 & 123, 449-54 (1984).

4. S. J. Zinkle and R. W. Knoll, "A Literature Review of Radiation Damage Data for Copper and Copper Alloys," University of Wisconsin Fusion Technology Institute Report UWFDM-578, June, 1984.

THE EFFECTS OF LOW DOSES OF 14 MeV NEUTRONS ON THE TENSILE PROPERTIES OF THREE BINARY COPPER ALLOYS - H. L. Heinisch and J. S. Pintler (Westinghouse Hanford Company)

OBJECTIVE

The objective of this experiment is to determine the effect of 14 MeV neutrons on radiation-induced changes in mechanical properties of three alloys of copper, Cu5%Al, Cu5%Mn and Cu5%Ni, and to compare the effects of 14 MeV and fission reactor neutrons.

SUMMARY

Miniature tensile specimens of high purity copper and copper alloyed respectively with five atom percent of Al, Mn, and Ni were irradiated with D-T fusion neutrons in the RTNS-II to fluences up to 1.3 x 10^{18} n/cm^2 at 90°C. To compare fission and fusion neutron effects, some specimens were also irradiated at the same temperature to similar damage levels in the Omega West Reactor (OWR). Tensile tests were performed at room temperature, and the radiation-induced changes in tensile properties were examined as functions of displacements per atom (dpa). The irradiation-induced strengthening of Cu5%Mn is greater than that of Cu5%Al and Cu5%Ni, which behave about the same. However, all the alloys sustain less irradiation-induced strengthening by 14 MeV neutrons than pure copper, which is in contrast to the reported results of earlier work using hardness measurements. The effects of fission and fusion neutrons on the yield stress of Cu5%Al and Cu5%Ni correlate well on the basis of dpa, but the data for Cu5%Mn suggest that dpa may not be a good correlation parameter for this alloy in this fluence and temperature range.

PROGRESS AND STATUS

Introduction

The correlation of fission and fusion neutron effects for the development of fusion reactor materials will be aided by developing an understanding of any differences in the fundamental production of damage by low and high energy (14 MeV) neutrons. Toward this end, many metals and alloys have been irradiated with the RTNS-II 14 MeV neutron source and in the Omega West Reactor. One means of investigating the fundamental damage state is through changes in mechanical properties as measured in tensile tests. Among the materials irradiated as part of the Low Exposure Spectral Effects Experiment[1] were a series of three binary copper alloys in the form of flat miniature tensile specimens. Tensile tests were performed on these specimens, and the results are compared with hardness data obtained earlier on the same alloys.[2,3]

Brager, et al.,[2] (hereafter referred to as "Brager") produced three binary copper alloys, having, respectively, five atom percent aluminum, manganese and nickel.[1] They irradiated 3 mm diameter by 0.25 mm thick microscopy disks of these alloys and pure (99.99+%) copper at 25°C in RTNS-II to a maximum fluence of 7.5 x 10^{17} n/cm^2. Diamond pyramid hardness measurements were made on the specimens, and their microstructures were examined by TEM, with the objective of determining the visibility and survivability of defect clusters. The same materials were supplied to Zinkle and Kulcinski[3] (hereafter referred to as Zinkle), who also irradiated them at 25°C in RTNS-II to 3 x 10^{17} n/cm^2. Zinkle examined the irradiated materials using resistivity and hardness measurements. The results were also analyzed to determine the survivability of defects using simple hardening models.

In both the earlier studies the radiation-induced change in yield stress was examined as a function of 14 MeV neutron fluence. The yield stress changes were obtained from the measured change in diamond pyramid hardness by applying a simple empirical correlation. In the present work the yield stress changes of these alloys are determined directly from tensile tests on irradiated sheet-type miniature tensile specimens punched from the same stock used in the earlier studies.

Experimental procedure

Annealed miniature tensile specimens of the alloys and pure copper were irradiated at 90°C in RTNS-II to a maximum fluence of 1.3 x 10^{18} n/cm^2 and at 90°C in OWR to similar damage levels. The RTNS-II irradiations were performed as part of the joint US/Japan long-term elevated temperature irradiation (R-2 in Ref. 1, where details of the irradiations are given). The tensile tests were performed at room temperature using a tensile frame made specifically for testing miniature specimens. Tensile tests were performed on five or six specimens of each alloy from each neutron environment. Two specimens of each unirradiated alloy were also tested. Some of the data on pure copper were reported in Ref. 1, but further testing of pure copper from the R-2 run has been done, and the results are reported here.

Results and discussion

The value of the 0.2% offset yield stress was determined for each tensile test. Table 1 contains the values of the yield stress for the unirradiated materials. The yield stress of Cu5%Mn is about 33% larger

than the value for the other materials, indicating a measurable effect of solute hardening for this alloy. Brager reported about the same fraction of solute hardening of Cu5%Mn determined from hardness measurements. Brager also reported a measurable solute hardening in Cu5%Al, but no hardening in Cu5%Ni. Zinkle reported little effect of solute hardening in hardness tests of any of the alloys.

Table 1. The 0.2% offset yield stress of unirradiated binary copper alloys

Alloy	Yield Stress, MPa
Cu (99.999%)	49 ± 5
Cu-5% Al	48 ± 8
Cu-5% Mn	66 ± 2
Cu-5% Ni	51 ± 5

The radiation-induced yield stress changes for the alloys as a function of dpa in RTNS-II are shown in Fig. 1, where they are compared to the yield stress changes in pure copper. The dpa values were calculated for the alloys from the total neutron fluences using the spectral averaged displacement cross sections for pure copper, 3396 b in RTNS-II and 293 b in OWR. Thus, in the same neutron spectrum, plotting with respect to dpa is equivalent to plotting with respect to neutron fluence. Cu5%Mn strengthens more with increasing neutron fluence than Cu5%Al or Cu5%Ni, but all three alloys experience less irradiation strengthening than pure copper.

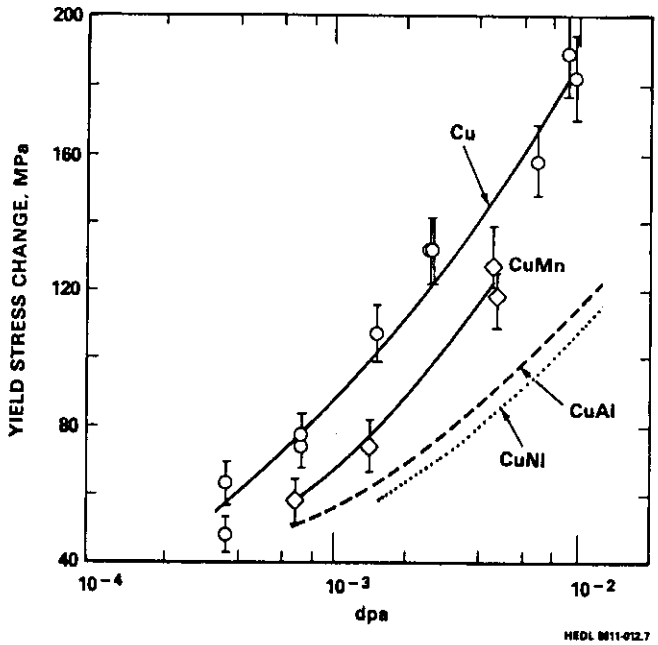

Fig. 1. Radiation induced yield stress changes as a function of dpa for pure copper and binary copper alloys having 5 atom percent of aluminum, manganese or nickel. The data for Cu5%Al and Cu5%Ni are represented by dashed lines. The bars on the data points represent the estimated precision of the measurement of the individual absolute yield stress measurements. Irradiations were performed at 90°C, tests at 25°C.

The results can be compared with the earlier work in Brager and Zinkle, although the higher fluence range of the present work overlaps the fluence range of the earlier work only slightly. The radiation strengthening of pure copper as a function of fluence is about the same in Brager, Zinkle and the present work (the data for pure copper in Zinkle was taken from RTNS-I irradiated copper examined by Mitchell, et al.[4]). Brager, Zinkle and the present work also agree that Cu5%Mn strengthens more with irradiation than the other binary alloys. However, all three disagree on the amount of strengthening of the alloys relative to pure copper. Zinkle shows Cu5%Mn strengthening by about 25 MPa more than pure copper at any

fluence, while the present work shows Cu5%Mn strengthening by about 20 MPa less than pure copper. Brager shows Cu5%Mn and pure copper strengthening by about the same amount.

It is interesting that the results for pure copper are the same in the three investigations, since three different heats of copper having slightly different impurity levels were used, and one set of yield stress data was determined by an empirical correlation of hardness data. Also, in the present work the copper was irradiated at 90°C, while the other irradiations were performed at room temperature. The copper binary alloy specimens in all three investigations were taken from the same material stock.

The Cu5%Mn alloy exhibits measurably different behavior from the other two alloys. However, in the only direct examination of the microstructures of these alloys, by Brager, it is the irradiated Cu5%Al alloy that is markedly different from the Cu5%Mn and Cu5%Ni alloys, exhibiting a higher density of smaller defect clusters. It can be argued that the large mass difference between Al and Cu atoms has an effect on the dynamics of displacement cascade production. The difference in energy transfer in collisions due to mass differences, resulting for example in the disruption of replacement collision sequences, would lead to fewer large defect clusters. This would result in a more finely distributed defect cluster structure in Cu5%Al than in pure copper or the other alloys. There is nothing in the limited information on the microstructure to explain the behavior of Cu5%Mn.

Figures 2, 3 and 4 show the increase in yield stress due to irradiation in RTNS-II and OWR for Cu5%Al, Cu5%Mn and Cu5%Ni, respectively. Yield stress changes are plotted as a function of dpa determined with displacement cross sections for pure copper. While the actual displacement cross sections for pure copper and the three alloys may differ somewhat in the same spectrum, it is unlikely that the cross section in RTNS-II relative to that in OWR would be very different for any of them. The data points in Figs. 2, 3 an 4 are for single tensile tests. The error bars indicate the estimated precision in the measurement of the absolute yield stress for each point. For Cu5%Al and Cu5%Ni there is no difference between RTNS-II and OWR on the basis of dpa.

For Cu5%Mn separate curves can be drawn through the RTNS-II and OWR data. Statistics applied to the double points at the same fluences would result in error bars about half the size of those shown for the overall estimated precision. According to the curves drawn in Fig. 3 about 1.7 times more dpa are needed in OWR to produce the same yield stress change as at the highest fluence RTNS-II data. This is on the order of the factors of 1.8 to 2.9 for pure copper reported in Ref. 1. More data are needed to provide convincing evidence of a difference in behavior of Cu5%Mn in the two spectra, especially at higher fluences in RTNS-II. Unfortunately, there are no specimens of this material that have been irradiated to higher fluences.

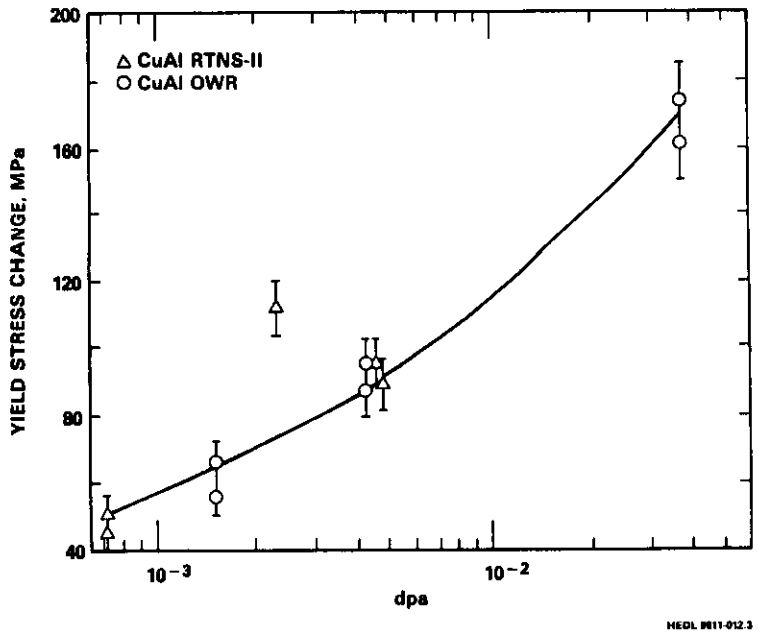

Fig. 2. Yield stress changes of Cu5%Al due to irradiation in RTNS-II and OWR as a function of dpa. The bars on the data points represent the estimated precision of the measurement of the individual absolute yield stress measurements. Irradiations were performed at 90°C, tests at 25°C.

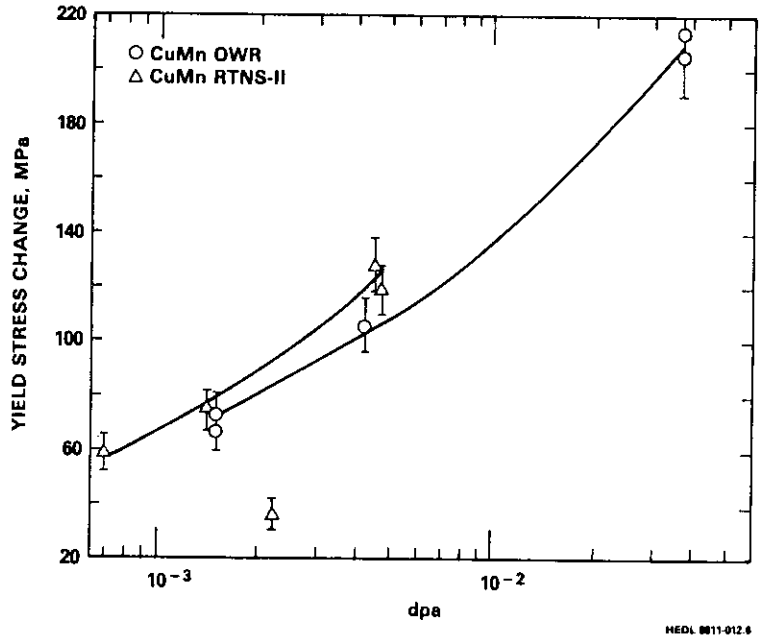

Fig. 3. Yield stress changes of Cu5%Mn due to irradiation in RTNS-II and OWR as a function of dpa. The bars on the data points represent the estimated precision of the measurement of the individual absolute yield stress measurements. Irradiations were performed at 90°C, tests at 25°C.

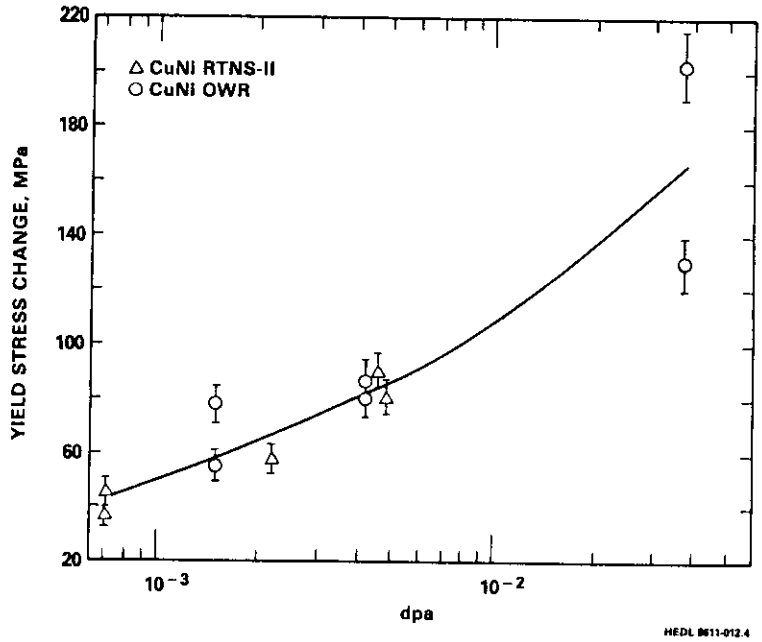

Fig. 4. Yield stress changes of Cu5%Ni due to irradiation in RTNS-II and OWR as a function of dpa. The bars on the data points represent the estimated precision of the measurement of the individual absolute yield stress measurements. Irradiations were performed at 90°C, tests at 25°C.

CONCLUSIONS

Irradiation strengthening of Cu5%Mn is different from that of Cu5%Al and Cu5%Ni and pure copper, but the present study and two earlier studies fail to agree on the magnitude and sign of the difference relative to pure copper. Dpa appears to be a good correlation parameter for yield stress changes in RTNS-II and OWR for Cu5%Al and Cu5%Ni, but not for Cu5%Mn or pure copper.

FUTURE WORK

Only a few irradiated tensile specimens of these alloys remain, and they will be used for TEM studies of their microstructure. No further irradiations are planned. However, further analysis of the existing tensile data will be done, and explanations of the behavior of these alloys under low fluence irradiation will be pursued.

REFERENCES

1. H. L. Heinisch, S. D. Atkin and C. Martinez, "Spectral Effects in Low-dose Fission and Fusion Neutron Irradiated Metals and Alloys," in Proceedings of the Second International Conference on Fusion Reactor Materials, Chicago, April 13-17, 1986, to be published in J. Nucl. Mat.

2. H. R. Brager, F. A. Garner and N. F. Panayotou, "Damage Development and Hardening in 14 MeV Neutron Irradiation of Copper Alloys at 25°C," J. Nucl. Mat., 103/104, 955-60 (1981).

3. S. J. Zinkle and G. C. Kulcinski, "14 MeV Neutron Irradiation of Copper Alloys," J. Nucl. Mat., 122/123, 449-54 (1984).

4. J. B. Mitchell, R. A. VanKonynenburg, C. J. Echer and D. M. Parkin, in Radiation Effects and Tritium Technology for Fusion Reactors, J. S. Watson and F. W. Wiffen, eds, Gatlinburg, TN, 172 (1975).

EFFECTS OF SUBSTITUTIONAL ALLOYING ELEMENTS ON MICROSTRUCTURAL EVOLUTION IN NEUTRON IRRADIATED FE-10CR - D. S. Gelles (Westinghouse Hanford Company)

OBJECTIVE

The objective of this effort is to determine the effects of substitutional alloying elements in an Fe-10Cr base composition on microstructural development due to neutron irradiation. The alloying elements selected are of interest in reduced activation applications and include a wide range of atom sizes.

SUMMARY

The effect of solute additions on microstructural development in the base alloy Fe-10Cr following neutron irradiation at 426°C to 33.5 dpa has been examined. Additions of Si, V, Mn, W, Ta, and Zr were considered at 0.1 and 1.0 wt. % levels. It was found that solute additions affect the level of swelling, the void morphology and the dislocation evolution. The results are interpreted in terms of solute segregation to point defect sinks.

PROGRESS AND STATUS

Introduction

This report is intended to provide insights into the effects of solid solution hardening elements on microstructural evolution due to neutron irradiation in a base composition, Fe-10Cr, similar to that of commercial martensitic stainless steels. The purpose is to examine effects of substitutional alloying elements covering a wide range of atomic misfits on radiation damage to a simple ferritic alloy and to study those elements which would be most pertinent to low activation ferritic alloy design. The alloying elements selected for study (in order of increasing atomic size) were Si, V, Mn, W, Ta and Zr at levels of 0.1 and 1.0 weight percent. The basis for alloy selection and description of alloy preparation are given in Ref. 1. Table 1, taken from Ref. 1 gives a comparison of atomic sizes for the elements of interest.

The present effort examines the series of Fe-10Cr substitutional alloy specimens irradiated in the FFTF to ≈30 dpa at 420°C. Identical specimens irradiated at 370°C to 11 dpa were removed from reactor but have not yet been examined. Irradiation is continuing on another set of specimens at each temperature aiming for a 100 dpa goal. However, identical specimens irradiated at 520 and 600°C were removed from reactor due to temperature instability difficulties and were replaced with new specimens. The present examinations along with specimens irradiated at the same temperature to higher dose are expected to be of greatest interest.

Table 1. Atomic size comparison of alloying elements of interest

Element	Atomic No.	Atomic Wt.	Atomic Radius	Misfit*
Fe	26	55.8	1.24	---
Cr	24	52.0	1.25	0.0081
Si	14	28.1	1.17	-0.0565
V	23	50.9	1.31	0.0565
Mn	25	54.9	1.23-1.48	-0.0081-0.1935
W	74	183.9	1.37	0.1048
Ta	73	180.9	1.43	0.1532
Zr	40	91.2	1.58-1.61	0.2742-0.2984

*Misfit = $(r_M - r_{Fe})/r_{Fe}$

Only the work of Smidt and co-workers[2,3] previously considered the consequences of various solute additions to neutron induced microstructural evolution in ferritic alloys. In those studies, additions of 0.3 at.% Cu, V, Ni, and P, and 0.1 at.% C were made to zone refined high purity iron in order to determine the mechanism by which residual elements influenced the embrittlement of pressure vessel steels. The corresponding misfits are Cu = 0.0323, V = 0.0565, Ni = 0, P = -0.1210 and C = -0.4274 to -0.3790. Irradiations were primarily at 280-290°C to doses considerably below 1 dpa but included one run in EBR-II at 596°C to 7.4×10^{21} n/cm^2 (E > 0.1 MeV) or 5.5 dpa. They concluded, based on microstructural examinations of neutron irradiated specimens and ion bombarded specimens, that small solute additions can markedly influence the damage produced. The major effect was a shift in the temperature at which voids formed and the dislocation structure grew into a recovered structure. Vanadium had the greatest influence. A

correlation between reduction of swelling in dilute solid solution alloy systems and the presence of oversized solute atoms was found.

Experimental procedures

Alloy selection, specimen fabrication and irradiation condition goals are given in Ref. 1. Table 2 lists the alloy compositions and specimen engraving codes. The specimens examined in this study are from TEM specimen packet K1 irradiated in MOTA 1C basket 2C4 during FFTF Cycles 5 and 6. The average temperature was 426°C and the accumulated fluence is estimated at 7.27×10^{22} n/cm^2 (E > 0.1 MeV) or 33.5 dpa.[4]

Table 2. Alloy compositions and engraving codes

Alloy	Composition	Code
R117	Fe-10Cr-0.1Si	R9
R118	-1.0Si	AH
R119	-0.1Mn	AU
R120	-1.0Mn	AX
R121	-0.1V	AZ
R122	-1.0V	A1
R123	-0.1W	A3
R124	-1.0W	A4
R125	-0.1Ta	A5
R126	-1.0Ta	A6
R127	-0.1Zr	A7
R128	-1.0Zr	A9

Specimen handling, preparation and examination followed standard procedures. However, it was noted that the addition of 1.0% Ta resulted in an eight-fold increase in specimen radioactivity.

Results and analysis

Microstructural examinations

The heat treatment given all specimens (1040°C/1 hr/AC + 760°C/2 hr/AC) resulted in a structure resembling tempered martensite in all alloys except Fe-10Cr-1.0Si and Fe-10Cr-1.0V which had larger and more equiaxed grain structures. In all cases the density of carbide particles on boundaries was low indicating that carbon contamination was on the order of 0.03% or less.

Irradiation produced voids and dislocation loops in all cases. However, significant differences were found in accumulated void swelling, void shape, dislocation structure and distribution as a function of composition. Some of these differences can be shown in Fig. 1 which provides low magnification examples of alloys containing 1.0% solute additions. Martensite lath structure is encountered in alloys containing Mn, W, Ta and Zr. Voids were non-uniformly distributed only in alloys containing Si and Mn and voids appear smaller in alloys containing Si an V. Also, small voids indicative of recent nucleation, were only present in alloys containing Si, V and Mn. Differences were less pronounced at solute levels of 0.1% as shown in Fig. 2 which provides low magnification examples for comparison. All alloys showed evidence of martensite formation and all contained small voids indicative of continuing void nucleation. However, differences can be identified. For example, voids had grown largest in alloys containing Mn and Zr and void development appeared to be delayed in alloys containing Si and Ta. The non-uniform distribution of voids in alloys containing Mn and Ta is expected to be due to the narrow subgrain structure retained from the martensite transformation.

In order to examine the microstructural development in greater detail, higher magnification micrographs are shown for all alloys with 1.0% solute additions. Fig. 3 shows a specimen of Fe-10Cr-1.0Si following irradiation at 426°C to 33.5 dpa. Figs. 3a and b compare an area in (001) orientation using image contrast of $\vec{g}$ = 110 and 200, respectively. Fig. 3c provides an example of the same area in void contrast and Fig. 3d shows an adjacent area at higher magnification under the same imaging conditions as Fig. 3a. The area shown contains a non-uniform distribution of small voids. The dislocation structure is also non-uniform consisting predominantly of a<001> loops in regions where voids are not present, but in regions containing voids, a dislocation network has evolved containing both a<001> and a/2 <111> loops and line segments. (It should be noted that in $\vec{g}$ = 110 contrast, two of the four sets of dislocations with a/2 <111> Burgers vectors and two of the three sets of dislocations with a<001> Burgers vectors can be seen whereas in $\vec{g}$ = 200 contrast, all with a/2 <111> Burgers vectors and only one of the three with a<001> Burgers vectors can be seen and the a[100] dislocations are in much stronger contrast.) Therefore, it appears likely that in this alloy, dislocation network evolution is required prior to the onset of void

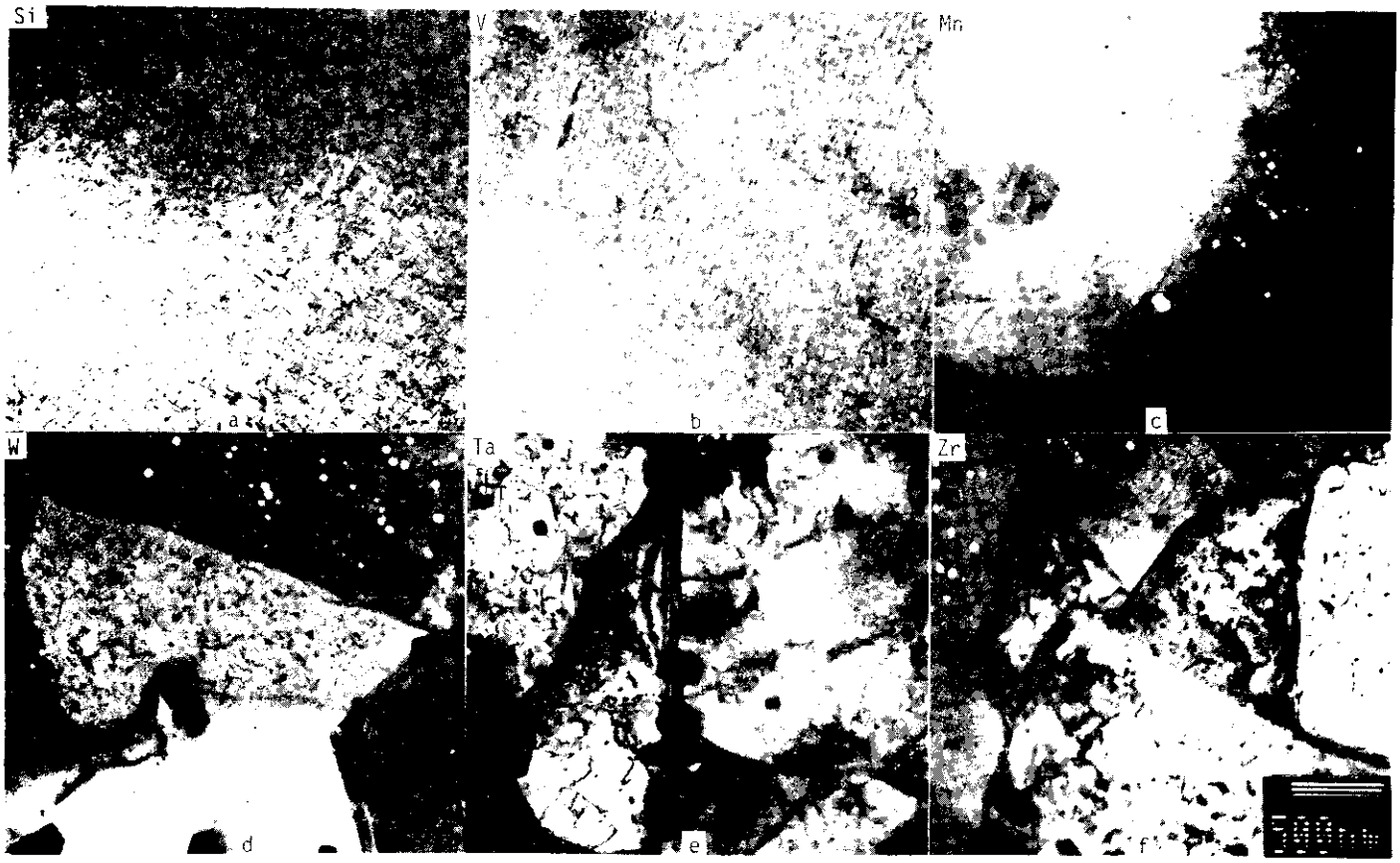

Fig. 1. Examples of microstructures at low magnification in alloys with 1.0% solute additions following irradiation at 426°C to 33.5 dpa.

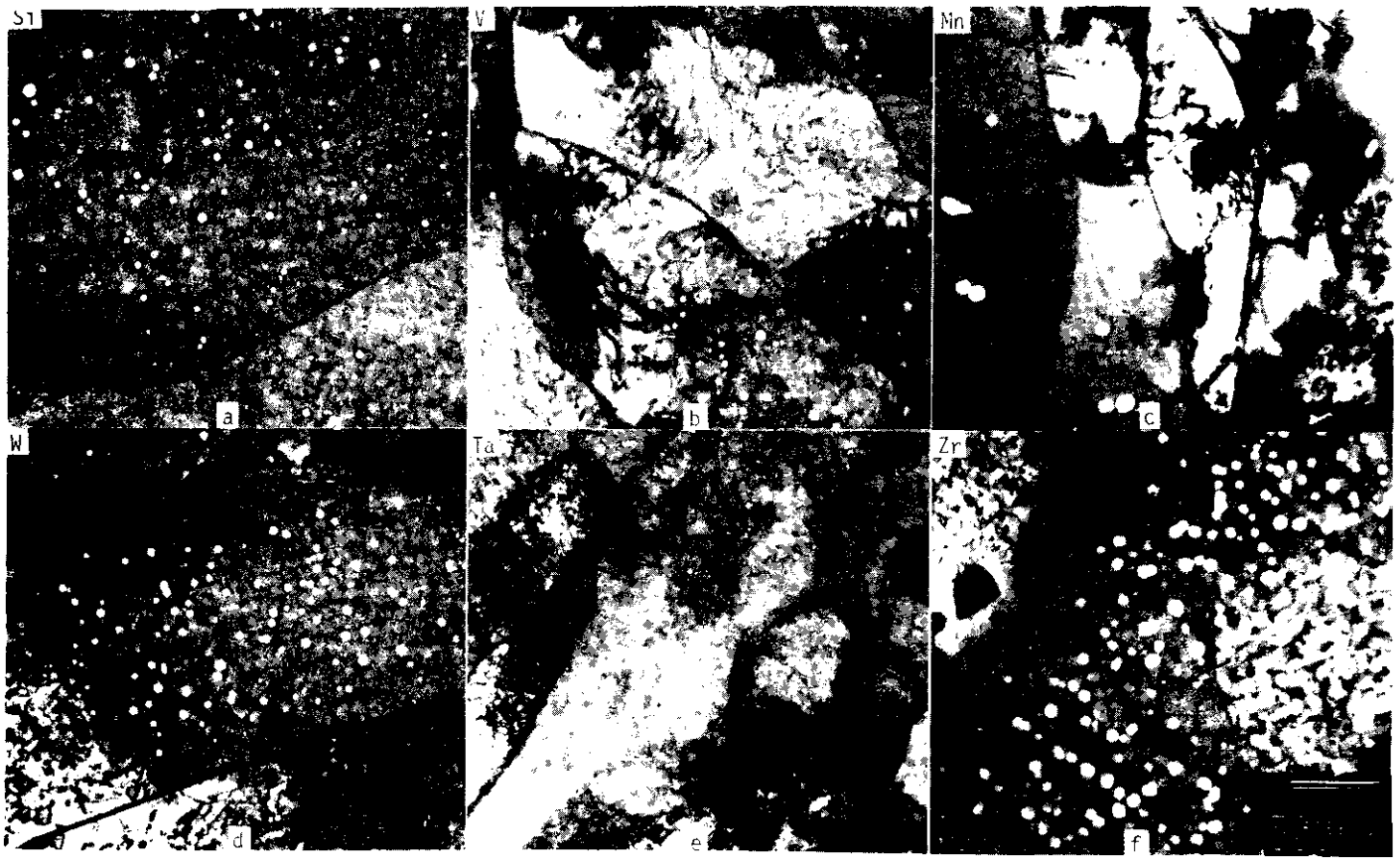

Fig. 2. Examples of microstructures at low magnifications in alloys with 0.1% solute additions following irradiation at 426°C to 33.5 dpa.

swelling. The presence of a/2 <111> dislocations prior to irradiation may also be important. Fig. 3d demonstrates more clearly that the voids appear as slightly truncated squares in an (001) orientation and the void edges are parallel to <100>. Other examples confirm that voids in Fe-10Cr-1.0Si are slightly truncated cubes with {001} faces. The truncation is probably on {011} planes!

Fig. 4 provides similar microstructural examples for Fe-10Cr-1.0V irradiated at 426°C to 33.5 dpa and comparisons reveal several differences. Precipitation is evident consisting of rod shaped particles oriented in <001> directions. The precipitates are expected to be V_4C_3. Also, the void distribution is more uniform and many of the voids are larger than those in the alloy containing Si. The dislocation structure consists predominantly of a<001> loops but several a/2 <111> line segments can be identified. However, of greatest surprise is a change in void shape. The voids appear as truncated squares with <011> edges. The (001) orientation does not allow easy differentiation between octahedral and dodecahedral voids but evidence of fringes on the void images indicates that these are in fact dodecahedral voids!

Fig. 5 shows similar views for a specimen of Fe-10Cr-1.0Mn. The structure again appears different. Voids have grown much larger than in the V alloy case but several examples of very small voids can be found indicating that void nucleation is continuing. The dislocation density is considerably reduced and the dislocation structure is a network containing a large fraction of a/2 <111> line segments. The void shape is again cuboidal with {011} truncations. Both Figs. 5a, c and d were taken some distance from the (001) pole and the cubic shape of the voids are clearly shown. Also of note is the distribution of small equiaxed particles found in Fig. 5c. In general, these are identified as α', the chromium rich body centered cubic phase. However, this identification has not yet been verified in the present work. Similar particles are identifiable in each of the other alloys, although not as clearly.

The results obtained for Fe-10Cr-1.0W are summarized in Fig. 6. The voids are uniformly distributed but are not quite as large as those in the Mn containing alloy. A few small voids can be identified in regions where swelling is not yet developed and α' precipitation is indicated. The dislocation structure is a network containing both a<001> and a/2 <111> Burgers vectors with some a<001> loops still present. Void shapes are dodecahedral with (001) truncations.

Fig. 7 shows microstructural development in Fe-10Cr-1.0Ta following irradiation at 426°C to 33.5 dpa. Behavior is similar to that found in the W containing alloy except that voids appear to have grown larger. The dislocation structure is a network with both a<001> and a/2 <111> Burgers vectors present but several examples of both a<001> and a/2 <111> loops can be identified. Void shape is generally dodecahedral with (001) truncation but several examples were found where equal (001) and (011) truncation had developed.

Fig. 8 provides examples of microstructural development in Fe-10Cr-1.0Zr following irradiation at 426°C to 33.5 dpa. In this case, the specimen orientation is near (011). Voids are uniformly distributed but a few small voids can be identified indicating that void nucleation is continuing. The dislocation structure consists of dislocation line segments and loops of predominantly a/2 <111> character. Precipitation present in the form of small equiaxed particles is expected to be α' phase. Void shape appears to be intermediate between cuboidal and dodecahedral. However, several examples appear to be almost spherical.

At solute levels of 0.1%, microstructural response can be summarized as follows. Void shapes were found to be generally truncated dodecahedra with {011} faces and {001} truncations. Exceptions were in Fe-10Cr-0.1Ta where smaller voids were cuboidal with {011} truncations and larger voids included equal amounts of {011} and {001} truncation. In Fe-10Cr-0.1Si, a few examples of cuboidal voids were found. Therefore, changes in void morphology occurred as Si, Mn and Ta solute additions were increased from 0.1 to 1.0%. Dislocation evolution was less sensitive to solute addition. In all cases, dislocation networks were found containing about equal parts of a<001> and a/2 <111> Burgers vectors. All conditions also contain loops of both Burgers vectors. The only notable difference was the fact that in Fe-10Cr-0.1Si the a<001> loops were smaller that the a/2 <111> loops whereas in Fe-10Cr-0.1V, the a<001> loops were larger. Therefore, increases in solute concentration had the greatest effect on dislocation evolution in the cases of V and Zr additions: further V additions promoted the formation of a<001> loops and further Zr additions promoted the formation of a/2 <111> loops.

In summary, additions of various solutes to an Fe-10Cr base composition leads to large changes in swelling and dislocation evolution. Differences are evident with each change in solute addition. It is apparent that radiation induced solute segregation must play an important role in controlling the microstructural development.

Microstructural measurements

Void swelling and dislocation density measurements have been made for one area of many of the alloy conditions examined. A listing of the conditions involved and the resulting measurements are given in Table 3. From Table 3 it can be shown that swelling appears to increase with increasing solute atom misfit but that this is not a straightforward variation with void density or mean void size. Reduction in the level of solute additions of W from 1.0 to 0.1% results in a small increase in void swelling due to small increases in void density and mean void size. The variations in swelling, void density and mean void size as a function of solute atom misfit for solute levels of 1% are plotted in Fig. 9. Except for uncertainty

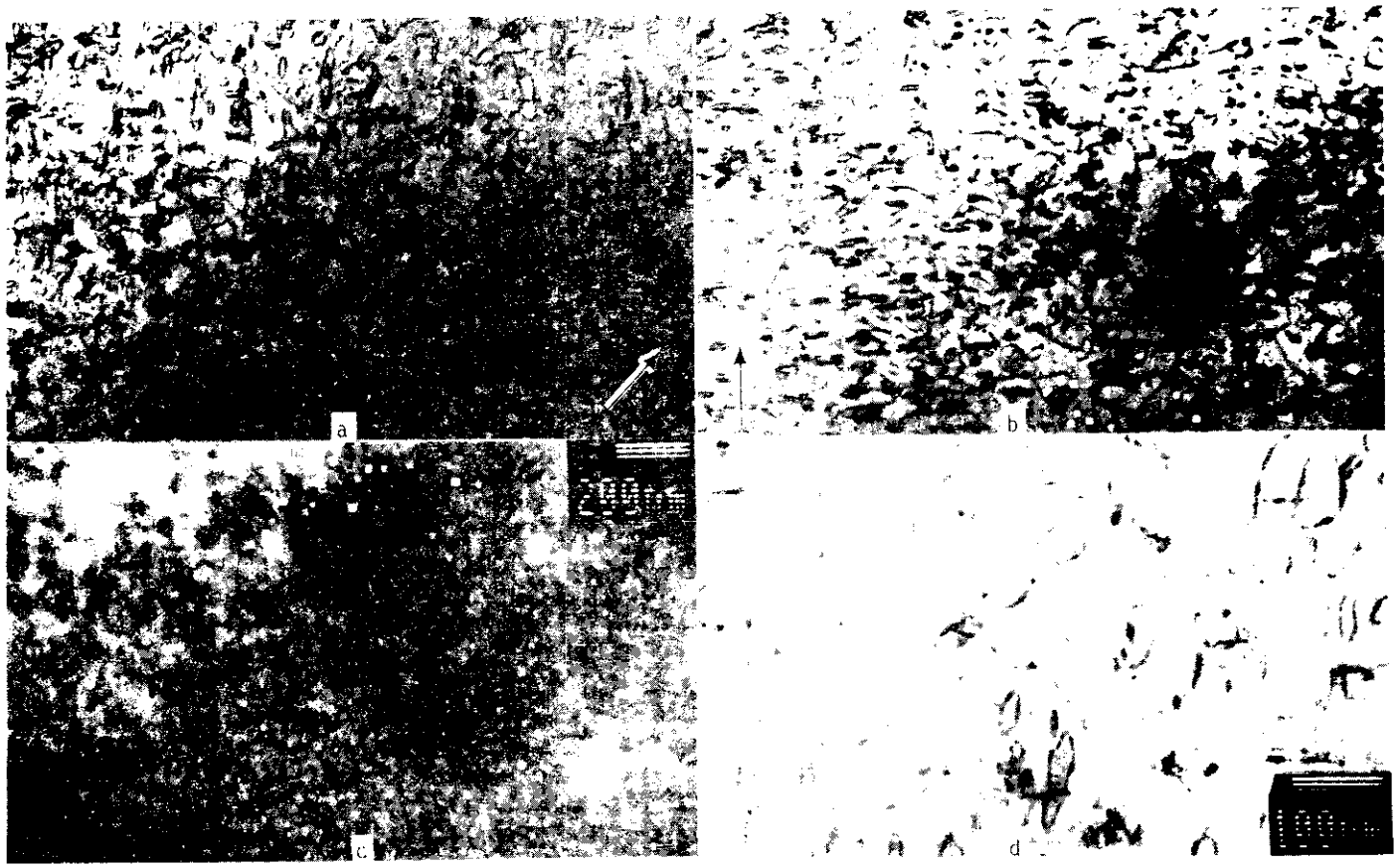

Fig. 3. Microstructure of neutron irradiated Fe-10Cr-1.0Si in a) 110 dislocation contrast, b) 200 dislocation contrast, c) void contrast and d) 110 contrast at higher magnification for a specimen in (001) orientation.

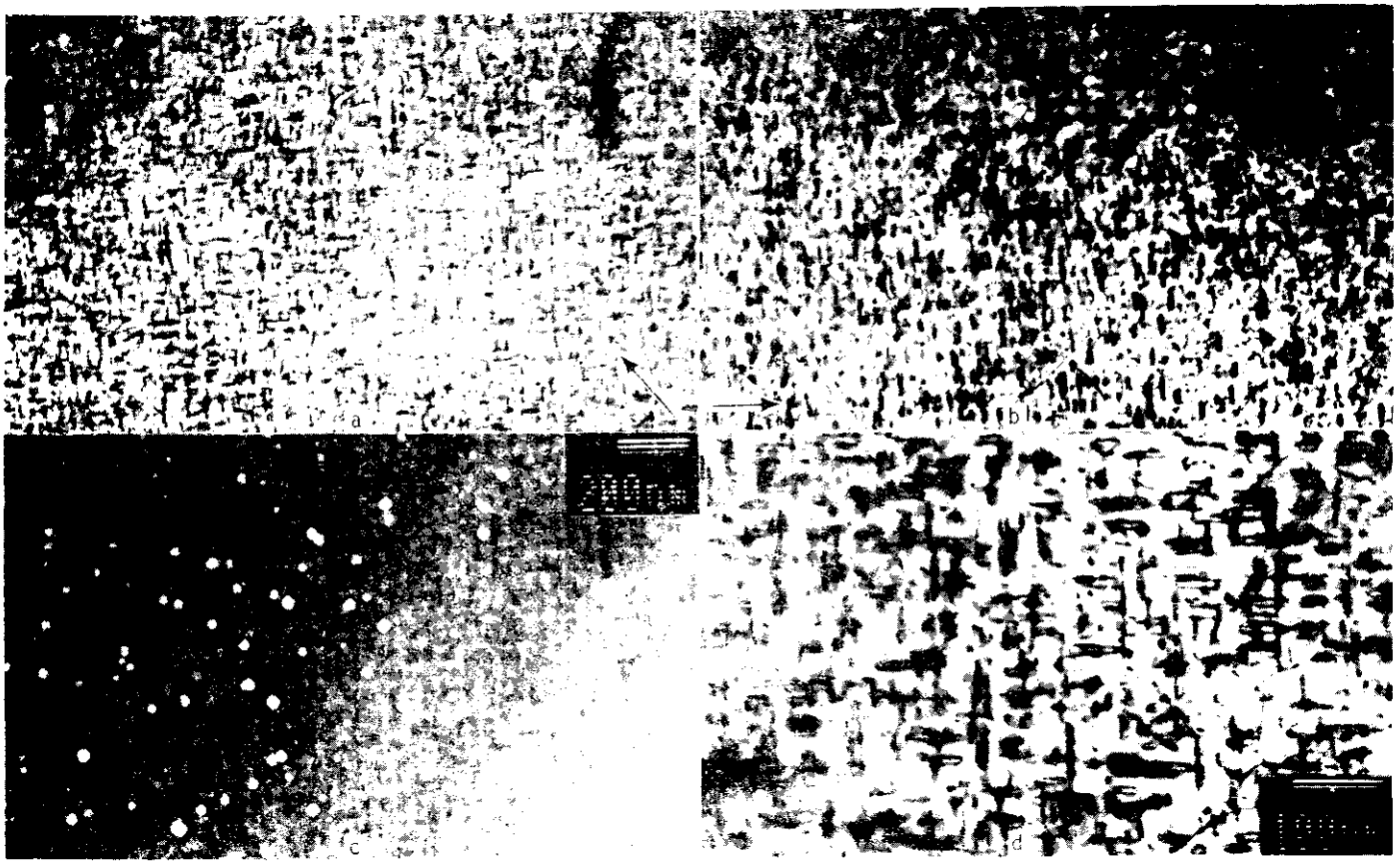

Fig. 4. Microstructure of neutron irradiated Fe-10Cr-1.0V in a) 110 dislocation contrast, b) 200 dislocation contrast, c) void contrast and d) 110 contrast at higher magnification for a specimen in (001) orientation.

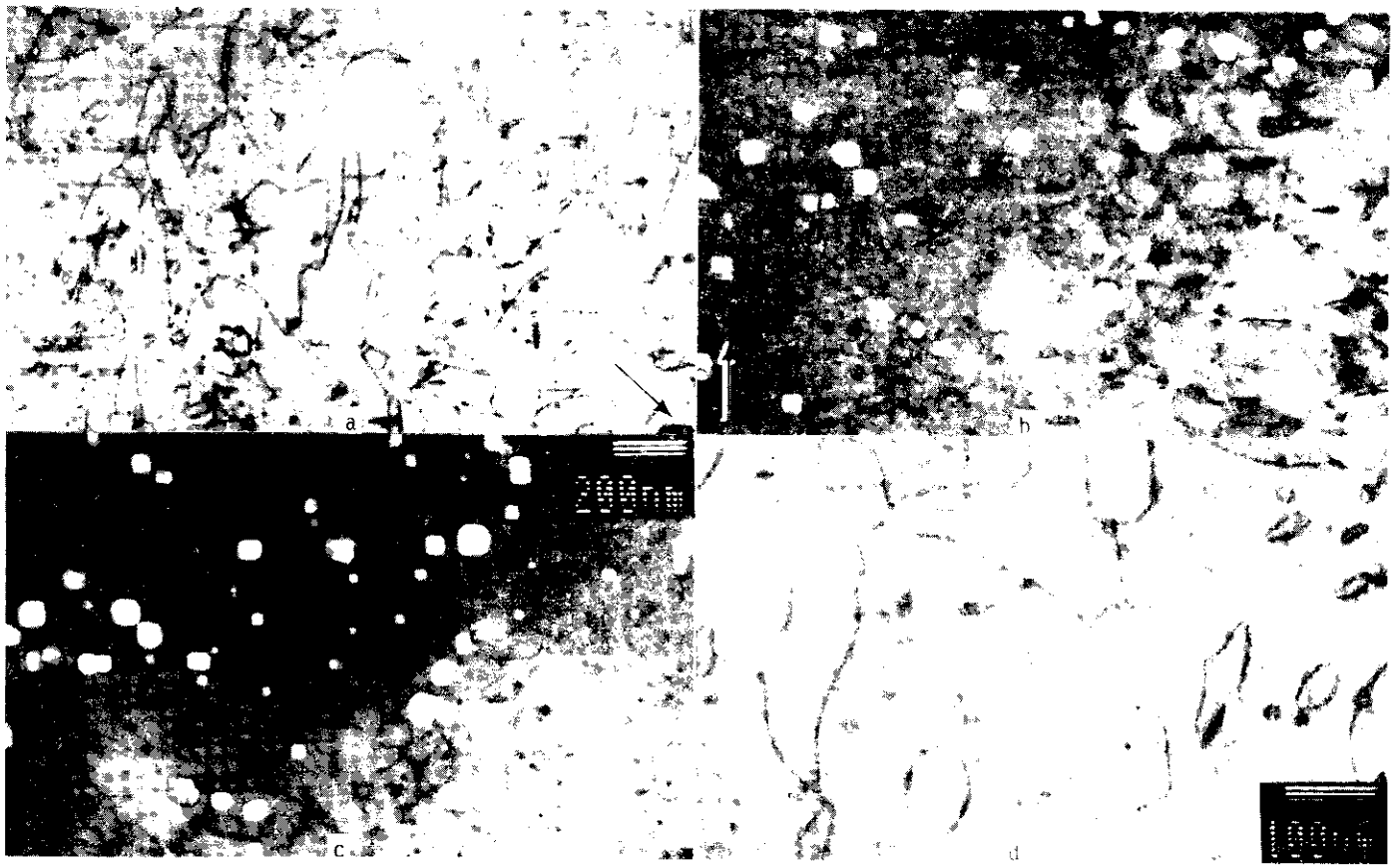

Fig. 5. Microstructure of neutron irradiated Fe-10Cr-1.0Mn in a) 110 dislocation contrast, b) 200 dislocation contrast, c) void contrast and d) 110 contrast at higher magnification for a specimen near (001) orientation.

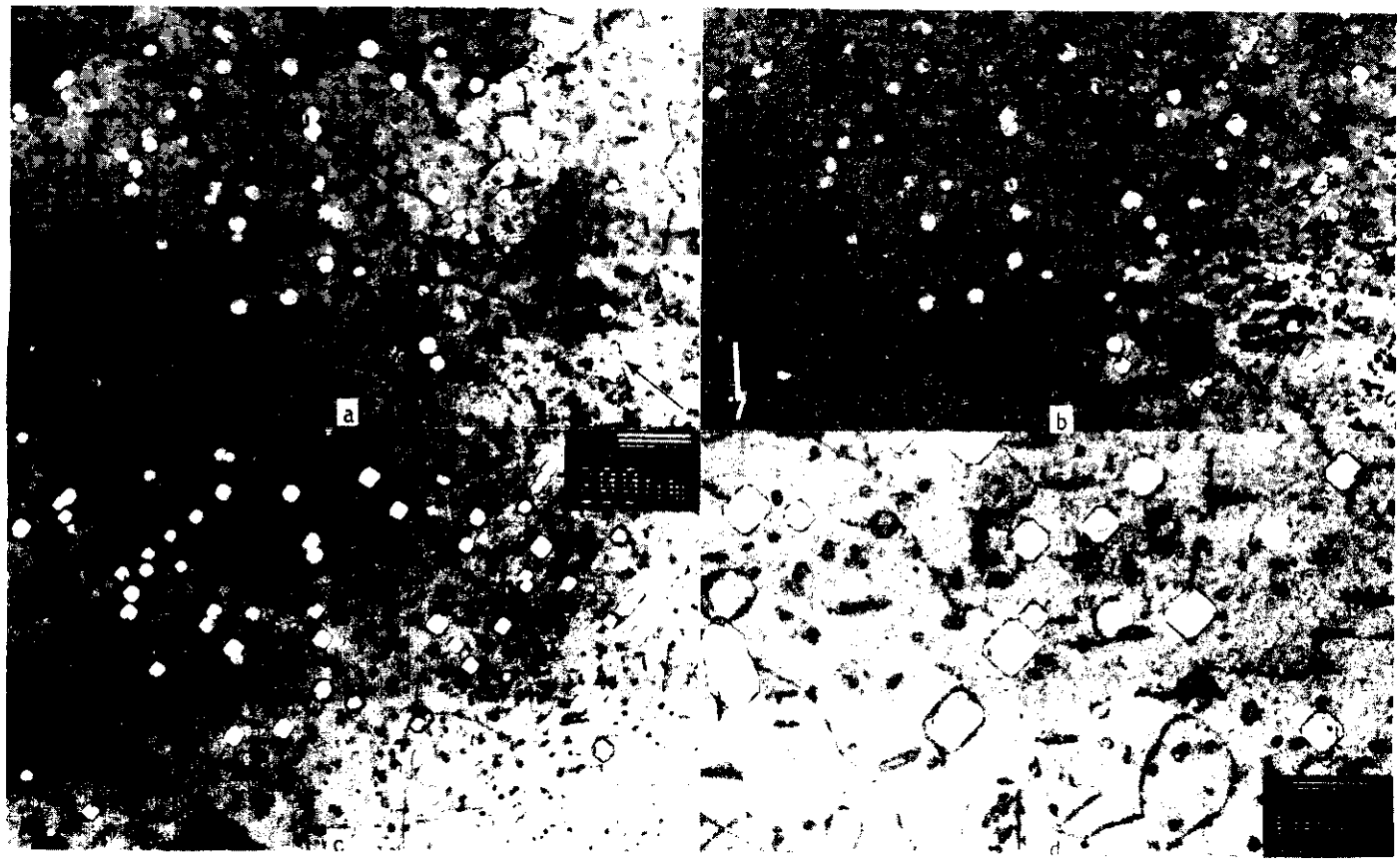

Fig. 6. Microstructure of neutron irradiated Fe-10Cr-1.0W in a) 110 dislocation contrast, b) 200 dislocation contrast, c) void contrast and d) 110 contrast at higher magnification for a specimen in (001) orientation.

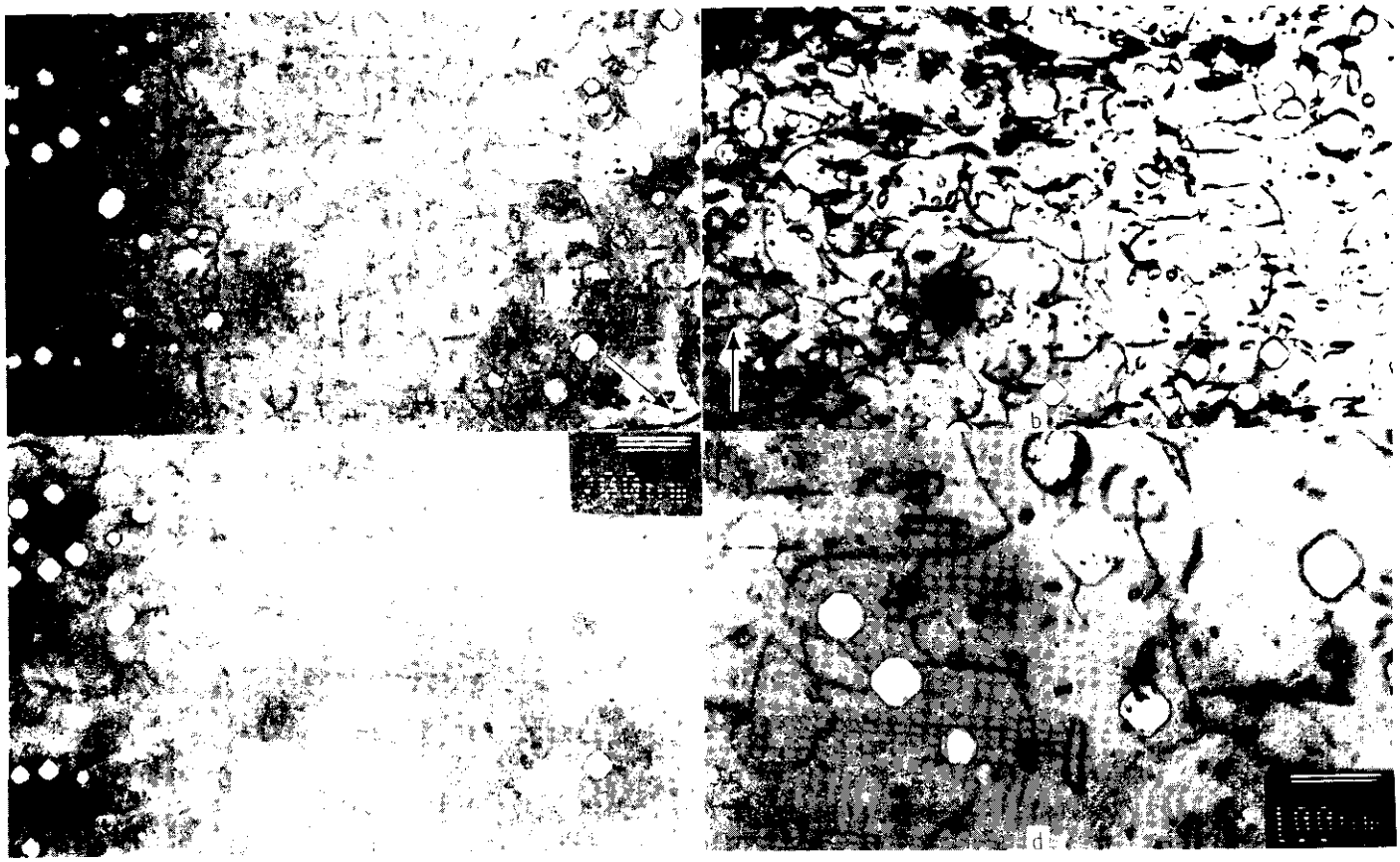

Fig. 7. Microstructure of neutron irradiated Fe-10Cr-1.0Ta in a) 110 dislocation contrast, b) 200 dislocation contrast, c) void contrast and d) 110 contrast at higher magnification for a specimen in (001) orientation.

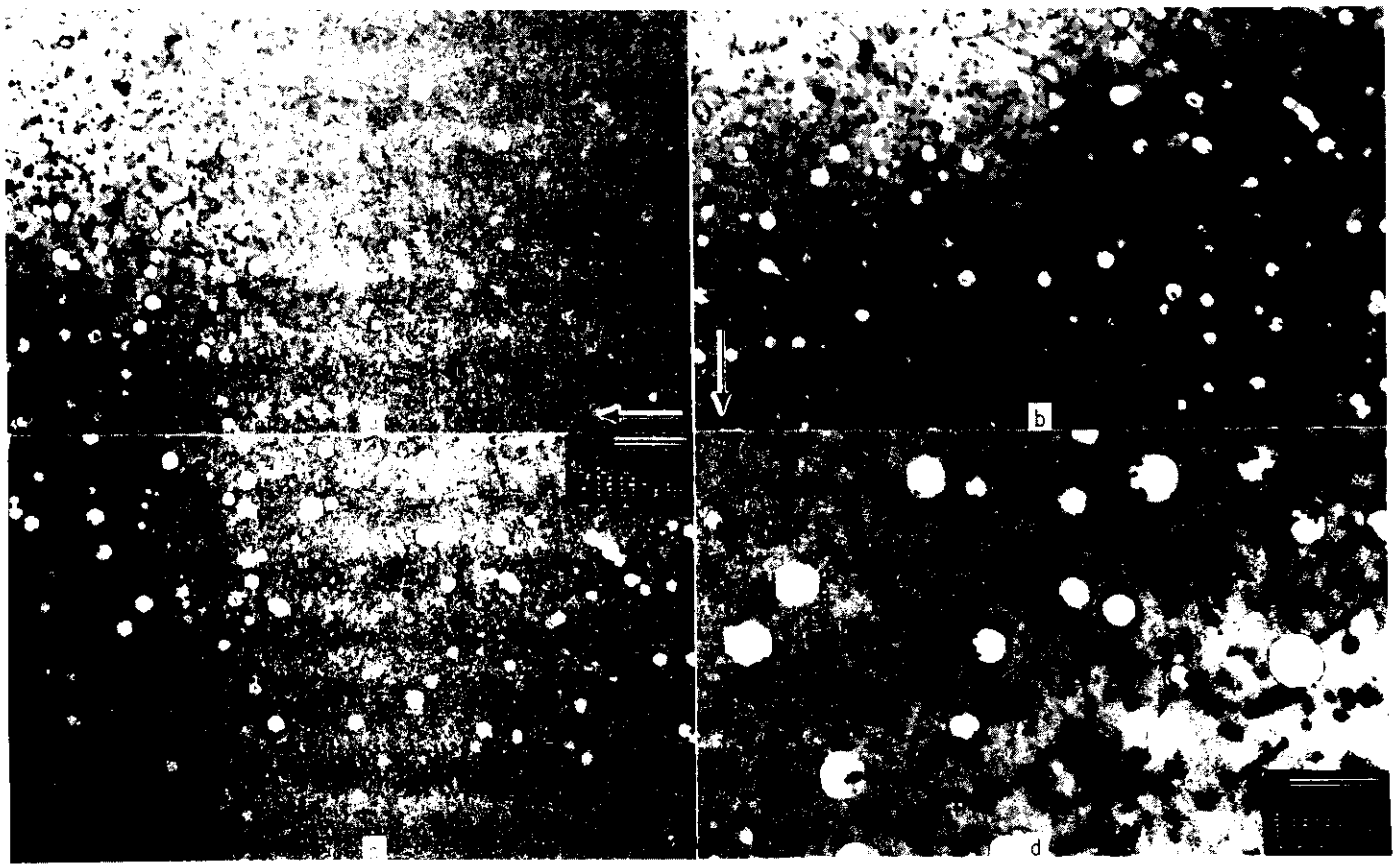

Fig. 8. Microstructure of neutron irradiated Fe-10Cr-1.0Zr in a) 110 dislocation contrast, b) 002 dislocation contrast, c) void contrast and d) 110 contrast at higher magnification for a specimen in (011) orientation.

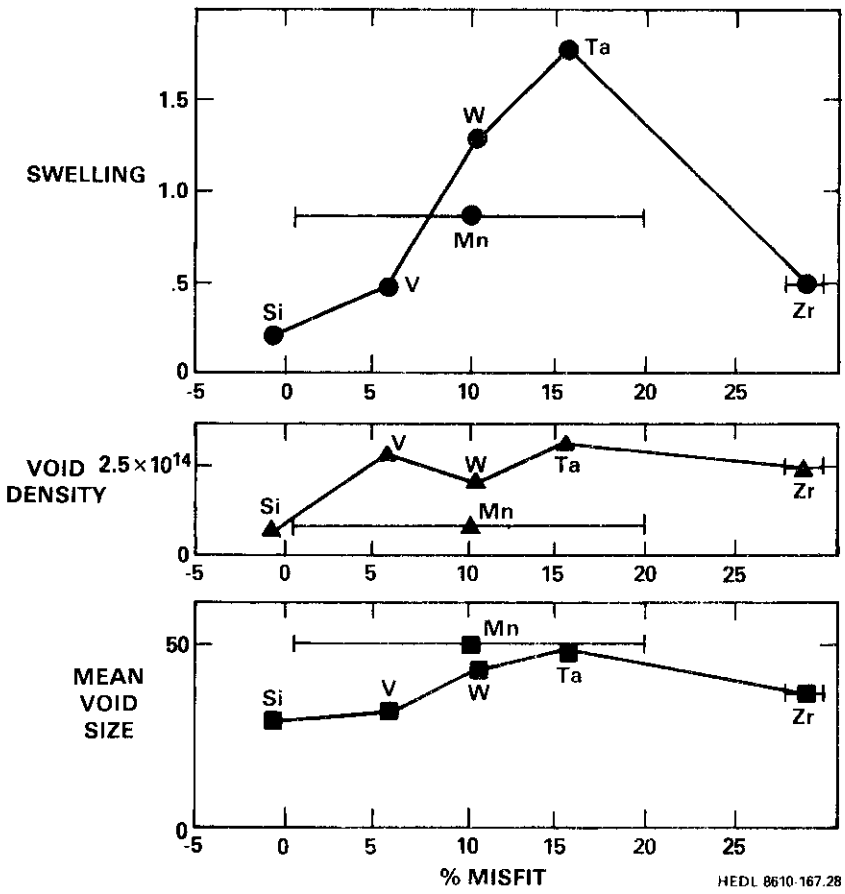

Fig. 9. Void swelling, void density and mean void size as a function of solute atom misfit.

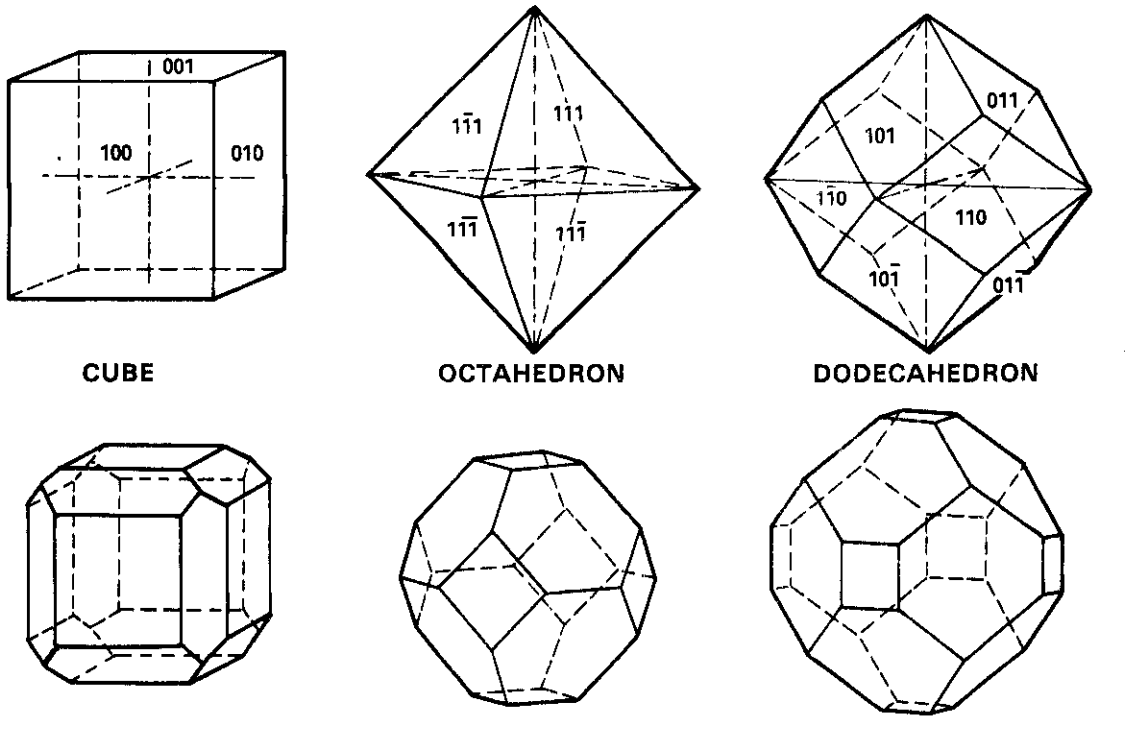

Fig. 10. Examples of the void shapes found in ferritic alloys.

in the misfit for Mn and the low swelling observed in the case of Zr, a linear trend in swelling as a function of misfit is found. The trends are not as clear in the case of void density and mean void size, however, because manganese proves to be an exception in each case. The reason for a linear swelling response as a function of misfit is not yet understood and may be fortuitous. The dislocation density measurements do not provide a simple explanation for variations in swelling. The measurements show high a<001> dislocation densities for V and Ta additions and high a/2<111> densities for Si and Ta additions with less variation in a/2<111> densities as a function of solute addition. Comparison of the results raises the concern that specimen A6K1 with 1 Ta has been evaluated with an incorrect specimen thickness. If the specimen were twice as thick the void swelling would be halved, the void density halved and each of the dislocation densities halved, all of which appear to follow reasonable trends.

Table 3. Quantitative microstructural measurements on selected specimens

I.D. No.	Alloy Composition	Swelling V/V_o (%)	Swelling Density (10^{14} cm^{-3})	Swelling d (nm)	Dislocation Density a<001> (10^9 cm^{-3})	Dislocation Density a/2 <111> (10^9 cm^{-3})
AHK1	-10Cr-1Si	0.19	1.24	29.3	6.5	9.1
A1K1	-10Cr-1V	0.44	2.86	31.4	20.8	7.1
AXK1	-10Cr-1Mn	0.88	1.23	49.1	3.8	4.8
A3K1	-10Cr-0.1W	1.29	3.10	43.3	4.5	7.4
A4K1	-10Cr-1W	1.05	2.41	42.0	5.7	6.5
A6K1	-10Cr-1Ta	1.79	3.02	47.2	21.9	11.9
A9K1	-10Cr-1Zr	0.46	2.22	35.3	2.4	5.1

Discussion

This effort has raised several very interesting points for discussion. It is now apparent that void swelling in ferritic alloys is very sensitive to solute additions particularly with regard to void shape but also to dislocation evolution. A review of the literature and classification of the response is called for. The present work suggests that solute segregation plays an important role, a result shown by several other experiments. A definition of that role in controlling response will be attempted.

Void shape in ferritic alloys

Horton has reviewed the literature on radiation damage in iron and Fe-Cr alloys through 1982[5] and reports that cavity morphologies vary considerably. Truncated octahedra with {110} faces, cubes with {100} faces and truncated octahedra with {111} faces have all been reported. Kulcinski, et al.,[6] incorrectly reported truncated octahedra with {110} planes in 99.999% pure iron following irradiation in EBR-II at 450°C to $3x10^{21}$ n/cm^2 (E > 0.1 MeV) or 1.5 dpa. If the voids were defined by {110} planes, a dodecahedral void shape must have existed. Dodecahedral voids are the common morphology in bcc metals. However, for neutron irradiated pure iron[7] and Fe-Cr binary alloys[5,8], truncated octahedra with {111} faces and {001} truncations have been found. However, Ohnuki, et al., have reported cuboidal cavities with {001} faces in iron irradiated at 525°C with 200 keV C^+ ions.[9]

The present observations extend these results to include truncated dodecahedral voids with {011} faces and {001} truncations, and truncated cuboidal voids with {001} faces and {011} truncations both found in fast neutron irradiated Fe-10Cr alloys with solute additions. The various void shapes found in ferritic alloys are summarized in Fig. 10. The cube, octahedron and dodecahedron morphologies are shown with labelled faces and examples of the pertinent truncations for these shapes are demonstrated. Therefore, strong evidence now exists for all three void morphologies in ferritic alloys.

Explanations for the existence of all three morphologies are not yet clear. The properties which are expected to control are the surface energies for the various close-packed planes, and it is now apparent that the various surface energies are affected by alloy composition. It appears likely that in iron and Fe-Cr alloys the lowest energy planes are {111} followed by {001}. (The Kulcinski, et al., results[6] were probably affected by impurities because the voids found were not equiaxed. This is probably a result of the low dose achieved which would tend to concentrate available solute at void surfaces even in pure alloy systems.) However, with the addition of many solutes, {111} planes are the least favored and either {011} or {001} are the lowest energy planes.

Solute segregation

Because void shape is altered in Fe-10Cr alloys by minor additions of several alloying elements of interest, it is quite likely that those solute additions are being concentrated at void surfaces by

radiation driven solute segregation. If segregation is occurring at voids, dislocations and grain boundaries are also likely to be affected. Solute atmosphere effects on dislocation climb are most likely responsible for differences in dislocation evolution as well. However, in simple Fe-Cr binary alloys it is found that α' precipitation does not form near voids[10] indicating that chromium depletion occurs at point defect sinks and that chromium does not play a role in void shape or dislocation evolution control. In the case of void stability, one can conclude that Si and Mn segregation causes {001} planes to be more stable than {011} planes which are more stable than {111} planes. However, V, W, Ta and Zr segregation cause {011} planes to be more stable than {001} planes which are more stable than {111} planes. To complicate matters further, reduced amounts of Si, Mn or Ta (to 0.1% solute levels) reverse the behavior, altering the relative stability of {001} and {011} planes. In the case of dislocation development, one can conclude that V additions promote a<001> Burgers vectors, Zr additions promote a/2 <111> Burgers vectors and Si, Mn, W and Ta additions allow both to form.

Much of the above discussion is based on the assumption that solute segregation controls behavior. This remains to be proven. Therefore, one of the major consequences of this effort is to encourage experimental verification of radiation induced solute segregation in ferritic alloys. To date, this has not been easily done. The most pertinent results have been provided by electron and C^+ ion irradiation experiments[11] where it is found that Cr and Mn are depleted on grain boundaries, Mo is depleted at voids, Ti is unaffected and Ni rich precipitates were found adjacent to voids. Behavior at voids has not been easy to identify because associated precipitation does not seem to occur.

CONCLUSIONS

The effect of various solute additions on microstructural development in the base alloy Fe-10Cr following neutron irradiation at 426°C to 33.5 dpa has been examined. Additions of Si, V, Mn, W, Ta, and Zr were considered at 0.1 and 1.0 wt. % levels. It was found that solute additions affect the level of swelling, the void morphology and the dislocation evolution.

Swelling was found to vary linearly with solute atom size misfit for solute levels of 1.0%. At solute levels of 0.1%, swelling response was controlled by martensite lath size considerations.

Void morphology was found to vary in a complex manner with solute addition for both 0.1 and 1.0 wt. % solute levels. Octahedra with {001} truncations, the normal void shape for Fe-Cr alloys, were not found. Instead, the common shapes were dodecahedra with {011} faces and {001} truncations at corners. However, with solute additions of 1.0 Si and Mn, the void shapes were shifted to cubes with {001} faces and {011} truncations at corners.

In general, dislocation evolution created a dislocation network containing equal components of a<001> and a/2 <111> Burgers vectors but including loops of both type. However, additions of 1.0% V promoted the formation of a<001> loops and additions of 1.0% Zr promoted the formation of a network dominated by a/2 <111> Burgers vectors.

These results are interpreted to show that radiation induced solute segregation controls microstructural development in ferritic alloys but the details of the segregation behavior remain to be demonstrated.

FUTURE WORK

This work will be continued. If funding is available, solute segregation measurements will be made. Specimens will be examined at a higher dose and at other irradiation temperatures.

REFERENCES

1. D. S. Gelles and W. L. Beem, "The Effects of Substitutional Alloying Elements in an Fe-10Cr Ferritic Alloy," p. 26 in Damage Analysis and Fundamental Studies Quarterly Progress Report, April-June 1984, DOE/ER-0046/18, U.S. DOE, Office of Fusion Energy.

2. F. A. Smidt, Jr. and J. A. Sprague, "Property Changes Resulting from Impurity-Defect Interactions in Iron and Pressure Vessel Steel Alloys," p. 78 in Effects of Radiation on Substructure and Mechanical Properties, ASTM STP 529, American Society for Testing and Materials, 1973.

3. F. A. Smidt, Jr., J. A. Sprague, J. E. Westmoreland and P. R. Malmberg, "The Effect of Alloy Additions on Void Nucleation and Growth," p. 341 in Defects and Defect Clusters in B.C.C. Metals and Their Alloys, National Bureau of Standards, 1973.

4. Letter, A. E. Ermi to Distribution, "Fusion Materials Specimens from MOTA-1C FFTF Cycles 5-6," dated October 11, 1985, HEDL-7630, Westinghouse Hanford Company, Richland, WA.

5. L. L. S. Horton, "A Transmission Electon Microscope Study of Fusion Environment Radiation Damage in Iron and Iron-Chromium Alloys," ORNL/TM-8303, Oak Ridge National Laboratory, Oak Ridge, TN, July 1982.

6. G. L. Kulcinski, B. Mastel and J. L. Brimhall, "Formation of Voids in Iron During High Temperature Neutron Irradiation," Rad. Eff., 2, 57 (1969).

7. L. L. S. Horton, J. Bentley and K. Farrell, "A TEM Study of Neutron-Irradiated Iron," J. Nucl. Matl., 108/109, 222 (1982).

8. D. S. Gelles, "Microstructural Examination of Neutron-Irradiated Simple Ferritic Alloys," ibid, 515 (1982).

9. S. Ohnuki, H Takahashi and T. Takeyama, ibid, 103/104, 1121 (1981).

10. E. A. Little and D. A. Stow, "Effects of Chromium Additions on Irradiation-Induced Void Swelling in α-Iron," Met. Sci. J., 14, 89 (1980).

11. T. Takeyama, H. Takahashi and S. Ohnuki, "Radiation-Induced Segregation in Austenitic and Ferritic Steels," Bul. Faculty Engrg. Hokkaido Univ., N. 121, 85 (1984).

SWELLING OF SOLUTE-MODIFIED Fe-Cr-Mn ALLOYS IN FFTF - F. A. Garner (Westinghouse Hanford Company)

OBJECTIVE

The object of this effort is to assess the suitability of austenitic Fe-Cr-Mn alloys as low activation candidates for fusion reactor structural materials.

SUMMARY

Density change data continue to be accumulated on solute-modified and commercial Fe-Cr-Mn alloys irradiated at 520°C and 50 dpa. The tendency toward saturation of density change observed in the simple ternary alloys in the annealed condition is accentuated by cold-working and solute addition. Irradiation at 420°C appears to further accelerate the tendency toward saturation.

PROGRESS AND STATUS

Introduction

The neutron-induced swelling of the annealed condition of simple Fe-Cr-Mn austenitic alloys at 9-14 dpa and 420-600°C has been described in previous reports.[1-4] Data on these same annealed alloys at 49.8 dpa and 520°C has also been presented.[5] As shown in Fig. 1, it appeared from these data that simple Fe-Cr-Mn austenitic alloys in the range 420-520°C initially swell at a rate of ∿1%/dpa after an incubation period of ∿10 dpa, consistent with the behavior observed in annealed Fe-Cr-Ni austenitic alloys.[6] At 520°C and 50 dpa, however, saturation of swelling appeared be developing,[5] as shown in Fig. 2.

Swelling data continue to be accumulated, with the major emphasis directed toward the solute-modified ternary alloys (See Table 1) and the commercial alloys (See Table 2) irradiated at 520°C. A limited amount of data on simple ternary alloys at 420°C and 46 dpa is also available.

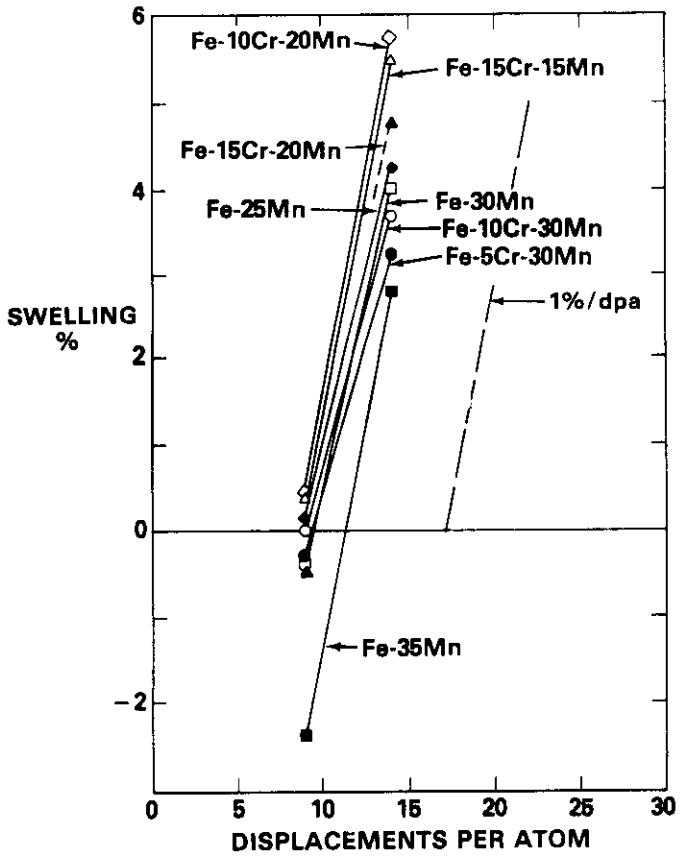

Fig. 1. Swelling at 9-14 dpa of simple Fe-Mn and Fe-Cr-Mn alloys at (420°C,9 dpa) and (520°C, 14 dpa) in FFTF-MOTA.[3]

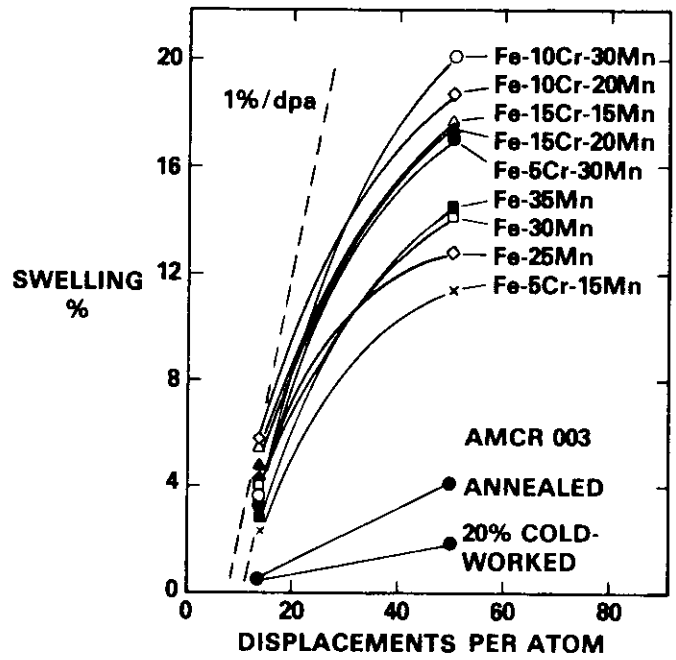

Fig. 2. Swelling of simple Fe-Mn and Fe-Cr-Mn alloys at 520°C.[5] The swelling of commercial alloy AMCR 003 is also shown for comparison.

Table 1. Composition of phase IV solute-modified Fe-Cr-Mn alloys (wt.%)

	Mn	Cr	C	N	V	P	B	Al	W	Ni	Si
X-75	30	2.0	0.10	0.15	-	-	-	-	-	0.5	0.4
R76	30	2.0	0.60	0.05	-	0.05	0.005	-	-	0.5	0.4
R77	30	2.0	0.40	0.15	1.0	0.05	0.005	-	1.0	0.5	0.4
R78	30	5.0	0.05	0.15	-	-	-	-	-	0.5	0.4
R79	30	10	0.05	0.10	-	-	-	-	-	0.5	0.4
R80	30	10	0.50	0.10	2.0	-	0.005	1.0	2.0	0.5	0.4
R81	20	15	0.05	0.10	-	-	-	-	-	0.5	0.4
R82	15	5	0.40	0.10	-	-	-	-	-	0.5	0.4
R83	15	5	0.60	0.05	-	0.05	0.005	-	-	0.5	1.0
R84	15	5	0.70	0.10	2.0	-	-	1.0	-	0.5	0.4
R85	15	15	0.05	0.15	-	-	-	-	-	0.5	0.4
R86	15	15	0.10	0.35	-	-	-	-	-	0.5	0.4
R87	15	15	0.10	0.10	-	0.05	0.005	-	-	0.5	1.0
R88	15	15	0.30	0.30	2.0	0.05	0.005	-	2.0	0.5	0.4
R89	15	15	0.50	0.10	2.0	-	-	1.0	2.0	0.5	0.4

Table 2. Composition of commercial Fe-Cr-Mn austenitic alloys

Designation	Vendor	Composition (wt.%)
NITRONIC ALLOY 32	ARMCO	18Cr-12Mn-1.5Ni-0.6Si-0.2Cu-0.2Mo-0.4N-0.1C-0.02P
18/18 PLUS	CARTECH	18Cr-18Mn-0.5Ni-0.6Si-1.0Cu-1.1Mo-0.4N-0.1C-0.02P
AMCR 0033	CREUSOT-MARREL	10Cr-18Mn-0.7Ni-0.6Si-0.06N-0.2C
NMF3	CREUSOT-MARREL	4Cr-19Mn-0.2Ni-0.7Si-0.09N-0.02P-0.6C
NONMAG 30	KOBE	2Cr-14Mn-2.0Ni-0.3Si-0.02N-0.02P-0.6C

Results

Fig. 3 shows that the tendency toward saturation in simple ternary Fe-Cr-Mn alloys occurs even faster at 420°C than it does at 520°C. Fig. 4 shows the swelling of solute-modified alloys in the 15% manganese range compared to that of the simple ternary alloys on which they are based. At this point it is not possible to separate the various factors which control the swelling, but one can see that aging after cold-working appears to increase the swelling and that varying the levels of various solutes also influences the swelling.

Fig. 5 shows that at 30% manganese the addition of solute can also have a pronounced effect on swelling. Note in Fig. 5b that cold-working of Fe-10Cr-30Mn after addition of 0.05C, 0.1N, 0.5Ni and 0.45Si causes a substantial reduction of swelling in alloy R79. An even greater reduction is realized in Alloy R80 by increasing the carbon level to 0.5% and by adding precipitate-forming elements such as tungsten, vanadium and aluminum.

In both Figs. 4 and 5 the tendency toward saturation is seen to be enhanced relative to that of the base ternary alloys. A similar behavior is observed in the commercial alloys as shown in Table 3. In general, the commercial alloys tend not to swell at 9-14 dpa, and most of them actually densify, as shown in Table 3. At ∿50 dpa and 520°C, most of these alloys have begun to swell, however. It appears that the annealed and aged condition of commercial alloys is the most vulnerable to the earliest onset of swelling.

Discussion

The discussion of these results will be deferred until more density change data are available and microscopy has been performed to provide insight on the relative contribution of voidage and phase-related strains.

FUTURE WORK

The accumulation of density change and microscopy data will continue.

Table 3 Swelling of commercial alloys

Alloy	Condition	Swelling, %			
		9dpa,420°C	14dpa,520°C	14dpa,600°C	49.8dpa,520°C
Nitronic 32	CW*	-0.11	-0.02	-0.19	3.5
18/18 Plus	CW	-0.10	-0.28	-0.56	2.2
18/8 Plus	CWA+	-0.05	---	-0.07	---
AMCR 0033	CW	0.42	0.62	---	1.9
AMCR 0033	CWA	-0.24	-0.02	-0.02	2.5
AMCR 0033	SAA[X]	0.03	0.61	0.22	4.4
NMF3	CW	-0.24	-0.23	---	0.1
NONMAG 30	SAA	0.07	0.17	-0.42	2.87
NONMAG 30	CW	0.42	0.62	---	1.0
NONMAG 30	CWA	-0.24	-0.02	0.20	0.42

*CW = 1030°C/0.5 hr/air cool + 20% cold-work
+CWA = cold-worked condition + 650°C/1 hr/air cool
[X]SAA = 1030°C/1 hr/air cool + 760°C/2 hr/air cool

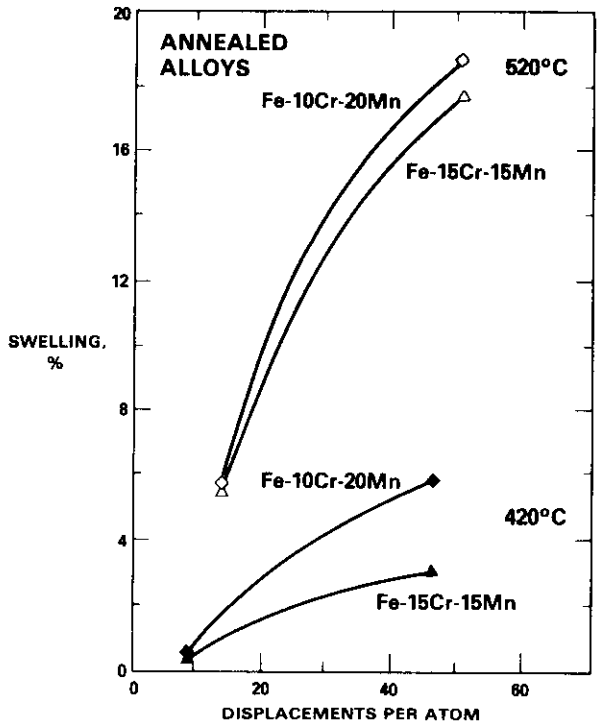

Fig. 3. Comparison of swelling of two simple Fe-Cr-Mn alloys at 420°C and 520°C.

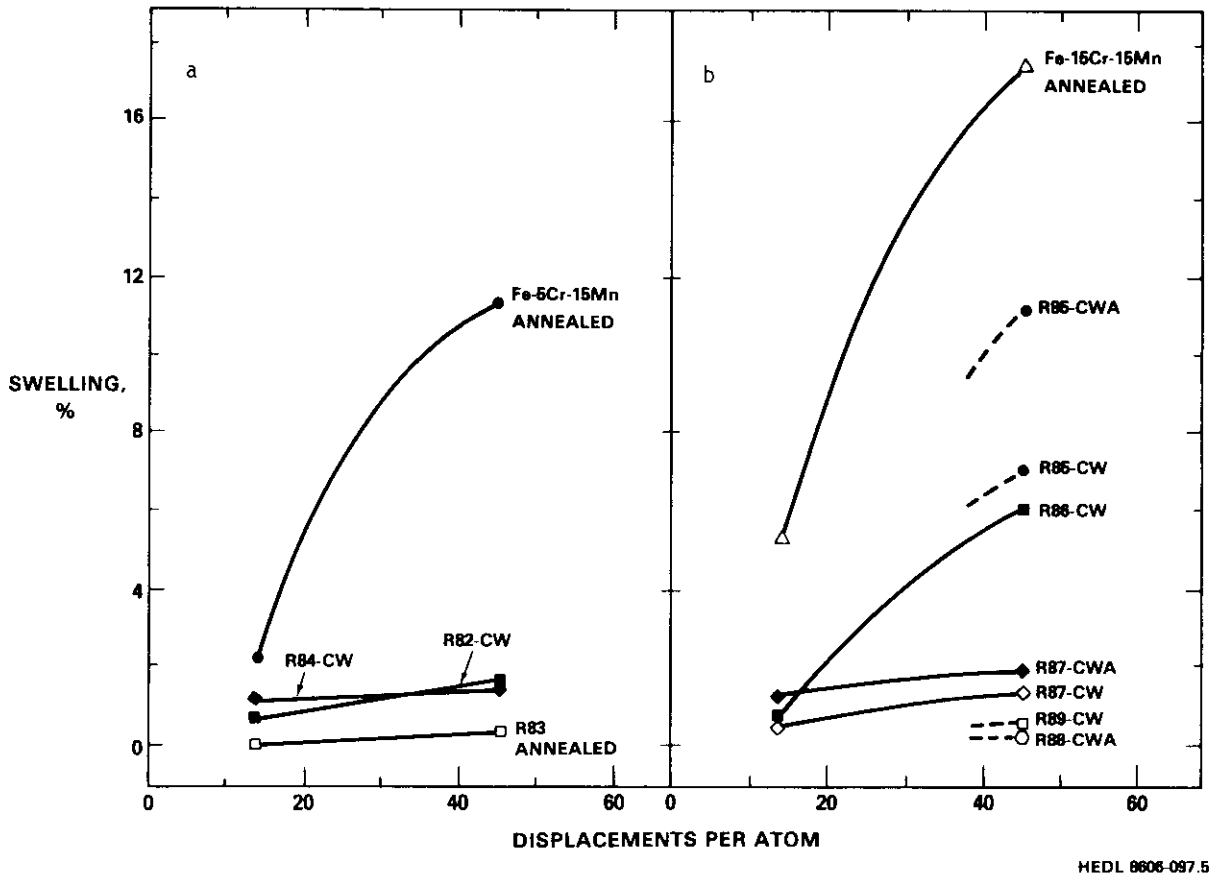

Fig. 4. Swelling of both simple and solute-modified alloys with 15% manganese at ∿50 dpa and 520°C. See Table I for definition of alloys codes and conditions.

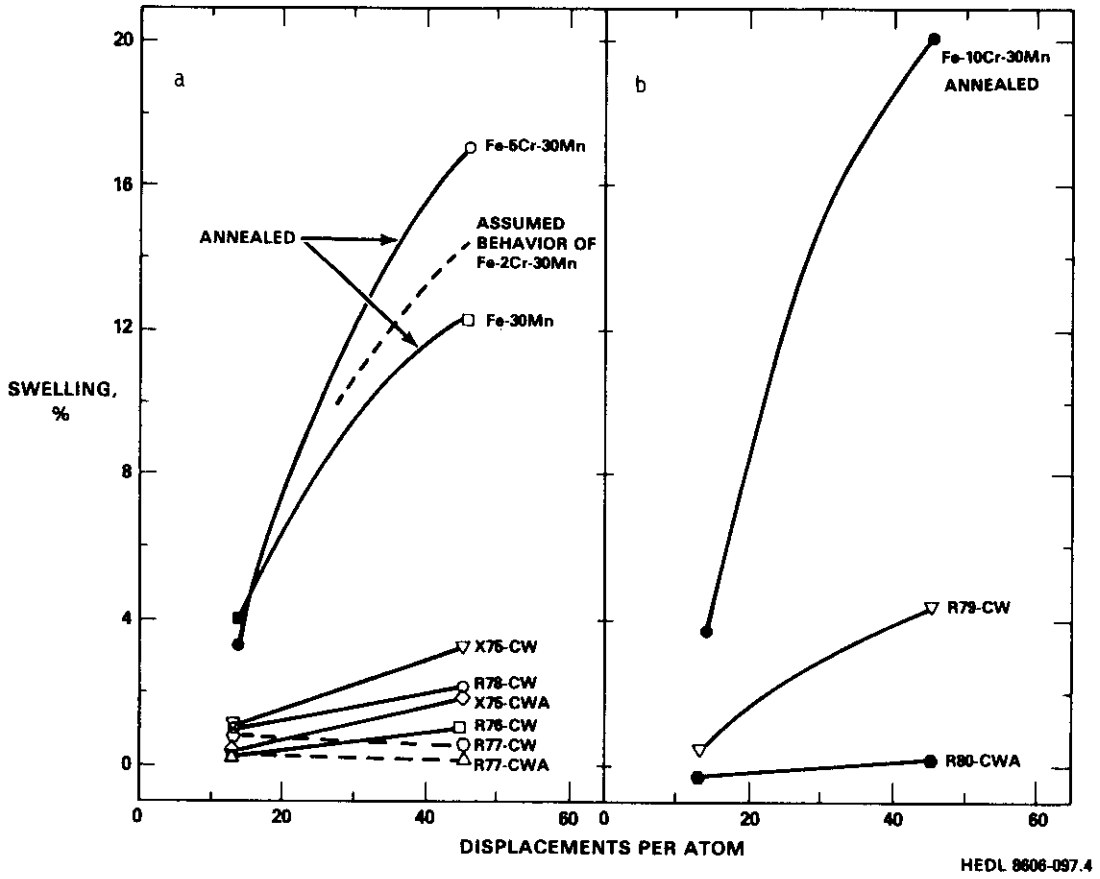

Fig. 5. Swelling of both simple and solute-modified alloys with 30% manganese at ~50 dpa and 520°C. With the exception of R78 all solute-modified alloys in Fig. 5b have 2% chromium; R78 has 5% chromium.

REFERENCES

1. H. R. Brager and F. A. Garner, "Swelling of Fe-Cr-Mn Ternary Alloys in FFTF," pp. 41-43 in Damage Analysis and Fundamental Studies Quarterly Progress Report, DOE/ER-0046/19, U.S. Department of Energy, Office of Fusion Energy, November 1984.

2. F. A. Garner and H. R. Brager, "Neutron-Induced Swelling of Fe-Cr-Mn Ternary Alloys," pp. 41-45 in Damage Analysis and Fundamental Studies Quarterly Progress Report, DOE/ER-0046/21, U.S. Department of Energy, Office of Fusion Energy, May 1985.

3. F. A. Garner and H. R. Brager, "Neutron-Induced Swelling and Microstructural Development of Simple Fe-Mn and Fe-Cr-Mn Alloys in FFTF," pp. 18-23 in Damage Analysis and Fundamental Studies Quarterly Progress Report, DOE/ER-0046/23, U.S. Department of Energy, Office of Fusion Energy, November 1985.

4. F. A. Garner, D. S. Gelles, H. R. Brager and J. M. McCarthy, "Phase Development and Swelling in Fe-Mn and Fe-Cr-Mn alloys During Neutron Irradiation," pp. 22-29 in Damage Analysis and Fundamental Studies Quarterly Progress Report, DOE/ER-0046/24, U.S. Department of Energy, Office of Fusion Energy, February 1986.

5. F. A. Garner and H. R. Brager, "Swelling of Fe-Mn and Fe-Cr-Mn Alloys at High Neutron Fluences," pp. 28-30 in Damage Analysis and Fundamental Studies Quarterly Progress Report DOE/ER-0046/25, U.S. Department of Energy, Office of Fusion Energy, May 1986.

6. F. A. Garner, J. Nucl. Mater., 122/123, 459-471 (1984).

CESSATION OF IRRADIATION CREEP IN AISI 316 CONCURRENT WITH HIGH LEVELS OF SWELLING - D. L. Porter (EBR-II Project, Argonne National Laboratory) and F. A. Garner (Westinghouse Hanford Company)

OBJECTIVE

The object of this effort is to study the relationship between radiation-induced microstructural alterations in metals and the associated macroscopic consequences of swelling, creep, mechanical properties and fracture modes.

SUMMARY

At high neutron exposures where the swelling of AISI 316 exceeds ∿5% the irradiation creep rate at 550°C begins to decline and eventually disappear. Swelling continues to proceed, however, leading to a maximum deformation rate dictated only by that of the steady-state swelling rate or ∿0.33%/dpa. It is not clear at this point whether large levels of voidage are directly responsible for the decrease in creep rate. There is some evidence to support the possible role of intermetallic precipitate formation, although the mechanism of creep suppression by such precipitates is not known.

PROGRESS AND STATUS

Introduction

In a series of recently published studies it was shown that the relationship of creep to concurrent void swelling is more complex than previously envisioned.[1-3] Whereas it has been commonly accepted that the irradiation-induced creep rate accelerates with the onset of swelling and would continue at a rate proportional to that of the swelling, it now appears that the creep rate in AISI 316 stainless steel subsequently declines as swelling approaches levels in excess of ∿5%. Creep also appears to be coupled to swelling in a manner such that the total rate of diametral deformation in pressurized tubes does not exceed ∿0.33%/dpa, regardless of how the swelling and creep strains are partitioned. Since 0.33%/dpa represents the anticipated steady-state swelling rate[4], this implies that the creep rate must eventually vanish.

These somewhat perplexing developments first were brought to light when the measured creep strains of fuel pin cladding at high neutron fluence often fell substantially below that predicted by creep correlations developed at lower fluence but higher stress levels.[1,3] The tendency toward underprediction appears to increase as the fluence to burn-up ratio is increased. (Burn-up refers to the percentage of fissile atoms which have undergone fission). This ratio is controlled primarily by the fissile enrichment of the fuel and governs the rate of increase of fission gas pressure. Since fuel cladding usually has very low initial stress levels which then increase primarily due to fission gas pressure as burn-up proceeds, the fluence to burn-up ratio determines the relative amounts of creep and swelling strain. Although the onset of swelling is somewhat sensitive to the stress level, swelling does not require stress to proceed in AISI 316.[5,6]

At this point it is relevant to note that there is a fundamental difference in the conditions under which stress-driven creep data are collected and the manner in which stresses arise in most reactor components. On the whole, creep data are very expensive to obtain compared to swelling data. This cost and the space constraints in available reactors necessitates several compromises in the experimental derivation of a comprehensive creep data base. First, creep experiments usually proceed on small creep capsules in order to cover the range of fluence and temperature desired. While the use of short tubes has been shown to yield results representative of longer tubes with minimum end effects, the gas pressures are chosen to maximize the creep strain, using constant stress levels that usually exceed the time-dependent levels encountered in fuel pin cladding and other reactor components.[7] This approach guarantees that creep strains develop in pressurized tubes prior to the onset of swelling. The opposite situation where swelling develops before much creep occurs would never happen in a typical highly-pressurized tube. However, swelling can start prior to substantial creep in fuel pins which have a high fluence to burn-up ratio.

The second compromise involves the method of calculating the creep strain. The usual practice is to calculate the creep strain by subtracting from the diametral change of the stressed tube the diametral change of a companion tube without stress. After measurement of both tubes, they are returned to the reactor for further irradiation and subsequent measurements. The alternative approach would be much more expensive and require the destructive examination of a stressed tube at every fluence and stress level.

One consequence of the current approach is the inclusion of some non-creep components of deformation in the calculated creep rate. These non-creep strains are the stress-affected component of swelling and the texture and stress-dependent anisotropies associated with the formation of various precipitate phases.[8,9] As long as these non-creep components are small relative to that of creep and providing that

these non-creep strains saturate with continued exposure, the errors associated with the trade-off between cost and necessity are small and can be compensated partially by using an appropriately coupled set of creep, swelling and densification equations. However, this approach also requires that the creep rate continue to develop in a manner which is proportional to the swelling rate. Otherwise, the potential exists for a misprediction of creep strains subject either to large levels of void swelling or phase-related volume changes. The latter consideration has been demonstrated to have a large effect on creep strains and creep predictions in AISI 316.[9] It may also be involved in the decrease of creep rates at high fluence, as discussed later.

In this paper we examine the relationship between strains arising from precipitation, irradiation creep and swelling in AISI 316 using rather long creep tubes irradiated to higher fluence levels than currently probed by most short creep tube experiments. One can also make use of the length of the tube to study at one stress level the influence of both fluence and displacement rate on the various components of strain, using the neutron flux and energy gradients along the tube axis.

Experimental details

Another way to assess the interrelationships between swelling and creep strains is to employ different thermal-mechanical starting conditions that affect the duration of the transient regime of swelling. The steel employed was the V87210 reference heat of AISI 316 used in the U.S. Breeder Reactor Program. Its composition in wt% was Fe-13.57Ni-16.36Cr-2.88Mo-1.42Mn-0.47Si-0.07C-0.02P-0.01S with <0.005 B. This steel was irradiated in five metallurgical conditions: solution annealed, 10% cold-worked, 20% cold-worked, 20% cold-worked followed by aging for 24 hr at 482°C (designated Heat Treat C), and Heat Treat C followed by another aging for 216 hr at 704°C to cause extensive carbide precipitation. This latter heat treatment is hereafter designated as Heat Treat D but is often called the Garafalo treatment. All conditions were prepared using vendor-produced 20% cold-worked steel as the starting condition. Thus the 10% cold-worked condition was prepared by working the annealed condition prepared in the laboratory from the 20% cold-worked condition.

The creep capsules have been described in detail elsewhere.[10,11] In brief, the capsules are 1.02 m long and have an outer diameter of 0.584 cm and a wall thickness of 0.038 cm, but only the top 0.28 m length of the capsules is pressurized with helium to yield hoop stresses varying from of 0 to 200 MPa (0-30 ksi). The pressurized portion is welded to the lower portion of the capsule which contains a tantalum rod to heat the sodium to ~550°C ±10°C as it flows upward. The irradiations proceeded in Row 7 of the Experimental Breeder Reactor EBR-II in Idaho Falls, Idaho. Approximately 5 dpa (±10%) are produced in this reactor for each 1.0×10^{22} n cm^{-2} (E > 0.1 MeV). The dpa levels cited for each datum are derived from the neutron spectrum and flux for the reactor position examined.

Diameter measurements were made with a contact profilometer on a spiral trace along the entire length of the capsule after each irradiation period. Some tubes had obviously failed during a given irradiation period and were withdrawn. Those that did not fail were returned for reirradiation until a decision was made to terminate the irradiation of that particular pin. At that point the tube was punctured and the gas volume measured to confirm that the design stress level had been maintained throughout the irradiation. Some pins, particularly those that were in the annealed condition, were found not to have gas pressure and thus to have failed by some not quite so obvious mode such as a pin-hole failure. The stress history of these pins was therefore unknown and they were not used in this analysis.

Some pins were sectioned into one inch axial increments and immersion density measurements performed on them in order to determine the contribution of the various strain components.

Results

Fig. 1 shows typical strain profiles for both an unstressed and a stressed pin, as well as a photograph of a typical pin in the unirradiated condition. The discontinuity in each profile shows the location of the weld at the bottom of the pressurized section. The oscillations in the spiral trace reflect a slight ovality that often develops in the pin during irradiation.

The swelling of the five metallurgical conditions of this steel in general has been found to be Heat Treat D >annealed> 20% cold-worked> Heat Treat C >10% cold-worked.[10,11] The lesser swelling of the 10% cold worked condition probably reflects the different annealing conditions it received in the laboratory compared to that of the mill-prepared 20% cold-worked condition. Normally, the swelling decreases as the cold-worked level increases, providing that the intermediate annealing conditions between cold-worked passes does not change. The onset of swelling for AISI 316 is known to be sensitive to many production variables including the rate of feed of the tube through the annealing furnace.[6] Laboratory anneals are in general conducted for times that exceed the residence time of mill-prepared steels.

Since the creep rate is thought to increase as swelling accumulates, one would expect that the total deformation would exhibit the same dependence on starting condition as seen in the swelling behavior. Fig. 2 shows that the total deformation behavior of a typical series of pins follows the trend observed in the swelling behavior of earlier studies.

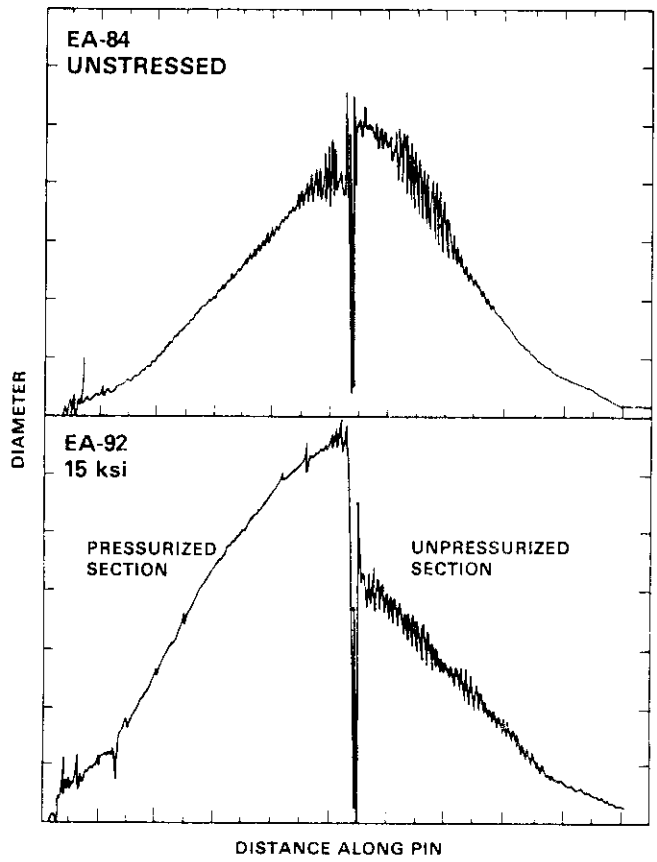

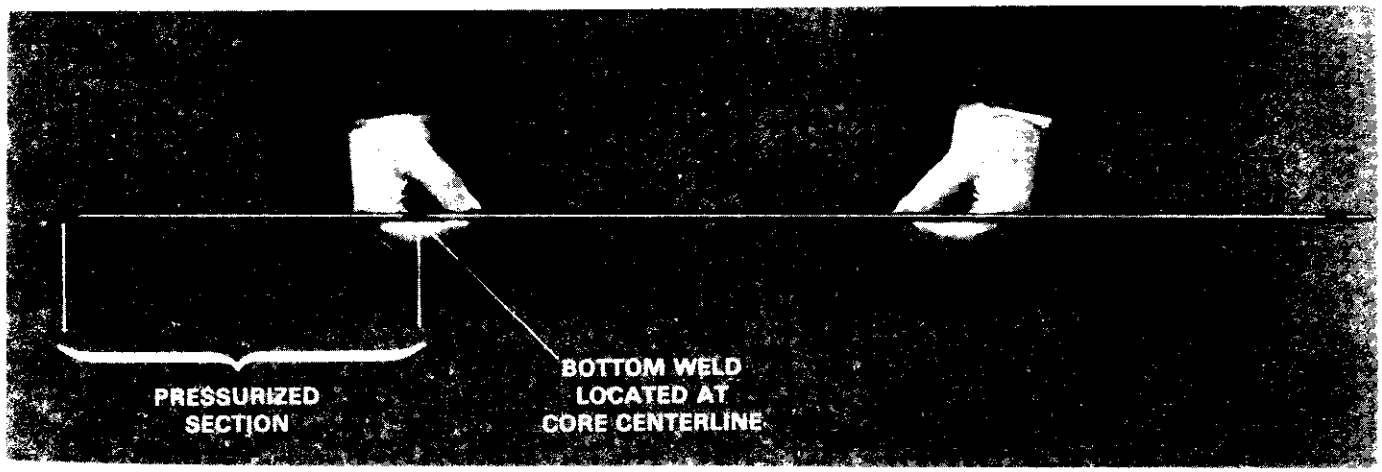

Fig. 1. Picture of creep capsule and typical profilometer traces of stressed and unstressed capsules.

Fig. 3a shows the total diametral strains measured at the position of maximum displacement rate for three high fluence capsules in the Heat Treat D condition. Note that while the transient regime of diametral deformation decreases in duration with increasing stress, the post-transient deformation rate does not appear to change. Even more significantly, the total deformation rate does not exceed the 0.33%/dpa expected from steady-state swelling alone. Instead it appears that the well-known linear stress dependence of creep rate has disappeared somewhere between hoop stress levels of 0 and 100 MPa (15ksi). Based on the current conception of irradiation creep where the largest component of the creep rate is proportional to the swelling rate[4] one would expect at 200 MPa a creep rate at high fluence that approaches the swelling-induced deformation rate. The swelling of these three pins was not measured so we cannot at this time separate the swelling and creep strains.

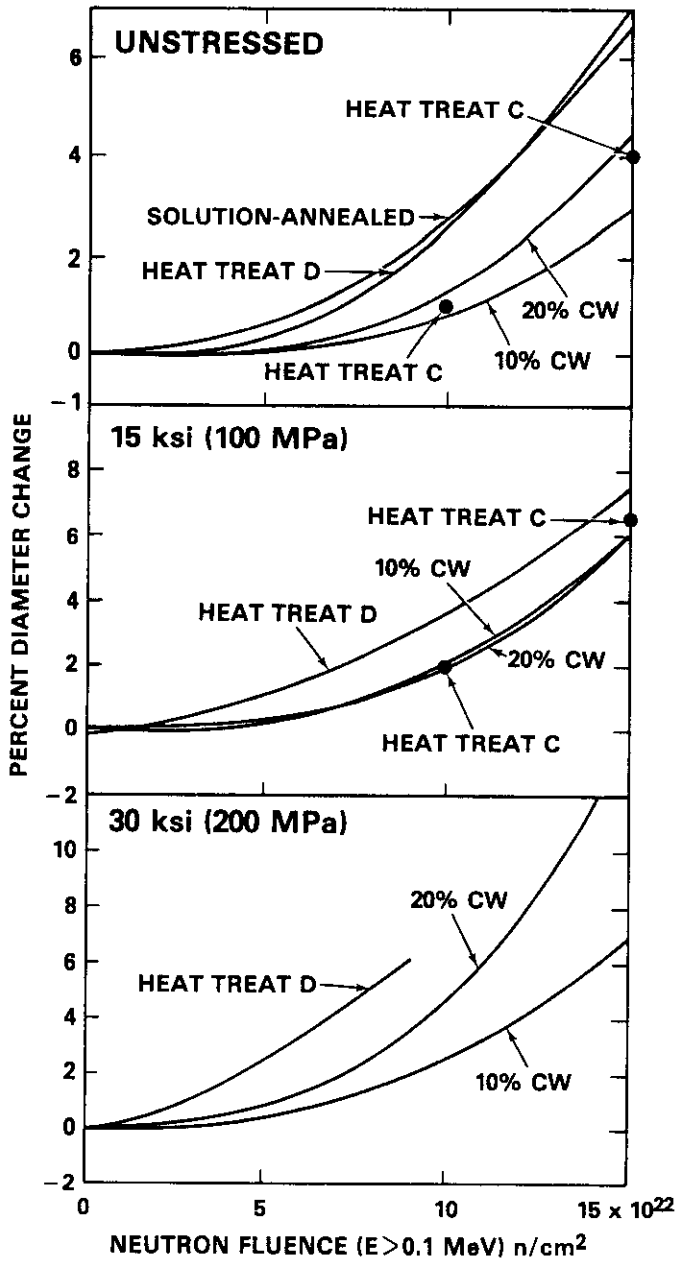

Fig. 2. Typical deformation behavior at core centerline of creep capsules with different stress levels and starting metallurgical conditions.

Fig. 3b shows three pins which were removed from reactor at a lower fluence level when the 200 MPa (30 ksi) pin (designated EA-223) failed. The creep rates for the two pressurized pins were calculated two ways as shown in Fig. 4. First, the swelling-induced change in diameter of the stress-free tube was subtracted from the total diametral change of the pressurized tubes. Note, however, that the total deformation data was taken as a function of time at one position while the swelling-induced deformation data was taken as a function of position, all at one time in-reactor, representing the time of removal of the capsule. This approach assumes that there is no dependence of swelling on displacement rate. In the second calculation, the swelling-induced deformation of the pressurized tube was used, once again assuming that there is no effect of displacement rate. The swelling-induced strain of the pressurized tube is obviously a better choice than that of the unpressurized tube, but as explained previously, such data are very expensive to obtain and are usually not available.

Fig. 4 shows that the inclusion of the stress-affected portion of swelling in the creep rate camouflages a trend toward saturation in the creep rate. While the high fluence portion of these data obviously have no influence of flux differences, one can question whether the low fluence (and therefore low flux) results reflect some interference from flux effects. Since capsule EA-223 failed it was not used to answer this question but we can address it using a pin that did not fail.

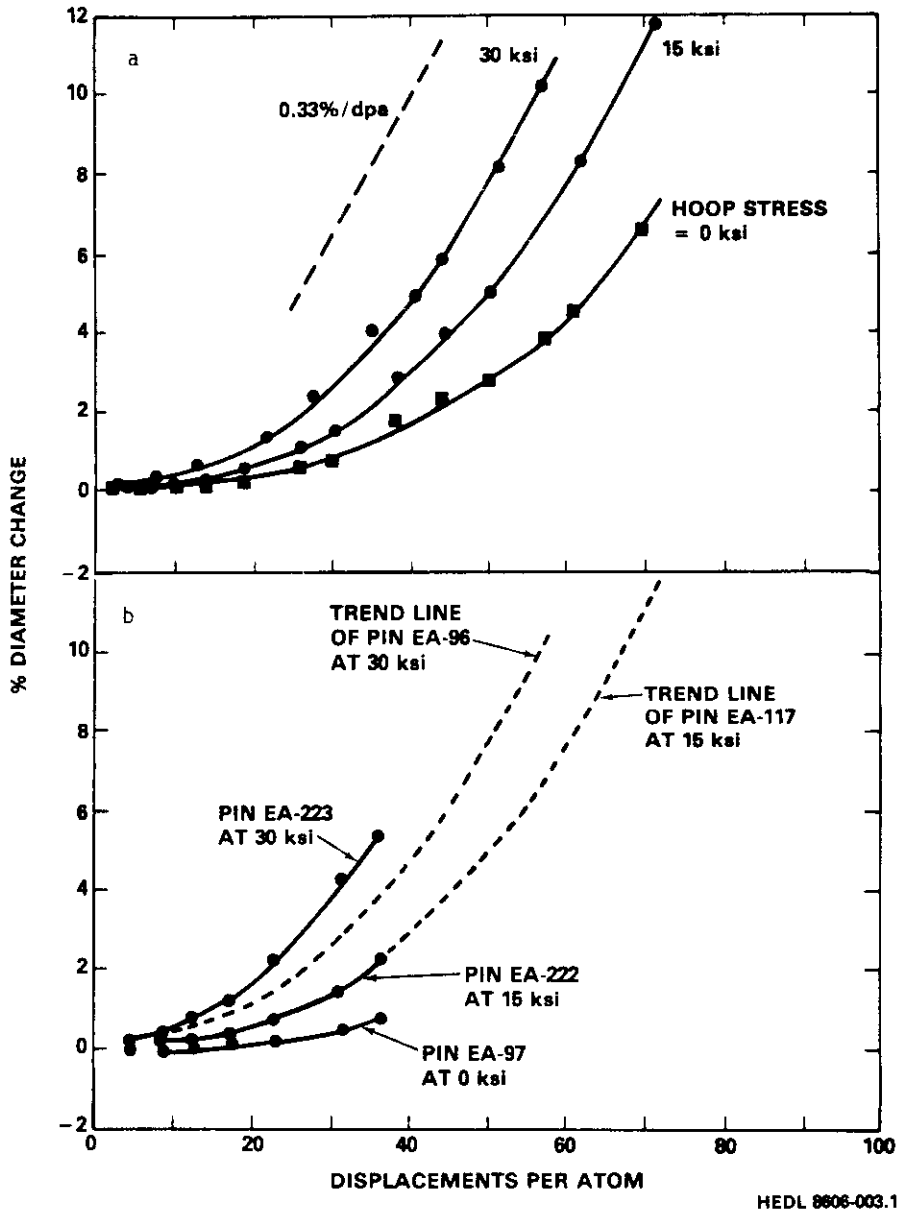

Fig. 3. (a) Diametral strains observed at core centerline position of EBR-II for three creep capsules irradiated at 550°C in the Heat Treat D condition, (b) Comparison of the strains above with those of another set of Heat Treat D capsules removed at lower fluence.

Fig. 5 shows the total deformation measured for another Heat Treat D pin. One trace is that recorded for the core center position as a function of time, the other is that determined as a function of position along the pin upon its removal. There obviously is a small but discernible influence of displacement rate on the total deformation of the Heat Treat D pin at lower flux levels. It is important to note, however, that the trend shown in Fig. 5 would tend to further accentuate the tendency toward saturation when applied to Fig. 4 in that it should steepen the slope of the 15 ksi (100 MPa) curve at lower fluence while not affecting the higher fluence portion of the curve.

We can see the trend toward saturation of the creep rate even more clearly in the data derived from the 20% cold-worked condition. As shown in Fig. 6 there is once again a strain rate that approaches but does not exceed 0.33%/dpa. Capsule EA-38 at 30 ksi (200 MPa) also failed after the last examination shown in Fig. 6 but once again we calculate for the 30 ksi capsule an irradiation creep behavior that exhibits saturation. In this case, however, the actual stress-affected swelling of EA-38 was measured below the region where failure occurred and was included in the calculation of creep rate.

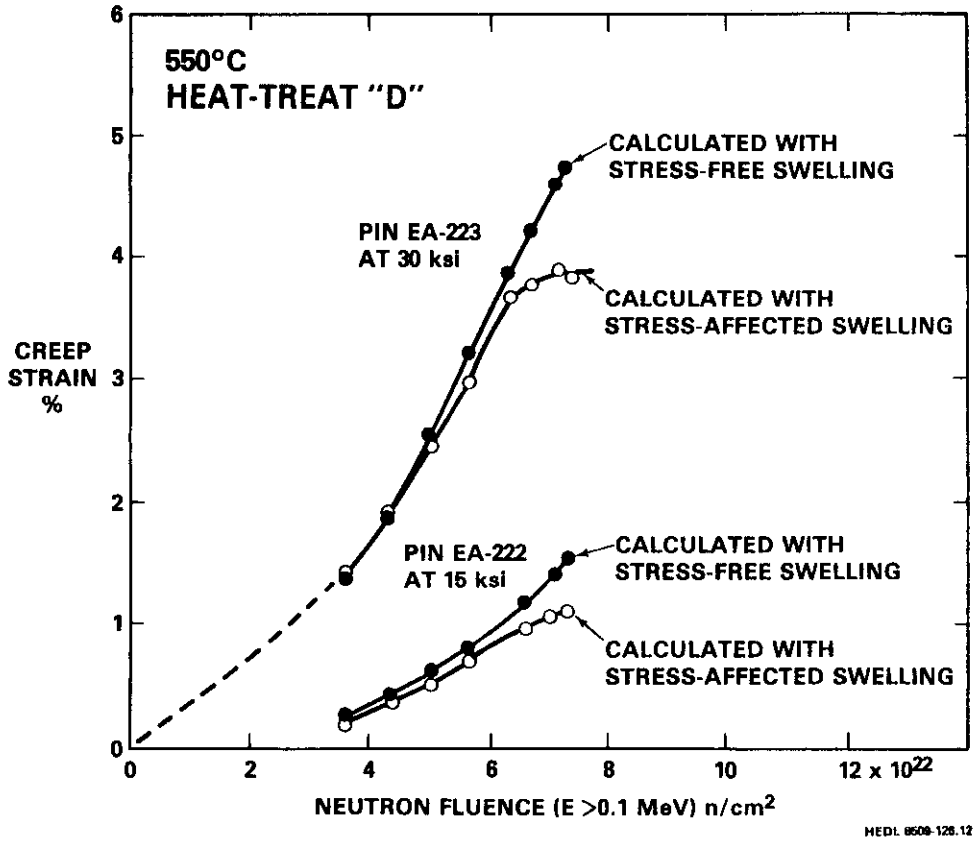

Fig. 4. Calculated creep strains for the two pressurized pins shown in Fig. 3b, showing how the use of stress-free swelling camouflages the onset of the saturation stage of creep.

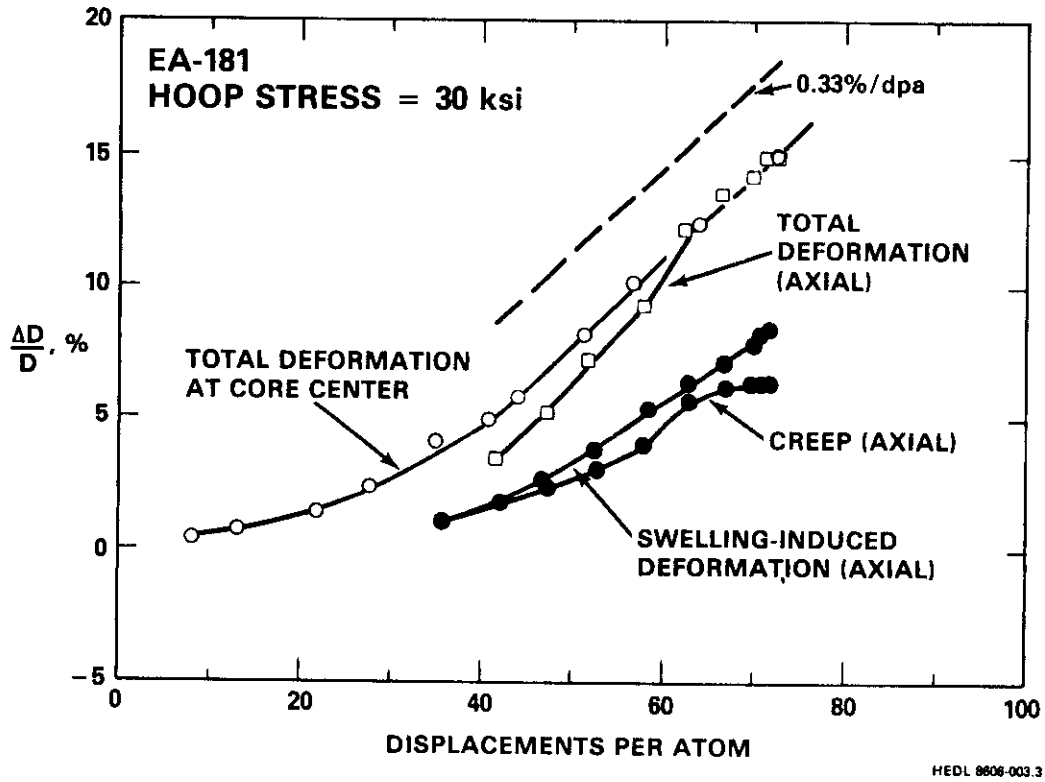

Fig. 5. Analysis of strains of another capsule in the Heat Treat D condition, showing influence of flux effects on analysis, but only at the lower displacement levels.

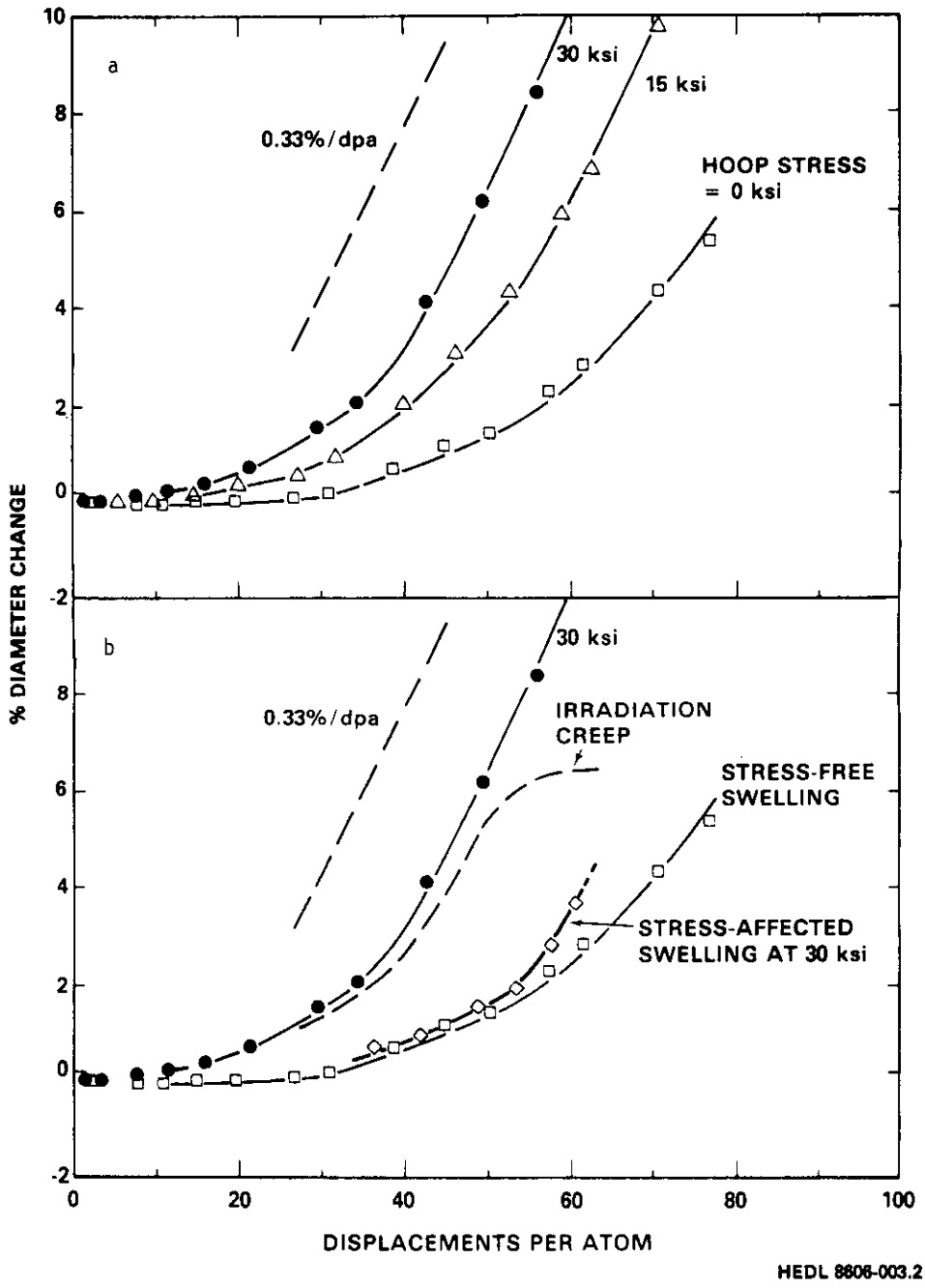

Fig. 6. a) Deformation observed in pressurized tubes of 20% cold-worked AISI 316 irradiated in EBR-II at 550°C. Note that the total strain rate does not exceed 0.33%/dpa, even at very high stress levels. b) Density measurements on the 30 ksi pressurized tube show that stress accelerates the rate of swelling and its approach to 1%/dpa, but also causes the creep rate to approach zero at high swelling levels.

A similar behavior is seen in the Heat Treat C condition at 15 ksi (100 MPa) as shown in Fig. 7b. In the Heat Treat C case the trend toward saturation is not obscured by flux effects. Note that the axial and core center determinations of total deformation are nearly identical, indicating that flux effects do not operate on the Heat Treat C condition.

Fig. 7a shows an apparent flux effect on the stress-free swelling portion of the deformation, however. While the swelling and swelling-induced deformation agree at core center, they do not agree as the dpa level decreases. Note, however, that the difference quickly becomes constant at ~1%. It has earlier been shown that intermetallic phase formation at relatively high temperatures can lead to increases in lattice parameter and an apparent swelling that is on the order of several percent.[9] Most importantly, this volume increase is distributed anisotropically, with the diameter absorbing most of the strain.[9]

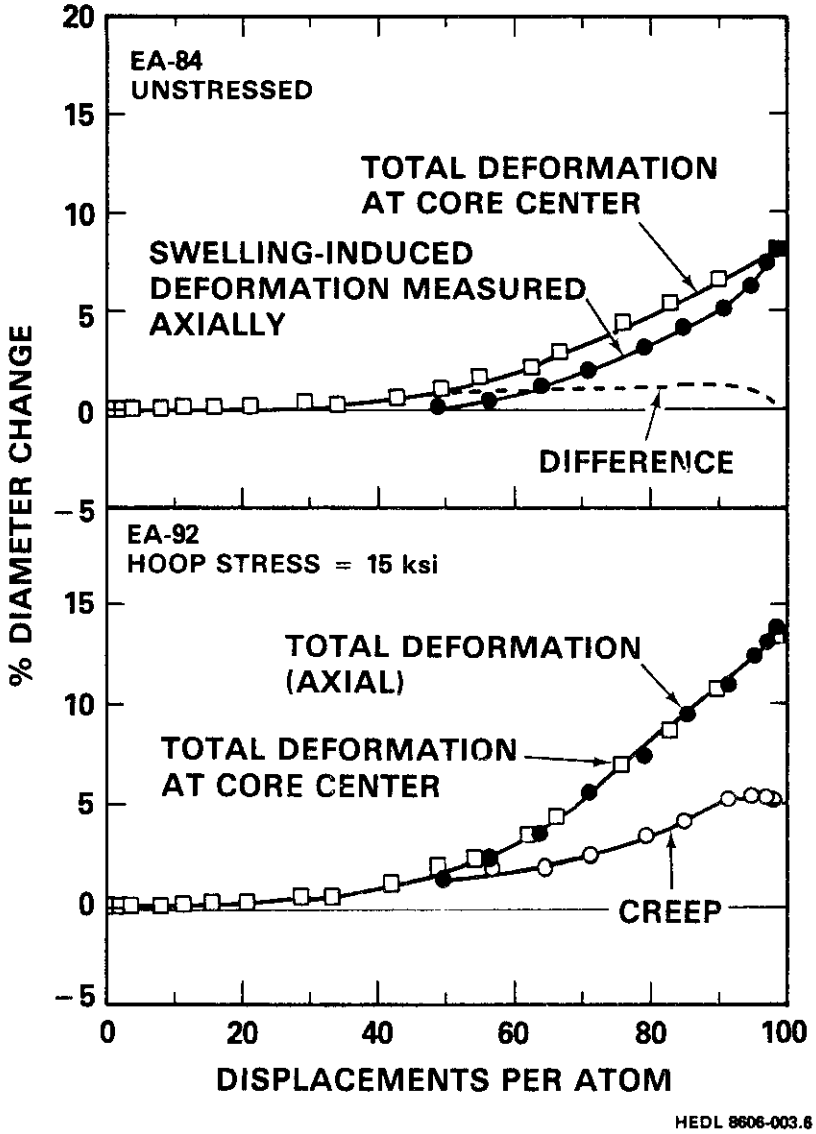

Fig. 7. Analysis of strains developed in capsules constructed of AISI 316 irradiated in the Heat Treat C condition.

The difference seen in Fig. 7a probably represents not only the anisotropy of intermetallic-induced volume changes but also the fact that intermetallic formation requires thousands of hours to occur. At a given low displacement level the axial data represent much longer times than that of the core center data.

The total deformation data for annealed and 10% cold-worked material have been presented in a previous paper[3] and will not be reproduced here. The annealed tubes had all failed in a manner which rendered their stress history to be indeterminate. The 10% cold-worked tubes were not subjected to sufficient tests to separate the creep and swelling components of strain.

Discussion

There are two ways in which to characterize the major findings of this study. One is to assume that the emergence of voids at relatively large volumes is directly responsible for the decline in creep rate. This would be a natural extension of the current creep model which states that the creep rate has a small athermal component unrelated to swelling and a much larger second component which is proportional to swelling.[4] This second component is often interpreted to imply a direct coupling of swelling and creep.

Another interpretation would be that creep and swelling both respond to the same developments in microstructure and microchemistry and therefore are not directly coupled to each other.[4] In this viewpoint creep might respond to late-term changes in microchemistry or microstructure that do not affect

swelling. Post-transient swelling has recently been shown to be a phenomenom which is dictated only by the crystal structure. This occurs after the completion of a transient regime in which only void nucleation has been found to be sensitive to all swelling-relevant variables.[4] Post-transient swelling of fcc metals does not seem to be affected by the softness or hardness of the alloy[2-4] while one would expect the irradiation creep rate to be related to the yield strength of the alloy.[12] The increase in hardness due to swelling at higher levels has been determined,[13] however, and is insufficient in itself to account for the near cessation of creep.

There are other direct-coupled types of mechanisms which might be invoked to partially explain the observed results. First of all, at these swelling levels the overwhelming majority of dislocations terminate at void surfaces, a situation in which the climb rate of dislocations can be strongly affected by pipe diffusion of defects into the voids. This might tend to change the bias of the dislocation network. Second, the glide distance of dislocations will be decreased as the voids become the dominant obstacle. This will make dislocation climb the dominant creep mechanism and reduce the amount of creep that can occur for a given level of irradiation. Third, if the creep process is now restricted primarily to irradiation-induced climb of dislocations, one can envision a situation in which the SIPA creep mechanism[14] may no longer operate effectively. This mechanism requires that the climb of dislocations lying on some planes be enhanced by the applied stress state while other less favorably oriented dislocations are inhibited in their climb rate. In short, this mechanism requires that dislocations lie on different planes and have different Burgers vectors. Gelles and coworkers have recently shown that large applied stresses lead to a strong anisotropy of dislocations such that unfavorably oriented dislocations exist at substantially reduced densities while favorably oriented dislocations increase in density.[15,16] Similar stress-induced anisotropies have been observed in the Frank loop population.[17,18] Hence, the SIPA creep mechanism may not function very effectively after the stress state has substantially altered the dislocation and loop microstructure.

There is one indication in the data presented in this paper that suggests that the near-cessation of creep may be only coincident with large swelling levels and not directly related to void growth. This is the suggestion that intermetallic formation may be occurring and affecting the creep rate, while not affecting the swelling rate. In an earlier paper it was shown that intermetallic formation during thermal annealing of AISI 316[9] leads to an abrupt decrease in the thermal creep rate at 649, 705 and 760°C as shown in Fig. 8. While the thermal creep experiment did not proceed for a sufficient time at 594°C to cause a convincing down-turn in creep rate it is reasonable to assume that longer times might cause a similar effect to occur at 594°C and that the additional influence of irradiation-enhanced diffusion might cause precipitation to occur at the 550°C temperature of this experiment.

Whatever the cause or causes of creep cessation it appears to be a reproducible phenomenon. Attempts to confirm this observation using current short tube experiments were unsuccessful, however. These experiments have diametral deformation rates that have currently reached only ~0.2%/dpa.

Since the diametral creep rate does saturate at approximately one-third of 1%/dpa, the latter being the steady-state swelling rate, this implies that stress-affected swelling itself is isotropic. Increases in volume obviously require dislocation motion but the apparent disappearance of creep implies a greatly reduced mobility of dislocations, or at least a reduction in their ability to sense and react to the stress state. This apparent paradox awaits the acquisition of more data before it can be resolved.

It is difficult to imagine, however, how the applied and swelling-generated stresses are being relieved on a microscopic level when the macroscopic creep rate seems to have disappeared.

CONCLUSIONS

At displacement levels of $\lesssim$50 dpa, the creep rate at 550°C of AISI 316 in a variety of metallurgical starting conditions begins to decline and eventually disappear. Once consequence of this is that the total diametral deformation rate of pressurized tubes cannot exceed that dictated by steady-state swelling (0.33%/dpa). It is not yet clear whether the cessation of creep arises as a direct consequences of large swelling levels or whether other late-term microstructural developments are responsible.

FUTURE WORK

This effort is complete, although the investigation may be reopened when short-tubes from other studies reaches fluence levels that approach those of this study.

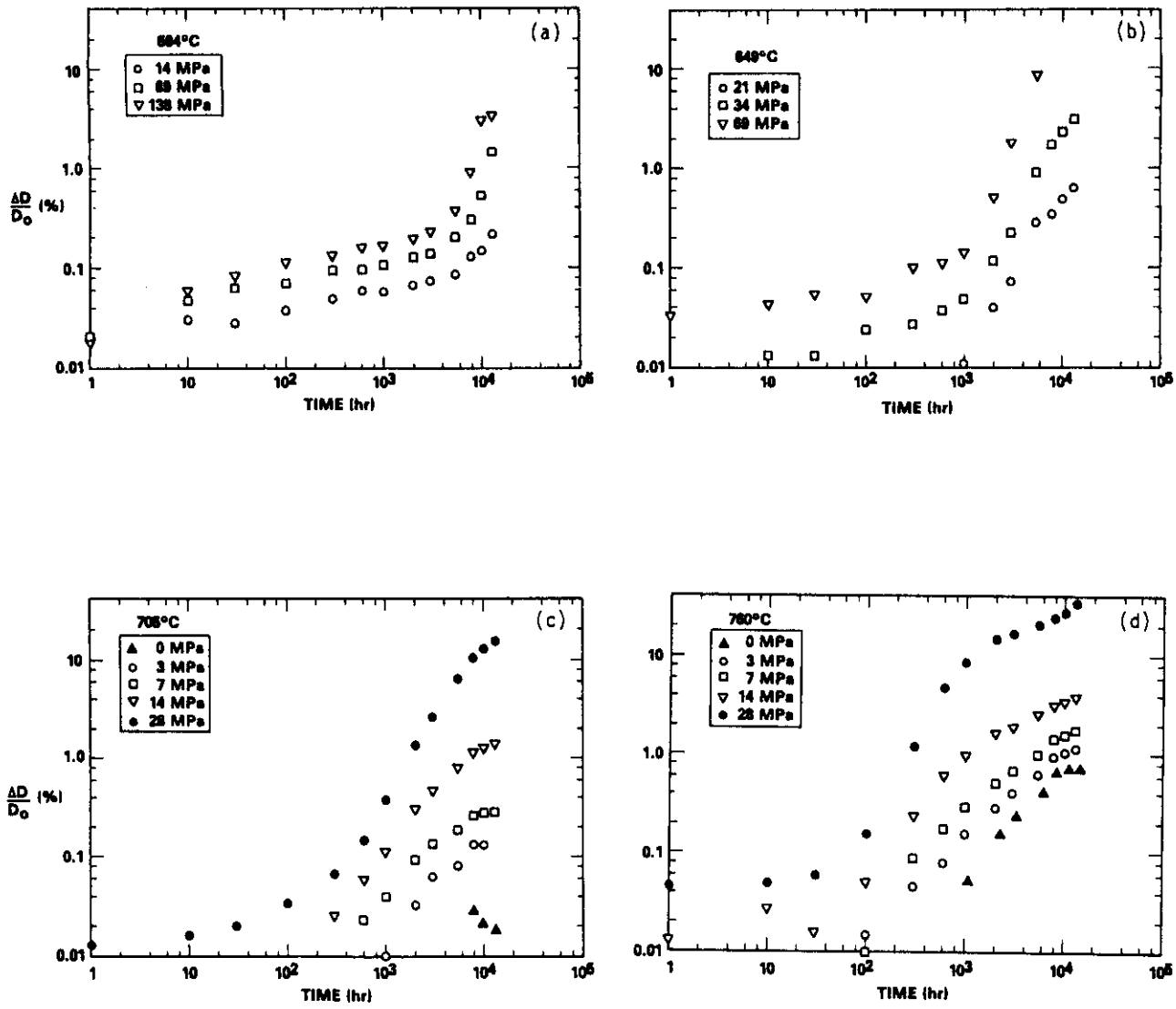

Fig. 8. Thermal creep strains observed in the diameter of gas-pressurized tubes constructed from AISI 316 heat K81581.[9] The stresses shown are midwall hoop stress levels.

REFERENCES

1. B. J. Makenas, pp. 202-11 in Effects of Radiation on Materials: Twelfth International Symposium, ASTM STP 870, F. A. Garner and J. S. Perrin, Eds., 1985.

2. F. A. Garner, H. R. Brager, M. L. Hamilton, R. A. Dodd and D. L. Porter, "New Developments in Irradiation-Induced Microstructural Evolution of Austenitic Alloys and Their Consequences on Mechanical Properties," HEDL-SA-3353, Westinghouse Hanford Company, August 1985, accepted for publication in Radiation Effects.

3. F. A. Garner, D. L. Porter and B. J. Makenas, "A Third Stage of Irradiation Creep Involving Its Cessation at High Neutron Exposures," HEDL-SA-3402, Westinghouse Hanford Company, November 1985, accepted for publication in J. Nucl. Mater.

4. F. A. Garner, J. Nucl. Mater., 122/123, 459-71 (1984).

5. F. A. Garner, E. R. Gilbert and D. L. Porter, pp. 680-97 in Effects of Radiation on Materials: Tenth Conference, ASTM STP 725, D. Kramer, H. R. Brager and J. S. Perrin, Eds., 1981.

6. F. A. Garner, pp. 111-39 in Optimizing Materials for Nuclear Applications, F. A. Garner, D. S. Gelles and F. W. Wiffen, Eds., TMS-AIME, Warrendale, PA, 1985.

7. J. L. Straalsund, pp. 191-207 in Radiation Effects in Breeder Reactor Structural Materials, M. L. Blieberg and J. W. Bennett, Eds., The Metallurgical Society of AIME, New York, NY, 1977.

8. F. A. Garner, W. V. Cummings, J. F. Bates and E. R. Gilbert, "Densification-Induced Strains in 20% Cold Worked 316 Stainless Steel During Neutron Irradiation," HEDL-TME 78-9, Westinghouse Hanford Company, Richland, WA, June 1978.

9. R. J. Puigh, A. J. Lovell and F. A. Garner, J. Nucl. Mater., 122/123, 242-45 (1984).

10. L. C. Walters, G. L. McVay and G. D. Hudman, pp. 277-94 in Radiation Effects in Breeder Reactor Structural Material, M. L. Blieberg and J. W. Bennett, Eds., The Metallurgical Society of AIME, New York, NY, 1977.

11. G. L. McVay, R. E. Einziger, G. L. Hofman and L. C. Walters, J. Nucl. Mater., 78, 201-9 (1978).

12. P. Jung and M. I. Ansari, J. Nucl. Mater., 138, 40-5 (1986).

13. F. A. Garner, M. L. Hamilton, N. F. Panayotou and G. D. Johnson, J. Nucl. Mater., 103/104, 803-8 (1981).

14. W. G. Wolfer, J. Nucl. Mater., 90, 175 (1980).

15. D. S. Gelles, pp. 98-112 in Effects of Radiation on Material: Twelfth International Symposium, ASTM STP 870, F. A. Garner and J. S. Perrin, Eds., 1985.

16. D. S. Gelles, F. A. Garner and B. L. Adams, pp. 81-100 in Damage Analysis and Fundamental Studies Quarterly Progress Report, DOE/ER-0046/11, U.S. Department of Energy, Office of Fusion Energy, August 1982.

17. H. R. Brager, F. A. Garner and G. L. Guthrie, J. Nucl. Mater., 66, 301-321 (1977).

18. D. S. Gelles, F. A. Garner and H. R. Brager, pp. 735-53 in Effects of Radiation on Materials: Tenth Conference, ASTM STP 725, D. Kramer, H. R. Brager and J. S. Perrin, Eds., 1981.

ANALYSIS OF HIGH DOSE SWELLING DATA FROM THE RS-1 EXPERIMENT — R. E. Stoller (Oak Ridge National Laboratory)

OBJECTIVE

The objective of this work is to compile and analyze the available swelling data base for austenitic stainless steels to help provide direction for alloy development and support for theoretical modeling efforts.

SUMMARY

A large amount of swelling data from several irradiation experiments has been entered into a computerized data base to facilitate the analysis of the data. This data includes that from the RS-1 experiment in the EBR-II in which several heats of 20% cold-worked type 316 stainless steel were irradiated to a maximum dose of about 85 dpa in the temperature range of 370 to 600°C. The actual irradiation temperatures in this experiment deviated from the design values by up to 100°C and the present report provides corrected average values. Contrary to some published reports, preliminary analysis of the RS-1 swelling data indicates that a significant temperature dependence of the steady-state swelling rate appears to persist at fairly high swelling levels.

PROGRESS AND STATUS

Introduction

As part of the effort by the U.S. fast breeder and fusion reactor programs to develop structural materials for use in these reactors, a number of irradiation experiments have been carried out to investigate the swelling behavior of austenitic stainless steels. A large amount of this swelling data has been collected and entered into a computerized data base to facilitate its analysis in support of the complementary goals of improving our fundamental understanding of the phenomenon of void swelling and the development of alloys that are swelling resistant. The swelling data from one particularly comprehensive experiment have been analyzed to determine whether or not the steady-state swelling rate exhibits any temperature dependence.

An overview of the swelling behavior of AISI type 316 stainless steel in the RS-1 experiment in the EBR-II has been given by other workers.[1-3] This experiment was designed to irradiate a number of heats of 20% cold-worked type 316 stainless steel to doses up to 85 dpa in the temperature range of 370 to 650°C. These conditions exceeded the requirements of temperature and dose for service as cladding material in the first core of the Fast Flux Test Facility (FFTF). Several of the heats included in the RS-1 experiment were melted and formed in accordance with the specification for FFTF first core cladding.[1] These heats were designated BB, CN-13, CN-17, X and 81615C and will be collectively referred to below as the first core heats. The RS-1 experiment also included several other heats which did not meet first core specifications because of deviations in either composition or fabrication history. When included in the analysis with the first core heats, these heats increased the amount of scatter in the swelling data at any one temperature or fluence condition.

Analysis of the RS-1 Swelling Data

The swelling of the first core heats is shown as a function of irradiation dose in Fig. 1(a) and (b). The irradiation dose in dpa was obtained by multiplying the reported fast fluence by a conversion factor which is dependent upon the neutron flux and hence upon the axial position in the core.[3] This is reflected in different fluence-to-dpa conversion factors for different irradiation temperatures. A typical conversion factor for fast-reactor irradiations is 5 dpa per 10^{26} n/m^2 (E > 0.1 MeV). The actual values in the RS-1 experiment range from 4.6 to 5.2 (ref. 3). In Fig. 1 the data have been shown as three trend bands for the temperature ranges indicated. These temperatures do not correspond to the design temperatures mentioned above since analysis subsequent to the experiment has indicated that the actual irradiation temperatures deviated from the design values.[4] Most earlier analysis of this data has not taken this information into account.[1-3,5,6] Not only were the irradiation temperatures generally lower than the design values, but the deviations from the design temperatures also increased with exposure due to unpredicted declines in the gamma heating.[4] Hence, the experiment was not completely isothermal — the largest decrease was 30°C for the specimens designed to be at 650°C. This is potentially significant to the analysis of these results because of the reported sensitivity of swelling to temperature changes.[2,7,8] The temperatures used in the present work are averages of the recalculated temperatures for the four discharges of the RS-1 experiment. These values are compared to the design values in Table 1. The actual temperatures shown in Table 1 reflect a significant compression of the temperature range when compared to the design values.

The data in Fig. 1 show the typical, approximately bilinear swelling behavior. There is a temperature-dependent incubation time followed by a transition to "steady state" swelling. The width of the data band is not solely due to the range of temperatures. The representative data points at each of the three temperatures in Fig. 1(b) give an indication of the scatter at any one temperature. In addition, there are

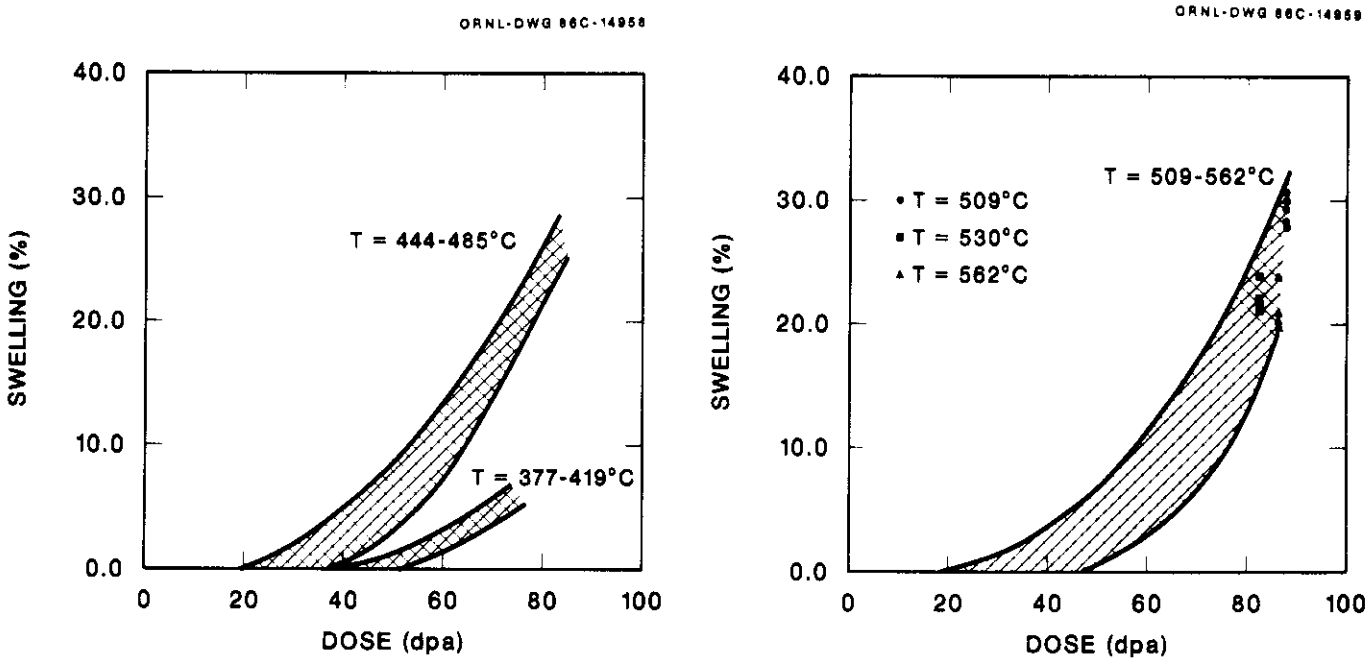

Fig. 1. Fluence dependence of swelling of 20% cold-worked type 316 stainless steel in three temperature ranges. FFTF first core heats from the RS-1 experiment. Data from Bates and Korenko, ref. 1, Yang and Garner, ref. 2, and Garner, ref. 3.

Table 1. Revised average and design irradiation temperatures in the RS-1 experiment

Temperature, °C	
Average Actual	Design
377	370
396	400
419	433
444	467
465	500
485	533
509	567
530	600
562	650

heat-to-heat variations in swelling. This is illustrated by comparing Fig. 1 with Fig. 2, where all of the U.S. heats of 20%-cold-worked 316 stainless steel from the RS-1 experiment have been included. In the latter figure, the scatter in the data at 80 dpa has almost doubled.

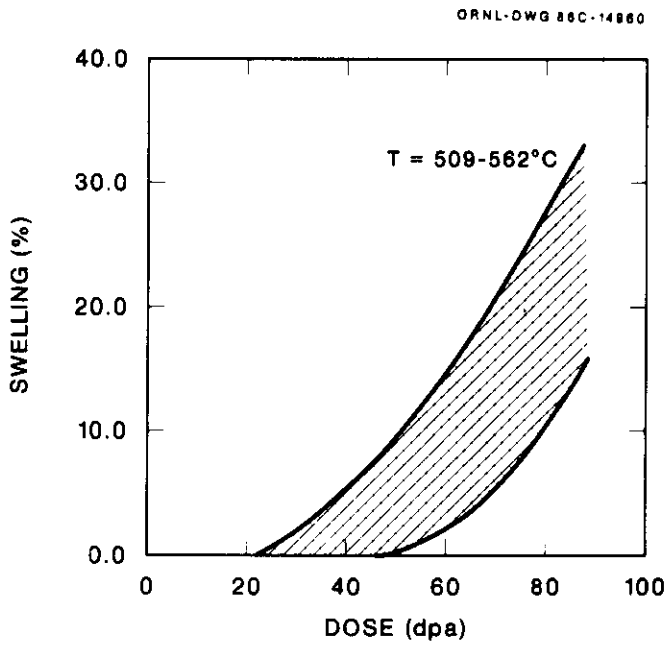

Fig. 2. Fluence dependence of swelling at 509 to 562°C for all U.S. heats in the RS-1 experiment. Data from Bates and Korenko, ref. 1, Yang and Garner, ref. 2, and Garner, ref. 3.

From an engineering standpoint, data such as shown in Figs. 1 and 2 can be useful in spite of the scatter. For any reactor design, it is unlikely that the actual operating temperature of a component will be known with much greater certainty than the temperature ranges shown in these figures, and some temperature fluctuations may be anticipated. One can make conservative use of such data by using the upper bound of the data trend curves. It is more difficult to use these data for fundamental studies of the behavior of fast-neutron-irradiated materials. Nonetheless, in a sufficiently large data base, valid trends may be observed.

An attempt has been made to determine the temperature dependence of the swelling rate in the materials irradiated in the RS-1 experiment. Garner has pointed out the hazard of looking at the swelling rate when the irradiation dose is too low.[3,9] The approach here was to calculate the swelling rate assuming linear swelling between the values measured at the two highest doses. This dose increment was 50 to 59 dpa at 396°C, 62 to 72 dpa at 419°C, 51 to 60 dpa at 445°C, 69 to 82 dpa at 466°C, 62 to 74 dpa at 485°C, 74 to 87 dpa at 509°C, 70 to 81 dpa at 530°C, and 73 to 85 dpa at 562°C. Reference to Fig. 1 indicates that, except for the lowest temperatures, such swelling measurements would be well beyond the incubation and transition regimes.

The average linear swelling rate has been plotted as a function of swelling in Fig. 3. The swelling values on the abscissa of Fig. 3 are the average of the two values over which the swelling rate was calculated. Figure 3(a) shows all the data broken into two rough temperature bands with most of the data approaching a value of about 0.8%/dpa at the highest swellings. The trend with swelling is more clear in Fig. 3(b) where only the lowest four temperatures are plotted. Here the influence of the transition regime is clearly seen at the lowest swellings, as Garner indicated. No clear influence of temperature can be determined for these four temperatures at these low doses.

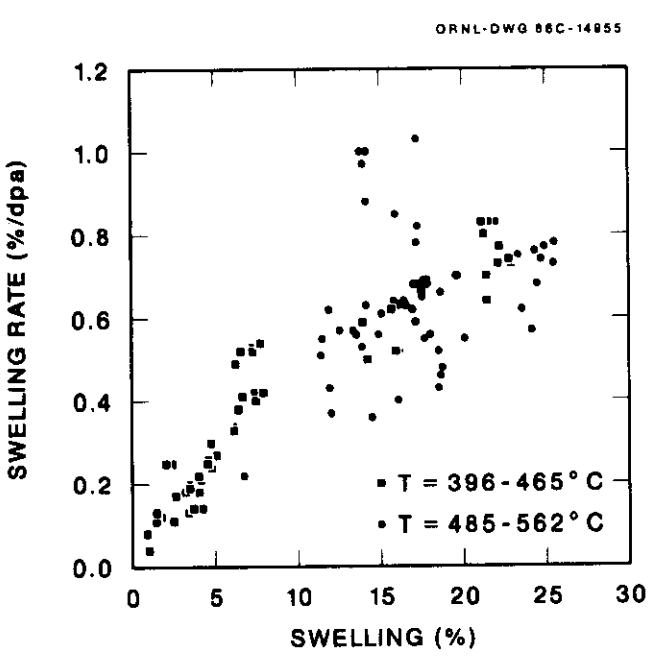

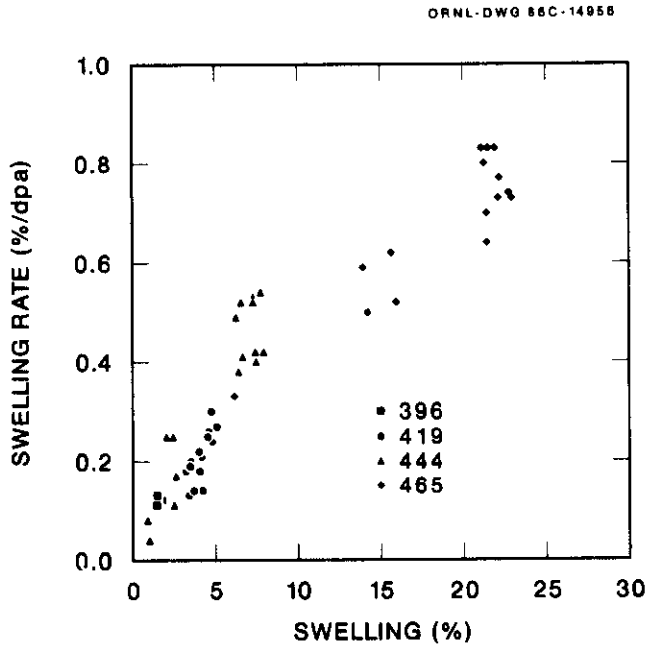

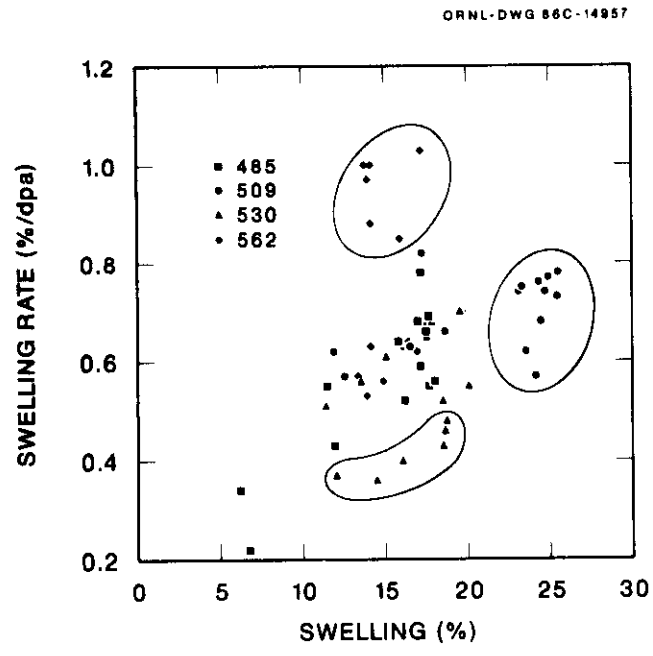

Fig. 3. Swelling rate as a function of swelling for the indicated temperatures. Data from Bates and Korenko, ref. 1, Yang and Garner, ref. 2, and Garner, ref. 3.

However, Fig. 3(c) indicates that there may be some temperature dependence at the higher temperatures. This figure shows a region of considerable data scatter around 0.6%/dpa for all four temperatures. This scatter is to be expected given the scatter in the swelling data in Figs. 1 and 2. However, there is also a clear separation of three groups of data at 509, 530 and 562°C. Data are available over the largest dose range at 509°C and the calculated swelling rates indicate that at this temperature the swelling rate is fairly constant between swellings of 12 and 25%. This supports the assumption that the calculated swelling rate of ~0.7%/dpa at 25% swelling represents a steady-state value. Therefore, the data at 562°C is particularly significant because the swelling rate is almost a factor of 2 greater than at 530°C at the same swelling and 50% higher than the 509°C data which is at an even higher swelling. Heat-to-heat variations cannot be responsible for this grouping because each temperature set has all five first-core heats included. The observed scatter at the three highest temperatures in Fig. 3(c) do reflect specimen-to-specimen variations at any one dose and temperature condition. These variations have been neglected in the data which were highlighted. Examining all the data indicates some overlap of the calculated swelling rates at the extremes, but this does not alter the conclusion of an apparent marked temperature dependence.

CONCLUSIONS

Garner and Wolfer[10] have used a simple rate theory expression for the steady-state swelling rate to show that for specific values of the vacancy migration energy and the total system sink strength this rate is essentially temperature independent. Specifically, they note that a vacancy migration energy (E_v^m) on the order of 1.1 eV and a sink strength greater than about 5×10^{14} m^{-2} is required. They cite[11,12] recent measurements of the vacancy formation energy in pure nickel to suggest that such a low value of the vacancy migration energy is appropriate for austenitic stainless steel. However, recent measurements of E_v^m in both high-purity austenitic Fe-Cr-Ni alloys and in type 316 stainless steel indicate that E_v^m = 1.3 to 1.4 eV.[13,14] Garner and Wolfer's results for E_v^m = 1.3 eV predict that the swelling rate would be somewhat temperature dependent even with a temperature-independent total system sink strength of 5×10^{14} m^{-2}. In addition, the sink strength would exhibit a fairly strong temperature dependence above about 600°C and the value of 5×10^{14} m^{-2} would be too high. The importance of using appropriate temperature dependent sink strengths in the rate theory has been pointed out elsewhere. Using values for the material and microstructural parameters characteristic of fast-neutron-irradiated austenitic stainless steel, the results of the simple theory[10] would be in agreement with the present analysis of the RS-1 data. A more comprehensive microstructural model[15] also predicts that the peak swelling rate would exhibit such temperature dependence.

The contention that the steady-state swelling rate is independent of temperature has been advanced by Garner and coworkers.[2,3,10] The present analysis of the RS-1 irradiation experiment does not support this interpretation of the data. Certainly this analysis was simple, but it was consistently applied at all temperatures so that any errors should be systematic. Other factors may be affecting the swelling at 562°C; for example, the 30°C temperature decrease which these specimens experienced in the course of the experiment. But the fairly large variations in the swelling rate observed for swellings between 15 and 25% swelling indicate that the temperature dependence of the swelling rate does persist until quite high doses. The degree to which the swelling rate will remain dependent on temperature at higher doses cannot be determined from this data set. Only the data at 509°C is extensive enough to verify that the material is exhibiting linear swelling behavior. The fact that the swelling rate at 562°C is a third greater at a similar fluence and at a lower swelling suggests that some temperature dependence is likely to persist.

FUTURE WORK

This work will continue as more data are entered into the data base and further analysis will be carried out in support of the objectives stated above. The swelling data from the MFE-IV spectral tailoring experiment will be included to permit a comparison of the swelling behavior of similar heats of austenitic stainless steel when they are exposed at different He/dpa ratios.

REFERENCES

1. J. F. Bates and M. K. Korenko, Nucl. Tech. 48 (1980) 303–314.

2. W.J.S. Yang and F. A. Garner, pp. 186–206 in "Effects of Radiation on Materials: Eleventh Conf.," ASTM STP 782, ASTM, Philadelphia, 1982.

3. F. A. Garner, pp. 111–139 in "Optimizing Materials for Nuclear Applications," AIME Symp. Proc., AIME, New York, 1984.

4. R. W. Clark, Dimensional Change Correlations for 20% Cold-Worked AISI 316 Stainless Steel for Fusion Applications, Master's Degree Thesis, University of Missouri, Rolla, 1985.

5. P. J. Maziasz, J. Nucl. Mater. 122&123 (1984) 472 486.

6. B. J. Makenas, J. F. Bates and J. W. Yost, pp. 17–29 in "Effects of Radiation on Materials: Eleventh Conf.," ASTM STP 782, ASTM, Philadelphia, 1982.

7. J. F. Bates and D. S. Gelles, J. Nucl. Mater. 71 (1978) 365–367.

8. J. F. Bates, J. Nucl. Mater. 98 (1981) 71–85.

9. F. A. Garner, H. R. Brager and R. J. Puigh, J. Nucl. Mater. 133&134 (1985) 535 539.

10. F. A. Garner and W. G. Wolfer, J. Nucl. Mater. 122&123 (1984) pp. 201–206.

11. S. K. Khanna and S. Sonnenberg, Rad. Effects 59 (1981) 91–92.

12. L. C. Smedskjaer, M. J. Fluss, D. G. Legnini, M. K. Chason and R. W. Seigel, J. Phys. F: Metal Phys. 11 (1981) 2221 2230.

13. O. Dimitrov and C. Dimitrov, J. Nucl. Mater. 105 (1982) 39–47.

14. A.O.O. Mekhrabov, E. Sato, M. Shimotomai, M. Doyama, T. Iwata, and T. Kawanishi, J. Nucl. Mater. 133&134 (1985) 549–552.

15. R. E. Stoller and G. R. Odette, "A Composite Model of Microstructural Evolution in Austenitic Stainless Steel Under Fast Neutron Irradiation", presented at the Thirteenth International Symposium on the Effects of Radiation on Materials, June 23-25, 1986, Seattle, WA, to be published by ASTM.

SPINODAL-LIKE DECOMPOSITION OF Fe-Ni AND Fe-Ni-Cr INVAR ALLOYS IN BOTH RADIATION AND NON-RADIATION ENVIRONMENTS - F. A. Garner and J. M. McCarthy (Westinghouse Hanford Company), R. A. Dodd (University of Wisconsin), and K. C. Russell (Massachusetts Institute of Technology)

OBJECTIVE

The objectives of this effort are to determine the mechanisms by which alloys evolve during irradiation and to use this information to develop a low swelling austenitic alloy in the invar compositional range.

SUMMARY

The radiation-induced development of spinodal-like compositional fluctuations in Fe-Ni-Cr invar alloys leads to several fortuitous methods of visualizing the three-dimensional nature of the decomposition process. In low dose neutron-irradiated Fe-Ni-Cr specimens, the use of high electropolishing rates during preparation of microscopy foils leads to a preferential attack of those regions which are low in nickel. In high dose ion-bombarded specimens of Fe-35Ni, the absence of chromium leads to formation of cellular martensite in the nickel-poor regions upon cooling to room temperature.

The scale of the fluctuations at temperatures >600°C is comparable to that found in the Santa Catharina meteorite, which is roughly Fe-35%Ni in composition. This and other non-radiation data support the proposal that the Fe-Ni system in the absence of irradiation tends to spinodally decompose in the invar regime but at a very sluggish rate. Thus it appears that radiation accelerates rather than induces the decomposition of Fe-Ni and Fe-Ni-Cr invar alloys.

PROGRESS AND STATUS

Introduction

In recent reports it has been shown that Fe-Ni-Cr alloys in the invar compositional range (30-40% nickel) decompose in a spinodal-like manner above ~500°C when irradiated with either neutrons or Ni^+ ions.[1-5] The nature of the compositional fluctuations can be assessed in terms of their impact on mechanical properties or by the use of EDX micro-analysis. The fluctuations cannot be observed directly by electron microscopy since Fe, Cr, and Ni are indistinguishable using conventional diffraction or absorption contrast.

An opportunity to image these fluctuations on a global scale was shown to arise in an earlier report[5] when Fe-35Ni irradiated at 625°C to 117 dpa with 5 MeV Ni^+ ions developed cellular martensite in the nickel-poor regions upon cooling. Since increases in nickel or additions of chromium both raise the M_s temperature, it was not surprising to find the absence of martensite in irradiated Fe-45Ni, Fe-7Cr-XNi, or Fe-15Cr-XNi where X = 30, 35, 40.

A preliminary survey of Fe-35Ni specimens irradiated at 675 and 725°C did find martensite formation, however.[5] This report details the further examination of these two specimens as well as the examination of several neutron-irradiated specimens.

Ion-irradiated specimens

Since earlier studies[1-3] have shown that the average wavelength of the compositional fluctuations tends to increase with temperature, the martensitic regions of Fe-35Ni irradiated to 675 and 725°C were compared to those produced at 625°C. As shown in Fig. 1, both the size and spacing of the martensitic domains increase with temperature between 625 and 675°C. While the micrographs shown in Fig. 1 are representative of the entire foil, the microstructure of the specimen irradiated at 725°C is much more heterogeneous, with typical micrographs shown in Figs. 2-4.

Even more importantly, the martensitic regions of Fig. 2 were found to average ~21% nickel, and the non-martensitic regions were measured at ~33% nickel. This leads to the conclusion that the average local nickel concentration has dropped well below the 35% level of the original homogeneous alloy. At 625°C the average postirradiation nickel level was found to be 32-34%.[2,5]

The increasing level of heterogeneity and decreasing average nickel content signal that another process is superimposed on the spinodal-like decomposition and subsequent formation of cellular martensite. Figure 5 shows that although the ion irradiations proceeded entirely within the austenite regime, the spinodal-like decomposition causes some microvolumes of material to fall under the M_s line upon cooling to room temperature. The martensitic transformation may also be assisted by the internal stresses inherent in ion-bombarded foils[6] and their relief when the constrained low-nickel volumes find themselves near the as-polished surface of the thin foil.

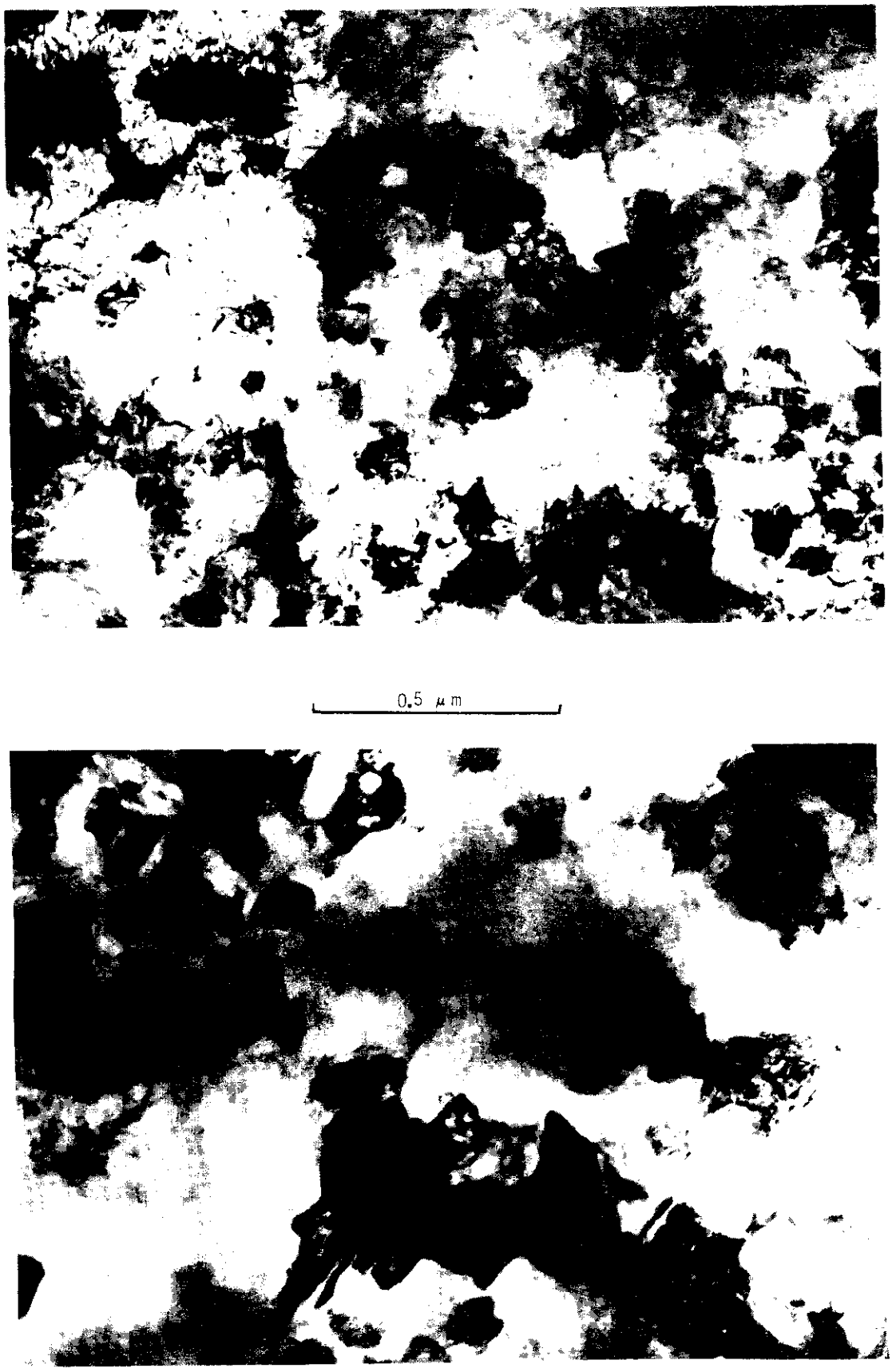

Fig. 1. Cellular martensite formed in Fe-35Ni after 5 MeV Ni^+ bombardment to 117 dpa. The upper micrograph is taken from the 625°C irradiation and the lower micrograph from the 675°C irradiation.

Fig. 2. Micrograph showing relatively small martensitic cells produced in one area of Fe-35Ni irradiated at 725°C to 117 dpa with 5 MeV Ni^+ ions.

Fig. 3. Another area of the Fe-35Ni specimen shown in Fig. 2, with much larger martensite domains and a larger local fraction of martensite.

Fig. 4. Another illustration of the non-uniformity of martensite formation after irradiation of Fe-35Ni at 725°C with nickel ions. Note the unusual distorted internal appearance of the martensite and the high density of small loops formed in the retained austenite matrix.

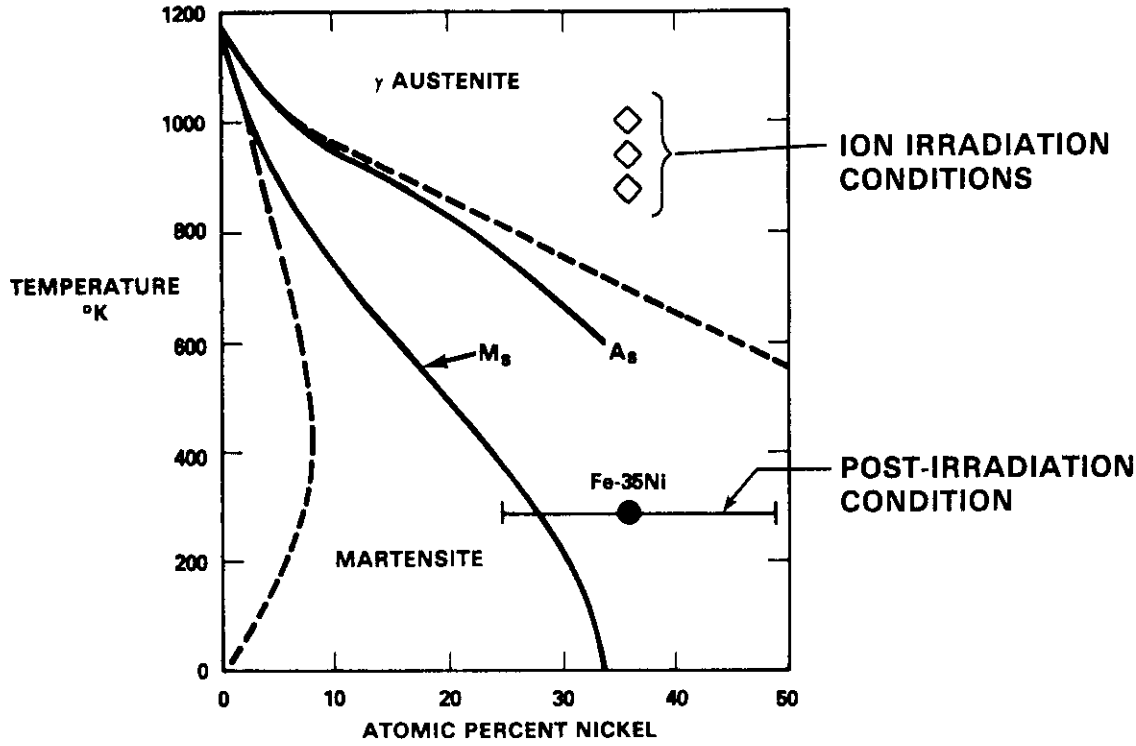

Fig. 5. Schematic diagram showing both the initial irradiation conditions and the final state of ion-irradiated Fe-35Ni after decomposing in a spinodal-like manner toward Fe-25Ni and Fe-50Ni. This diagram does not include the shift of the mean composition to lower nickel content that was observed at the higher irradiation temperatures.

This scenario assumes that during irradiation the average composition of the alloy does not change in the volume to be examined. It is known, however, that nickel flows down displacement gradients and also accumulates at the specimen surface via the inverse-Kirkendall effect and possibly as a result of nickel-interstitial binding.[7-9]

There are several consequences of the out-migration of nickel from the volume examined in this study. First, the higher nickel levels produced outside the peak damage region (especially near the front surface) lead to earlier swelling than in the peak damage region and to a very unusual swelling vs. depth profile, as shown in Fig. 6 for an ion irradiation of Fe-35Ni-15Cr. Second, the composition of the peak damage region of the foil has moved toward the M_S line, predisposing that volume to martensitic transformation even before the spinodal-like decomposition begins. Given the nature of the inverse-Kirkendall effect and its dependence on temperature, it is not surprising that the degree of out-migration of nickel will increase with increasing temperature. Unfortunately, this phenomenon interferes with our efforts to determine the upper limit of the temperature regime of the spinodal-like decomposition.

Neutron-irradiated specimens

During neutron irradiation of typical TEM disks, there are no significant gradients in temperature or displacement rate, and the influence of grain boundaries and surfaces is very small. Therefore, one would expect to see the martensite transformation without the complication of changes in average composition. Unfortunately, this promise has not been realized to date due to the unavailability of Fe-35Ni alloys at high dose and high temperature, although this problem is now being resolved.[10] The few chromium-free specimens that are currently available exist at much lower doses (12-15 dpa) than available for the ion studies (>100 dpa) and also exist only for temperatures ≤600°C. Therefore, it is not surprising that martensitic transformations have yet to be observed in neutron-irradiated specimens. Another fortuitous development allows us to visualize the compositional fluctuations at these lower temperatures and doses, however, even in the presence of chromium.

Two methods of specimen preparation have been employed in this study. One involves a low temperature electropolish using dry ice to cool the electrolyte and to produce a more uniform polish. Another method involves the use of an electrolyte maintained at room temperature which produces a faster and sometimes less uniform foil. As shown in Figs. 7 and 8, this faster polishing condition leads to a highly irregular

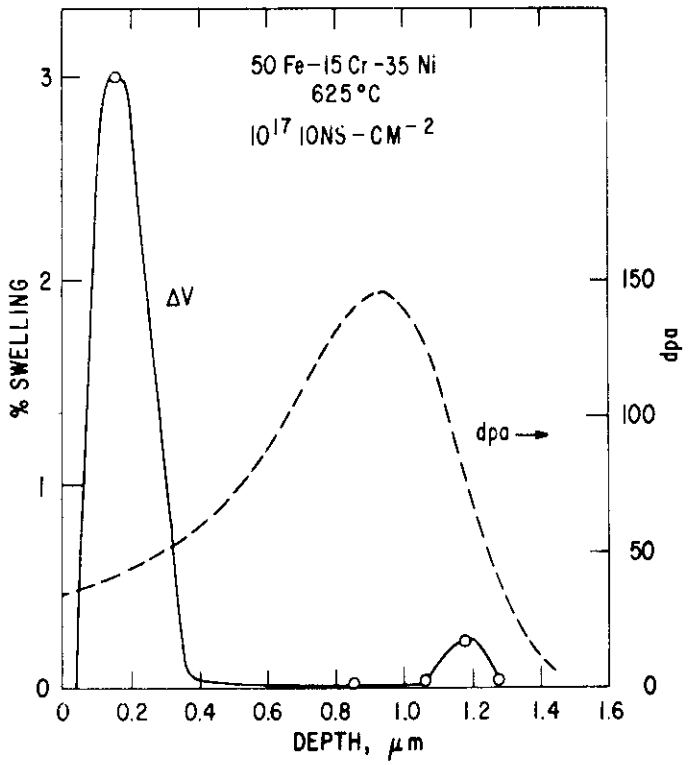

Fig. 6. Swelling profile for Fe-15Cr-35Ni after irradiation with 5 MeV Ni^+ ions, as published in Ref. 19. The displacement profile is shown for comparison.

foil surface in Fe-7.5Cr-35.5Ni irradiated to 12.5 dpa in FFTF-MOTA at 550°C. The foil exhibits thickness variations that appear to be uniformly spaced along crystallographic directions. At the edge of the foil this leads to very irregular boundaries. EDX analysis shows that the low nickel areas are being preferentially attacked by the electropolishing. One consequence of this selectivity is that grain boundaries are preserved due to their tendency to segregate nickel via the inverse-Kirkendall effect. Often these grain boundaries are found to extend far beyond the edge of the foil.

When there is no chromium in the alloy the preferential attack becomes even more pronounced, leading to perforation and tunneling of the electrolyte through the foil, as shown in Figs. 9 and 10 for Fe-35Ni irradiated to 14 dpa at 520°C in EBR-II. Figure 10 illustrates the crystallographic regularity of the spinodal-like process in several grains and also illustrates the resistance to electropolishing of the nickel-rich grain boundaries that separate the grains. Note in Figs. 7-10 that the mean distance between low nickel regions is smaller than that seen in Fig. 1, reflecting the lower irradiation temperature. As noted earlier,[3] the wavelength does not appear to be very sensitive to displacement rate, which varies four orders of magnitude between the neutron and ion irradiations.

Nature of the decomposition process

The relative insensitivity of the wavelength to displacement rate suggests that radiation-induced segregation is not the sole cause of the decomposition and that the Fe-Ni system may have a tendency toward spinodal decomposition. Based on studies of magnetic behavior, elastic moduli, thermoelectric power and interdiffusion coefficients of Fe-Ni alloys,[11-14] Tanji and co-workers have stated that there is cause to suspect that a very sluggish spinodal decomposition occurs in the absence of radiation, with a critical temperature of ~1000°C at Fe-35Ni.

The best test of Tanji's proposal would be to compare the fluctuations developed during irradiation with those produced by long-term thermal aging. Unfortunately, the Fe-Ni system is so sluggish in its diffusion that hundreds or thousands of years would be required for the thermal aging in order to reproduce the total amount of diffusion that occurs during irradiation at 500-650°C. There is another way to approach this problem, however, using Fe-Ni alloys subjected to millions of years of slow cooling in the cores of meteorites.

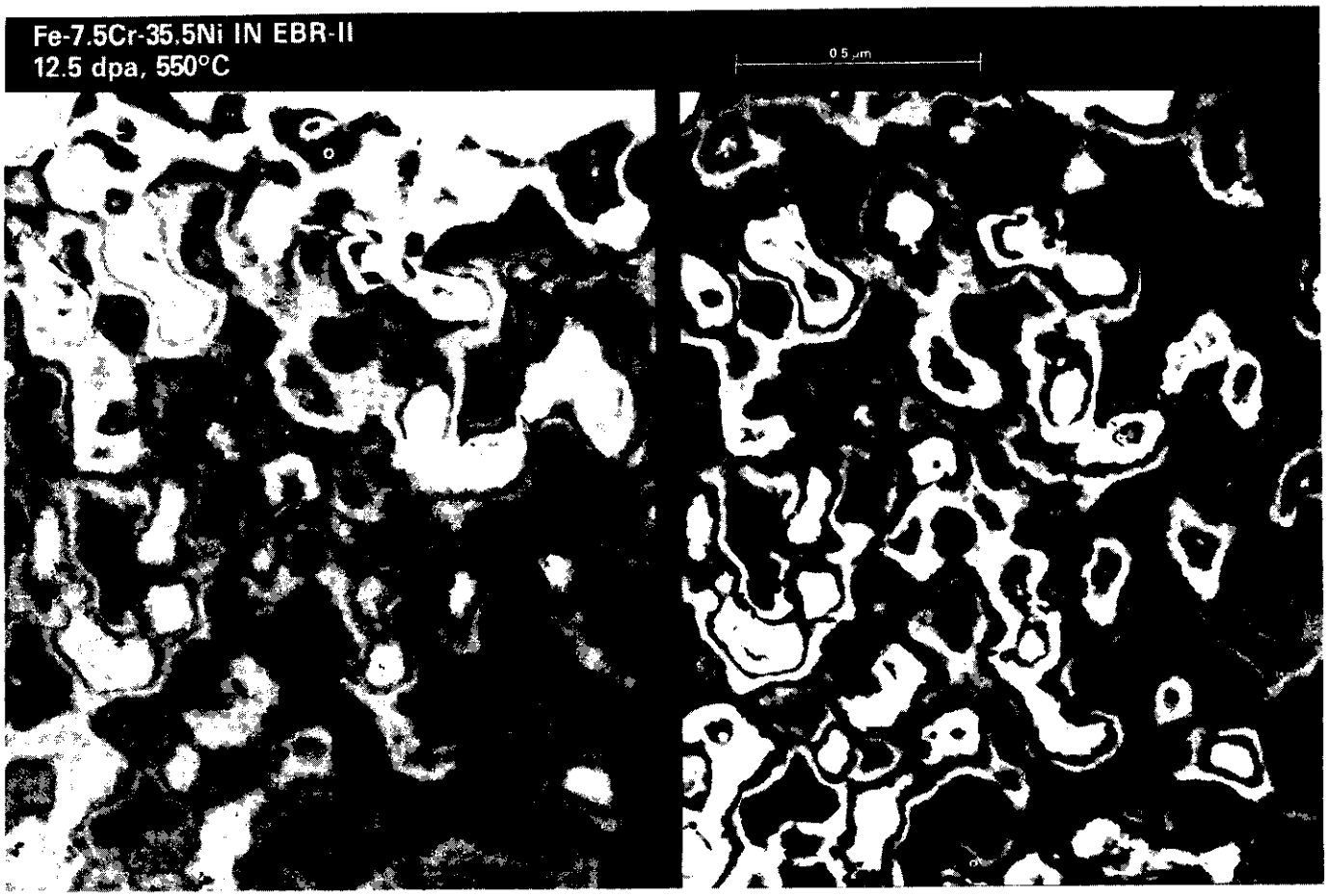

Fig. 7. Thickness differences near the edge of an electropolished foil of Fe-7.5Cr-35.5Ni irradiated in EBR-II to 12.5 dpa at 550°C. The micrograph on the left employs diffraction contrast to image the Frank loops and dislocations and interference thickness contours to image the variations in thickness. The micrograph on the right employs a stronger interference condition in order to maximize the contrast.

The Santa Catharina meteorite has been exhaustively studied since its finding in 1875, having an average composition of Fe-35Ni-0.2P and a possible original mass of 25,000 Kg.[15] In more recent studies,[16,17] Mossbauer and electron microprobe techniques on the non-weathered portion of the meteorite have been used to show that on the average 50% of the meteorite is ordered FeNi (50-51 wt.% Ni) with a size and spacing on the micron scale. These ordered domains are embedded in a matrix of ~27 wt.% nickel. This corresponds closely to the compositional boundaries of Fe_3Ni and FeNi observed in the ion and neutron-irradiated specimens.

The investigators of the meteorite note that the microstructure is consistent with that of a late stage of spinodal decomposition, exhibiting a modulated microstructure along well-defined crystallographic directions.[17] Figures 11 and 12 show some of the spinodal-like features observed in this meteorite.

Large meteorites cool at very slow rates, ~1°C per million years.[18] This would allow sufficient time for large wavelength decomposition and aging of the spinodal at temperatures in the range 500-1000°C and also for the even slower reaction required to produce the ordered FeNi, whose critical ordering temperature is 320°C. Therefore, it appears plausible that Fe-Ni alloys in the invar compositional regime have a tendency toward spinodal decomposition that is accelerated by irradiation. In addition, the decomposition may be further accelerated at lower temperatures by radiation-induced segregation of nickel at Frank loops which form at high densities at lower temperatures. Some of these loops are visible in Fig. 7. At higher neutron irradiation temperatures, however, there did not appear to be loops or other microstructural sinks which could serve as segregation sites.[3]

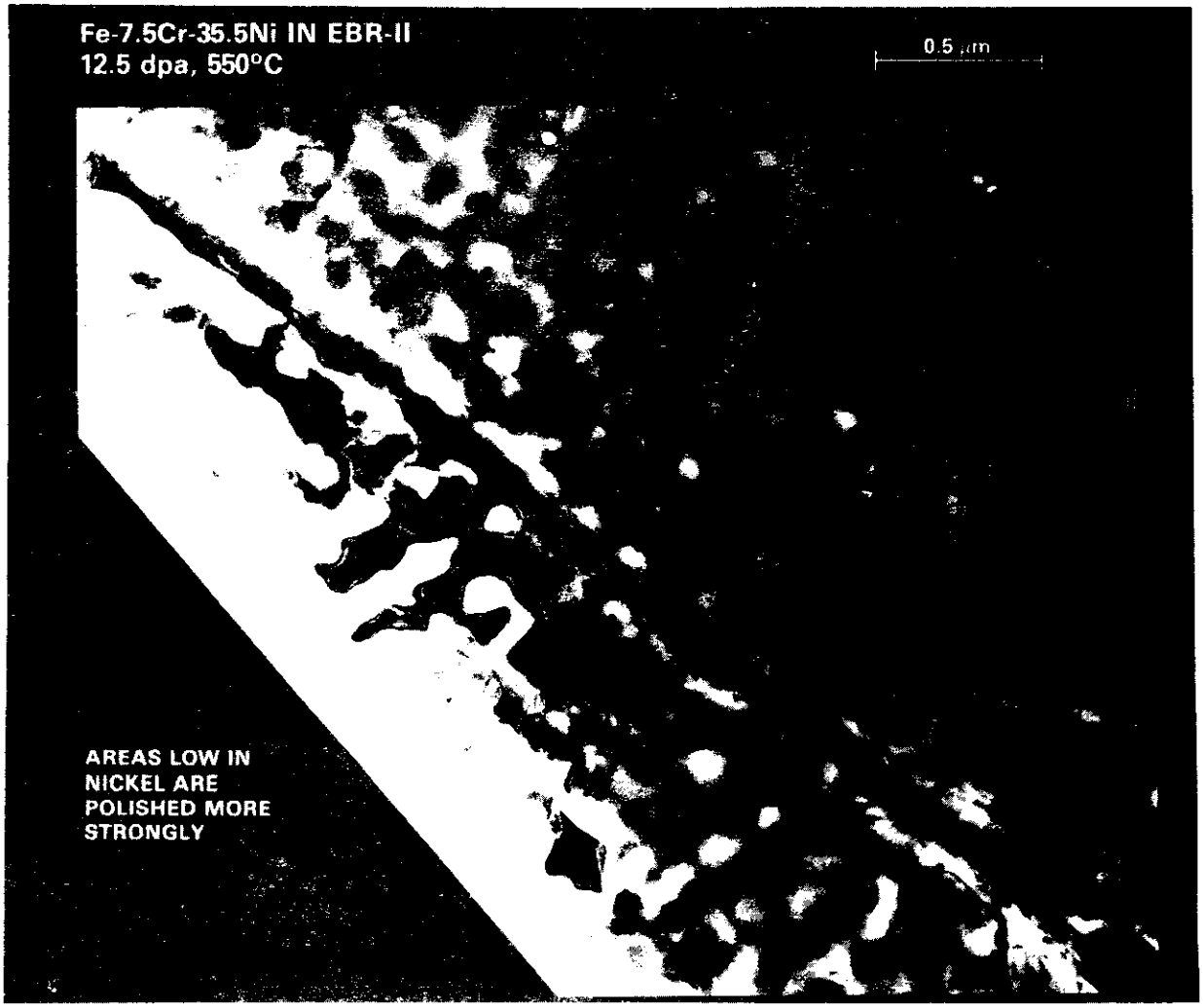

Fig. 8. Same specimen as that of Fig. 7, showing the irregular polished edge of the foil and the preservation of a nickel-rich zone containing a grain boundary.

An analysis is now in progress of the compositional dependence of free energy and strain energy. It shows that the latter forces the alloy to undergo spinodal decomposition in a compositional range which is very narrow, except at low temperatures where thermal diffusion is very slow. Radiation-enhanced diffusion at these low temperatures allows the spinodal decomposition to proceed at rates much faster than that relevant to thermal evolution of meteorites. This analysis will be presented in the next report.[20]

FUTURE WORK

Examination of both ion and neutron irradiated specimens will continue, along with the development of a theoretical treatment of the spinodal process.

REFERENCES

1. F. A. Garner, H. R. Brager, R. A. Dodd, and T. Lauritzen, Nuclear Instruments and Methods in Physics Research, B16, 244 (1986).

2. H. R. Brager and F. A. Garner, p. 141 in Optimizing Materials for Nuclear Applications, F. A. Garner, D. S. Gelles and F. W. Wiffen, eds., TMS-AIME, Warrendale, PA (1985).

3. H. R. Brager and F. A. Garner, p. 139 in Effects of Radiation on Materials: Twelfth International Symposium, F. A. Garner and J. S. Perrin, eds., ASTM, Philadelphia, PA (1985).

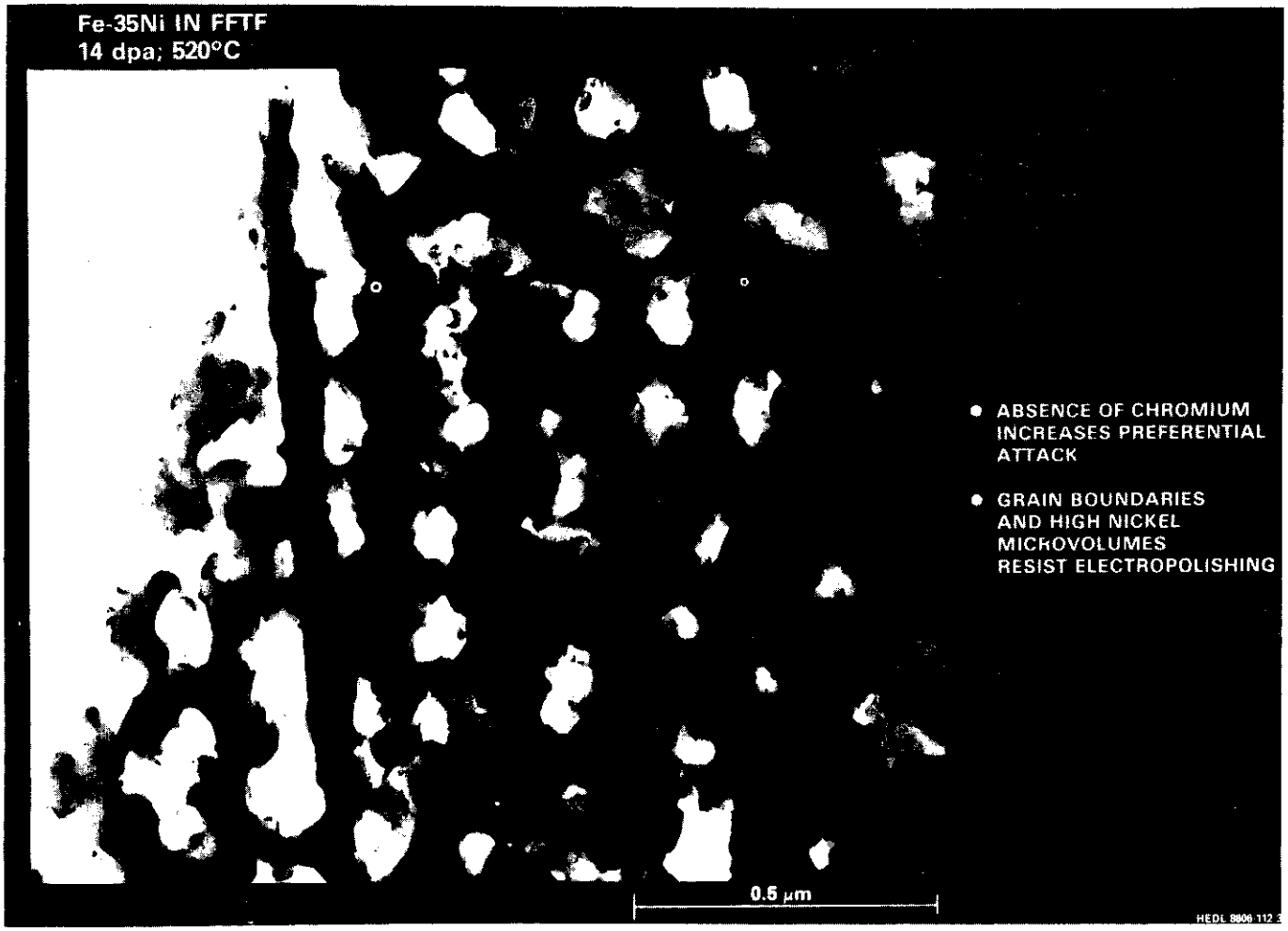

Fig. 9. Preferential attack of low nickel microvolumes in Fe-35Ni (14 dpa at 520°C in FFTF) after electropolishing. The electrolyte has tunneled through the foil in many places. The linear feature on the left is a nickel-rich zone containing a grain boundary.

4. F. A. Garner and H. R. Brager, p. 71 in Damage Analysis and Fundamental Studies Quarterly Progress Report, February 1986, DOE/ER-0046/24, U. S. Department of Energy, Office of Fusion Energy.

5. R. A. Dodd and F. A. Garner, p. 98 in Damage Analysis and Fundamental Studies Quarterly Progress Report, May 1986, DOE/ER-0046/25, U. S. Department of Energy, Office of Fusion Energy.

6. F. A. Garner, G. L. Wire, and E. R. Gilbert, p. 474 in Proc. Inter. Conf. on Radiation Effects and Tritium Technology for Fusion Reactors, CONF-750959, Gatlinburg, TN (1974).

7. W. G. Johnston, W. G. Morris and A. M. Turkalo, p. 421 in Radiation Effects in Breeder Reactor Structural Materials, M. L. Bleiberg and J. W. Bennett, eds., TMS-AIME, New York, NY (1977).

8. N. Q. Lam, J. Nucl. Mater. 117, 106 (1983).

9. A. D. Marwick, R. C. Pillar, and M. E. Horton, p. 11 in Vol. 2 of Dimensional Stability and Mechanical Behaviour of Irradiated Metals and Alloys, British Nuclear Energy Society, London, England (1984).

10. F. A. Garner, "Irradiation of Fe-Ni-Cr Austenitic Alloys at 420-750°C in the MOTA-1E Experiment", this report.

11. Y. Tanji, Y. Nakagawa, Y. Saito, K. Nishimura, and K. Nakatsuka, Physica Status Solidi A 56, 513 (1979).

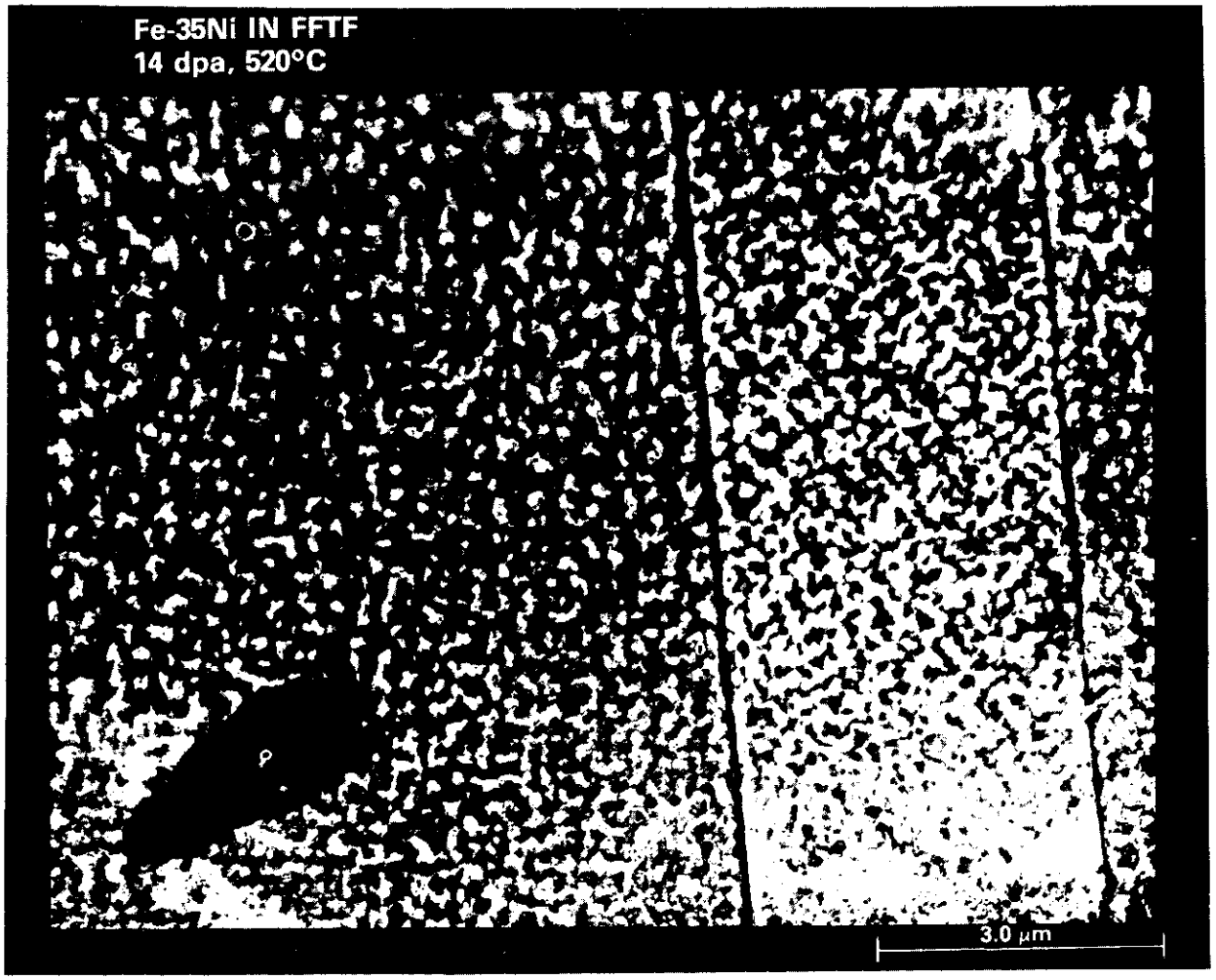

Fig. 10. Lower magnification micrograph of the specimen shown in Fig. 9. Three grains are visible, separated by grain boundaries. Note the crystallographic orientation of the etched-out microvolumes.

12. Y. Tanji, Y. Nakagawa, and S. Steinemann, Physica B+C 119, 109 (1983).

13. Y. Nakagawa, Y. Tanji, H. Morita, H. Hiroyoshi, and H. Fujimori, J. Magnetism and Magnetic Materials 10, 145 (1979).

14. Y. Tanji, H. Morita and Y. Nakagawa, J. Phys. Soc. Japan 45, 1244 (1978).

15. V. F. Buchwald, p. 1068 in Vol. 3 of Handbook of Iron Meteorites, Their History, Composition and Structure, University of California Press (1975).

16. J. Danon, R. B. Scorzelli, I. Souza Azevedo, W. Curvello, J. F. Albertsen, and J. M. Knudsen, Nature 277, 284 (1979).

17. R. B. Scorzelli, and J. Danon, Physica Scripta 32(2), 143 (1985).

18. J. I. Goldstein and J. M. Short, Geochim. Cosmochim. Acta 31, 1733 (1967).

19. W. G. Johnston, T. Lauritzen, J. H. Rosolowski, and A. M. Turkalo, J. Nucl. Mater. 62, 167 (1976).

20. K. C. Russell and F. A. Garner, "Unexpected Phase Transformation in Fe-Ni Invar Alloys", HEDL-SA-3592A, to be presented at The Metals Society Annual Meeting, Denver, CO, February 24-27, 1987.

Fig. 11. Back-scatter electron image from electron microprobe analysis of a polished surface of a Santa Catharina sample.[16] It was found that the dark areas correspond to the Fe-50Ni ordered phase whereas the light areas correspond to the Fe-rich paramagnetic phase. (Micrograph courtesy of R. B. Scorzelli).

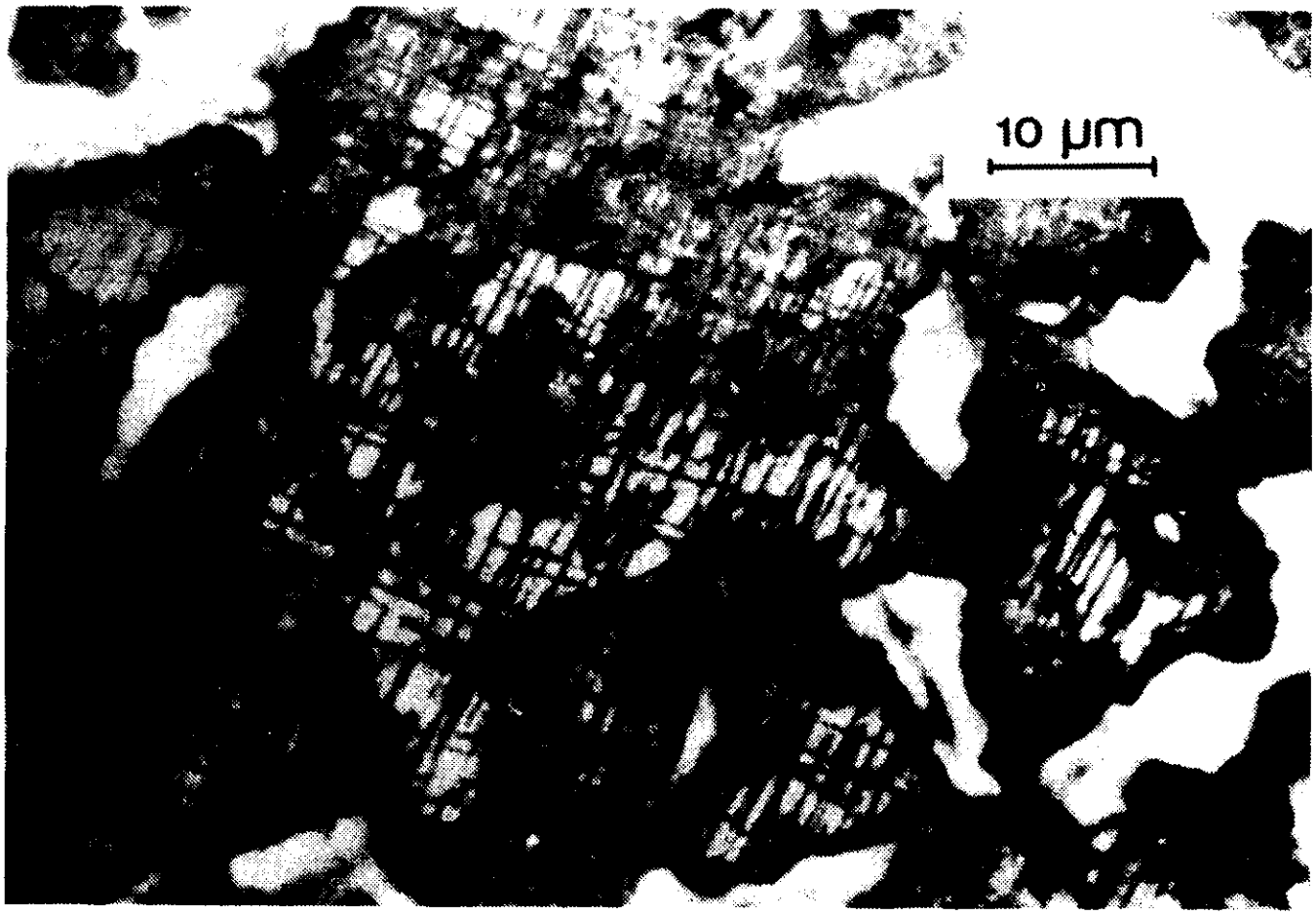

Fig. 12. Optical photomicrograph of Santa Catharina meteorite after etching,[17] showing finer structure, with plate-like precipitates in low-nickel matrix exhibiting well-defined crystallographic habit planes.

EFFECT OF NICKEL CONTENT ON THE MINIMUM CRITICAL RADIUS OF Fe-Cr-Ni ALLOYS - W. A. Coghlan (Arizona State University) and F. A. Garner (Westinghouse Hanford Company)

OBJECTIVE

The object of this effort is to determine the mechanisms by which materials evolve under irradiation and to predict the changes that will occur in fusion neutron environments.

SUMMARY

Swelling data from both ion and neutron irradiations of Fe-Cr-Ni alloys are analyzed in terms of the critical radius concept for bubble-to-void conversion. It is shown that while the dependence of critical radius on temperature, displacement rate and helium can explain many features of the data, one must also consider the dependence of vacancy diffusion on nickel content in order to be able to explain the compositional dependence of void nucleation.

PROGRESS AND STATUS

Introduction

In a series of recent papers it has been shown that much of the compositional dependence of radiation-induced swelling in austenitic alloys can be explained in terms of the effects on vacancy diffusivity that arise from increases in solutes and solvent atoms[1-5] or from spatial heterogeneities which develop in composition during irradiation.[6-9] Additional changes in matrix composition can arise from precipitation and precipitates may also contribute in other ways to void nucleation, but these effects are not addressed in this paper.

There are two major conclusions of these earlier studies. First, the compositional dependence of swelling is most significant in that temperature regime where nucleation of voids becomes increasingly more difficult with temperature. In the temperature-insensitive regime, the influence of composition on swelling is much smaller. Second, the nucleation rate in the temperature-sensitive regime can be affected strongly by minor changes in displacement rate, gas availability or vacancy diffusivity. The latter is sufficiently sensitive to nickel, chromium and silicon to account for the majority of the observed effects of these elements on void nucleation.[4]

Figs. 1 and 2 show the influence of these three variables on void nucleation in ion-irradiated Fe-15Cr-XNi alloys.[9,10] Note that the effect of nickel on void nucleation is still visible but becomes less pronounced at higher displacement rates and higher levels of helium. This is particularly evident in the preinjection experiment of Fig. 2 when compared to the dual ion experiment in that same figure.

It is generally accepted that in order for voids to grow they must first nucleate as small defect clusters and grow to a critical size. During this early stage the cavities are not stable and will spontaneously shrink unless they are stabilized by gas atoms or by some other mechanism. Theoretical analyses of this process have been recently summarized and extended to include the influence of assuming a van der Waals gas[11] and variations in microstructure.[12] These reports have shown that the critical radius is strongly dependent on the microstructure, temperature, defect bias, surface energy and helium level. Based on previous studies[1-5] we would add the composition dependence of vacancy diffusivity to the list of variables which strongly affect the critical radius.

Evidence to support this proposal is available from experiments which attempt to measure the critical radius directly. The technique was first employed by Mazey and Nelson[13] who injected 1000 appm of helium at high temperatures into two high nickel alloys in order to produce a distribution of bubble sizes which spanned the presumed value of critical radius. Subsequent irradiation then caused those bubbles with radii greater than the critical value to grow into voids. Those below the critical radius were left behind and provided a microstructural record of the critical radius.

This technique has also been employed by others to study the critical radius in the simple ferritic alloy Fe-10Cr[14] and the simple austenitic alloys Fe-15Cr-15Ni and Fe-15Cr-35Ni.[10] This latter experiment is one of the two shown in Fig. 2, namely the preinjection series. Each alloy was preinjected with 400 appm helium at 675°C and then aged at that temperature for an additional hour to coarsen the bubble distribution. The helium bubble distributions were found to be relatively uniform but the average bubble diameter in the 15% nickel alloy was ~7.5 nm, about 50% larger than the 4.9 nm diameter found in the 35% nickel alloy.

Subsequent irradiation with 4 MeV Ni^+ ions yielded a bimodal cavity distribution in the 35% nickel alloy with a critical radius at ~5 nm. In the 15% nickel alloy a unimodal rather than a bimodal distribution of cavities was found. Fig. 3 shows the cavity distributions for these two alloys at ~40 dpa.

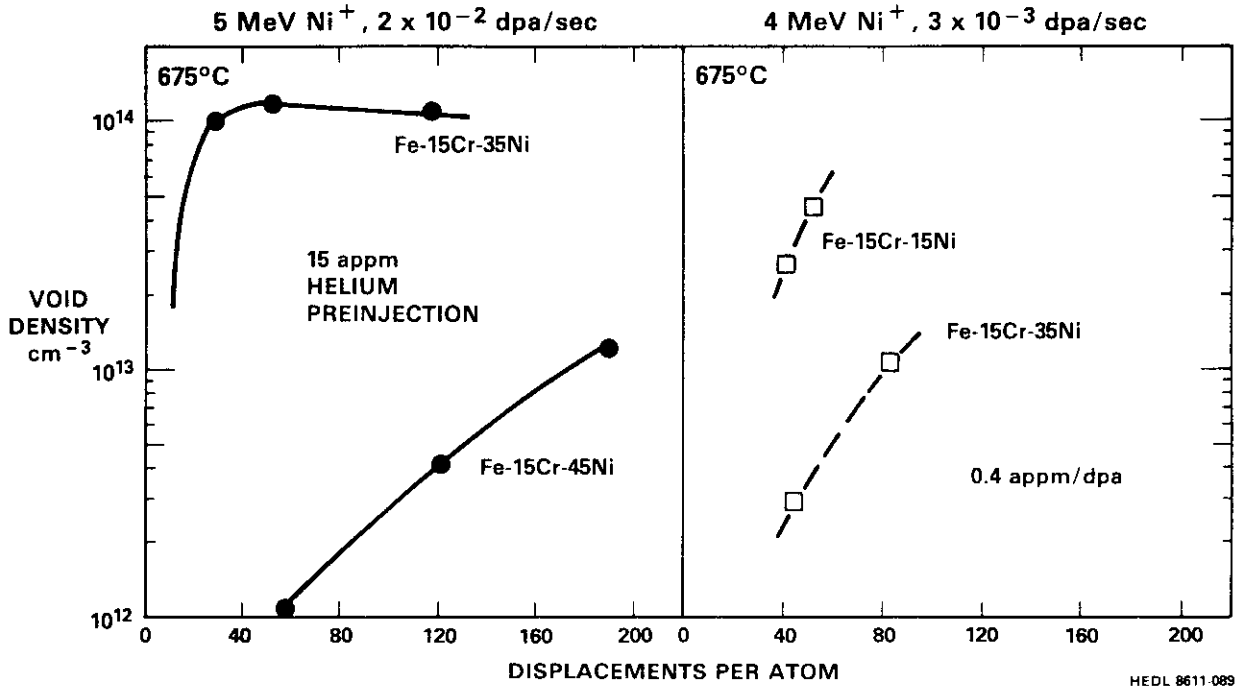

Fig. 1. Void Nucleation in two ion bombardment experiments[9,10] on Fe-15Cr-XNi alloys at 675°C showing effect of nickel content for different helium introduction methods, ion energies and displacement rates.

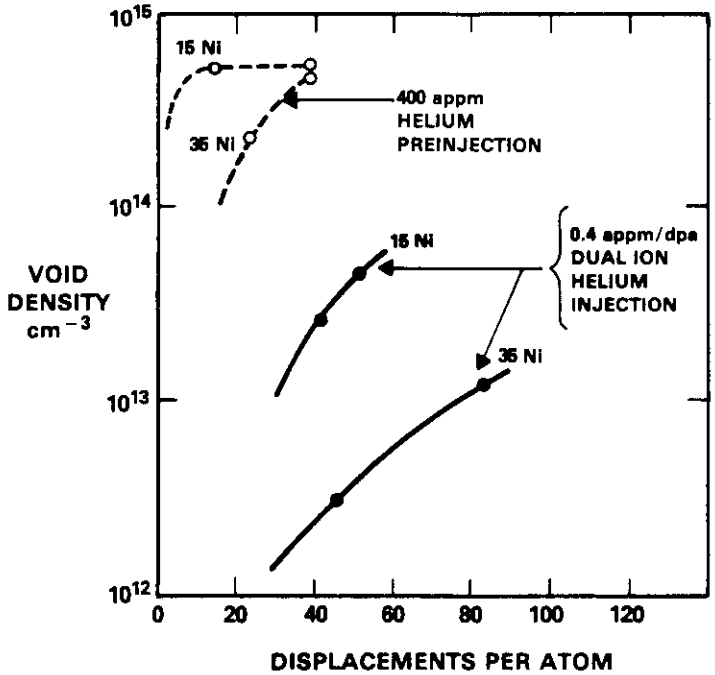

Fig. 2. Void densities observed in two experiments conducted by Lee and Mansur with 4 MeV Ni^+ ions at 675°C and 3 x 10^{-3} dpa/sec, showing effect of composition and helium injection.[10]

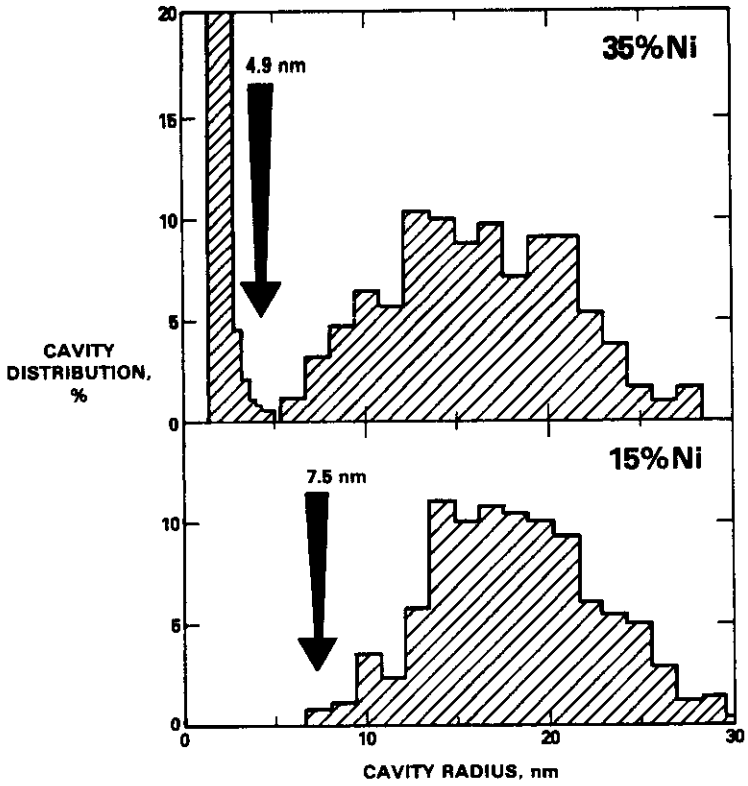

Fig. 3. Histograms of cavity size distributions observed in Fe-15Cr-15Ni and Fe-15Cr-35Ni after ∿40 dpa ion irradiation following preinjection of 400 appm helium and aging to coarsen the bubble distribution.[10] The arrows denote the mean bubble size prior to irradiation.

From these results Lee and Mansur concluded that the critical radius at 15% nickel lay below the microscopy resolution limit of ∿0.5 nm. This conclusion in turn implies a factor of ten reduction or more in critical radius when the nickel content drops from 35% to 15%.

As we will show later an equally plausible interpretation is available that will produce the same results with only a factor of two reduction in critical radius. This factor of two can easily arise from the difference in effective vacancy diffusion coefficient of the two alloys.[4] This reduction in critical radius means there has been almost an order of magnitude reduction in the amount of gas needed to stabilize the cavities. Under conditions where the gas is generated during the irradiation this could lead to large differences in the duration of the transient regime of swelling.

Under neutron irradiation conditions the critical radius argument should be equally effective. In fact, the same alloys used by Johnston and coworkers, and also by Lee and Mansur, have been studied using neutron irradiation.[15] For neutron irradiation conditions the boundary between the temperature-insensitive and the temperature-sensitive regimes of void nucleation is at much lower temperatures compared to that of typical ion irradiation conditions. This difference is primarily due to the much lower displacement rate of neutron irradiations and the fact that helium must first be produced by transmutation rather than be preinjected. In some instances the high nickel alloys have been observed during neutron irradiation to resist swelling while exhibiting high densities of ($\sim 10^{16}$ cm^{-3}) of small cavities which are assumed to be helium bubbles.[6] These appear to be waiting for some signal before growing, while alloys with lesser nickel content have already begun to swell. This is particularly significant when you consider that the helium level is actually higher in the high nickel alloy, since nickel is the major source of transmutation-induced helium in Fe-Ni-Cr alloys.

In the following sections we first describe the calculational procedure used to provide estimates of the critical radius and explore the sensitivity of the model to relevant environmental variables and material parameters. Then we choose the necessary adjustable parameters to reproduce the 5.0 nm critical radius of the Fe-15Cr-35Ni alloy and calculate the change in critical radius that occurs when the nickel level drops to 15%. We also apply the results of this study to describe various features of two neutron irradiation studies.

Description of the critical radius calculation

Critical radii for void nucleation from bubbles containing helium gas (as described by the van der Waals equation) have been presented recently[11,12] and only a summary of the equations used for these calculations will be presented. A much more compact form for the equations will be given here than appears in the cited references. This equivalent form was derived by Trinkhaus and Mansur[16] and greatly simplifies their use.

Prior to irradiation a material is assumed to contain thermal equilibrium concentration of vacancies and no interstitials. The formation energy of the latter is too high to allow an appreciable equilibrium concentration. The equilibrium concentration of vacancies is

$$C_v^o = \Omega^{-1} \exp(S_v^f/k) \exp(-E_v^f/kT). \quad (1)$$

The terms S_v^f, k, and T are the vacancy formation entropy, Boltzmann's constant, and the temperature, respectively. The remaining expressions are given in Table 1 along with the values used for the calculations to follow. We have assumed a value of zero for the entropy which simplifies Eq. (1) and does not change the general results calculated.

The model will be used to compare neutron and ion irradiations; and in order to make this comparison, we have included the injected interstitials which are implanted during ion irradiation. The generation rates of vacancies and interstitials are

$$G_v = f_c G + G_T, \text{ and} \quad (2)$$

$$G_i = f_c G + E_i, \quad (3)$$

where G is the generation rate of Frenkel pairs, G_T is the thermal production of vacancies, f_c is the fraction that survive immediate recombination, and E_i is the fraction of injected interstitials.

The defects that are produced accumulate in the sample or annihilate by recombination or diffuse to dislocations. The recombination coefficient is

$$R = 4\pi r_o (D_v + D_i)/\Omega, \quad (4)$$

and the loss rate of defects to dislocations is

$$K_{v,i} = D_{v,i} Z_{v,i}^d L \quad (5)$$

where the v,i subscript implies either vacancy or interstitial. All other parameters are defined in Table 1.

With the above definitions, the vacancy and interstitial concentrations can be found algebraically and are given in Eqs. (6) and (7).

$$C_v = \frac{[K_i K_v + R(G_i - G_v)]}{2RK_v} \left[\left(1 + \frac{4RG_v K_i K_v}{[K_i K_v + R(G_i - G_v)]^2} \right)^{1/2} - 1 \right] \quad (6)$$

$$C_v = \frac{[K_i K_v + R(G_v - G_i)]}{2RK_i} \left[\left(1 + \frac{4RG_i K_i K_v}{[K_i K_v + R(G_v - G_i)]^2} \right)^{1/2} - 1 \right] \quad (7)$$

If the dominant sink is the dislocation network, the bulk of the thermally produced defects will be emitted by dislocations and the thermal vacancy production will be

$$G_T = Z_v^d D_v C_v^o L. \quad (8)$$

Using the above defect concentrations the minimum critical radius is

$$r_c^* = \frac{4\gamma}{3f} \quad \frac{3}{2} \quad \frac{1+\delta}{2+\delta} \quad (9)$$

Table 1. Parameters used for calculations

Vacancy motion energy, E_v^m	1.1 eV
Vacancy formation energy, E_v^f	1.7 eV
Interstitial pre-exponential, D_i^o	1×10^{-6} m^2/s
Interstitial motion enthalpy, E_i^m	0.15 eV
Recombination radius, r_o	0.4 nm
Cascade efficiency, f_c	0.3
Lattice parameter, a_o	3.5×10^{-10} m
Atomic volume, Ω	1.07×10^{-29} m^3
Ion Implantation:	
Defect production, G	3×10^{-3} dpa/s
Fraction of injected interstitials, E_i	5×10^{-4}
Dislocation density, L	5×10^{13} /m^2
Neutron Irradiation:	
Defect production, G	1×10^{-6} dpa/s
Dislocation density, L	5×10^{14} /m^2

where: $\delta = \sqrt{1 + 3Bf/kT}$,

$$f = kT \ln [(1-Z)C_v/C_v^o + Z]/\Omega$$

$$Z = Z_i^c Z_v^d / Z_v^c Z_i^d,$$

and the van der Waals constant, B, according to reference 17 is

$$B = 6.65 \times 10^{-27}[4.5 \times 10^{-4} + 5.42/(1890 + T)].$$

In our calculation all the sink efficiencies are chosen to be equal to 1 except for Z_i^d which we use as a parameter to fit the observed results.

Calculated critical radii

As can be seen from the previous section, calculation of the critical radius requires a knowledge of the microstructure and of the diffusion properties of the material. Some of the microstructural parameters have been determined for the experiment being considered, and several of the physical parameters of the materials are known for the iron-based alloys being studied. Other parameters such as the energy of bubble and void surfaces, the sink efficiency factor for dislocations, and the pre-exponential constant for vacancy diffusion are less well known for these alloys. Each of these parameters may also depend on the alloy composition. Table 1 shows the values chosen for the material and diffusion parameters. Several calculations were performed for sets of values chosen for the surface energy and the dislocation sink

efficiency for interstitials. In each case D_v^o was adjusted to obtain the experimental value of 5 nm for the minimum critical radius, at 675°C reported by Lee and Mansur for Fe-15Cr-35Ni.[10] A lower value of 5×10^{13} m^{-2} was chosen for the dislocation density for the ion irradiation because this is the density observed in dual ion irradiations and the value that preirradiated specimens approach at high dose. For our calculations an increase in the dislocation density would cause a corresponding decrease in the required diffusion pre-exponential. The values of D_v^o required to fit the ion data are summarized in Table 2.

Table 2. D_v^o required for r_c^* =5 nm at 675°C

Cascade Efficiency	Z_i^d	γ, J/m^2	D_v^o, m^2/s
8%	1.05	0.5	4.80×10^{-4}
8%	1.05	1.0	2.15×10^{-4}
8%	1.1	0.5	2.78×10^{-3}
8%	1.1	1.0	1.23×10^{-3}
30%	1.05	0.5	5.35×10^{-3}
30%	1.05	1.0	2.41×10^{-3}
30%	1.1	0.5	1.04×10^{-2}
30%	1.1	1.0	4.72×10^{-3}

After the critical radius for Fe-15Cr-35Ni was calculated, the parameters were modified to simulate the ion irradiation of Fe-15Cr-15Ni and then to simulate in turn the neutron irradiation of the Fe-15Cr-15Ni. The value for D_v^o used for Fe-15Cr-35Ni was that of Fe-15Cr-15Ni divided by two to take into account the effect of nickel on diffusion.[4] The neutron-irradiation conditions are summarized in Table 1 and reflect a large decrease in the damage rate, an increase in dislocation density, relative to the lower values found in ion experiments, and the absence of injected interstitials. It has recently been suggested that a higher sink efficiency may pertain for dislocations under neutron irradiation than under ion irradiation because at high dislocation velocity the defects are less influenced by the dislocation stress field,[18] but this insight will not be used in this analysis.

The resulting calculated critical radii for two sets of assumed values of surface energy and sink efficiency are shown in Fig. 4. The values of D_v^o used for each case is given in Table 2. The general shape of the curves are the same and all the curves labeled D_v^o pass through the observed critical radius of 5 nm at 675°C. Very little difference is seen in the two cases shown. However, the decrease in the surface energy results in a decrease in the values found at low temperature. It should be noted, however, that even including a decrease of a factor of two in D_v^o and also in γ, the calculated minimum critical radius is larger than the <0.5 nm value assumed by Lee and Mansur for Fe-15Cr-15Ni. For the factor of two reduction in D_v^o, the magnitude of the change in r_c^* can be more easily seen in Fig. 5.

In Fig. 5 the absolute and the fractional changes in the minimum critical radius are plotted versus temperature for Z_i^d=1.1 (a 10% bias) for two different surface energies, 0.5 and 1.0 J/m^2. In Fig. 5a the absolute change in critical radius is found to be independent of surface energy, but strongly dependent on temperature. In Fig. 5b, a difference in the fractional change is seen for the two values of surface energy. For both values a change of almost 50% in the radius is seen with a small change in the temperature dependence resulting from the difference in the surface energy. This calculation was performed using values of 8% and 30% for the cascade efficiency, f_c, and the results were exactly the same. The change in the D_v^o required to match the measured critical radii completely removed any dependence on cascade efficiency.

The parameters that have the strongest effect on the minimum critical radius are temperature, defect production rate, surface energy, dislocation density, bias, and the pre-exponential constant for vacancy diffusion. The activation energies for vacancy formation and motion can also have strong effects if they are changed independently from each other. If the sum of the activation enthalpies for motion and formation is held constant almost no effect is predicted. Figs. 6 and 7 illustrate all the above strong dependencies. In each case we have plotted the minimum critical radius versus temperature for γ =1.0 J/m^2, Z_i^d=1.1, f_c=8%, and D_v^o=1.23 x 10^{-3} m^2/s. We have then repeated the calculation by varying each parameter in turn over a range of values. Analysis of the plots shows that change in every parameter is effective in changing the temperature where the minimum critical radius rises very quickly but only the surface energy is effective in significantly changing the minimum critical radius in the temperature-insensitive regime.

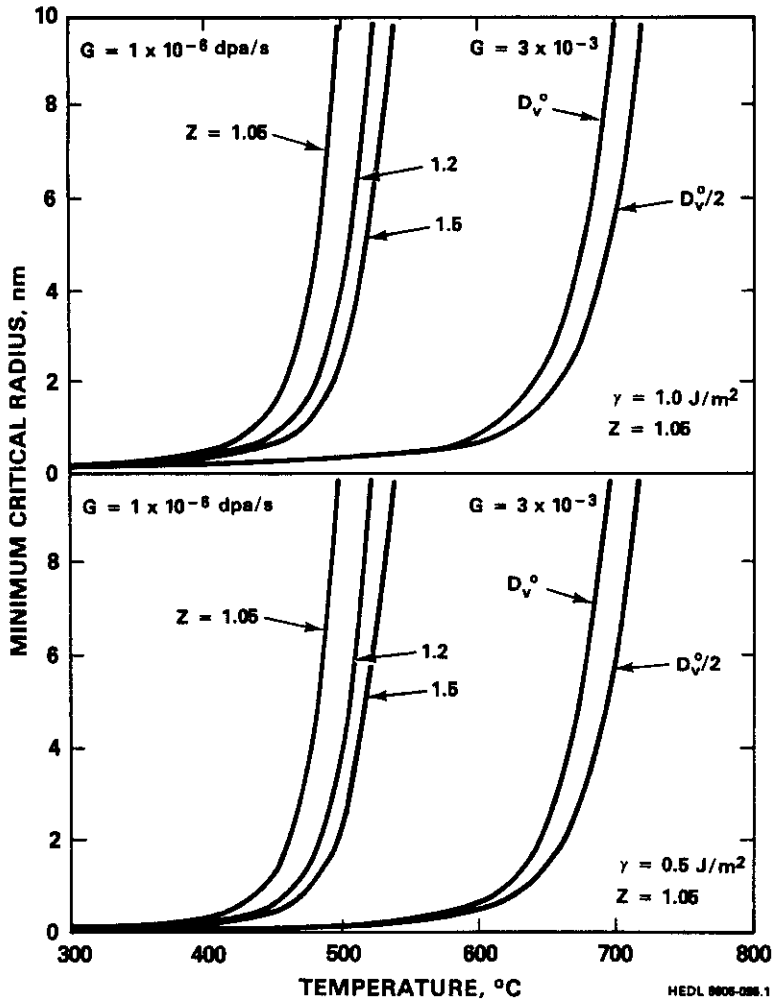

Fig. 4. Dependence of minimum critical radius on temperature, displacement rate, D_v^o and Z for two values of surface energy.

Discussion

In another paper it is demonstrated that an increase in D_v^o is comparable to an increase in temperature and can be characterized by a temperature shift comparable to that used to characterize the effect of changes in displacement rate.[4] If we select values of irradiation and material parameters to match the 5 nm radius of Fe-15Cr-35Ni found at 675°C by Lee and Mansur,[10] we predict a factor of two reduction in critical radius based only on a factor of two change in the preexponential for vacancy diffusion. It is important to note that this factor of two change in D_v^o arises from measurements of nickel's influence on diffusivity and not from arbitrary assumptions.

This apparent shift in temperature leads to a critical radius of 2.5 nm, which is well below the mean of the original bubble distribution, namely 7.5 nm. This means that the overwhelming majority of the bubbles would be promoted to voids by bias-driven growth, leaving only a few bubbles behind. It is assumed that many of these remaining bubbles would also be swept up by the considerable dislocation activity that accompanies the swelling. Thus it is not necessary to assume that the critical radius of the Fe-15Ni-15Cr alloy lies below the resolution limit of electron microscopy.

Support for the preceding interpretation arises from the results of Mazey and Nelson.[13] In that study two related but different alloys were used which developed significantly different distributions of bubbles in the preimplantation stage. In one case the distribution peaked at a diameter of 4.8 nm and the other peaked at 11.3 nm. In both alloys a critical radius of about 4 nm (critical diameter of ~8 nm) was predicted. In the case where the critical radius lay well within the initial distribution, a bimodal cavity distribution developed. In the case where the critical radius lay well below the mean, a unimodal distribution developed. These results are thus in agreement with our interpretation of the experiment of Lee and Mansur such that it is not necessary to invoke the assumption that the critical radius lies below the resolution limit of microscopy.

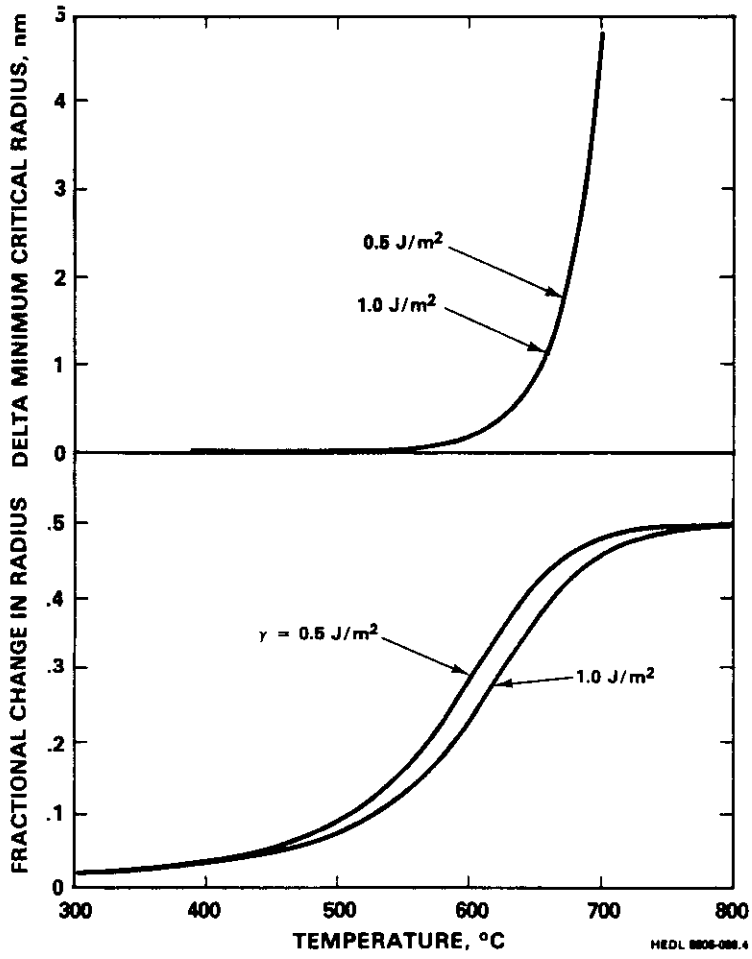

Fig. 5. Change in critical radius for a factor of two reduction in D_v^o.

There is another result of the experiment of Lee and Mansur that is useful for the present study. Note in Fig. 2 that the saturation density of voids for the preinjection case appears to be unaffected by the difference in early void nucleation rates. The swelling at ∿40 dpa is also not very different (1.7 vs 1.2%), whereas in the dual-ion case there are substantial differences in both void density and swelling. Thus we find support for our contention that compositional effects on void nucleation are only important in that temperature regime where void nucleation becomes increasingly more difficult.[4] In the presence of large amounts of helium the difficulty of nucleation is reduced substantially and the effect of composition is reduced.

This paper has focused only on the compositional influence on vacancy diffusion. There are certainly other material parameters dependent on nickel content. There is a strong compositional dependence of stacking fault energy on nickel for instance.[19] Lee and Mansur note that Frank loops in the 35% Ni alloy appear to be more stable than those at 15% Ni in the dual-ion experiment. In fact Frank loops are very hard to find in the 15% Ni alloy at any fluence examined, as shown in Fig. 8b. This implies that loops either grow slower at 35% Ni or are more stable against unfaulting. Since the higher nickel alloy possesses the higher stacking fault energy, one would expect that this would promote earlier unfaulting. The opposite is observed, however.

It is important to realize that Frank loops are known to segregate nickel around themselves.[20-23] Therefore the loops exist at higher nickel levels than that of the matrix. For Fe-15Cr-35Ni this would probably place the loops at the >50% level where a substantial amount of short-range order occurs, even at temperature in the range of 600-700°C.[24] This is also the regime where this alloy has been shown to develop spinodal-like micro-oscillations, density changes, and hardness increases characteristic of irradiated alloys in the Invar composition regime.[6-9] Perhaps these and other mechanisms contribute to the stability of the loops at the 35% Ni level.

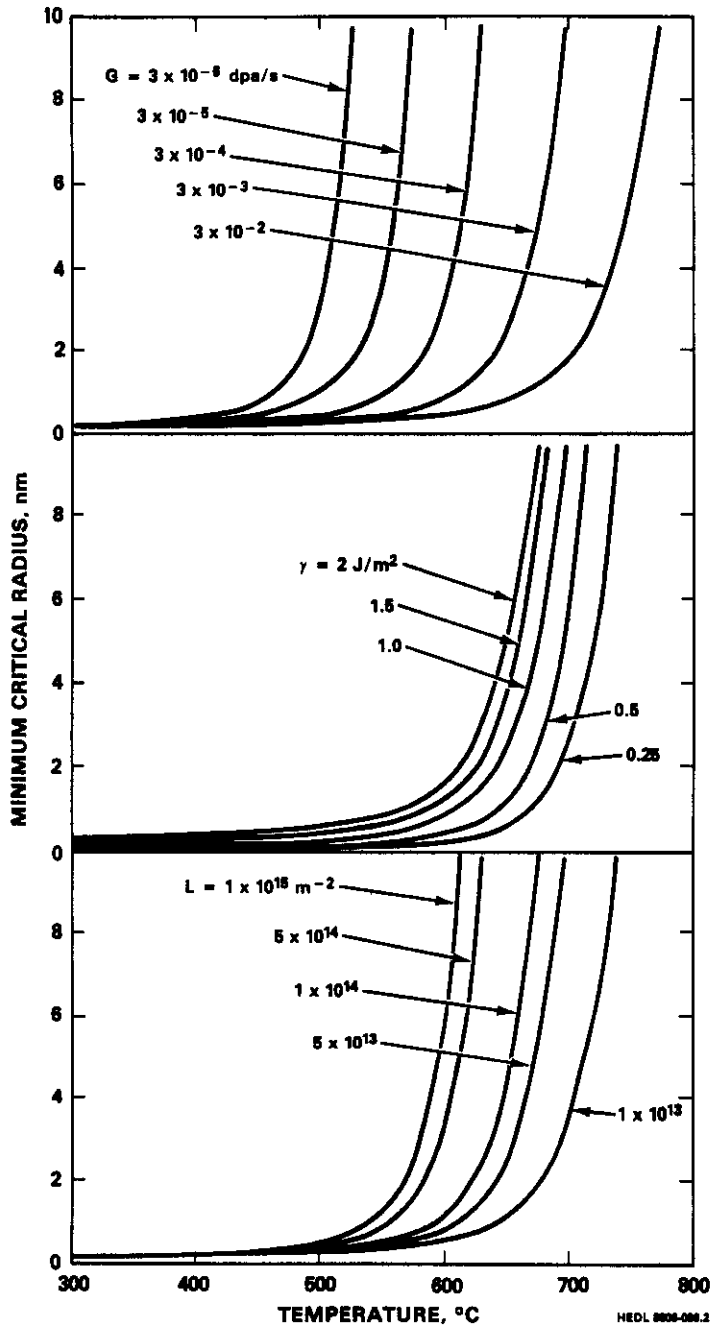

Fig. 6. Dependence of minimum critical radius on displacement rate G, surface energy γ and dislocation density L.

Lee and Mansur attribute the stability of the loops at 35% Ni to the assumption of an increased difficulty of interstitial absorption at Frank loops. They assert that this difficulty would lead to a lower system bias, a parameter which has a strong effect on void nucleation as shown in Fig. 7. As evidence for this they point out that in Fe-15Cr-35Ni, unfaulted loops in doublet or triplet clusters are frequently observed with each loop lying on a different {110} plane. The implication is that the interstitials are drawn to and collect near the loops because of their interaction with the stress field, but they have difficulty in joining the loop and therefore nucleate new loops instead.

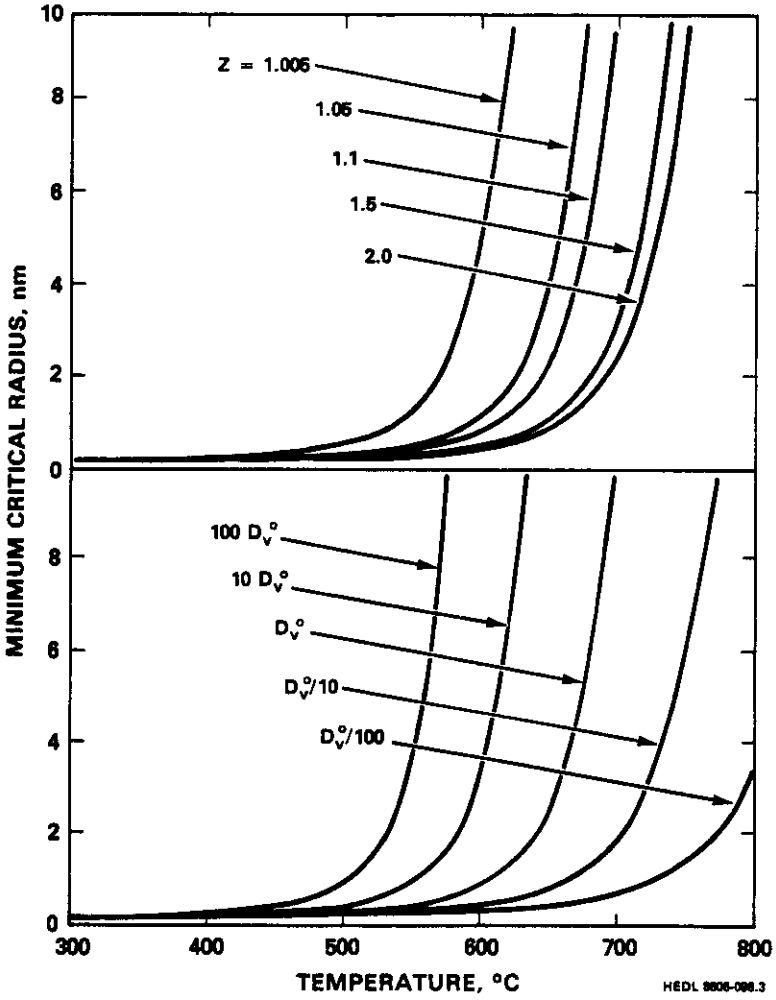

Fig. 7. Dependence of minimum critical radius on bias Z and pre-exponential coefficient D_v^o for vacancy diffusion.

The validity of this proposal cannot be assessed in this paper without evidence that loops in Fe-15Cr-15Ni did not also exhibit doublet or triplet behavior. As shown in Fig. 8, however, loops in Fe-15Cr-15Ni unfaulted in the irradiation interval before the first examination. Perhaps multiple loops were present in the lower nickel alloy during that interval. If so, this would tend to discount a strong dependence of loop bias on nickel content.

It appears, however, that multiple loops indeed do form in low nickel alloys as observed by Boulanger in Ni^+ ion irradiations of Fe-19Cr-13Ni at 650°C.[25] As summarized by Chen and Ardell multiple layer loops have been observed in many systems.[26] They cite a number of factors which encourage multiple loop formation, primarily gaseous impurities such as nitrogen and oxygen; but even more importantly, high displacement rates favor formation of multiple loops. Both Kenik[27] and Das and Mitchell[28] have shown that high dose rates and hence high vacancy supersaturations are necessary for multiple loop formation during high voltage electron irradiation. Remember that we cited earlier that Rauh and Bullough[18] predict that the bias will decrease strongly at high displacement rates but composition is not the important factor. We therefore consider it unlikely that the observations of Lee and Mansur support a strong dependence of the bias on nickel content.

Figs. 3 and 8 show another facet of this experiment coupling the short transients in void nucleation with equally short transients in dislocation evolution. Before void swelling begins the dislocation density provides the dominant sink and the critical radius increases as the dislocation density increases. After swelling begins the vacancy concentration decreases and bubble-to-void conversion ceases. One consequence of this turn of events is that late-forming bubbles might never be promoted into voids if the microstructural evolution is already well in progress and substantial swelling and dislocation levels have been reached.

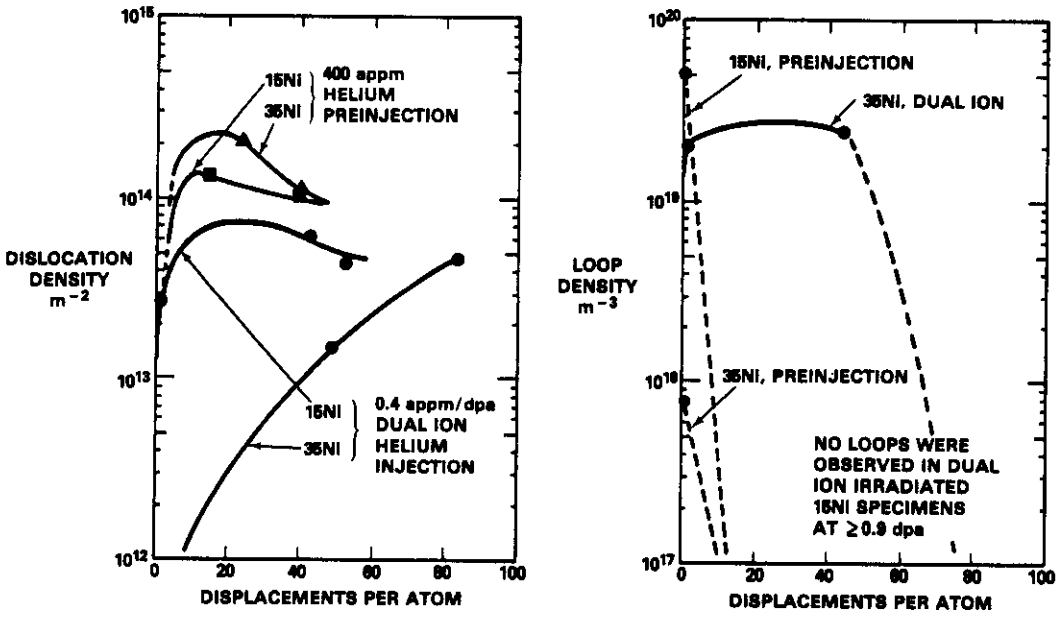

Fig. 8. Dislocation and loop evolution observed by Lee and Mansur in preinjection and dual-ion irradiation experiments at 675°C.[10]

Support for this contention can be seen in Fig. 9, where annealed AISI 316 stainless steel has been irradiated in the High Flux Isotope Reactor (HFIR) at Oak Ridge, TN.[29] In this case the helium production is very large and is also non-linear. A factor of two increase in the helium production rate occurs after the onset of swelling. After irradiation to ∿45 dpa at 480°C there is about 9% swelling with voids of mean diameter of ∿40 nm and density of ∿1.4 x 10^{15} cm^{-3}. The dislocation density is ∿6 x 10^{10} cm^{-2}. However, there are also 1.7 x 10^{17} cm^{-3} small helium bubbles (∿2 nm) between the voids. Most of these bubbles probably developed as a consequence of the high helium generation rate but formed after the micro-structural sink strength had reached levels where the critical radius was too large to allow promotion of these bubbles to voids.

In the HFIR specimen just discussed it is important to note that the displacement rate was much lower (∿1 x 10^{-6} dpa/sec) than that at which the ion irradiation experiments were conducted. As shown in Figs. 10 and 11, the void densities in Fe-15Cr-XNi alloys irradiated in EBR-II exhibits their temperature-sensitive and composition-sensitive regime at much lower temperatures, reflecting the very large influence of displacement rate on void nucleation.

Often during neutron irradiation helium bubbles are observed to form in higher nickel and/or lower chromium alloys but appear to be waiting to accumulate enough helium and vacancies to begin bubble-to-void conversion, while lower nickel and higher chromium alloys irradiated side-by-side have begun to swell substantially. Since these lower nickel alloys have proportionately lower helium transmutation rates, the strong role of composition on bubble-to-void conversion is particularly evident. An example of this tendency for bubbles to resist promotion is shown in Fig. 12 for neutron-irradiated Fe-7.5Cr-35.5Ni at 593°C and 38 dpa where bubbles of size ≤5 nm and 1 x 10^{16} cm^{-3} density are found along with a low density of dislocations.[6] The helium level at this point is ∿30 appm but alloys with lower nickel and helium levels are already swelling at this exposure and temperature.[15]

If we refer to Fig. 6 we can see that the critical radius at 1 x 10^{-6} dpa/sec is very large at 593°C. In fact it is so large compared to the observed 5 nm radius shown in Fig. 12 that we might never expect bubble-to-void conversion to occur until more helium is collected or till the critical radius is changed by some other factor. That factor appears to have been identified in that fairly large scale micro-oscillations in composition have been found to be developing in this specimen due to irradiation.[6-8] This process eventually leads to volumes poor in nickel and rich in chromium, two conditions which both decrease D_v^0 and encourage bubble-to-void conversion.[4]

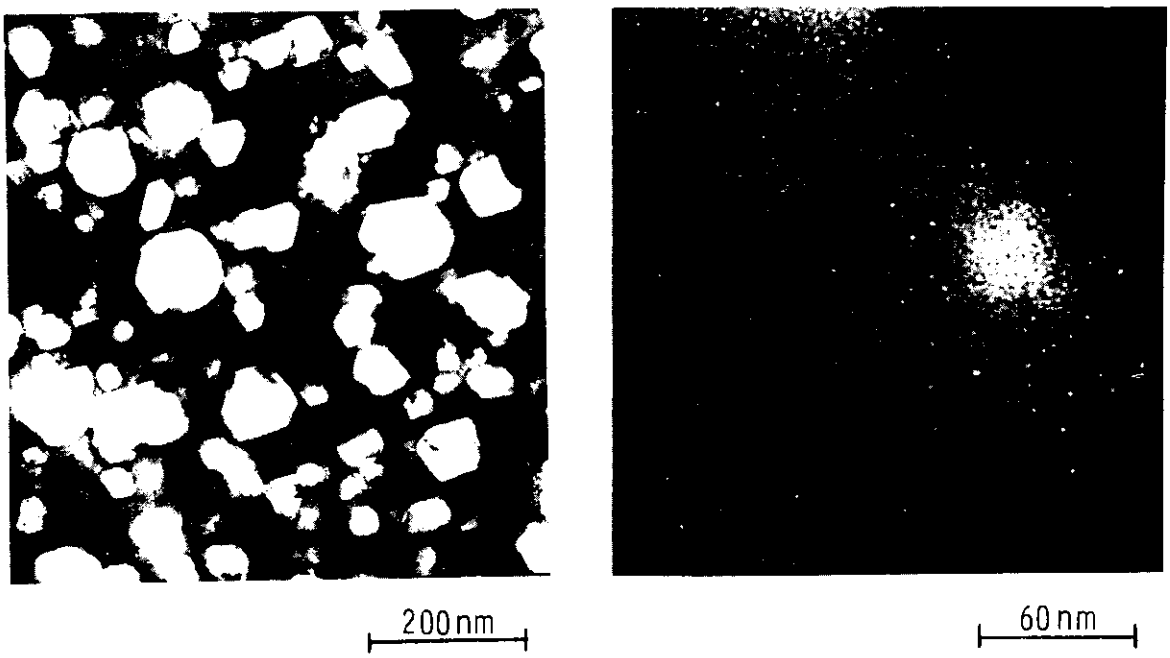

Fig. 9. Voids and late-term bubbles observed in HFIR irradiation of annealed AISI at 480°C and ~45 dpa.[29] The bubbles between the larger voids exist at a density of ~1.7 x 10^{17} cm^{-3}.

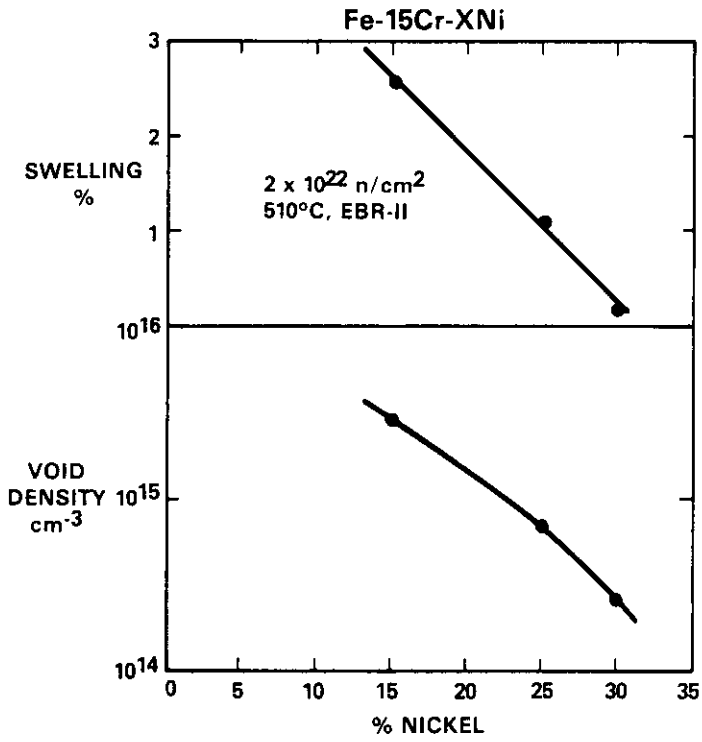

Fig. 10. Dependence of swelling and void density on nickel content observed in Fe-15Cr-XNi alloys at 510°C to 10 dpa in EBR-II.[15]

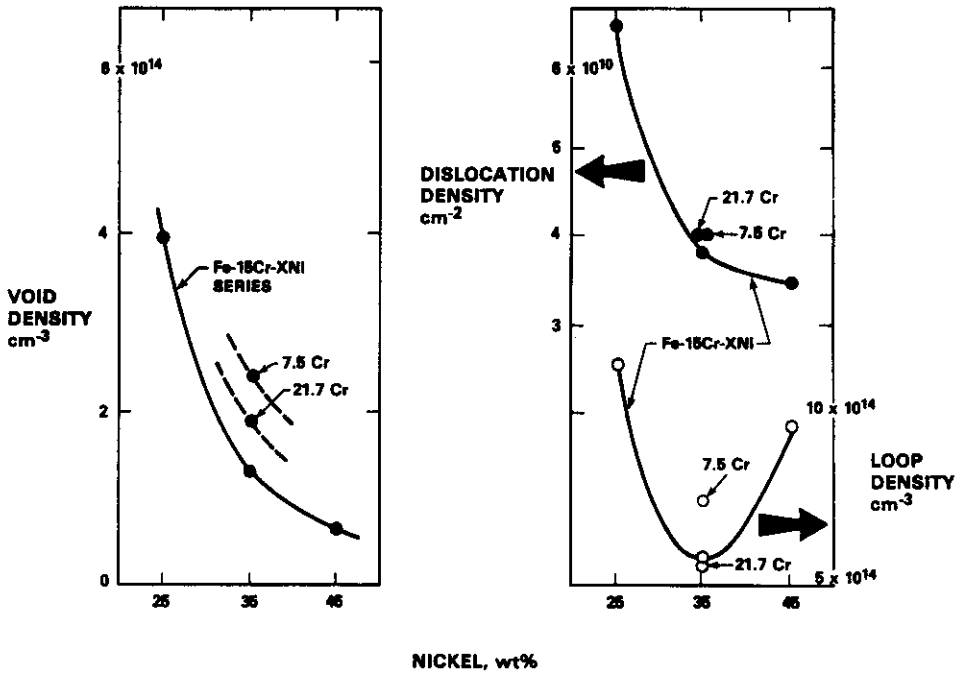

Fig. 11. Dependence of microstructural evolution in Fe-Ni-Cr alloys as a function of nickel and chromium content at 450°C and 12.5 dpa in EBR-II.[30]

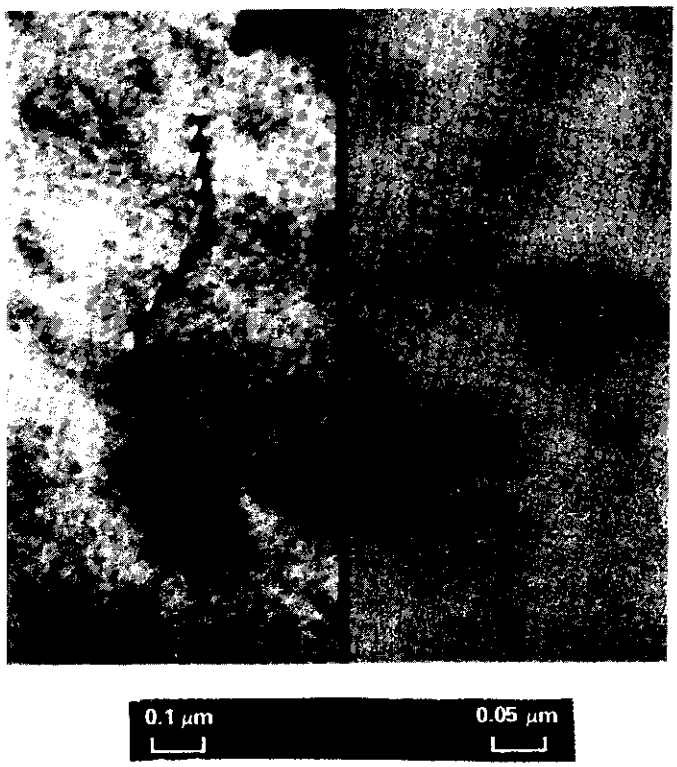

Fig. 12. Micrographs of Fe-35.5Ni-7.5Cr after irradiation to 7.6 x 10^{22} n/cm^2 (E > 0.1 MeV) at 593°C, showing a very low density of dislocations, an absence of Frank dislocation loops and a high density ($\sim 10^{16}$ cm^{-3}) of small cavities assumed to be helium bubbles.[6]

CONCLUSIONS

There are two temperature regimes of void nucleation which can be explained in terms of the critical radius concept. In the first regime r_c^* is relatively insensitive to temperature and is relatively small. At higher temperatures the minimum critical radius becomes exceptionally sensitive to temperature and increases rapidly. Two variables which affect the transition point between regimes of different temperature sensitivity are the displacement rate and the effective vacancy diffusion coefficient. The preexponential coefficient D_v^0 for vacancy self-diffusion is known to be moderately dependent on nickel content. This dependence on nickel content appears to be sufficient to explain the major features of the differences in void nucleation rate and minimum critical radius observed in Fe-15Cr-15Ni and Fe-15Cr-35Ni during ion irradiation at 675°C. It also appears to explain the observation of subcritical bubbles in neutron irradiated Fe-7.5Cr-35.5Ni which fail to grow at a lower temperature (593°C) and a much lower displacement rate.

FUTURE WORK

This effort will continue with the primary effort directed toward the effect of phosphorus and other minor elements on the critical radius of both austenitic and ferritic alloys.

REFERENCES

1. F. A. Garner and W. G. Wolfer, J. Nucl. Mater., 102, 143-150 (1981).

2. F. A. Garner and W. G. Wolfer, J. Nucl. Mater., 122/123, 201-205 (1984).

3. B. Esmailzadeh and A. Kumar, pp. 468-480 in Effects of Radiation on Materials: Twelfth International Symposium, ASTM STP 870, F. A. Garner and J. S. Perrin, Eds., ASTM, Philadelphia, PA, 1985.

4. F. A. Garner and A. Kumar, this report.

5. F. A. Garner and H. R. Brager, J. Nucl. Mater., 133/134, 511-514 (1985).

6. H. R. Brager and F. A. Garner, pp. 139-150 in Effects of Radiation on Materials: Twelfth International Symposium, ASTM STP 870, F. A. Garner and J. S. Perrin, Eds., ASTM, Philadelphia, PA, 1985.

7. F. A. Garner, H. R. Brager, R. A. Dodd and T. Lauritzen, Nuclear Instruments and Methods in Physics Research B16, 244-250 (1986).

8. F. A. Garner, H. R. Brager and J. M. McCarthy, to be published in Proceedings of 13th International Symposium on Effects of Radiation on Materials, June 23-25, 1986, Seattle, WA.

9. R. A. Dodd, F. A. Garner, J. -J. Kai, T. Lauritzen and W. G. Johnston, ibid.

10. E. H. Lee and L. K. Mansur, Phil. Mag. A, 52, 493-508 (1985).

11. W. A. Coghlan and L. K. Mansur, J. Nucl. Mater., 122/123, 495-501 (1984).

12. W. A. Coghlan and L. K. Mansur, pp. 481-492 in Effects of Radiation on Materials: Twelfth International Symposium, ASTM STP 870, F. A. Garner and J. S. Perrin, Eds., ASTM, Philadelphia, PA, 1985.

13. D. J. Mazey and R. S. Nelson, J. Nucl. Mater., 85/86, 671-675 (1979).

14. L. L. Horton and L. K. Mansur, pp. 345-361 in Effects of Radiation on Materials: Twelfth International Symposium, ASTM STP 870, F. A. Garner and J. S. Perrin, Eds., ASTM, Philadelphia, PA, 1985.

15. F. A. Garner and H. R. Brager, ibid, pp. 187-201

16. H. Trinkhaus and L. K. Mansur, to be published.

17. N. V. Tsederberg, V. N. Popov, and N. A. Morozova, "Thermodynamic and Thermophysical Properties of Helium," Israel Program for Scientific Translations, Keter Press, Jerusalem, 1971, p. 18-19.

18. H. Rauh and R. Bullough, Phil. Mag. 52A, 333-356 (1985).

19. D. Dulien and J. Nutting, Iron and Steel Institute Special Report No. 86, 140 (1964).

20. E. A. Kenik, Scripta Met. 10, 733 (1976).

21. E. A. Kenik, "Measurements of Equilibrium and Non-equilibrium Segregation by X-Ray Microanalysis," Accepted for publication in the Proceedings of the MRS Symposium on Materials Problem Solving with Transmission Electron Microscopy, Boston, Mass., Dec. 1985.

22. N. Q. Lam, P. R. Okamoto and H. Wiedersich, J. Nucl. Mater., 74, 101 (1978).

23. L. E. Thomas, Proc. 38th Annual Meeting of the EMSA Society of America, (1982) Washington, D.C., Claitors, pp. 594-597.

24. Y. A. Chang, F. A. Garner and Ying-Yu Chuang, to be published.

25. L. Boulanger, J. Nucl. Mater., 89, 129-135 (1980).

26. L. J. Chen and A. J. Ardell, Phys. Stat. Sol. A, 34, 679-690 (1976).

27. E. A. Kenik, Ph. D. Thesis, Case Western Reserve Univ., Cleveland, Ohio, 1974.

28. G. Das and T. E. Mitchell, J. Nucl. Mater., 56, 297 (1975).

29. H. R. Brager and F. A. Garner, J. Nucl. Mater., 117, 159-176 (1983).

30. H. R. Brager, F. A. Garner and M. L. Hamilton, J. Nucl. Mater., 133/134, 594-598 (1985).

THE INFLUENCE OF PHOSPHORUS ON THE NEUTRON OR ION-INDUCED SWELLING OF Fe-Cr-Ni ALLOYS - F. A. Garner (Westinghouse Hanford Company)

OBJECTIVE

The object of this effort is to 1) determine the effect of phosphorus on radiation-induced swelling, creep and microstructural development and 2) explore the interaction of phosphorus with other important factors such as the displacement rate, the helium/dpa ratio, the concentration of other minor solute elements and the identity of the damage-producing particle.

SUMMARY

A recent ion bombardment study has called into question a fundamental assumption used to design a Ni^{59} isotopic tailoring experiment. This assumption involves the synergistic roles of phosphorus and helium in void nucleation and therefore the assumption was tested by analysis of the results of an earlier irradiation experiment. Neutron irradiation of Fe-25Ni-15Cr with three different phosphorus levels was found to yield density changes which support the design assumption. Based on the role proposed for phosphorus an alternative explanation is also offered to describe the results of the ion bombardment experiment. It appears that ion bombardment experiments may not be suitable for the simulation of the influence of phosphorus on neutron-induced microstructural development.

PROGRESS AND STATUS

Introduction

Phosphorus has been shown to be much more effective per atom than other solutes in suppressing the onset of radiation-induced creep and swelling of AISI 316 stainless steel, both when increased alone[1-3] or when phosphorus and silicon are simultaneously increased.[4] As shown in Figs. 1 and 2 recent neutron-induced swelling studies on phosphorus effects have proceeded primarily on AISI 316 steels which contain significant levels of silicon, titanium and zirconium.

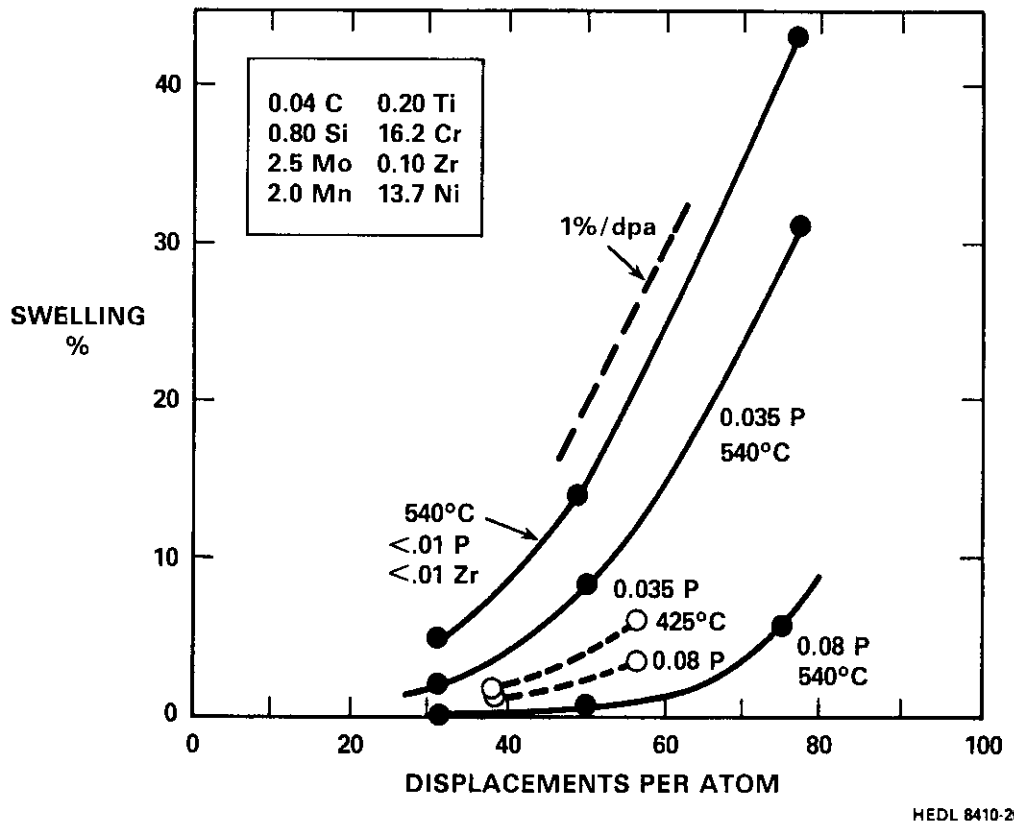

Fig. 1. Effect of phosphorus and irradiation temperature on swelling of annealed AISI 316 with 0.80 wt.% silicon in EBR-II.[3] The compositions shown are in weight percent.

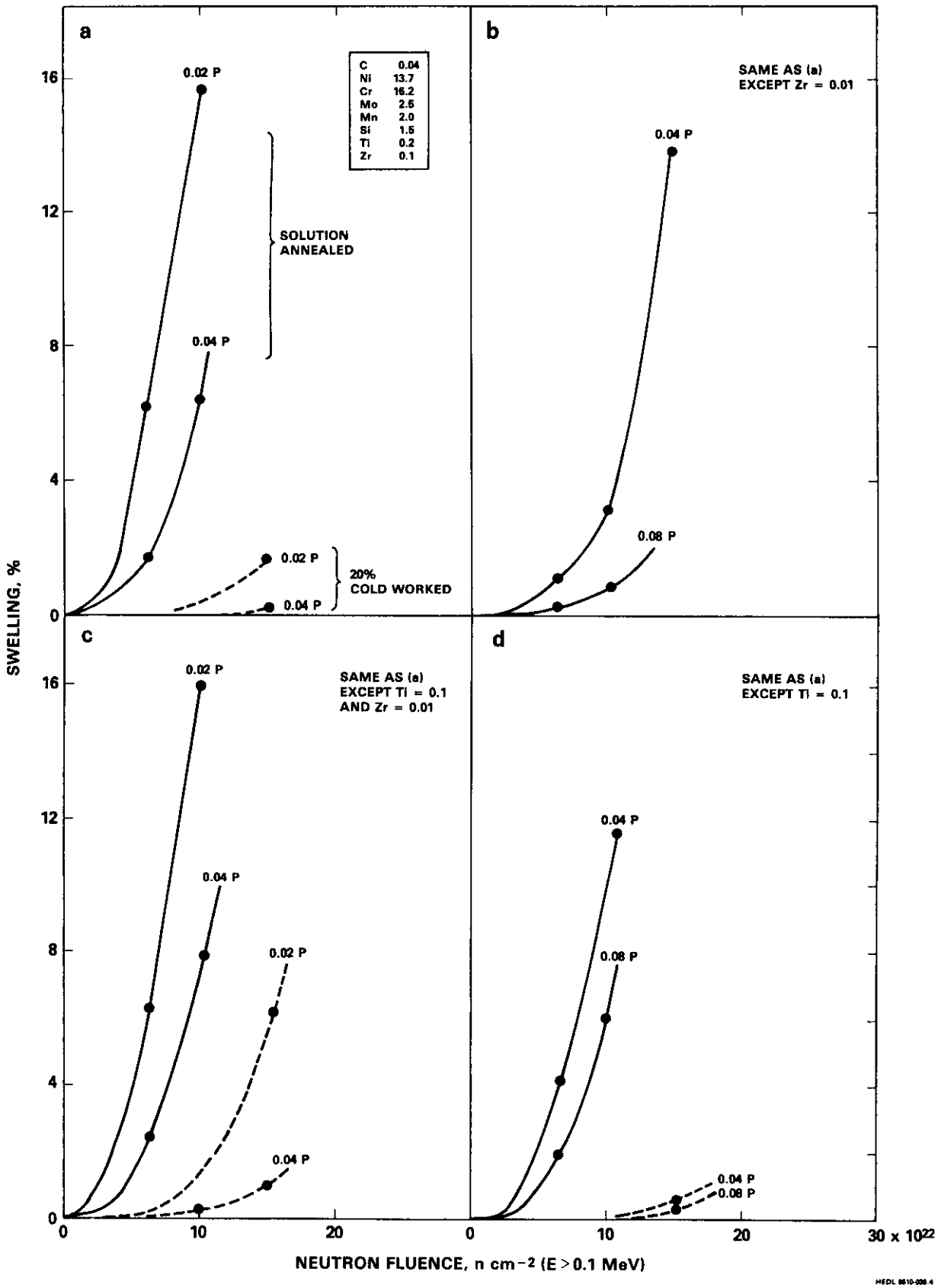

Fig. 2. Effect of phosphorus, titanium, zirconium and cold work on swelling of AISI 316 with 1.5 wt.% silicon after irradiation at 540°C in EBR-II. These data were derived from the same experiment that produced the data in Fig. 1, but have not been previously published.

However, a recent study by Lee and Mansur using 4.0 MeV Ni^+ ion bombardment at 675°C showed that the single addition of 0.05 wt.% phosphorus to the ternary alloy Fe-15Ni-13Cr did not significantly affect swelling at 86-95 dpa.[5] This study also concluded that the suppression usually attributed to phosphorus was only observed when other phosphide precipitate-forming elements such as titanium (0.18 wt.%) or silicon (0.84 wt.%) were added. (Carbon at 0.04 wt.% was also added in the alloys containing titanium). The studies cited earlier[1-4] all involved alloys which contained moderate-to-high levels of silicon and carbon and some contained titanium levels in the range explored in the ion bombardment study of Lee and Mansur. If we accept these ion bombardment results as being representative of neutron-induced behavior, then our previous perception[3] of the role of phosphorus would be incorrect. Such a misperception would also strongly influence the interpretation of the results of other on-going irradiation experiments.

There is doubt in the mind of this author, however, that one can dismiss the action of phosphorus when operating alone based solely on the results of Lee and Mansur. First of all, there are neutron data which support the previous perception and as will be discussed later, there are a number of reasons to suspect the ion results to be unrepresentative of neutron-induced swelling.

The best test of the role of phosphorus and its interactions with other variables would be to conduct the irradiation using a uniform neutron irradiation field and bulk material. This would avoid the influence of both displacement gradients and free surfaces and the additional influence of the injected interstitial associated with self-ion bombardment.[6] However, it would not address the potentially synergistic effects of phosphides and helium that were also explored by Lee and Mansur, since the helium/dpa ratio is usually fixed by the composition of the alloy and the neutron spectrum.

There is an experiment now in progress in FFTF-MOTA, however, which can be used to address the role of phosphorus in the absence of these other solutes and also address the synergistic effect of helium. However, this experiment (described in Table 1) employs a higher nickel level (Fe-25Ni-15Cr) than explored in previous experiments on phosphorus effects. In this experiment each of Fe-25Ni-15Cr and Fe-25Ni-15Cr-0.04P have been prepared in two conditions.[7] The first utilizes the natural isotopic distribution of nickel and the second employs the addition of the radiosotope Ni^{59} to enhance the helium/dpa ratio. This experiment also investigates the separate and synergistic effects of increasing both the nickel level (Fe-45Ni-15Cr) and the helium/dpa ratio, but does not explore the role of phosphorous at the 45% nickel level. The Fe-45Ni-15Cr alloy is expected to develop a spinodal-like decomposition observed in other experiments[8-10] and thought to be related to the break-down of swelling resistance of Fe-Ni binary and Fe-Cr-Ni ternary alloys at higher nickel levels.[9,10] The interaction of the decomposition and helium influence is of particular interest for development of low swelling alloys for fusion applications.

Table 1. Irradiation parameters for the ^{59}Ni enriched ternary alloys[7]

MOTA Level	MOTA Irrad. Cycles	Temp. (°C)	Dose (dpa)	hpa/dpa (appm/dpa)	hpa* (appm)	Initial hpa/dpa Enhancement**
6E2	1	490	2.2	11	24	150
	2		4.4		48	
	4		8.8		97	
5D1	1	600	8.8	8	70	22
	2		18		144	
	4		35		280	
Below Core Canister	1	360	5.2	11	57	113
	2		10		110	
	4		21		231	
8E1	1	450	0.19	33	6	50
	2		0.38		13	
	4		0.76		25	

*hpa = helium per atom.

**This column describes the enhancement of helium expected between the three alloys enriched in Ni^{59} compared to the three alloys without the isotope.

While the first exposure level of this experiment has been attained and the specimens removed from reactor, it will be about a year before these alloys can be examined. However, we can address the issue of whether simple addition of phosphorus is sufficient in itself to depress swelling in Fe-25Ni-15Cr, using another previously unpublished irradiation experiment conducted in 1976-1977.

Experimental details

In an experiment designated AA-IX and described in Table 2, Fe-25Ni-15Cr was irradiated in Row 2 of EBR-II with three separate phosphorus levels (0.013, 0.055 and 0.10 wt.%). These alloys were part of an experiment designed to explore the influence of residual solute elements and contained negligible levels of Si, Ti, Zr, Mo and other important solutes. The neutron exposures ranged from 1.63 to 2.86 x 10^{22} n/cm^2 (E > 0.1 MeV), causing damage levels of 8.2 to 14.3 dpa. There were eight nominal irradiation temperatures which varied from 399 to 649°C. The alloys were irradiated as small microscopy disks (3 mm diameter, 0.25 mm thick) in the annealed condition (1030°C/0.5 hr/air cool) in sodium-filled subcapsules. The temperatures drifted somewhat during irradiation, varying ±5°C at 400°C and ±15°C at 650°C. The swelling was measured by an immersion density technique accurate to ±0.16%.

Table 2. Description of the phosphorus alloy series irradiated in the AA-IX experiment in EBR-II

Alloy Code	Composition, wt.%
E103	Fe-24.65Ni-14.34Cr-0.01Mn-0.005C-0.0027N_2-0.0129O_2-0.013P
E104	Fe-25.20Ni-15.05Cr-0.01Mn-0.004C-0.0025N_2-0.0136O_2-0.055P
E105	Fe-25.35Ni-15.00Cr-0.02Mn-0.007C-0.0021N_2-0.0157O_2-0.10P

Condition: Annealed (1030°C/0.5 hr/air cool)

Irradiation Conditions		
Design Temperatures, °C	Fluence (10^{22} n/cm^2, E > 0.1 MeV)	dpa*
399	1.63	8.2
427	2.23	11.2
454	1.89	9.5
482	2.37	11.9
510	2.63	13.2
538	2.73	13.6
593	2.86	14.3
649	2.86	14.3

*Calculated assuming 5.0 dpa per 10^{22} n cm^{-2} (E > 0.1 MeV).

Results

As shown in Fig. 3 phosphorus additions to Fe-25Ni-15Cr suppress swelling at 399 and 427°C at exposures of 8.2 and 11.2 dpa, respectively. At temperatures above 427°C the swelling falls quickly and the effect of phosphorus on the net density change is more complex. Doan and Goldstein[11] have investigated the Fe-Ni-P phase equilibrium to temperatures as low as 550°C and show that both the α and phosphide phases form in this composition and temperature regime. Unfortunately, we have no previous experience with phosphide or α-phase formation at these nickel and chromium levels to allow us to separate the volume changes associated with phase instabilities from those due to voids. Microscopy is required for this purpose.

The uniformity of the six curves at temperatures ≥454°C leads us to suspect that the observed density changes reflect the following contributions. First, swelling decreases with temperature and increases with fluence, trends well established at all three phosphorus levels. Second, there is a decrease in void swelling with phosphorus additions that is offset by phase-related density changes which appear to lead to a net increase in volume. Third, the solubility limit for phosphorus increases with temperature,[12,13] such that fewer α or phosphide precipitates form. Thus, the net density change at higher temperatures is relatively independent of the phosphorus level and approaches zero.

Discussion

The data at 399 and 427°C clearly show that phosphorus additions can suppress swelling in Fe-25Ni-15Cr in the absence of other solutes such as Ti, Si and Zr. Thus the conclusion of Lee and Mansur on the role of phosphorus cannot be taken to apply in general to all material and irradiation conditions. Until we perform microscopy on the specimens irradiated at higher temperatures, however, we cannot on the basis of these data alone exclude the possibility that their conclusion may apply at higher temperatures, such as the 675°C used in their experiment.

Before addressing the disparity between the results of the neutron irradiation and those of the ion study of Lee and Mansur, we should examine the roles played by phosphorus in microstructural evolution during irradiation. We have earlier shown that very small amounts of phosphorus have a pronounced effect on the migration and equilibrium concentration of vacancies, leading to a strong suppression of void nucleation via a reduction in the vacancy supersaturation.[3] This suppression is partially the consequence of the higher diffusivity of phosphorus[14] but primarily represents the very large binding energy (0.4 eV) of phosphorus with vacancies, as measured in Fe-14Ni-18Cr by positron annihilation.[15,16] This primary influence of phosphorus is thus directed toward its role while in solution. The action of phosphide precipitates is considered to be secondary, with the exception that phosphorus additions have been found to delay the removal of nickel and silicon from solution and into precipitates.[3] These elements (especially silicon) are also known to have a large effect on void nucleation while in solution.[17-19]

In a recent paper Itoh and coworkers[20] have shown in a variety of neutron-irradiated 316 stainless steels that phosphorus exerts its major influence while in solution and not after precipitation. Phosphorus in solution was found by Itoh to retard the recovery of dislocations in cold-worked steels and the development of Y and G-phase precipitates. These precipitates form by concentrating nickel and silicon from the matrix. This delay in microchemical evolution of the matrix occurs despite the fact that the phosphide phase is in itself rich in nickel and silicon as observed by Itoh and coworkers,[20] Lee and coworkers[21] and Yang.[22] However, the amount of phosphide formed and its associated removal of nickel and silicon is limited by the small amount of phosphorus available. Itoh and coworkers did not address the nature of the interaction of phosphorus and vacancies but cited the work of Garner and Brager[3] as a possible explanation.

The studies and theories of Lee and coworkers[4,5,21,23,24] do not recognize a role for phosphorus while in solution but are directed primarily toward its role as a precipitate-former. The precipitates are postulated to increase the sink density for point defects and serve as nucleation sites for stable helium bubbles which are too small to easily grow into voids.

In a more recent study[19] Garner and Kumar have expanded on the role of phosphorus while in solution. They show that phosphorus affects the vacancy supersaturation that provides the driving force for void nucleation, but does so in a manner which is fundamentally different from the action of nickel and silicon. As we shall see later, this difference may also account for the disparity of results obtained from neutron and ion irradiation studies.

Whereas nickel and silicon affect the pre-exponential term D_0 of the vacancy diffusion coefficient and thereby reduce the concentration C_v of vacancies during irradiation, phosphorus primarily affects C_{vo}, the equilibrium concentration of thermally-produced vacancies.[3,19] A change in nickel level thus exerts roughly the same percentage increase in vacancy diffusivity and decrease in vacancy super-saturation (C_v/C_{vo}) at all temperatures and displacement rates. Silicon behaves in a similar manner, but is more effective than nickel on a per-atom basis. Phosphorus, however, exerts an even stronger influence per atom, but operates primarily on the thermal vacancy concentration. Its influence increases only until its solubility limit is reached, however, and the solubility limit falls strongly as a function of declining temperature. Below the solubility limit the effect is roughly proportional to the percentage of solubility and not the total phosphorus level. Therefore, a given level of phosphorus can exert different effects on the vacancy supersaturation at different temperatures. The maximum effect of phosphorus at any temperature is to reduce the supersaturation by almost exactly an order of magnitude.[19]

Fig. 4 illustrates the impact of the temperature and solubility dependence of phosphorus on the neutron and ion studies discussed in this report. (We must assume in this analysis that the solubility of phosphorus is not strongly affected by the presence of 15% chromium, since data are available only for the Fe-Ni-P system). In the neutron study the Fe-15Cr-25Ni-0.013P alloy is undersaturated at all irradiation temperatures, the Fe-15Cr-25Ni-0.055P alloy is undersaturated only above ~500°C and the Fe-15-25Ni-0.10P alloy is under-saturated only above ~600°C. Thus the maximum effect of phosphorus on vacancy supersaturation is maintained throughout much of the experimental matrix of the neutron study as shown in Fig. 4b. At this point we cannot factor into the analysis the possible effects of radiation-induced segregration on solubility.

The ion experiment of Lee and Mansur was conducted at 675°C and 0.055 wt.% phosphorus. As shown in Fig. 4a this is a condition which represents only 25% of the solubility limit, illustrating a possible short-coming of charged particle studies which are traditionally conducted at very high displacement

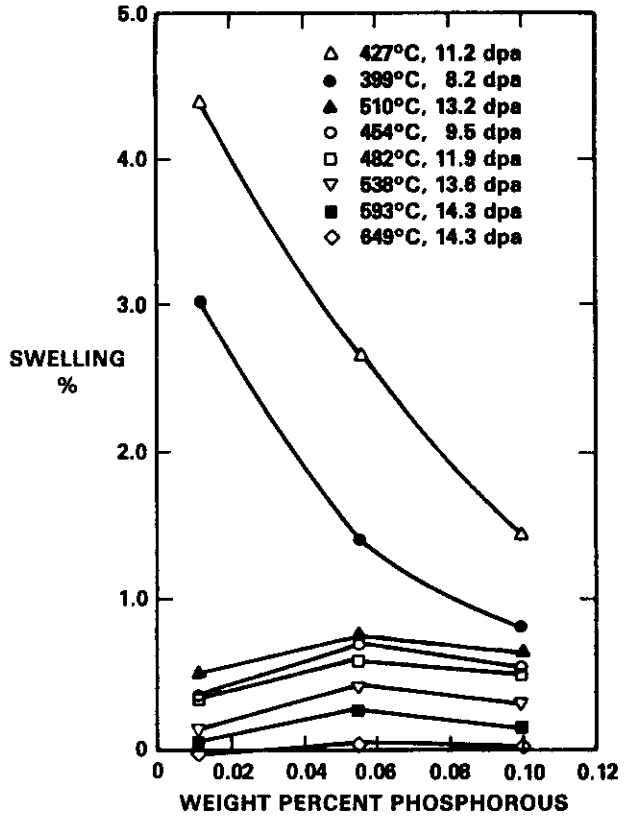

Fig. 3. Effect of phosphorus and temperature on the swelling of Fe-25Ni-15Cr during irradiation in the AA-IX experiment in EBR-II.

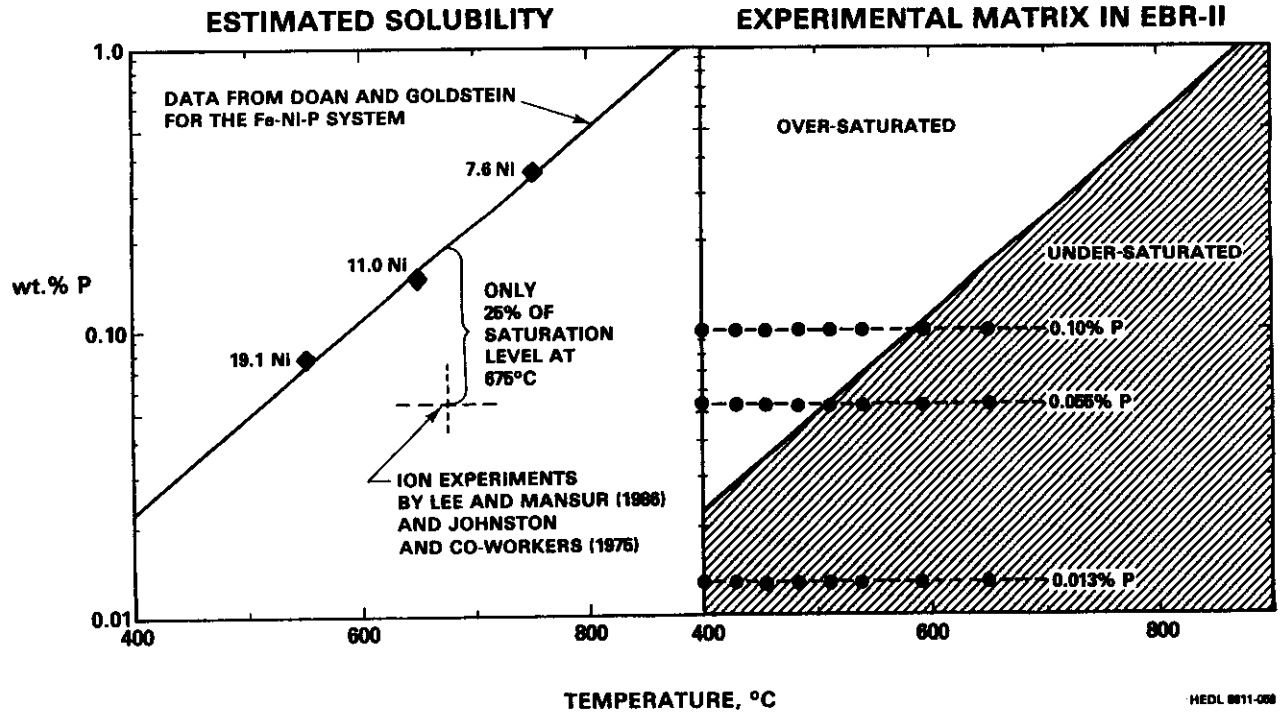

Fig. 4. Solubility-based analysis of phosphorus effects on vacancy concentrations in Fe-Ni-P alloys. The solubility vs. temperature curve is plotted from the points where the four phase fields meet (γ, $\gamma + \alpha$, $\gamma + \alpha$ + phosphide, γ + phosphide) as described by Doan and Goldstein.[11] The nickel level for each four-phase point is shown, but the solubility of phosphorus in the γ phase does not change very much with increasing nickel level.

rates. This requires irradiation temperatures which must be higher by 100-150°C to account for the well-known "temperature-shift" effect. In effect the temperature shift guarantees that the role of phosphorus in ion irradiations will be strongly reduced relative to that of typical neutron irradiations.

It is doubtful, however, that this is the only shortcoming of such an experiment. The combined action of the higher diffusivity of phosphorus and its strong binding with vacancies will most likely cause it to couple with the large gradients in vacancy concentration associated with the use of 4.0 MeV Ni^+ ions as well as the additional strong influence of the surface at 675°C. The latter effect has been shown analytically to be very large at $\geq$625°C by Bullough and Haynes[25] and by the analysis of denunded zone data by Garner and Laidler.[26]

There is a large amount of evidence that shows that such coupling will lead to rapid depletion of elements which bind with vacancies or interstitials.[27-30] Due to the particularly strong binding of phosphorus with vacancies, much of the phosphorus in the ion-bombarded Fe-15Ni-13Cr-0.055P alloy may have been depleted in the peak damage region before it could exert its full influence on void nucleation. This would give the erroneous impression that phosphorus had very little effect, even less than anticipated at the 25% solubility level.

If this assessment of the ion experiment is correct, one must address the issue of why phosphorus, when combined with either silicon and/or titanium, appeared to lead to void suppression in the ion bombardment experiment. Whereas Lee and Mansur attribute this directly to the present of phosphides, it must be pointed out that they did not demonstrate the separate influence of silicon and titanium in the absence of phosphorus. Both of these elements are known to strongly affect swelling in neutron irradiation experiments.

Based on this one short-coming alone, the ion experiment of Lee and Mansur must be considered inconclusive with respect to its conclusion about the single role of phosphorus. Using the same bombardment facility, Gessel and Rowcliffe have shown large effects of both silicon and titanium on the swelling of Fe-7.5Cr-20Ni-0.002P at 170 dpa in the range 500-730°C.[31] Johnston and coworkers have also shown that the separate and synergistic effects of silicon and titanium are very large on the swelling of Fe-15Cr-20Ni at 116 dpa using 5 MeV Ni^+ ions.[32] Interestingly, they also found that addition of 0.05 wt. % phosphorus did not reduce swelling at 675°C. In fact, the step height produced by swelling was actually somewhat larger in the alloy containing phosphorus.

There are other factors which may be operating in ion-bombarded specimens containing silicon and titanium. First, Marwick and co-workers have shown that silicon and titanium additions impede the redistribution process that occurs during ion bombardment.[33,34] This is accomplished via their own interactions with point defects, reducing the defect concentrations available for redistribution of other solutes. Second, silicon and titanium probably change the solubility of phosphorus, the consequences of which are unknown in this experiment. (The 0.4% carbon added with the titanium probably also affects the solubility of phosphorus). Third, the enhanced formation of phosphide precipitates by silicon, titanium and carbon will interpose a high density of alternate sinks for phosphorus and impede its migration down the vacancy gradients and to the surface.

The net effect of these and the preceding considerations is to cast considerable doubt on the validity of ion bombardment experiments directed toward the study of the role of phosphorus on microstructural evolution. The neutron-induced swelling data clearly show a response to phosphorus not found in the ion studies of Lee and Mansur or that of Johnston and coworkers.

Returning to our original purpose of this investigation, remember that the Ni^{59} experiment was designed in part on the assumption that phosphorus plays a role in swelling suppression without requiring the assistance of other solutes. Based on the results of the EBR-II study (and the higher displacement rate of FFTF compared with that of EBR-II) it appears safe to predict that the two low temperature MOTA canisters (360, 450°C) will yield results which reflect the validity of this assumption. At this point, however, we cannot on the basis of the data in Fig. 3 alone make a similar fully confident statement about the two high temperature canisters (490, 600°C). Data at higher fluence are required before such a statement can be made.

CONCLUSION

Phosphorus plays a strong role in void nucleation and swelling of neutron-irradiated Fe-Cr-Ni alloys even when unaccompanied by other solute elements such as silicon or titanium. Based on the proposed role of binding with vacancies it is anticipated that the influence of phosphorus during neutron irradiation cannot be realistically simulated using ion bombardment studies which employ ions of shallow penetration and thus proceed at higher displacement rates and subsequently higher "shifted" temperatures. The influence of phosphide precipitates as nucleation sites for helium bubbles has not been addressed in this report and awaits the examination of the isotopic tailoring experiment using the Ni^{59} isotope.

FUTURE WORK

The specimens discussed in this report will be retrieved from storage and microscopy performed on them. A search for specimens irradiated to higher fluence will also be pursued and if successful, the specimens will be measured using immersion density. The first discharge of the Ni^{59} experiment from MOTA-FFTF has occurred and the synergistic effects of phosphorus, helium and nickel will be examined as the specimens become available. The effect of phosphorus on thermal creep and radiation creep will also be analyzed.

REFERENCES

1. J. F. Bates, R. W. Powell and E. R. Gilbert, p. 713 in Effects of Radiation on Materials: Tenth Conference, ASTM STP 725, D. Kramer, H. R. Brager, J. S. Perrin, Eds., 1981.

2. M. Terasawa et al., p. 687 in Proceedings Conference on Radiation Effects in Breeder Reactor Structural Materials, Scottsdale, AZ, M. L. Bleiberg and J. W. Bennett, Eds., TMS-AIME, June 19-23, 1977.

3. F. A. Garner and H. R. Brager, J. Nucl. Mater., 133/134, 511 (1985).

4. E. A. Lee, L. K. Mansur and A. F. Rowcliffe, J. Nucl. Mater., 122/123, 299 (1984).

5. E. H. Lee and L. K. Mansur, accepted for publication in J. Nucl. Mater.

6. F. A. Garner, J. Nucl. Mater., 117, 177 (1983).

7. R. L. Simons, "Isotopic Tailoring with Nickel-59 to Enhance Helium Production in Fission Reactor Irradiations," p. 19 in Damage Analysis and Fundamental Studies Quarterly Progress Report, DOE/ER-0046/21, U.S. Department of Energy, Office of Fusion Energy, May 1985.

8. H. R. Brager, F. A. Garner and M. L. Hamilton, J. Nucl. Mater., 133/134, 594 (1985).

9. F. A. Garner, H. R. Brager, R. A. Dodd and T. Lauritzen, Nucl. Instr. and Meths. in Physics Research, B16, 244 (1986).

10. F. A. Garner and H. R. Brager, p. 87 in Optimizing Materials for Nuclear Applications, F. A. Garner, D. S. Gelles and F. W. Wiffen, Eds., The Metallurgical Society Inc. Warrendale, PA, 1985.

11. A. S. Doan, Jr. and J. I. Goldstein, Met. Trans., 1, 1759 (1970).

12. D. C. Dean and J. I. Goldstein, Met. Trans. A, 17A, 1131 (1986).

13. T. R. Heyward and J. I. Goldstein, Met. Trans., 4, 2335 (1973).

14. H. Oikawa, Technical Reports, Tohoku University, 47, No. 2, 215 (1982); 48, No. 1, 7 (1983).

15. A. Azarian and K. Kheloufi, J. Nucl. Mater., 97, 25 (1981).

16. A. Azarian, Doctoral Thesis, University of Paris (1974).

17. F. A. Garner, J. Nucl. Mater., 122/123, 459 (1984).

18. F. A. Garner and W. G. Wolfer, J. Nucl. Mater., 122/123, 201 (1984).

19. F. A. Garner and A. S. Kumar, to be published in Proceedings of 13th International Symposium on Effects of Radiation on Materials, June 23-25, 1986, Seattle, WA, also in this semiannual report.

20. M. Itoh, S. Onose and S. Yuhara, ibid.

21. E. H. Lee, P. J. Maziasz and A. F. Rowcliffe, p. 191 in Phase Stability During Irradiation, J. R. Holland, L. K. Mansur and D. I. Potter, Eds., The Metallurgical Society of AIME, Warrendale, PA, 1981.

22. W. J. S. Yang, Precipitate Evolution in 316 Type Stainless Steels Irradiated in EBR-II, in Proceedings of 13th International Symposium on Effects of Radiation on Materials, June 23-25, 1986, Seattle, WA.

23. L. K. Mansur, M. H. Haynes and E. H. Lee, J. Nucl. Mater., 103/104, 359 (1981).

24. A. D. Brailsford and L. K. Mansur, ibid, 1403 (1981).

25. R. Bullough and M. R. Haynes, J. Nucl. Mater., 68, 286 (1977).

26. F. A. Garner and J. J. Laidler, p. 177 in Proceedings of Workshop on Correlation of Neutron and Charged Particle Damage, CONF-760673, 1976.

27. N. Q. Lam, J. Nucl. Mater., 117, 106 (1983).

28. N. Q. Lam and P. R. Okamoto, p. 403 in Effects of Radiation on Materials: Twelfth International Conference, ASTM STP 870, F. A. Garner and J. S. Perrin, Eds., 1985.

29. A. D. Marwick, R. C. Pillar and M. E. Horten, p. 11 in Dimensional Stability and Mechanical Behaviour of Irradiated Metals and Alloys, Vol. 2, British Nuclear Energy Society, London, 1984.

30. F. Rotman, D. Gilbon, H. Lorant and O. Dimitrov, in Proceedings International Conference on Vacancies and Interstitials in Metals and Alloys, Berlin, Germany, September 14-19, 1986 (in press).

31. G. R. Gessel and A. F. Rowcliffe, p. 431 in Radiation Effects In Breeder Reactor Structural Materials, M. L. Bleiberg and J. W. Bennett, Eds., TMS-AIME, 1977.

32. W. G. Johnston, T. Lauritzen, J. H. Rosolowski and A. M. Turkalo, J. Metals, 19 (1976).

33. R. C. Pillar, A. D. Marwick, J. Nucl. Mater., 83, 5 (1979); also 83, 42 (1979).

34. A. D. Marwick, R. C. Pillar, Rad. Eff., 47, 195 (1980).

THE SWELLING OF NICKEL AND NICKEL-CHROMIUM ALLOYS DURING NETURON OR ION IRRADIATION - F. A. Garner (Westinghouse Hanford Company)

OBJECTIVE

The object of this effort is to determine those factors which control the swelling, creep and mechanical properties of irradiated metals.

SUMMARY

Data on the neutron and ion-induced swelling of pure nickel and nickel-chromium alloys are reviewed to test the hypothesis that long or short range ordering will reduce swelling. The concept of order-induced swelling suppression appears to be valid, but the influence of chromium on ordering and swelling of nickel-chromium alloys is complicated by the action of at least one other as-yet-undetermined mechanism. The swelling rate of pure nickel depends on temperature and metal purity, reaching ∿1%/dpa at low temperatures and high purity. Nickel also saturates in swelling at a pace dictated by purity, cold-work level and temperature, while Ni-Cr alloys do not appear to be subject to saturation.

PROGRESS AND STATUS

Introduction

In a series of earlier reports it was shown that the parametric dependence of neutron-induced swelling in Fe-Ni-Cr and Fe-Mn-Cr austenitic alloys lies primarily in the effect of material and environmental parameters on the duration of the transient regime of swelling.[1-3] It was also shown that the post-transient rate of swelling in both of these alloy systems and that of pure nickel was ∿1%/dpa, essentially independent of composition. The dependence of the transient duration on nickel content in Fe-Ni-Cr alloys was explained in terms of the competition between the increase in the effective vacancy diffusion coefficent (which lowers the vacancy supersaturation and decreases the void nucleation rate) and the increasing tendency of Fe-Ni alloys to form short-range and long-range order with increasing nickel content.[3] One manifestation of this tendency toward ordering is the generation of compositional micro-oscillations found in both ion and neutron-irradiated Invar alloys.[4,5] These micro-oscillations tend to destroy the swelling resistance of high nickel alloys by generating relatively large volumes which are enriched in chromium and depleted in nickel, both of which favor void nucleation.[6] Prior to the onset of swelling, however, these micro-oscillations also lead to significant changes in lattice parameter, causing such alloys to densify. Densification is also known to be a general consequence of disorder-order transitions in the Fe-Ni[7] and Ni-Cr systems.[8]

As discussed later, ordered alloys are predicted to resist swelling and irradiation creep. In order to study the possible correlation between swelling resistance and the tendency toward ordering, the isothermal swelling of 85Ni-15Cr in EBR-II was investigated at eight temperatures. (The actual composition in weight percent is 84.9% Ni, 15.1% Cr, 0.002% C, 0.0064% O, and 0.001% N and the temperatures are subject to ±15°C uncertainty.) This model alloy was irradiated as small microscopy disks in the same experiment in the EBR-II fast reactor which contained the Fe-Ni-Cr alloys described earlier.[1-3] Approximately 5 dpa occur in this alloy in EBR-II for an exposure of 1.0×10^{26} n m^{-2} (E > 0.1 MeV). The swelling levels were determined using an immersion density technique accurate to ±0.16%. No microscopy data are available for these specimens since each specimen was returned to the reactor for further irradiation.

Unfortunately, pure nickel was not included in that study for comparison. However, there are published data on the swelling of nickel available from both thermal and other fast reactor irradiations. In addition, there are a number of published ion bombardment studies involving nickel and nickel-chromium alloys. The results of one previously unpublished ion study, and another unpublished neutron study are also available; both are presented in this report.

Results

Fig. 1 shows that the neutron-induced swelling of 85Ni-15Cr in EBR-II is remarkably insensitive to temperature in the range 400-538°C and that the rate of swelling is initially rather low but increases continually with accumulated exposure. Even at 2.0×10^{27} n m^{-2} (E > 0.1 MeV) or ∿100 dpa, however, this alloy has not yet reached the swelling rate of ∿1%/dpa which is characteristic of pure nickel and Fe-Ni-Cr austenitic alloys.[1] Above 538°C the transients are longer, but a reversal occurs, with the transient at 650°C shorter than that at 593°C. Note also that prior to the onset of significant swelling, the density of the alloy at 593 and 650°C increases by ∿0.15%, suggesting that some micro-segregation has probably occurred.

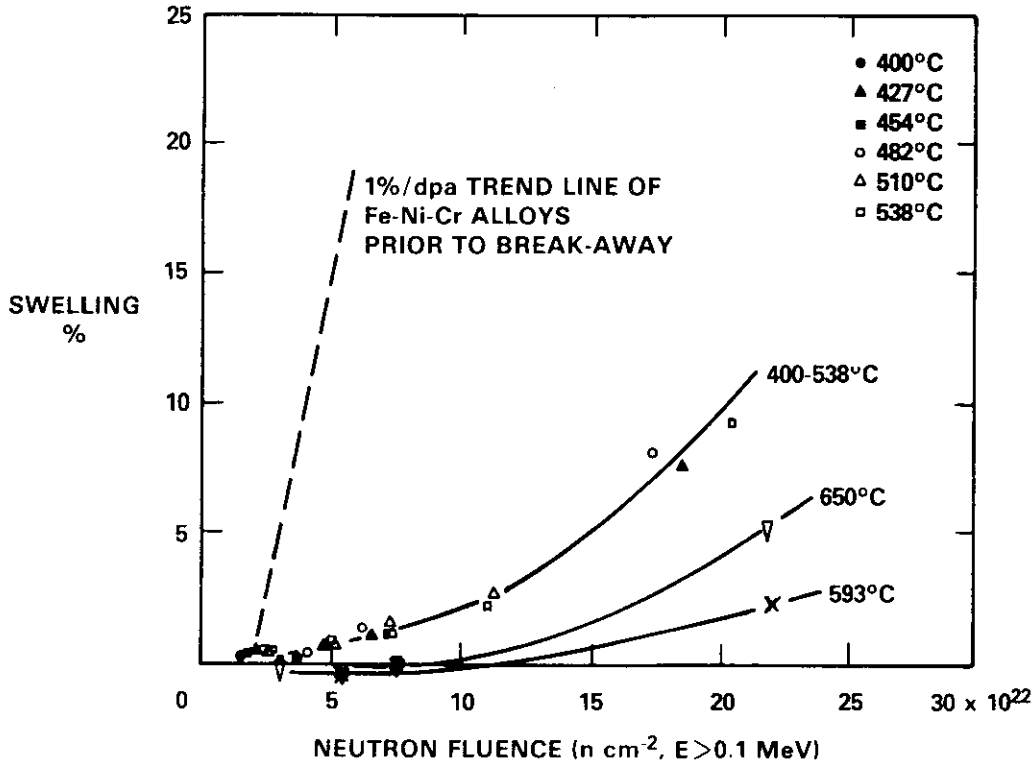

Fig. 1. Swelling of 85Ni-15Cr irradiated in EBR-II, measured by immersion density. Note that 1×10^{26} n m^{-2} (E > 0.1 MeV) yields ~5 dpa in this alloy in EBR-II.

Discussion

There are only limited neutron irradiation data available on the dose dependence of swelling for pure nickel at high displacement levels. Fig. 2 shows that at very low exposure and temperatures in the range 380-450°C the swelling of 99.99% nickel is linear with exposure at ~1%/dpa.[9] A similar linearity was observed by Holmes[10] in EBR-II, but he found the swelling rate to be dependent on the purity of the nickel, as shown in Fig. 3. Fig. 4 shows that for irradiation temperatures in the range of 400-460°C[11-15] nickel of purity >99.9% initially swells at ~1%/dpa but tends to saturate in swelling shortly thereafter. At 500°C saturation sets in much more quickly, however, as shown in Fig. 5, depicting data on 99.8% nickel from the Russian BR-10 reactor.[16] Harbottle has also observed a decreasing rate of swelling in 99.995% nickel during irradiation in the SILOE reactor at 350°C.[7]

Recent data from the Russian BOR-60 reactor shows that in the range 450-550°C the swelling of 99.99% pure nickel reaches only 8 to 9% at 59-65 dpa, as shown in Fig. 6.[18] This suggests that the saturation level is relatively insensitive to temperature. In an unpublished study by Brager and Straalsund[19] relatively impure (99.6%) annealed nickel was found to reach swelling levels in EBR-II at 15-25 dpa and 420-700°C that are consistent with those of pure nickel at comparable temperatures in Figs. 3 and 4. As shown in Fig. 7, there is a slight decline in swelling with temperature in these data suggesting once again that the tendency toward saturation increases with temperature. In contrast to the data of Holmes[10] in Fig. 3 there appears to be an effect of cold work on the swelling behavior in the data of Brager and Straalsund.

The tendency toward saturation at levels below 10% has also been observed in ion and electron irradiation experiments conducted on nickel.[19-24] The relative insensitivity of the saturation level to temperature can be seen in the nickel ion irradiations conducted by several groups. As shown in Fig. 8, Hudson and Ashby, using 45 MeV Ni^+ ions, found that 1-2% swelling was reached in the range 525-700°C at 9 dpa but only 5-7% was reached by 60 dpa.[24] Whereas Pinizzotto and coworkers[25] reached 5-6% swelling with 3.5 MeV Ni^+ ions at 18-20 dpa and 550-600°C, Johnston and coworkers[26] reached only 8-12% with 5 MeV Ni^+ ions in the range 565-675°C.

Since the neutron-induced swelling rate of 85Ni-15Cr is continuously increasing and that of nickel is decreasing, one would expect that pure nickel would swell more at low displacement levels but that 85Ni-15Cr would eventually swell more at higher displacement levels. (This assumes that Ni-Cr alloys do

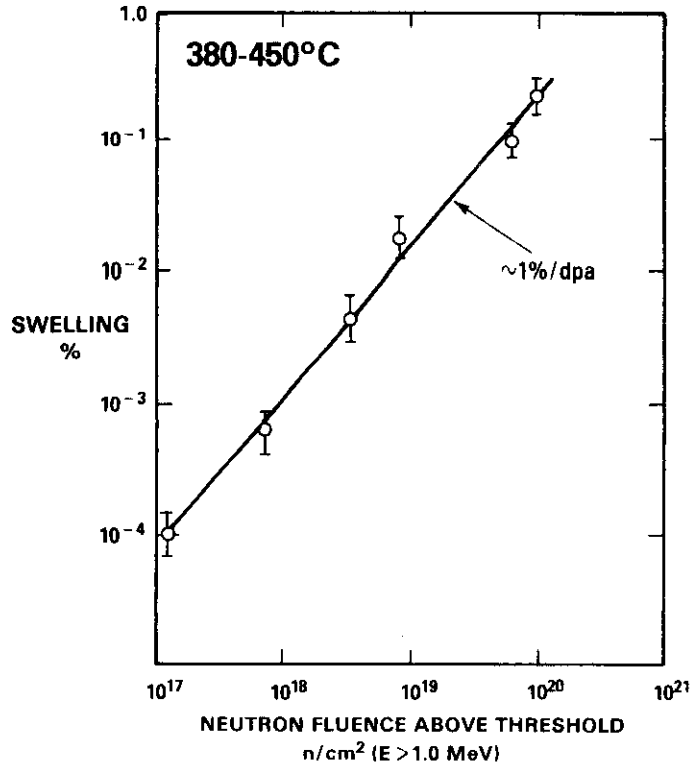

Fig. 2. Swelling observed in thermal reactor irradiation of 99.995% pure nickel at 380-450°C by Harbottle and Dickerson.[9] The estimated swelling rate shown was determined in the current study from knowledge of reactors with comparable spectra.

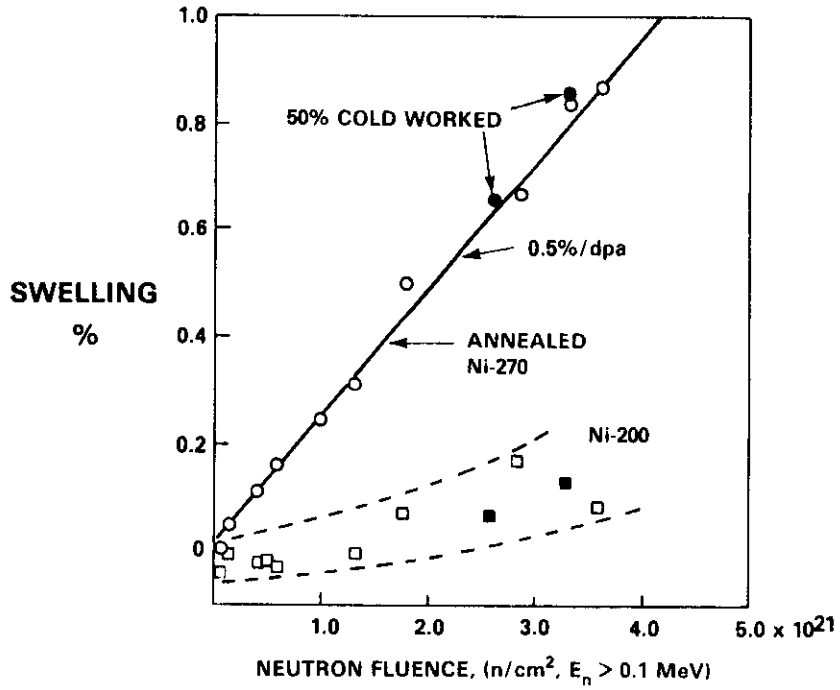

Fig. 3. Swelling observed by Holmes in nickel of varying purity and cold-work levels at 399-455°C in EBR-II.[10] Each datum was derived from a specimen which had the same residence time in reactor but which was irradiated at a different displacement rate.

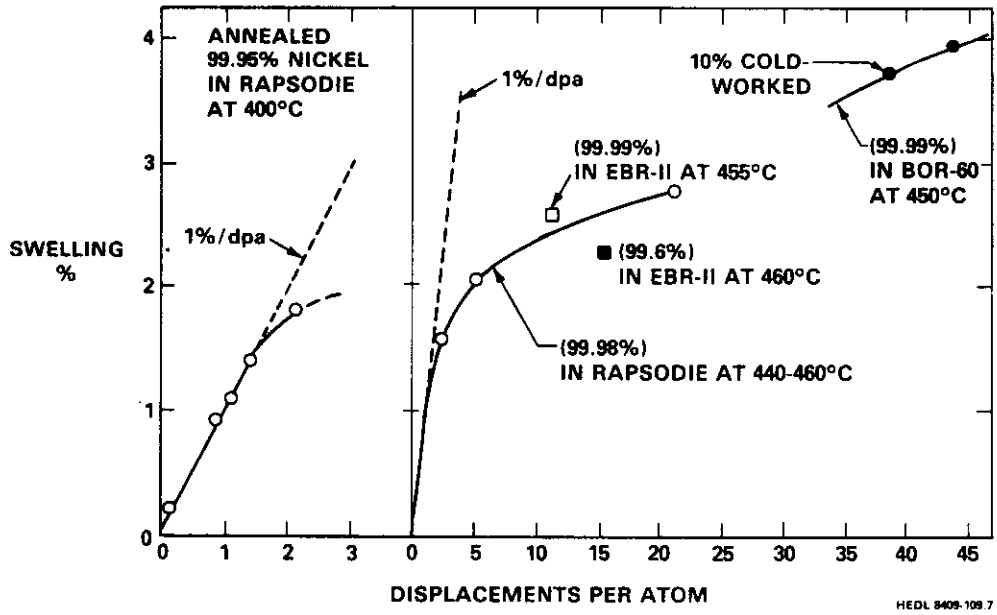

Fig. 4. Swelling observed in relatively pure nickel in fast reactors at quoted temperatures of 400°C[11] and at 440-460°C.[12-15] All data are for annealed specimens except for one 10% cold-worked datum.

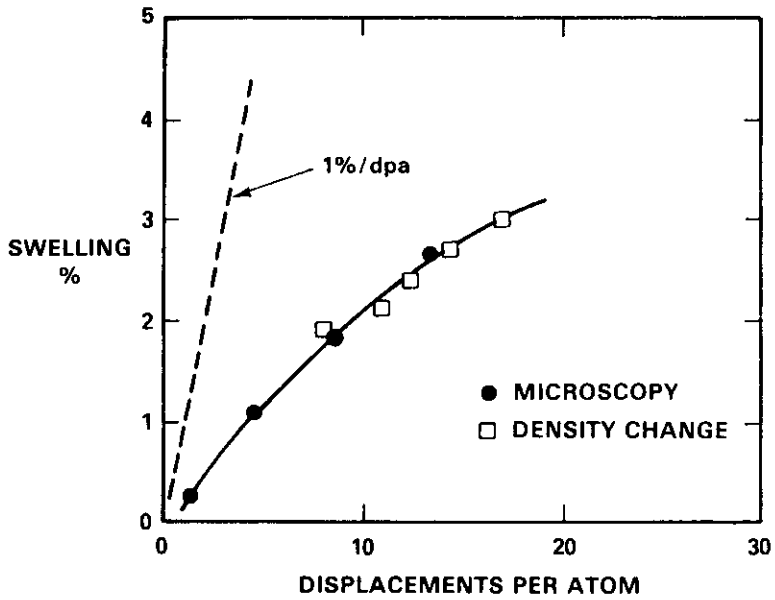

Fig. 5. Neutron induced swelling of 99.8% pure nickel at 500°C in the BOR-10 Reactor.[16]

not saturate in swelling, an observation yet to be made in either neutron or charged particle experiments.) As shown in Fig. 8, a reversal in swelling has actually been observed at a higher chromium level by Hudson and Ashby in comparative 46.5 MeV Ni^+ ion irradiations of nickel and Ni-27.5Cr.[24] The ion-induced swelling of Ni-27.5Cr only exceeded that of nickel above 650°C, however. Remember that there was a reversal in the neutron-induced swelling of Ni-15Cr somewhere between 600 and 650°C such that the swelling at 650°C proceeded at a faster rate than that below 650°C. Is it possible that the two observations are related to each other and to the densification observed prior to the onset of neutron-induced swelling?

While we cannot answer this question at the moment, we can independently confirm that the influence of chromium above ~650°C is different from that at lower temperatures. In a previously unpublished experiment by Johnston and coworkers[27] the swelling of nickel at 675°C and 116 dpa was found to increase

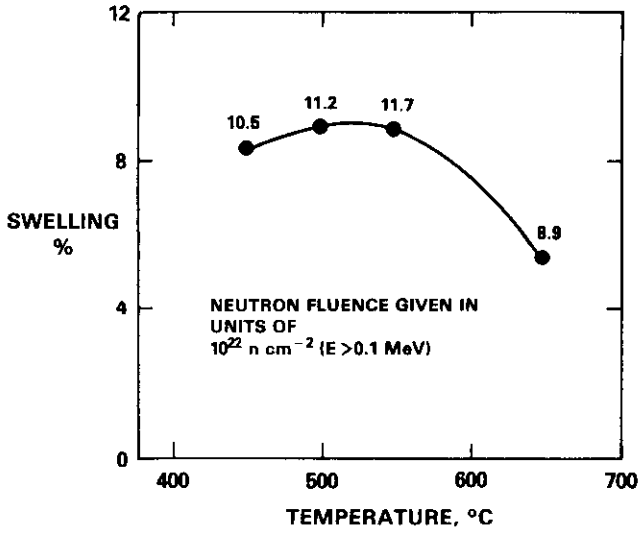

Fig. 6. Neutron-induced swelling in 99.99% nickel irradiated in BOR-60 fast reactor.[18] The authors indicate that 5.6 dpa results from 1.0 x 10^{26} n m^{-2} (E > 0.1 MeV).

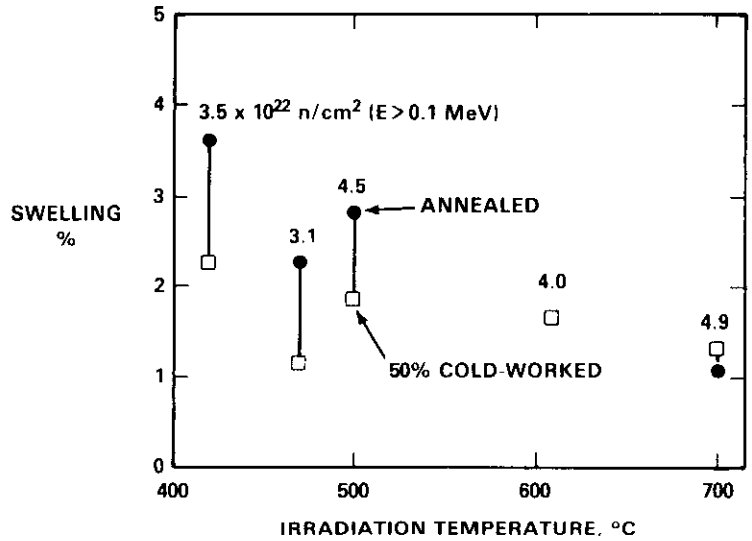

Fig. 7. Neutron-induced swelling in 99.6% nickel irradiated in EBR-II in both the annealed and 50% cold-worked conditions (previously unpublished). A fluence of 1 x 10^{22} n cm^{-2} (E > 0.1 MeV) produces ~5 dpa in this reactor.

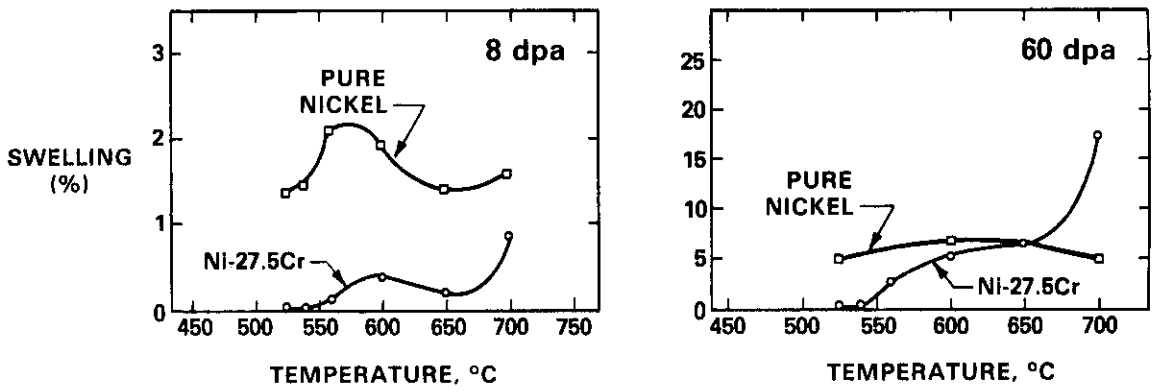

Fig. 8. Swelling observed in comparative irradiations of pure nickel and Ni-27.5Cr at 8 and 60 dpa with 46.5 MeV Ni$^+$ ions.[24]

with chromium additions of 5 and 15%, as shown in Fig. 9. The void density was non-monotonic but not strongly affected by the chromium level. This is in contrast to the results of ion studies conducted at lower temperatures where chromium additions were found to delay swelling and to strongly suppress void nucleation.[24,25]

Figs. 10a and 10b show the dependence of ion-induced swelling in Ni-27.5Cr on both temperature and displacement level. Note that below ~550°C there is very little swelling while above this temperature swelling increases sharply. There also does not appear to be any tendency for swelling to saturate. Hudson and Ashby also performed irradiations on Ni-9Cr at 525°C.[24] Fig. 11 shows that the onset of swelling is progressively delayed with increasing chromium content at 525°C, and Fig. 12 indicates that the effect of chromium additions is to progressively depress the void nucleation rate in nickel. This is opposite to the effect of chromium additions on the swelling of Fe-Ni-Cr austenitic alloys.[1-3,6] There is another interesting difference in behavior, however, between the Ni-9Cr and Ni-27.5Cr alloys at 525°C. Both pure nickel and the Ni-27.5Cr alloy were observed to cease nucleation by ~2 dpa but the nucleation in Ni-9Cr at 525°C was relatively continuous.[24] However, the eventual density of voids in the two Ni-Cr alloys at 525°C was essentially identical.

In another study using 3.5 MeV Ni^+ ions Pinizzotto and coworkers found that chromium additions of 2, 4, 6 and 8% progressively suppressed the swelling of nickel at 550°C.[25] The void sizes found at 9 and 18 dpa were identical and the primary influence of adding chromium was to suppress the rate of void nucleation. These same researchers also found the swelling of nickel to be increasingly suppressed by chromium at levels of 2, 4, 6, 8 and 16% when irradiated by 0.4 MeV N_2^+ ions to 10 dpa at 500°C. In this case, however, nitrogen's role in the void nucleation process somewhat obscured that of chromium, particularly at the lower chromium levels.

If the depression of void nucleation by chromium additions is to be explained in terms of the previously advanced model,[3,6] then either the effective vacancy diffusion coefficient D_v^{eff} of Ni-Cr alloys must be higher than that of pure nickel or the tendency of Ni-Cr alloys to order must be very large. As can be seen from Fig. 13, however, the addition of chromium to nickel at 1100°C tends to depress rather than to enhance the diffusion of both nickel and chromium.[28] Another researcher has found that additions of 0-14% chromium to nickel at 1250°C have essentially no effect on the diffusion of either chromium or nickel.[29]

There is, however, ample evidence that both long and short-range order exist in the Ni-Cr system. Short-range order has been found in Ni-11.4Cr[30,31] and Ni-19.4 Cr.[32] A review of numerous papers describing ordering in a wide range of Ni-Cr alloys is also contained in ref. 33. Although short-range order has been observed by many investigators, long-range order has also been observed in Ni-25.0Cr, Ni-29.2Cr and Ni-33.3Cr with critical ordering temperatures of 550, 580 and 590°C.[34] Thus the Ni-27.5Cr alloy, whose ion-induced swelling was described earlier, was irradiated in the temperature regime encompassing the critical temperature. Note in Fig. 10 that at ~550°C there is an abrupt transition from low swelling to high swelling behavior as the alloy probably becomes disordered. Interpolation of the estimated critical ordering temperatures of Ni-11.4Cr and Ni-25Cr yields a critical temperature in the range 520°C-540°C for the 85Ni-15Cr alloy, which is close to the transition temperature observed in its neutron-induced swelling behavior.

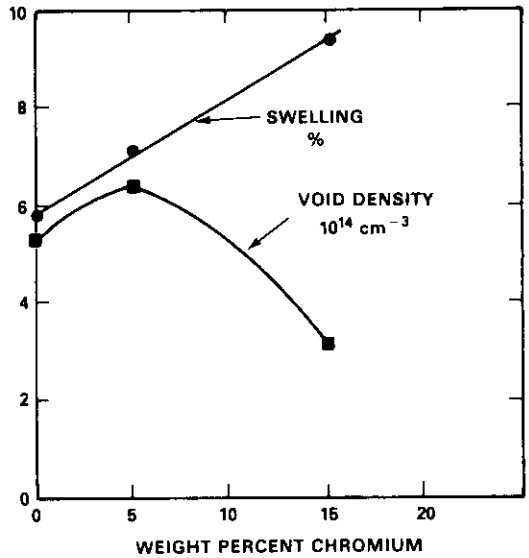

Fig. 9. Ion-induced swelling observed at 675°C and 116 dpa in a previously unpublished study by Johnston and coworkers. Preinjection of 15 appm helium was used in this study.

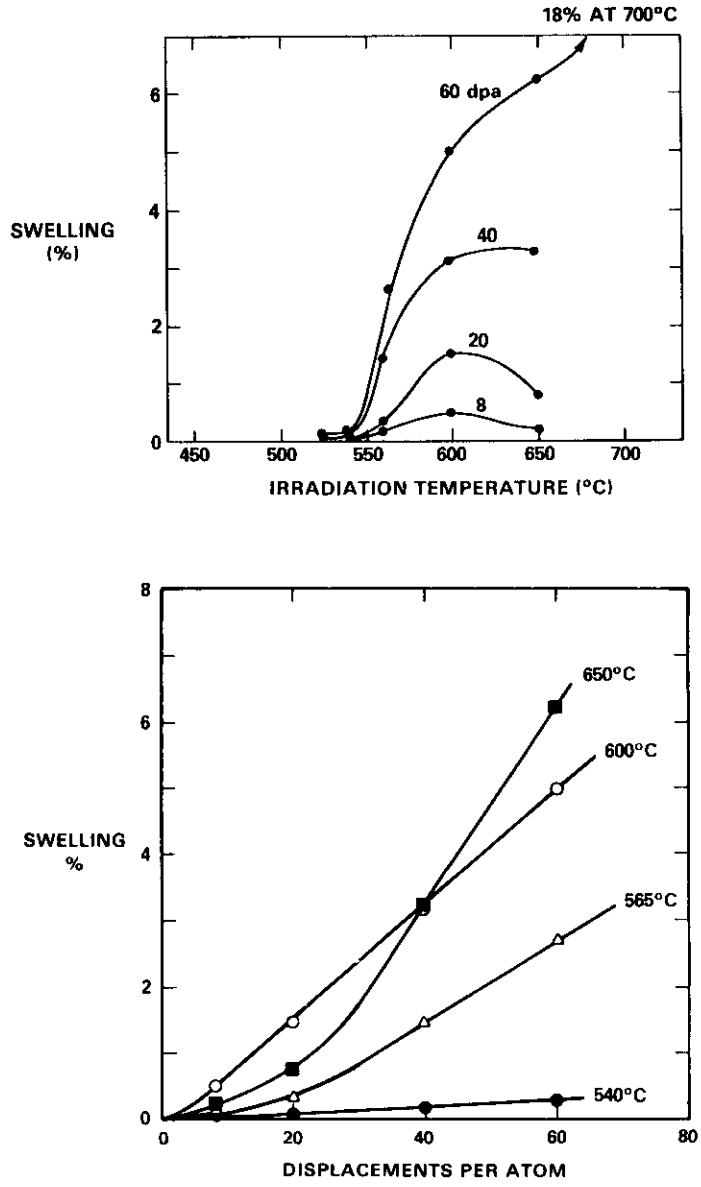

Fig. 10. Temperature and dose dependence of swelling observed in Ni-27.5Cr irradiated with 46.5 MeV Ni^+ ions.[24] Note the abrupt transition in swelling at ~550°C and the absence of a tendency toward saturation of swelling.

Ordering has been invoked by several theoreticians as a mechanism that influences swelling. Schulson proposed that ordering impedes the mobility of irradiation-produced vacancies and thus increases the direct recombination of vacancies and interstitials[35,36] Akhiezer and Davydov note that alloys which tend to order (but which are not long-range ordered) are characterized by a greater vacancy formation energy and, therefore, by a smaller thermal vacancy concentration compared with the disordered pure metal.[37] This would lead to larger vacancy supersaturations and greater rates of void nucleation. Alternatively, however, they note that in alloys that do not order at any temperature, the nucleation of voids is impeded compared with that of the corresponding pure metal. Several experimental studies on long-range ordered alloys, $(Co,Fe)_3V$ and $(Fe,Ni)_3V$, have shown a low swelling rate below their order-disorder transformation temperatures.[38,39]

Nickel is not the only fcc metal to exhibit a tendency toward void saturation and an initial neutron-induced swelling rate of ~1%/dpa. Copper and various copper alloys have shown this behavior during neutron[40] and charged particle irradiations.[41,42] It is hoped that a study of neutron-irradiated copper and copper alloys will provide some insight on the causes of the saturation phenomena, the onset of which appears to be sensitive to variables such as cold-work, temperature and metal purity.

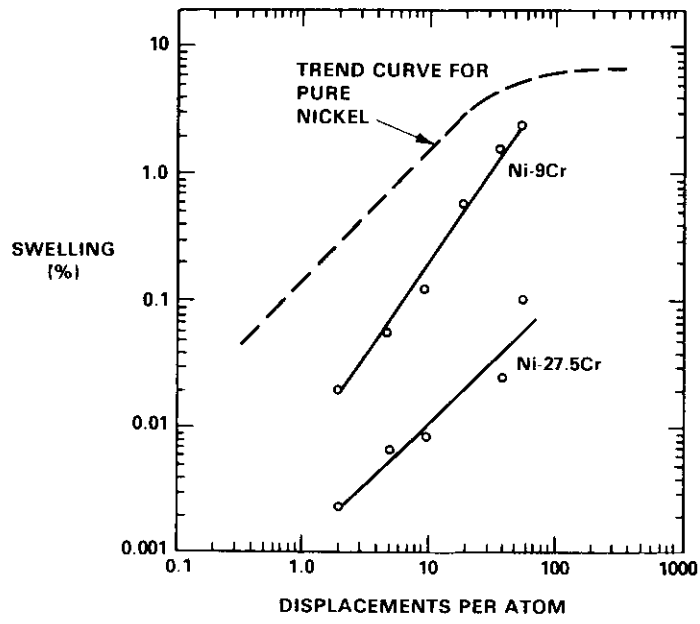

Fig. 11. Comparison of ion-induced swelling of nickel and two nickel-chromium alloys at 525°C.[22,24]

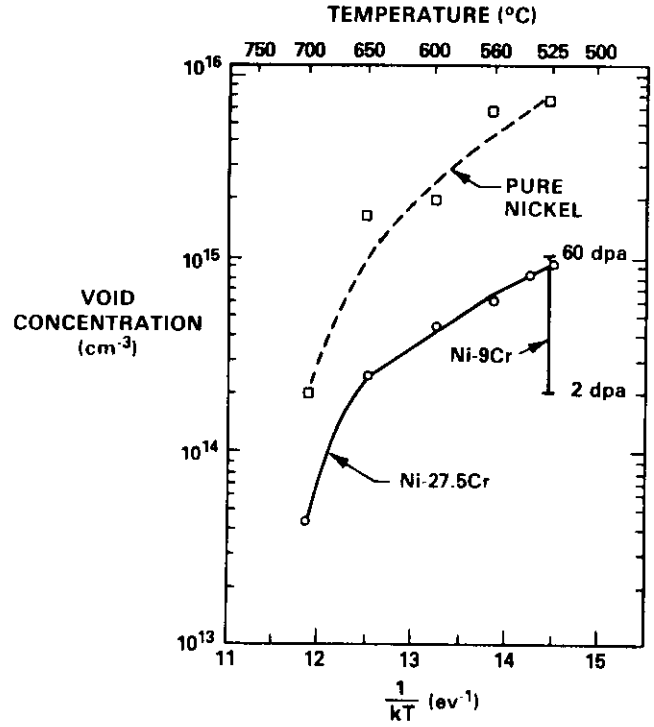

Fig. 12. Void densities observed in ion-irradiated nickel and Ni-27.5Cr at 8 dpa.[24] Data for Ni-9Cr are shown at 2 and 60 dpa.

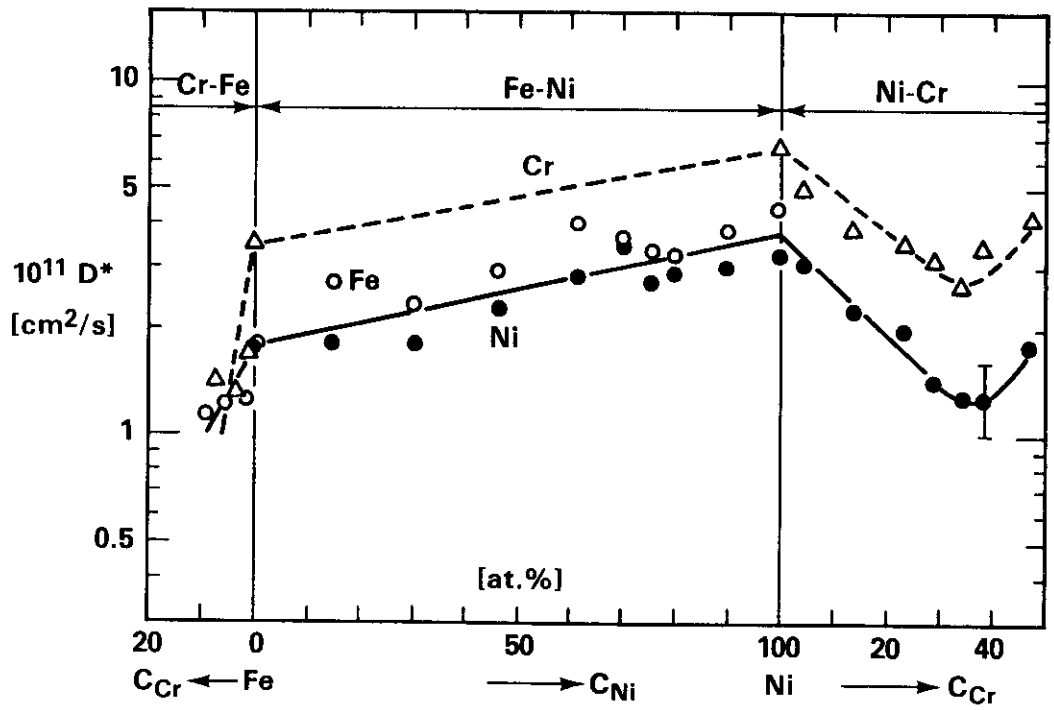

Fig. 13. Diffusivities of elemental components in the f.c.c. phases of binary solid solutions in the Fe-Ni-Cr system at 1100°C.[28]

CONCLUSIONS

Void formation in either relatively pure or impure nickel tends to saturate at moderately low swelling levels during ion or neutron irradiation, but nickel-chromium alloys do not exhibit this tendency. It is postulated that chromium additions to nickel lead to some form of radiation-enhanced micro-segregation above 650°C and an order-disorder transformation below ~550°C. This may account for the unusual swelling behavior of the alloy compared to that of pure nickel or Fe-Ni-Cr alloys. Void nucleation appears to be impeded by chromium additions below 550°C, and induces a swelling behavior that is remarkably insensitive to irradiation temperature below that corresponding to the order-disorder transformation temperature. These observations lend support to the concept that ordered alloys can be developed which will exhibit low swelling and creep rates in fusion neutron environments, providing that they are employed below their order-disorder transformation temperature.

FUTURE WORK

This effort will continue, concentrating on data analysis and microscopy for both nickel and copper alloys.

REFERENCES

1. F. A. Garner, J. Nucl. Mater., 122/123, 459 (1984).

2. F. A. Garner and H. R. Brager, p. 187-201 in Effects of Radiation on Materials: Twelfth International Symposium, ASTM STP 870, F. A. Garner and J. S. Perrin, Eds., American Society for Testing and Materials, Philadelphia, 1985.

3. F. A. Garner and H. R. Brager, p. 87-110 in Optimizing Materials for Nuclear Applications, F. A. Garner, D. S. Gelles, F. W. Wiffen, Eds., The Metallurgical Society of AIME, Warrendale, PA, 1985.

4. H. R. Brager and F. A. Garner, in Ref. 2, pp. 139-150 and in Ref. 3, pp. 141-166.

5. F. A. Garner, H. R. Brager, R. A. Dodd, and T. Lauritzen, Nuclear Instruments and Methods in Physics Research, B16, 244 (1986).

6. F. A. Garner and A. S. Kumar, this report.

7. A. Chamberod, J. Laugier and J.M. Pennison, J. Magnetism and Magnetic Materials, 10, 139 (1979).

8. A. Marucco, E. Metcalfe and B. Nath, p. 237 in Solid-State Phase Transformations, H.I. Aaronson, et al. Eds., The Metallurgical Society of AIME, 1982.

9. J. E. Harbottle and S. M. Dickerson, J. Nucl. Mater., 44, 313 (1972).

10. J. J. Holmes, Trans. ANS, 12, 701 (1969).

11. Y. Adda, p. 31 in Proc. Inter. Conf. on Radiation-Induced Voids in Metals, CONF-710601, Albany, N.Y., (1971).

12. G. Silvestre, A. Silvent, C. Regnard and G. Sainfort, J. Nucl. Mater., 57, 125 (1975).

13. N. P. Agapova, et al., Atomnaya Energiya, 45 (6), 433 (1978).

14. K. B. Roarty, J. A. Sprague, R. A. Johnson and F. A. Smidt, J. Nucl. Mater., 97, 67 (1981).

15. H. R. Brager and J. L. Straalsund, "Irradiation Swelling Resistance of Inconel 600," HEDL-SA-322 S, (Oral Presentation Only), Westinghouse Hanford Company, Richland, WA, 1972.

16. V. I. Scherbak, Fiz. Metal. Metalloved., 50, No. 6, 1314 (1980).

17. J. E. Harbottle, J. Nucl. Mater., 66, 258 (1977).

18. N. K. Vasina, I. P. Kursevich, O. A. Kozhevmikov, V. K. Shamardin and V. N. Golovanov, Atomnaya Energiya, 59, 265 (1985).

19. J. B. Whitley, G. L. Kulcinsky, P. Wilkes and J. Billen, J. Nucl. Mater., 85/86, 701 (1979).

20. G. L. Kulcinsky, J. L. Brimhall and H.E. Kissinger, p. 449 in Proc. Inter. Conf. on Radiation-Induced Voids in Metals, CONF-710601, Albany, N.Y., 1971.

21. R. S. Nelson, J. A. Hudson, D. J. Mazey, G. P. Walters and T. M. Williams, ibid., 430.

22. J. A. Hudson, S. Francis, D. J. Mazey and R. S. Nelson, p. 326 in Effects of Radiation on Substructure and Mechanical Properties of Metals and Alloys, ASTM STP 529, 1973.

23. D. I. R. Norris, J. Nucl. Mater., 40, 66 (1971).

24. J. A. Hudson and S. J. Ashby, p. 140 in The Physics of Irradiation Produced Voids, R. S. Nelson, Ed., AERE-R-7934, Harwell U.K., September 9-11, 1974.

25. R. F. Pinizzotto, Jr., L. J. Chen and A. J. Ardell, Met. Trans. A, 9A, 1715 (1978).

26. W. G. Johnston, T. Lauritzen, J. H. Rosolowski and A. M. Turkalo, p. 227 in Radiation Damage in Metals, American Society for Metals, Metals Park, Ohio, 1976.

27. Unpublished data supplied by T. Lauritzen and W. G. Johnston of General Electric Company.

28. J. Ruzickova and B. Million, Mat. Sci. and Engr., 50, 59 (1981).

29. G. R. Johnston, High Temperatures - High Pressures, 14, 695 (1982).

30. H. Heidsiek, R. Scheffel and K. Lücke, Journal de Physique, Colloque C7, n° 12, 38, C7-174 (1977).

31. H. Heidsiek, K. Lücke, and R. Scheffel, J. Phys. Chem. Solids, 43, 825 (1982).

32. B. Schönfeld, F. Klaiber, G. Kostorz, U. Zaune and G. McIntyre, Scripta Met., 20, 385 (1986).

33. R. L. Klueh, Mat. Sci. and Engr., 54, 65 (1982).

34. Y. Z. Vintaykin and G. G. Urshadze, Fiz. Met. Metalloved., 27 (5), 895 (1969).

35. E. M. Schulson, J. Nucl. Mater., 66, 322 (1977).

36. E. M. Schulson, J. Nucl. Mater., 83, 239 (1979).

37. I. A. Akhiezer and L. N. Davydov, J. Nucl. Mater., 96, 155 (1981).

38. D. N. Braski, J. Nucl. Mater., 122/123, 676 (1984).

39. D. N. Braski and K. Farrell, J. Nucl. Mater., 136, 48 (1985).

40. F. A. Garner and H. R. Brager, Damage Analysis and Fundamental Studies Quarterly Progress Reports, DOE/ER-0046/24 (p. 89) and DOE/ER-0046/25 (p. 110), U.S. Department of Energy, Office of Fusion Energy, 1986.

41. M. K. Makin p. 269 in Voids Formed by Irradiation of Reactor Materials, S. F. Pugh, Ed., British Nuclear Energy Society, 1971.

42. K. H. Leister, Kernforschungzentrum Karlsruhe Report, KFK 3499, (in German) May 1983.

TEM CROSS-SECTION OBSERVATION OF GAS EFFECT ON VOID FORMATION IN ION IRRADIATED NICKEL - L.M. Wang, R.A. Dodd and G.L. Kulcinski (University of Wisconsin)

OBJECTIVE

To better understand the role of helium and oxygen atoms in void nucleation and growth in irradiated materials.

SUMMARY

Nickel samples with various helium and oxygen concentrations have been irradiated with 14 MeV Ni ions at 500°C to a fluence of 8 x 10^{19} ions/m^2 (2 dpa at a 1-μm depth). Helium atoms with energy varying from 200 to 700 keV were pre-injected at room temperature. The samples with low oxygen content were obtained by a hydrogen reduction treatment and high vacuum outgassing. The density and the average diameter of voids were determined by TEM examination of cross-section specimens.

The residual oxygen plays an important role in promoting void formation. Lowering the oxygen content from 180 appm to 75 appm reduces void density and increases void size remarkably.

Small amounts of helium (10 appm) enhanced the void nucleation remarkably in both high (180 appm) and low (75 appm) oxygen content samples, while larger amounts of helium (30 appm) reduced the observable void density in the high oxygen content sample.

PROGRESS AND STATUS

Introduction

Nickel has long been selected as a model material in radiation-induced void swelling studies to avoid the complex analysis problems imposed by phase changes,[1-3] and thereby to better understand the void formation mechanism(s). The effect of helium, produced either by the transmutation reaction in neutron irradiated Ni or by pre- or co-implantion in ion irradiations of pure Ni, has been studied extensively.[4-6] However, the effect of oxygen on void formation in irradiated pure Ni has been neglected. Oxygen is the most common residual gas in metals and has been shown to promote void formation both by theoretical analysis[7,8] and by some experiments on other materials.[9-13] Therefore, it seems that any quantitative approach of gas effects on void formation would be incomplete without considering the effect of residual oxygen in the material. In the present experiments, we have investigated the effects of both helium and oxygen on void formation in ion irradiated pure Ni.

Experimental Procedure

The Ni used in this study was Marz grade (99.995 wt.% pure) foil from the Materials Research Corporation. Foil samples with 1 cm x 0.5 cm dimensions were mechanically polished with 0.3 μm alumina abrasive. Seven samples with different pre-irradiation treatments were irradiated with 14-MeV Ni^{3+} ions at the University of Wisconsin Heavy-Ion Irradiation Facility. One sample was irradiated in the as-received state (cold worked), while three were annealed at 800°C for 3.6 x 10^3 s in a vacuum of 4 x 10^{-5} Pa to remove the cold-worked structure. Two of the annealed samples were then injected with either 10 appm or 30 appm helium before Ni-ion irradiation. The remaining three samples (with a thickness of about 0.25 mm) were first heated at 1000°C in flowing dry hydrogen for 4.3 x 10^4 s to reduce the oxygen content, and then annealed at 150°C in a vacuum of 6.6 x 10^{-7} Pa for 1.8 x 10^3 s to remove residual hydrogen. Analyses performed by Los Alamos National Laboratory, using a vacuum fusion technique, indicated that the oxygen content in the Ni foil was reduced from the original 180 appm to 75 appm after such treatment. Two foils with reduced oxygen content were then pre-injected with either 10 or 50 appm helium before Ni-ion irradiation.

The helium atoms with energy varying from 200 to 700 keV were pre-injected in the Ni samples at room temperature using the University of Wisconsin 700 kV Accelerator. This produced a zone with relatively uniform helium concentration extending from the sample surface to a depth of about 1 μm, which is separated from the injected interstitials introduced during the 14 MeV Ni self-ion irradiation.

All the samples were finally irradiated at 500°C with a flux of 3 x 10^{16} $Ni^{3+}/m^2/s$ to a fluence of 8 x 10^{19} Ni^{3+}/m^2. The displacement damage as a function of depth for 14 MeV Ni ions on pure Ni was calculated using the Brice code[14] and is plotted in Fig. 1. According to this calculation, Ni-ion irradiation in our study would produce a displacement level of 2 dpa at 1 μm or about 8 dpa at the damage peak. It should be noted that a displacement efficiency factor of k = 0.8 was used in the displacement damage calculation to be consistent with previous ion bombardment studies, even though k = 0.3 is probably a more appropriate factor for neutron or ion irradiations.[15,16]

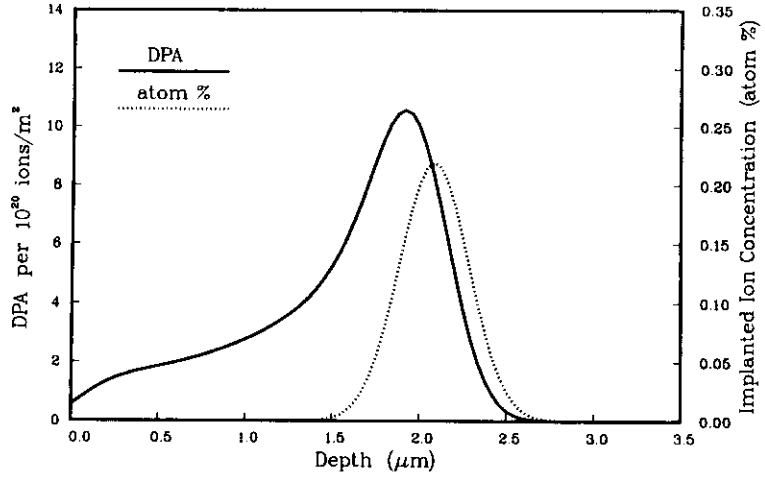

Figure 1. Displacement damage and implanted ion concentration versus depth from the irradiated surface for 14 MeV Ni-ion irradiated pure Ni calculated using the Brice code. The damage efficiency (k) used is 0.8.

After irradiation, the specimens were prepared in cross-section[3] for observation by Transmission Electron Microscopy (TEM), which allows the entire damage region to be studied in one single foil. TEM analysis was performed on a JEOL 100B and a JEOL TEMSCAN-200CX electron microscope.

Results and Discussion

After irradiation, a heterogeneous void distribution was observed in the cold-worked (as-received) Ni containing 180 appm oxygen, as can be seen from Figs. 2 and 3. In Fig. 3 (a), it can be seen that voids formed preferentially around a very occasional impurity particle. An Energy Dispersive X-ray Spectroscopy (EDXS) analysis on the particle showed only the presence of Ni (elements with Z < 10 can not be detected by EDXS). It is believed that the particle was an oxide. If that is the case, then the high void density around the particle might be attributed to the higher local free oxygen content because of the re-solution of Ni oxide during irradiation. Voids were also found to form preferentially on dislocations and along grain boundaries as shown in Figs. 3 (b) and (c), where the oxygen concentration could also be higher than in the bulk material. The average void density was determined to be 6×10^{19} m^{-3} at the depth of 1 μm and 2×10^{20} m^{-3} at the damage peak. The corresponding average void diameter was 35 nm at the 1-μm depth and 30 nm at the damage peak.

Figure 4 shows the entire damage region of the three annealed specimens which contain 180 appm oxygen and varying levels of helium in the first micrometer region. The variation of void density and average diameter with depth is shown in Fig. 5. It is clear from Fig. 4 (a) that the heterogeneous void distribution in the irradiated, cold-worked Ni (Figs. 2 and 3) is not a feature of irradiated, annealed Ni specimens. Also, compared to the cold-worked specimen, the void density is much higher, and voids are much smaller in diameter in the annealed material. This change might be explained by homogeneous distribution of oxygen atoms due to thermal diffusion during annealing.

The effect of pre-injected helium in the annealed, high oxygen content (180 appm) Ni is shown by comparison of the micrographs and curves presented in Figs. 4 and 5, respectively. Pre-injection of 10 appm helium enhanced the void nucleation remarkably, while pre-injection of 30 appm helium reduced the void density. Compared to the sample without helium pre-injection, pre-injection of 10 appm helium increased the void density at 1 μm (2 dpa) by about three times, but pre-injection of 30 appm helium reduced the void density by a factor of 2.6. The suppression of void formation by pre-injected helium was previously reported for higher helium levels than used in this study,[6] and the suppression was considered to be the result of copious nucleation of sub-microscopic cavities in the implanted region. To verify this explanation, the region pre-injected with 30 appm helium was observed very carefully at a magnification of 200,000X for sub-microscopic cavities in addition to the voids. Sub-microscopic cavities were not resolved. Another possibility is that large levels of pre-injected helium tend to suppress void nucleation by increasing the vacancy-interstitial recombination rate, because helium has a high possibility of trapping a vacancy[17] and these trapped vacancies function as recombination sites when their density is high.

Figure 2. TEM micrograph which shows the cross-section of 14 MeV Ni-ion irradiated, cold-worked Ni (the first half micron was lost during sample preparation). The oxygen content is 180 appm in the sample.

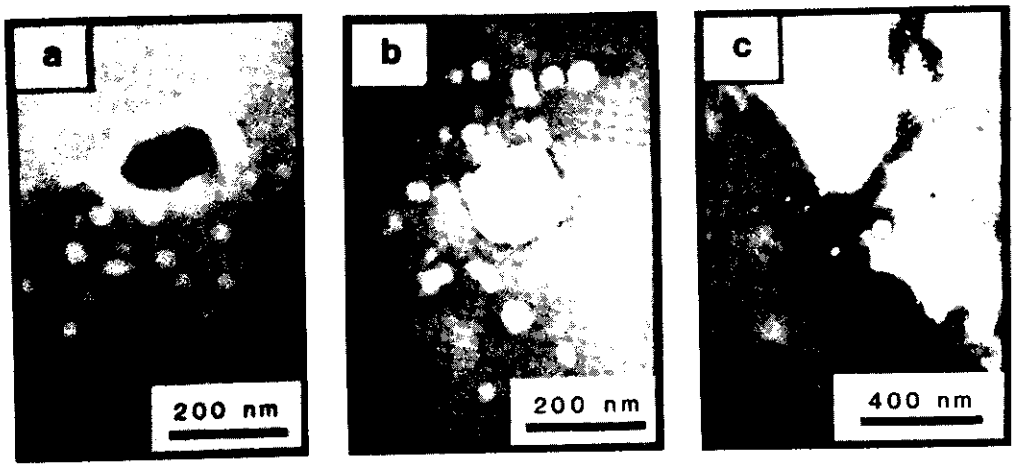

Figure 3. Heterogeneous void distribution in 14 MeV Ni-ion irradiated cold-worked Ni containing 180 appm oxygen. Voids formed preferentially around an impurity particle (a), on dislocations (b), and along the grain boundary (c).

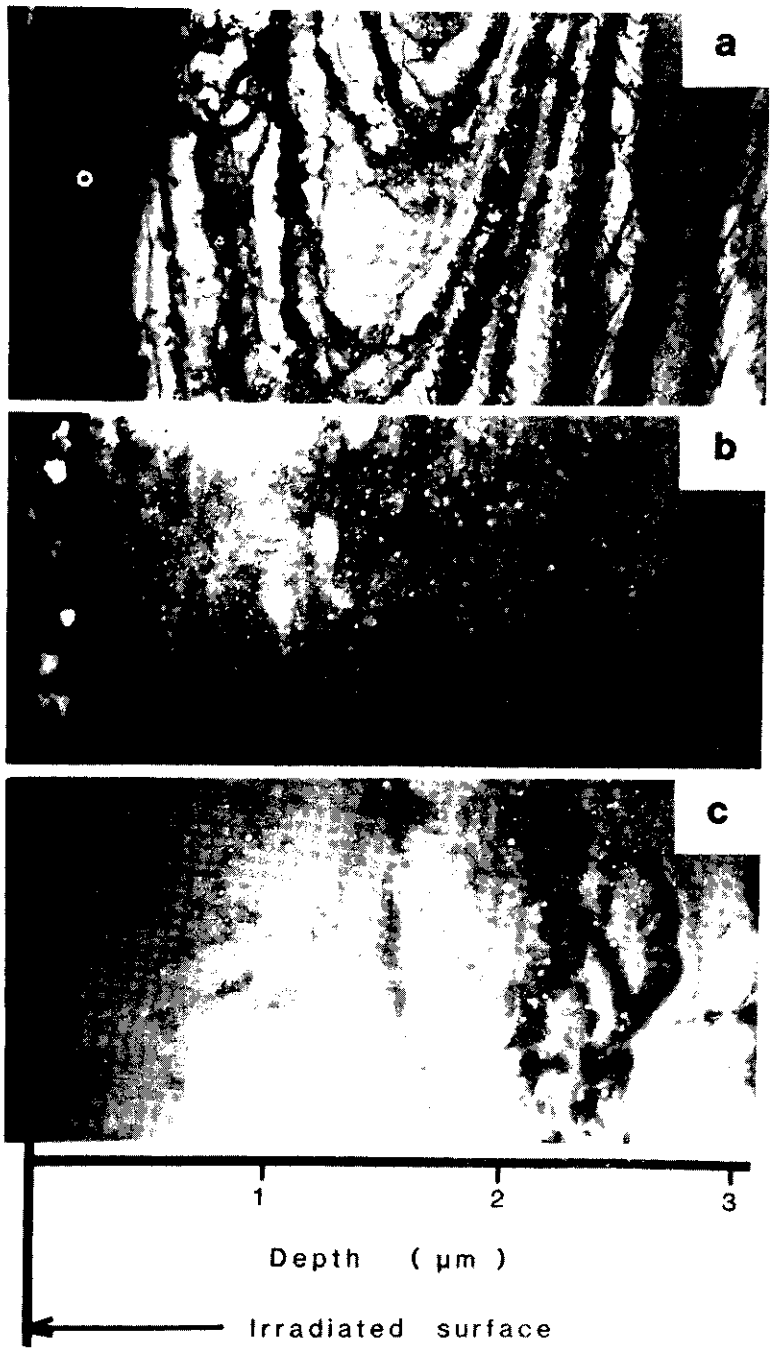

Figure 4. Cross-section TEM micrographs which span the entire damage region of 14 MeV Ni-ion irradiated Ni containing 180 appm oxygen. The samples were annealed at 800°C, 4 x 10^{-5} Pa for one hour before helium pre-injection and Ni irradiation.
(a) without helium pre-injection;
(b) with 10 appm helium pre-injected in the first micrometer;
(c) with 30 appm helium pre-injected in the first micrometer.

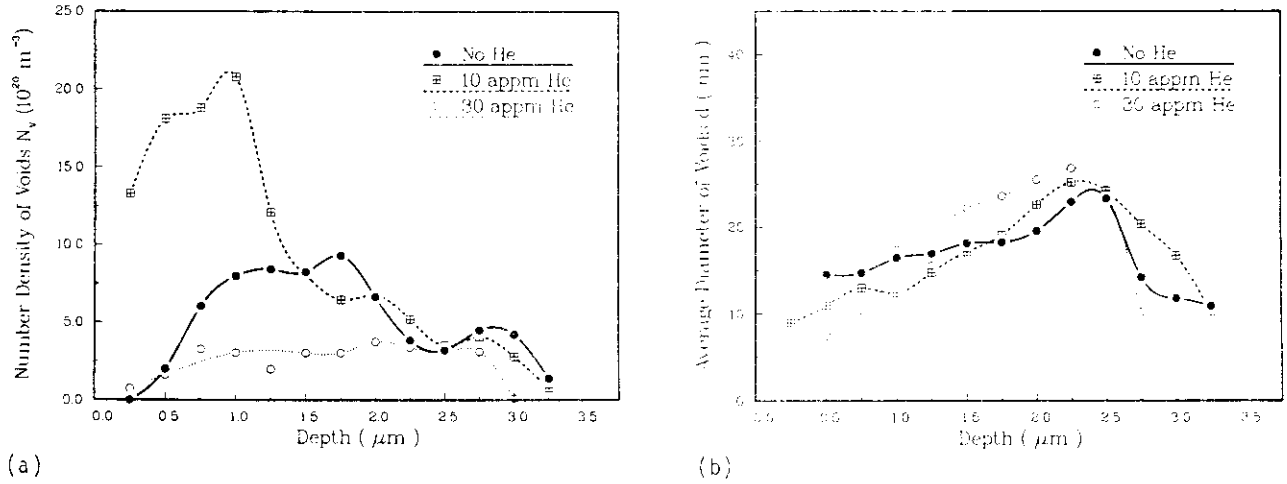

Figure 5. Number density of voids (a) and average diameter of voids (b) versus depth for the irradiated high oxygen content (180 appm) samples as shown in Figure 4.

The variation of the void distribution and the dependence of the void parameters along the depth in two irradiated low-oxygen content (75 appm) specimens are shown in Fig. 6 and Fig. 7, respectively. The sample shown in Fig. 6 (b) had 10 appm helium injected in the first micrometer region. For the purpose of comparison, the void parameter curves for the sample with high oxygen content (180 appm) and zero helium is also presented in Fig. 7. Also, it should be noted that the void density is drawn on a logarithmic scale in Fig. 7 (a) because the void density in the low oxygen content samples is at least one order of magnitude lower than that in the high oxygen sample except in the helium pre-injected region. On the other hand, the average void size in the low oxygen content samples is much larger. In the helium pre-injected region we have a high density of small diameter voids, but, compared to the 10 appm helium region in the sample with high oxygen content (Fig. 5), the void density in the same region of the low oxygen content sample is much lower and the average void size is larger. Another notable difference is that toward the end of the helium range (1 μm) in the low oxygen sample, the voids get progressively larger and the void density becomes progressively lower. There is a void denuded zone in the range of 1-2 μm because fewer gas atoms are available for void nucleation. This phenomenon was not seen in the high oxygen content sample that was pre-injected with the same amount of helium because there were oxygen atoms available to stabilize the void embryos.

Figure 8 and 9 show the void distribution and the variation of void parameters along the depth in the low-oxygen content (75 appm) sample pre-injected with 50 appm helium. Instead of a suppression of void formation in the helium injected region as seen in the high oxygen content sample pre-injected with 30 appm helium, a relatively high void density was observed. This indicates that the void suppression or "over nucleation" observed previously is the collective effect of high oxygen and helium contents.

In addition to the results shown above, Ni samples with different intrinsic oxygen contents and with pre-injected oxygen have also been irradiated to higher fluences. The results, which confirmed the observations of this study, are being presented separately.[12]

CONCLUSIONS

The effects of residual oxygen and pre-injected helium on void formation in pure Ni have been studied by cross-section technique following 14 MeV Ni ion irradiation to a fluence of 8×10^{19} ions/m^2 at 500°C. The following conclusions can be drawn:

(a) The residual oxygen plays an important role in promoting void formation in ion irradiated Ni. Lowering the oxygen content from 180 appm to 75 appm reduces the void density and increases void size remarkably.

(b) Voids tend to form in regions with high dissolved oxygen contents. The heterogeneity in void distribution observed in cold-worked Ni could be attributed mainly to the heterogeneous oxygen distribution.

Figure 6. Cross-section TEM micrographs of 14 MeV Ni-ion irradiated low oxygen content (75 appm) Ni samples without (a) or with (b) 10 appm helium pre-injected in the first micrometer region.

(c) Pre-injection of a small amount (10 appm) of helium enhances the void nucleation significantly in both high (180 appm) and low (75 appm) oxygen content Ni, but the void density in the low oxygen content sample is still much lower compared to that in the high oxygen content sample after the same amount of helium pre-injection.

(d) Pre-injection of a relatively large amount (30 appm) of helium reduced the observable void density in the Ni foil containing 180 appm oxygen. The void suppression or "over nucleation" is the collective effect of high oxygen and helium contents.

(e) The experimental results in this study support the theoretical model which predicts that gas is necessary for voids to form in Ni.[8,18]

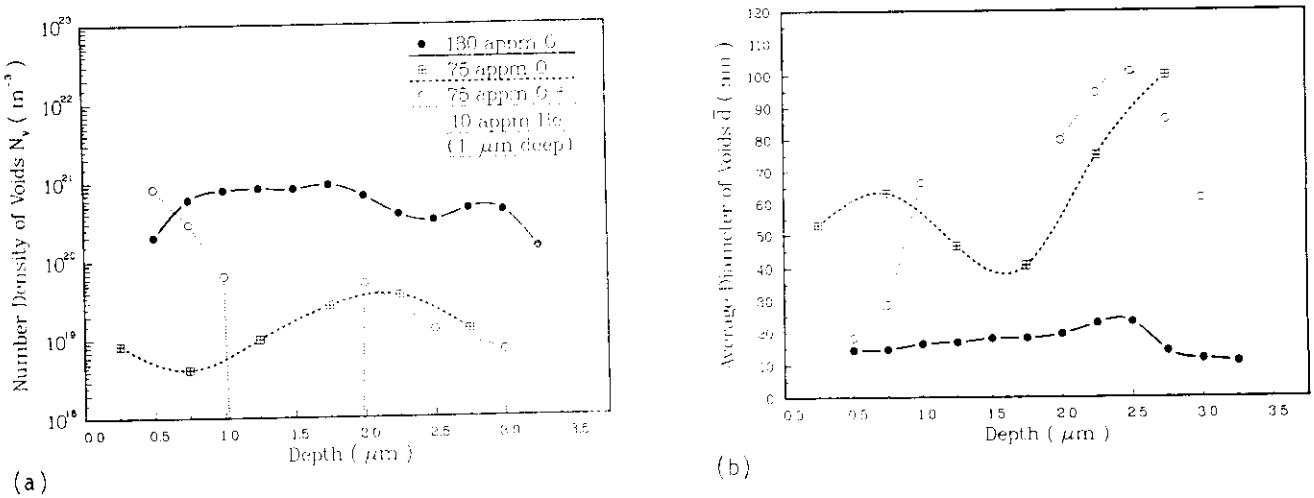

Figure 7. Number density of voids (a) and average diameter of voids (b) versus depth for the irradiated low oxygen content (75 appm) samples with or without 10 appm helium pre-injected in the first micrometer region. The curve for the high oxygen content (180 appm) zero helium sample shown in Figure 5 is repeated here for comparison.

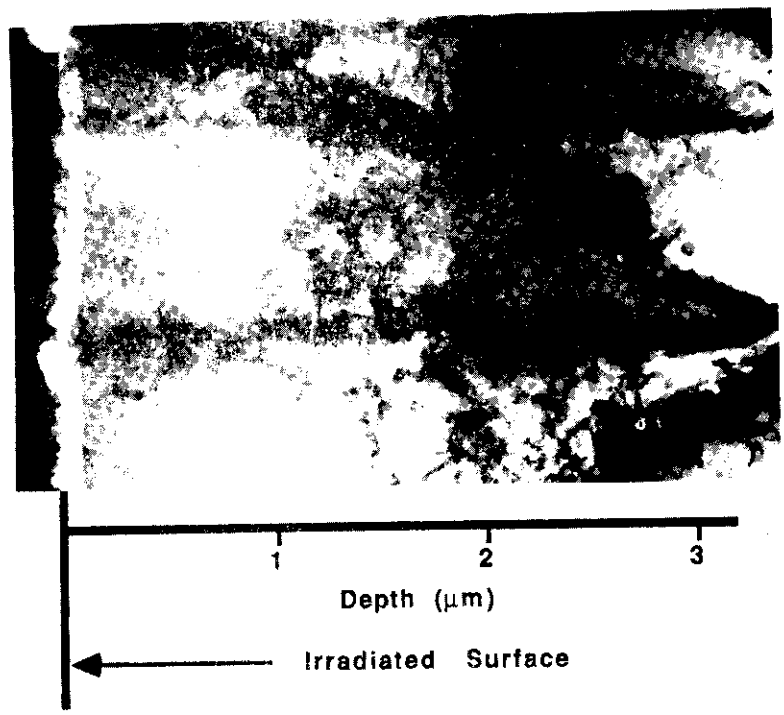

Figure 8. Cross-section TEM micrograph of 14 MeV Ni-ion irradiated low oxygen content (75 appm) Ni with 50 appm helium pre-injected.

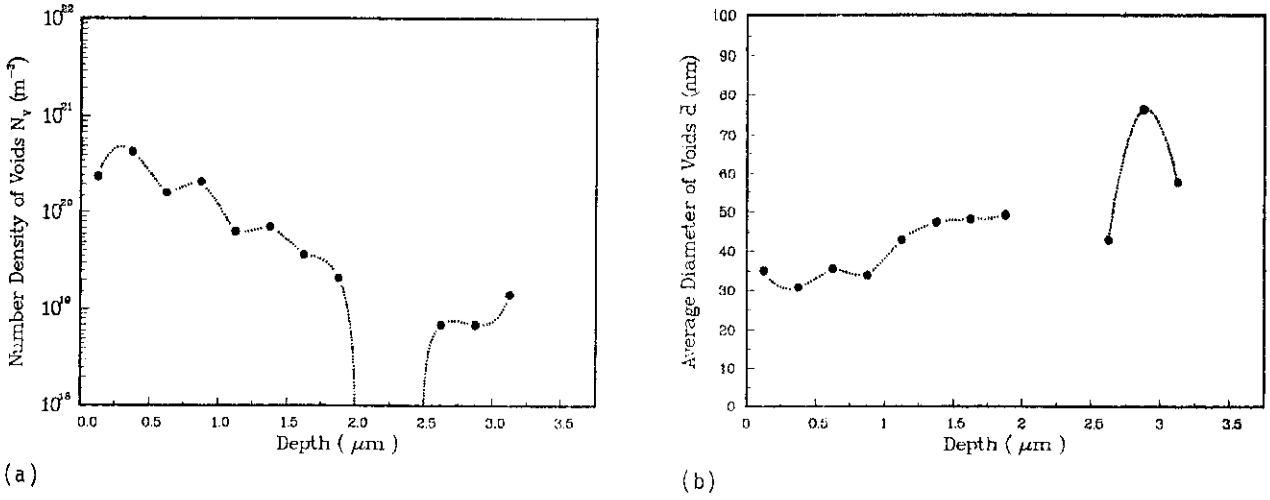

Figure 9. Number density of voids (a) and average diameter of voids (b) versus depth for the irradiated low oxygen content (75 appm) Ni with 50 appm helium pre-injected.

ACKNOWLEDGMENTS

The authors wish to thank L.E. Seitzman for some valuable discussions, D.J. Pertzborn for performing the helium pre-injection, and Pat Caliva for preparing the manuscript. This work was supported by the U.S. Department of Energy, Office of Fusion Energy.

REFERENCES

1. B. Mastel and J.L. Brimhall, "Voids Produced in High Purity Nickel by Neutron Irradiation," *J. Nucl. Mater.* 28 (1968) 115.

2. J.L. Brimhall, H.E. Kissinger and G.L. Kulcinski, "The Effect of Temperature on Void Formation in Irradiated Pure and Impure Metals," Proceedings of Int. Conf. on *Radiation-Induced Voids in Metals*, ed. J.W. Corbett and L.C. Ianniello, Albany, NY, 1971, CONF-710601, p. 338 (1972).

3. J.B. Whitley, "Depth-Dependent Damage in Heavy-Ion Irradiated Nickel," Ph.D. Thesis, University of Wisconsin-Madison (1978).

4. W.N. McElroy and H. Farrar, "Helium Production in Stainless Steel and Its Constituents as Related to LMFBR Development Programs," Proceedings of Int. Conf. on *Radiation-Induced Voids in Metals*, ed. J.W. Corbett and L.C. Ianniello, Albany, NY, 1971, CONF-710601, p. 187 (1972).

5. K. Farrell, N.H. Packan and J.T. Houston, "Depth Profiles of Nickel Ion Damage in Helium-Implanted Nickel," *Rad. Effects* 62 (1982) 39-52.

6. D.B. Bullen, "The Effects of Implanted Hydrogen and Helium on Cavity Formation in Self-Ion Irradiated Nickel," Ph.D. Thesis, University of Wisconsin-Madison (1984).

7. W.G. Wolfer, "Advances in Void Swelling and Helium Bubble Physics," *J. Nucl. Mater.*, 122 & 123 (1984) 367.

8. S.J. Zinkle, W.G. Wolfer, G.L. Kulcinski and L.E. Seitzman, "Stability of Vacancy Clusters in Metals II, Effect of Oxygen and Helium on Void Formation in Metals," to be published.

9. L.D. Glowinski and C. Fishe, "Etude de la Formation des Cavites D'irradiation Dans le Cuivre III - Irradiation Aux Ions Cuivre de 500 keV - Effet des Gaz Implantes," *J. Nucl. Mater.* 61 (1976) 29.

10. M.J. Makin, J.A. Hudson, D.J. Mazey, R.S. Nelson, G.P. Walters and T.M. Williams, "UKAEA Void Simulation in Fast Reactor Structural Materials," in *Radiation Effects in Breeder Reactor Structural Materials*, M.L. Bleiberg and J.W. Bennett (Eds.), TMS-AIME, 1977, 645-665.

11. S.C. Agaswal, D.I. Potter and A. Taylor, "Effects of Oxygen Addition on the Void Swelling Behavior of Vanadium," *Met. Trans. A* 9A (1978) 569.

12. B.A. Loomis and S.B. Gerber, "Similar Dependence on Dilute O Concentration of Void Formation in Ion-Irradiated Nb and Some Properties of Unirradiated Nb," *J. Nucl. Mater.* 97 (1981) 113-125.

13. R.L. Sindelar, "A Comparison of the Response of 316 SS and the P7 Alloy to Heavy-Ion Irradiation," Ph.D. Thesis, University of Wisconsin-Madison (1985).

14. D.K. Brice, "Ion Implantation Range and Energy Deposition Codes COREL, RASE4, and DAMG2," SAND77-0622, Sandia National Lab. (1977).

15. J.H. Kinney, M.W. Guinan, Z.A. Munir, "Defect Production Efficiencies in Thermal Neutron Irradiated Copper and Molybdenum," *J. Nucl. Mater.* 122 & 123 (1984) 1028-1032.

16. S.J. Zinkle, "Effects of Thermal Annealing and Ion Irradiation on the Properties and Microstructures of Copper Alloys," Ph.D. Thesis, University of Wisconsin-Madison (1985).

17. A. Kumar and F.A. Garner, "Dual-Ion Irradiation: Impact of the Conflicting Roles of Helium on Void Nucleation," Proceedings of 12th Inter. Symposium on *Effects of Radiation on Materials*, Williamsburg, June 18-29, 1984, p. 493.

18. L.E. Seitzman, L.M. Wang, G.L. Kulcinski and R.A. Dodd, "The Effect of Oxygen on Void Stability In Nickel and Austentic Steel," Proceedings of 2nd Intl. Conf. on *Fusion Reactor Materials*, 14-17 April 1986, Chicago, IL.

FUTURE WORK

The oxygen content in nickel is to be reduced to much lower level and small controlled amounts of oxygen will then be injected into the samples almost free of oxygen for more detailed study.

THE EFFECT OF OXYGEN ON VOID STABILITY IN NICKEL - L.E. Seitzman, L.M. Wang, G.L. Kulcinski and R.A. Dodd (University of Wisconsin)

OBJECTIVE

The object of this study is to calculate the minimum oxygen concentration capable of stabilizing voids in irradiated nickel.

SUMMARY

Surface energy values lower than those determined experimentally are often utilized in theories of void nucleation and growth in metals. Utilization of established surface energy values generally predicts no swelling in the absence of helium. However, swelling occurs in many metals even in the absence of helium. Surface active impurities, such as oxygen, can readily account for this discrepancy by reducing the surface energy of metals. This investigation shows that very low concentrations of oxygen in nickel can achieve the necessary decrease in surface energy.

A model has been developed to calculate the requisite quantity of oxygen in solution to stabilize voids. The criterion for void stability is that the void be the most energetically stable vacancy cluster in the metal. Knowing the fraction of oxygen which chemisorbs and the surface coverage required permits the determination of initial oxygen concentration needed to promote void stability. Calculations have been performed for nickel.

The model has been tested by irradiating nickel with 14-MeV Ni ions at 500°C. Oxygen was preinjected into one sample to a concentration of 75 appm. The irradiation reached a fluence of 3×10^{20} Ni-ion/m^2 (28 dpa at the damage peak). The irradiated foils were examined in cross section in the electron microscope.

PROGRESS AND STATUS

Introduction

Void nucleation and growth have been extensively studied for the last two decades. Several authors have attempted to model the physics of void formation in metals. Unfortunately, most of these theories assume a metal surface energy of 1.0 J/m^2, which is lower than the experimental values for most metals. Two notable exceptions to this are Mayer and co-workers[1] and Wehner and Wolfer.[2] Using the appropriate surface energy, Mayer concludes that gas is required for void formation. Wehner and Wolfer predict that small void embryos will nucleate at very low doses without gas assistance; however, they suggest that gas may be necessary to prevent the collapse of these unstable embryos to dislocation loops. Si-Ahmed and Wolfer[3] point out that in the absence of gas, exceedingly low concentrations of stable voids result from utilizing established surface energies.

Some experimental evidence also lends support to the notion that gas is necessary for void stability in some metals.[4-8] For neutron irradiated materials, the (n,α) nuclear reaction produces helium to aid void formation. However, in electron- and ion-irradiated metals, helium is absent unless introduced by implantation; yet voids exist in helium-free metals bombarded by charged particles.[5,9-11] Therefore, the possibility of void stability promoted by residual gas atoms must be considered. Oxygen, a common impurity in metals, is a likely candidate because of its reactive nature.

This paper focuses on the role of oxygen in void stabilization in nickel. A model introduced to calculate the required levels of oxygen needed for void formation in copper[12] after ion irradiation is extended to this metal. This model is then tested experimentally for nickel.

Theory

Elastic continuum theory applied to vacancy clusters in metals allows the determination of the most stable vacancy cluster type. In nickel, four defect clusters are found: the stacking fault tetrahedron (SFT), the faulted dislocation loop, the perfect dislocation loop, and the void. Recent calculations, using the best known values of the relevant materials parameters, indicate that the void is thermodynamically unstable at all sizes in both metals.[13] However, the void can be stabilized by surface energy reductions. The effect of a reduction in the surface energy of nickel from 2.1 to 1.5 J/m^2 on void stability is depicted in Fig. 1. The void becomes the energetically favorable vacancy cluster type. These reductions can be achieved by chemisorption of oxygen onto the metal surface.

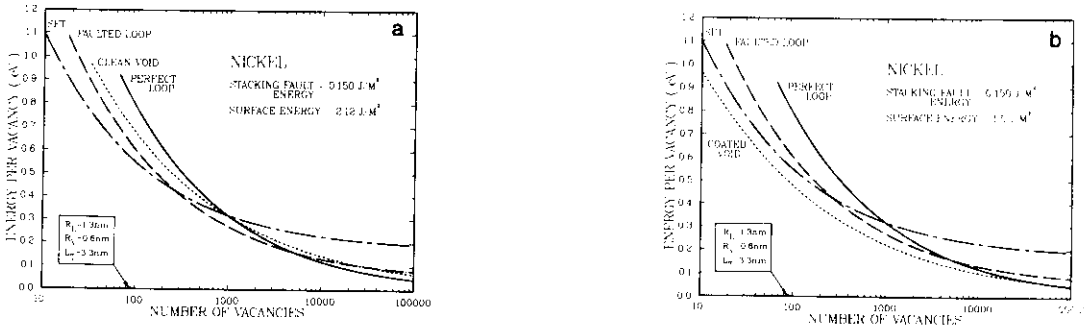

Figure 1. The effect of surface energy on void stability: (a) $\Gamma = 2.1\ J/m^2$, (b) $\Gamma = 1.5\ J/m^2$.

Bernard and Lupis[14] discussed the reduction in metal surface energy by surface reactive species. The Bernard-Lupis isotherm can be expressed as:

$$\Gamma(\theta) = \Gamma - \frac{RT}{mA} \ln \left(\frac{1}{1 - m\theta}\right) + mg\theta^2, \tag{1}$$

where $\Gamma(\theta)$ is the surface energy at a coverage of θ, Γ is the clean surface energy, θ is the fractional degree of surface covered by the impurity, m is an integer that depends on the stoichiometry of the impurity surface lattice, A is the metal molar surface area, and g is the magnitude of the interaction between impurity atoms.

For oxygen, metal surface contamination is a complex process. At relevant temperatures, free matrix oxygen is in atomic form on surfaces and in the bulk. Oxygen is distributed on the surfaces in a lattice configuration such as MO or M_3O. A comprehensive review of oxygen-metal interactions can be found in the literature.[15] The value of m in Eq. (1) is determined by the oxygen-saturated lattice type, $M_{m-1}O$. Once this lattice is fully formed, the lattice is saturated in oxygen. The introduction of additional oxygen results in the penetration of oxygen into the bulk and, ultimately, the formation of an oxide. This oxide can lead to an increase in the surface energy.[16,17]

A disagreement exists in the literature regarding the saturation coverage, θ_{sat}, of nickel by oxygen. Some researchers believe $\theta_{sat} = 0.25$[18,19] and others support $\theta_{sat} = 0.5$.[20,21] This paper uses a value of $\theta_{sat} = 0.5$ (m = 3) for nickel.

In view of the uncertainty in m and because the interaction energy between oxygen atoms is unknown, but often small,[22] the last term in Eq. (1) is assumed to be zero. The resultant equation for nickel is

$$\Gamma(\theta) = \Gamma - \frac{RT}{3A} \ln \left(\frac{1}{1 - 3\theta}\right) . \tag{2}$$

Knowledge of the surface energy needed for void stabilization permits the calculation of the corresponding surface coverage by Eq. (2).[23] To relate this coverage to the mole fraction, X, of oxygen in solution, the Langmuir-McLean isotherm may be used:

$$\frac{\theta}{1-\theta} = X \exp \left[\frac{G_B - G_S(\theta)}{RT}\right], \tag{3}$$

where G_B is the Gibbs free energy of atomic oxygen in the bulk and $G_S(\theta)$ is the Gibbs free energy of atomic oxygen on the covered surface. Assuming no change in G_S as a function of coverage up to $\theta = 0.5$, $G_S(\theta)$ is $G_S(0)$, the initial free energy of chemisorption. Brennan and Graham[24] find that the heat of adsorption of oxygen on nickel remains unchanged up to a coverage of one monolayer at 273°K.

Finally, to determine the fraction of oxygen in solution and on surfaces, a simple gas atom balance is employed. Before irradiation, some concentration of free oxygen exists in solution in the metal. When the irradiation commences, a terminal void density is rapidly reached.[2] The existing oxygen may now remain in solution, partition to the newly formed void surfaces, or re-associate in the interior of the embryos. The

sum of the gas atoms at these three locations must balance with the number of gas atoms originally in solution. Thus,

$$nX\Omega + N_o\left(\frac{4\pi R_v^2}{A}\right) n_v\theta\Omega + 2 N_o n_v Xg_2\Omega = nX_o\Omega, \quad (4)$$

where n is the matrix atom number density, Ω is the atomic volume, N_o is Avogadro's number, R_v is the average void embryo radius, n_v is the terminal void density, Xg_2 is the molar fraction of diatomic gas molecules inside the void, and X_o is the initial free oxygen mole fraction. Calculations using Eq. (4) reveal that the last term on the left-hand side of Eq. (4) is negligible compared to the other terms. Thus Eq. (4) can be reduced to

$$X_o - X = \frac{4\pi R_v^2 N_o \theta n_v}{A n}. \quad (5)$$

Equation (5) in conjunction with Eqs. (2) and (3) determines the initial free matrix oxygen concentration that will stabilize void formation by sufficient surface energy reduction.

Calculations

The Gibbs free energies of oxygen in the bulk, G_B, and on the surface, G_S, are not well known. These terms can be approximated by $G_B = -(H_u + E_D)/2$ and $G_S = -(H_{cs} + E_D)/2$, where H_u and H_{cs} are the heats of solution and adsorption of molecular oxygen and E_D is the dissociation energy of molecular oxygen.[23] This approximation assumes entropy terms cancel. The values used in this calculation are E_D = 498.4 kJ/mol,[25] H_u^{Ni} = 195 kJ/mol,[26] and H_{cs}^{Ni} = 420 kJ/mol.[27]

The void densities and radii used are taken from Wehner and Wolfer's data for a damage rate of 10^{-3} dpa/s.[2] The molar surface area is calculated according to Tyson[28] using his "average" population density factor. Table 1 lists all the parameters used in the calculations.

Table 1. Materials Parameters

Parameter	Nickel
Γ (J/m^2)	2.1
$\Gamma(\theta)_2$ (J/m^2)	1.5
A (m^2/mol)	4.84 x 10^4
G_B (kJ/mol O)	- 347
G_S (kJ/mol O)	- 459
n (m^{-3})	9.1 x 10^{28}

The calculated minimum free oxygen concentration needed for void stability is plotted versus temperature in Fig. 2. At low temperatures a greater oxygen concentration is needed due to the higher void density. At 650 to 700°C a minimum of about 1 appm is reached. Calculations, not shown in Fig. 2, reveal that the required oxygen levels increase above 700°C because of increasing oxygen solubility.

Experimental Procedure

A Marz-grade nickel (99.995% pure) was used in this experiment. The initial oxygen concentration, determined by inert-gas fusion analysis, was 180 appm. Samples were cut into 1 cm x 0.5 cm foils and mechanically polished to a thickness of approximately 0.25 mm. The foils were then treated in flowing dry hydrogen at 1000°C for 4.3 x 10^4 s hours to reduce the oxygen levels from 180 to 75 appm. The deoxidation step was followed by a 1.8 x 10^3 s anneal at 150°C in a vacuum of 6.6 x 10^{-7} Pa to remove any hydrogen that may have diffused into the metal.

The degassed foils were mechanically polished with 0.3 μm alumina abrasive in order to clean the surfaces. Electrochemical polishing was avoided because this procedure can introduce gas.[9] One degassed nickel sample was pre-injected with 75 appm of 5-MeV O^{2+} ions at room temperature to give a total of 150 appm oxygen at the peak depth of 2 μm using the University of Wisconsin Heavy-Ion Irradiation facility. The first micrometer of the surface of this specimen was removed by sputtering with 3.5-kV Ar^+ ions.

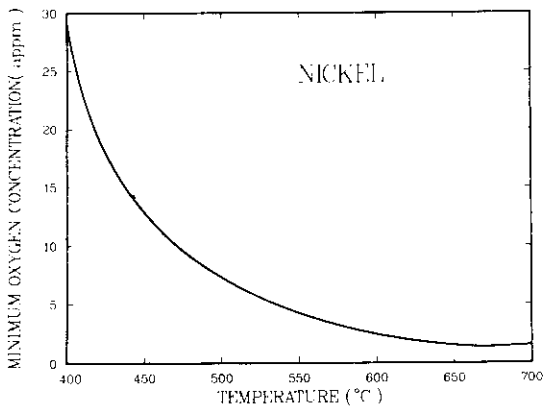

Figure 2. The minimum oxygen concentration needed for void stability.

Profilometer measurements indicate a surface removal of 0.8 to 1.0 μm. This procedure resulted in a specimen with 150 appm oxygen at the 1 μm depth and 75 appm oxygen at the peak nickel-ion damage depth (2 μm).

A total of three foils were irradiated with 14 MeV Ni^{3+} ions: the oxygen preinjected foil, a degassed foil, and an as-received foil. The specimens were irradiated at 500°C with 14-MeV Ni^{3+} ions at a flux of 3×10^{16} ions/m^2/s to a fluence of 3×10^{20} ions/m^2. These values correspond to a peak dose rate and dose of 3×10^{-3} dpa/s and 28 dpa, respectively. The damage at 1 μm is approximately one-fourth that of the peak damage. The oxygen-implanted foil received half this dose. After irradiation, the foils were prepared for analysis using a cross-section technique described elsewhere.[29] The microscopy was performed on a JEOL TEMSCAN-200CX electron microscope.

Results and Discussion

Figure 3 shows the irradiation damage throughout the damage region for the three foils. Each of the foils showed evidence of some void formation. This was expected because all samples contained oxygen concentrations exceeding the minimum for void stability. Table 2 lists the average void densities and diameters at the 1-μm depth and at the damage peak. In all cases the swelling at the damage peak resulted from a relatively low density of voids with diameter of 40-60 nm. The void density at the peak damage depth in the as-received nickel is approximately an order of magnitude greater than in the degassed or oxygen-implanted foils. In the first micrometer of the as-received and degassed nickel, a sparse, heterogeneous population of large voids exists. The void size at the 1-μm depth is smaller and the void density is two orders of magnitude high in the oxygen implanted foil in comparison to the as-received or degassed nickel foils.

Table 2. Void Paramters

Sample	Irradiation Temperature	Location	Oxygen Level	Peak Dose (dpa)	Average Void Density ($10^{20}/m^3$)	Average Void Diameter (nm)
As-Received Nickel	500°C	1 μm	180 appm	7	0.3	50
		Peak	180 appm	28	1.0	50
Degassed Nickel	500°C	1 μm	75 appm	7	0.1	50
		Peak	75 appm	28	0.07	60
Oxygen Implanted Nickel	500°C	1 μm	150 appm	3.5	20.0	14
		Peak	75 appm	14	0.2	40

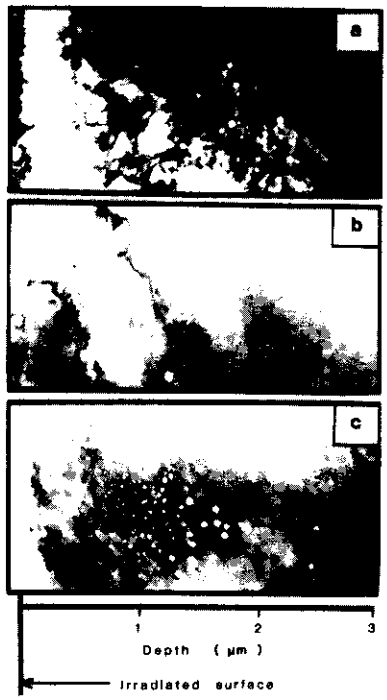

FIGURE 3. Void structure in nickel after 14 MeV Ni irradiation at 500°C.
(a) as-received nickel, 180 appm O
(b) degassed nickel, 75 appm O
(c) as (b) injected with additional 75 appm O to approximately 1-1.2 μm

This last result is important in the following respect. It should be noted that the oxygen level at the 1-μm depth in the oxygen implanted nickel is twice the oxygen level in the peak damage region, but there is a hundred-fold increase in void density at the 1-μm depth for approximately one-fourth the damage level. The void density at the 1-μm depth in the oxygen implanted nickel was also substantially higher than in the as-received and degassed samples. This difference can be explained by assuming that the implanted oxygen is bound differently from the initial matrix oxygen. At room temperature, the injected oxygen is immobile and probably remains in solution. Once the irradiation starts, this free oxygen is able to partition to embryo surfaces. The heterogeneous nature of the voids in the peak damage zone indicates that most of the oxygen originally in the bulk is tied up at grain boundaries, dislocations, internal oxides, or other binding sites. Bombarding or knock-on atoms may free some of these bound oxygen atoms but it is not expected that the density of these liberated oxygen atoms will be high enough to stabilize many embryos. The chance of such an event is greater near large oxide particles or other oxygen-rich areas.[30] Thus, it seems likely that the injection of oxygen increases the free oxygen levels from a very low value to 75 appm.

It should also be noted that the void density of 2×10^{21} m^{-3} does not exceed the theoretical prediction of the terminal void density of 2×10^{22} m^{-3}.[2] A major uncertainty in the model is the heat of chemisorption of oxygen, H_{cs}, on nickel.[28] A 25% change in H_{cs} can alter X_o by two orders of magnitude. This carries an uncertainty in the calculation of the oxygen level for void stabilization. The model also assumes that all embryos obtain at least a minimum coverage. A free oxygen concentration below the calculated minimum can still stabilize some fraction of the void embryos. In fact nine oxygen atoms can stabilize a 1.3 nm diameter embryo.

The maximum void density also may not be reached due to the kinetics of the process. This model examines only thermodynamic potential. The physics of oxygen partitioning to sinks may prevent the stabilization of all void embryos. Finally, the model presented here considers void stabilization and not growth. Stabilized void embryos may grow and coalesce according to classical growth mechanisms. The difficulties mentioned above preclude unequivocable proof that gas is needed to stabilize voids in many metals. The trends, however, support this conclusion for nickel. Reduction of the starting oxygen levels and the re-injection of oxygen atoms should be a valuable technique in testing the limits of this model.

ACKNOWLEDGMENTS

The authors wish to thank Dr. P.T. Cunningham and Mr. D.E. Vance of Los Alamos National Laboratory for performing the gas analysis, Dr. W.G. Wolfer and Dr. S.J. Zinkle for their invaluable advice, and Pat Caliva for preparing the manuscript. This work was supported by the U.S. Department of Energy, Office of Fusion Energy.

REFERENCES

1. R.M. Mayer, L.M. Brown and U. Gösele, *J. Nucl. Mat.* 95 (1980) 44 (8 parts).

2. M.F. Wehner and W.G. Wolfer, *Phil. Mag.* A. 52(2) (1985) 189.

3. A. Si-Ahmed and W.G. Wolfer, in: *Effects of Radiation on Materials*, Eleventh Conference, ASTM STP 782, Scottsdale, Arizona, 1982, Eds. H.R. Brager and J.S. Perrin (ASTM, 1982) p. 1008.

4. D.I.R. Norris, *Rad. Eff.* 14 (1972) 1.

5. B.L. Eyre, *J. Phys.* F. 3 (1973) 422.

6. J.M. Lanore, in: *Fundamental Aspects of Radiation Damage in Metals*, Vol. II, Gatlinburg, Tenn., 1975 (Conf. 75, 1006-P2, 1976) p. 1169.

7. S.K. McLaurin, Ph.D. Thesis, University of Wisconsin (1984).

8. S.J. Zinkle, Ph.D. Thesis, University of Wisconsin (1985).

9. J.B. Whitley, Ph.D. Thesis, University of Wisconsin (1978).

10. R.W. Knoll, Ph.D. Thesis, University of Wisconsin (1981).

11. R.L. Sindelar, G.L. Kulcinski and R.A. Dodd, *J. Nucl. Mat.* 122 & 123 (1984) 246.

12. S.J. Zinkle, W.G. Wolfer, G.L. Kulcinski and L.E. Seitzman, submitted to *Phil. Mag.*

13. S.J. Zinkle, L.E. Seitzman and W.G. Wolfer, submitted to *Phil. Mag.*

14. G. Bernard and C.H.P. Lupis, *Surf. Sci.* 42 (1974) 61.

15. K. Wandelt, *Surf. Sci.* Repts. 2 (1982) 1.

16. M. McLean and E.D. Hondros, *J. Mat. Sci.* 8 (1973) 349.

17. E.D. Hondros, *Pure & Appl. Chem.* 56 (12) (1984) 1677.

18. D.E. Taylor and R.L. Park, *Surf. Sci.* 125 (1983) L73.

19. J.B. Benziger and R.E. Preston, *Surf. Sci.* 141 (1984) 567.

20. C. Benndorf et al., *Surf. Sci.* 92 (1980) 636.

21. H.J. Grable and H. Viefhaus, *Surf. Sci.* 112 (1981) L779.

22. G.A. Somorjai, in: *Chemistry in Two Dimensions: Surfaces* (Cornell Univ. Press, 1981) Chpts. 3, 6.

23. R.H. Jones and W.G. Wolfer, *J. Nucl. Mat.* 122 & 123 (1984) 379.

24. D. Brennan and M.J. Graham, *Discuss. Faraday Soc.* 41 (1966) 95.

25. R.C. Weast, in: *CRC Handbook of Chemistry and Physics*, 59th Ed., (CRC Press, 1979) p. F-236.

26. W.A. Fischer and W. Ackermann, *Arch. Eisenhutt.* 37 (1966) 43.

27. I. Toyoshima and G.A. Somorjai, *Catal. Rev. - Sci. Eng.* 19 (1) (1979) 105.

28. W.R. Tyson, *Can. Met. Quart.* 14(4) (1975) 307.

29. S.J. Zinkle and R.L. Sindelar, *Nucl. Instr. & Meth. in Phys. Res. B*, in press.

30. L. Wang, R.A. Dodd and G.L. Kulcinski, "Gas Effects on Void Formation in 14 MeV Nickel Ion Irradiated Pure Nickel", Proc. of 2nd Intl. Conf. on Fusion Reactor Materials, 14-17 April 1986, Chicago, IL.

CONCLUSIONS

1. Voids are calculated to be thermodynamically unstable in extremely pure Ni.
2. In ion-irradiated nickel, unbound residual oxygen can stabilize voids by reducing the metal surface energy.
3. Pre-injection of Ni with 75 appm oxygen dramatically increases the void nucleation rate at 500°C.
4. Oxygen implanted in the nickel prior to ion irradiation is mostly unbound and able to partition readily to void embryos.

FUTURE WORK

This model is being extended to type 316 Stainless Steel. Also, efforts are being made to decrease the starting oxygen content in order to completely eliminate void formation.

6. DEVELOPMENT OF STRUCTURAL ALLOYS

6.1 Ferritic Stainless Steels

RADIATION EMBRITTLEMENT OF MANGANESE-STABILIZED MARTENSITIC STAINLESS STEEL - D. S. Gelles and W. L. Hu (Westinghouse Hanford Company)

OBJECTIVE

The object of this work is to evaluate the irradiation embrittlement behavior of manganese stabilized martensitic stainless steels in support of low activation ferritic alloy design.

SUMMARY

Fractographic examination has been performed on selected Charpy specimens of manganese stabilized martensitic stainless steels in order to identify the cause of irradiation embrittlement. Embrittlement was found to be partly due to enhanced failure at grain boundaries arising from precipitation. Microstructural examination of a specimen irradiated at higher temperature has demonstrated the presence of Fe-Cr-Mn chi phase, a body centered cubic intermetallic phase known to cause embrittlement. This work indicated that manganese stabilized martensitic stainless steels are prone to intermetallic phase formation which is detrimental to mechanical properties.

PROGRESS AND STATUS

Introduction

In a previous report, it was shown that manganese stabilized martensitic stainless steels underwent a large shift in ductile-to-brittle transition temperature (DBTT) as a result of irradiation at 365°C to 5.4 dpa and a further shift following irradiation to 11.3 dpa.[1] Higher manganese content increased the degradation. Although equivalent tests on HT-9 have not been performed, it is likely that this represents behavior that is worse than that found in HT-9. As the alloy design concepts used in manganese stabilized martensitic steels were used in 12% Cr low activation ferritic alloys, it was necessary to determine the cause of the embrittlement. The present effort is intended to determine the cause of embrittlement. The work includes fractographic examination of the Charpy test specimens and microstructural examination of TEM specimens irradiated at somewhat higher temperatures, 420 and 520°C, to 9.8 and 14.4 dpa, respectively.

The alloys of interest, coded F2 and F4 are Fe-12Cr-0.1C-1.0Mo-0.20V-0.15Nb with 3.33 and 6.57% Mn, respectively. The 1/3 size Charpy specimen test results[1] are provided in Fig. 1 with F2 as closed symbols and F4 as open symbols. From Fig. 1 it can be shown that the two alloys behaved similarly in the unirradiated state but F4 had a slightly lower upper shelf energy (USE). Following irradiation to 5.4 dpa, both alloys showed a shift in DBTT: for F2 115°C, comparable to HT-9 irradiated at 400°C and for F4 approximately 150°C. However, a further shift was found following irradiation to 11.3 dpa, to 130°C for F2 and to 225°C for F4. HT-9 does not show a further shift with irradiation. Also of note were recorded increases in USE such that for F4 following irradiation to 11.3 dpa, the USE had almost doubled. Therefore it was apparent that manganese additions to martensitic steels resulted in degradation of the DBTT but improvement in USE response due to irradiation.

The present effort is intended to provide an explanation for the above results. The work concentrates on fractographic examination of selected Charpy specimens but also includes companion transmission electron microscopy (TEM) specimens which were irradiated at somewhat higher temperatures, 420 and 520°C.

Experimental procedures

Details of the alloy design, composition, fabrication, Charpy testing and test results are given in Ref. 1. As noted, the results are shown graphically in Fig. 1. Fig. 1 also identifies specimens selected for fractographic examination by specimen identification number. The specimens were chosen to show transition temperature behavior (tested at the transition temperature) so that both brittle and ductile response could be observed in a single specimen. However, because unusual response was observed in USE as a function of dose, several specimens showing upper shelf response were chosen as well. The test conditions and results for these specimens are given in Table 1 along with the alloy compositions.

TEM specimens of these alloys were included in MOTA fusion canisters operating at 420, 520 and 600°C. Specimens of F4 (coded PZ for MOTA TEM tests) were therefore examined following irradiation in MOTA 1B irradiated in Cycle 4. The irradiation conditions for these specimens were: 407°C to a fluence of 2.23×10^{22} n/cm^2, which is equivalent to 9.8 dpa, and 518°C to a fluence of 3.12×10^{22} n/cm^2, which is equivalent to 14.4 dpa.[2] Specimen preparation and examination followed routine procedures.

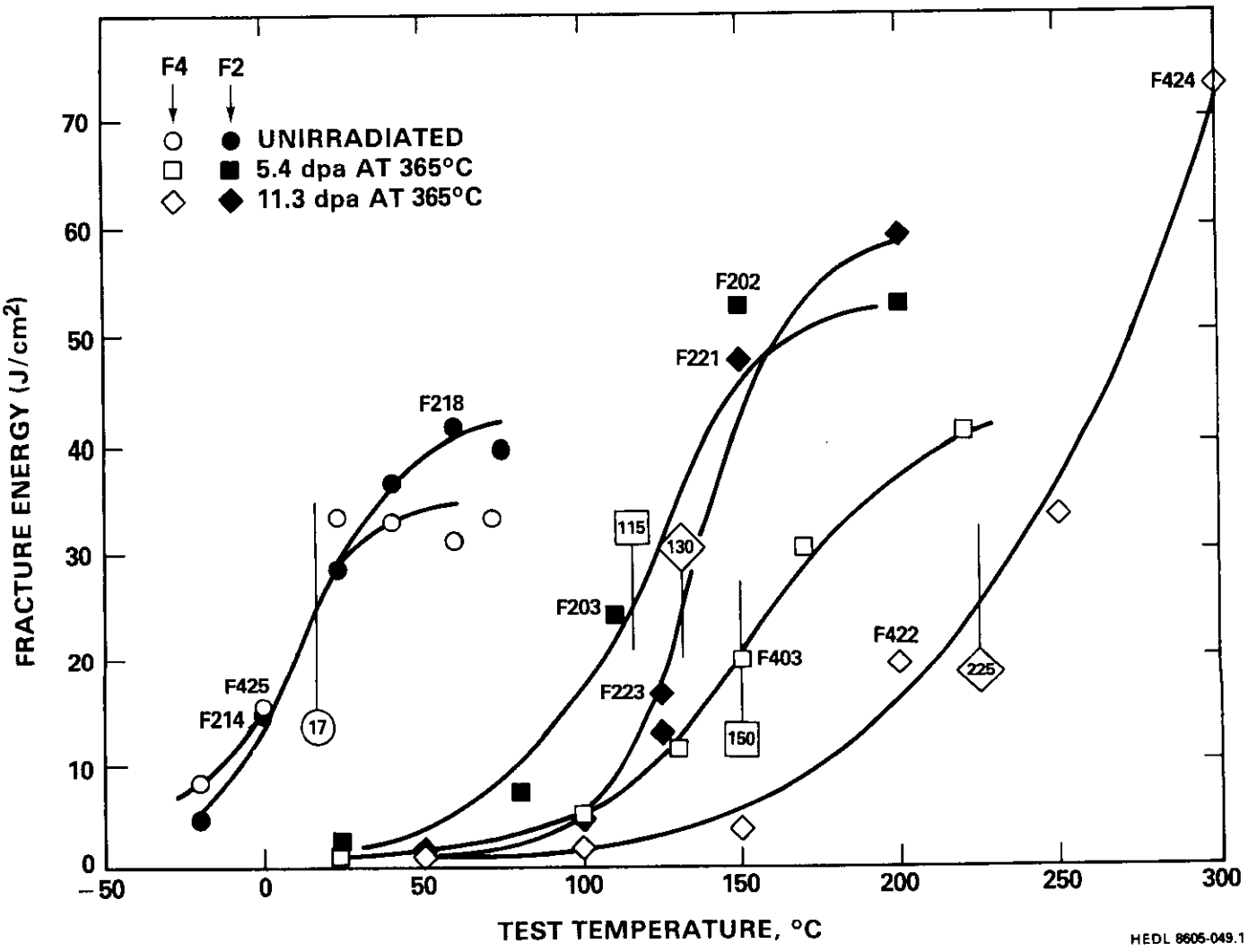

Fig. 1. Charpy impact fracture energy as a function of test temperature for manganese stabilized martensitic steels with specimens selected for examination indicated by identification number.

Table 1. Charpy specimens selected for fractographic examination

Specimen I.D.	Test Temperature (°C)	Total Fracture Energy (Joules)	Normalized Fracture Energy (J/cm²)
UNIRRADIATED			
F214*	0	2.152	14.56
F218	60	6.095	41.29
F425**	0	2.283	15.21
IRRADIATED AT 365°C TO 5.4 DPA			
F203	110	3.496	23.73
F202	150	7.665	52.67
F403	150	2.869	19.66
IRRADIATED AT 365°C TO 11.3 DPA			
F223	125	2.395	16.53
F221	150	6.963	47.36
F422	200	2.807	19.31
F424	300	10.626	73.04

*Composition of F2: Fe-11.8Cr-3.33Mn-0.96Mo-0.21V-0.16Nb-0.12C (wt. percent)
**Composition of F4: Fe-12.0Cr-6.57Mn-0.96Mo-0.20V-0.15Nb-0.11C

Results

Fractography

The results of fractographic examination will be presented by alloy, first showing results for alloy F2 with 3.3% Mn and then showing results for F4 with 6.5% Mn.

Specimens containing 3.3% Mn in the unirradiated condition showed behavior typical of a martensitic stainless steel. Examples of fracture surfaces at the transition temperature and on the upper shelf are shown in Figs. 2 and 3, respectively. In each case, part (a) provides a stereo pair at low magnification with the fatigue precrack on the left and the fracture surface created during the Charpy test adjacent to it. Therefore, crack propagation proceeded from left to right. Part (b) gives a higher magnification stereo pair example of the central region of the fracture surface immediately adjacent to the fatigue surface with the fatigue surface again shown on the left. The stretch zone adjacent to the fatigue surface at the transition temperature is on the order of 15 μm whereas on the upper shelf it is closer to 50 μm. Brittle failure consists of plateau regions of brittle failure connected by steeply inclined transitions which have been typically identified as prior austenite grain boundaries. Therefore, the prior austenite grain size is on the order of 350 μm. Failure on the upper shelf is by dimple rupture, with a fine dimple size on the order of 10 μm.

Following irradiation to 5.4 dpa at 365°C, the fracture behavior for specimens containing 3.3% Mn was similar to unirradiated specimens, but transition regions corresponding to martensite lath boundaries were in greater evidence. Examples of behavior at the transition temperature and on the upper shelf are given in Figs. 4 and 5. Examination of Fig. 4 in stereo reveals that the brittle plateaus have become rougher, and vertical transition regions can be found more frequently within prior austenite grains as seen at higher magnification. Upper shelf response appears to have generated a finer dimple size near the fatigue surface . Both observations suggest precipitation is occurring during irradiation, weakening lath boundaries and providing more cavity nucleation sites. The stretch zone at the transition temperature remains at about 15 μm whereas for the upper shelf it increases to about 100 μm based on the lower part of Fig. 5b.

Similar response is found following irradiation to 11.3 dpa at 365°C except that the dimple size for upper shelf behavior appears intermediate between unirradiated and low dose irradiation response. Examples are given in Figs. 6 and 7 for behavior at the transition temperature and on the upper shelf, respectively. Note that the stretch zone at the transition temperature is generally about 15 μm but a region at the lower part of Figure 6b shows a stretch zone closer to 30 μm. The stretch zone for upper shelf response varies between 35 and 60 μm. It can therefore be concluded that a straightforward relationship between fracture energy and stretch zone size does not exist. The variation of upper shelf energy with fluence is more likely a result of crack propagation than crack initiation.

The fracture surface of unirradiated alloy F4 with 6.5% Mn tested at the transition temperature is shown in Fig. 8. This specimen also shows normal response with a prior austenite grain poorly defined but on the order of 300 μm and a stretch zone on the order of 10 μm. Based on the appearance of the brittle fracture appearance, it is likely that the martensite lath structure is finer in alloy F4 than in F2.

Irradiation of alloy F4 at 365°C to 5.4 dpa altered the fracture appearance significantly. This can be shown in Fig. 9 which provides an example of failure at the transition temperature. Brittle cleavage plateaus are no longer apparent. Instead, smaller facets appear which is typical of grain boundary failure. Also of note is the presence of several deep fissures in the center of the specimen as shown in Fig. 9a. Both features indicate grain boundary and subgrain boundary embrittlement. An apparent change in fracture appearance can be seen creating a narrow band of fine structure separating two facetted regions. Such structure results when fracture goes from brittle to ductile and then back to brittle again.

The fracture surfaces of alloy F4 irradiated at 365°C to 11.3 dpa are shown in Figs. 10 and 11 for tests at the transition temperature and on the upper shelf, respectively. The brittle failure shown in Fig. 10 is more typical than in Fig. 9 but examples of some very deep fissures can be seen. Grain boundary embrittlement is evident. As in Fig. 9, there is an apparent change in fracture appearance creating a narrow band of fine structure separating two brittle regions and indicating a return to brittle failure after ductile failure begins. Fig. 11 shows the characteristic dimple rupture failure of upper shelf response but it too is unusual in that only a small triangular region adjacent to the fatigue crack is parallel to the fatigue surface. The rest is steeply inclined. Such response is common in miniature compact tension specimens where surface effects dominate most of the fracture process but is unusual in miniature Charpy specimens. This fracture morphology suggested that a great degree of plane stress state existed at the crack front and extensive plastic deformation occurred prior to failure initiation.

The cause of grain boundary embrittlement could be traced to precipitate development at grain boundaries. This is shown in Fig. 12 which provides higher magnification examples of structure on prior austenite grain boundaries in specimens F403 and F422. Fig. 12a shows a boundary region in alloy F4 irradiated to 5.4 dpa, and Fig. 12b shows a similar region in alloy F4 irradiated to 11.3 dpa. Precipitate particles can be clearly seen decorating the boundaries and many small cavities and fissures can be identified. However, failure is either by brittle fracture or shear because the cavities are not typical

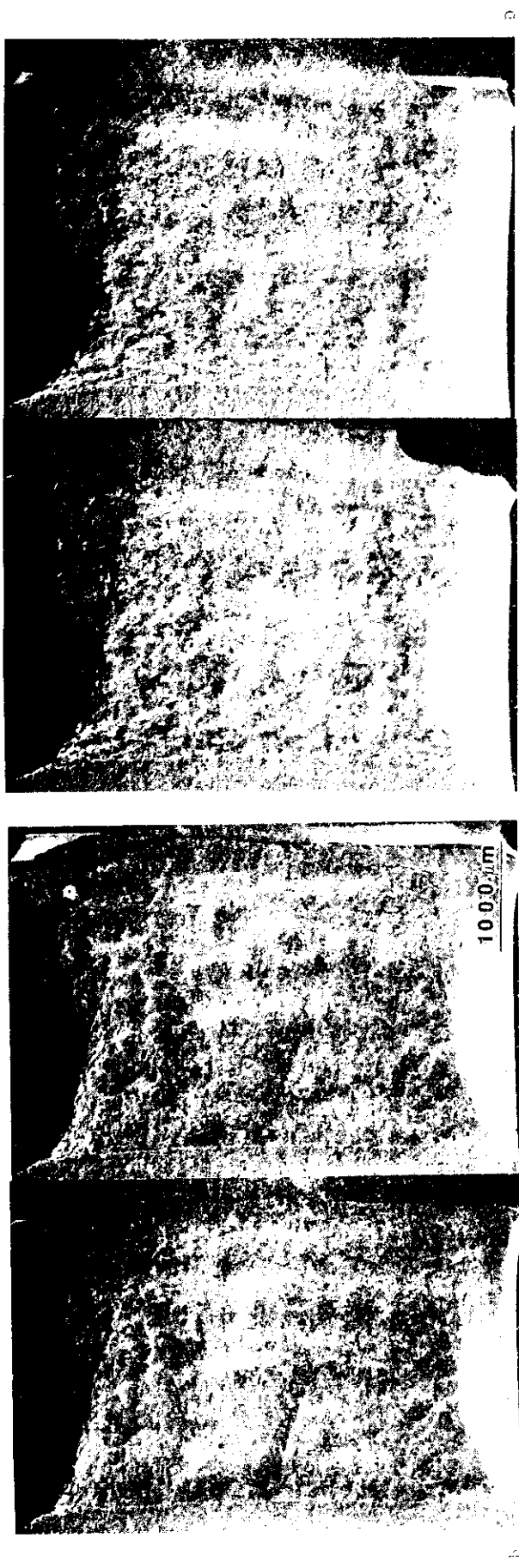

Fig. 2. Stereo fractograms of unirradiated alloy F2 specimen F214 tested at 0°C near the transition temperature a) at low magnification and b) higher magnification.

Fig. 3. Stereo fractograms of unirradiated alloy F2 specimen F218 tested at 60°C on the upper shelf a) at low magnification and b) higher magnification.

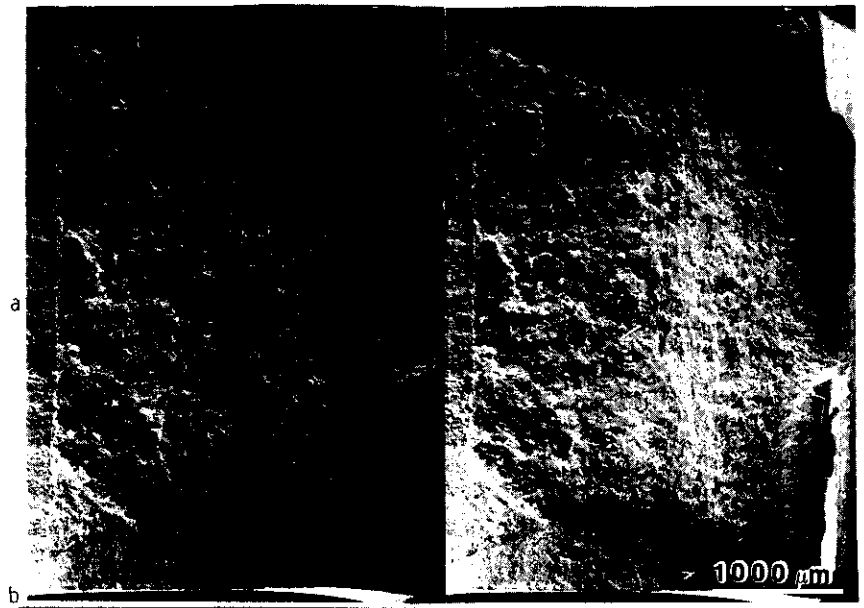

Fig. 4. Stereo fractograms of alloy F2 specimen F203 irradiated at 365°C to 5.4 dpa and tested at 110°C near the transition temperature a) at low magnification and b) higher magnification.

Fig. 5. Stereo fractograms of alloy F2 specimen F202 irradiated at 365°C to 5.4 dpa and tested at 150°C on the upper shelf a) at low magnification and b) higher magnification.

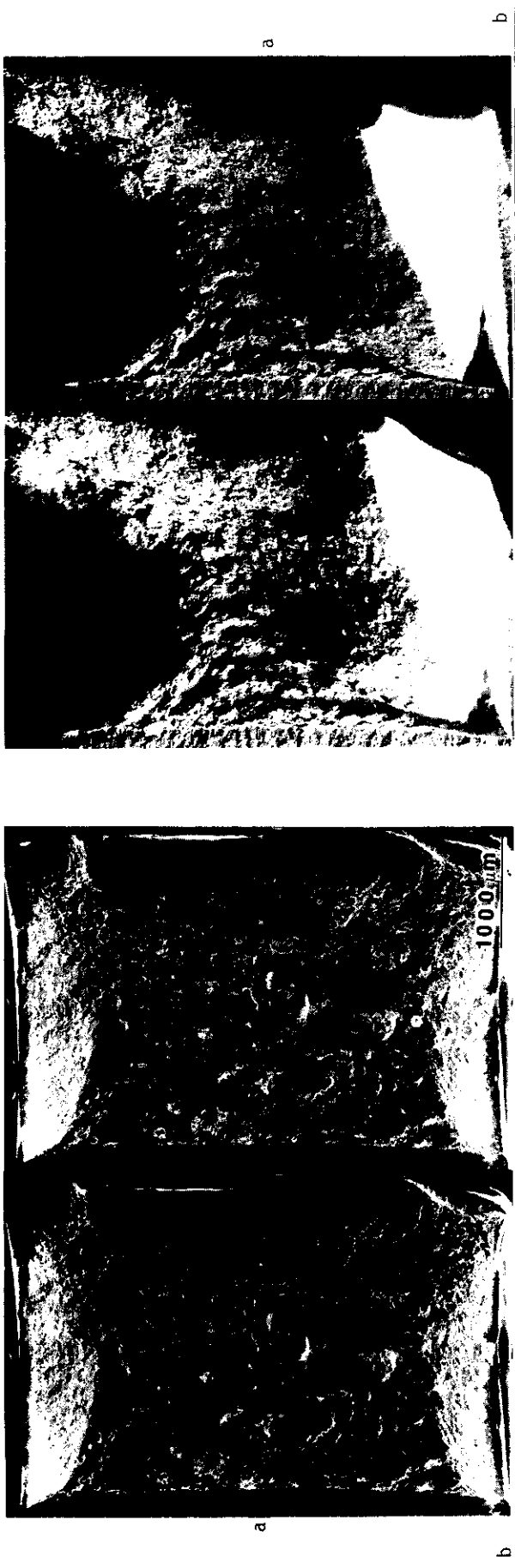

Fig. 6. Stereo fractograms of alloy F2 specimen F223 irradiated at 365°C to 11.3 dpa and tested at 125°C near the transition temperature a) at low magnification and b) higher magnification.

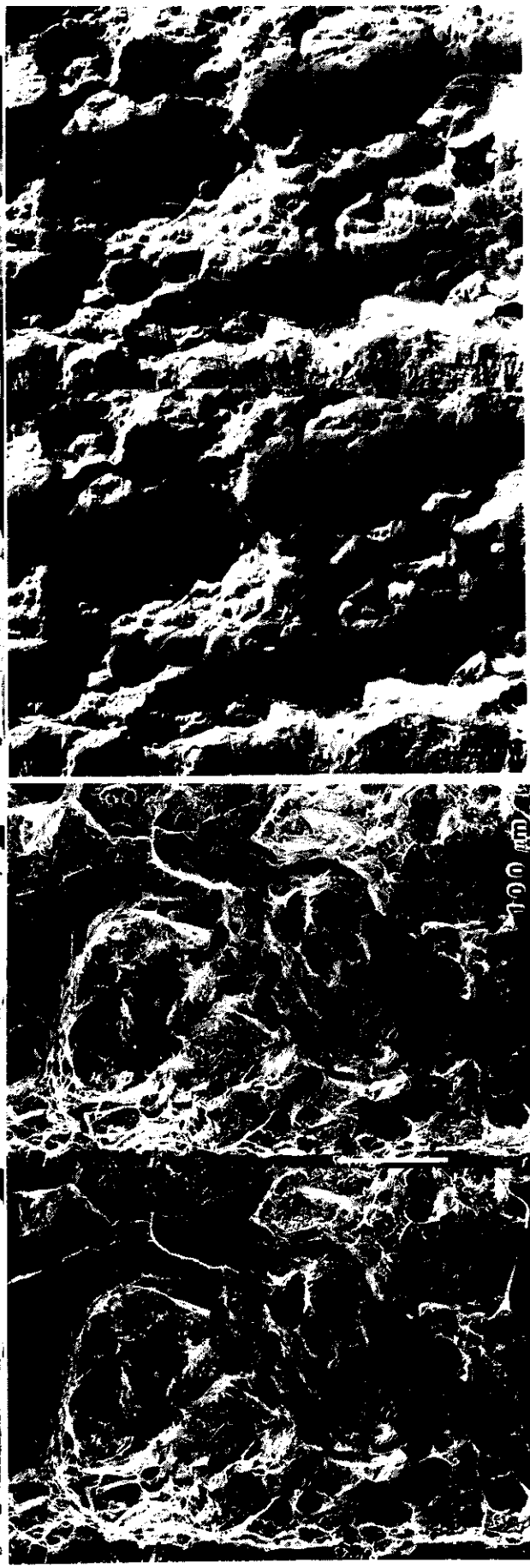

Fig. 7. Stereo fractograms of alloy F2 specimen F221 irradiated at 365°C to 11.3 dpa and tested at 150°C on the upper shelf a) at low magnification and b) higher magnification.

Fig. 8. Stereo fractograms of unirradiated alloy F4 specimen F425 tested at 0°C near the transition temperature a) at low magnification and b) higher magnification.

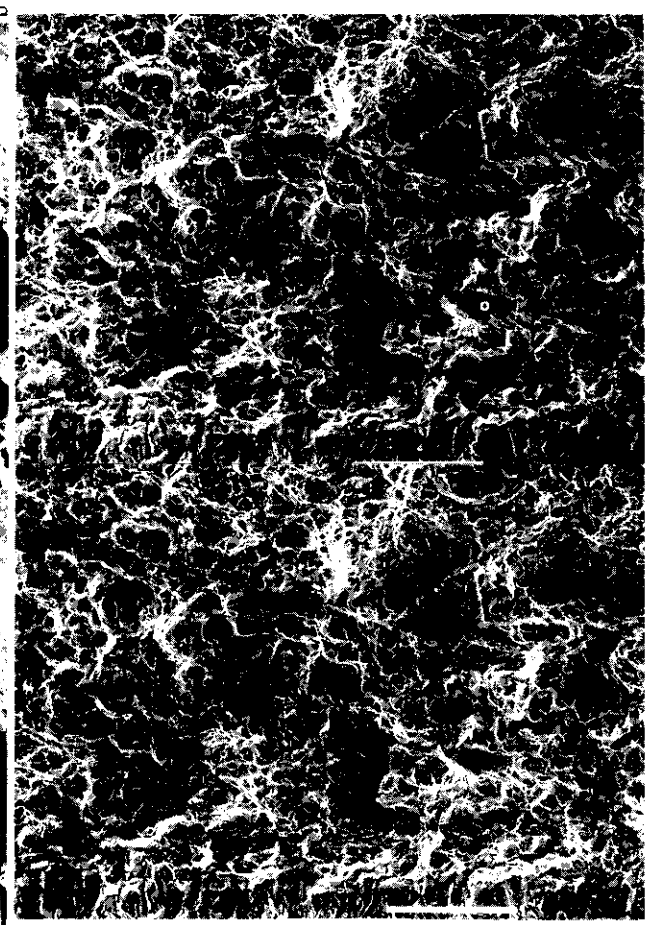

Fig. 9. Stereo fractograms of alloy F4 specimen F403 irradiated at 365°C to 5.4 dpa and tested at 150°C near the transition temperature a) at low magnification and b) higher magnification.

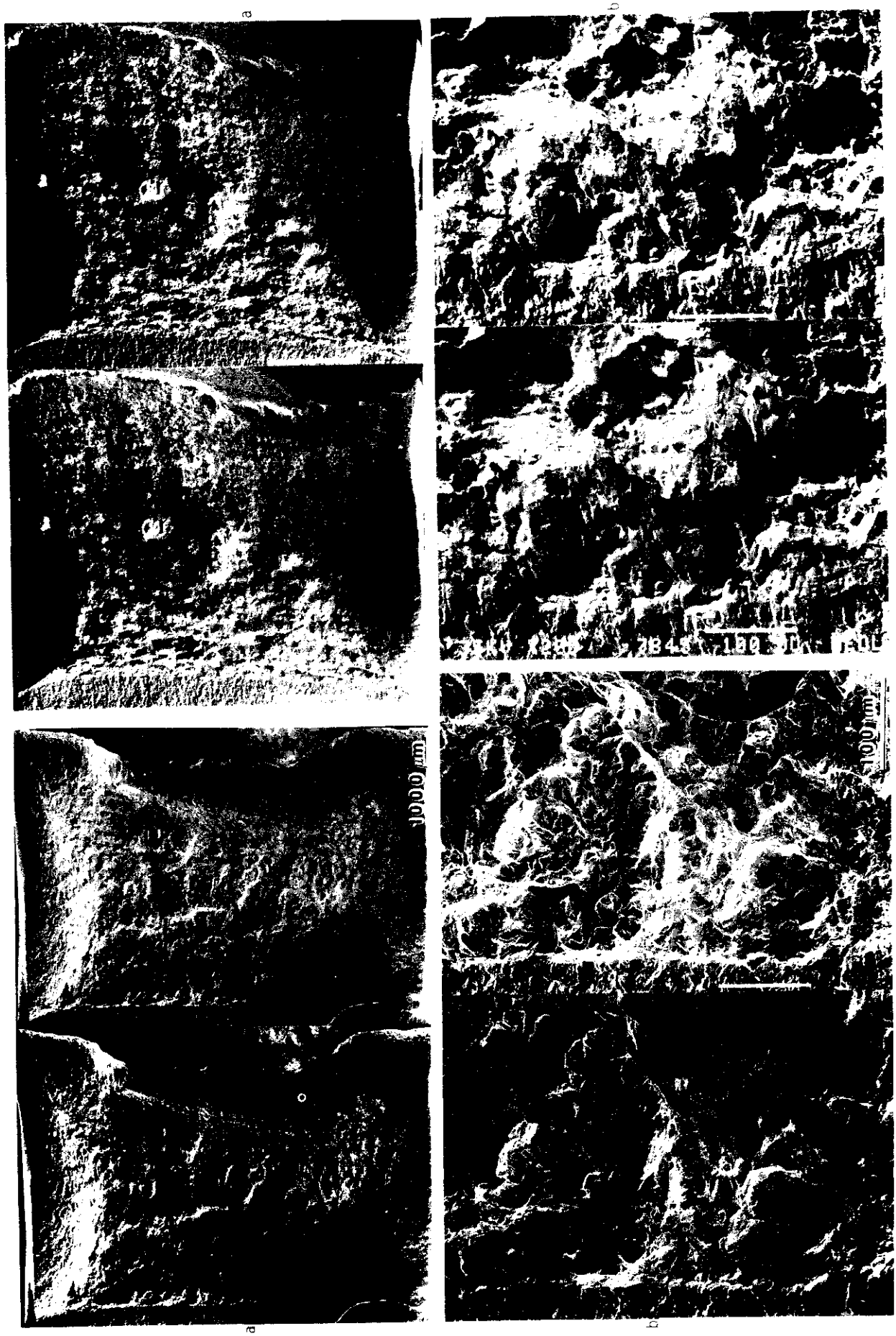

Fig. 10. Stereo fractograms of alloy F4 specimen F422 irradiated at 365°C to 11.3 dpa and tested at 200°C near the transition temperature a) at low magnification and b) higher magnification.

Fig. 11. Stereo fractograms of alloy F4 specimen F424 irradiated at 365°C to 11.3 dpa and tested at 300°C on the upper shelf a) at low magnification and b) higher magnification.

of dimple rupture. More likely, they are impressions of particles which remained attached to the other half of the fractured specimen.

Microscopy

Examples of prior austenite grain boundary structure in alloy F4 are given in Fig. 13. Fig. 13a shows a grain boundary region in the unirradiated alloy. The boundary is poorly defined by precipitate particles but an example of a larger carbide particle can be seen. Fig. 13b shows the structure following irradiation at 407°C to 9.8 dpa and includes a ferrite grain at the lower left. Precipitates are larger and more clearly defined in this structure, but grain boundary precipitates do not form a continuous coating. As is usually the case, precipitation on ferrite boundaries is more extensive than on boundaries between grains containing only martensite. Also of note is the observation of void swelling in the ferrite grain. Void swelling was not found in martensite grains. Fig. 13c provides an example of the microstructure at a prior austenite grain boundary in alloy F4 following irradiation at 518°C to 14.4 dpa. In this case, the precipitate structure forms in two distinctly different size distributions, a size characteristic of the starting structure and a much large size. Analysis demonstrated that the smaller particles were $M_{23}C_6$ but the larger particles were a body centered cubic phase identified as chi. Fig. 14 has been prepared to show this identification. The large precipitate particle shown was tilted to several major orientations of interest and microbeam diffraction patterns were taken as shown. The phase is clearly body centered cubic with a lattice parameter approximately three times that of the matrix. Attempts to define the composition of this phase in the foil indicated a composition of Fe-16.2Cr-10.2Mn-3.0Mo-0.7Si where the silicon peak probably represented tungsten. Therefore, the composition is similar to Fe-30Cr-30Mo chi phase except that manganese appears to be substituting for molybdenum and iron may also be occupying molybdenum sites. Extraction replicas to isolate this phase were not completely successful. Compositions similar to that above were obtained, but the particles being analyzed were not clean and were coated with debris which may have been rust. Extraction of chi phase is generally a difficult process.

Discussion

When the concept of manganese stabilized martensitic stainless steels was applied to alloy design for fusion reactor applications, it was assumed that manganese additions would be innocuous with regard to phase instability. The published phase diagrams[3-4] gave no indications that intermetallic phase instabilities would occur in Fe-Cr-Mn phase space to manganese levels as high as 30%. Therefore, the possibility of substituting manganese for nickel and carbon to reduce nickel and carbon contents but still retain a fully martensitic structure appeared promising. No adverse effects on mechanical properties due to phase instabilities were anticipated.

Experiments on the present series of manganese stabilized martensitic stainless steels proves otherwise. DBTT properties are degraded by irradiation to the point where properties are expected to be significantly worse than those of HT-9. The degradation appears to be a result of precipitate formation on grain boundaries. Examination of a TEM specimen irradiated at higher temperature demonstrates the existence of significant quantities of chi phase, an intermetallic phase rich in iron and containing significant quantities of chromium and manganese. The volume fraction of the phase may be as high as 10%. Chi phase may not in fact be the precipitate causing embrittlement at lower temperatures but its existence certainly demonstrates that phase instabilities can occur in these steels.

It is interesting to note that chi phase is generally referred to as having the α-manganese crystal structure. Yet the α-manganese phase field is clearly defined and does not extend across the phase diagram to the composition found in the present study. Instead, the presence of manganese tends to stabilize the more common Fe-Cr-Mo form. It is not yet known whether Fe-Cr-Mn chi phase forms thermally or whether the presence of molybdenum, tungsten and/or carbon is required. Evidence for it has not been located in the literature. Therefore, further study of the phase appears warranted.

The implications of this work to alloy design are significant. Manganese stabilization of martensitic stainless steels is likely to lead to embrittlement. Low activation martensitic alloy design will probably not be worthwhile in the Fe-12Cr composition range unless manganese is low and carbon levels are set above 0.2% which will probably be too high. Therefore the most promising composition range for low activation steel development is Fe-10Cr-W with possibly minor additions of vanadium and tantalum. Key questions which remain to be answered concern the levels of carbon, tungsten, vanadium and tantalum.

CONCLUSIONS

Fractographic examination has been performed on selected Charpy specimens of manganese stabilized martensitic stainless steels in order to identify the cause of irradiation-induced embrittlement. Embrittlement was found to be partly due to enhanced failure at grain boundaries arising from precipitation. Microstructural examination of a specimen irradiated at higher temperature has demonstrated the presence of Fe-Cr-Mn chi phase, a body centered cubic intermetallic phase known to cause embrittlement. This work indicated that manganese stabilized martensitic stainless steels are prone to intermetallic phase formation which is detrimental to mechanical properties.

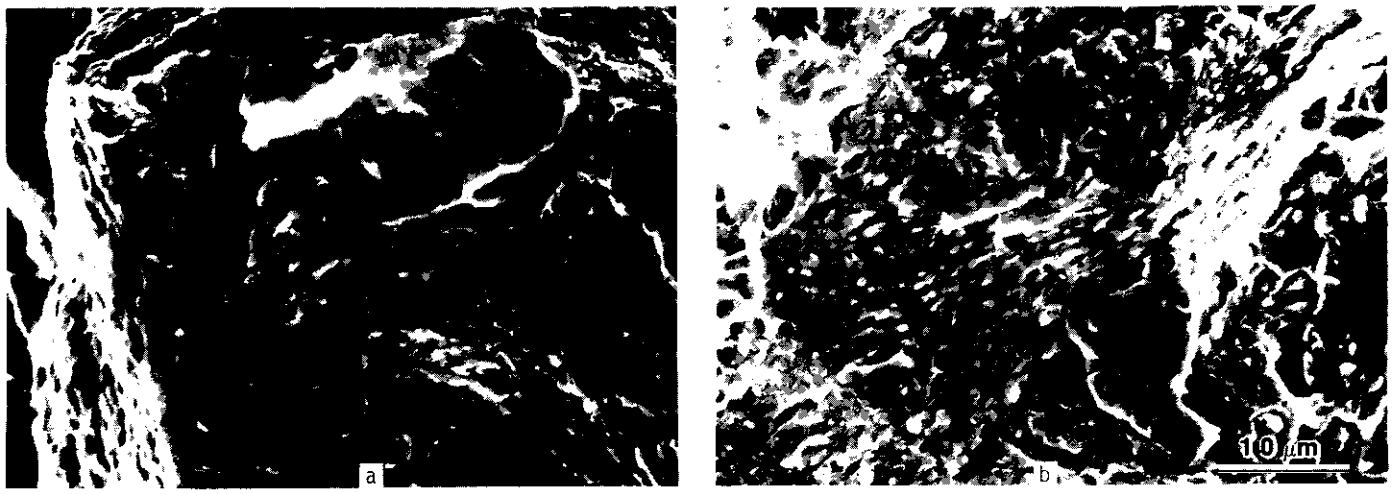

Fig. 12. Examples of precipitate structure on prior austenite boundaries in a) specimen F403 and b) specimen F422.

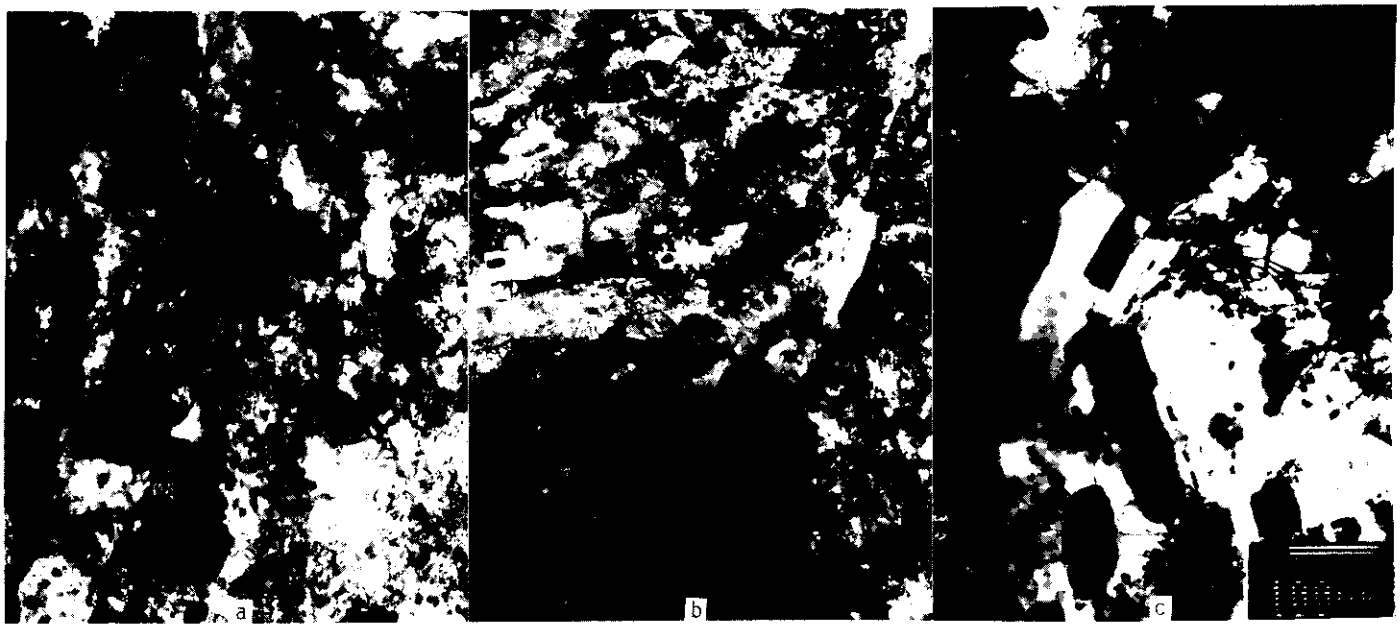

Fig. 13. Prior austenite grain boundaries in alloy F4 at low magnification a) unirradiated, b) irradiated at 407°C to 9.8 dpa and c) irradiated at 518°C to 14.4 dpa.

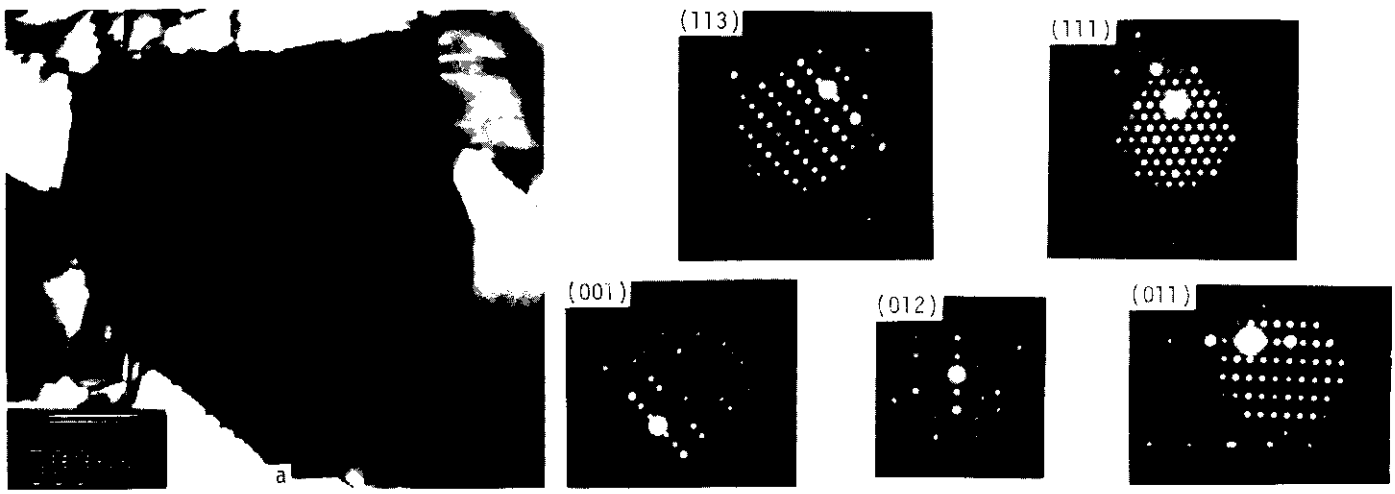

Fig. 14. A chi phase precipitate particle in alloy F4 following irradiation at 518°C to 14.4 dpa with several major pole microbeam diffraction patterns.

FUTURE WORK

This work will be concluded after it is established whether phase instability is thermally induced.

REFERENCES

1. W. L. Hu and D. S. Gelles, "Charpy Impact Behavior of Manganese Stabilized Martensitic Steels," DOE/ER-0045/16, to be published.

2. Letter, A. M. Ermi to Distribution, "Fusion Materials Specimens from MOTA-1C FFTF Cycles 5-6," dated October 11, 1985, HEDL-7630, Westinghouse Hanford Company, Richland, WA.

3. V. G. Rivlin and G. V. Raynor, "Critical Review of Constitution of Ternary Systems Fe-Mn-X (X = Ti, V, Cr, Co, Ni, Cu)," Int. Metals Rev., 28, 23 (1983).

4. E. A. Brandes and R. F. Flint, "The Cr-Fe-Mn System," Bull. of Alloy Phase Diagrams, 2, 103 (1981).

6.2 Austenitic Stainless Steels

TENSILE PROPERTIES OF HFIR-IRRADIATED AUSTENITIC STAINLESS STEELS AT 250 TO 400°C FROM THE EUROPEAN COMMUNITY/U.S./JAPAN FUSION MATERIALS COLLABORATION — M. L. Grossbeck (Oak Ridge National Laboratory)

OBJECTIVE

Austenitic steels are being irradiated in different experimental reactors to achieve a variation in He:dpa ratio. Mechanical properties at temperatures relevant to INTOR are being determined; in the present report, only tensile property results are presented.

Four alloys were selected for study: European Community (EC), type 316 stainless steel (EC316); U.S. type 316 stainless steel (US316); Japanese PCA (JPCA); and USPCA. All four alloys are being irradiated in the HFIR at Oak Ridge, the HFR at Petten, the BR-2 at Mol, Belgium, and the R2 at Studsvik, Sweden. Furthermore, the U.S. alloys are being irradiated in the ORR at Oak Ridge. The present report details the tensile property experiment using the HFIR.

SUMMARY

In the collaborative experiments, four austenitic stainless steels (EC316, US316, USPCA, JPCA) are being irradiated in four reactors to exploit the variation in neutron energy spectrum. In this way the effect of He:dpa ratio can be investigated. Tensile properties were determined for all four alloys irradiated to a maximum of 10 dpa and containing a maximum of 550 appm He, depending upon the nickel concentration in the alloy and position in the reactor. Irradiation temperatures of 250 to 400°C were chosen because of their particular relevance to INTOR. The U.S. alloys were prepared in the cold-worked condition, the EC and Japanese alloys in the annealed condition.

The tensile behavior more nearly reflected the differences in initial condition than the differences between irradiation properties of the alloys, the cold-worked material remaining stronger even after irradiation. In general, irradiation in this temperature range clearly produced hardening with accompanying reduction in ductility. All four alloys, with the possible exception of JPCA, exhibited rather low uniform elongation. There was no evidence for helium embrittlement.

PROGRESS AND STATUS

Introduction

Canada, the European Community, Japan, the United States, and Switzerland have signed an IEA Implementing Agreement for a program of research and development on radiation damage in fusion materials. The working group on the IEA Implementing Agreement, Annex II, arranged a workshop in Oak Ridge in August 1982 which developed an irradiation test plan. A total of five experimental reactors were chosen for the study: the HFIR in the United States, the HFR in Petten, the BR-2 in Belgium, the R2 in Sweden, and to a limited extent, the ORR in the United States. The purpose in using such a variety of reactors was to achieve a range of He:dpa values from the fusion reactor level of about 12 to about 50 appm/dpa. A broad range of properties is being investigated: in situ and postirradiation fatigue, irradiation creep, and postirradiation tensile properties. A test matrix appears in Table 1. Four alloys were chosen for the investigation: European Community type 316 stainless steel (EC316), U.S. Fusion Program type 316 stainless steel (HT X15893) (US316), Japanese PCA (JPCA), and U.S. fusion PCA (USPCA). The compositions of the alloys appear in Table 2.

In this report, only the tensile properties from the HFIR are discussed. These data will be combined with corresponding data from the HFR and published as a single report.[1]

Experimental Procedure

HFIR Irradiation Two irradiation capsules designated HFIR-CTR-44 and -45 were employed in which eleven specimens were arranged linearly along the capsule axes. The specimens were positioned in holders (Fig. 1) which provided a gas gap between the specimen and the aluminum holder to impede heat transfer and thus provide passive control of the irradiation temperature. The specimens were held in place by end spurs with the result that the axial temperature was very uniform along the specimen gage section but rather steep along the spurs (which were of no consequence to subsequent tests). The gas gaps were adjusted to compensate for the flux gradient along the capsule.

The capsules were filled with helium and irradiated with reactor coolant water, at an average of 55°C, in contact with the capsule outer wall. The capsules were positioned on the periphery of the target region adjacent to the inner fuel element in order to achieve a high fast flux as well as a high thermal flux.

Table 1. Oak Ridge Test Matrix

No.	Test	Parameter	A BR2 Mol		B HFIR Oak Ridge		C HFR Petten	D ORR Oak Ridge	E R2 Studsvik	Remarks	European Test Type
1	In-pile fatique	Experiment name									
		Material	(4)	(3)			To be defined				MAT
		Specimen geometry	HG	HG (2)							2
		Test Temp., °C	430	250			320 to 400				
		Exposure, dpa	10				3 to 10				
		Irradiation start	Begin 1987				Beyond 1986				
2	Post-irradiation fatique	Experiment name	FAFUMA 1	FAFUMA 2 (5)	CTR-14 15,20-22	CTR-52			Different alloys; flat bending	HG specimens for "push-pull" testing are included in the R2 Studsvik rig	MAT 1
		Material	(1)	(3)	(4)	(3)					
		Specimen geometry	HG	HG	HG	HG (7)			250		
		Test Temp., °C	430	250	430	430			5 to 10		
		Exposure, dpa	10	10	(PIE				09/33		
		Irradiation start	02/34	06/95	com-	01/94			06/86		
		Irradiation end	08/85	06/97	pleted 1982)	07/84					
3	In-pile crack growth		(design study on thin flat specimen)				INFANTE FATMAC (design studies)	HEDL sponsored capsule completed; no further action		Design studies are available from Mol, Saclay, and Petten	MAT 4
4	In-pile creep	Experiment name					TRIESTE + CRISP	TBC 07		CRISP: In-pile creep machine with on-line measurements. Start of prototype mid-1985. ORR pressurized tube rig uses sample recirculation	MAT 5
		Material					(9),(10)	(10),(11)			
		Specimen geometry					Cyl. Petten design	Tubes			
		Test Temp., °C					320 to 400	350,400,500, 600			
		Exposure, dpa					~5	5, 10, 20			
		Irradiation start					11/83	mid-1983			
		Irradiation end					beyond 1986				
5	Post-irradiation	Experiment name	FAFUMA 2		CTR-44, -45		FRUST 10	MFE-4A, 4B		Inter-laboratory tests. All clindr. CEC and U.S. steel specimens have been manufactured by Petten to ORNL drawings.	MAT 1
		Material	(3),(6),(10)		(3)		(3),(6), (10)	(10)	(3),(6),(10)		
		Specimen geometry	ORNL cylinder				ORNL cylinder	ORNL, flat	ORNL cylinder		
		Test Temp., °C	250		400		250	330 to 600	250		
		Exposure, dpa	5 and 10		10		10	10	5 to 10		
		Irradiation start	06/85 (5)		01/83		08/82	(8)	09/93		
		Irradiation end	06/97		05/83		06/85 (12)	Same rig as 4D	Same rig as 2E 06/86		

(1) Test 2A1 (BR2 Mol post-irr fatique) to contain samples of CEC, U.S. ref. 316, and U.S. PCA.
(2) HG = "hourglass" specimen.
(3) CEC ref. = Ispra stockpile of 316 L stainless steel.
(4) U.S. ref. 316 = ORNL stockpile 316 steel.
(5) Tests 2A-2 and 5A are carried out in the same in-pile rig (250°C) with CEC ref. incl. weldments, some CEC ref., U.S. ref. 316 + PCA, Japan PCA tensile.
(6) Japan prime candidate alloy.
(7) Assembly of CEC fatique capsule in 12/83; PIE not before end 1985.
(8) 340 to 400°C reached 10 dpa in 03/84; 500 to 600°C; reached 10 dpa in 12/84.
(9) Four types of high Mn AMCR type alloys.
(10) ORNL stockpile 316 stainless steel and U.S. PCA.
(11) 5 dpa data are available.
(12) PIE results are available.

Table 2. Chemical composition of the four alloys

Heat	Composition, wt %													
	Cr	Mn	Ni	Mo	Co	Cu	Si	Nb	Ta	Ti	B	C	S	P
JRC-Ispra type 316	17.5	1.8	12.3	2.4	0.18	0.21	0.43	--	<0.15	--	0.0023	0.021	<0.009	<0.029
ORNL (HT X15893) type 316	17.3	1.7	12.4	2.1	0.3	0.3	0.67	<0.05	<0.05	<0.05	0.0004	0.061	0.081	0.037
ORNL PCA	14.5	1.8	15.6	2.3	0.003	0.005	0.42	0.001	--	0.24	0.00003	--	<0.001	0.008
JAERI PCA	14.6	1.8	16.2	2.4	--	--	0.53	--	--	0.24	--	--	--	--

Table 3 shows the specimen loading, alloys, and irradiation parameters for the HFIR specimens. The values for displacement damage were computed from dosimetry measurements made by L. R. Greenwood.[2] The helium levels were calculated from relations developed by Greenwood from a series of HFIR experiments.[3] Helium produced from (n,α) reactions by fast neutrons in nickel, by thermal neutrons by the series of reactions $^{58}Ni(n,\gamma)$, $^{59}Ni(n,\alpha)$, and by (n,α) reactions in boron present in the alloys are all included in the reported values.

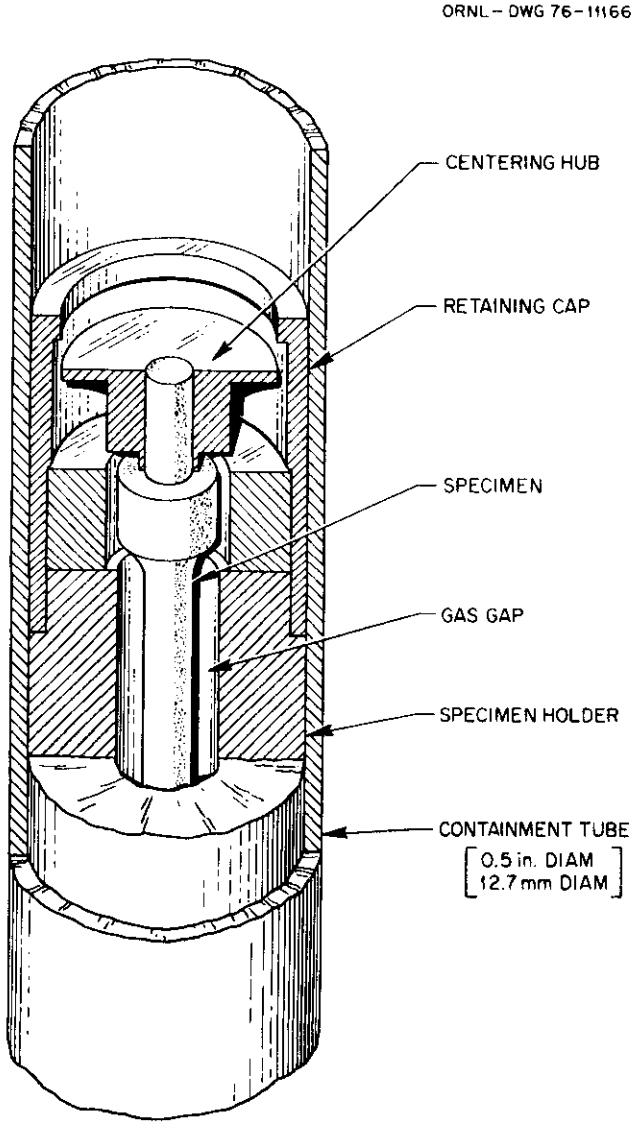

Fig. 1. Tensile specimens positioned in irradiation fixture for the HFIR.

Temperatures are values calculated using a two-dimensional heat transfer code (HEATING III)[4] and nuclear heating values determined by previous experiments using melt-wire monitors.

The HFIR specimens were tested on an Instron screw-driven tensile test system equipped with a resistance furnace and an ultrahigh vacuum system. The system is in a radiation hot cell and operates remotely. The load measuring system has a maximum load capability of 0.22 kN. Calibration following the testing showed that the accuracy was within 0.35% on all ranges.

All specimens were tested in vacuum at a pressure not exceeding 1.5×10^{-4} Pa. A strain rate of 4.6×10^{-4} s^{-1} was used for all tests.

Results

Tensile results have been tabulated in Table 4. Both the annealed and cold-worked alloys exhibit similar tensile behavior (Figs. 2 and 3). The annealed, unirradiated material work hardens gradually until the onset of necking; the load then decreases rapidly until fracture occurs by transgranular ductile rupture. In cold-worked materials, the ability to work harden becomes exhausted at lower elongations than in the annealed material, resulting in relatively rapid onset of necking and lower total elongation. The irradiated material exhibits irradiation hardening and irradiation embrittlement, both of which are illustrated in Figs. 2 and 3.

The 0.2% yield and ultimate strengths are plotted in Figs. 4 through 7. The early onset of necking is manifest in the similarity of the yield and ultimate tensile strengths. The differences between annealed and cold-worked materials are apparent after irradiation, but to a much lesser degree than prior to irradiation. There is little dependence on irradiation temperature within the range investigated, 250 to 400°C.

Tensile elongation follows trends corresponding to strength. As shown in Figs. 8 through 11, total

Table 3. HFIR irradiation parameters and capsule layout

Position	Specimen	Alloy	Temperature (K)	Fast Fluence ($n/m^2 \times 10^{26}$)	dpa	He (appm)
			HFIR-CTR-44			
Top						
1	E135	EC316	523	0.64	5.1	140
2	E139	EC316	543	0.85	6.8	220
3	E142	EC316	563	1.02	8.2	290
4	J41	JPCA	583	1.14	9.4	489
5	E143	EC316	673	1.21	9.7	380
6	E147	EC316	613	1.23	9.9	390
7	AA31	US316	673	1.21	9.7	380
8	E150	EC316	583	1.14	9.1	349
9	E159	EC316	563	1.02	8.2	294
10	J42	JPCA	543	0.85	7.0	319
11	J44	JPCA	523	0.64	5.3	210
			HFIR-CTR-45			
1	E161	EC316	250	0.64	5.1	139
2	EK11	USPCA	270	0.85	7.0	270
3	EK12	USPCA	290	1.02	8.4	370
4	EK13	USPCA	310	1.14	9.3	434
5	EK14	USPCA	400	1.21	9.9	480
6	J45	JPCA	340	1.23	10.2	550
7	J46	JPCA	400	1.21	10.0	530
8	J470	JPCA	310	1.14	9.4	489
9	E163	EC316	290	1.02	8.2	294
10	AA41	US316	270	0.85	6.8	220
11	AA100	US316	250	0.64	5.1	140

Table 4. Irradiation and Tensile Properties

Specimen	Alloy	Test Temperature (°C)	Fluence (E > 0.1 MeV) ($\times 10^{22}$ n/cm^2)	dpa	Total Helium (appm)	Yield Stress (MPa)	Ultimate Tensile Strength (MPa)	Fracture Stress (MPa)	Elongation, % Uniform	Elongation, % Total	Pressure (Pa)
134	EC316	250	0			289	481	261	28.7	36.5	5.9×10^{-5}
135	EC316		0.640	5.1	140	724	724	391	0.31	20.4	5.5×10^{-6}
AA80	US316		0			738	765	466	2.2	9.7	1.0×10^{-4}
AA100	US316		0.640	5.1	140	972	972	617	0.28	6.4	1.0×10^{-4}
J43	JPCA		0			207	474	205	30.7	38.5	7.3×10^{-5}
J44	JPCA		0.640	5.3	210	703	724	432	8.6	15.6	9.3×10^{-5}
172	EC316	270	0			272	512	294	25.3	31.9	5.5×10^{-5}
139	EC316		0.850	6.8	220	807	807	466	0.31	14.6	1.2×10^{-4}
AA75	US316		0			724	752	450	2.0	8.7	1.2×10^{-4}
AA41	US316		0.850	6.8	220	979	986	623	0.32	6.2	1.1×10^{-4}
J430	JPCA		0			215	479	281	30.8	38.0	4.0×10^{-5}
EK151	USPCA		0			731	731	415	0.28	6.5	1.2×10^{-4}
EK11	USPCA		0.850	7.0	270	924	924	548	0.21	5.5	1.5×10^{-4}
160	EC316	290	0			292	523	241	27.7	35.7	9.3×10^{-5}
142	EC316		1.02	8.2	290	827	827	690	0.23	9.4	1.3×10^{-4}
EK16	USPCA		0			703	703	403	0.22	6.5	1.1×10^{-4}
EK12	USPCA		1.02	8.4	370	1062	1069	658	0.34	5.7	8.8×10^{-5}
166	EC316	340	0			274	523	254	25.5	32.8	1.1×10^{-4}
147	EC316		1.23	9.9	390	821	821	485	0.33	9.3	1.1×10^{-4}
J48	JPCA		0			175	453	205	31.5	38.4	9.3×10^{-5}
J45	JPCA		1.23	10.2	550	807	807	485	0.38	8.3	1.2×10^{-4}
169	EC316	400	0			237	488	301	24.4	30.4	9.2×10^{-5}
143	EC316		1.21	9.7	380	765	772	439	0.95	7.0	1.3×10^{-4}
AA73	US316		0			703	710	433	1.0	7.3	1.3×10^{-4}
AA31	US316		1.21	9.7	380	1000	1007	690	0.35	4.7	1.3×10^{-5}
J49	JPCA		0			169	441	261	30.7	37.4	9.3×10^{-5}
J46	JPCA		1.21	10.0	530	800	807	532	1.4	7.2	8.4×10^{-5}
EK15	USPCA		0			676	676	605	0.18	6.2	1.5×10^{-4}
EK14	USPCA		1.21	9.9	480	945	952	605	0.31	4.8	1.5×10^{-4}

US316 — 20% CW. EC 316 — Annealed. JPCA — Annealed. USPCA — 25% CW.

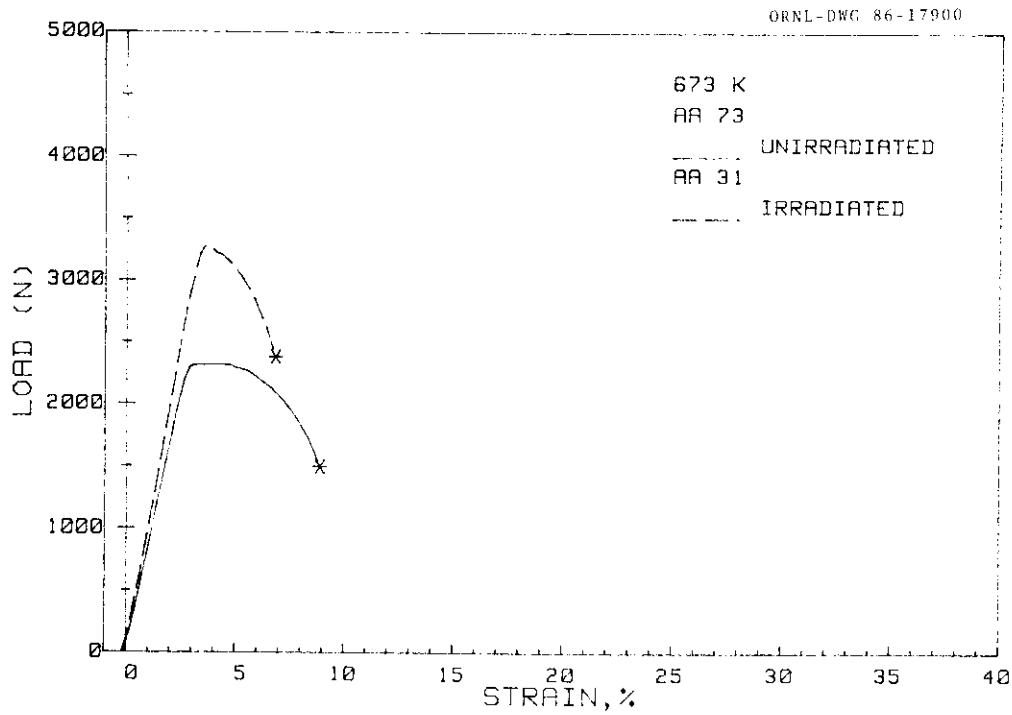

Fig. 2. Load as a function of engineering strain for 20% cold-worked U.S. type 316 stainless steel. The material was irradiated in the HFIR at 673 K (400°C) to a damage level of 9.7 dpa and a helium level of 380 appm.

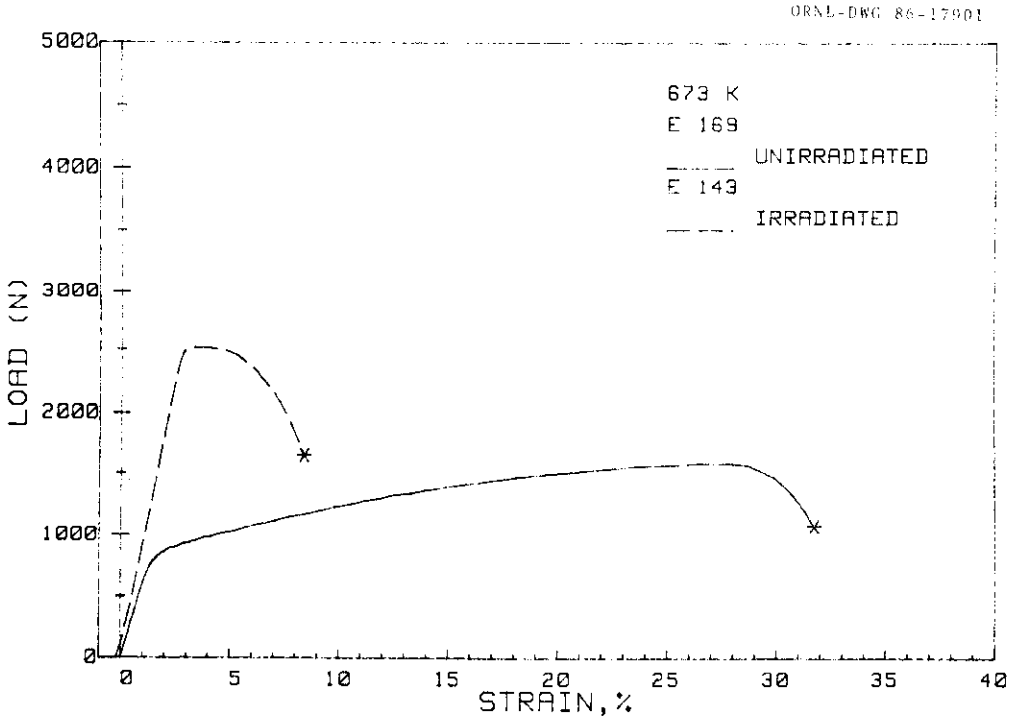

Fig. 3. Load as a function of engineering strain for annealed European community type 316 stainless. The irradiated material was irradiated in the HFIR at 673 K (400°C) to a damage level of 9.7 dpa and a helium level of 380 appm.

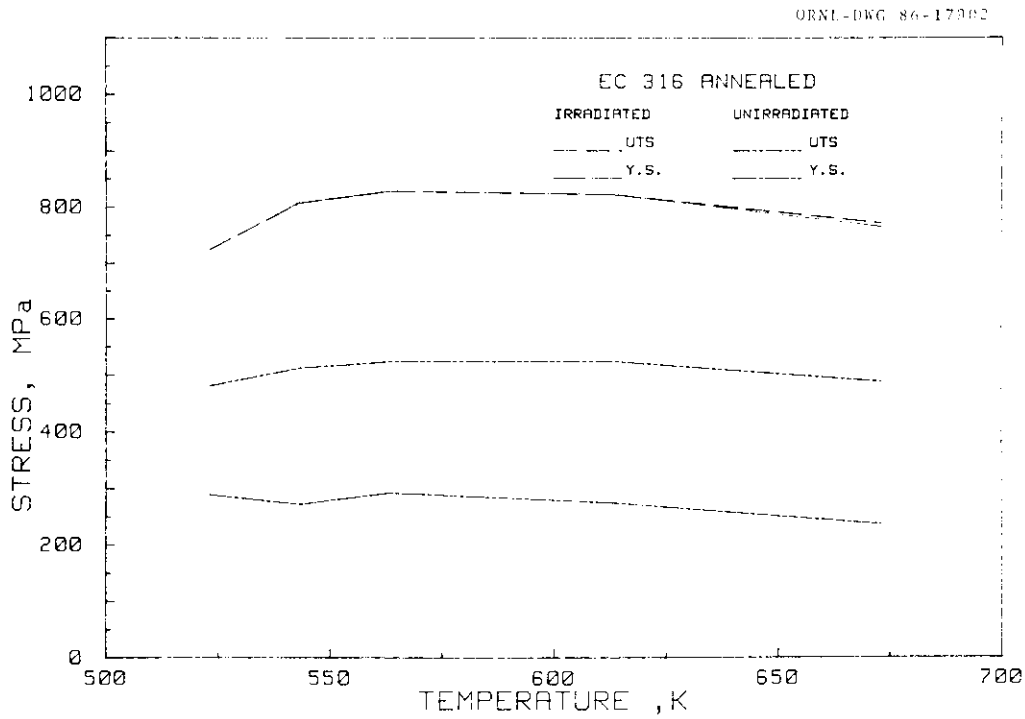

Fig. 4. Ultimate tensile strength (UTS) and 0.2% yield strength (YS) as a function of temperature (irradiation temperature = test temperature) of annealed European Community type 316 stainless steel. The irradiated material was irradiated in the HFIR up to damage levels of about 10 dpa.

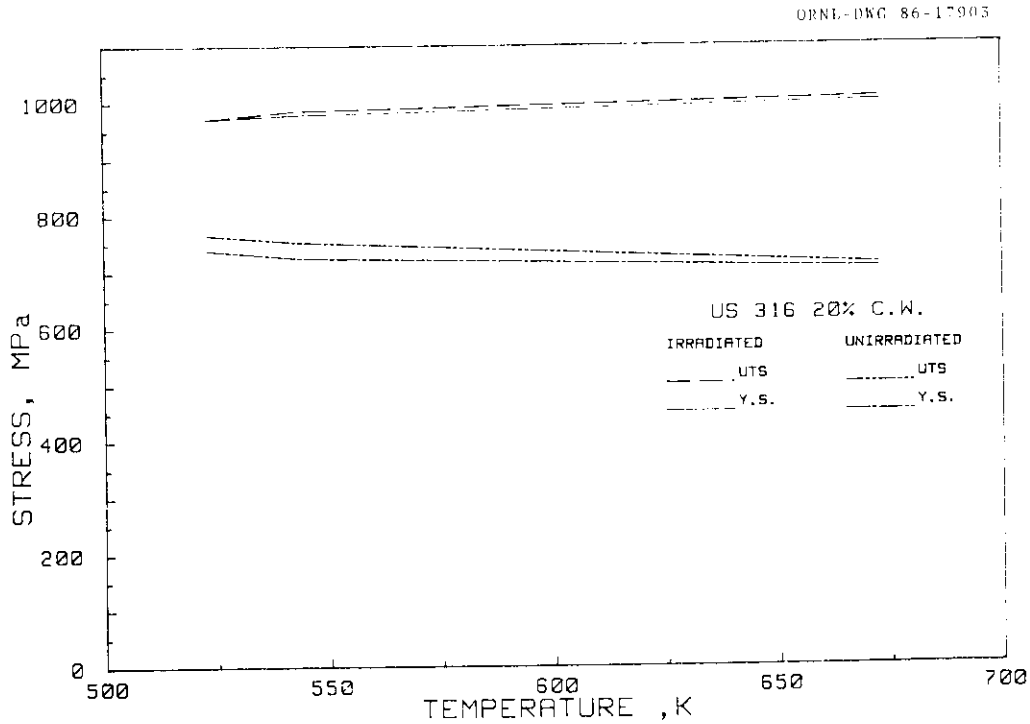

Fig. 5. Ultimate tensile strength (UTS) and 0.2% yield strength (YS) as a function of temperature (irradiation temperature = test temperature) of 20% cold-worked US type 316 stainless steel. The irradiated material was irradiated in the HFIR up to damage levels of about 10 dpa.

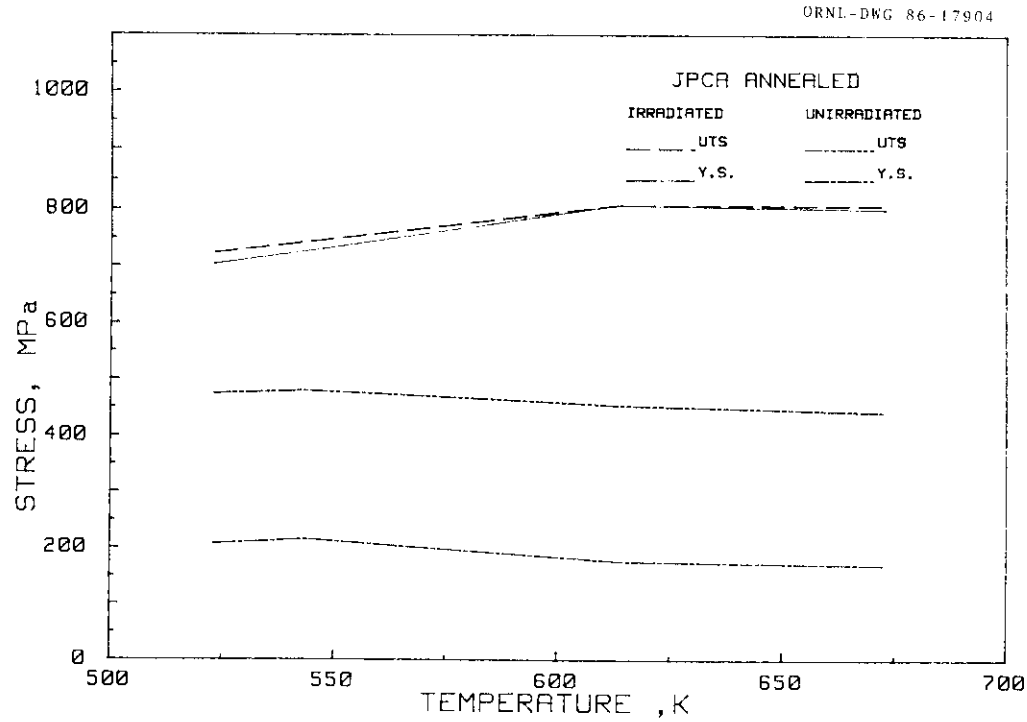

Fig. 6. Ultimate tensile strength (UTS) and 0.2% yield strength (YS) as a function of temperature (irradiation temperature = test temperature) of annealed Japanese PCA. The irradiated material was irradiated in the HFIR to a damage level of about 10 dpa.

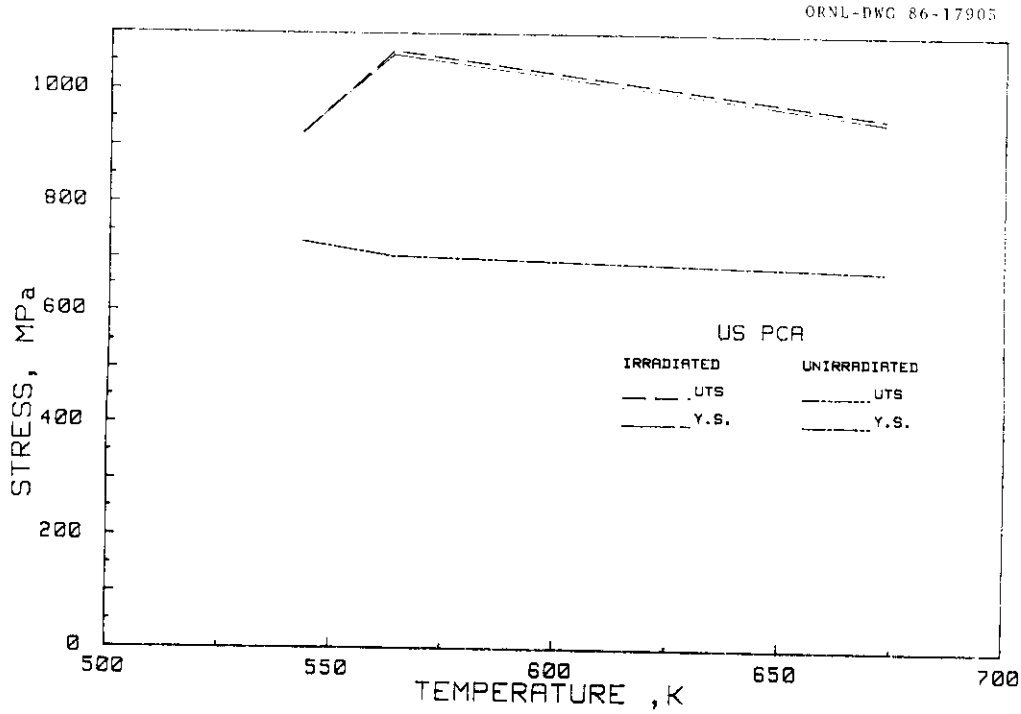

Fig. 7. Ultimate tensile strength (UTS) and 0.2% yield strength (YS) as a function of temperature (irradiation temperature = test temperature) of 25% cold-worked USPCA. The irradiated material was irradiated in the HFIR up to damage levels of about 10 dpa.

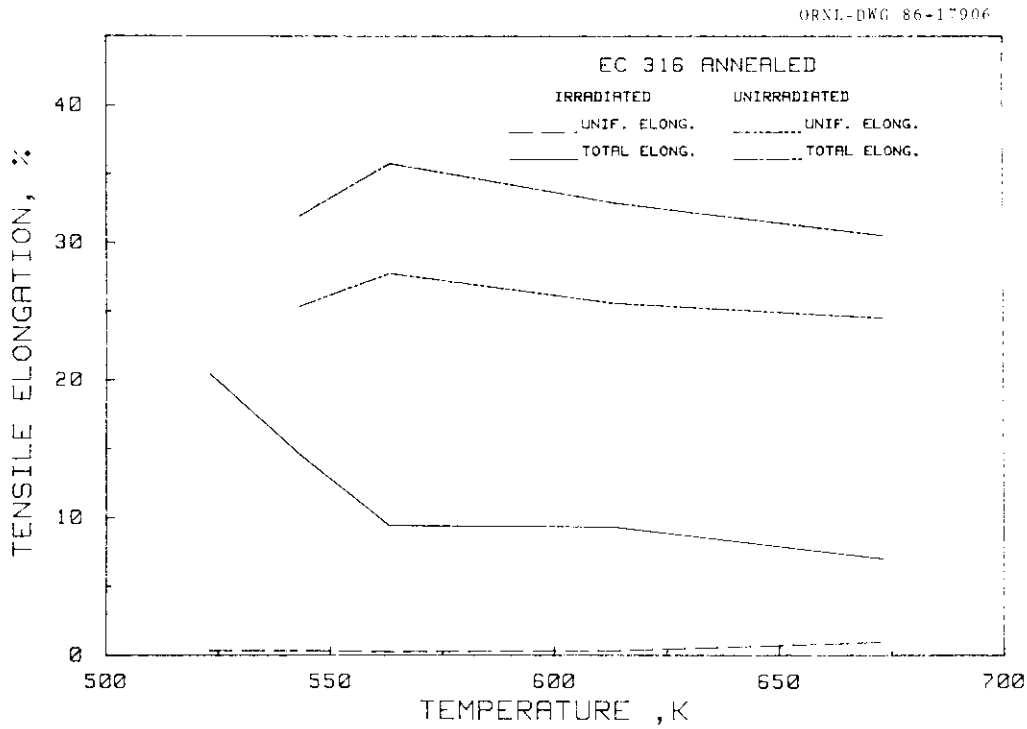

Fig. 8. Uniform and total elongation as a function of temperature (irradiation temperature = test temperature) or annealed European Community type 316 stainless steel. The irradiated material was irradiated in HFIR up to damage levels of about 10 dpa.

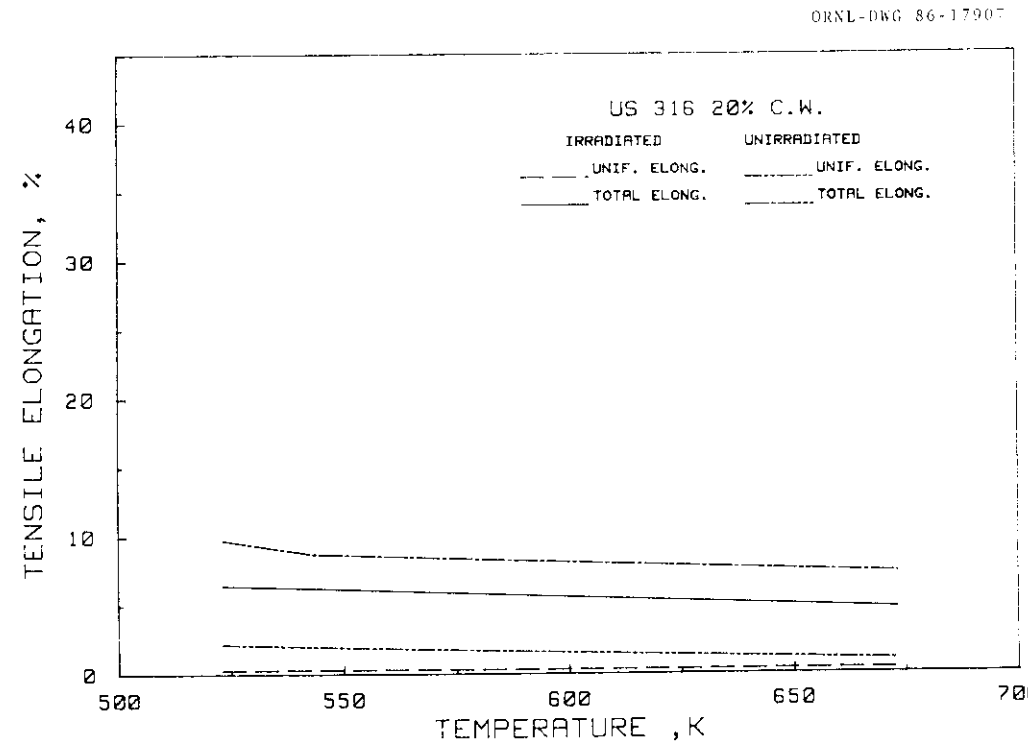

Fig. 9. Uniform and total elongation as a function of temperature (irradiation temperature = test temperature) of 20% cold-worked U.S. type 316 stainless steel. The irradiated material was irradiated in HFIR up to damage levels of about 10 dpa.

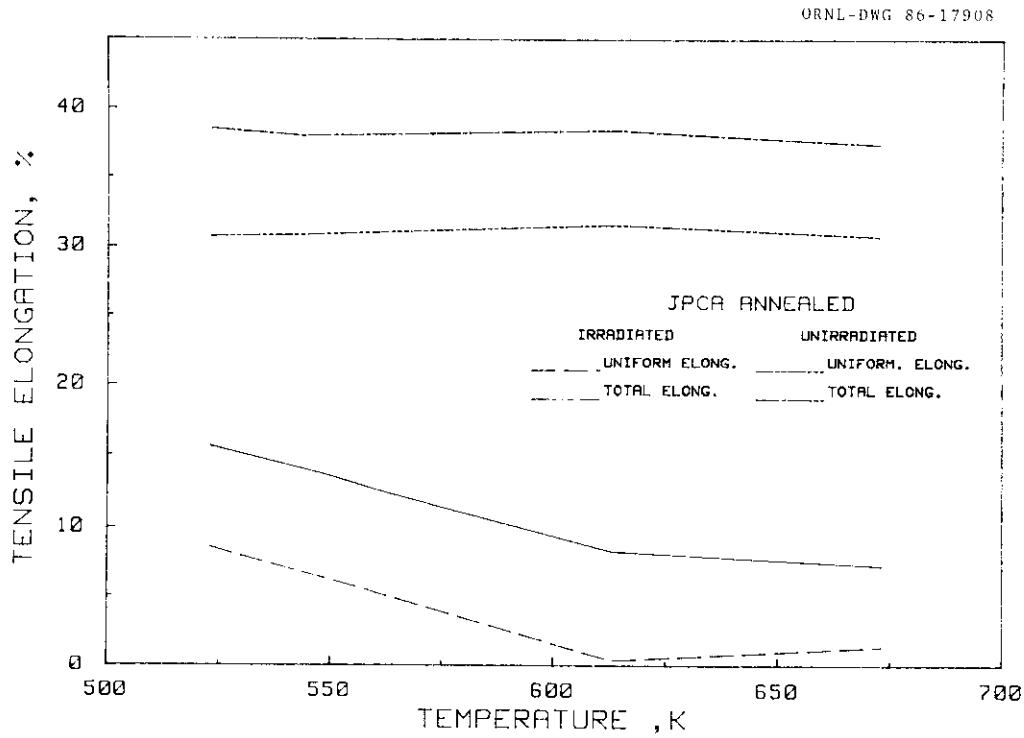

Fig. 10. Uniform and total elongation as a function of temperature (irradiation temperature = test temperature) of annealed Japanese PCA. The irradiated material was irradiated in HFIR up to damage levels of about 10 dpa.

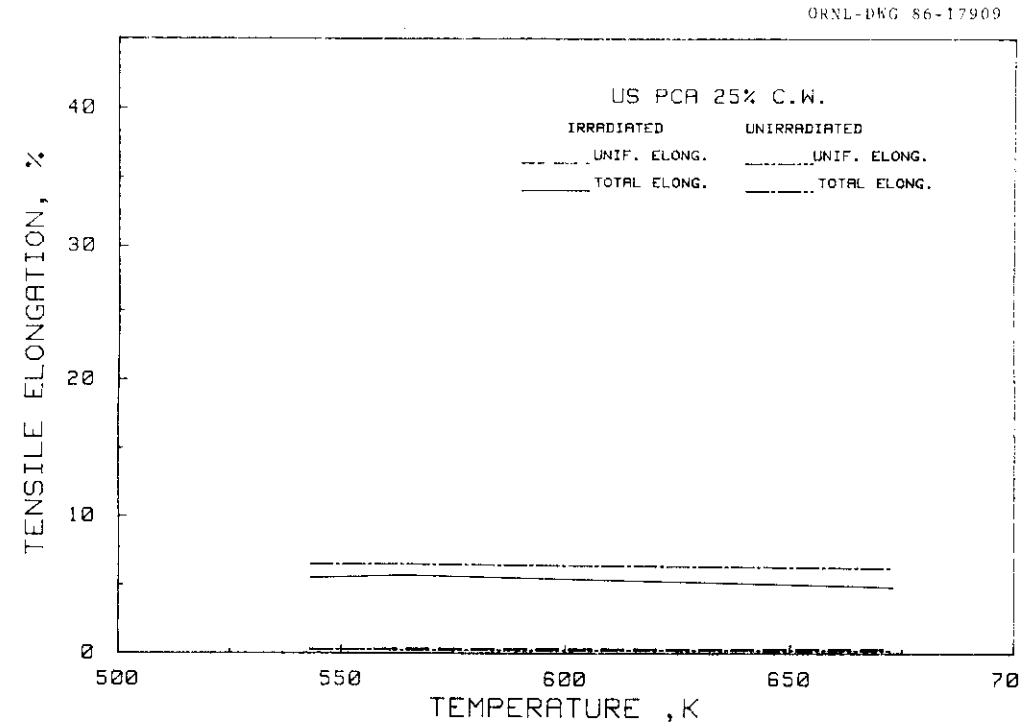

Fig. 11. Uniform and total elongation as a function of temperature (irradiation temperature = test temperature) of 25% cold-worked U.S. PCA. The irradiated material was irradiated in HFIR up to damage levels of about 10 dpa.

elongation decreases by about 60% upon irradiation in the annealed alloys. The total elongations of the cold-worked material are decreased slightly by irradiation over the entire temperature range. Total elongation remains above about 5% in the cold-worked alloys and about 10 to 20% in the annealed alloys following irradiation. Uniform elongation following irradiation is below 0.5% in the cold-worked alloys and even in EC316 in the annealed condition. The uniform elongation of JPCA reaches almost 9%, but only at the lowest temperature where the damage level is only about 5 dpa.

Discussion

This report describes only one phase of a rather large cooperative experimental program: tensile properties following HFIR irradiation. Assessment of the differences in the He:dpa value between the different reactors must await tests from the other reactors. Even then, helium effects might not be observed in mechanical properties at temperatures below 500°C. However, microstructural observations might provide data valuable in understanding helium effects.

The temperature and fluence ranges selected are relevant to the design of INTOR. Since the experiment evaluates candidate alloys for the next generation of experimental fusion devices, the irradiation data being produced will serve as guidance to the designers. The nearly constant values of strength and ductility with respect to temperature will facilitate design and operation of such devices.

The effects observed upon irradiation increase in strength, reduction in ductility, and reduction in work hardening coefficient as measured by uniform elongation — are all established effects of low temperature neutron irradiation of austenitic stainless steels. No unexpected behavior was observed. In comparing the four alloys, the differences can be interpreted mostly in terms of cold work level prior to irradiation. Other differences between the alloys appear to be minor. The PCA alloys were designed on the basis of swelling and high-temperature embrittlement. It is, therefore, not unexpected that significant differences were not observed.

It is believed that the observed tensile properties are adequate for fusion reactor application in a device with an end-of-life exposure level of 10 dpa. Although total elongation was high, the low values of uniform elongation require further consideration. If a structural member is stressed under constant load at a value above the ultimate tensile strength (an elongation equal to the uniform elongation), necking will begin and failure will result. If, however, the stress that produces the strain is relieved by it, as in the case of swelling stresses or thermal stresses, the low uniform elongation will not be detrimental. It is then concluded that as long as the design stresses are well below the yield stress of the material (which increases during irradiation), the structure will not fail. Of course, the total elongation must not be exceeded no matter what the source of the deformation.

CONCLUSIONS

1. Upon irradiation, little difference between cold-worked US316 and USPCA was observed. Also, little difference between annealed EC316 and JPCA was observed. The cold-worked alloys remained about 20% stronger than the annealed alloys, even after irradiation.

2. The total elongations of all four alloys remained above 5% throughout the range of 250 to 400°C.

3. Uniform elongation remained below 0.5% with the possible expection of JPCA at 250°C.

FUTURE WORK

The HFR tensile data are now available.[1] The report will be issued by JPC, Petten, the Netherlands, in the near future. Tensile and fatigue specimens will soon be available for testing at Mol, Belgium. The schedule in Table 1 remains current, but will be updated in 1987.

REFERENCES

1. B. van der Schaaf, H. Scheurer, and M. L. Grossbeck, "Irradiation and Postirradiation Tensile Tests of Austenitic Stainless Steels in HFR and HFIR," Joint Research Center, Petten, to be published.

2. L. R. Greenwood, "Fission Reactor Dosimetry — HFIR-CRT-40 45," pp. 5 8 in Damage Analysis and Fundamental Studies, Quart. Prog. Rep., September 1984, DOE/ER-0046/19, U.S. DOE, Office of Fusion Energy.

3. L. R. Greenwood, "A New Calculation of Thermal Neutron Damage and Helium Production in Nickel," J. Nucl. Mater. 115 (1983) 137 142.

4. W. D. Turner and M. Siman-Tov, Heating 3 An IBM 360 Heat Conduction Program, ORNL/TM-3208, Oak Ridge National Laboratory (February 1971).

IRRADIATION-ENHANCED PRECIPITATES IN TYPE 316 STAINLESS STEEL IRRADIATED IN HFIR — S. Hamada, M. P. Tanaka (Japan Atomic Energy Research Institute, assigned to ORNL), and P. J. Maziasz (Oak Ridge National Laboratory)

OBJECTIVE

The objective of this work is to determine the precipitation behavior of Japanese type 316 stainless steel during irradiation in the HFIR.

SUMMARY

Solution-annealed (SA) type 316 stainless steel was irradiated to 36 dpa at 600°C in HFIR. Large irradiation-produced (100 to 270 nm) precipitates were observed in irradiated specimens and many voids (3 to 30 nm in diameter) were attached to these precipitates. In addition, many fine helium bubbles (1 to 5 nm in diameter) and additional defects (~5 nm) were observed inside these precipitates. Most of these precipitates were identified as M_6C (eta) phase, enriched in Ni, Cr, Mo, and Si.

PROGRESS AND STATUS

Experimental Procedure

The chemical composition of specimens used in the experiment is given in Table 1. Solution-annealed (SA) specimens were irradiated in the JP-6 capsule at 600°C to ~36 dpa (exposure time 8800 h) and 2250 appm He in HFIR. Carbon-extraction replica films were prepared to analyze the composition of precipitates prior to thinning the specimens using the Tenupol electropolishing technique. Replicas and thin foils were examined in a JEM 2000FX transmission electron microscope. Precipitate compositions were analyzed using EDX and operating the microscope in the S mode to get a strong beam current as well as a small spot size; normally the 3S spot size (~65 nm) was used.

Table 1. Chemical composition of type 316 stainless steel

Composition, wt %												
Cr	Ni	Mo	Mn	C	Ti	Si	P	S	N	B	Co	Fe
16.75	13.52	2.50	1.80	0.058	0.005	0.61	0.028	0.013	---	---	<0.01	bal

Results and Discussion

Under irradiation, especially at elevated temperature, it is well known that precipitates appear to be different from those formed by normal thermal aging, and these precipitates affect the swelling behavior of materials. In the present work, many precipitates were observed throughout the matrix in specimens irradiated at 500°C and above up to 36 dpa, as shown in Fig. 1. At 500°C, medium sized precipitates formed with voids at the particle/matrix interface. The average diameter and number density of precipitates were 37 nm (range 15 to 65 nm) and 2.4×10^{21} m^{-3}, respectively. At 600°C, precipitates were coarser (average diameter 160 nm, range 100 to 270 nm) and their number density decreased (2.3×10^{19} m^{-3}).

The size of most of the voids associated with precipitates showed little difference between 500 and 600°C, in spite of coarsening of the precipitates at 600°C. At 600°C, however, it is interesting that many fine cavities were observed inside these large precipitates (we did not observe stereomicrographs, but the fact that the fine cavities could be observed on replicas as well as in thin foils indicates that they are inside the particles). Figure 2 shows typical extracted precipitates from irradiated material. This figure includes an electron diffraction pattern, an x-ray EDS spectrum, and a histogram of metallic element composition [Fig. 2(b,c,d)]. This precipitate has an fcc structure and a lattice parameter of a_0 = 1.10 nm, which agrees with that of eta phase (M_6C) (refs. 1,2). It contains nearly 30 wt % each of Cr and Ni and about 17% Mo and 7% Si. This phase is identified as eta phase (M_6C). The eta phase is considerably depleted in iron relative to the matrix. This result is in very good agreement with results reported by others.[1-3] Most of the precipitates observed were identified as eta phase. γ', G, Laves, and tau phases, which have been reported elsewhere,[4-6] were not found in the present work. The possibility of microsegregation of elements within the large precipitates was examined. The result given in Fig. 3 indicates uniform distribution of elements within the large precipitates for the size of electron beam used.

ORNL-PHOTO 8563-86

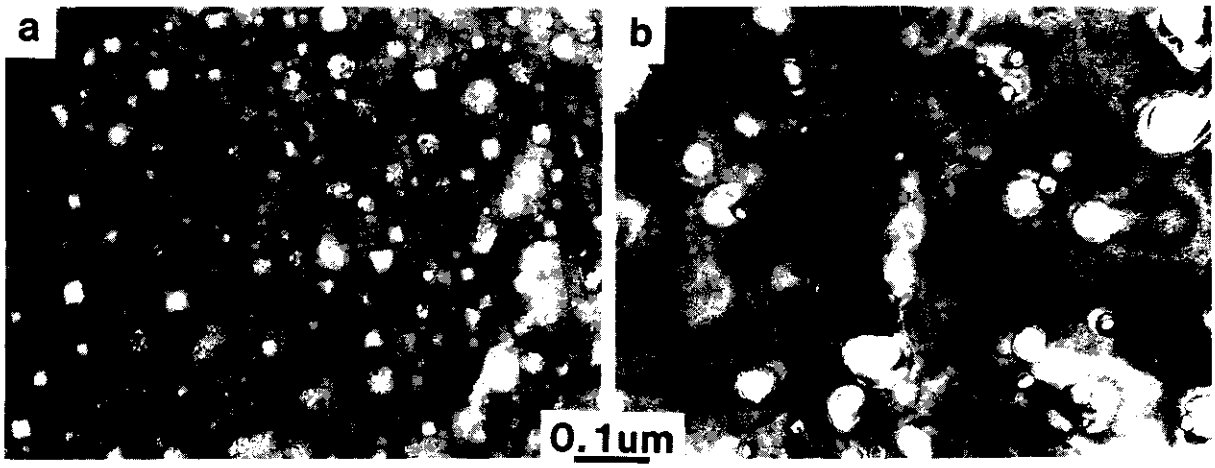

Fig. 1. Precipitates observed in SA type 316 stainless steel irradiated to 36 dpa at (a) 500°C and (b) 600°C in HFIR.

ORNL PHOTO 6788-86

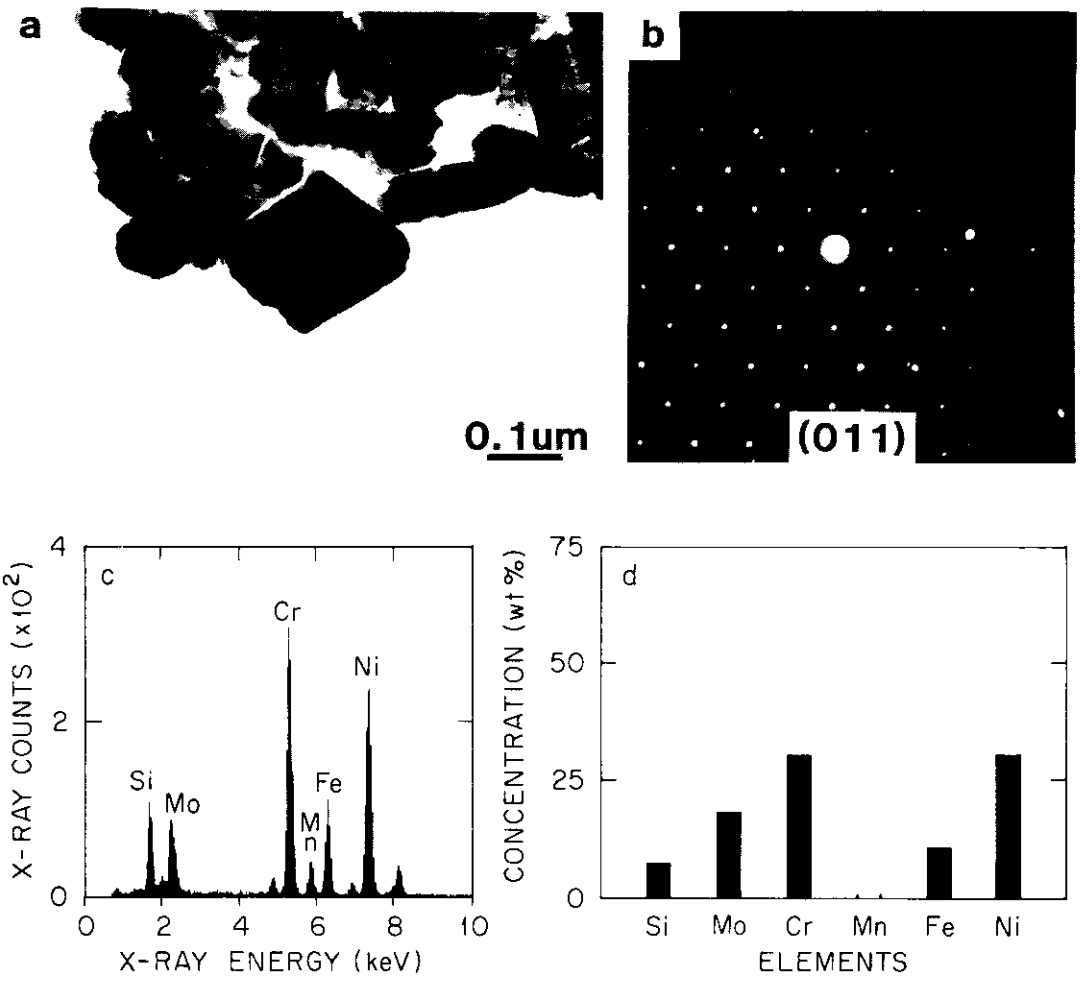

Fig. 2. Typical precipitate extracted on a replica produced from SA type 316 stainless steel irradiated in HFIR to 36 dpa at 600°C. (a) Bright-field image, (b) electron diffraction pattern, (c) characteristic x-ray EDS spectra, and (d) histogram of metallic element composition.

ORNL PHOTO 6789-86

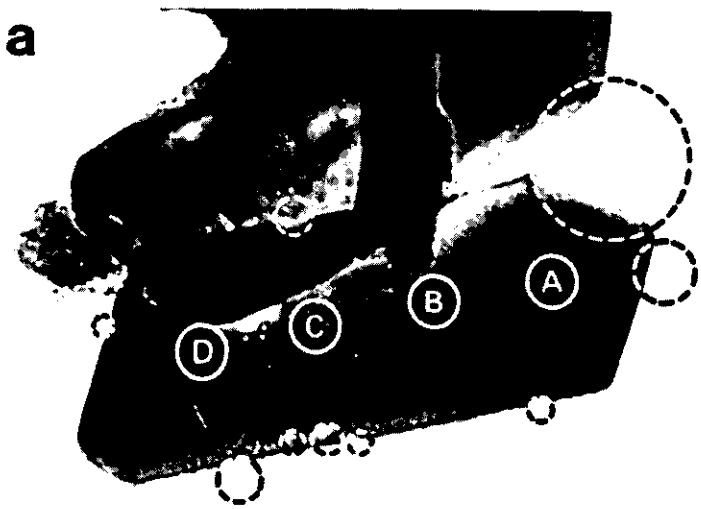

POSITION ANALYZED	COMPOSITION, wt %								
	Fe	Ni	Cr	Mn	Ti	Si	P	Mo	V
A	10.26	28.71	27.95	0.00	0.18	8.58	1.44	20.56	2.31
B	10.91	29.80	31.54	0.00	0.19	7.85	1.24	16.48	1.79
C	10.28	28.77	29.39	0.00	0.00	8.78	1.44	18.51	2.31
D	10.94	25.87	26.66	0.00	0.05	7.91	1.41	24.32	2.63
AVERAGE	10.60	28.29	28.89	0.00	0.09	8.28	1.38	19.97	2.26

Fig. 3. Dependence of chemical composition on analyzed area in eta phase observed in SA 316 irradiated to 36 dpa at 600°C in HFIR.

Figure 4 shows the same precipitate particle analyzed in Fig. 3. Some arcs along the edge of the precipitate appear to be the remaining impressions of voids that were attached to the surface of the precipitate as illustrated schematically by the circles drawn in Fig. 3(a). The fine (0.8 to 4.9 nm) white dots in Fig. 4(a) appear to exist on the inside of the blocky precipitate particles because they were not removed by the extraction process as were the interfacial voids. A through-focus series shows the tiny features to be white in the underfocused condition [Fig. 4(a)] and dark in the overfocused condition [Fig. 4(b)], further demonstrating that these fine internal defects are cavities or helium bubbles. However, there may be other internal defects in addition to the fine cavities. Figure 5 shows fringe images that are larger than and adjacent to the fine cavities within the precipitate under dynamical contrast conditions which rotate with g. This rotation behavior indicates that the second type of small defect is not a loop, but is some three-dimensional defect, possibly a tiny precipitate within the larger precipitate. In this case the fringes would probably be Moiré fringes which should be perpendicular to g, as observed.

Next, let us consider several mechanisms that could lead to the observed intraparticle defects, and several consequences of their existence. One possible mechanism that could produce the tiny cavities within the precipitate would be internal trapping of helium produced within the nickel-rich precipitates by nickel transmutation reactions. The denuded zone near the precipitate interface could be a result of helium atoms recoiling beyond the precipitate and into the nearby region. Another mechanism could be discontinuous growth of the precipitate particle with helium bubbles forming along the interface early in the irradiation to retard growth, and then the particle growing around the bubble obstacles and proceeding at faster rates to its final size. A third mechanism could be helium atoms collection at the interface followed by

ORNL-PHOTO 8564-86

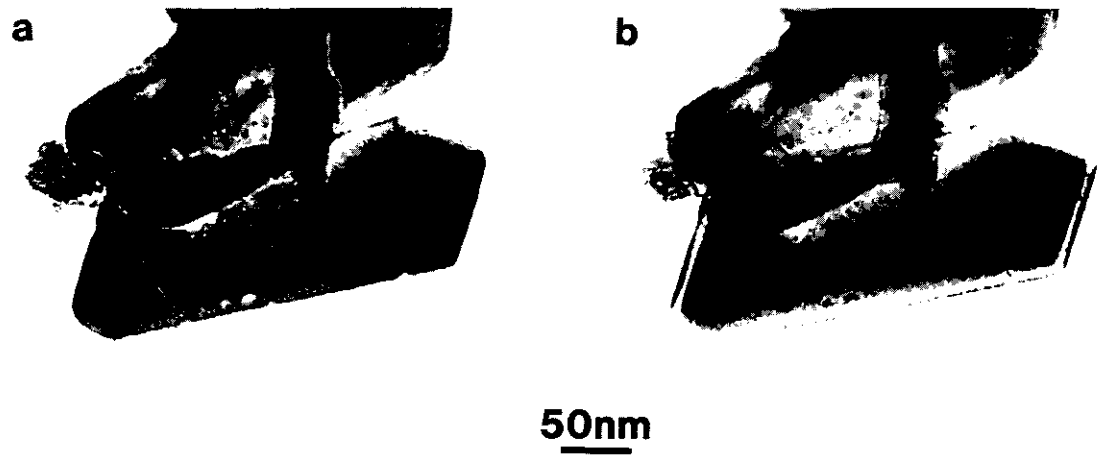

Fig. 4. Helium bubbles observed inside large eta phase. (a) Underfocused and (b) overfocused micrograph.

ORNL-PHOTO 8565-86

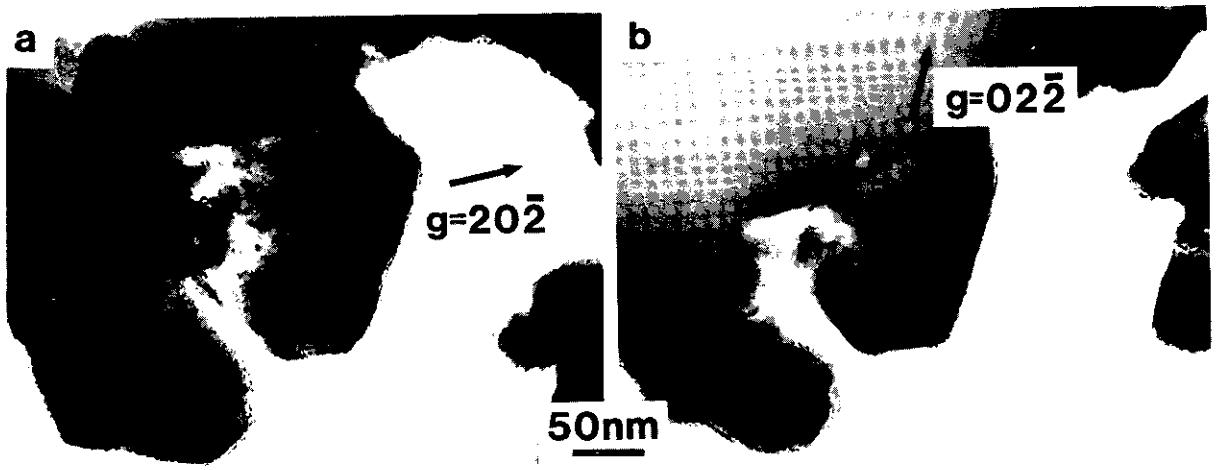

Fig. 5. Fringe images observed inside eta particle. (a) g = 20$\bar{2}$, (b) g = 02$\bar{2}$.

diffusion into the particle to nucleate the fine cavities. Experiments at higher and lower fluences would be required to sort out these possibilities with confidence, although consideration of helium atoms recoil and diffusion parameters within the eta phase particle may help to evaluate the first and third mechanisms. One important consequence of the internal defects, especially the tiny precipitate particles within the larger particle, is that if precipitate particles are large enough to have an inner region beyond the effect of the precipitate-matrix interfaces as strong sinks, then they may undergo their own microstructural evolution as the result of radiation damage and point defect processes within the phase particle. The internal processes may affect the stability of the larger phase particle at higher fluence. Furthermore, defect fluxes and internal segregation to the precipitate-matrix interface may influence the conversion of bubbles to voids at the particle interface, and their subsequent precipitate-enhanced growth rate.

Similar internal fine cavities and other defects that appear to be tiny precipitates are observed in eta phase formed in type 316 stainless steel irradiated to 36 dpa at 630°C in the EBR-II, which has a low helium generation rate compared to HFIR (Maziasz).[7] In this case, since the content of helium atoms is very low (18 appm He), the mechanism involving the precipitate growing around bubbles that were previously at the interface seems favored. However, more experiments at lower and higher fluence at the same temperature would be needed to know the behavior of cavities inside precipitates.

CONCLUSIONS

Solution-annealed type 316 stainless steels was irradiated in HFIR at 600°C up to 36 dpa and 2335 appm He. From direct TEM and x-ray analysis, we observe the following:

1. Most of the large precipitates are eta phase (M_6C), which has an fcc structure and a lattice parameter of a_0 = 1.10 nm and enriched Ni, Cr, Mo, and Si. Large voids are attached to the interface of the precipitates. Elements are uniformly distributed within the precipitate particles.

2. Many fine bubbles and other fine defects that may be tiny precipitate particles are observed inside the large eta precipitates.

FUTURE WORK

To further study the behavior of precipitates and discern the mechanisms responsible for forming cavities inside precipitates in type 316 stainless steel during neutron irradiation at 600°C, work should include specimens irradiated to lower and higher fluence at 600°C.

REFERENCES

1. B. Weiss and R. Stickler, "Phase Instabilities During High Temperature Exposure of 316 Austenitic Stainless Steel," Met. Trans. 3 (1972) 851–866.

2. Eal H. Lee, P. J. Maziasz, and A. F. Rowcliffe, "The Structure and Composition of Phases Occurring in Austenitic Stainless Steels in Thermal and Irradiation Environments," pp. 191–218 in Phase Stability During Irradiation (Proc. Symp., Pittsburgh, Pa., Oct. 5–9, 1980), ed. by J. R. Holland, L. K. Mansur, and D. I. Potter, The Metallurgical Society of AIME, Warrendale, Pa., 1981.

3. P. J. Maziasz, Effects of Helium Content on Microstructural Development in Type 316 Stainless Steel under Neutron Irradiation, ORNL-6121, Oak Ridge National Laboratory (November 1985).

4. P. J. Maziasz, "Some Effects of Increased Helium Content on Void Formation and Solute Segregation in Neutron-Irradiated Type 316 Stainless Steel," pp. 169–216 in ADIP Semiannu. Prog. Rep. Mar. 31, 1982, DOE/ER-0045/8, U.S. DOE, Office of Fusion Energy.

5. P. J. Maziasz, J. A. Horak, and B. L. Cox, "The Fluence of Both Helium and Neutron Irradiation on Precipitation in 20% Cold-Worked Austenitic Stainless Steel," pp. 271–292 in Phase Stability During Irradiation (Proc. Symp., Pittsburgh, Oct. 5–9, 1980), ed. by J. R. Holland, L. K. Mansur, and D. I. Potter, The Metallurgical Society of AIME, Warrendale, Pa., 1981.

6. P. J. Maziasz, "Composition and Microstructure of Precipitate Phases in Austenitic Stainless Steels," pp. 75–129 in ADIP Quart. Prog. Rep. June 30, 1980, DOE/ER-0045/3, U.S. DOE, Office of Fusion Energy.

7. P. J. Maziasz, Oak Ridge National Laboratory, unpublished data (1986) (available upon request).

TEMPERATURE DEPENDENCE OF SWELLING IN TYPE 316 STAINLESS STEEL IRRADIATED TO ABOUT 33 dpa IN HFIR — S. Hamada, M. P. Tanaka (Japan Atomic Energy Research Institute, assigned to ORNL), and P. J. Maziasz (Oak Ridge National Laboratory)

OBJECTIVE

The objective of this research is to obtain fundamental data on swelling in a Japanese heat of type 316 stainless steel irradiated in HFIR at 300 to 600°C and to evaluate heat-to-heat variations in behavior by comparison with U.S. heats of type 316 stainless steel. This work is a part of the U.S./Japan collaborative program.[1]

SUMMARY

Solution-annealed (SA) and 20%-cold-worked (20% CW) type 316 stainless steels were irradiated in HFIR up to 33 to 36 dpa and 2250 to 2335 appm He at irradiation temperatures of 300 and 400°C. Small bubbles (1.5 to 4.5 nm in diameter) were uniformly dispersed throughout the matrix at concentrations in the range 2 to 4 × 10^{23} m^{-3}. Swelling was very low (below 0.2%) in both materials. In SA materials, cavity size rapidly increased while the number density decreased at irradiation temperatures of 500°C and above. Swelling appeared to be a maximum at 500°C (>1%). Most of the cavities were voids at 600°C. On the other hand, in 20% CW specimens, cavities were much smaller, with diameters of 6 and 9 nm at 500 and 600°C, respectively. The cavity number density at both 500 and 600°C (~1 × 10^{22} m^{-3}) was about one order less than at 400°C. Swelling slightly increased as irradiation temperature increased, peaking at 600°C (0.3%). Inhibition of swelling by cold working was more effective at temperatures above 500°C.

PROGRESS AND STATUS

Experimental Procedure

The chemical composition of specimens used in the experiment is given in Table 1. SA (1050°C/30 min) and 20% CW (SA + 20% CW) disks were irradiated in the JP-1, -3, -6, and -7 capsule at 300, 400, 600, and 500°C in HFIR, respectively, to 33 to 36 dpa and 2250 to 2335 appm He. After irradiation, these disks were electropolished and examined with a JEM 2000FX transmission electron microscope operating at 200 kV. Cavity and loop size distributions were measured using a Zeiss particle analyzer. Two methods were used to estimate the thickness of the foil — one was to measure thickness fringes and the other was to deposit a contamination spot on the top and bottom surfaces of the thin foil.[2]

Table 1. Chemical composition of type 316 stainless steel

Composition, wt %												
Cr	Ni	Mo	Mn	C	Ti	Si	P	S	N	B	Co	Fe
16.75	13.52	2.50	1.80	0.058	0.005	0.61	0.028	0.013	---	---	<0.01	bal

Results and Discussion

The cavities observed in specimens irradiated at 300 to 600°C are shown in Fig. 1 for comparison of cavity development in both SA and 20% CW materials. At 300 and 400°C, cavities are uniformly observed in the matrix and there is no difference in cavity size distribution between SA and 20% CW materials. Calculation of gas atoms in the cavities from a modified Van der Waals equation suggests that these cavities are most likely helium bubbles. At 400°C, a portion of the bubbles have probably converted to voids [Fig. 1(c) and (d)]. At 500°C, cavities in SA material are much larger than at 400°C, but in the 20% CW material, cavities were only slightly larger than at 400°C. The size distributions of the cavity microstructure of SA and 20% CW at 500 and 600°C are plotted in Fig. 2. At 500°C, both materials have the sharp, narrow peak that suggests subcritical bubbles, with sizes below 5 nm, but the SA material has the broad tail at larger sizes that suggests bias-driven voids. In this case, we should note the following: cavities that appear diffuse are being affected by the electropolishing and therefore are eliminated from swelling estimates; this may lead to an underestimate of swelling. Immersion density measurements in progress should provide a more reliable measurement of swelling. At 600°C, the large, faceted voids (10 to 65 nm in diameter) are observed in the SA steel, whereas many small cavities are uniformly found in the matrix of the 20% CW steel. The cavity size distribution of the former [Fig. 2(c)] shows a Gaussian distribution, with the peak at about 30 nm in diameter, while the distribution in the latter shows a sharp, narrow peak at 10 nm in diameter [Fig. 2(d)].

ORNL-PHOTO 8562-86

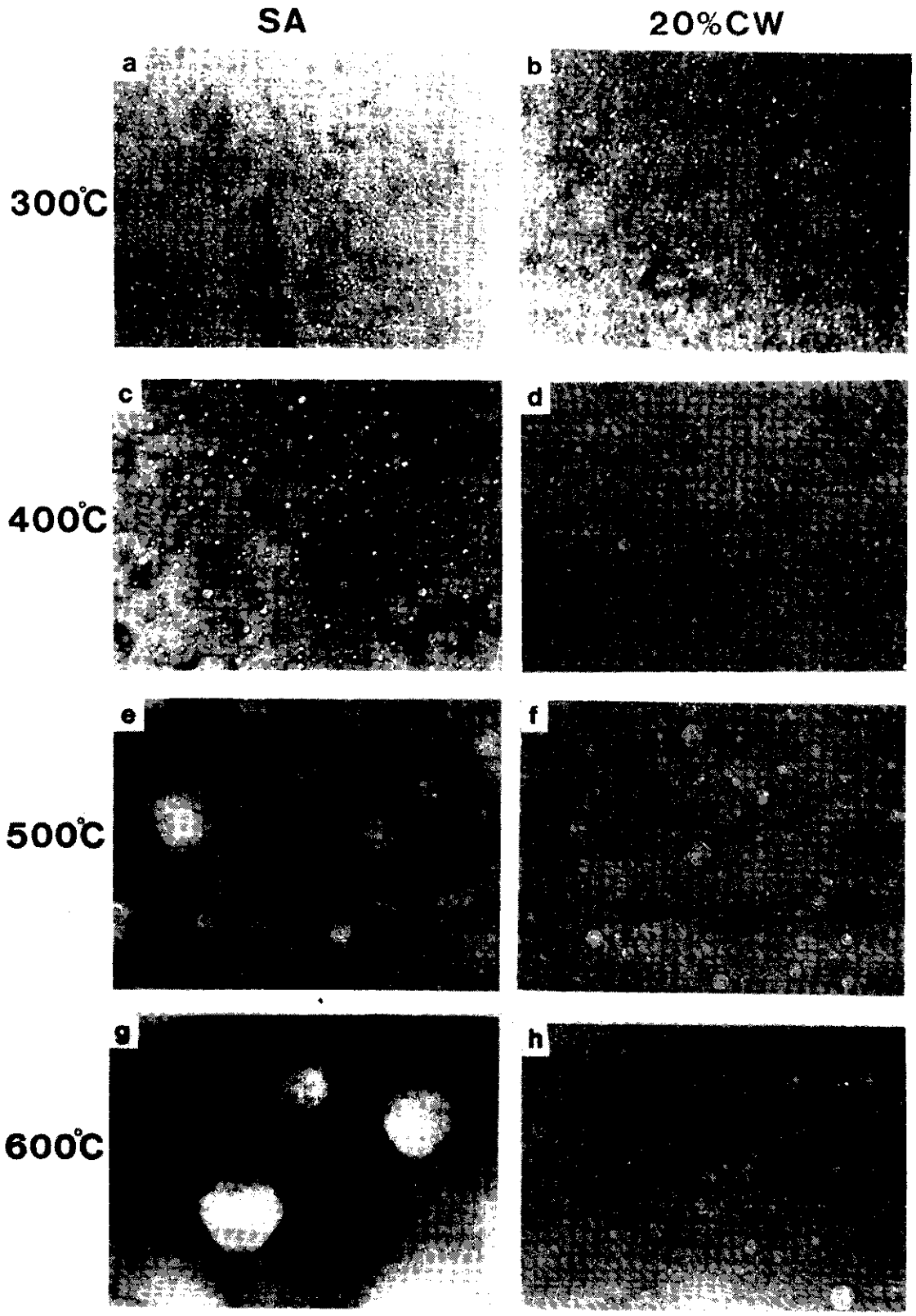

Fig. 1. A comparison of cavities for SA (a,c,e,g) and 20% CW (b,d,f,h) type 316 stainless steel irradiated in HFIR at 300 to 600°C up to 33 to 36 dpa and 2250 to 2335 appm He.

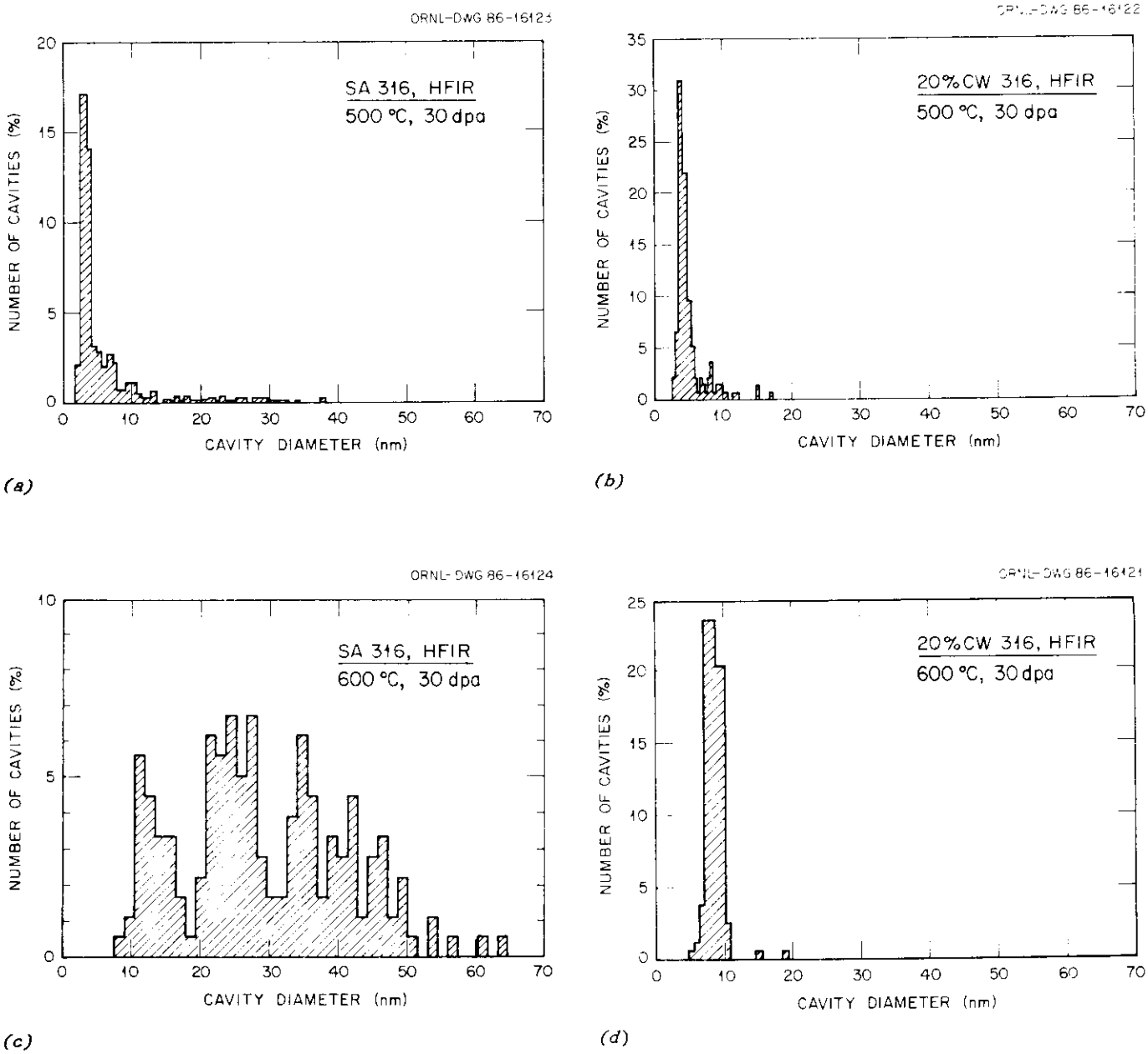

Fig. 2. Histograms of cavity size distribution in SA (a,c) and 20% CW (b,d) type 316 stainless steel after 33 and 36 dpa HFIR irradiation at 500 and 600°C, respectively.

The temperature dependencies of cavity diameter, cavity concentration, and cavity swelling are shown in Fig. 3. Figure 3(c) includes cavity swelling data for 20% CW DO-heat and N-lot determined at various fluences by Maziasz.[4] Figure 3(a) shows that for SA material the sizes of cavities increase as the irradiation temperature increases, particularly at temperatures above 500°C, while cavities observed in the CW material depend only weakly on irradiation temperature. The temperature dependence of cavity concentration is opposite to their size dependence; cavity concentrations in the SA material continue to decrease steeply with increased temperature above 500°C while those in the CW material are parallel to the SA material at 300 to 500°C, and show much less decrease at 600°C.

At temperatures below 400°C, swelling is low because of the high concentration of fine bubbles [Fig. 3(a)]. These bubbles are strong, dominant sinks and the conversion of bubbles to voids is suppressed.[5] Swelling of SA material peaks at 500°C (>1%). This tendency was reported in SA (DO-heat) 316 stainless steel irradiated in HFIR.[6] The actual magnitude of the swelling at 500°C is uncertain due to the reason mentioned above. At 600°C, dislocation concentration decreases to further reduce the concentration of bubbles that serve as void nuclei, so the cavity density decreases steeply [Fig. 3(b)]. Voids are much larger than subcritical bubbles at 500 and 600°C.

In 20% CW, total swelling shows a flat temperature dependence below 500°C, and increases slightly at 600°C. At temperatures below 400°C, swelling is similar in SA and 20% CW material because fine bubbles in higher concentrations have much larger sink strengths than dislocations either induced by cold work or developed during irradiation in SA material. However, at temperatures above 500°C, dislocations induced by cold work would give more nucleation sites for bubbles even as the structure recovers, and suppress bubble-to-void conversion relative to SA material. Therefore, 20% CW is more effective in resisting swelling in materials irradiated in HFIR at temperatures above 500°C. Finally, data in Fig. 3(c) show that swelling varies from heat-to-heat for 20% CW 316 stainless steel irradiated in HFIR to below 30 dpa. Most of the data could be covered in hatched regions. This suggests that in the right heat of 316 stainless steel, 20% CW could suppress swelling to below 0.5% during HFIR irradiation up to 36 dpa to 600°C.

CONCLUSIONS

Solution-annealed and 20% CW type 316 stainless steels have been irradiated in HFIR up to 33 to 36 dpa and 2250 to 2335 appm He at temperatures in the range of 300 to 600°C. Cavity development in various specimens was examined by transmission electron microscopy. The conclusions are as follows:

1. Swelling in solution-annealed type 316 stainless steel is a maximum at 500°C.

2. In 20% CW material, swelling is lower than SA material at all irradiation temperatures and is at maximum at 600°C (0.3%).

3. 20% CW is more effective for swelling resistance at temperatures above 500°C.

4. Swelling data on heat-to-heat variations of type 316 stainless steel suggest that swelling in 20% CW type 316 stainless steel is below 0.5% in HFIR irradiations up to ~36 dpa at below 600°C.

FUTURE WORK

The work will continue for heat-to-heat variations irradiated up to 30 and 50 dpa to obtain fundamental data on swelling in type 316 stainless steel irradiated in HFIR.

REFERENCES

1. J. L. Scott and T. Kondo, "Introduction to U.S./Japan Collaborative Testing Program in HFIR and ORR" pp. 35–36 in ADIP Semiannu. Prog. Rep., March 31, 1984, DOE/ER-0045/12, U.S. DOE, Office of Fusion Energy.

2. G. Fenske, S. K. Das, and M. Kaminsky, "A Technique for Determining the Depth Distribution of Cavities in He^+-Irradiated Nickel," J. Nucl. Mater. 80 (1979) 373–378.

3. P. J. Maziasz, Effects of Helium Content on Microstructural Development in Type 316 Stainless Steel under Neutron Irradiation, ORNL-6121, Oak Ridge National Laboratory (November 1985).

4. P. J. Maziasz and D. N. Braski, "Swelling and Microstructural Development in Path A PCA and Type 316 Stainless Steel Irradiated in HFIR to about 22 dpa," ADIP Semiannu. Prog. Rep. Sept. 30, 1982, DOE/ER-0045/9, U.S. DOE, Office of Fusion Energy.

5. R. E. Stoller and G. R. Odette, "A Model Based Fission-Fusion Correlation of Cavity Swelling in Stainless Steel," J. Nucl. Mater. 103&104 (1981) 1361–1366.

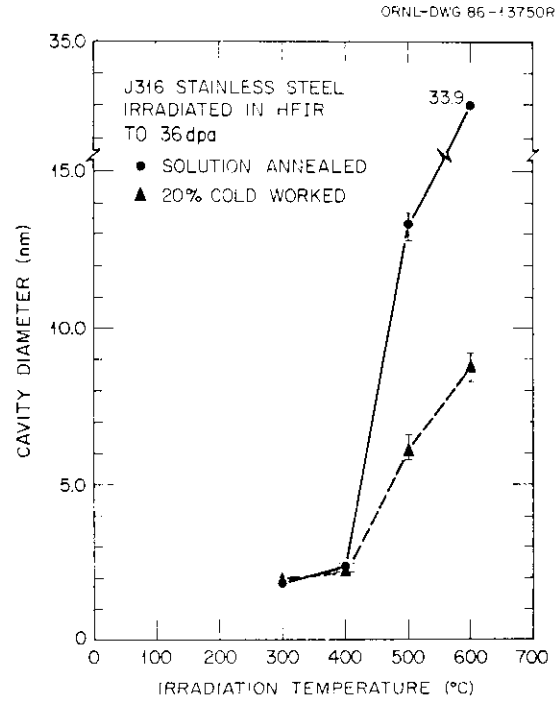

(a)

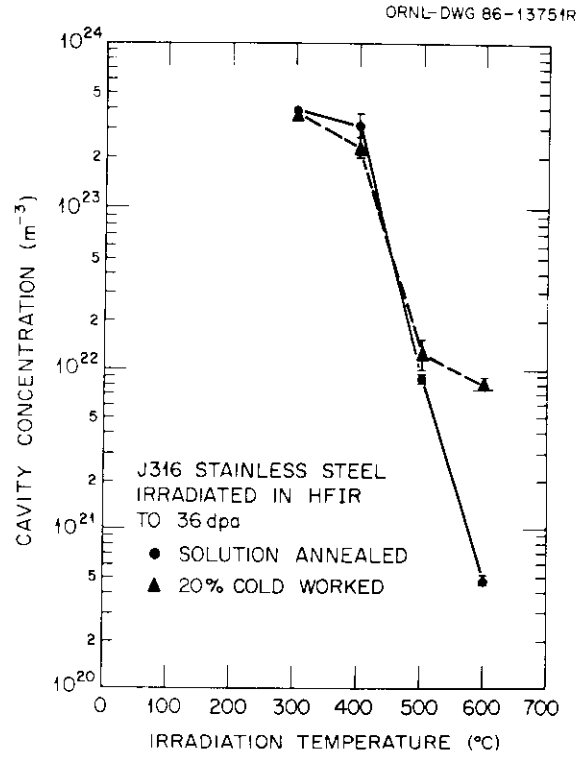

(b)

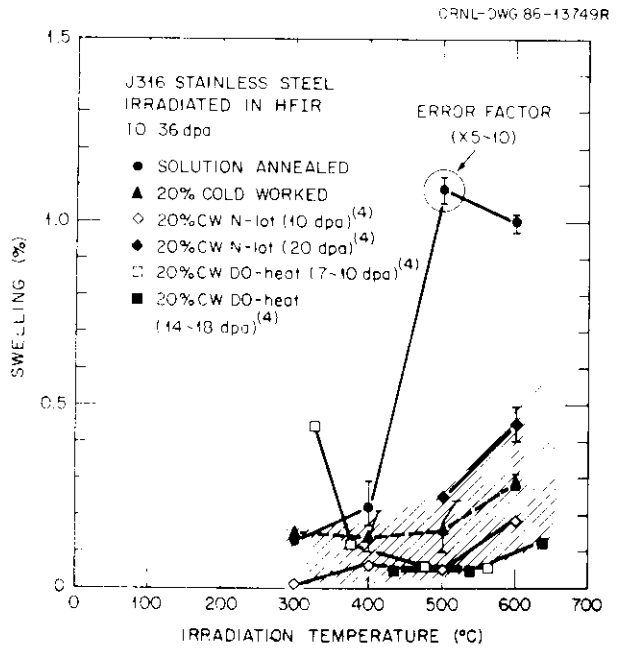

(c)

Fig. 3. Cavity size, cavity concentration, and cavity swelling are plotted as functions of irradiation temperature for SA and 20% CW type 316 stainless steel irradiated in HFIR at 300 to 600°C up to 36 dpa and 2250 to 2335 appm He. Data indicated with ref. 4 were reported (Maziasz and Braski).

6. P. J. Maziasz, "Comparison of Swelling and Cavity Microstructural Development for Type 316 Stainless Steel Irradiated in EBR-II and HFIR," J. Nucl. Mater. 122 (Nos. 1–3) (1984) 236–241.

7. G. R. Odette, P. J. Maziasz, and J. A. Spitznagel, "Fission-Fusion Correlations for Swelling and Microstructure in Stainless Steels: Effect of the Helium to Displacement per Atom Ratio," J. Nucl. Mater. 104 (Nos. 1–3) (1981) 1289–1303.

8. G. R. Odette, "Modeling of Microstructural Evolution under Irradiation," J. Nucl. Mater. 85&86 (Part A) (1979) 533–545.

THE DEVELOPMENT OF AUSTENITIC STAINLESS STEELS FOR FAST INDUCED-RADIOACTIVITY DECAY — R. L. Klueh and P. J. Maziasz (Oak Ridge National Laboratory)

OBJECTIVE

During the operation of a fusion reactor, the structural material of the first-wall and blanket structure will become highly radioactive from activation by the fusion neutrons. Disposal of this material after the service lifetime will be a difficult radioactive waste-management problem. One way to minimize the disposal problem is to use structural materials in which radioactive isotopes induced by irradiation rapidly decay to levels that allow simplified disposal techniques. We are assessing the feasibility of developing such austenitic stainless steels.

SUMMARY

Tensile properties were determined for six Fe-Mn-Cr-C alloys that were used previously to determine the austenite-stable region in that system. The steels were tested in the solution-annealed and 20%-cold-worked conditions. When the results were compared with type 316 stainless steel, the average behavior of the five steels compared favorably with the tensile behavior of type 316 stainless steel.

PROGRESS AND STATUS

Introduction

During the operation of a fusion reactor, the various alloying elements of the alloys that are proposed for the first wall and blanket structure of a fusion reactor undergo transmutation reactions when irradiated by high-energy neutrons. After the service lifetime of the reactor, these radioactive components must be properly disposed of. The complexity of this waste-disposal procedure depends on the time required for the induced radioactivity to decay to levels that no longer pose a threat to people and the environment. The more rapid the decay, the simpler is the disposal task.

We have proposed an alloy-development program for fast induced-radioactivity decay (FIRD) versions of present conventional first-wall and blanket structural candidate alloys.[1] For the austenitic alloys, manganese was proposed as a replacement for nickel, although it was recognized[1] that this may be difficult, because manganese is not as strong an austenite stabilizer as nickel. Hence, it is not possible to simply replace nickel with manganese on an atom-for-atom basis. It was proposed that an effort be made to determine Fe-Cr-Mn-C compositions that are austenitic and that would remain austenitic when further alloyed to obtain the strength and irradiation-resistant properties required for a fusion-reactor structural material.[1]

We initially reported on the microstructure of ten heats of Fe-Mn-Cr-C steels with compositions of 15 or 20% Mn, 10, 15, or 20% Cr, and 0.05, 0.1, 0.2, or 0.4% C (ref. 2). Those alloys were selected on the basis of the Schaeffler diagram. The results indicated that either the boundaries of the Schaeffler diagram, which were determined for Fe-Cr-Ni-C alloys, need to be modified, or the multiplying factor for manganese (taken as 0.5) needs to be changed. This latter approach has been suggested by several investigators.

Regardless of the explanation for the discrepancy with the Schaeffler diagram, the investigation of these ten heats of steel provided insight into possible manganese-stabilized, austenitic-base compositions. Five additional button heats were obtained to verify those observations.[3] The results of the microstructural studies on those five alloys provided further information on the austenite-stable region for the high-manganese alloys. Seven alloy compositions based on that work have been melted and are being examined and tested, and the results of that work will be reported in the future. In this report, the tensile behavior of the five alloys previously examined[3] will be discussed.

Experimental Procedure

The tensile specimens were taken from the five 600-g button heats that were melted and cast with goal compositions of 20% Mn for all heats. Three heats were to have 0.1% C and 10, 12, and 14% Cr. Two heats with 0.2% C were to have 12 and 16% Cr. The actual compositions are given in Table 1.

The alloys were cast into an ingot of rectangular cross section of 12.7 by 25.4 by 152 mm. The ingots were hot rolled at 1050°C to 6.4-mm thickness, after which they were homogenized 5 h at 1200°C. Each steel was cold rolled to 0.76- and 0.25-mm sheet. The reductions from the 6.4-mm bar were made by successively reducing the cross section 50% and then annealing 1 h at 1150°C. The final sheet was 20% cold worked.

For these preliminary comparative tests, miniature specimens with a 12.7-mm-long by 1.02-mm-wide gage section were punched from the 0.25-mm sheet. Tests were made at room temperature, 300, 450, and 600°C on 20%-cold-worked and solution-annealed material. The solution anneal treatment was 2 h at 1150°C. Tensile

Table 1. Chemical compositions of button heats melted for fast induced-radioactivity decay (FIRD) alloy-development program

Alloy	Chemical composition, wt %										
	C	Mn	Cr	Si	Ni	Mo	V	Nb	Cu	N	Fe
PCMA-10	0.081	19.92	9.97	0.04	0.01	0.01	0.01	0.01	0.02	0.005	bal
-11	0.084	19.99	11.94	0.03	0.01	0.01	0.01	0.01	0.02	0.009	bal
-12	0.180	20.04	11.95	0.02	0.01	0.01	0.01	0.01	0.02	0.008	bal
-13	0.088	19.14	14.01	0.03	0.01	0.01	0.01	0.01	0.04	0.013	bal
-14	0.170	19.85	15.89	0.05	0.01	0.01	0.01	0.01	0.02	0.0012	bal

tests were conducted in a vacuum chamber on a 120-kN-capacity Instron closed-loop, servohydraulic materials test machine using a crosshead speed of 0.0085 mm/s.

Results and Discussion

The tensile results are given in Tables 2 and 3. Figure 1 shows the data for the solution-annealed steels and Fig. 2 shows the data for the cold-worked material. Also shown are data for type 316 stainless steel (fusion reference heat) taken from previous work.[4] In order that the tensile properties can be correlated with the microstructures previously determined,[3] the microstructures are given in Table 4.

Table 2. Tensile properties of solution-annealed Fe-Mn-Cr-C steels

Test Temperature (°C)	Yield Stress (MPa)	Ultimate Tensile Strength (MPa)	Elongation, %	
			Uniform	Total
Fe–20Mn–10Cr–0.1C (PCMA-10)				
21	164	638	25.0	25.0
300	95	448	46.8	51.4
450	55	398	42.0	43.4
600	83	193	9.8	11.2
Fe–20Mn–12Cr–0.1C (PCMA-11)				
21	69	652	48.0	48.4
300	72	431	47.4	51.6
450	60	405	47.4	48.2
600	66	310	33.0	34.8
Fe–20Mn–12Cr–0.2C (PCMA-12)				
21	66	607	46.6	47.4
300	90	448	48.2	50.0
450	100	445	47.0	49.0
600	55	286	31.6	33.6
Fe–20Mn–14Cr–0.1C (PCMA-13)				
21	172	824	77.6	79.8
300	140	486	39.8	42.2
450	134	483	43.8	46.2
600	95	345	30.0	32.4
Fe–20Mn–16Cr–0.2C (PCMA-14)				
21	190	688	47.4	50.4
300	159	431	31.4	33.8
450	186	431	26.8	28.8
600	105	207	23.6	28.8

Table 3. Tensile properties of 20%-cold-worked Fe-Mn-Cr-C steels

Test Temperature (°C)	Yield Stress (MPa)	Ultimate Tensile Strength (MPa)	Elongation, %	
			Uniform	Total
Fe–20Mn–10Cr–0.1C (PCMA-10)				
21	793	848	0.6	2.6
300	733	839	1.6	2.4
450	431	445	0.4	1.6
600	383	396	0.3	2.4
Fe–20Mn–12Cr–0.1C (PCMA-11)				
21	776	934	5.6	7.0
300	664	833	4.0	4.8
450	500	690	2.8	3.6
600	314	414	3.6	6.0
Fe–20Mn–12Cr–0.2C (PCMA-12)				
21	543	693	2.2	2.8
300	483	638	2.6	3.6
450	452	619	3.4	4.4
600	328	457	4.0	5.2
Fe–20Mn–14Cr–0.1C (PCMA-13)				
21	741	934	11.4	13.2
300	586	753	4.2	6.8
450	534	722	4.4	5.8
600	353	443	4.6	10.8
Fe–20Mn–16Cr–0.2C (PCMA-14)				
21	750	870	2.8	3.0
300	612	777	2.2	2.6
450	596	758	3.2	3.6
600	391	495	3.6	5.6

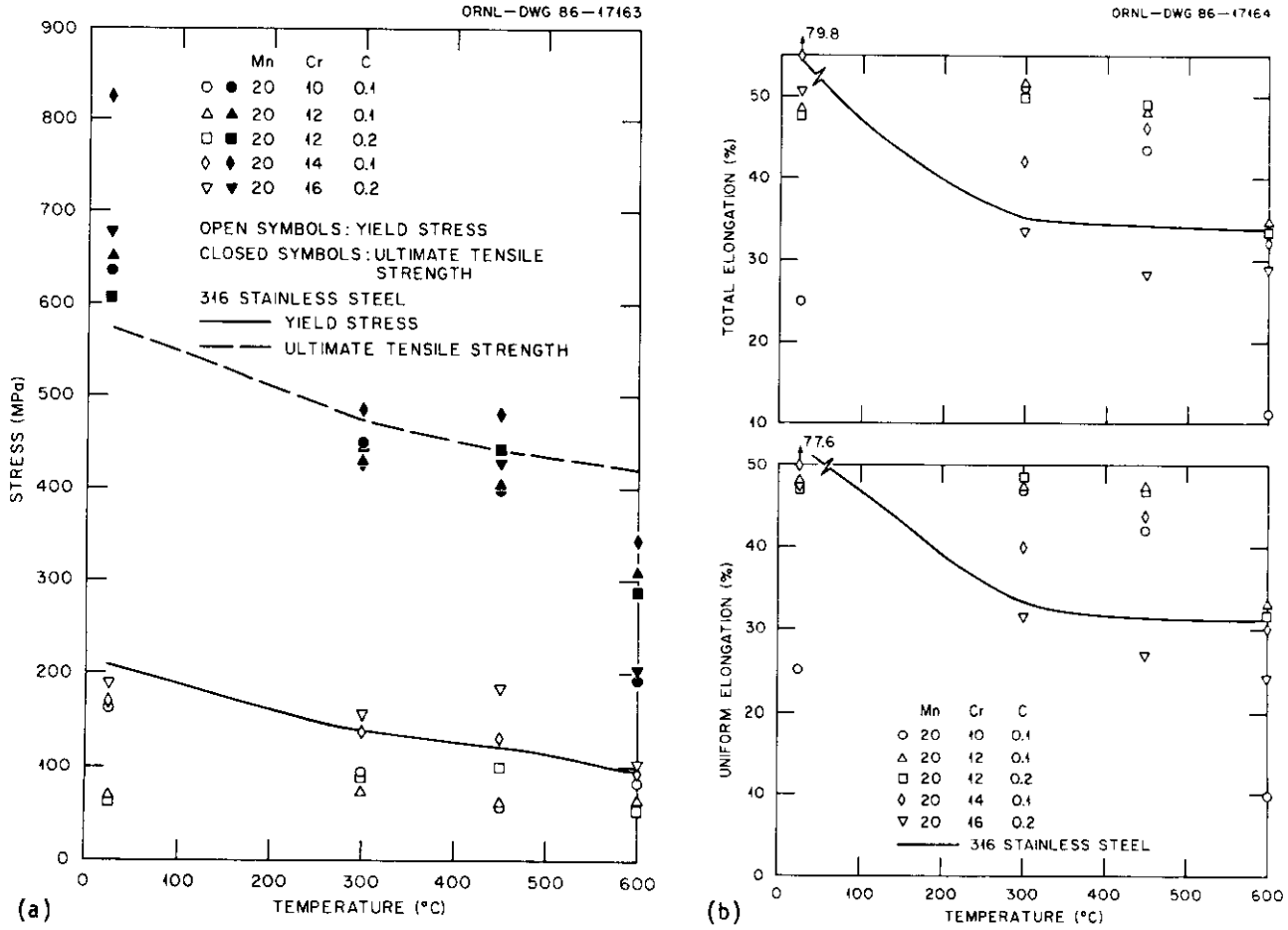

Fig. 1. Tensile properties of Fe-Mn-Cr-C steels in the solution-annealed condition as a function of test temperature: (a) 0.2% yield stress and ultimate tensile strength and (b) uniform and total elongation.

Table 4. Microstructural constituents[a] of Fe-Mn-Cr-C steels for various heat treatments

Alloy	Constituents[b]		
	1250°C/5 h	1150°C/1 h	1050°C/8 h
PCMA-10	γ + M	γ + M	γ + M
-11	γ + M	γ + M	γ + M
-12	γ + P	γ	γ
-13	γ + δ	γ + δ	γ + δ
-14	γ + δ	γ + δ	γ + δ

[a]Identified by optical microscopy.

[b]γ = austenite, δ = δ ferrite, M = martensite, and P = precipitate.

The tensile results indicate that it should be possible to develop manganese-stabilized stainless steels that have strength and ductility comparable to the values of type 316 stainless steel. In fact, these five steels have tensile properties that approach those for type 316 stainless steel in the cold-worked and annealed conditions (the type 316 stainless steel was annealed 1 h at 1050°C). This has been achieved without the addition of any type of strengthening elements (e.g., titanium).

An examination of the results for the five experimental heats in the solution-annealed condition reveals some information on strengthening mechanisms for these steels. Although there is considerable scatter in the data, the weakest steels are generally those that are entirely austenite, PCMA-11 and -12 (the 12%Cr–0.1%C and 12%Cr–0.2%C steels). The PCMA-10 alloy (10%Cr–0.1%C steel), which contains some martensite, is also quite weak. The two-phase alloys with austenite and delta-ferrite, PCMA-13 and PCMA-14 (14%Cr–0.2%C and 16%Cr–0.2%C steels), are generally the strongest. This is probably a reflection of the strengthening effect of the delta-ferrite. However, it is probably not possible to use such a two-phase alloy at elevated temperatures, because of the potential for sigma-phase formation. Previous goals have identified the entirely austenitic structure as desirable. Steel compositions that have a small fraction of martensite in the austenite might be useable, but these have a lower relative priority at the present time.

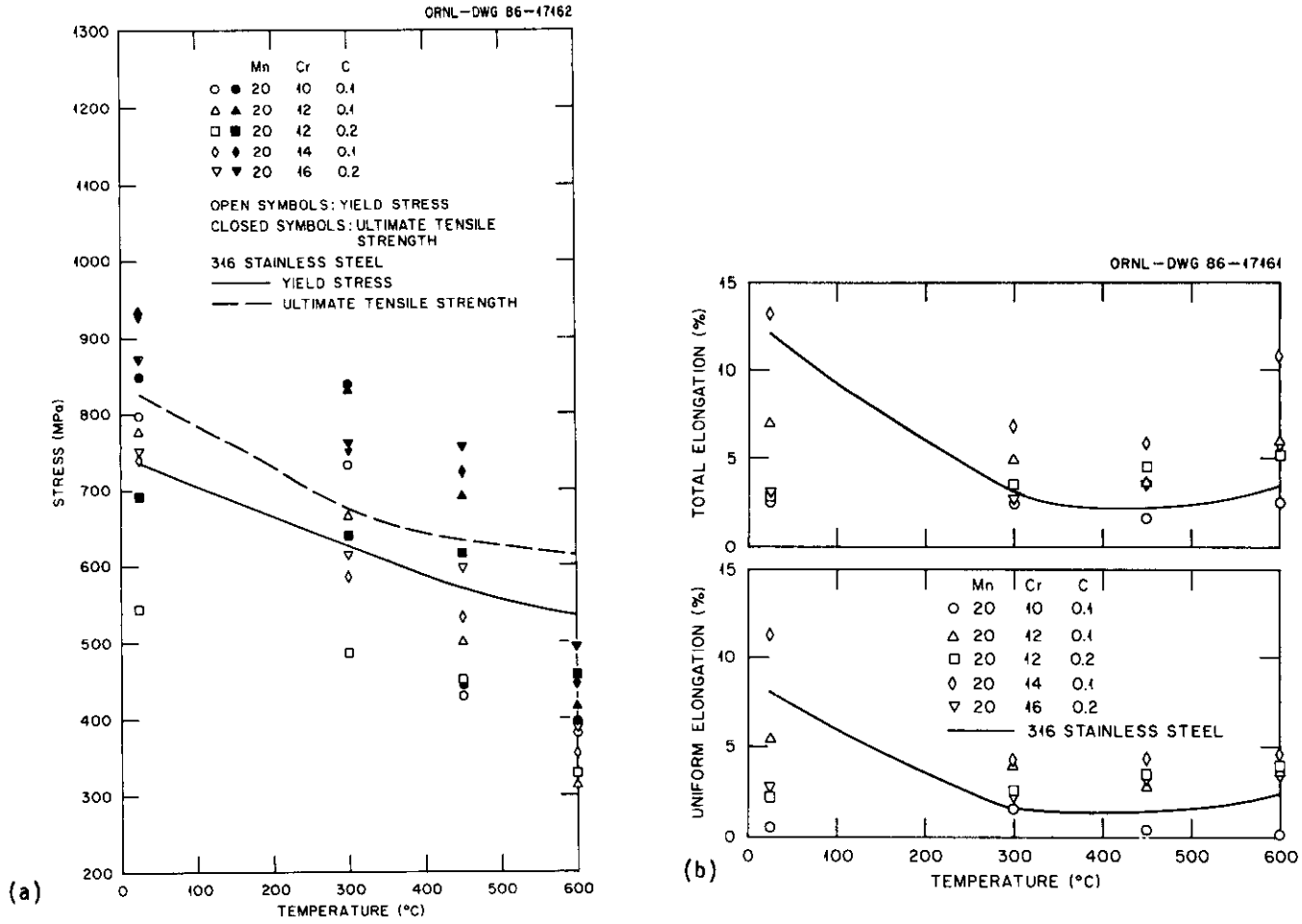

Fig. 2. Tensile properties of Fe-Mn-Cr-C steels in the 20%-cold-worked condition as a function of test temperature: (a) 0.2% yield stress and ultimate tensile strength and (b) uniform and total elongation.

CONCLUSIONS

The results of the work on the alloys discussed in this and the previous report[3] indicate that austenitic alloys can be produced with compositions containing about 20% Mn, 12 to 14% Cr, and 0.1 to 0.25% C. The tensile results on alloys produced to date indicate that by a suitable choice of alloying elements it should be possible to obtain unirradiated tensile properties that will be equivalent to or exceed those for type 316 stainless steel.

FUTURE WORK

Future work will be concentrated on producing alloys with a stable austenite base that will then be further alloyed for strength and irradiation resistance, using the elements that can be used to produce a FIRD alloy. It is proposed to improve the strength of the austenite-base composition by such alloying to produce steels with properties similar to the austenitic, nickel-stabilized PCA alloy presently being considered for fusion applications.

REFERENCES

1. R. L. Klueh and E. E. Bloom, "The Development of Austenitic Steels for Fast Induced-Radioactivity Decay for Fusion Reactor Applications," pp. 73–85 in Optimizing Materials for Nuclear Applications, The Metallurgical Society of AIME, Warrendale, Pa., 1985.

2. R. L. Klueh and P. J. Maziasz, "The Development of Austenitic Steels for Fast Induced-Radioactivity Decay," pp. 69–75 in ADIP Semiannu. Prog. Rep. Sept. 30, 1984, DOE/ER-0045/13, U.S. DOE, Office of Fusion Energy.

3. R. L. Klueh and P. J. Maziasz, "The Development of Austenitic Steels for Fast Induced-Radioactivity Decay," pp. 69–75 in ADIP Semiannu. Prog. Rep. Sept. 30, 1985, DOE/ER-0045/15, U.S. DOE, Office of Fusion Energy.

4. R. L. Klueh, "Miniature Tensile Test Specimens for Fusion Reactor Irradiation Studies," Nucl. Eng. Design/Fusion 2, 407–416 (1985).

6.3 Vanadium Alloys

PREPARATION AND FABRICATION OF VANADIUM BASE ALLOYS - H. R. Thresh and A. G. Hins (Argonne National Laboratory)

OBJECTIVE

The objective of this task is twofold: (1) to provide an inventory of vanadium alloy sheet material for testing in other parts of the development program and (2) to investigate the importance of process variables on the properties of the candidate vanadium alloys. This objective provides for the establishing of a materials processing flowstream that is capable of synthesizing vanadium base alloys and fabricating cast alloys to a final flat stock form. Initial efforts are focused on the V-Cr-Ti alloy system, with priority being given to the V-15Cr-5Ti alloy. Other alloys selected for development include V-10Cr-5Ti and V-10Cr-10Ti. This work also provides for the coordination of complimentary activities at Teledyne Wah Chang Albany.

SUMMARY

Initial phases in the production of V-Cr-Ti alloys have been completed. All steps in the process flow sheet (1) have been activated on production of the V-15Cr-5Ti ternary alloy. Sufficient material was processed to generate a 9.65 cm (3.8") diameter cast ingot weighing 13.1 kg (29 pounds). Subsequent hot extrusion provided a change in geometry to the billet to remove the cast structure and produce a rectangular shape to initiate hot rolling procedures. This extrusion has been subdivided and is currently passing through final processing operations, which include hot rolling, warm rolling and cold finishing steps. Flat stock is now being accumulated, while characterization work such as chemistry, non-destructive testing and metallography is on-going. Plans for the fabrication of the V-10Cr-5Ti alloy have been defined and the initial alloy consolidation is under way.

In addition, this effort provides for correlation of complimentary fabrication work on V-12Cr-5Ti and V-10Cr-10Ti alloys at Teledyne Wah Chang Albany.

PROGRESS AND STATUS

Introduction

All processing steps outlined in the ANL revised flowsheet for the fabrication of V-15Cr-5Ti alloy have been activated. Emphasis has been placed on optimizing the process stream to minimize the pickup of interstitial elements C, O, H and N by controlling the surface/volume ratio of the vanadium stock at the alloy synthesizing stage. Replacement of the formerly used vanadium turnings feedstock with sheared flat stock has permitted the particulate compaction stage to be substituted by direct alloying with a D.C. arc melting operation. All further high temperature operations have employed cladding, coatings or other atmosphere protection to control interstitial pick-up during material processing.

Alloy Processing

Alloy consolidation arc melting operations were continued in order to produce three additional 2.5 cm (1") alloy electrodes. These in turn were converted into three 5.8 cm (2.3") diameter consumable arc melted ingots as described previously (1). The five castings at this diameter were each machined to permit end to end contact for assembly into a second-stage consumable electrode by GTAW welding. Argon atmosphere protection in the welding glovebox minimized contamination pickup from this operation. A 9.65 cm (3.8") diameter copper mold was fitted to the NRC model 2721 arc melter and the 5.8 cm (2.3") consumable alloy electrode was processed into a 9.65 cm (3.8") diameter ingot employing a melting rate of 0.9 kg (2 pounds) per minute. This ingot was judged suitable as feedstock for the extrusion breakdown step. Minor billet size adjustments by machining produced a billet 9.017 cm (3.550") diameter by 26.7 cm (10.5") in length, weighing 10.5 kg (23.2 pounds).

To minimize contamination during the high temperature extrusion operation, a 304 stainless steel protective can was used to shroud the alloy billet. The components for this assembly are shown in Figure 1. Final sealing was accomplished by a GTAW welding operation. An extrusion ratio (input cross-section/exit cross-section) of 3.9:1 was adopted using a die contained in the external die holder. A new die was fabricated from an H-13 alloy steel blank and had a rectangular opening of 6.53 cm (2.57") by 3.18 cm (1.25"). The billet assembly was equilibrated at 1125°C for 2 hours and extruded through the 1250 ton Lake Erie Press with due attention to tooling preheat and lubrication. The 114 cm (45") long extruded bar was straightened while hot and measured 6.5 cm (2.56") x 3.20 cm (1.26"). This bar was cut into five 18 cm (7") pieces and the units were homogenized at 900°C for two hours under vacuum conditions. A hot rolling schedule reduced the thickness of three pieces from 3.20 cm (1.26") to 1.3 cm (0.51") employing 6 passes at 900°C. Employing a roll diameter of 23 cm (9") and a roll gap of 3.3 cm (1.3"), the ends of the hot rolled pieces showed some evidence of forming alligators. Processing

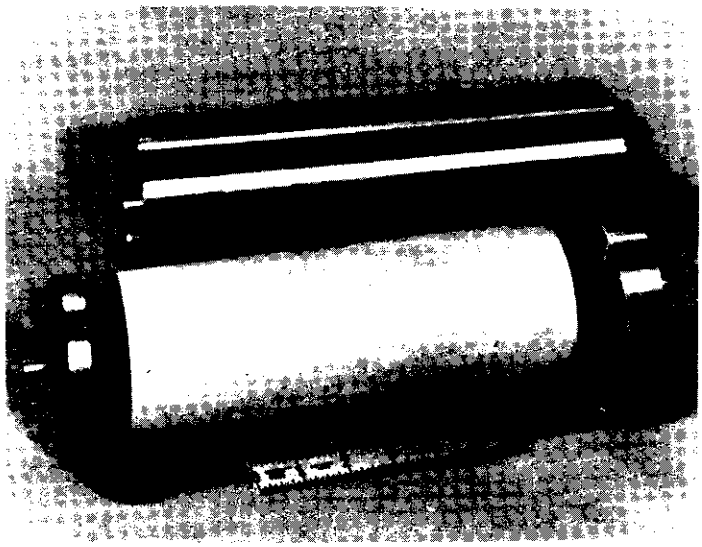

Figure 1. Billet Assembly Components for the Extrusion of the 8.9 cm (3.5") Diameter V-15Cr-5Ti Alloy Casting.

conditions need to be further optimized to minimize this condition. Warm rolling at 500°C reduced the thickness from 1.3 cm (0.51") to 0.76 cm (0.30"). The stainless steel cladding (extrusion can residual) was removed at this point. The final cold rolling sequence used a reduction of 50% before removing cold work with a process vacuum anneal at 900°C for one hour. All finished material will contain 50% cold work. Samples of finished 1.27 mm (0.050") thick and 0.51 mm (0.020") thick strip are shown in Figure 2.

Material Characterization

As sheet stock of V-15Cr-5Ti is accumulated, it is important to define certain parameters before this material is used in engineering scoping studies for the fusion community. At this time, chemistry, metallographic and non-destructive testing examinations are on-going to define the quality of the material. Chemistry data on the alloy content from samples removed from the large arc cast billet are recorded in Table I.

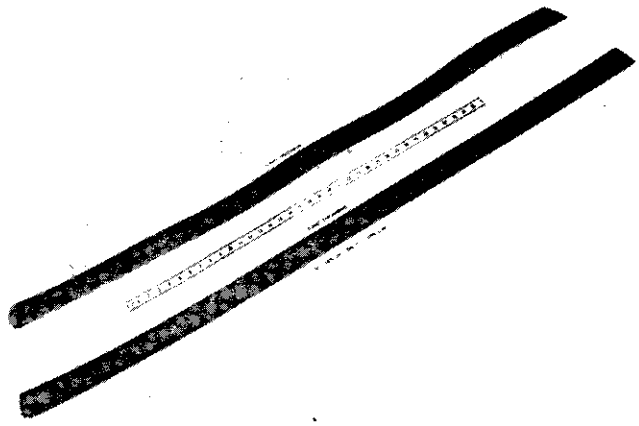

Figure 2. V-15Cr-5Ti Alloy Strip Finished to 0.51 mm (0.020") and 1.27 mm (0.050") Thickness and With 50% Cold Work.

The analytical results from three positions of the large as-cast ingot demonstrate that the target composition has been attained with good homogeneity throughout the material. Good control over the effects of Cr vapor pressure by the alloy consolidation method (1) is shown in the Cr results. Early interstitial analyses on the casting were made. The results are also shown in Table I. Additional analytical chemistry measurements are under way at this time.

Table I. Cast V-15Cr-5Ti Ingot Constituents

	Cr[a]	Ti[a]	C[b]	N[b]	O[b]
Ingot Top Sample	15.5	5.01	65	77	381
Ingot Center Sample	15.5	4.88	--	--	--
Ingot Bottom Sample	15.5	5.03	73	65	394

[a]In weight percent. [b]In ppm.

At the selected alloy composition, V, Cr and Ti are completely soluble as a beta phase. During the arc casting process an acicular precipitate is observed to separate in zones associated with final liquid solidification. Subsequent processing redistributes this precipitate to give the appearance of banding in the alloy structure. Banding has been observed in the current alloy. The nature and role of this precipitate on the material properties of this alloy has yet to be defined. All inventory material of this alloy will be finished with a cold work content of 50%. A typical microstructure of the as-finished condition is shown in Figure 3 where heavily deformed beta grains contain a redistributed dark precipitate.

As some degree of alligator formation has been experienced in the breakdown steps of this material, non-destructive examination has been introduced to ensure that all separated material has been removed at the appropriate process step. The detection of material laminations was performed by the use of a Kraut Kramer Branson ultrasonic test unit in conjuction with a hand-held portable probe.

Approximately 0.5 kg of V-12Cr-5Ti alloy sheet has been received from Teledyne Wah Chang Albany for characterization and comparison with the ANL vanadium alloy heats.

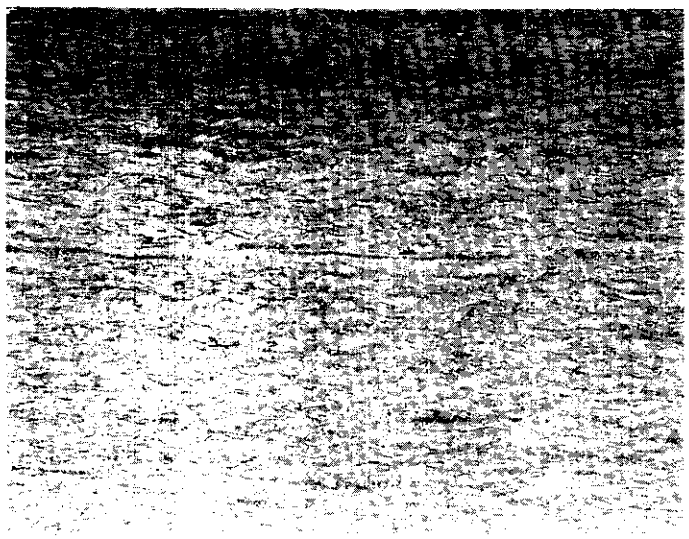

Figure 3. Typical Microstructure of Cold Rolled V-15Cr-5Ti Finished Sheet (50% C.W.), 200X Magnification in Transverse Direction.

FUTURE WORK

Processing of the current lot of V-15Cr-5Ti will continue through complete conversion of this material to sheet stock. Original plans to fabricate additional amounts of this particular alloy will be curtailed at this time. Priority will be placed on moving V-10Cr-5Ti into the processing stream. Corresponding materials characterization work will define the quality of these materials.

The Teledyne Wah Chang Albany effort will concentrate on providing a small test heat of V-10Cr-10Ti alloy sheet material.

REFERENCES

1. A. G. Hins and H. R. Thresh, "Preparation and Fabrication of Vanadium Base Alloys," pp. 73-77 in Alloy Development for Irradiation Performance: Semiannual Progress Report for Period Ending March 31, 1986, DOE/ER-0045-16, Oak Ridge National Laboratory, Oak Ridge, TN, Sept., 1986.

DEVELOPMENT OF A VANADIUM-BASE ALLOY STRUCTURAL MATERIAL - B. A. Loomis (Argonne National Laboratory)

OBJECTIVE

The objective of this research is to determine the composition of a vanadium-base alloy with the optimum combination of swelling resistance, corrosion resistance, and mechanical properties in the environment of a magnetic fusion reactor.

SUMMARY

The V-3Ti-1Si, V-5Ti, V-20Ti, and V-15Cr-5Ti alloys were irradiated at 650°C with 4.0-MeV $^{51}V^{++}$ ions to 50 dpa. Voids were not visible in the irradiated alloys. Coherent precipitates were produced in the irradiated V-5Ti and V-15Cr-5Ti alloys. The precipitates were noncoherent with the matrix in the V-20Ti alloy and partially coherent in the V-3Ti-1Si alloy. The formation of coherent precipitates may contribute to the greater susceptibility of the V-15Cr-5Ti alloy, in comparison to the V-20Ti and V-3Ti-1Si alloys, to irradiation hardening and loss of ductility after neutron irradiation. A test matrix for irradiation of V-base alloys in the FFTF reactor during cycle 9 is presented.

PROGRESS AND STATUS

Introduction

The microstructures for single- and dual-ion irradiated pure V and V-base alloys containing Ni, Fe, Cr, Ti, Mo, or W solute show that Ti solute is the most effective for the reduction of swelling of irradiated V-base alloys.[1] Furthermore, the microstructures show that the swelling of V-base alloys containing at least 3 wt % Ti is less than 0.01% per atom displacement per atom (dpa) if the helium implantation rate is less than 10 appm per dpa.[2] In the case of the ion-irradiated V-15Cr-5Ti alloy, the increase in yield stress and decrease in ductility have been computed from the number density of irradiation-produced dislocations and precipitates in the microstructures. The results of these computations suggest that the ductility for this alloy at a damage level of ~50 dpa may be unacceptable for a structural material in a magnetic fusion reactor (MFR).[3] Neutron irradiations of the V-15Cr-5Ti alloy have also shown that this alloy is susceptible to significant irradiation hardening and loss of ductility.[4] However, the V-3Ti-1Si and V-20Ti alloys are less susceptible to irradiation hardening and loss of ductility on neutron irradiation.[4] A previous investigation on the effects of thermal-mechanical treatment and impurity level on the yield strength of the unirradiated V-15Cr-5Ti alloy has shown that a suitable preirradiation heat treatment may result in reduced irradiation hardening and loss of ductility of the alloy.[5] Investigations on the influence of Cr additions on the long-time stress-rupture properties of unirradiated V-Ti alloys suggest that the pronounced strengthening of V-Ti alloys by Cr additions may be attributed to the formation of more-coherent TiO precipitates.[6] If this is the correct explanation for these results, the different irradiation hardening of V-15Cr-5Ti, V-20Ti, and V-3Ti-1Si alloys may also be attributed to the degree of coherency of the irradiation-produced precipitates.

In this report, the results of an investigation on the coherency of precipitates in ion-irradiated V-15Cr-5Ti, V-10Ti, V-5Ti, and V-3Ti-1Si alloys are presented. Also presented is the test matrix of V-15Cr-5Ti, V-15Ti-7.5Cr, V-3Ti-1Si, and V-20Ti alloy tensile and transmission electron microscopy (TEM) specimens that have been inserted in the FFTF reactor. These neutron-irradiated specimens are intended for an evaluation of the effects of thermal-mechanical treatment and coherency of irradiation-produced precipitates on irradiation hardening and loss of ductility of the alloys.

Experimental procedures

The V-3Ti-1Si and V-20Ti alloys (nominal composition in wt %) for this investigation were obtained from the Fusion Materials Inventory (Oak Ridge National Laboratory). The V-15Cr-5Ti, V-5Ti, and V-15Ti-7.5Cr alloys were supplied from the Argonne National Laboratory (ANL) Materials Inventory.

FFTF irradiation

Miniature tensile specimens with a nominal thickness of 0.4 mm and a gauge length and width of 7.6 and 1.5 mm, respectively, were machined from the as-rolled material (25-50% cold work). The tensile specimens (wrapped in tantalum foil) were annealed in quartz tubes containing high-purity argon for 1 h at 850, 950, 1100, or 1200°C and quenched in the capsules in water. Some of the annealed V-15Cr-5Ti and V-15Ti-7.5Cr material received subsequently a 10% reduction in thickness at ambient room temperature. The annealed specimen surfaces were polished to a 0.3-μm finish before insertion in the FFTF. The alloy designations for the FFTF irradiation were:

Designation	Alloy
BL-24	V-15Cr-5Ti
BL-10	V-15Ti-7.5Cr
BL-27	V-3Ti-1Si
BL-15	V-20Ti
BL-37	V-15Cr-5Ti (10% cold work)
BL-38	V-15Ti-7.5Cr (10% cold work)

The heat treatment designations for the FFTF irradiation were:

Designation	Heat Treatment
A	Annealed 1 h at 1200°C
B	Annealed 1 h at 1100°C
C	Annealed 1 h at 950°C
D	Annealed 1 h at 850°C
E	Annealed 1 h at 1125°C + 10% cold work

The distribution of the tensile specimens in the FFTF MOTA 1-E for cycle 9 is presented in Table 1. The distribution of TEM discs in the MOTA is approximately the same as for the tensile specimens. The goal irradiation damage level for the tensile specimens and the TEM discs is approximately 30 dpa.

Table 1. Tensile specimens for FFTF irradiation

	Irradiation Temperature (°C)		
	420	520	620
Alloy	Number of Specimens		
BL-24-A	2	1	
BL-24-B	2	1	1
BL-24-C	2	1	
BL-24-D	2	1	1
BL-10-A	1	1	
BL-10-B	2	1	1
BL-10-C	3	1	
BL-10-D	2	1	1
BL-27-A	1	1	
BL-27-B	1	1	
BL-27-C	1	1	
BL-27-D	1	1	1
BL-15-A			
BL-15-B	1	1	
BL-15-C	1	1	
BL-15-D	1	1	1
BL-37-E	1	1	1
BL-38-E	1	1	1

Ion irradiation

Disc-shape specimens of the V-5Ti, V-15Cr-5Ti, V-3Ti-1Si, and V-20Ti alloys, each with a diameter of 3.05 mm, were annealed for 1 h at 1125°C. The specimens were mounted in a tungsten holder for irradiation in the 2-MeV Tandem irradiation facility at ANL. The specimens were irradiated with 4-MeV $^{51}V^{++}$ ions at a nominal atomic displacement rate of 5×10^{-3} dpa per second to an irradiation damage level of 55 dpa at the depth for the maximum calculated damage. The dpa levels were calculated by the use of the Brice computer codes RASE 3 and DAMG 2 with some modifications.[7] The depth of the maximum irradiation damage for 4-MeV $^{51}V^{++}$ ions impinging on V was calculated to be 1100 nm. The specimens at 650°C were irradiated in an all-metal system evacuated to a total pressure of 3×10^{-6} Pa. The irradiated specimens were prepared for

observation by TEM by sectioning the specimens to a depth that was approximately 100 nm less than the peak damage depth. The sectioning of the specimens was accomplished by electrolytic polishing of the irradiated surface in a 15% H_2SO_4-15% butyl cellosolve-70% methanol solution at -25°C.

Results and analysis

The TEM microstructures for the V-3Ti-1Si, V-5Ti, V-20Ti, and V-15Cr-5Ti alloys after ion irradiation at 650°C to 50 dpa are shown in Fig. 1. Voids were not visible in the microstructures. The microstructures for the V-3Ti-1Si (Fig. 1a) and the V-20Ti (Fig. 1c) alloys contained a high density (~10^{23} m^{-3}) of disc-shape precipitates with a diameter of ~60 nm. The microstructures for the V-5Ti (Fig. 1b) and V-15Cr-5Ti (Fig. 1d) alloys also contained a high density (~5 x 10^{23} m^{-3}) of disc-shape precipitates but the diameter of these precipitates was ~6 nm. The addition of Cr to the V-5Ti alloy did not result in a visible change in the microstructure for the irradiated V-5Ti alloy.

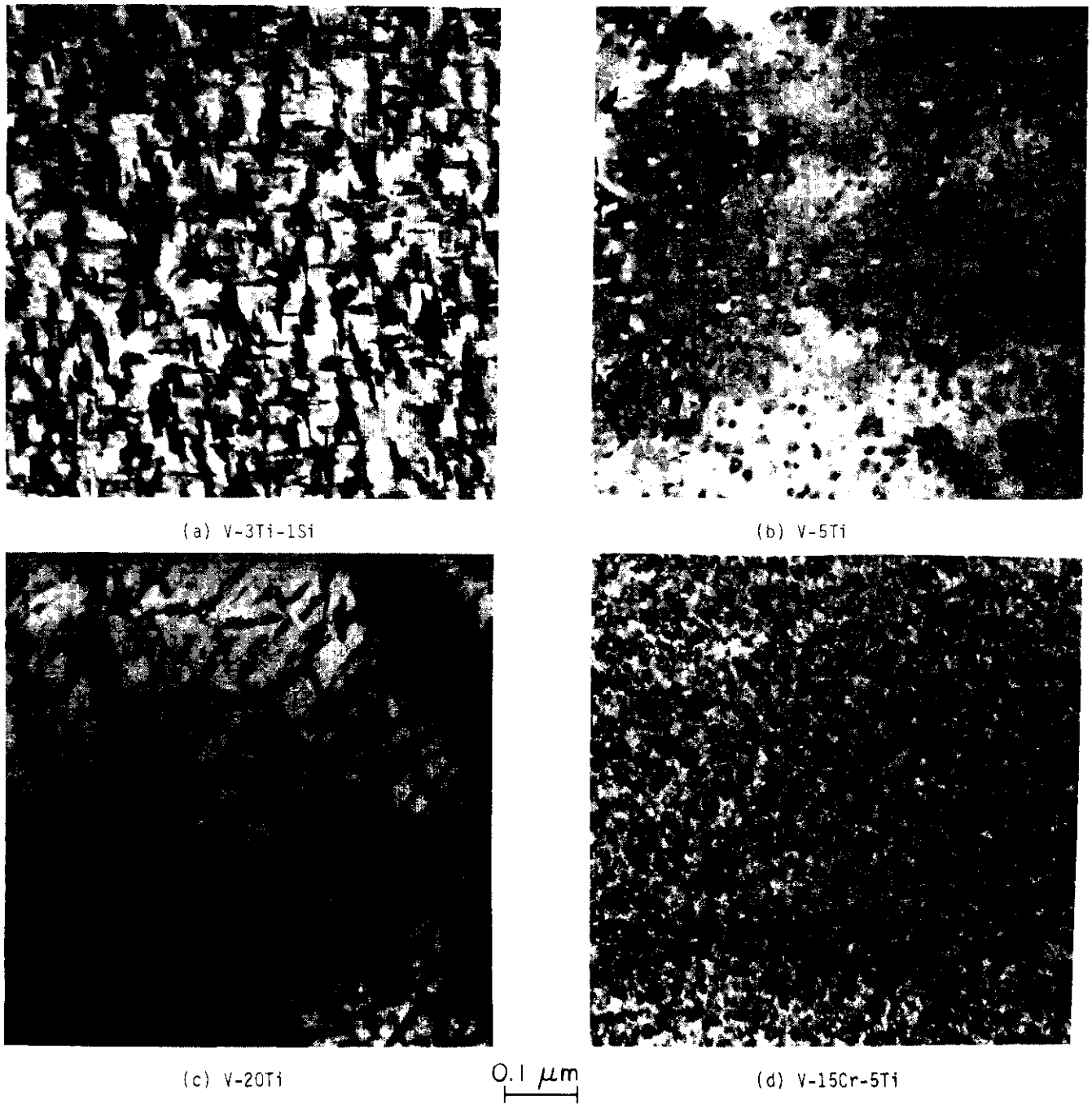

Fig. 1. Microstructures for the (a) V-3Ti-1Si, (b) V-5Ti, (c) V-20Ti, and (d) V-15Cr-5Ti alloys after ion irradiation at 650°C to 50 dpa.

The presence of strain field contrast in the vicinity of the precipitates in the V-5Ti and V-15Cr-5Ti microstructures suggests that these precipitates are coherent with the matrix. That is, the lattice constants for the precipitates and the matrix differ by less than 2%. Strain field contrast was clearly absent around the precipitates in the microstructure for the V-20Ti alloy (Fig. 1c). In the case of the V-3Ti-1Si alloy (Fig. 1a), some of the precipitates appeared to have strain field contrast, i.e., a partially coherent precipitate structure.

The composition of the precipitates in the ion-irradiated V-15Cr-5Ti alloy has been previously determined to be Ti_3O.[8] The composition of the precipitates in the other alloys has not been determined. The precipitates in all of the alloys had a {100} habit plane.

Discussion

The misfit on the boundary plane between the matrix and the precipitates is given by

$$\frac{a_m \sqrt{2} - a_{TiO}}{a_m \sqrt{2}},$$

where a_m is the lattice constant for the matrix and a_{TiO} is the lattice constant for the precipitate. Since the lattice constant of the matrix, a_m, increases with an increase of the Ti concentration, the misfit at the boundary plane of the precipitates increases with an increase of the Ti concentration from 5 to 20 wt %.[8] The misfit is 2% for a 5 wt % Ti concentration, but the misfit increases to >4% for the 20 wt % Ti concentration.[8] Hence, it may be expected, in agreement with the TEM observations, that the Ti_3O precipitates in the V-5Ti alloy are coherent with the matrix whereas the precipitates in the V-20Ti alloy are noncoherent with the matrix. The addition of Cr to the 5 wt % Ti alloy is expected to decrease the misfit of the precipitates with a corresponding increase of coherency since Cr atoms are undersized in the V solid solution alloy.[9] The greater susceptibility of the V-15Cr-5Ti alloy, in comparison to the V-20Ti and V-3Ti-1Si alloys, to irradiation hardening and loss of ductility after neutron irradiation may be due to the formation of coherent precipitates rather than noncoherent or partially coherent precipitates.

CONCLUSIONS

1. Voids are not visible in V-5Ti, V-15Cr-5Ti, V-3Ti-1Si, and V-20Ti alloys after ion irradiation at 650°C with 4-MeV $^{51}V^{++}$ ions to 50 dpa.

2. The irradiation-produced precipitates in V-5Ti and V-15Cr-5Ti alloys on ion irradiation at 650°C to 50 dpa are coherent with the matrix.

3. The irradiation-produced precipitates in the V-3Ti-1Si alloy are partially coherent whereas the precipitates in the V-20Ti alloy are noncoherent on ion irradiation at 650°C to 50 dpa.

4. The greater susceptibility of the V-15Cr-5Ti alloy, in comparison to the V-3Ti-1Si and V-20Ti alloys, to irradiation hardening and loss of ductility may be due to the formation of coherent precipitates.

FUTURE WORK

1. The lattice constant of the matrix material and precipitates in V-3Ti-1Si, V-20Ti, V-5Ti, and V-15Cr-5Ti alloys will be determined to see whether a quantitative relationship exists with the irradiation hardening of V alloys.

2. The effect of thermal-mechanical treatment on the ductility of neutron-irradiated (FFTF reactor) V-base alloys will be evaluated.

3. The coherency of the irradiation-produced precipitates in neutron-irradiated V-base alloys will be evaluated.

REFERENCES

1. B. A. Loomis, B. J. Kestel, and S. B. Gerber, "Solute Segregation and Microstructural Evolution in Ion-Irradiated Vanadium-Base Alloys," Thirteenth International Symposium on Effects of Radiation on Materials, Seattle, WA, June 23-25, 1986.

2. B. A. Loomis, B. J. Kestel, S. B. Gerber, and G. Ayrault, "Effect of Helium on Swelling and Microstructural Evolution in Ion-Irradiated V-15Cr-5Ti Alloy," Second International Congress on Fusion Reactor Materials, Chicago, IL, April 13-17, 1986.

3. B. A. Loomis and B. J. Kestel, "Microstructural Evolution and Computed Yield Stress Increase for Ion-Irradiated V-15Cr-5Ti Alloy," pp. 65-70 in Alloy Development for Irradiation Performance: Semiannual Progress Report for Period Ending March 31, 1986, DOE/ER-0045-16, Oak Ridge National Laboratory, Oak Ridge, TN, September 1986.

4. D. N. Braski, "The Effect of Neutron Irradiation on the Tensile Properties and Microstructure of Several Vanadium Alloys," Thirteenth International Symposium on Effects of Radiation on Materials, Seattle, WA, June 23-25, 1986.

5. B. A. Loomis and B. J. Kestel, "Effect of Thermal-Mechanical Treatment and Impurity Level on the Yield Strength and Microstructure of V-15Cr-5Ti Alloy," pp. 78-82 in Alloy Development for Irradiation Performance: Semiannual Progress Report for Period Ending September 30, 1985, DOE/ER-0045/15, Oak Ridge National Laboratory, Oak Ridge, TN, February 1986.

6. H. Böhn, "Strengthening Mechanism in Vanadium-Titanium Alloys," pp. 341-345 in Second International Conference on the Strength of Metals and Alloys, August 30-September 4, 1970, Pacific Grove, CA, Vol. 1.

7. D. K. Brice, Ion Implantation Range and Energy Deposition, IFI/Plenum Publishers, New York, 1975.

8. K. H. Kramer, "Precipitation Processes in Pure Vanadium and Vanadium-Titanium Alloys," J. Less-Common Metals 21, 365-382 (1970).

9. Handbook of Chemistry and Physics, 65th edition, 1984, CRC Press, Inc., p. F167.

EFFECT OF PREINJECTED HELIUM ON THE RESPONSE OF V–20Ti PRESSURIZED TUBES TO NEUTRON IRRADIATION — J. M. Vitek, D. N. Braski, and J. A. Horak (Oak Ridge National Laboratory)

OBJECTIVE

The goal of this experiment was to investigate the combined effects of displacement damage and helium generation on the behavior of pressurized vanadium alloy tubes.

SUMMARY

Vanadium–20% titanium tubes, pressurized to stresses of 34 and 39 MPa, were irradiated in the Experimental Breeder Reactor (EBR-II) at 700°C to a fluence of 3.9×10^{26} n/m^2, corresponding to a displacement damage level of 22 dpa. Sections of the tubes were injected with 15 appm He prior to irradiation to determine the effect of helium on the microstructural and creep response of this alloy to irradiation. It was found that helium promoted cavity formation, primarily within existing precipitates, but total swelling remained low. Under some conditions, an apparent enhanced creep deformation due to the presence of helium was found. The results suggest that the increase in creep deformation in the presence of helium may be very sensitive to stress.

PROGRESS AND STATUS

Introduction

Vanadium alloys are of interest as candidate alloys for possible structural applications in fusion reactor devices. One of the advantages of this class of alloy is its potential for use at a higher service temperature than other candidate alloys such as ferritic or austenitic stainless steels. More recently, interest in vanadium alloys has increased because of their inherent low activation following neutron irradiation.[1] Some vanadium alloys maintain promising properties following irradiation.[2] As candidate materials for fusion applications, though, one concern that requires investigation, in addition to displacement damage effects, is how the properties are affected by stress and the helium production inherent in a fusion environment. Unfortunately, a direct evaluation of simultaneous helium production and displacement damage during neutron irradiation is not possible at present. Therefore, one must resort to techniques which simulate the fusion environment as closely as possible. One such technique is to implant helium into the specimens prior to neutron irradiation. In order to make as direct a comparison as possible to evaluate helium effects on the irradiation response of the vanadium alloys, helium was implanted into only a section of the vanadium tubes prior to being pressurized and irradiated with neutrons. In this way, comparisons could be made between stressed regions with and without helium in the same specimen. Thus, possible variations in temperature, neutron spectrum, or preparation would be avoided in the analysis of helium effects.

The use of helium implantation prior to irradiation has often been utilized. Examination of tensile properties of specimens preinjected with helium has shown that helium decreases the postirradiation ductility for a number of vanadium alloys.[2,3] In addition, in the temperature range of 400 to 700°C and to damage levels up to 40 dpa, preinjected helium promoted cavity formation although negligible total swelling was found.[3,4] In the present study, the helium was injected into pressurized tube samples so that the additional factor of irradiation under stress could be examined. In a similar study on helium injected pressurized tubes of type 316 stainless steel,[5] it was found that the helium preinjection suppressed swelling.

Experimental Procedure

The alloy used in the present investigation was vanadium with 20 wt % Ti (V–20Ti), one of the several vanadium alloys being evaluated for potential fusion applications. A list of minor element concentrations in the alloy is given in Table 1. The tubing was manufactured by Superior Tube Company and swaged down to its final size at the Oak Ridge National Laboratory (ORNL). After swaging, the tube was given a final anneal at 900°C for 30 min at $\sim 5 \times 10^{-5}$ Pa.

The tubing had an outer diameter of 4.57 mm and a wall thickness of 0.25 mm. They were approximately 51 mm in length and had welded end caps. Tubes V23 and V24 were pressurized to produce a hoop stress of 34 MPa (5000 psi) at the irradiation temperature, whereas tube V22 had a hoop stress of 39 MPa (5700 psi). The central section (~13 mm in length) of each specimen was preinjected with helium at 20°C at the Oak Ridge Isochronous Cyclotron (ORIC). The end sections of the tubes contained no preinjected helium. An accelerator energy of 51.6 MeV was degraded with a beryllium wedge-shaped wheel in order to uniformly distribute the helium throughout the thickness of the tube walls. The degrader wheel rotation speed was appoximately 100 times greater than the rate of revolution of the tube, thereby ensuring uniformity of the helium distribution along the tube circumference. Helium preinjection levels of 15 appm were attained. The tube specimens

Table 1. Impurity element concentrations in V–20%Ti tubing (wt ppm)

Mg	Al	Si	S	Ca	Cr	Fe	Ni	Cu	Sn	W	O	C	N	H
10	10	80	20	10	90	200	20	30	40	20	730	330	290	20

were then irradiated in the EBR-II in sodium at a nominal temperature of 700°C to a dose of 3.9×10^{26} neutrons/m^2 (E > 0.1 MeV), corresponding to a total damage of 22 dpa and a direct helium production of 1 appm (ref. 6).

The diameters of the tube specimens were measured after filling with helium (prior to irradiation) and after neutron irradiation. These measurements were made at the Hanford Engineering Development Laboratory by E. R. Gilbert. After the diameter measurements, the tubes were cut into ring sections corresponding to the regions with and without pre-injected helium. Immersion density measurements were made at ORNL on these ring sections prior to the preparation of TEM specimens. Specimens for TEM examination were cut from the ring sections and ground flat on 600-grit emery paper. The wafers were subsequently jet polished in a 12.5 vol % solution of H_2SO_4 in methanol at –25°C and then examined in a 100 kV analytical electron microscope.

RESULTS

Dimensional Measurements

Tube diameter measurements are available for tubes V22 and V24 and the change in tube diameter is plotted in Fig. 1 for both of these specimens. The increase in tube diameter found for both specimens is a combination of plastic deformation and swelling. Except for the last data point in Fig. 1(a), which seems to be an outlier, the tube expansion was fairly uniform across its length. A marginal increase in the tube expansion may exist in the helium preinjected area. For the tube with the greatest hoop stress

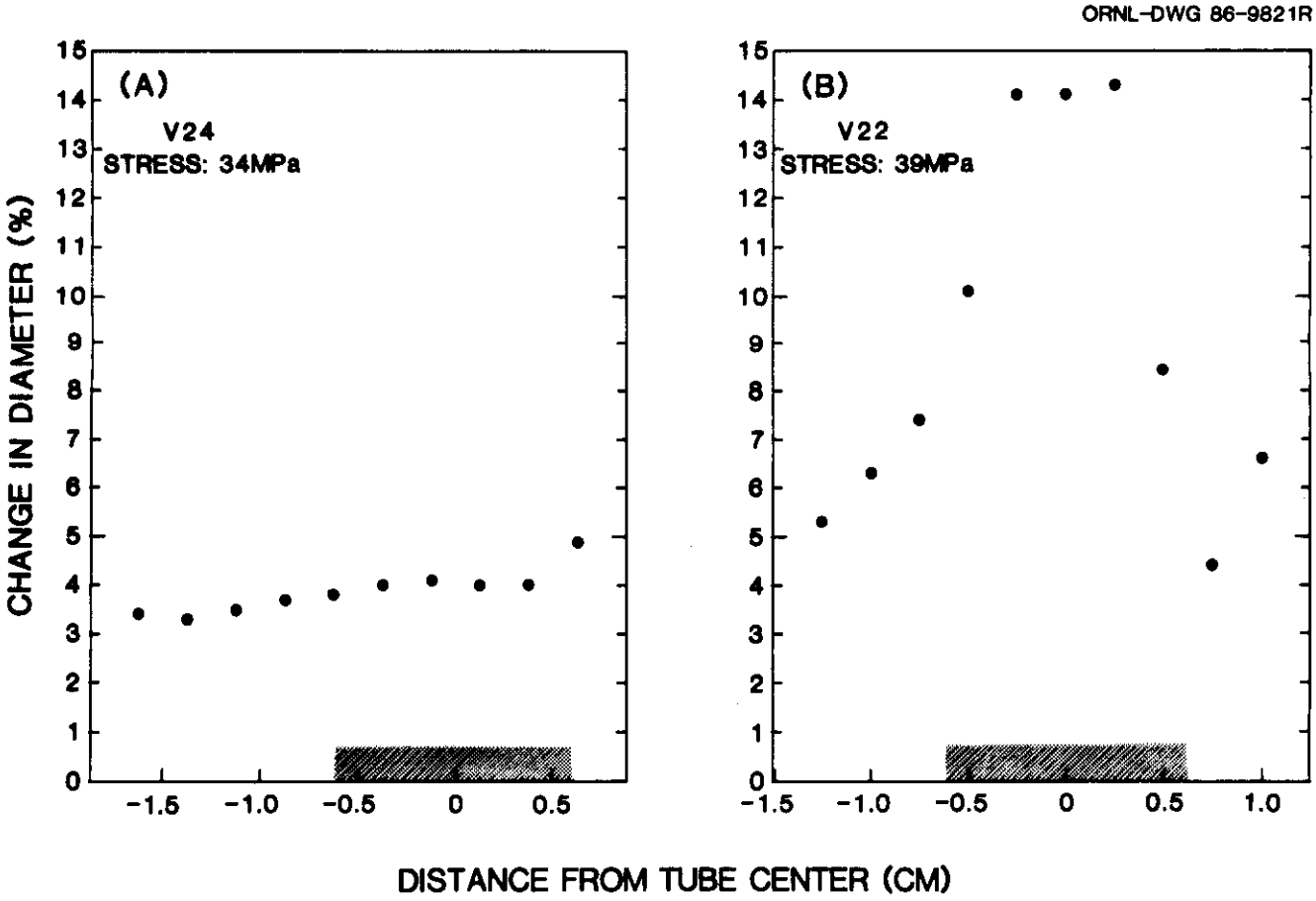

Fig. 1. Percent change in tube diameter vs. position for tubes (a) V24 and (b) V22. Shaded region corresponds approximately to helium-containing section.

[V22, Fig. 1(b)], a large increase in tube expansion is found in the center section of the tube, corresponding to the region that contains 15 appm preinjected helium. Thus, for sample V22, it is clear that the presence of helium leads to a larger tube expansion.

Density Measurements

After irradiation, the three tubes were cut into rings approximately 7.5 mm long and density measurements were made on these rings from all three tubes. The results are plotted in Fig. 2. Also shown is a dashed line representing the density for identical, but unirradiated, ring sections. The data show that a slight decrease in density occurs upon irradiation. No significant difference in density is seen between the regions with and without helium.

Microstructure

The microstructure of the unirradiated vanadium tube is typical of that for a cold-worked material that has undergone some recovery as shown in Fig. 3(a). The microstructure contains an extensive network of dislocation segments and subgrain boundaries. Second phase particles, ranging in size from less than 0.1 μm to several microns in diameter, were scattered throughout the material [Fig. 3(b)]. Quantitative x-ray dispersive spectroscopy (EDS) analyses performed on an analytical electron microscope showed that the detectable element composition (Z > 11) of the second phase was 96 wt % Ti and 4 wt % V. It is likely that the phase is a Ti-V oxide, nitride, or carbide. Unpublished electron diffraction data by Tanaka[7] indicate that it is probably an oxide.

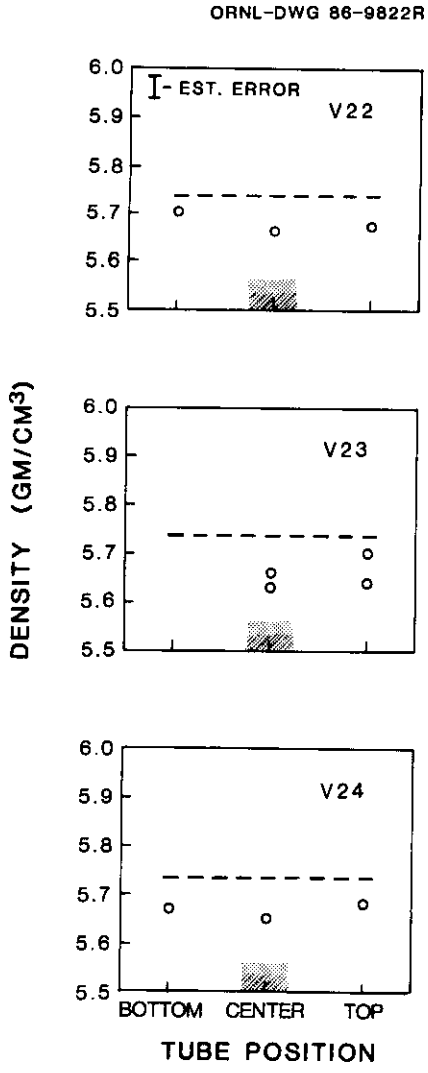

Fig. 2. Immersion density measurements vs. tube position for ring sections from tubes (a) V22, (b) V23, and (c) V24. Dashed lines indicate density of unirradiated material; shaded shaded region corresponds to helium-containing section. Estimated error bar for the measurements is shown in Fig. 2(a).

Sections of V–20Ti tubes without implanted helium showed cavities in the second phase following irradiation to 22 dpa, as revealed in Fig. 4. Stereo-microscopy confirmed that the cavities were within the second phase particles and not along the particle/matrix interface. Cavities were not observed in the matrix. Under the same irradiation conditions, much larger and often elongated cavities in the second phase particles were found in the helium-implanted section of the same tube, as illustrated in Fig. 5. Stereo-microscopy showed that the unusual cavity distribution was within the particles and appeared to be aligned along a specific crystallographic plane. Such alignment of cavities was observed frequently in the second phase particles. Although no quantitative measurements were made, it was obvious that cavitation or swelling in the second phase was significantly greater in the section of the tube containing helium. Limited matrix swelling of the helium-injected sections was also found, but the actual volume change was small as evident from the micrograph in Fig. 6. In this typical matrix area, only a few small cavities are present. Cavity formation was quite heterogeneous but under all conditions, in sections with and without preinjected helium, the total swelling was minimal, well below 0.5%.

Discussion

The aim of the present study was to evaluate the effect of helium on the irradiation behavior of the V–20%Ti alloy. Two effects can be identified, one on the microstructural behavior and the other on the creep response. Considering the former effect first, it is apparent that helium promoted swelling within the titanium-rich second phase particles (cf Figs. 4 and 5). The region with implanted helium also experienced some limited cavity formation within the matrix. Thus, although V–20Ti is quite resistant to swelling when irradiated in the absence of helium,[8] some limited swelling is found when helium is present. The promotion of swelling by helium is characteristic of systems in which cavity formation is restricted

ORNL-PHOTO 8566-86

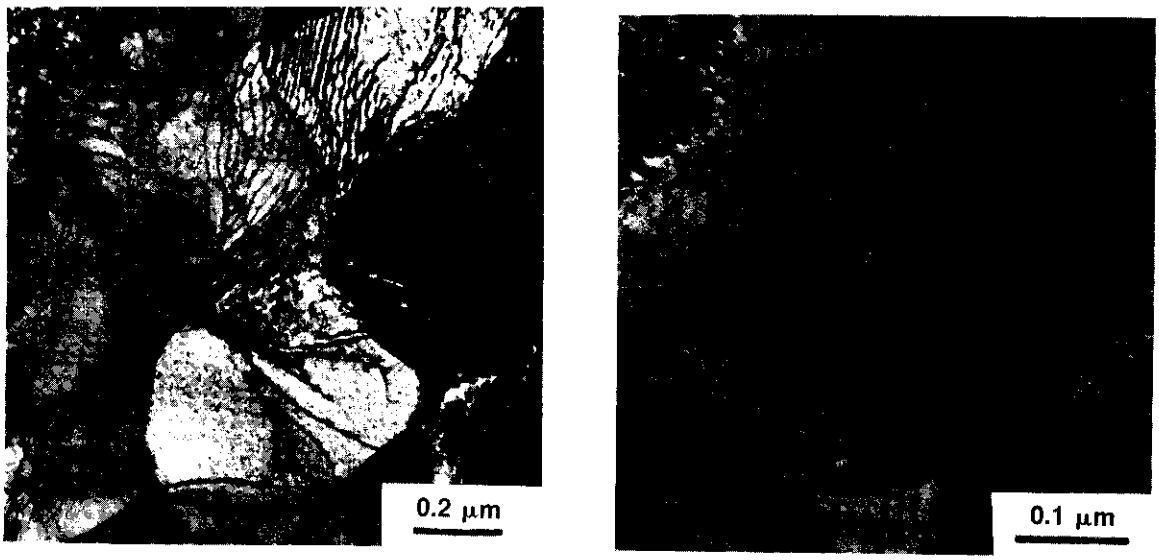

Fig. 3. Microstructure of unirradiated V–20Ti tube showing (a) the cold-work and recovered structure with characteristic dislocation networks and numerous subgrain boundaries, and (b) a second phase particle in the grain matrix.

ORNL-PHOTO 8670-86

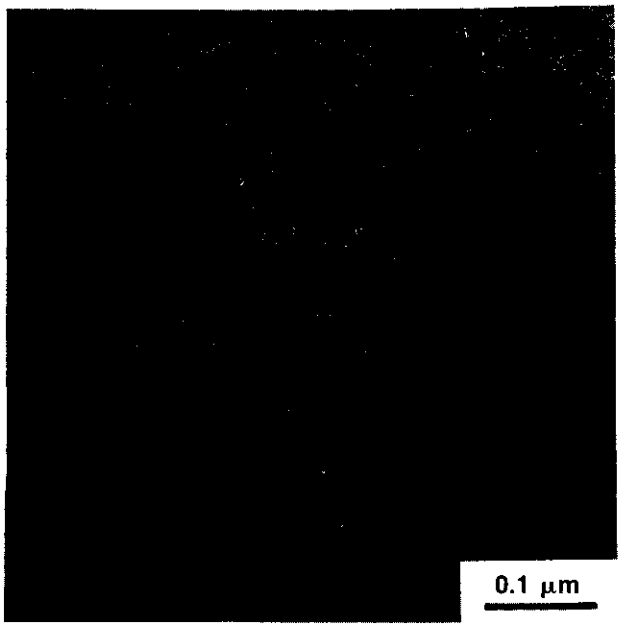

Fig. 4. Cavities within a second phase particle found in a section of tube V23 without helium.

The helium bubbles act as nuclei for cavities. Such an effect has been observed in other vanadium alloys[4,9] as well as in other systems, such as ferritic steels.[10] The opposite effect was found in helium-injected pressurized tubes of type 316 stainless steel,[5] where helium inhibited swelling. The difference in behavior can be attributed to the fact that cavities form in the stainless steel without helium and the presence of helium changes the cavity growth rates by influencing the relative sink strengths.[5]

It is interesting to note that nearly all of the cavities observed were located within second phase particles. Such behavior is unusual, but not unique. The presence of cavities within precipitates has recently been observed in other EBR-II-irradiated vanadium alloys[9] as well as in large precipitates in nickel-doped ferritic alloys.[11] In the present case, such void formation within precipitates may be due to helium production during irradiation. Although the average amount of helium produced in the matrix during irradiation is small (1 appm), within the titanium-rich precipitates over 5 appm He is produced due to the titanium concentration alone.[6] In the region with preinjected helium, bubbles already exist and the irradiation-produced helium may preferentially segregate to these bubbles. With this additional helium, the critical radius for cavity growth may be surpassed, leading to void growth during irradiation.

The dimensional changes measured on the pressurized tubes can be due to three factors: creep deformation, cavitational swelling, and phase-related changes in lattice parameters. Based on the TEM observations, swelling is minimal and therefore contributes only marginally to the change in tube diameters. The decrease in density may be responsible in part for the increase in tube diameter, but this contribution should correspond to considerably less than a 1% change in linear dimensions, which is small compared to the measured tube expansion. Furthermore, no phase transformations were observed by TEM. Therefore, the diameter changes can be attributed primarily to creep deformation. The fact that the diameter change was significantly greater in the tube with a higher stress (V22) supports this conclusion. The creep deformation may

ORNL-PHOTO 8671-86

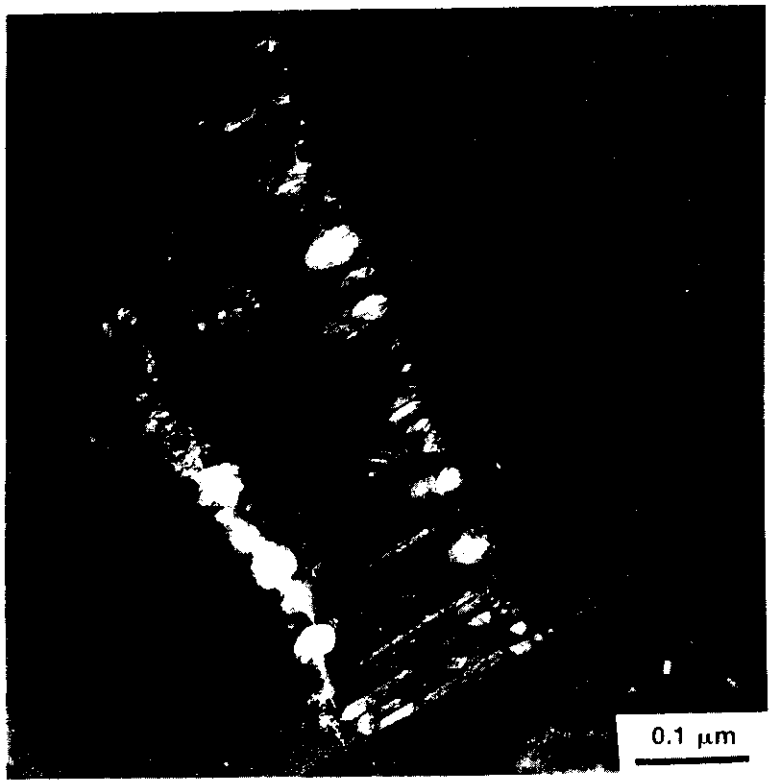

Fig. 5. Large elongated cavities aligned in a second phase particle in the section of the irradiated tube V23 which contained ~15 appm He.

ORNL-PHOTO 8567-86

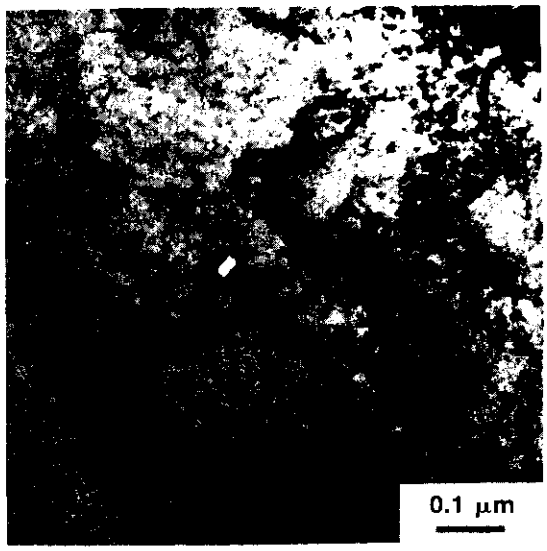

Fig. 6. Typical matrix region in the section of the irradiated V–20Ti tube containing ~15 appm He that contains a few small cavities.

be a combination of thermal and irradiation creep, but these two mechanisms cannot be separated with the available data, so they will not be distinguished in the sugsequent discussion.

Since the major portion of the diameter changes measured was due to creep deformation, Fig. 1(b) indicates that helium promotes creep. This result is in agreement with an earlier study on stainless steels[12] which showed that helium promoted creep when grain boundaries were free to slide and were not inhibited by precipitates, as in the case of V–20Ti. The increase in creep deformation due to helium for tube V22 is quite dramatic and the effect is unexpectedly strong. However, this enhanced creep effect was not found in the other tube, where the stress and resultant creep deformation were smaller [Fig. 1(a)]. A nominal increase in stress of only 15% showed a 250% increase in tube expansion. This sensitivity to stress should be confirmed by additional experimentation. It is possible that the stress difference was greater than 15% if the tube wall thicknesses were not equal for both tubes. However, even with the uncertainty in the absolute values of the stresses, the large increase in the tube expansion in the helium-containing region of tube V22 indicates that helium has a strong influence on creep behavior under some conditions. This effect, if verified by further work, should have major consequences on the evaluation of the irradiation creep behavior of vanadium alloys. It should be noted that among the vanadium alloys under consideration for fusion applications, other alloys, such as V–15Cr–5Ti, have better creep resistance than the V–20Ti alloy considered here.[13] The V–15Cr–5Ti alloy also has precipitates along its grain boundaries and therefore it may not show the same helium-enhanced creep found here. Such considerations should be important in any future vanadium alloy development work.

CONCLUSIONS

1. Preimplanted helium promoted cavity formation in the V–20Ti pressurized tubes irradiated at 700°C, primarily within existing precipitates, but total swelling was low.

2. Under some conditions, helium enhanced creep deformation.

FUTURE WORK

There are no pressurized vanadium alloy tubes being irradiated or investigated at the present time.

REFERENCES

1. D. L. Smith, B. A. Loomis, and D. R. Diercks, "Vanadium-Base Alloys for Fusion Reactor Applications — A Review," J. Nucl. Mater. 135 (1985) 125–137.

2. D. N. Braski, "The Tensile Properties of Several Vanadium Alloys after Irradiation in FFTF," pp. 54–61 in ADIP Semiannu. Prog. Rep. Mar. 31, 1985, DOE/ER-0045/14, U.S. DOE, Office of Fusion Energy.

3. M. P. Tanaka, E. E. Bloom, and J. A. Horak, "Tensile Properties and Microstructure of Helium Injected and Reactor Irradiated V–20Ti," J. Nucl. Mater. 103&104 (1981) 895–900.

4. D. N. Braski, "The Effect of Neutron Irradiation on the Tensile Properties and Microstructure of Several Vanadium Alloys," presented at 13th Int. Symp. on Effects of Radiation on Materials, Seattle, WA, June 1986 and to be published in ASTM STP.

5. A. Hishinuma, J. M. Vitek, J. A. Horak, and E. E. Bloom, "Effect of Preinjected Helium on Swelling and Microstructure of Neutron Irradiated Pressurized Tubes of Type 316 Stainless Steel," pp. 92–107 in ASTM-STP-782 (1982).

6. L. R. Greenwood, "Fusion Reactor Dosimetry," pp. 8–16 in DAFS Quarterly, November 1981, DOE/ER-0046/7.

7. M. P. Tanaka, Japan Atomic Energy Research Institute, Tokai, Japan, on assignment to Oak Ridge National Laboratory, Oak Ridge, Tennessee, personal communication.

8. J. Bentley and F. W. Wiffen, "Swelling and Microstructural Changes in Irradiated Vanadium Alloys," Nucl. Technol. 30 (1976) 376–384.

9. M. L. Grossbeck and J. A. Horak, "Tensile and Fracture Properties of EBR-II-Irradiated V–15Cr–5Ti Containing Helium," presented at 13th Int. Symp. on Effects of Radiation on Materials, Seattle, WA, June 1986 and to be published in ASTM STP.

10. J. M. Vitek and R. L. Klueh, "Microstructure of HFIR-Irradiated 12Cr–1MoVW Ferritic Steel," p. 151 in Proc. Top. Conf. on Ferritic Alloys for Use in Nuclear Energy Technologies, Snowbird, UT, June 1983, J. W. Davis and D. Michel, Eds., AIME Publ., Warrendale, PA, 1984.

11. P. J. Maziasz, R. L. Klueh, and J. M. Vitek, "The Effects of Increased Helium Generation on Microstructure and Swelling of Nickel-Doped 9Cr–1MoVNb and 12Cr–1MoVW Steels Irradiated in HFIR," pp. 91–101 in: ADIP Semiannu. Prog. Rep. Sept. 30, 1985, DOE/ER-0045/15, Office of Fusion Energy.

12. H. Schroeder and D. N. Braski, "The Effect of Implanted Helium on the High Temperature Mechanical Properties of a Model Austenitic Fe–17%Cr–17%Ni Alloy," J. Nucl. Mater. 115 (1983) 297–306.

13. Private communication from R. Mattas, Argonne National Laboratory, Argonne, IL, concerning unpublished data of F. L. Yaggee, March 17, 1986.

6.4 Copper Alloys

EFFECTS OF NEUTRON IRRADIATION TO 63 dpa ON THE PROPERTIES OF VARIOUS COMMERCIAL COPPER ALLOYS -
H. R. Brager (Westinghouse Hanford Company)

OBJECTIVE

The objective of this effort is to determine the effect of high neutron fluence on the properties of high purity copper and of a range of conventional commercial high-conductivity, high-strength, copper-base alloys.

SUMMARY

High purity copper and six commercial copper alloys were neutron irradiated to 47 and 63 dpa at about 450°C in the FFTF. Immersion density measurements showed a wide range of swelling behavior after irradiation to 63 dpa. At one extreme was CuBe in the aged and tempered (AT) condition which had densified slightly. At the other extreme was 20% CW Cu-0.1% Ag which swelled over 45%. Electrical resistivity measurements of high-conductivity alloys followed trends similar to previously published results for the same alloys irradiated to 16 dpa, namely a continued reduction in conductivity with fluence which appears to relate to transmutation products and, somewhat, to void formation and defect cluster development. At 63 dpa, the electrical conductivity of zone-refined copper had decreased significantly. The reduction was to a value comparable with that of the irradiated Cu-Al25 -- the Al_2O_3 dispersion strengthened alloy. Conversely, for the moderate conductivity alloy CuBe, the electrical conductivity was unaffected for irradiation greater than 16 dpa. These results of the irradiated material were compared with electrical conductivity of unirradiated alloys examined after aging for 10,000 hours.

The most irradiation resistant high-conductivity, high-strength copper alloy examined after 63 dpa is Cu-Al25 followed by MZC. Cu-2.0Be, only a moderate-conductivity alloy, exhibits very consistent irradiation resistant properties. Thus, Cu-Al25 and MZC appear to be acceptable candidates for high heat flux materials in fusion reactor applications.

PROGRESS AND STATUS

Introduction

In an earlier paper,[1] presented at ICFRM-1, the swelling, electrical conductivity and tensile properties of pure copper and six commercial copper alloys were described. These materials had been neutron irradiated at approximately 450°C to the lowest neutron fluence attained by specimens in this irradiation series -- 16 dpa. The microstructure of the specimen of pure copper and of the three high-strength, high-conductivity alloys which showed the most resistance to irradiation after 16 dpa was characterized.[2] The current paper presents information on the same commercial copper alloys which now have been neutron irradiated to the next two higher neutron fluence levels -- approximately 47 and 63 dpa. A fourth, and final, set of specimens in this series is still being irradiated in the FFTF.

Experimental procedure

The alloys listed in Table 1 were irradiated in the form of miniature tensile specimens and standard microscopy disks, both of which were punched from the same sheet stock. The discs were used for changes in density, electrical conductivity, and microscopy and were all measured at room temperature. Tensile specimens were also subjected to thermal aging at 300 to 600°C for 10,000 hours. The specimens were irradiated in 4 mm diameter helium-filled subcapsules and were tightly packed with the copper specimens separated by aluminum foil spacers and with specially machined copper bars included to improve the thermal conductivity in the subcapsules and minimize the specimen's irradiation temperature. The aluminum was included in an attempt to eliminate self-welding of the copper specimens. The copper specimens span four classes: pure metal, and solution-strengthened, precipitation-hardened and dispersion-strengthened alloys.

Results

Swelling

The 16 dpa swelling data shown on Table 1 were derived from the miniature tensile specimens; the higher fluence data were extracted from TEM disks. There was often more than one disk, allowing for an estimate of the variability of swelling. The miniature tensile specimens in the second irradiation exhibited considerable self-welding and have been set aside for later examination.

Figure 1 shows the swelling behavior observed for those alloys which exhibit a moderate-to-high amount of swelling. Pure copper reaches 31% after 63 dpa. Consistent with its swelling behavior at lower fluence[1], copper with 0.1 wt% silver exhibits the greatest amount of swelling. Its swelling rate is compared, Fig. 1, with a 1% per dpa line. This line represents the peak swelling rate reported for reactor

Table 1. Swelling of various commercial copper alloys at ~450°C (irradiated in MOTA/FFTF)

Alloy	Alloy Composition (wt%)	Condition	Swelling (%) Neutron Fluence 16.2 dpa	47.2 dpa	63.3 dpa
Cu (MARZ)	Cu (99.999%)	annealed	6.5	22.2, 23.3	30.1, 31.3 33.2
CuAg	Cu-0.1 Ag	20% CW	16.6	35.4, 38.2	47.4
CuAgP	Cu-0.3 Ag-0.06 P-0.08 Mg	20% CW	7.9	16.0, 16.2	17.1
CuNiBe (½ HT)*	Cu-1.8 Ni-0.3 Be	20% CW and aged (3 h at 480°C)	1.70	13.9, 14.6	22.3, 24.6
CuNiBe (AT)*	Cu-1.8 Ni-0.3 Be	20% CW and aged (3 h at 480°C)	0.29	3.05	5.73, 6.59
CuBe (½ HT)	Cu-2.0 Be	20% CW and aged (2 h at 320°C)	-0.18	0.18, 1.11 1.71	1.09, 1.61
CuBe (AT)	Cu-2.0 Be	annealed and aged (2 h at 320°C)	-0.66	-0.45 -0.24 +0.12	-0.43 -0.25
MZC	Cu-0.9 Cr-0.1 Zr-0.05 Mg	90% CW, aged ½ h at 470°C	1.03	0.79	5.15, 7.90
Cu-Al25 (CW)	Cu-0.25 Al (as Al_2O_3)	20% CW	0.13	0.23, 0.36 0.86	0.28
Cu-Al25 (CWA)	Cu-0.25 Al (as Al_2O_3)	20% CW + aged 1 h at 550°C	---	-0.18, 0.05 0.52	0.04,1.45 1.85
Ni-Be	Ni-1.9Be	Annealed and aged 1½ h @ 500°C	-0.37	0.05	-0.11
AISI 316	Fe-18Cr-13Ni-2.5Mo	Annealed	-0.20	1.30	2.28

*½ HT and AT are industry designations for half-hard and tempered, and annealed and tempered, respectively.

irradiated fcc alloys.[3] At higher fluences, the swelling rate decreases with the swelling reaching 47% at 63 dpa. The copper alloy CuAgP with three times as much silver and small amount of phosphorus and magnesium swells less but with a pronounced S-shaped behavior. CuNiBe swelled less than pure copper or CuAg, the amount depending on the preirradiation heat treatment.

The low swelling alloys consisted of Cu-Al25, CuBe and MZC. The Cu-Al25 in the cold worked (CW) condition exhibited virtually no measurable swelling (0.28%) after 63 dpa, Fig. 2. The same material in the cold worked and aged (CWA) condition showed some scatter with swelling ranging from slight densification to nearly two percent swelling. Scatter of the density measurements could have been due to surface irregularities. Commercial grade pure aluminum foil was placed between the copper specimens to prevent self-welding. At 16 dpa,[1] this concept worked quite well. At the higher fluences reported here, some of the specimens had aluminum partially adhered to the surface. Removal of the aluminum could have been incomplete. The accuracy of each measurement is estimated to be ±0.16%.

The swelling of CuBe alloy in the hardened and tempered condition (½HT) measured swelling of about 1% after 63 dpa, Fig. 2. However, the same alloy in the aged and tempered condition (AT), on average, densified slightly.

The MZC alloy swelled about 1% after 16 dpa and was shown earlier to be the result of phase-related density changes and not due to void swelling.[2] Swelling of the alloy irradiated to 47 dpa showed practically no change while further irradiation to 63 dpa indicated swelling in the six to eight percent range.

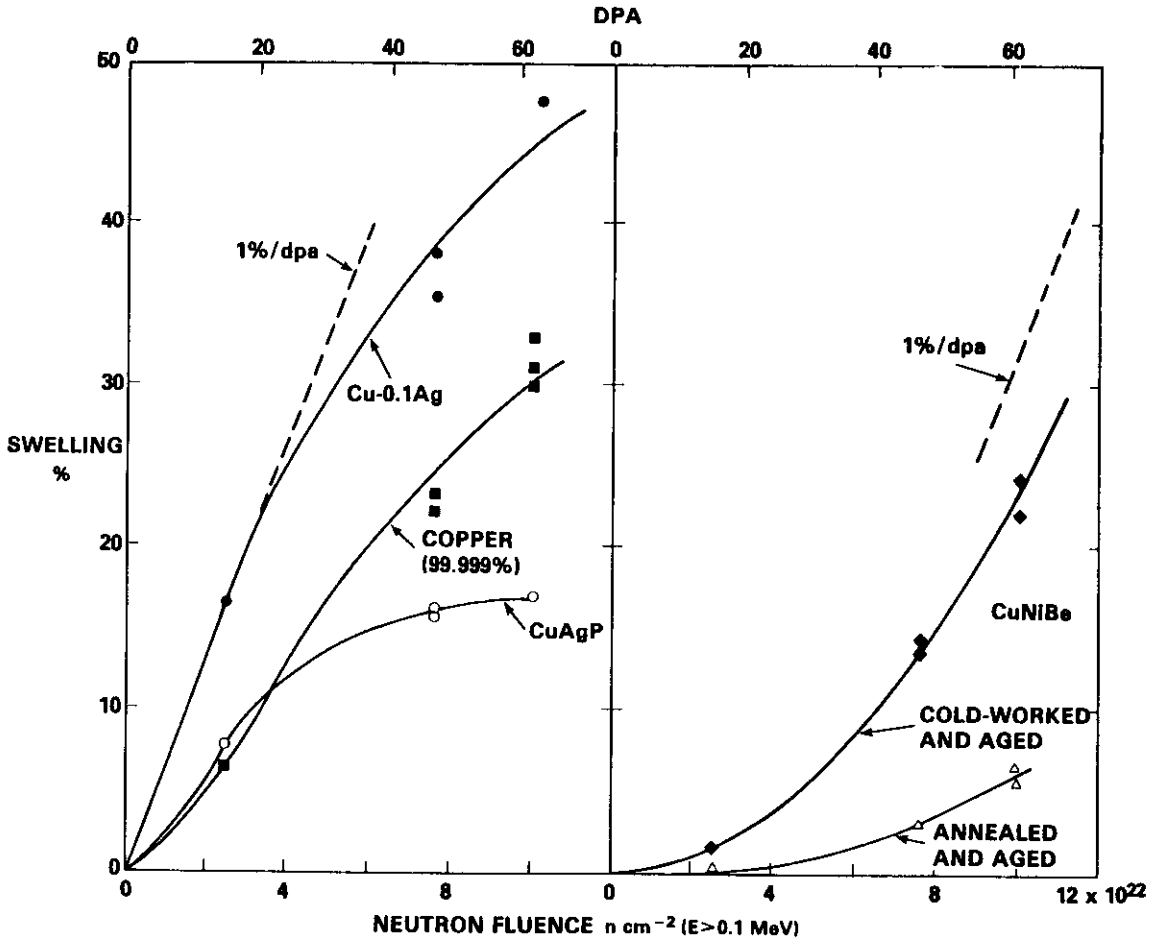

Fig. 1. Swelling behavior of zone-refined copper and copper alloys which exhibit a moderate to high amount of swelling.

The NiBe alloy was included in the experiment due to its high strength characteristics. Its potential use is as a structural reinforcing material although it has only limited current carrying characteristics. AISI 316 was included so as to reference the behavior of this well investigated alloy to other irradiation studies, if needed.

Electrical conductivity, and electron microscopy, measurements of this study focused on the three commercial copper alloys showing the most promise: Cu-Al25, MZC and CuBe. For comparison, the MARZ grade copper was also examined.

Electrical conductivity

The electrical conductivity measurements were all determined relative to that obtained for the unirradiated zone-refined copper specimen, which was assumed to have an International Annealed Copper Standard (IACS) value of 103%. The pre- and postirradiation conductivities were determined using a four point resistivity technique.

For zone refined copper, the electrical conductivity appears to decrease asymptodically with increasing neutron fluence, Fig. 3. The principal causes for the reduction in conductivity was expected to be due to void and defect cluster development and transmutation product formation. The principal transmutation products formed from copper irradiated in the FFTF are nickel and zinc.[4] The change in electrical conductivity was estimated from literature data[5] assuming that the nickel and zinc transmutation products are maintained in solution in the copper and was included in Fig. 3. These transmutation products appears to be the primary influence in the reduction in electrical conductivity of zone refined copper with increasing neutron fluence. The change due to void formation was estimated assuming that isotropic swelling decreased the conducting material between the probe point positions. The balance was attributed to the other transmutation products and defect clusters.

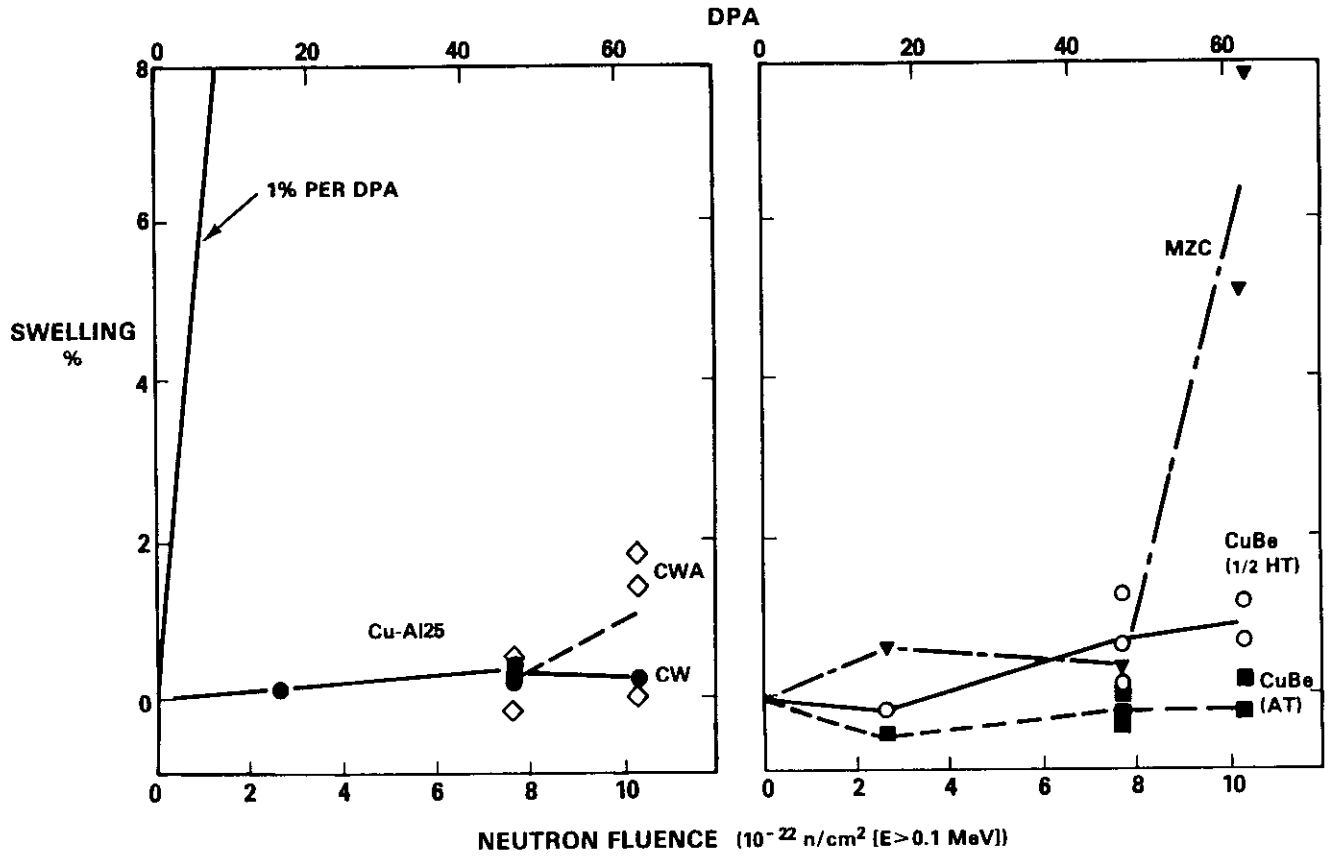

Fig. 2. Swelling behavior of copper alloys (Cu-Al25, MZC, and Cu-Be) which exhibit a low level of swelling.

The effect of neutron fluence on the electrical conductivity of the Cu-Al25 appears to follow the same trend as for zone-refined copper, Fig. 4. That is, a reduction in conductivity with increasing neutron fluence. Since Cu-Al25 consists of high-purity commercial grade copper with a low volume fraction of small sized Al_2O_3 particles, the nickel and zinc transmutation products should have a first order influence on the conductivity of the effectively single phase copper matrix. For the solution-strengthened, work-hardened MZC alloy, the general trend of a lower conductivity with increased neutron exposure was also observed. The MZC's conductivity at 63 dpa was 64% IACS or slightly lower than the 71% IACS value measured for the alloy irradiated to 16 dpa.

The effect of neutron irradiation on the electrical conductivity of the CuBe alloy was quite different from that of the single-phase, zone-refined copper. The conductivity of the unirradiated CuBe alloy is not high (about 18% IACS) and was shown to increase after irradiation to 16 dpa.[1] At higher fluences, the data of this study show that the conductivity appears to be unaffected, Fig. 5. This independence of conductivity with neutron exposure above 16 dpa is also shown to be independent of the two preirradiation thermal-mechanical-treatments given to the alloy. Both the aged and tempered (AT) and the hardened and tempered (½HT) conditions behave similarly. This behavior follows very closely the conductivity measurements of the unirradiated and aged CuBe alloy. Aging 10,000 hours at 300°C or at 500°C increased the IACS value from 18% to 25% and 33%, respectively. Both the irradiation at about 450°C and long-term aging would enhance the formation of second phase precipitates thereby reducing the amount of beryllium in solution in the matrix. This would result in an increase in conductivity of the CiBe alloy. Aging the unirradiated CuBe alloy at 600°C for 10,000 hours induced an IACS value of 22% indicating a significant resolution of beryllium back into the copper matrix at this temperature.

Electron microscopy

Electron microscopy examination was conducted on thin foils of irradiated pure copper and on the two swelling resistent high-strength, high-conductivity commercial copper alloys -- Cu-Al25 and MZC.

Zone-refined copper. The zone refined copper (99.999%) was in the solution annealed condition. The irradiation was conducted at approximately 450°C which represents a homologous temperature of 0.53. For a pure fcc metal in the solution annealed condition, one would expect a significant level of vacancy mobility at this temperature and a relatively low void density. Figure 6 shows that only a low density

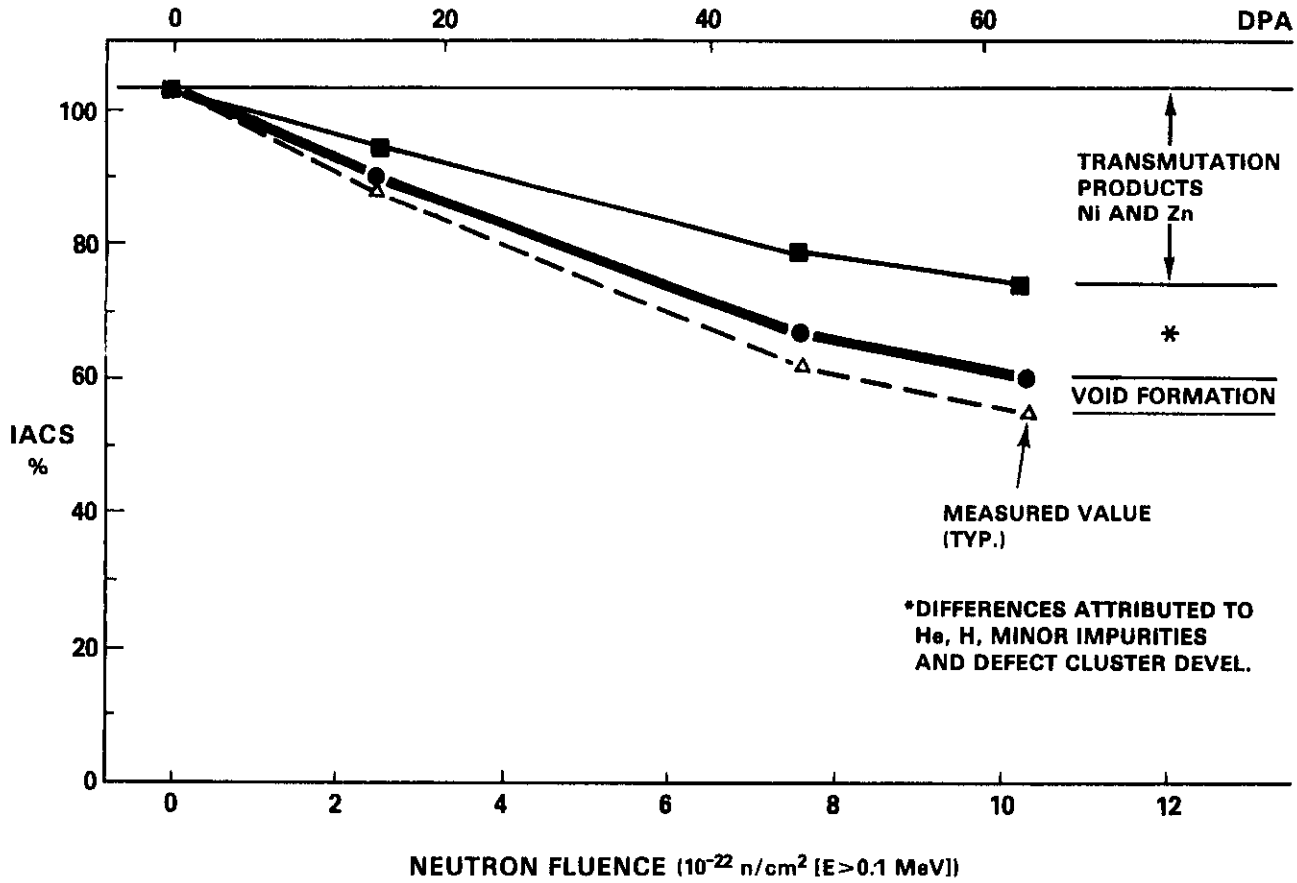

Fig. 3. Electrical conductivity measurements of zone-refined copper irradiated to a neutron fluence of up to 63 dpa. The estimated affect of transmutation products and defect cluster development on electrical conductivity of pure copper is shown.

(approximately 4 x 10^{12} cm^{-3}) of quite large and faceted voids were observed. The average diameter of these voids is nearly 500 nm. The local swelling in the region shown in Fig. 6 is approximately 20% compared to the measured change in bulk density of approximately 30%. The difference is probably associated with the difficulty in measuring voids in very thick foils.

A low density of small unidentified defect clusters is also present. These defects might be associated with the estimated 0.5 wt% Ni formed by transmutation of the copper.

Al_2O_3 dispersion-strengthened copper. The commercial alloy Cu-Al25 was irradiated in the 20% cold-worked (CW) and the cold-worked and aged (CWA) conditions and is essentially pure copper strengthened with a high number density of very small alumina particles formed by internal oxidation of a small amount of aluminum solute. In contrast to the pure copper, which had large grains on the order of tens of microns, Cu-Al25 contains grains and subgrains of micron and submicron sizes. In this particular alloy, the Al_2O_3 is 0.25 percent by weight and in the as-fabricated condition is dispersed in particles with a mean of approximately 7 nm and with a density of approximately 3 x 10^{16} cm^{-3}.

An examination of the microstructure after irradiation showed that this alloy was remarkably insensitive to irradiation, with only a low density of small cavities observed and a high density of small objects which exhibit fringe contrast that are independent of the reciprocal lattice vector, Fig. 7. The small cavities could well be helium bubbles which would represent a portion of the approximately 20 appm helium formed in the copper after 63 dpa irradiation in the FFTF.[4] To a lesser extent than for results at 16 dpa,[2] when different diffraction vectors are used to image the Al_2O_3 precipitates, only a small number of black-white contrast images with vectors parallel to the diffraction vector are visible. This result indicates that the normal radially-symmetric strain field around the Al_2O_3 particles formed during alloy preparation and observed after 16 dpa irradiation[2] is decreased after the 63 dpa neutron irradiation. However, the high concentration of small Al_2O_3 particles uniformly dispersed throughout the matrix appears to be maintained, Fig. 8.

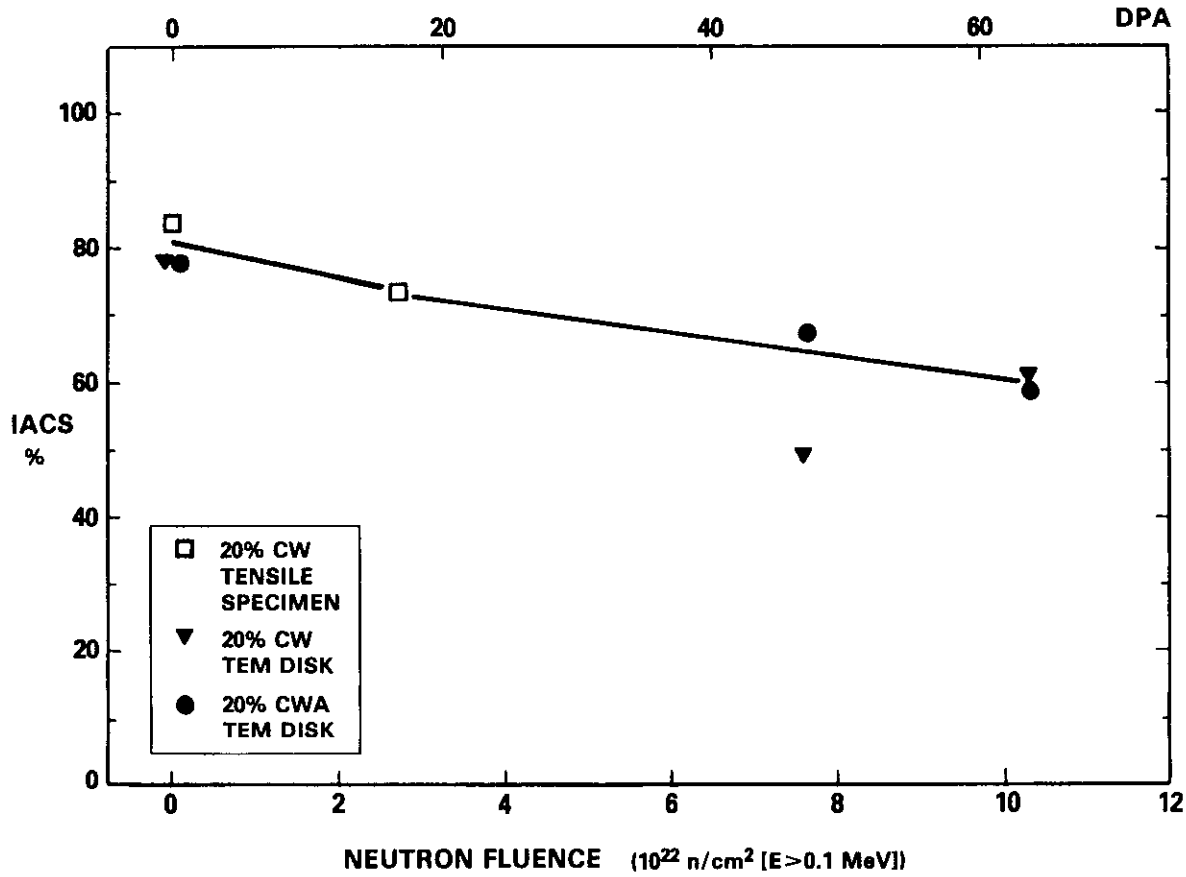

Fig. 4. The effect of neutron irradiation on the electrical conductivity of Cu-Al25 dispersion strengthened alloy.

MZC (precipitation-strengthened cold-worked alloy). The MZC copper-base alloy contains small amounts of magnesium, zirconium and chromium which provide both solid solution strengthening and precipitation hardening. When combined with work hardening, this alloy provides a good combination of high strength and high conductivity. The properties of the alloy are somewhat dependent on thermal-mechanical treatment. The recommended treatments are directed toward production of a high concentration of small precipitates. The purpose of introducing these precipitates is to stabilize the dislocation network at high temperatures.

After a less detailed examination than that employed for the Cu-Al25 alloy, it appeared that few, if any, large voids and a low density of cavities had formed in the irradiated MZC alloy, Fig. 9. This apparent absence of significant void volume in the MZC specimen is inconsistent with the measured value of about 7% swelling by immersion density change. Previously, no voidage was observed in this alloy after irradiation to 16 dpa that had a 1.0% density change.[2] While it is suspected that at least a part of this apparent swelling is principally a consequence of a lattice parameter change of the matrix arising from precipitation, a more thorough examination is required to settle this discrepancy. The possibility of having aluminum on the specimen surface and this influencing the immersion density measurements will be reviewed. While Fig. 9 also shows a high number density ($>10^{15}$/cc) of precipitates with sizes in the range 2-10 nm which exist after irradiation to 63 dpa, there is still a second population of larger (~50 nm) precipitates at approximately 10^{14} cm^{-3} which existed after 16 dpa irradiation.

Discussion

The results of neutron irradiation at near 450°C to 63 dpa of a series of commercial copper alloys have shown a mixed response. The behavior of the zone-refined copper was, in general, consistent with expectations of a pure fcc metal irradiated at a high homologeous temperature. After 16 dpa, a moderate density of large voids formed. Irradiation further to 63 dpa resulted in a substantial increase in swelling but with over an order of magnitude reduction in void density (from about 1×10^{14} cm^{-3} to about 4×10^{12} cm^{-3}). The void size increase to nearly 500 nm diameter would have occurred by both void growth and coalescence.

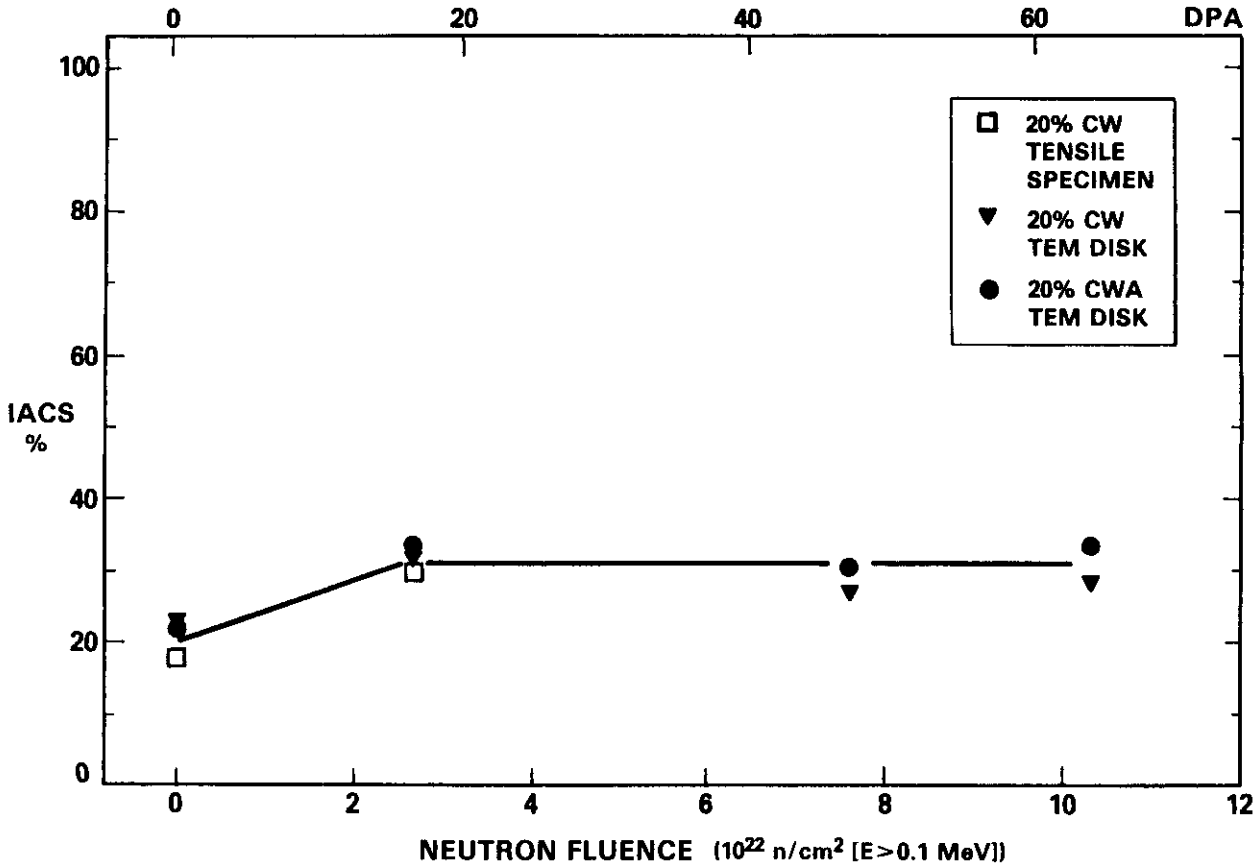

Fig. 5. The effect of neutron irradiation on the electrical conductivity of Cu-Be alloy. The conductivity appears to be unaffected by exposure above 2.7 x 10^{22} n/cm^2 (16 dpa) and by pre-irradiation thermal mechanical treatment.

The electrical conductivity of the zone-refined copper alloy was quite drastically reduced to about 60% IACS after 63 dpa. It would appear that zone refined copper should only be considered in applications with fusion reactors which will irradiate material to less than about 10 dpa. In addition, the spectral effect on transmutation products need be evaluated to estimate their effect on altering the type and amount of elements formed. In single phase materials, the effect of alloying addition on electrical conductivity should be cumulative.[5] The addition of a small (0.25%) amount of Al_2O_3 in the form of a high density (>10^{16}/cm^3) of small stable particles (~7 nm diameter) uniformly distributed in the matrix substantially improves the irradiation response of copper. This alloy, Cu-Al25, appears to be the most irradiation-resistant, high-conductivity, high-strength alloy examined in this study.

Comparison of the electrical conductivity of the zone-refined copper, Fig. 3, and of the Cu-Al25 dispersion strengthened alloy, Fig. 4, after 63 dpa shows that both materials have similar values --near 60% IACS. For applications designed for high neutron fluence -- greater than about 50 dpa, the use of the Cu-Al25 alloy appears to be clearly superior to that of pure copper.

A more thorough examination is required to better evaluate the irradiation response of the MZC alloy with its apparent resistance to void formation. This alloy appears to have high-conductivity values, maintain its high-strength at elevated temperatures and can be welded.

The CuBe alloys show excellent swelling resistant but have low conductivity. It is interesting to note that the Cu-Ni-Be alloy, with 1.8%Ni and 0.3%Be for both the ½HT and the AT conditions, exhibited poor irradiation resistance to void formation at 16 dpa.[2] The inferior behavior of this beryllium bearing alloy became very pronounced at the high neutron fluence of 63 dpa.

CONCLUSIONS

High purity copper and six commercial copper alloys were neutron irradiated to 47 and 63 dpa at about 450°C in the FFTF. Immersion density measurements showed a wide range of swelling behavior after irradiation to 63 dpa. At one extreme was CuBe in the aged and tempered (AT) condition which had densified

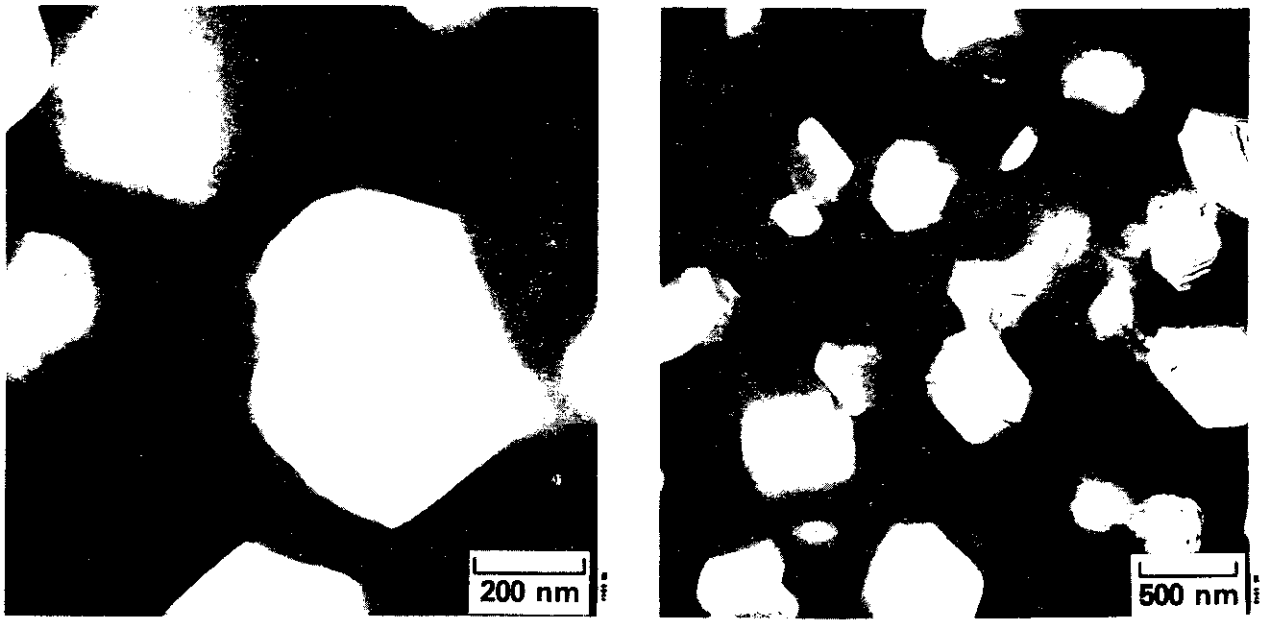

Fig. 6. A low density (~4 x 10^{12} cm^{-3}) of large voids (mean value nears 500 mm) formed in zone-refined copper irradiated at ~450°C to 63 dpa.

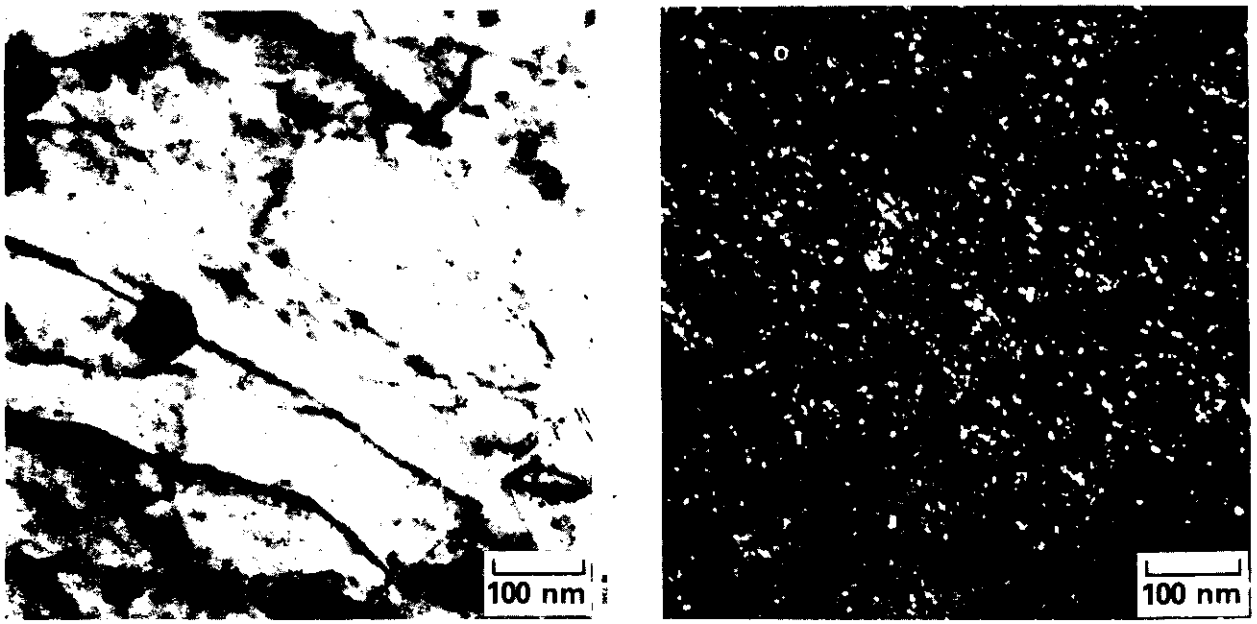

Fig. 7. Bright field and dark field micrographs of Cu-Al25 alloy which exhibit a high resistance to neutron damage of 63 dpa.

slightly. At the other extreme was 20% CW Cu-0.1% Ag which swelled over 45%. Electrical resistivity measurements of high-conductivity alloys followed trends similar to previously published results for the same alloys irradiated to 16 dpa, namely a continued reduction in conductivity with fluence which appears to relate to transmutation products and, somewhat, to void formation and defect cluster development. At 63 dpa, the electrical conductivity of zone-refined copper had decreased significantly. The reduction was to a value comparable with that of the irradiated Cu-Al25 -- the Al_2O_3 dispersion strengthened alloy. Conversely, for the moderate conductivity alloy CuBe, the electrical conductivity was unaffected for irradiation greater than 16 dpa. The most irradiation resistant high-conductivity, high-strength copper alloy examined after 63 dpa is Cu-Al25 followed by MZC. Cu-2.0Be, only a moderate-conductivity alloy, exhibits very consistent irradiation resistant properties. Thus, Cu-Al25 and MZC appear to be acceptable candidates for high heat flux materials in fusion reactor applications.

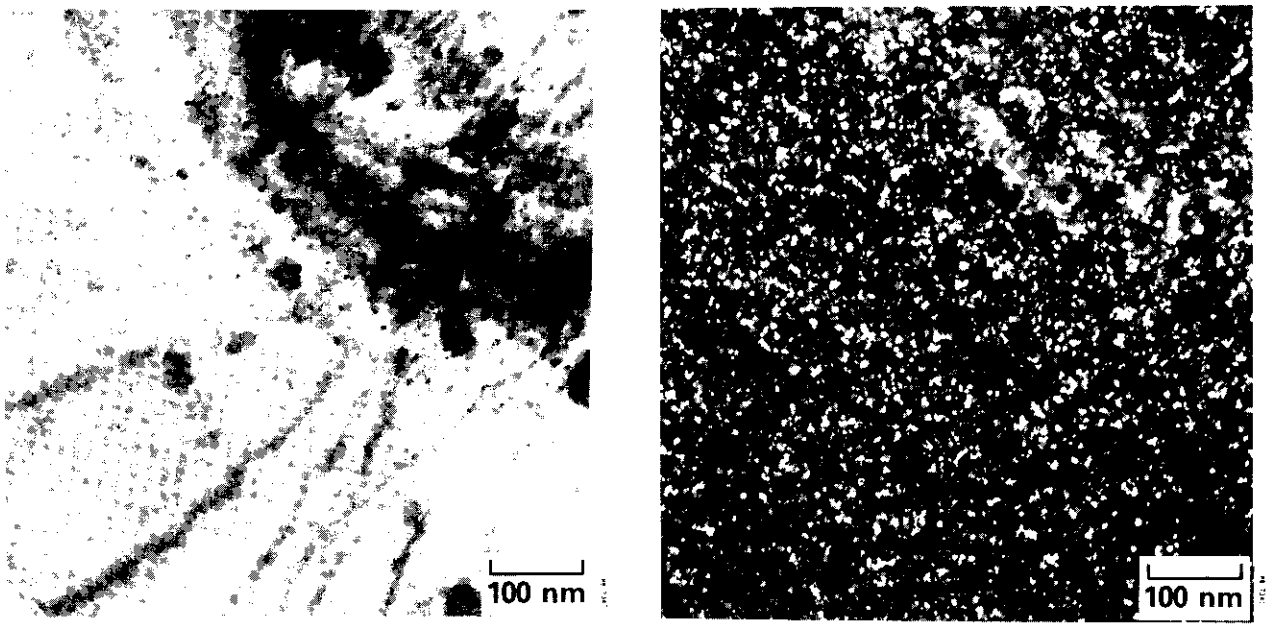

Fig. 8. Bright field and dark micrographs of Cu-Al25 alloy irradiated to 63 dpa and showing a high concentration of small, uniformly dispersed Al_2O_3 particles.

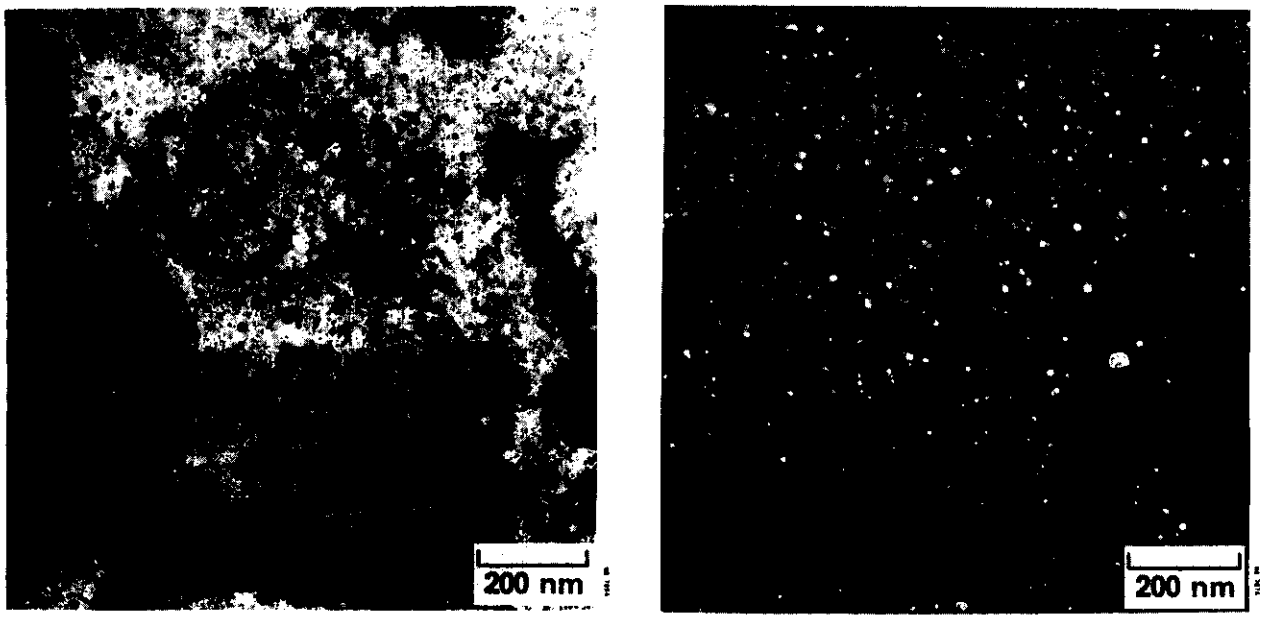

Fig. 9. Bright field and dark field micrographs of MZC alloy irradiated to 63 dpa. Preliminary examination showed no significant voidage was observed by stereographic analysis.

FUTURE WORK

The next higher fluence level, and the last of four sets, of the same copper alloy specimens irradiated in the FFTF has been discharged with MOTA 1D. These specimens, with a fluence in excess of 100 dpa, are being processed for examination covering the same topics described in the present report.

Based on the information generated by the current report, a second generation of copper alloy specimens have been prepared for irradiation. Four sets of specimens were prepared and inserted in MOTA 1E for irradiation. Details of this experiment are described elsewhere in this progress report.[6]

REFERENCES

1. H. R. Brager, H. L. Heinisch and F. A. Garner, J. Nucl. Mater. 133/134, 676-9 (1985).

2. H. R. Brager and F. A. Garner, "Microstructural Examination of Pure Copper and Three Copper Alloys Irradiated in FFTF", p. 63-70 in Damage Analysis and Fundamental Studies Quarterly Progress Report, July-September 1985, DOE/ER-0046/23, U. S. Department of Energy, Office of Fusion Energy.

3. F. A. Garner, J. Nucl. Mater. 122/123, 459-71 (1984).

4. F. M. Mann, "Transmutations in Fusion Test Facilities", p. 10-20 in Damage Analysis and Fundamental Studies Quarterly Progress Report, October-December 1985, DOE/ER-0046/24, U. S. Department of Energy, Office of Fusion Energy.

5. P. Gregory, A. J. Bangay and T. L. Bird, "The Electrical Conductivity of Copper", Metall. 71, 207-14 (1965).

6. H. R. Brager, "Neutron Irradiation of Copper Alloys", this progress report.

NEUTRON IRRADIATION OF COPPER ALLOYS -- PHASE II - H. R. Brager (Westinghouse Hanford Company)

OBJECTIVE

Using fast reactor irradiated copper alloy data, investigate the effects of neutron irradiation on the properties of high-conductivity, high-strength, irradiation-resistant copper base alloys for use in the design of MFE systems.

SUMMARY

A second generation copper alloy experiment has been designed, built, and inserted into the Fast Flux Test Facility (FFTF) for irradiation. The experiment test matrix is heavily biased toward the examination of oxide-dispersion-strengthened (ODS) copper-based alloys. This material exhibited the most irradiation resistance of the alloys examined after fast reactor irradiation to fluences up to 63 dpa. The current experiment included matrix and weldment specimens of commercial ODS alloys that were designed to be weldable.

PROGRESS AND STATUS

Introduction

A series of specimens made from commercial copper-base alloys and zone-refined copper were irradiated in the FFTF/Materials Open Test Facility (MOTA). The specimens were irradiated at ~450°C to fluences of 16, 47, 63, and ~110 dpa. Data for specimens irradiated at the three lower fluences have been obtained.[1-3] One conclusion drawn from these studies is the remarkably high level of irradiation resistance shown by ODS specimens irradiated to fluences of 63 dpa.[3] Based on that information, a second generation of alloy specimens were prepared and inserted into the FFTF/MOTA-1E for irradiation to high neutron fluences.

Experimental procedure

Zone refined copper and sixteen copper base alloys, Table 1, were obtained for inclusion in the experiment. They were processed by cold-work and annealing to produce foil thicknesses of 0.010 inch thick. A high percentage of these materials (twelve of seventeen) are ODS alloys. The same 0.010 inch thick processes material was used for punching out miniature tensile specimens having an overall length of 1.2 cm as well as 0.3 cm diameter TEM disks.

Table 1. Copper alloy specimens engraving code

Alloy	Condition		Specimen Engraving Code	Neutron Fluence							
				30 DPA (ET)*		60 DPA (IV)		120 DPA (E9)		240 DPA (17)	
				Tensile	TEM	Tensile	TEM	Tensile	TEM	Tensile	TEM
MARZ	--	SA	R0	1	4	1	4		4		4
AL25	--	CW1	R4	1	4	1	4	1	4	1	4
AL25	--	CW&W	3N	1	4	1	4	1	4	1	4
CuBe	--	HTA	R1		4		4		4		4
CuBe	--	HTB	R3	1	4	1	4	1	4	1	4
A120	--	CW1	UX	1	4	1	4	1	4	1	4
MZC	--	HTA	U6		4		4		4		4
MZC	--	HTB	U7		4		4		4		4
MZC	MIT#2	STA	U9	1	4	1	4	1	4	1	4
MZC	MIT#3	HT	VB	1	4	1	4	1	4	1	4
Cu-5Ni-2.5Ti	MIT#6	HT	VK		4		4		4		4
Cu-5Ni-2.5Ti	LANL	HT	VL		4		4		4		4
A115+B	LANL	HT	VO		4		4		4		4
CuCr	MIT	HT	3A	1	4	1	4	1	4	1	4
CuHf	MIT	HT	3B	1	4	1	4	1	4	1	4
CuCrZr	JRC	HT	3E		4		4		4		4
ODS-1	TRAA	CW	3F	1	4	1	4	1	4	1	4
ODS-1	TRAA	CW&W	3H	1	4	1	4	1	4	1	4
ODS-2	TRAB	CW	3K		4		4		4		4
ODS-3	TRAC	CW	3L		4		4	1	4	1	4
ODS-4	TRAD	CW	3M	1	4	1	4	1	4	1	4
				12	84	12	84	12	84	12	84

*Location codes engraved on specimens are shown in parentheses.

The punched specimens were assembled into four sets of two each (eight total) with each set loaded into a steel packet and backfilled with helium. To minimize self-welding between specimens, a 0.001 inch thick punched same of molybdenum was interspersed between the copper specimens. Machine blocks of iron were used to fill the gap around the tensile specimens and decrease the specimen temperature to near the reactor coolant value.

Each packet contained one miniature tensile specimen from each of six select alloys and two TEM disks from all of the twenty-one different alloy conditions. Each set of specimens is scheduled to be irradiated to a different fluence level at a comparable neutron flux of about 2×10^{15} n/cm^2 (E > 0.1 MeV).

Discussion

There are three types of ODS alloys: two are made by United States' companies and one is supplied by Professor N. Grant (Massachusetts Institute of Technology [MIT]). Conventional ODS alloys were purchased from SCM Metals. Four heats were provided by TRA Inc., a company that is working on developing weldable ODS copper alloys. Professor Grant provided experimental ODS alloys prepared at MIT. Dr. Livak, Los Alamos National Laboratory, provided a boron deoxidized ODS alloy.

The alloys Cu-2Be and MZC were included based on the absence of swelling in the former alloy and generally favorable irradiation response of the latter.[3] Zone-refined copper was included as a reference.

Two alloys, conventional ODS alloy and one of the TRA Inc. weldable ODS alloys, were processed by translating an electron beam weld trace across the surface of the 0.010 inch thick sheet. Miniature tensile and TEM disks were punched from the sheet with the weld area centered within the specimen. The condition of these specimens are shown in a CW&W, Table 1.

Miniature tensile specimens were punched and are being processed for thermal aging of the material. Specimens are expected to be aged 10^3, 10^4, and 3×10^4 hours at 300, 400, 500, 600, and 700°C in argon. Electrical resistivity measurements will be compared between the unirradiated and irradiated specimens.

The first set of specimens is expected to be discharged from the FFTF in September 1987.

CONCLUSIONS

A second generation copper alloy experiment has been designed, built, and inserted into the Fast Flux Test Facility (FFTF) for irradiation. The experiment test matrix is heavily biased toward the examination of oxide-dispersion-strengthened (ODS) copper-based alloys. This material exhibited the most irradiation resistance of the alloys examined after fast reactor irradiation to fluences up to 63 dpa. The current experiment included matrix and weldment specimens of commercial ODS alloys that were designed to be weldable.

FUTURE WORK

Specimen examination will proceed as material completes scheduled treatment or irradiation.

REFERENCES

1. H. R. Brager, H. L. Heinisch, and F. A. Garner, J. Nucl. Mater. 133/134, 676-9 (1985).

2. H. R. Brager and F. A. Garner, "Microstructural Examination of Pure Copper and Three Copper Alloys Irradiated in FFTF", p. 63-70 in Damage Analysis and Fundamental Studies Quarterly Progress Report, November 1985, DOE/ER-0046, U. S. Department of Energy, Office of Fusion Energy. [Also, Proceedings of ICFRM-2, Chicago, IL, April 14-17, 1986, to be published in J. Nucl. Mater.]

3. H. R. Brager, "Effects of Neutron Irradiation to 63 dpa on the Properties of Various Commercial Copper Alloys", this report. [Also, Proceedings of ICFRM-2, Chicago, IL, April 14-17, 1986, to be published in J. Nucl. Mater.]

6.5 Environmental Effects On Structural Alloys

ENVIRONMENTAL AND CHEMICAL EFFECTS ON THE PROPERTIES OF VANADIUM-BASE ALLOYS - D. R. Diercks and D. L. Smith (Argonne National Laboratory)

OBJECTIVE

The objective of this task is to experimentally evaluate the corrosion behavior of selected vanadium-base alloys in aqueous, liquid-metal, and gaseous environments and to investigate chemical effects on the mechanical and physical properties of the alloys. The results of these investigations will be used in the selection of appropriate vanadium-base alloys for structural applications in fusion reactors.

SUMMARY

The susceptibility of V-15Cr-5Ti to stress corrosion cracking in water at 288°C has been evaluated by means of constant extension rate tensile (CERT) tests. The test environments include high-purity water as well as water containing controlled levels of SO_4^{2-} and NO_3^-. Strain rates from 1×10^{-6} to 5×10^{-8} s^{-1} were employed, and dissolved oxygen levels ranged from <0.005 to 7.9 wppm. No stress corrosion cracking was observed under any of the test conditions. Electrochemical potential values as a function of dissolved oxygen content were obtained from V-15Cr-5Ti, Type 304 stainless steel, and platinum electrodes in the high-temperature water.

PROGRESS AND STATUS

Introduction

Interim results from a series of experiments to evaluate the stress corrosion cracking susceptibility of V-15Cr-5Ti in high-purity water at 288°C have been reported previously.[1] No indication of stress corrosion cracking was observed in tests conducted at a strain rate of 1×10^{-6} s^{-1} and dissolved oxygen levels in the range <0.005 to 7.7 ppm. The results described in the present report are from additional tests conducted under similar conditions as well as tests conducted under more-severe conditions, namely lower strain rates and with the addition of 10 wppm SO_4^{2-} or NO_3^- as acid.

Experimental procedures

Constant extension rate tensile (CERT) tests were conducted using a loading system consisting of a worm gear Jactuator, gear reducer, and variable-speed motor. The test specimen was enclosed in a small-diameter autoclave with a once-through water system. The dissolved oxygen level in the water was controlled by bubbling the appropriate nitrogen-oxygen gas mixture through deoxygenated/deionized feedwater (conductivity <0.2 μS/cm) in a 120-L stainless steel feedwater tank. A flow rate of ~10 mL/s was maintained in the autoclave. An external silver chloride (0.1M KCl) reference electrode and a thermocouple were located at the outlet of the autoclave, along with platinum and V-15Cr-5Ti electrodes to establish the redox and open-circuit corrosion potentials, respectively. Commercial instruments were used to monitor the pH, conductivity, and dissolved oxygen concentrations at the influent and effluent lines of the autoclave. The dissolved oxygen concentration was verified by the colorimetric (CHEMetrics ampules) method.

The CERT test specimens were fabricated from 6.35-mm (0.25-in.) dia. V-15Cr-5Ti rod material obtained from the Fusion Program Materials Inventory (Heat No. CAM 835 B-2). A chemical analysis supplied with the as-fabricated rod indicated the following composition (in wt %): 15.3% Cr, 5% Ti, 0.017% C, 0.023% O, and 0.052% N. Cylindrical tensile specimens with 4.1-mm (0.161-in.) diameters and 19.1-mm (0.75-in.) gage lengths were machined from the rod material. The rod material was tested in the as-received, cold-worked condition without prior annealing. The gage sections of the specimens were wet-abraded with 600-grit metallographic paper in the circumferential direction immediately before insertion into the autoclave. The specimens were exposed to the oxygenated water environment of ~20 h at 288°C before straining.

After testing, total elongation and reduction in area were determined for the failed specimens. In addition, the fracture surfaces were examined optically and under the scanning electron microscope to determine the fracture mode.

Results and analysis

The results of all of the CERT tests conducted in the current test series, as well as the four tests reported previously,[1] are summarized in Table 1. The tests fall into two categories: (1) those conducted in pure water with several dissolved oxygen levels and two strain rates, and (2) those conducted in water containing 10 wppm SO_4^{2-} or NO_3^- over a narrower range of strain rates at approximately the same dissolved oxygen level. In addition, the results of four experiments to determine the electrochemical potentials as a function of dissolved oxygen content are included in Table 1.

Table 1. Results obtained from CERT tests conducted at several strain rates on V-15Cr-5Ti in 288°C water containing various levels of dissolved oxygen, sulfate, and nitrate

Dissolved Oxygen (wppm)	Impurity Species	Anion Conc. (wppm)	Conductivity (μS/cm)	pH at 25°C	Strain Rate (s^{-1})	Failure Time (h)	Maximum Stress (MPa)	Total Elongation (%)	Reduction in Area (%)	Fracture Mode	Potentials [mV (SHE)] V-15Cr-5Ti	Pt	Type 304 SS
<0.005	-	-	0.07	6.57	1×10^{-6}	32.0	846	12	48	ductile	-422	-398	-419
0.025	-	-	0.08	6.67	1×10^{-6}	32.5	847	12	49	ductile	-428	-410	-427
0.20	-	-	0.20	6.31	1×10^{-6}	32.9	833	12	50	ductile	-351	83	-39
0.20[a]	-	-	0.35	6.29	-	-	-	-	-	-	-312	139	87
0.20[a]	-	-	0.21	6.43	-	-	-	-	-	-	-323	158	98
0.80[a]	-	-	0.50	6.27	-	-	-	-	-	-	-69	227	170
2.0[a]	-	-	0.54	6.30	-	-	-	-	-	-	4	188	139
7.7	-	-	0.09	6.61	1×10^{-6}	31.7	834	11	48	ductile	23	150	80
7.2	-	-	0.15	6.21	5×10^{-8}	619	848	11	46	ductile	103	223	185
7.9	H_2SO_4	10.0	89.0	3.77	1×10^{-5}	3.2	817	12	52	ductile	318	453	307
7.6	H_2SO_4	10.0	88.0	3.81	4×10^{-6}	7.5	836	11	49	ductile	327	464	288
7.2	H_2SO_4	10.0	86.0	3.75	2×10^{-7}	149	854	11	45	ductile	312	446	331
7.0	HNO_3	10.0	67.0	3.87	4×10^{-6}	7.4	843	11	50	ductile	306	440	407
7.6	HNO_3	10.0	66.0	3.87	5×10^{-7}	58.0	845	10	44	ductile	313	462	423

[a] Electrochemical potential data for several dissolved oxygen concentrations in high-purity water.

The CERT tests in pure water at 1×10^{-6} s^{-1} were conducted at dissolved oxygen levels of <0.005, 0.025, 0.20, and 7.7 wppm. The values of maximum stress, total elongation, and reduction in area were essentially the same for all four specimens, and the observed fracture mode was completely ductile in all cases. The ductile fracture mode, in conjunction with the relatively high measured ductilities, clearly indicates the complete absence of stress corrosion cracking under these test conditions.

An additional CERT test was conducted in pure water containing 7.7 wppm dissolved oxygen at a strain rate of 5×10^{-8} s^{-1}. This much slower strain rate, which resulted in a time to failure of 619 h as compared with 31.7 h for a similar test conducted at 1×10^{-6} s^{-1}, would normally be considered more conducive to stress corrosion cracking. However, the observed total elongation and reduction in area are similar to those obtained for the companion test conducted at the higher strain rate, and the fracture mode was again entirely ductile. Thus, this relatively slow strain rate in pure water containing a high level of dissolved oxygen failed to induce stress corrosion cracking in V-15Cr-5Ti.

In an attempt to produce even more severe conditions with respect to stress corrosion cracking, five tests were conducted at high dissolved oxygen levels (7.0 to 7.9 wppm) with the addition of 10 wppm SO_4^{2-} or NO_3^- as sulfuric and nitric acid. Both anions (particularly SO_4^{2-}) have been found to promote stress corrosion cracking in lightly sensitized Type 304 stainless steel in water at 289°C, with noticeable effects at concentrations as low as 0.1 wppm.[2,3] However, the ductility and fracture mode indicate that these anions failed to produce stress corrosion cracking in V-15Cr-5Ti, even at these very high levels.

Discussion

Further evidence that stress corrosion cracking did not occur under the test conditions considered here is provided by Fig. 1, in which the time to failure is plotted against the strain rate for all of the CERT tests in Table 1. The observed slope of -1 is consistent with a recently developed phenomenological model of stress corrosion cracking in which the applied strain rate was related to parameters such as the time and strain to failure, the crack length at failure, and the average crack growth rate.[4,5] In the absence of stress corrosion cracking, the model predicts a reciprocal relationship between time to failure and strain rate, as seen in Fig. 1. This result indicates that the strain to failure is essentially constant for these tests, as evidenced by the total elongation values in Table 1. Under conditions of stress corrosion cracking, the model predicts a slope of approximately -2/3 for such a plot. Thus, data points corresponding to tests in which stress corrosion cracking occurred would be expected to fall below the straight line in Fig. 1.

The measured electrochemical potentials for the three electrodes versus the standard hydrogen electrode are plotted as a function of dissolved oxygen content in Figs. 2-4. The platinum redox potential curve and Type 304 stainless steel curve (Figs. 2 and 3) are similar, with a lower potential of about -400 to -430 mV, an upper potential of about 150 to 200 mV, and a rather sharp break at about 0.1 ppm dissolved oxygen. For Type 304 stainless steel, this break is normally associated with the transition from active corrosion behavior at the lower potential to passivity at the higher potential. The V-15Cr-5Ti open-circuit corrosion potential curve (Fig. 4) differs somewhat from the other two curves in that the higher potential is somewhat less positive (~30 mV) than for the other two electrodes, and the transition between the upper and lower potentials is more gradual. For all three curves, the potentials for the acidified solutions lie at higher values than for pure water at a similar oxygen content.

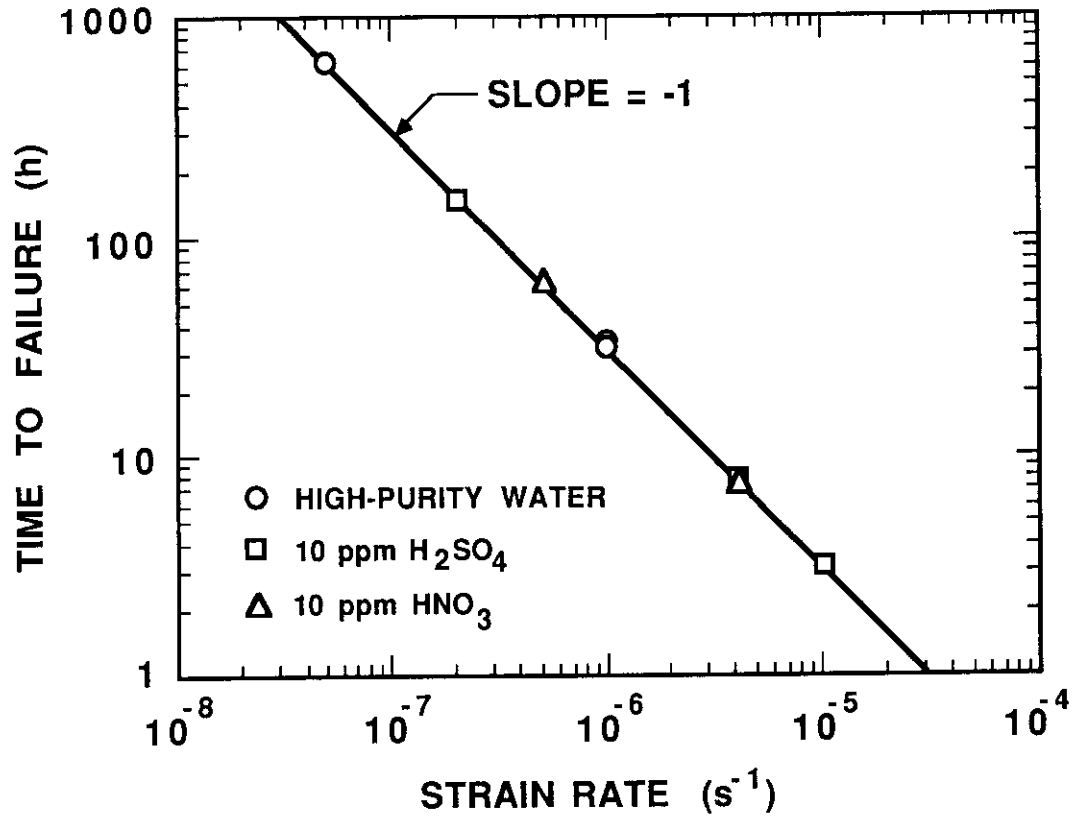

Fig. 1. Time to failure versus strain to failure for CERT tests in Table 1.

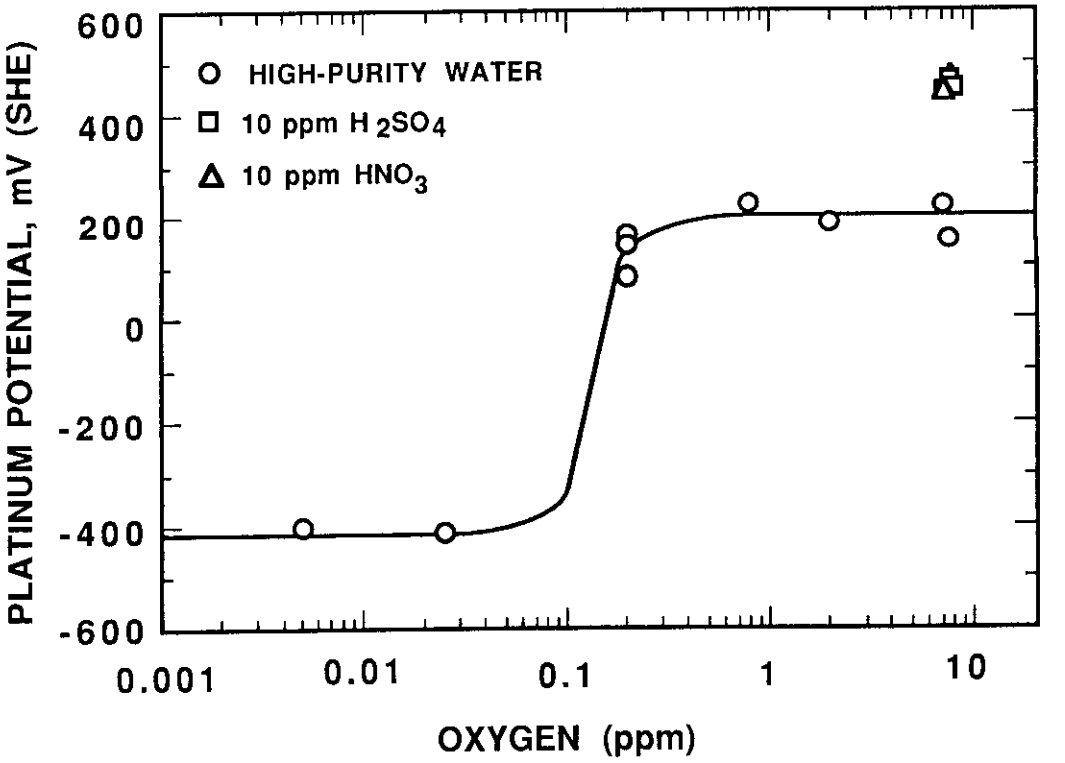

Fig. 2. Platinum electrode (redox) potential versus dissolved oxygen content for CERT tests and supplemental potential data in Table 1.

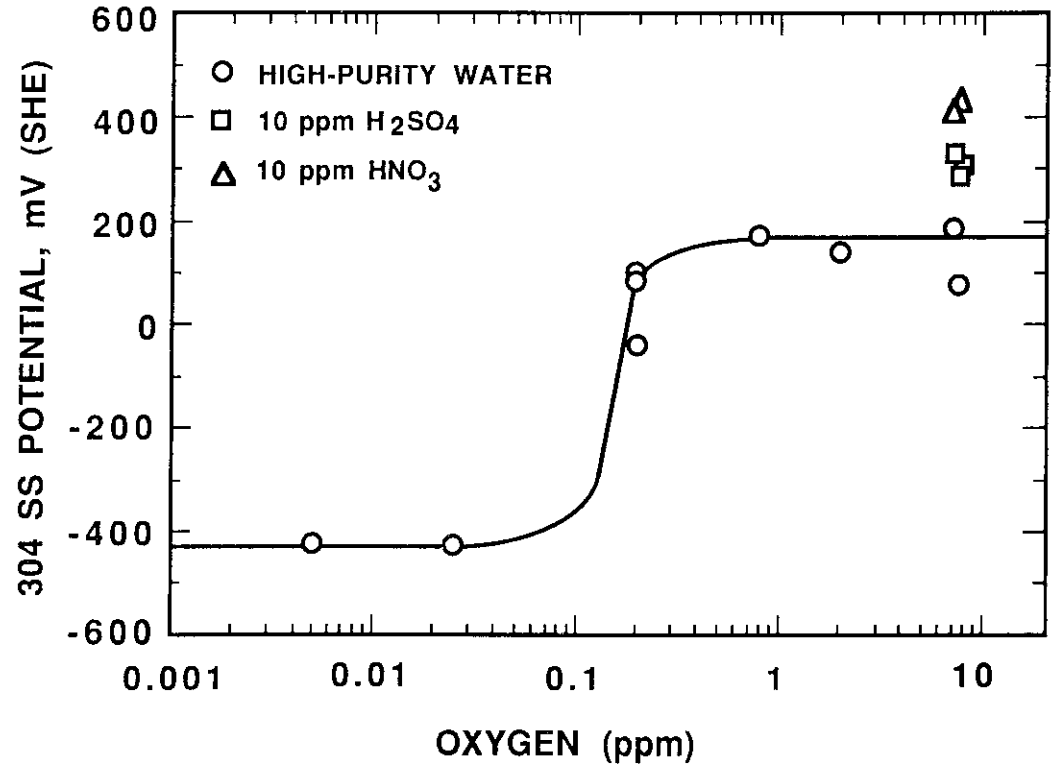

Fig. 3. Type 304 stainless steel electrode potential versus dissolved oxygen content for CERT tests and supplemental potential data in Table 1.

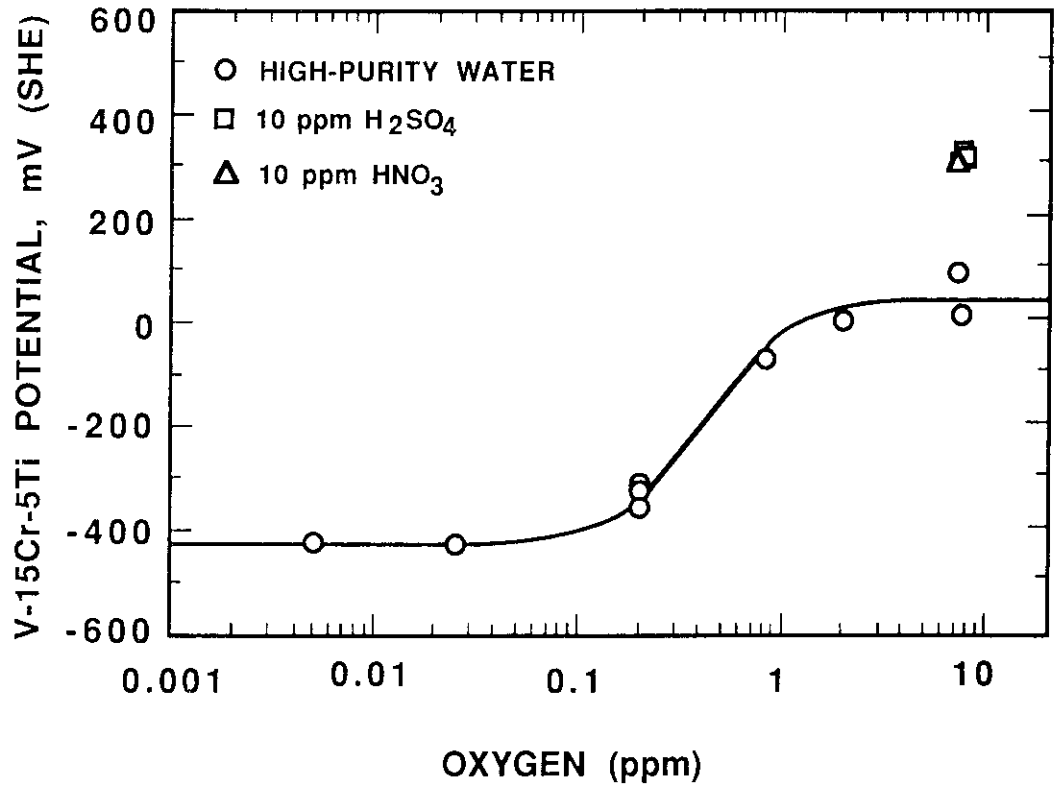

Fig. 4. V-15Cr-5Ti electrode (open-circuit corrosion) potential versus dissolved oxygen content for CERT tests and supplemental corrosion data in Table 1.

The above electrochemical potential and pH information can, in principle, be used to rationalize the corrosion and stress corrosion cracking behavior of V-15Cr-5Ti with the stability of corrosion product phases indicated in the equilibrium potential-pH (Pourbaix) diagram for vanadium. Unfortunately, no such diagram has been developed for V-15Cr-5Ti, and the Pourbaix diagram for vanadium[6] (Fig. 5) refers to room temperature. Nonetheless, several observations can be made relative to Fig. 5.

The shaded V area in Fig. 5 is the region of potential and pH values for which metallic vanadium is stable, i.e., the region where the metal is considered to be immune to corrosion. In the lightly cross-hatched regions of V_2O_2 and V_2O_3 stability, the metal can be in a passive state if the surface oxides provide a degree of protection to the underlying base metal. Stress corrosion cracking is generally considered possible when the corrosion potential lies in this passive region and passivity is lost at the tip of a crack following mechanical straining that ruptures the protective film and enables local rapid active corrosion. Over the remainder of the Pourbaix diagram, numerous soluble ionic species are stable, and active general corrosion is predicted. In accordance with standard practice, the boundaries between the regions of solid phases and ionic species correspond to an ionic concentration of 10^{-6} mole per liter in equilibrium with the solid. The dashed lines a and a' correspond to the potentials above which oxygen is evolved at 25 and 288°C, respectively, and the lines b and b' correspond to the potentials below which hydrogen is evolved at these two temperatures.

The pH of pure water (i.e., water containing dissolved oxygen but no other species) at 288°C is about 5.6. The redox potentials from the platinum electrode over which the present experiments were conducted ranged from about -420 to +200 mV. The corresponding heavily cross-hatched rectangular region is labeled "pure water" in Fig. 5. This region corresponds to general corrosion at room temperature. However, the stability regions for the V_2O_2 and V_2O_3 oxides (i.e., passive behavior) can be expected to move somewhat to the left at 288°C. Unfortunately, thermodynamic data are not available to predict whether these experimental conditions fall within the region of predicted passive behavior at this temperature. Since stress corrosion cracking did not occur under the "pure water" experimental conditions, one must conclude that either (1) these conditions did not fall within the region of oxide stability at 288°C, or (2) a surface oxide did form but the passivity regime was not conducive to stress corrosion cracking. The visual appearance of the CERT specimens suggests the latter alternative. It should also be noted that the alloy V-15Cr-5Ti forms somewhat different oxides than pure vanadium,[7] and the stability regions of these oxides is not indicated in Fig. 5.

For the tests in which 10 ppm H_2SO_4 or HNO_3 were added to the water, the potential-pH conditions fall within the heavily cross-hatched rectangle labeled "acid solutions" in Fig. 5. The lower pH and higher potential both favor general corrosion, and, based upon the Pourbaix diagram, stress corrosion would be even less likely to occur under these conditions than under the "pure water" conditions. As described above, no stress corrosion cracking was observed.

CONCLUSIONS

A series of CERT tests has been completed on V-15Cr-5Ti at 288°C in water containing varying levels of dissolved oxygen and, for some tests, 10 wppm SO_4^{2-} or NO_3^-. No stress corrosion cracking was observed in pure water containing dissolved oxygen levels ranging from <0.005 to 7.7 wppm at a strain rate of 1×10^{-6} s^{-1} or in pure water containing 7.2 wppm dissolved oxygen at a strain rate of 5×10^{-8} s^{-1}. In addition, stress corrosion cracking was not observed in solutions containing 10 wppm dissolved SO_4^{2-} or NO_3^- along with 7.0 to 7.9 wppm oxygen at strain rates ranging from 1×10^{-5} to 2×10^{-7} s^{-1}. These results indicate that V-15Cr-5Ti is resistant to stress corrosion cracking in aqueous environments of the type anticipated for water-cooled fusion reactor applications. Based upon electrochemical potential measurements, available Pourbaix diagram information, and observed oxidation behavior, it appears that the surface oxide formed during the tests was not sufficiently protective to promote localized active behavior and thus create the necessary conditions for stress corrosion cracking.

FUTURE WORK

The present experiments complete the planned experimental program on the aqueous corrosion behavior of vanadium-base alloys. Subsequent corrosion experiments on these alloys will focus on their behavior in lithium and lead/lithium coolants.

REFERENCES

1. D. R. Diercks and D. L. Smith, "Environmental and Chemical Effects on the Properties of Vanadium-base Alloys," pp. 71-72 in Alloy Development for Irradiation Performance: Semiannual Progress Report for Period Ending March 31, 1986, DOE/ER-0045/16, Oak Ridge National Laboratory, Oak Ridge, TN, September 1986.

2. W. E. Ruther, W. K. Soppet, G. Ayrault, and T. F. Kassner, "Effect of Sulfuric Acid, Oxygen, and Hydrogen in High-Temperature Water on Stress Corrosion Cracking of Sensitized AISI 304 Stainless Steel," Corrosion 40(10), 518-527 (1984).

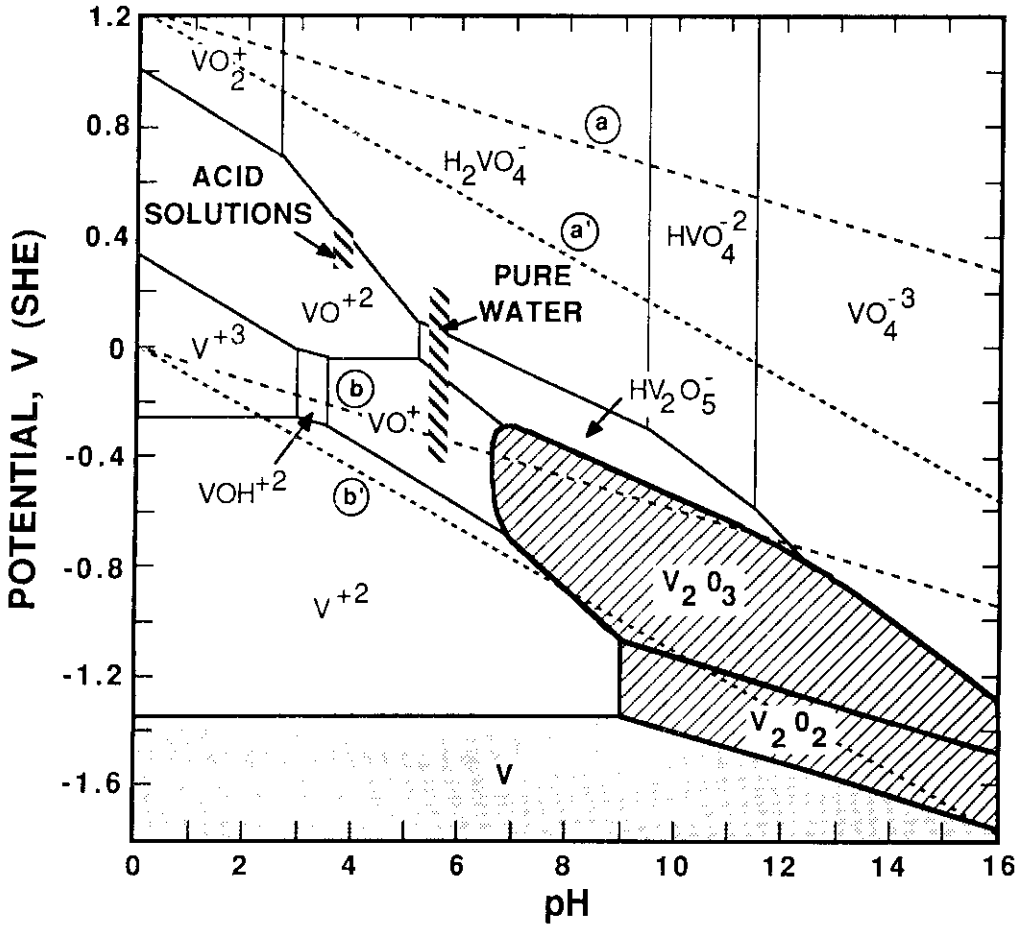

Fig. 5. Potential-pH (Pourbaix) equilibrium diagram for vanadium in an aqueous environment at 25°C. The dashed lines a and a' indicate the potentials above which oxygen is evolved at 25 and 288°C, respectively, and the dashed lines b and b' denote the potentials below which hydrogen is evolved at the same temperatures. The cross-hatched rectangular regions labeled "pure water" and "acid solutions" indicate the experimental conditions evaluated here (adapted from Ref. 6).

3. W. E. Ruther, W. K. Soppet, and T. F. Kassner, "Effect of Temperature and Ionic Impurities at Very Low Concentrations on Stress Corrosion Cracking of Type 304 Stainless Steel," Paper 102 presented at Corrosion 85, Boston, MA, March 25-29, 1985.

4. P. S. Maiya, "Prediction of Environmental and Strain-Rate Effects on the Stress Corrosion Cracking of Austenitic Stainless Steels," in Predictive Capabilities in Environmentally Assisted Cracking, PVP-Vol. 99 (R. Rungta, ed.), American Society of Mechanical Engineers, New York, 1985, pp. 39-54.

5. P. S. Maiya and W. J. Shack, "Stress Corrosion Cracking Susceptibility of AISI 316NG and 316 Stainless Steel in an Impurity Environment," Corrosion 41(11), 630-634 (1985).

6. Marcel Pourbaix, Atlas of Electrochemical Equilibria in Aqueous Solutions, (J. A. Franklin, tr.), Pergamon Press, New York, 1966.

7. D. R. Diercks and D. L. Smith, "Environmental and Chemical Effects on the Properties of Vanadium-base Alloys," pp. 192-196 in Alloy Development for Irradiation Performance: Semiannual Progress Report for Period Ending March 31, 1985, DOE/ER-0045/14, Oak Ridge National Laboratory, Oak Ridge, TN, July 1985.

CORROSION STUDIES IN THERMALLY CONVECTIVE LITHIUM: 12Cr-1MoVW STEEL AND LOW ACTIVATION AUSTENITIC AND FERRITIC ALLOYS - P. F. Tortorelli (Oak Ridge National Laboratory)

OBJECTIVE

The purpose of this task is to determine the corrosion resistance of candidate first-wall materials to slowly flowing lithium in the presence of a temperature gradient. Corrosion and deposition rates are measured as functions of time, temperature, additions to the lithium, and flow conditions. These measurements are combined with chemical and metallographic examinations of specimen surfaces to establish the mechanisms and rate-controlling processes for dissolution and deposition reactions.

SUMMARY

Results from experiments with austenitic and ferritic steels exposed to lithium yielded further evidence for the important role of chromium reactions in the corrosion process. Preliminary indications from the analysis of weight change data for a low nitrogen Fe-Cr-Mn steel exposed to thermally convective lithium at 500°C for 2856 h revealed that the nitrogen concentration alone cannot account for the chromium reactions observed for Fe-Cr-Mn alloys in molten lithium. Additional surface analysis of standard 12Cr-1MoVW steel specimens exposed in a thermal convection loop circulating lithium between 600 and 450°C confirmed the presence of chromium enrichment at intermediate temperatures. An initial study of low activation ferritic steels in thermally convective lithium at 500°C was completed. Results showed low weight losses typical of standard ferritic steels exposed under similar conditions. Steels containing a significant concentration of manganese appear to be slightly less corrosion resistant than one containing only 0.02 wt % of this element.

STATUS AND PROGRESS

A major component of the fusion energy materials effort involves the development of alloys of low residual radioactivity. To this end, the corrosion of both austenitic and ferritic "low activation" alloys by thermally convective lithium has been studied. Initial data for such ferritic alloys are discussed below. With respect to the austenitic steels, previous weight change and surface characterization results from simultaneous exposure of Fe-Cr-(12–30 wt %)Mn alloys to lithium circulating between 500 and 350°C revealed competing mechanisms of weight loss resulting from manganese dissolution and transport and weight gain due to chromium reactions.[1,2] While the exact nature of the reaction(s) involving chromium is not known, it was hypothesized that they could be driven by the relatively high nitrogen concentrations of some of the Fe-Cr-Mn alloys in the loop and the concentration gradient transfer among the various alloy specimens. In order to determine if the elevated nitrogen concentration of certain of these alloys contributed to the observed chromium reactions, a low nitrogen Fe-Cr-Mn steel (PCMA-2: Fe-15Cr-17Mn-0.01Ni-0.04Si-0.06C-0.001N, wt. %) was singly exposed in the same lithium thermal convection loop (TCL) used for the earlier exposures of Fe-Cr-Mn alloys. The PCMA-2 specimen was held at the hottest position of the TCL for a total exposure of 2856 h. Weight change data as a function of time is shown in Fig. 1, which also includes the 495°C data for a PCMA-2 specimen when it was exposed in the prior TCL experiment with several other Fe-Cr-Mn alloys.[2] While the weight change values from the two exposures differ somewhat, they show the same qualitative behavior with time: initial weight losses followed by weight gains. This weight change pattern has previously been interpreted in terms of a time dependent process in which manganese depletion makes the principal contribution to the weight change during the early stages of exposure, while, at later times, chromium transport and reaction become dominant and lead to weight gains.[2] It thus appears that the starting nitrogen concentration of the Fe-Cr-Mn alloys does not play a key role in the corrosion process, although, in the second TCL experiment, such reactions could have possibly been exacerbated by residual nitrogen from the loop walls. Results from forthcoming surface analysis of the recently exposed PCMA-2 specimen will be compared to similar data from the earlier experiment to check for any differences in surface morphology and/or composition.

Chromium reactions have also been considered to be important in Cr-Mo steel-lithium TCL systems.[1,3,4] Results presented in the preceding progress report[1] showed chromium depletion in a 12Cr-1MoVW steel exposed at 600°C in a TCL circulating lithium between 600 and 450°C for 6962 h. However, chromium surface products formed at intermediate temperature specimen positions in the loop. During the current reporting period, surface analyses of additional specimens from this loop experiment were completed and confirmed the previous limited observations of the temperature dependence of chromium enrichment and the changes in surface morphology around the loop.[1] Using Fig. 2 for reference, the micrographs of Fig. 3 and the surface composition results in Table 1 (which includes some previously reported data[1] for completeness) summarize surface morphology and composition data as a function of loop position. The enrichment in chromium at intermediate loop temperatures was due to the presence of nodules highly enriched in this element. Such observations illustrate the propensity for surface reactions that form chromium-containing products [possibly Li_8CrN_6] (ref. 5)]. Since such features are also detected on exposed Fe-Cr-Mn alloys,[1,2] the role of chromium reactions in influencing overall corrosion behavior in lithium is obviously quite important regardless of the particular alloy being exposed to this liquid metal.

ORNL-DWG 86-17645

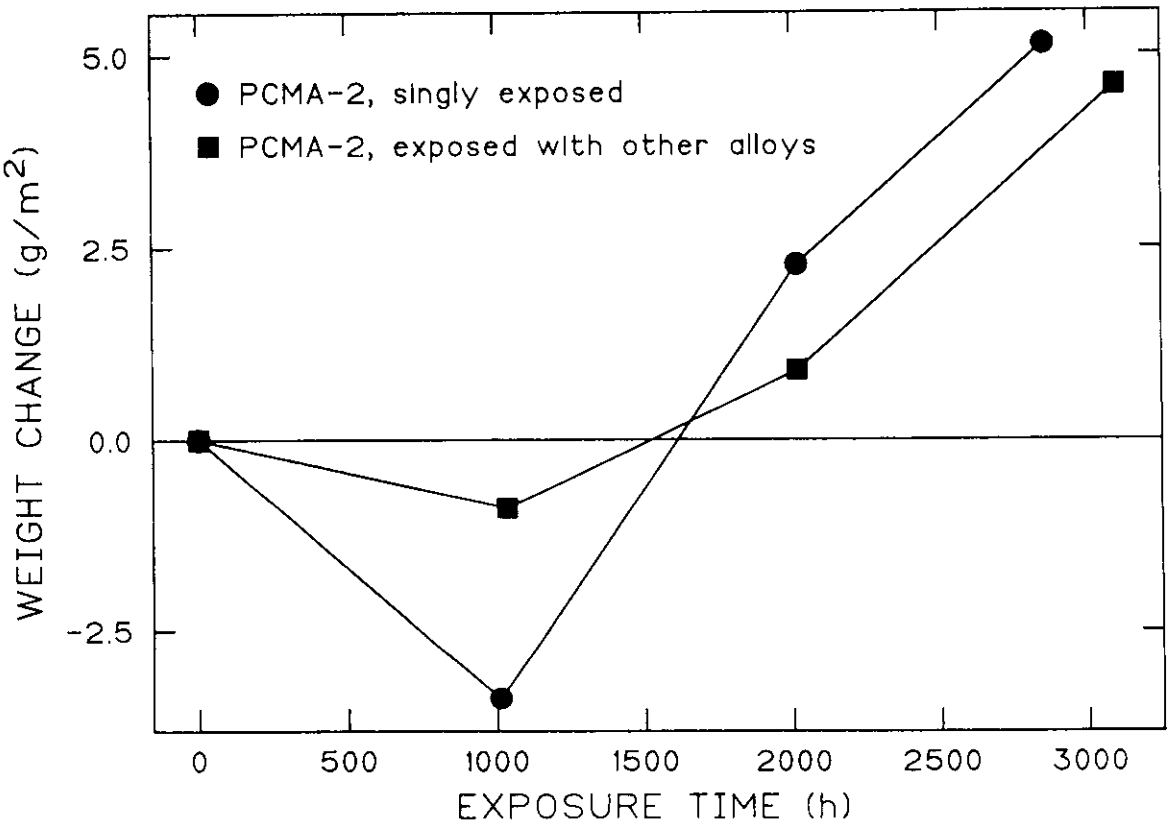

Fig. 1. Weight change versus time for PCMA-2 exposed to thermally convective lithium at 500°C.

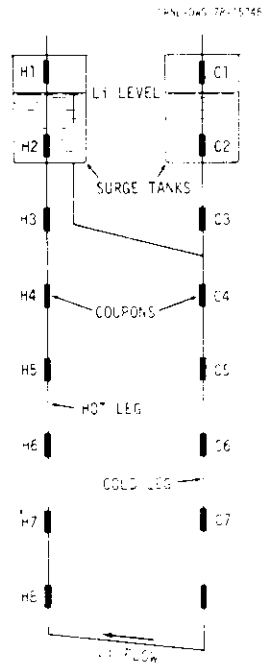

Fig. 2. Schematic drawing of thermal convection loop showing positions of coupons during typical loop experiment.

Table 1. Weight changes and surface compositions of 12Cr-1MoVW steel exposed to thermally convective lithium for 6962 h

Loop position	T (°C)	Weight change (g/m^2)	Surface composition (wt %)[a]			
			Fe	Cr	Ni	Mo
H3	600	−20.7	90.2	9.1	0.4	0.3
H4	580	0.0	87.8	10.5	0.9	0.6
H5	560	+13.3	50.3	45.6	1.9	2.1
H6	540	+1.7	72.3	25.5	1.6	0.5
H7	520	+8.8	92.2	5.2	1.9	0.5
C4	530	+18.7	60.7	36.7	1.3	1.2
C5	510	+17.0	73.7	21.8	1.0	0.6
C6	490	+10.5	91.6	6.7	0.9	0.4
C7	470	+7.7	92.2	5.7	1.3	0.5
C8	450	+9.7	92.1	5.6	1.9	0.6

[a]As determined by semiquantitative energy dispersive x-ray analysis.

ORNL DWG 86-18384

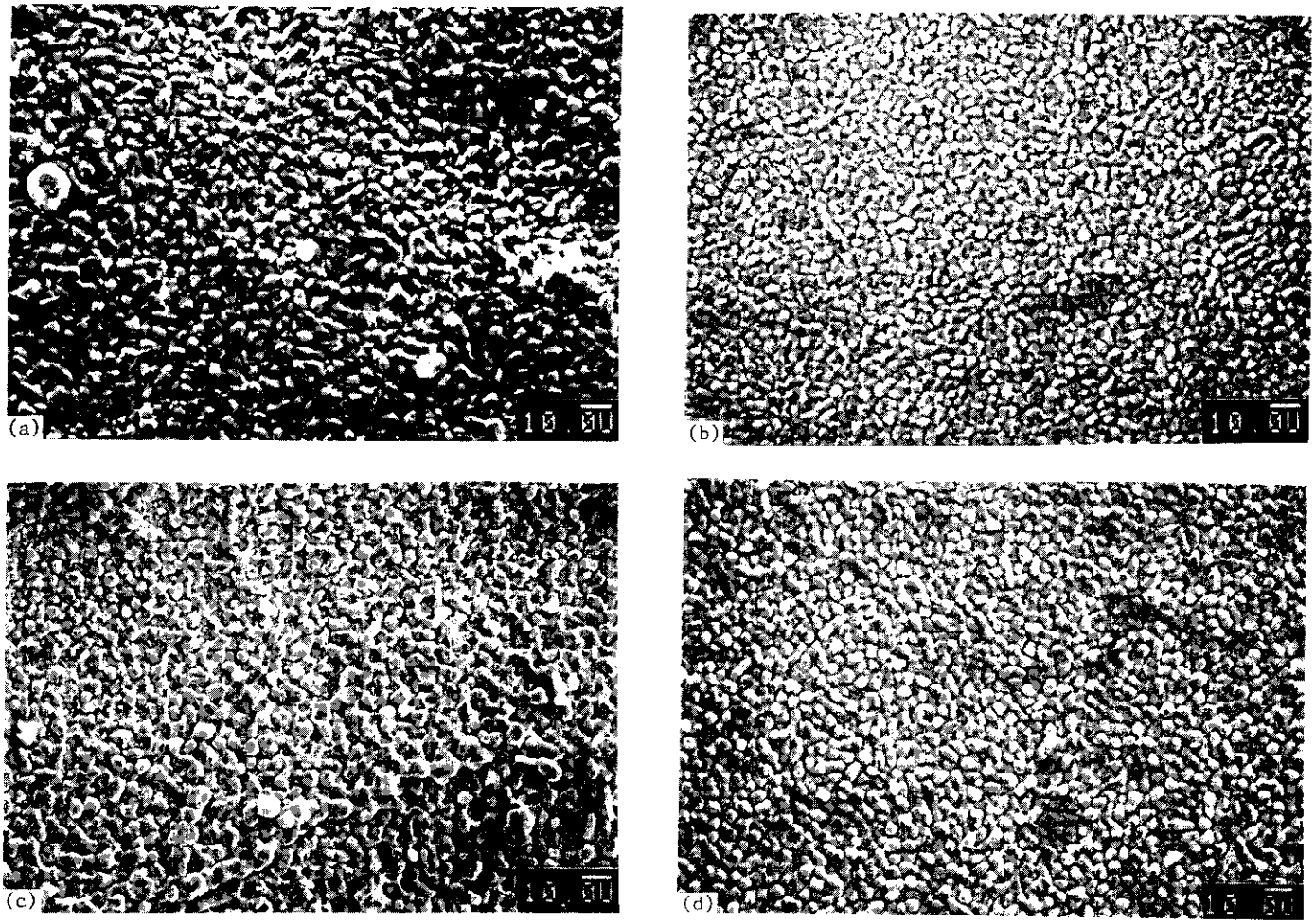

Fig. 3. Scanning election micrographs of 12Cr-1MoVW steel exposed to thermally convective lithium for 6962 h (maximum temperature = 600°C). (a) H4, 580°C. (b) H7, 525°C. (c) C5, 510°C. (d) C7, 470°C. (cf. Fig. 2 for specimen positions in loop).

As mentioned above, some research on the corrosion of developmental "low activation" ferritic alloys by molten lithium has been included as part of the chemical compatibility program. During the current reporting period, an initial TCL experiment was completed after 4802 h of specimen exposure to lithium circulating between 500 and 350°C. Four coupons of three alloys were grouped at the hottest position of the loop and were weighed at selected times during the course of the experiment. The compositions of these alloys are shown in Table 2. The V-64 and V-68 alloys were developed at Hanford Engineering Development

Table 2. Starting compositions of low activation ferritic alloys exposed to thermally convective lithium for 4802 h at 500°C

Alloy	Composition (wt %)[a]								
	Cr	Mn	V	W	Si	N	P	S	C
V02264 ("V-64")[b]	9.1	0.02	0.52	0.01	0.09	0.003	<0.005	0.003	0.001
V02268 ("V-68")[b]	8.8	2.44	0.27	0.89	0.10	0.002	<0.005	0.004	0.101
90E, steel 13[c]	9.2	0.7	0.25	2.9	0.42				0.17

[a]Balance is Fe.

[b]Provided by D. S. Gelles of Hanford Engineering Development Laboratory.

[c]Provided by G. J. Butterworth of Culham Laboratory.

Laboratory. The "steel 13" is one of the European Community's developmental alloys and was provided by Culham Laboratory. Weight change results as a function of time are shown in Fig. 4. The weight changes of all the specimens are relatively low and are quite similar to each other. However, the lower weight loss of the V-64 alloy may be significant: preferential dissolution of the manganese in the other two steels (see Table 2) can occur (as discussed above and elsewhere)[2] and contribute to the slightly higher weight losses observed for steel 13 and V-68. Indeed, there is evidence from energy dispersive analysis of the exposed surfaces that there has been some depletion of manganese from these latter two steels (see Table 3).

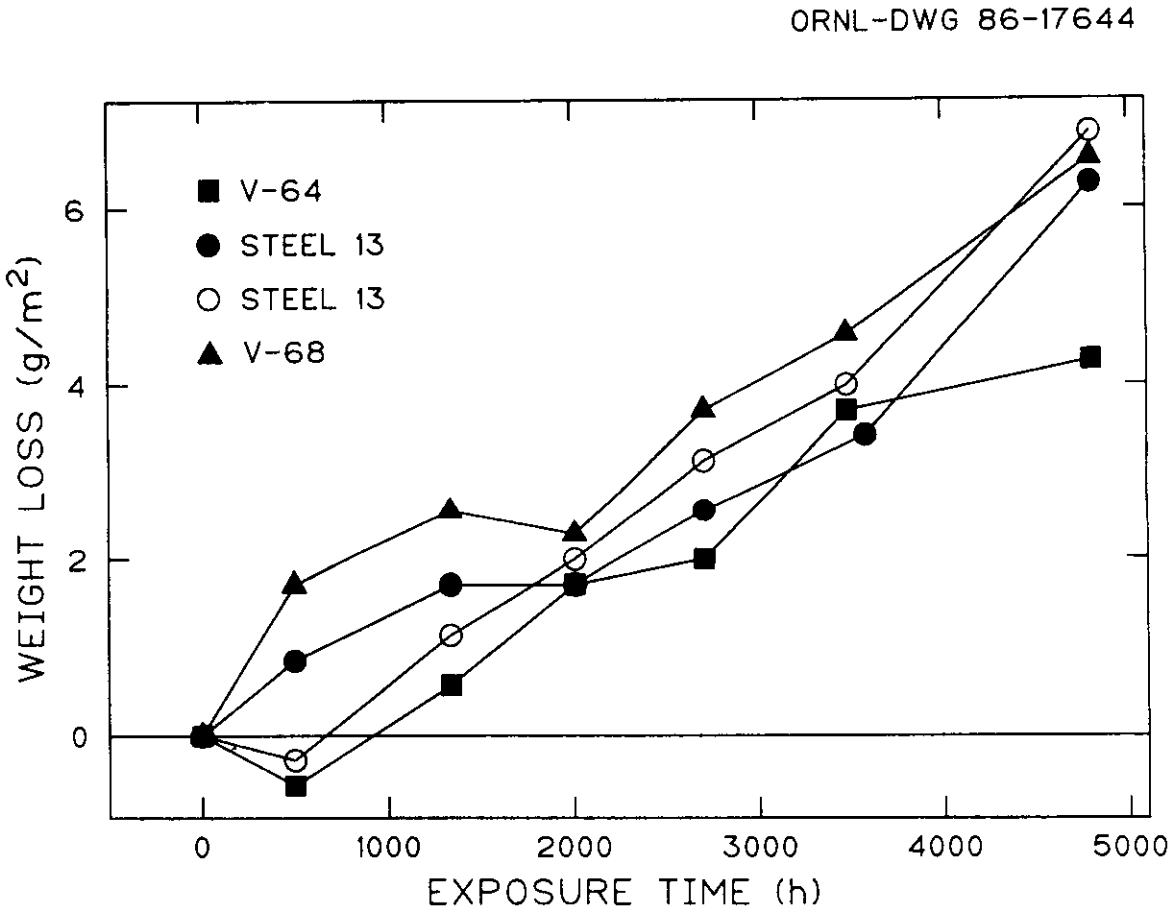

Fig. 4. Weight losses versus time for low activation ferritic steels exposed to thermally convective lithium at 500°C.

Table 3. Surface compositions of specimens exposed to thermally convective lithium for 4802 h at 500°C

Specimen	Composition (wt %)[a]		
	Cr	Mn	Fe
V-64	6	0.0	94
V-68	6	0.6	93
Steel 13	6	0.0	93
Steel 13	6	0.2	93

[a]As determined by semi-quantitative energy dispersive x-ray analysis.

Compositional analyses of polished cross sections of these specimens will yield more quantitative information about the extent of manganese depletion, while the surfaces of coupons located in the cold leg of the loop during the 4802 h of this experiment will also be examined for mass transfer deposits containing manganese. The surface composition data in Table 3 indicate that some preferential dissolution of chromium also occurred. Such behavior has also been noted for standard 12Cr-1MoVW steel exposed to thermally convective lithium at 500 (ref. 4) and 600°C (ref. 3). Scanning electron micrographs of the surfaces of the four specimens exposed to thermally convective lithium at 500°C are shown in Fig. 5. As with other ferritic steels, the effect of lithium exposure on surface morphology was not substantial when compared to the effects of this environment on austenitic steels. However, there is some evidence for the "dimpling" that has been observed on standard Cr-Mo steels.[6]

ORNL DWG 86-18385

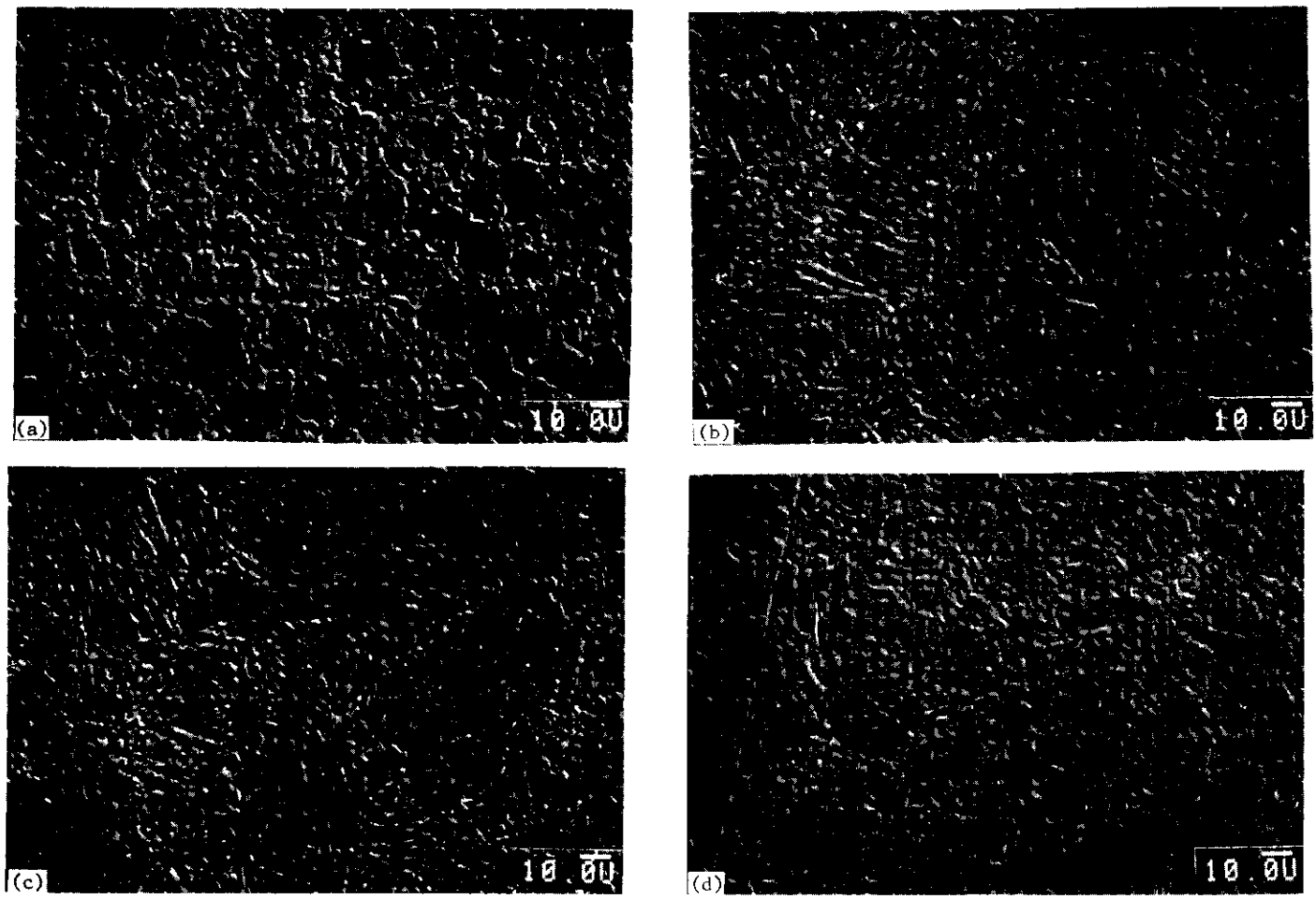

Fig. 5. Scanning electron micrographs of low activation ferritic steels exposed to thermally convective lithium at 500°C for 4802 h. (a) V-64. (b) Steel 13. (c) Steel 13. (d) V-68.

CONCLUSIONS

1. Preliminary indications from the analysis of weight change data for a low nitrogen Fe-Cr-Mn steel exposed to thermally convective lithium at 500°C for 2856 h revealed that nitrogen concentration alone cannot account for the observed chromium reactions for Fe-Cr-Mn alloys in molten lithium.

2. Additional surface analysis of standard 12Cr-1MoVW steel exposed to thermally convective lithium between 600 and 450°C confirmed the presence of chromium enrichment at intermediate temperatures and again showed the importance of chromium reactions in lithium systems.

3. An initial study of low activation ferritic steels in thermally convective lithium at 500°C was completed. Results showed low weight losses typical of standard ferritic steels exposed under similar conditions. Steels containing significant concentrations of manganese appear to be less corrosion resistant than one containing only 0.02 wt %. Preliminary surface composition data indicate preferential depletion of manganese and chromium.

FUTURE WORK

During the next reporting period, research on corrosion in thermally convective lithium environments will focus on low activation austenitic and ferritic alloys. Further analysis of the exposed PCMA-2 specimen and additional exposure of low nitrogen Fe-Cr-Mn steel in fresh lithium will help to definitively determine the role of nitrogen in the alloy on the corrosion process. Additional compositions of the low activation ferritic steels will be exposed in a TCL experiment. A wider range of manganese concentrations in these alloys will allow a better definition of the importance of manganese depletion with respect to the corrosion resistance of such steels.

REFERENCES

1. P. F. Tortorelli and J. H. DeVan, "Corrosion of Fe-Cr-Mn and Fe-Cr-Mo Alloys in Thermally Convective Lithium," pp. 169–80 in *ADIP Semiann. Prog. Rep. Mar. 31, 1986,* DOE/ER-0045/16, U.S. DOE, Office of Fusion Energy.

2. P. F. Tortorelli and J. H. DeVan. "Corrosion of Fe-Cr-Mn Alloys in Thermally Convective Lithium," *J. Nucl. Mater.* 141-143 (1986) 579-783

3. P. F. Tortorelli and J. H. DeVan, "Thermal Convection Loop Studies of the Lithium Corrosion of Low Activation Austenitic Alloys and Standard Fe-12Cr-1MoVW Steel," pp. 197–204 in *ADIP Semiann. Prog. Rep. Mar. 31, 1985,* DOE/ER-0045/14, U.S. DOE, Office of Fusion Energy.

4. P. F. Tortorelli and J. H. DeVan, "Corrosion of an Fe-12Cr-1MoVW Steel in Thermally Convective Lithium," pp. 215–21 in *Proc. Topical Conf. on Ferritic Alloys for Use in Nuclear Energy Technologies,* ed. J. W. Davis and D. J. Michel, AIME, 1984.

5. M. G. Barker et al., "The Interaction of Chromium with Nitrogen Dissolved in Liquid Lithium," *J. Nucl. Mater.* 114 (1983) 143–49.

6. O. K. Chopra and D. L. Smith, "Corrosion of Austenitic and Ferritic Steels in Flowing Lithium Environment," pp. 171–79 in *ADIP Semiann. Prog. Rep. Sept. 30, 1985,* DOE/ER-0045/15, U.S. DOE, Office of Fusion Energy.

LONG-TERM CORROSION OF TYPE 316 STAINLESS AND 12Cr-1MoVW STEELS IN THERMALLY CONVECTIVE Pb-17 at. % Li - P. F. Tortorelli (Oak Ridge National Laboratory)

OBJECTIVE

The purpose of this work is to determine the corrosion resistance of candidate first-wall materials to slowly flowing Pb-17 at. % Li in the presence of a temperature gradient. Dissolution and deposition rates are measured as functions of time, temperature, and additions of minor elements to the lead-lithium. These measurements are combined with chemical and metallographic examinations of specimen surfaces to establish the mechanisms and rate-controlling processes for the dissolution and deposition reactions.

SUMMARY

During the current reporting period, long-term (10,000 h) baseline thermal convection loop experiments with austenitic and ferritic steels exposed to Pb-17 at. % Li were completed. The 500°C data confirmed the aggressiveness of the lead-lithium environment. Surface analysis revealed uniform attack of 12Cr-1MoVW steel with minimal change in surface composition. In contrast, the type 316 stainless steel suffered irregular attack and preferential dissolution of nickel and chromium. These observations are in accord with a model that predicts such nonuniform attack under conditions of selective leaching. Mass transfer profiles revealed that, in the case of type 316 stainless steel, the maximum deposition was not at the coldest point in the loop. Such behavior can be attributed to the product of thermodynamic and kinetic factors that vary oppositely with respect to temperature.

PROGRESS AND STATUS

During the current reporting period, long-term baseline thermal convection loop (TCL) experiments with austenitic and ferritic steels were completed. Specimens of type 316 stainless and 12Cr-1MoVW steels were exposed to thermally convective Pb-17 at. % Li for just over 10,000 h in two different TCLs. In one loop, type 316 stainless steel coupons were contained in type 316 stainless steel piping that previously had circulated lithium for over 10,000 h. The second TCL contained 12Cr-1MoVW steel specimens and was made from modified 9Cr-1Mo steel. It had not seen service prior to the lead-lithium experiment. Both loops circulated Pb-17 at. % Li at a maximum temperature of 500°C, but the temperature differential was higher in the case of the 12Cr-1MoWV steel (150°C) than the type 316 stainless steel (100°C).

At all times during the experiments, four specimens were grouped at the hottest location in both loops (500°C) and these specimens were selectively removed and replaced at various times. This resulted in 500°C data at about 1000, 2000, 3000 (two different specimens), 4000 (2), 6000, 7000, and 10,000 h of exposure. Some of these data were reported previously;[1,2] updated weight loss versus time curves are shown in Fig. 1. The results confirm the previous findings[1,2] that the molten lead-lithium environment was quite aggressive. Large weight losses were measured for both type 316 stainless and 12Cr-1MoVW steels throughout the 10,000 h of exposure. As discussed in detail previously,[2] the use of low temperature molten lithium to remove residual lead-lithium from exposed specimens was quite effective, but can sometimes lead to partial or complete detachment of the penetrated layer on type 316 stainless steel. This would result in more rapid corrosion than if the layer had not been disturbed.[2] Therefore, the data in Fig. 1 represent measurements from individual coupons, which were cleaned in the standard manner after loop exposure and not re-exposed. Although the specimen cleaning procedure does not strip any corrosion layer from the 12Cr-1MoVW steel specimens,[3] the same coupon exposure methodology was used for these specimens to generate the mass loss kinetics in a consistent manner.

Analysis of the type 316 stainless steel data of Fig. 1 revealed similar kinetic behavior to what was observed over a shorter time period;[2,3] a power curve fit adequately describes the data and is consistent with mixed reaction rate control. Since, at longer times, the data can be adequately described by linear kinetics, the slope of a fitted straight line for times greater than 3000 h can be used to determine a "steady-state" dissolution rate.[3,4] In this case, such a procedure yielded a value of 77 mg/m^2·h. This dissolution rate is essentially the same as that obtained earlier for limited data between 3000 and 6000 h: 76 mg/m^2·h. It is much greater than that measured in lithium.[4] In contrast to the type 316 stainless steel data, a straight line best describes the 12Cr-1MoVW data over its entire exposure range, although there is substantial scatter among the data points (see Fig. 1). The dissolution rate obtained from the slope of this fitted line was 14 mg/m^2·h, which is significantly different from that determined previously[3] from just five data points between 0 and 6000 h. Again, this rate is greater than that measured at 500°C in lithium.[5]

It is interesting to note that while there is significant scatter in the weight loss measurements (see Fig. 1), there is extremely close agreement between such data when coupons of both steels were exposed for identical periods of time and then were cleaned under the same conditions. In the case of type 316 stainless steel, two specimens simultaneously exposed for 3886 h showed weight losses of 461 and 466 g/m^2. Each of two specimens of 12Cr-1MoVW steel exposed for 4027 h suffered weight losses of 50 g/m^2. These

results indicate that, under identical exposure and handling conditions, weight loss data from lead-lithium exposures are quite reproducible and that the observed scatter in the accumulated data probably arises from differences in the efficacy of a particular lithium rinsing procedure in removing the residual lead. While part of the scatter in the type 316 stainless steel data can be expected from partial detachment of the corrosion layer[2,3] during postexposure cleaning, such a process does not occur in the Cr-Mo steel case. It is thus reasonable to assume that variations in the amount of residual lead remaining on the surfaces after repeated cleaning can cause significant variations in the weight change measurements. However, the amount of such residual lead must be small since energy dispersive x-ray analysis of exposed surfaces normally failed to detect the presence of lead.

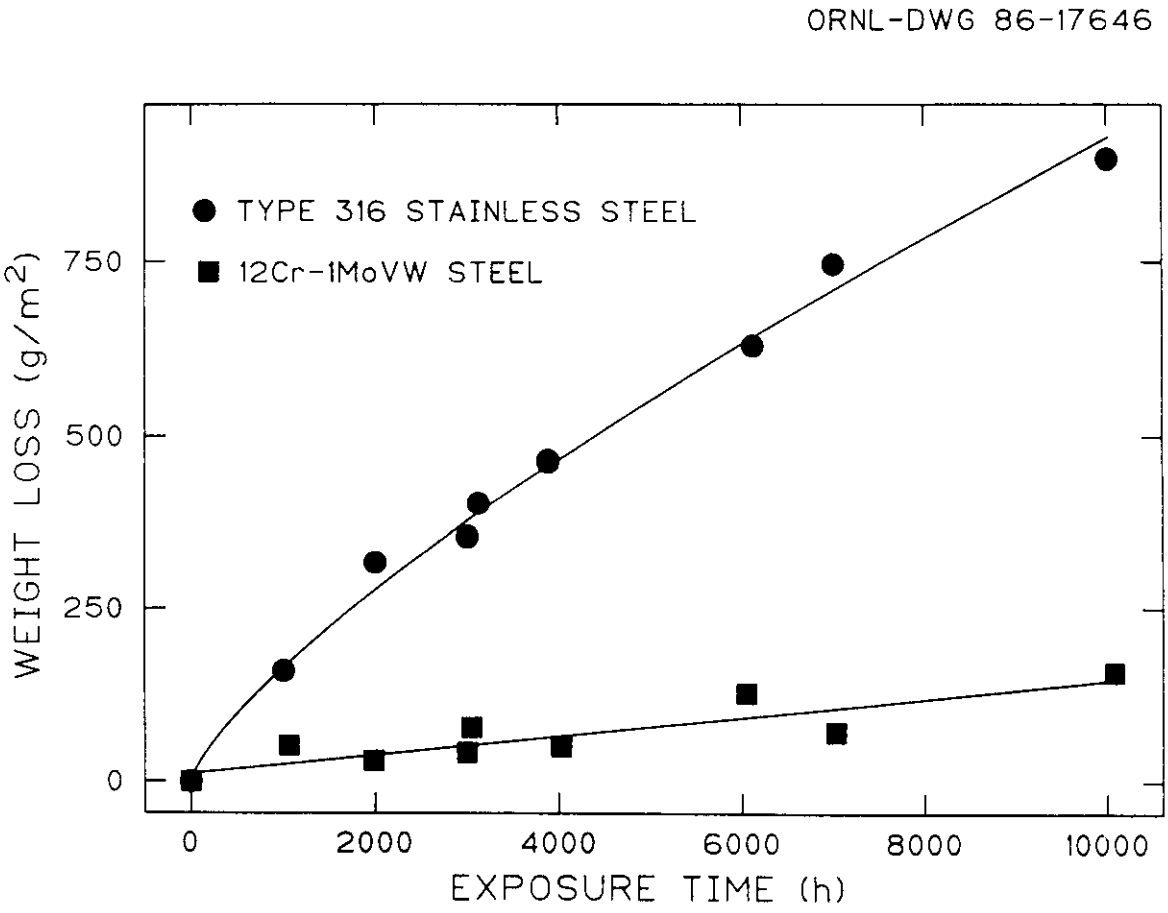

Fig. 1. Weight loss versus exposure time for type 316 stainless steel and 12Cr-1MoVW steel exposed to thermally convective Pb-17 at. % Li at 500°C.

The surfaces of type 316 stainless and 12Cr-1MoVW steels after about 7000 h of exposure are shown in Fig. 2. Note the very rough surface of the type 316 stainless steel relative to that of the Cr-Mo alloy. Such differences in corrosion-induced morphologies have also been noted previously[2,3] and are even more striking when such specimens are examined in cross section. Whereas the Cr-Mo alloys tend to corrode uniformly, the Fe-Ni-Cr austenitic stainless steel suffers severe localized corrosion resulting in deep penetrations into the specimens. Such a difference in surface recession behavior for the two types of steel has been shown to be adequately explained by the destabilization of a surface that undergoes preferential dissolution, as in the case of austenitic stainless steel, from which nickel and chromium are selectively removed due to exposure to molten Pb-17 at. % Li.[3] Although the roughness of the surface shown in Fig. 2(a) precludes strict quantitative analysis, energy dispersive x-ray analysis did indeed indicate such preferential dissolution for the type 316 stainless steel specimen. In contrast, according to this model, a planar surface should recede uniformly in the absence of selective leaching and this is exactly what is observed for the 12Cr-1MoVW steel: the surface concentration after 7027 h of exposure to lead-lithium was approximately the same as its starting concentration (see Table 1). Forthcoming cross sectional analysis of these specimens will yield more quantitative compositional data. The relative uniform corrosion of the 12Cr-1MoVW steel was still evident after 10,000 h (see Fig. 3). As also shown in Table 1, the surface composition of this specimen was again similar to its starting concentration.

ORNL DWG 86-18386

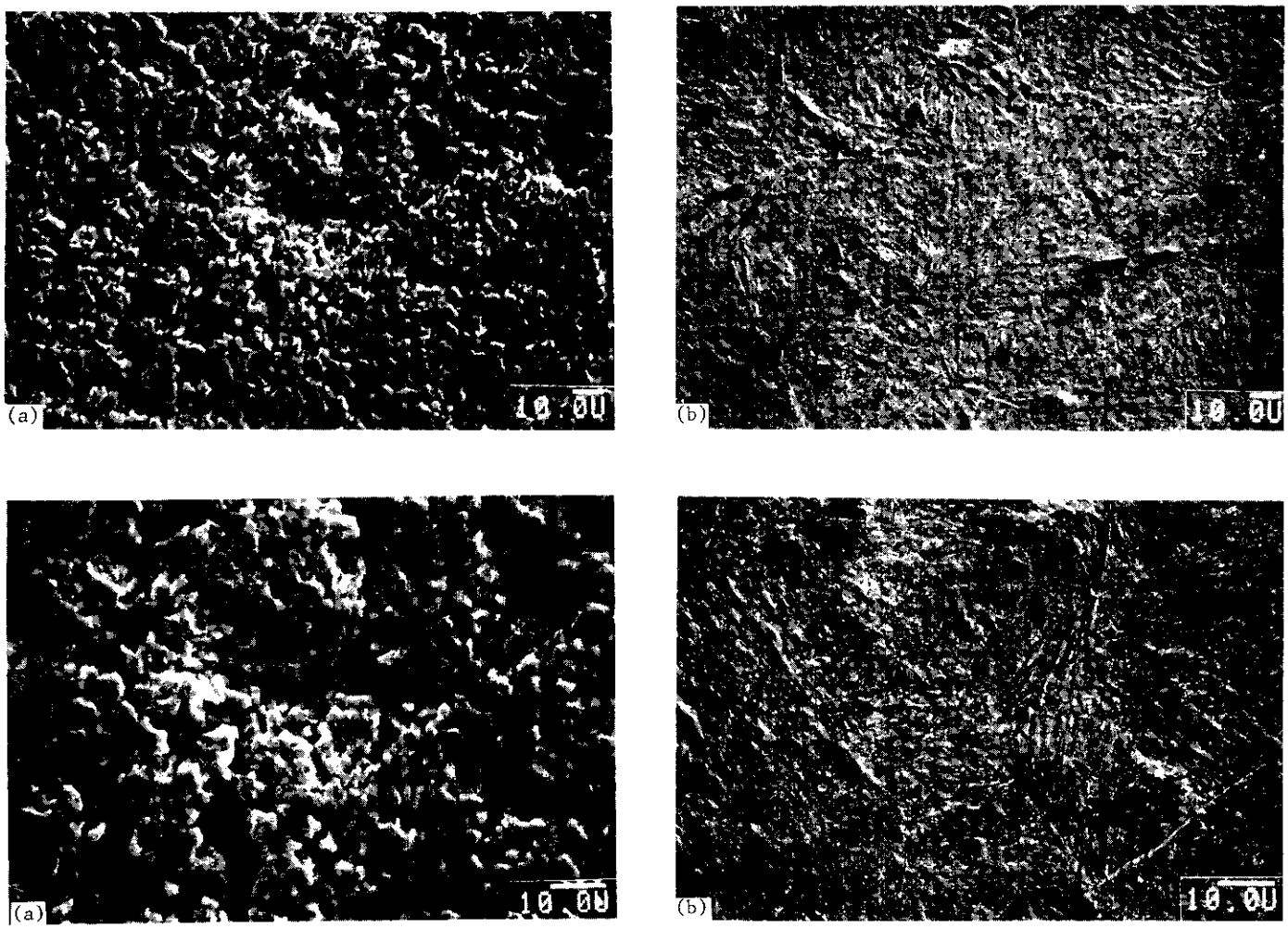

Fig. 2. Scanning electron micrographs of steels exposed to thermally convective Pb-17 at. % Li at 500°C. (a) Type 316 stainless steel, 7007 h. (b) 12Cr-1MoVW steel, 7027 h.

Table 1. Surface compositions of specimens exposed to thermally convective Pb-17 at. % Li at 500°C[a]

Alloy	Exposure time (h)	Composition (wt %)		
		Fe	Cr	Ni
type 316 stainless steel	7007	88	8	3
12Cr-1MoVW	7027	87	12	0.2
12Cr-1MoVW	10076	87	12	0.4

[a]As determined by standardless semiquantitative energy dispersive x-ray analysis.

ORNL DWG 86-18387

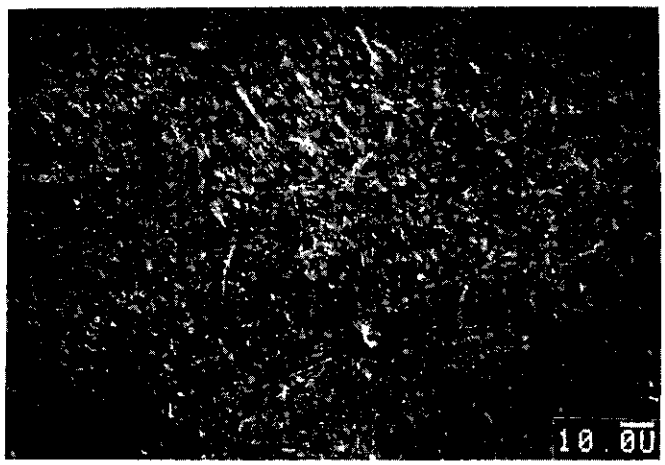

Fig. 3. Scanning electron micrograph of 12Cr-1MoVW steel exposed to thermally convective Pb-17 at. % Li for 10,076 h at 500°C.

The net flux, J, of a given element out of a specimen exposed to the molten lead-lithium can be expressed as

$$J = k(C_0 - C) \ , \qquad (1)$$

where k is the overall rate constant for dissolution or deposition, C_0 is the solubility of that element in the liquid metal at a particular temperature, and C is the actual concentration of the element in the liquid. For the present purposes, C can be considered constant around the loop so that the variation of the solubility with temperature determines whether dissolution ($C_0>C$, $J>0$) or deposition ($C_0<C$, $J<0$) occurs. Therefore, the positioning of coupons around the loops allows the measurement of mass transfer profiles for a given exposure time. Such profiles are shown in Figs. 4 and 5 for the type 316 stainless steel and the 12Cr-1MoVW steel loop experiments, respectively, and indicate substantial amounts of mass transport. (The weight losses and gains do not balance because coupons are not positioned in every part of the loop.) In the case of the type 316 stainless steel, the position of maximum deposition is not at the coldest point of the loop. This observation is similar to what has been found in similar loop experiments with lithium[4] and can most probably be ascribed to the fact that when $C_0<C$ [see Eq. (1)], k and $|C_0-C|$ vary in opposite directions with respect to temperature. Depending on the relative magnitudes of these kinetic and thermodynamic terms, this can then result in a maximum weight gain at an intermediate temperature.

CONCLUSIONS

1. Long-term (10,000 h) baseline thermal convection loop experiments of type 316 stainless and 12Cr-1MoVW steels in thermally convective Pb-17 at. % Li were completed. The results confirmed the aggressive behavior of this environment.

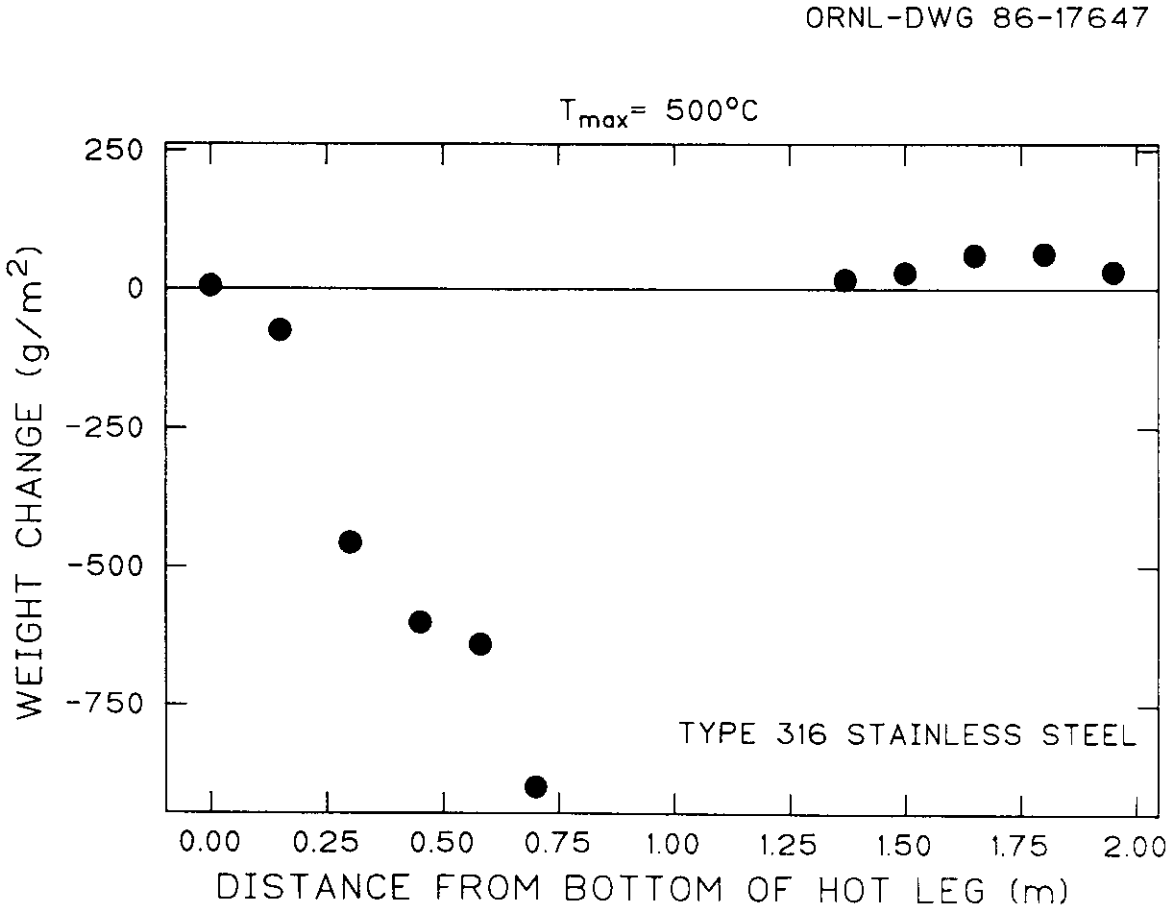

Fig. 4. Weight change versus loop position for type 316 stainless steel exposed to thermally convective Pb-17 at. % Li for 10,008 h at 500°C.

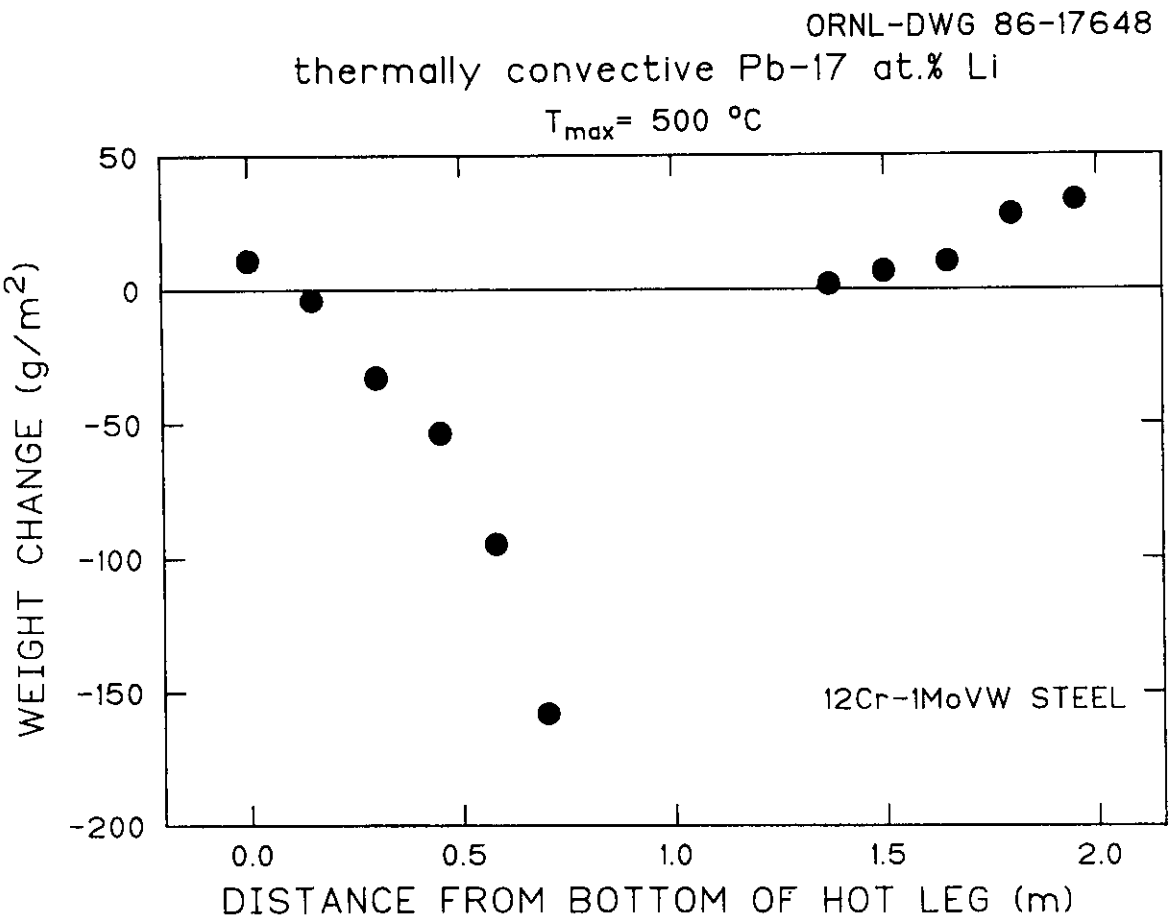

Fig. 5. Weight change versus loop position for 12 Cr-1MoVW steel exposed to thermally convective Pb-17 at. % Li for 10,008 h at 500°C.

2. Under identical exposure and cleaning conditions, measured weight losses were the same. Scatter in the weight loss data appears to be caused by variations in the amount of residual lead left on cleaned specimens and the effect of the cleaning process on the stability of the corrosion layer on type 316 stainless steel.

3. Surface analysis of type 316 stainless steel exposed to thermally convective lithium for 7007 h at 500°C showed preferential dissolution of nickel and chromium, whereas analysis of similarly exposed 12Cr-1MoVW steel revealed no significant change in surface concentration relative to the starting composition. Such observations are in accord with the model used to explain differences between the localized attack of type 316 stainless steel exposed to lead-lithium and the uniform surface recession of 12Cr-1MoVW steel.

4. Mass transfer profiles for the type 316 stainless steel revealed that the maximum deposition was not at the coldest point in the loop. Such behavior can be attributed to the product of thermodynamic and kinetic factors that vary oppositely with respect to temperature.

FUTURE WORK

During the next reporting period, the microstructural analysis of exposed specimens will be completed and corrosion inhibition experiments in the lead-lithium TCLs will be started. The purpose of the inhibition work will be to determine if additions to the melt will reduce corrosion and, if so, whether such additives inhibit corrosion by forming resistant surface layers or by influencing dissolution/deposition kinetics because of their presence in the liquid metal. The completion of the long-term thermal convection loop experiments in lead-lithium during the current reporting period will provide the necessary baseline data for comparison with results from these inhibition experiments.

REFERENCES

1. P. F. Tortorelli and J. H. DeVan, "Corrosion of Type 316 Stainless Steel and 12Cr-1MoVW Steel in Thermally Convective Pb-17 at. % Li," pp. 188–94 in *ADIP Semiann. Prog. Rep. Sept. 30, 1985*, DOE/ER-0045/15, U.S. DOE, Office of Fusion Energy.

2. P. F. Tortorelli and J. H. DeVan, "Thermal Convection Loop Studies of Ferrous Alloys Exposed to Molten Pb-17 at. % Li," pp. 181–85 in *ADIP Semiann. Prog. Rep. Mar. 31, 1986*, DOE/ER-0045/16, U.S. DOE, Office of Fusion Energy.

3. P. F. Tortorelli and J. H. DeVan, "Corrosion of Ferrous Alloys Exposed to Thermally Convective Pb-17 at. % Li, " *J. Nucl. Mater.* 141-143 (1986) 592-98

4. P. F. Tortorelli and J. H. DeVan, "Mass Transfer Kinetics in Lithium-Stainless Steel Systems," pp. 81–88 in *Proc. 3rd Intern. Conf. on Liquid Metal Engineering and Technol.*, vol. 3, The British Nuclear Energy Society, 1985.

5. P. F. Tortorelli and J. H. DeVan, "Corrosion of an Fe-12Cr-1MoVW Steel in Thermally Convective Lithium," pp. 215–22 in *Proc. Topical Conf. on Ferritic Alloys for Use in Nuclear Energy Technologies*, ed. J. W. Davis and D. J. Michel, AIME, 1984.

CORROSION OF FERRITIC STEELS AND V-15Cr-5Ti ALLOY IN FLOWING LITHIUM - O. K. Chopra and D. L. Smith (Argonne National Laboratory)

OBJECTIVE

The objective of this program is to investigate the influence of a flowing lithium environment on the corrosion behavior and mechanical properties of structural alloys under conditions of interest for fusion reactors. Corrosion rates are determined by measuring the weight change and depth of internal corrosive penetration as a function of time and temperature. These measurements, coupled with metallographic evaluation of the alloy surface, are used to establish the mechanism and rate-controlling process for the corrosion reactions. Initial effort on mechanical properties is focused on fatigue and tensile tests in a flowing lithium environment of controlled purity.

SUMMARY

Corrosion data are presented for several ferritic steels and the V-15Cr-5Ti alloy in a flowing lithium environment. The dissolution rates of low-activation ferritic steels and V-15Cr-5Ti alloy are compared with those for HT-9 and Fe-9Cr-1Mo steels. The influence of nitrogen content in lithium on the corrosion behavior of these alloys is discussed.

PROGRESS AND STATUS

Introduction

The corrosion behavior of several ferritic and austenitic steels has been investigated in a flowing lithium environment. A detailed description of the loop and the test procedure have been presented earlier.[1-3] The corrosion data and metallographic evaluation of ferritic HT-9 and Fe-9Cr-1Mo steel exposed to flowing lithium at temperatures between 538 and 372°C have been reported previously.[4,5] The results indicate that after an initial transient period of ~500 h, the weight losses for ferritic steels increase linearly with time and yield a constant dissolution rate. The dissolution rates increase with an increase in temperature. The dissolution behavior of HT-9 is comparable to that of Fe-9Cr-1Mo steel. After exposure to lithium, the alloy surfaces develop a dimpled appearance due to depletion of chromium from the steel. The dimpled structure is fully developed after ~1000 h of exposure and is associated with the significant weight loss during the initial period of exposure. An Arrhenius plot for the steady-state dissolution rates yield an activation energy of 16.3 kcal/mole.

Limited data indicate that an increase in nitrogen in lithium increases the dissolution rates of ferrous alloys. Metallic elements detected on the corrosion specimens indicate the presence of corrosion products on the alloy surfaces.[5] These products are most likely ternary nitrides of lithium and major alloy elements, e.g., Li_9CrN_5. In capsule tests, the Li_9CrN_5 compound has been observed on Type 316 stainless steel exposed at 600°C to lithium containing 20 wppm nitrogen.[6] The formation of this compound is associated with depletion of chromium from the steel. Recent measurements using an electrochemical nitrogen meter in liquid lithium yield a value of 12 wppm at 558°C as the equilibrium value for nitrogen in lithium for the formation of Li_9CrN_5.[6] The corrosion data for the present investigation were obtained in flowing lithium containing 50 to 100 wppm nitrogen, i.e., a nitrogen content above the equilibrium value required for the formation of ternary nitride. For these conditions of lithium purity, the dissolution of major elements as well as chemical reactions between nitrogen and chromium and/or iron control the corrosion behavior of ferrous alloys.

During this reporting period, the nitrogen content in lithium was decreased by hot trapping with titanium foils to values between 15 and 25 wppm. Corrosion tests were conducted at 482 and 427°C to assess the influence of nitrogen on corrosion, and the results are presented in this report. Corrosion data for some low-activation ferritic steels and the V-15Cr-5Ti alloy are also presented.

Corrosion behavior of ferritic steels

The chemical composition of the various ferritic steels is given in Table 1. The low-activation ferritic steels were supplied by D. S. Gelles of Westinghouse Hanford Company. The temperature and time of exposure and the loop operating conditions for the various corrosion tests are given in Table 2. Lithium was circulated at ~1 L/min in the primary loop.

The weight losses of the various ferritic steels exposed during run 8 to lithium at 482 and 427°C are shown in Fig. 1. The corrosion behavior of HT-9 and Fe-9Cr-1Mo steel is similar to that observed earlier in test runs 4-6, viz., a steady-state dissolution rate is achieved after an initial transient period. However, the weight losses of these steels after the transient period are lower than those observed in runs 4-6, e.g., the weight losses after 1000-h exposure at 482°C are 0.3 to 0.6 g/m^2 during run 8 relative to 1 to 1.2 g/m^2 during run 4, and at 427°C the weight losses are 0.2 to 0.4 g/m^2 compared to ~0.8 g/m^2 during runs 4 and 5.[5] The differences in the initial weight loss may be attributed to the chemical interactions

Table 1. Chemical compositions of ferritic steels

Alloy	Content (wt %)									
	Cr	Ni	Mo	Mn	Si	P	S	C	N	Other
HT-9	12.0	0.6	1.03	0.50	0.22	0.006	0.002	0.210	0.003	0.32V, 0.5W
9Cr-1Mo	8.8	-	0.92	0.40	0.36	-	-	0.098	0.011	0.21V, 0.06Nb
9Cr-0.5V	9.13	-	-	0.02	0.09	0.005	0.003	0.010	0.003	0.52V
9Cr-2.5Mn	8.82	-	-	2.44	0.10	0.005	0.004	0.101	0.002	0.27V, 0.89W
12Cr-6.5Mn	11.81	-	-	6.47	0.11	0.005	0.005	0.097	0.003	0.28V, 0.89W

Table 2. Lithium loop operating conditions for various corrosion tests

Test Run	Loop Temperature (°C)				N Content in Li (wppm)	Exposure Time (h)	
	Test Vessel	Spec. Exp. Vessel[a]	Supply Vessel	Cold Trap		Test Vessel	Spec. Exp. Vessel
4	482	427	410	212	50-100	5521	6501
5	427	372	372	206	~100	5023	4955
6	538	482	410	208	~50	3655	3330
8	482	427	426	213	15-20	2158	2062

[a]Lithium flow was from test vessel to specimen exposure vessel.

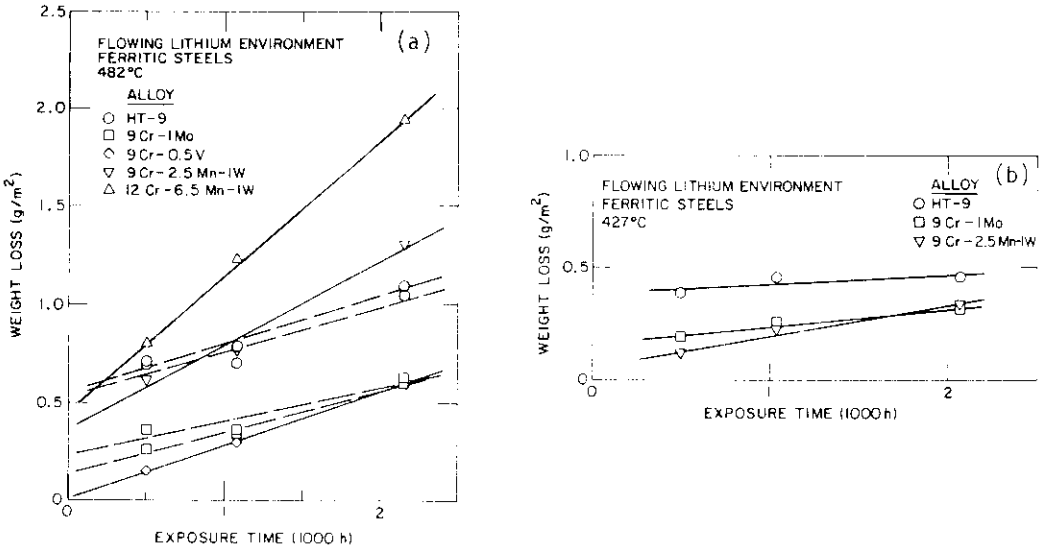

Fig. 1. Weight loss versus exposure time for several ferritic steels exposed to flowing lithium at (a) 482°C and (b) 427°C.

between nitrogen and chromium; the nitrogen content in lithium during runs 4 and 5 was ~100 wppm and it was 15-25 wppm for run 8. For both steels, the steady-state dissolution rates, however, are comparable to those obtained from runs 4 and 5.

The corrosion behavior of the low-activation Fe-9Cr-0.5V ferritic steel is similar to that for HT-9 or Fe-9Cr-1Mo steel, while the Mn-containing low-activation alloys exhibit higher dissolution rates. The Mn-containing steels are expected to yield higher dissolution rates since significant depletion of Mn has been observed in several ferritic and austenitic steels exposed to flowing lithium.

Corrosion behavior of V-15Cr-5Ti

The V-15Cr-5Ti alloy was exposed to lithium at 538, 482, 427, and 372°C during test runs 4-6. The maximum duration of most of the tests was between 1600 and 2500 h. The concentration of N and C in lithium was 50 to 100 and 6 to 12 wppm, respectively. For these conditions of lithium purity, nitrides of V and Ti and carbides of V, Ti, and Cr are expected to be stable (Fig. 2). The data from Ref. 6 for the equilibrium values of nitrogen concentration in lithium for the formation of Li_9CrN_5 are also plotted in Fig. 2. The results indicate that ternary Li_9CrN_5 nitride is also stable. The chemical interactions to form these compounds will have a dominant role in controlling the corrosion behavior of V-15Cr-5Ti alloy.

The weight losses of V-15Cr-5Ti exposed to flowing lithium at 538, 482, and 427°C are shown in Fig. 3. Weight losses at 372°C were <0.1 g/m^2 for times up to 3000 h and are not plotted in Fig. 3. The results indicate that the weight losses increase with an increase in time. Specimens exposed for ~5000 h at 372°C (run 5) yielded a linear increase in weight loss with time. Consequently, the results at higher temperatures are also represented by a linear law.

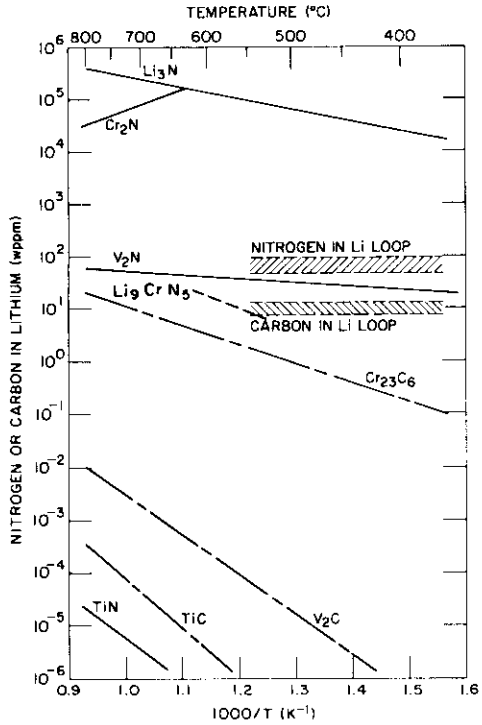

Fig. 2. Temperature dependence of the nitrogen and carbon concentrations in lithium at which selected structural metal nitrides and carbides are stable.

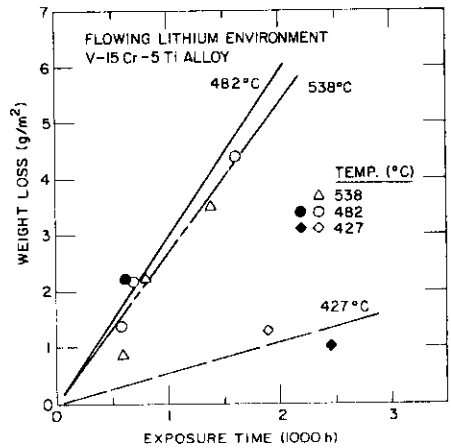

Fig. 3. Weight loss versus exposure time for V-15Cr-5Ti alloy exposed to lithium. Each symbol type represents weight loss for a single specimen after various exposure times.

Dissolution rates

The steady-state dissolution rates for the various ferritic steels and the V-15Cr-5Ti alloy are given in Table 3. The Arrhenius plot of the data for HT-9 and Fe-9Cr-1Mo steel is shown in Fig. 4. The temperature dependence of the rates may be represented by an activation energy of 16.3 kcal/mole. The results show that the dissolution rates in lithium are more than an order of magnitude lower than in the Pb-17Li environment. A maximum operating temperature of 550°C would yield an uniform corrosion rate of ~0.5 μm/yr.

The dissolution rates for HT-9 in a thermal convection loop at 500 and 600°C[7] and of Fe-9Cr-1Mo steel in a forced-circulation loop at 538°C[8] are also plotted in Fig. 4. The dissolution rate for Fe-9Cr-1Mo steel was obtained at a flow velocity of 1.82 m/s and is normalized to a value of 0.03 m/s using the relationship for corrosion of stainless steel in sodium. The corrosion rate R is expressed as

$$R \alpha (2.97 + 2.71\ V),$$

where V is the velocity in meters per second. The dissolution rates at 538 and 600°C are a factor of ~4 higher than those predicted from the best-fit line in Fig. 4. The variation is probably due to differences in the nitrogen content in lithium.

Table 3. Dissolution rates of ferritic and V-15Cr-5Ti exposed to flowing lithium

Test Run	Temp. (°C)	N Content in Li (wppm)	Maximum Time (h)	Dissolution Rate (mg/m^2 h)					
				HT-9	9Cr-1Mo	9Cr-1/2V	9Cr-2-1/2Mn	12Cr-6-1/2Mn	V-15Cr-5Ti
6	538	~50	3655[a]	0.401	0.391	-	-	-	2.66
6[b]	482	~50	1618	-	-	-	-	-	2.95
4	482	50-100	5521	0.173	0.144	-	-	-	-
8	482	15-25	2158	0.244	0.211	0.272	0.429	0.692	-
			2158	0.226	0.172	-	-	-	-
4[b]	427	50-100	5739	0.064	0.066	-	-	-	-
			6501	0.070	0.070	-	-	-	-
5	427	~100	5023[c]	0.077	0.062	-	-	-	0.54
8[b]	427	15-25	2062	0.042	0.078	-	0.138	-	-
5[b]	372	~100	4955	0.029	0.030	-	-	-	0.036

[a]Maximum exposure time for V-15Cr-5Ti was 1384 h.
[b]Specimens exposed in the specimen exposure vessel located downstream from the maximum temperature position in the test vessel.
[c]Maximum exposure time for V-15Cr-5Ti was 2465 h.

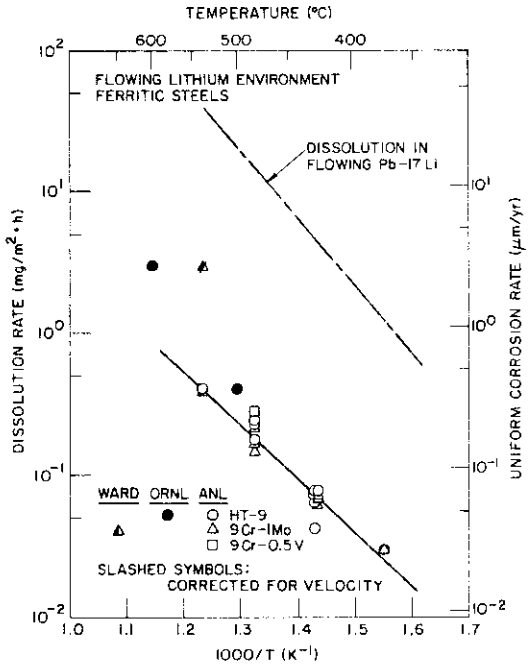

Fig. 4. Arrhenius plot of dissolution rate data for ferritic steels exposed to flowing lithium. ANL: Argonne National Laboratory; ORNL: Oak Ridge National Laboratory; WARD: Westinghouse Advanced Reactor Division.

The dissolution rates for the low-activation ferritic and the V-15Cr-5Ti alloy are compared with the best-fit curve for HT-9 or Fe-9Cr-1Mo steel in Fig. 5. The dissolution rates for the Mn-containing steels are a factor of 2 to 3 higher than for the other ferritic steels. The higher rates may be attributed to selective leaching of Mn from the steel. The data also indicate that at temperatures >450°C, the dissolution rates for V-15Cr-5Ti are an order of magnitude greater than for the HT-9 alloy. These results were obtained in lithium containing 50 to 100 wppm nitrogen, a value significantly above the equilibrium nitrogen content required for the formation of V_2N. The nitrides formed during lithium exposure may spall, thus increasing the corrosion rates. Preliminary examination of the V-15Cr-5Ti specimens exposed at 538 and 482°C show a very uneven surface with heavily corroded regions. These results indicate preferential attack of the surfaces.

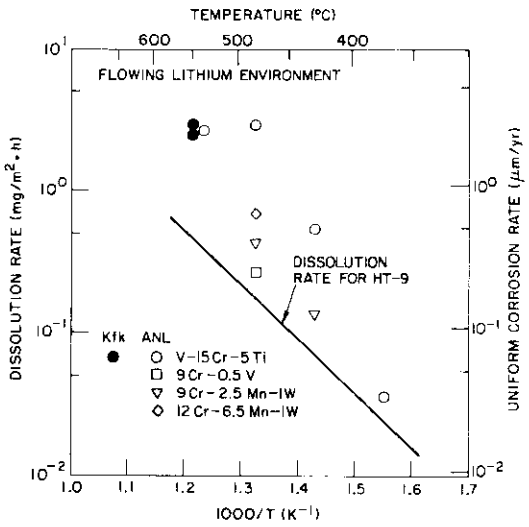

Fig. 5. Arrhenius plot of dissolution rates for low-activation ferritic steels and V-15Cr-5Ti alloy exposed to lithium containing 50-100 wppm N and 8-12 wppm C. KfK: Kernforschungszentrum, Karlsruhe.

The dissolution rates in Fig. 5 for V-15Cr-5Ti obtained at Karlsruhe[9] in lithium at 550°C show a good agreement with the results from the present study. These tests were conducted in lithium containing 10 wppm nitrogen (calculated from foil equilibration data). Although Fig. 2 indicates that V_2N is not stable at 550°C in lithium containing 10 wppm nitrogen, the specimens from the KfK study show hardened surface layers with very high nitrogen concentrations (i.e., 2-4 wt. %). Additional data are needed to establish standard procedures for more precisely determining the concentration of nitrogen in lithium and for quantifying the effects of nitrogen on the corrosion behavior of V-15Cr-5Ti alloy. Furthermore, although the influence of the carbon content in lithium on corrosion is not known, the calculated curves in Fig. 2 indicate that carbides should form at the measured carbon concentrations in lithium. Chemical interactions between carbon and metallic elements may also affect the corrosion behavior and need to be investigated.

CONCLUSIONS

Corrosion data for ferritic HT-9 and Fe-9Cr-1Mo steel indicate that the weight loss after the initial transient period decreases with a decrease in the nitrogen content in lithium. However, the steady-state dissolution rates are not significantly affected. Preliminary results for low-activation ferritic steels indicate that the dissolution rates for Fe-9Cr-0.5V steel are comparable to those for HT-9 or Fe-9Cr-1Mo steel while the rates for Mn-containing Fe-9Cr-2.5Mn and Fe-12Cr-6.5Mn steels are a factor of 2 to 3 higher. The data for V-15Cr-5Ti alloy indicate that chemical interactions between alloy elements and nitrogen or carbon in lithium play a dominant role in the corrosion behavior of this alloy when exposed to lithium containing 50 to 100 wppm nitrogen and 8 to 12 wppm carbon.

FUTURE WORK

Corrosion tests on several low-activation ferritic steels and V-15Cr-5Ti alloy are in progress at 482 and 427°C in lithium containing 15 to 25 wppm nitrogen. Tests are also planned in lithium containing <10 wppm nitrogen to evaluate the corrosion kinetics of vanadium alloys under conditions where nitride formation does not occur. The nitrogen content in lithium will be controlled by hot trapping using titanium foils. A lithium mass-transfer loop is also being constructed from Fe-9Cr-1Mo steel to study the dissolution/mass-transfer behavior as a function of temperature, velocity, and system temperature gradient.

REFERENCES

1. O. K. Chopra and D. L. Smith, "Environmental Effects on Properties of Structural Alloys in Flowing Lithium," pp. 176-182 in Alloy Development for Irradiation Performance: Semiannual Progress Report for Period Ending March 31, 1984, DOE/ER-0045/12, Oak Ridge National Laboratory, Oak Ridge, TN, July 1984.

2. O. K. Chopra and D. L. Smith, "Environmental Effects on Properties of Structural Alloys in Flowing Lithium," pp. 182-191 in Alloy Development for Irradiation Performance: Semiannual Progress Report for Period Ending March 31, 1985, DOE/ER-0045/14, Oak Ridge National Laboratory, Oak Ridge, TN, July 1985.

3. O. K. Chopra and D. L. Smith, "Corrosion of Ferrous Alloys in a Flowing Lithium Environment," J. Nucl. Mat. 133&134, 861-866 (1985).

4. O. K. Chopra and D. L. Smith, "Corrosion of Austenitic and Ferritic Steels in Flowing Lithium Environment," pp. 171-179 in Alloy Development for Irradiation Performance: Semiannual Progress Report for Period Ending September 30, 1985, DOE/ER-0045/15, Oak Ridge National Laboratory, Oak Ridge, TN, February 1986.

5. O. K. Chopra and D. L. Smith, "Influence of Temperature and Lithium Purity on Corrosion of Ferrous Alloys in Flowing Lithium Environment," to be published in J. Nucl. Mater.

6. M. G. Barker, J. A. Lees, and I. E. Schreinlechner, "The Corrosion of Type 316 Stainless Steels in Static and Dynamic Liquid Lithium," to be published in Proc. 14th Symposium on Fusion Technology, Avignon, September 1986.

7. P. F. Tortorelli and J. H. DeVan, "Thermal Convection Loop Studies of the Lithium Corrosion of Low-Activation Austenitic Alloys and Standard Fe-12Cr-1Mo VW Steel," pp. 197-204 in Alloy Development for Irradiation Performance: Semiannual Progress Report for Period Ending March 31, 1985, DOE/ER-0045/14, Oak Ridge National Laboratory, Oak Ridge, TN, July 1985.

8. G. A. Whitlow, W. L. Wilson, W. E. Ray, and M. G. Down, "Materials Behavior in Lithium Systems for Fusion Reactor Applications," J. Nucl. Mater. 85&86, 283-287 (1979).

9. H. V. Borgstedt and J. Konys, "Lithium Corrosion of the Alloys V15Cr5Ti and V3Ti1Si," presented at the Workshop on Lithium and Pb17Li Eutectic, Kernforschungszentrum, Karlsruhe, IMF II, May 1986.

CORROSION OF FERROUS ALLOYS IN FLOWING Pb-17Li ENVIRONMENT - O. K. Chopra and D. L. Smith (Argonne National Laboratory)

OBJECTIVE

The objective of this program is to investigate the influence of a flowing Pb-17 at. % Li environment on the corrosion behavior and mechanical properties of structural alloys under conditions of interest for fusion reactors. Corrosion behavior is evaluated by measuring the weight change and depth of internal corrosive penetration of alloy specimens exposed to flowing Pb-17Li for various times. The dissolution rates are determined as a function of temperature. Metallographic examination of the alloy surface is used to establish the mechanism and rate-controlling process for the corrosion reactions. Initial effort on mechanical properties is focused on tensile tests in a flowing Pb-17Li environment.

SUMMARY

Corrosion data have been obtained on low-activation ferritic steels in flowing Pb-17 at. % Li environment at temperatures of 482 and 371°C. The results are compared with the dissolution behavior of ferritic HT-9 and Fe-9Cr-1Mo steels and the austenitic Type 316 stainless steel.

PROGRESS AND STATUS

Introduction

The effects of a flowing Pb-17Li environment on the corrosion behavior of ferritic and austenitic steels are being investigated.[1-6] Tests are being conducted in a forced-circulation loop consisting of a high-temperature test vessel, a heat exchanger section, and a cold-temperature chamber. A detailed description of the loop and the experimental procedure have been presented earlier.[2,6] Four corrosion test runs of 2000 to 4000 h each were conducted at maximum temperatures of 371, 427, 454, and 482°C, respectively. For all corrosion tests, the cold-leg temperature was maintained at 300°C and the Pb-17Li alloy was circulated at a rate of ~350 cm^3/min.

The results indicate that the disssolution rates of ferritic HT-9 and Fe-9Cr-1Mo steel are an order of magnitude lower than those for Type 316 stainless steel. The weight losses for ferritic and austenitic steels increase linearly with time after an initial 500-h period characterized by large weight loss. The initial weight loss for ferritic steels is significant only at 482°C and is associated with preferential attack along grain boundaries and martensitic lathe boundaries. The large initial weight loss for Type 316 stainless steel is associated with the depletion of nickel and chromium from the steel and the subsequent formation of a ferrite surface layer. The ferrite layer is very porous and its thickness increases with time.

For all alloys, the dissolution rates increase with temperature and the Arrhenius plots of dissolution rates yield activation energies of 22.1 and 28.6 kcal/mol for the ferritic steels and Type 316 stainless steel, respectively. The data also indicate that corrosion/mass transfer is likely to be the most restrictive criterion for establishing the operating temperature limit for liquid Pb-17Li first wall/blanket systems. Assuming a corrosion limit of 20 μm/yr would yield a maximum operating temperature of ~500°C for HT-9 or Fe-9Cr-1Mo steel and ~410°C for Type 316 stainless steel in circulating Pb-17Li systems.

During the current reporting period, corrosion test run 4 was continued up to ~5600 h of exposure to evaluate the long-term dissolution behavior of several ferrous alloys. Corrosion specimens were exposed at the maximum temperature position as well as at a downstream location. The temperature at both locations was 371°C. The corrosion data from test run 4 are presented in this report. The corrosion behavior of two low-activation ferritic steels exposed to Pb-17Li during test runs 3 and 4 is also described. The low-activation ferritic steels were supplied by D. S. Gelles of Westinghouse Hanford Company.

Corrosion behavior

The corrosion behavior was evaluated by measuring the change in weight of the specimens exposed to flowing Pb-17Li for different times. The chemical compositions of the various alloys are given in Table 1. The weight losses for HT-9, Fe-9Cr-1Mo, and Type 316 stainless steel exposed at 371°C (run 4) are shown in Fig. 1. The weight losses for Fe-9Cr-1Mo steel are comparable to those for the HT-9 alloy. For all alloys, the weight losses increase linearly with time and yield average dissolution rates of 1.11 and 3.93 $mg/m^2 \cdot h$ for HT-9 or Fe-9Cr-1Mo steel and Type 316 stainless steel, respectively. The data for Type 316 stainless steel show significant scatter, probably due to the presence of a porous ferrite layer on the specimen surface. The ferrite layer often spalls during specimen cleaning, thus adding considerable variation in the weight change measurements.

Table 1. Chemical compositions of ferritic and austenitic steels

Alloy	Content (wt %)									
	Cr	Ni	Mo	Mn	Si	P	S	C	N	Other
HT-9	12.0	0.6	1.03	0.50	0.22	0.006	0.002	0.210	0.003	0.32V, 0.5W
9Cr-1Mo	8.8	-	0.92	0.40	0.36	-	-	0.098	0.011	0.21V, 0.06Nb
9Cr-0.5V	9.13	-	-	0.02	0.09	0.005	0.003	0.010	0.003	0.52V
12Cr-6.5Mn	11.81	-	-	6.47	0.11	0.005	0.005	0.097	0.003	0.28V, 0.89W
Type 316	17.00	13.4	2.49	1.90	0.64	0.024	0.020	0.070	0.034	

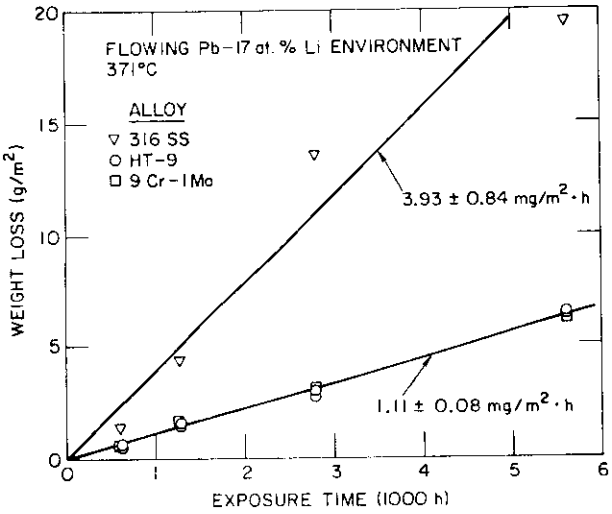

Fig. 1. Weight loss versus exposure time for ferritic and austenitic steels exposed to flowing Pb-17Li at 371°C. Each symbol type represents weight loss for a single specimen after various exposure times.

The weight losses of low-activation ferritic steels exposed to flowing Pb-17Li at 482°C (run 3) and 371°C (run 4) are shown in Fig. 2. The corrosion behavior of these steels is similar to that of HT-9 or Fe-9Cr-1Mo steel.[6] Specimens exposed at 482°C show significant weight loss after the initial 500-h exposure to Pb-17Li. At both temperatures, the weight losses and dissolution rates are comparable to those observed for the HT-9 alloy.

Dissolution rates

The Arrhenius plots of steady-state dissolution rates for the various ferritic steels and annealed and 20% cold-worked Type 316 stainless steel are shown in Fig. 3. Dissolution rate data obtained from other investigators[7-10] are also plotted in Fig. 3 and show good agreement with the results from the present study. The dissolution rate obtained at MOL for HT-9 at 450°C is, however, a factor of 4 higher. The difference is probably due to the method for calculating dissolution rates. The data from MOL were obtained from the total weight loss of the corrosion specimens after 1000-h exposure and do not represent the steady-state dissolution. At temperatures >450°C, the ferritic steels show significant weight loss during the initial 500 h due to preferential attack along grain and lathe boundaries. Consequently, the average dissolution rate after 1000 h would be higher than the steady-state rate achieved after longer times.

The dissolution rates for austenitic Type 316 stainless steel show significant variation at temperature above 450°C. When exposed to Pb-17Li, the austenitic steels develop a porous ferrite layer due to depletion of nickel from the steel. This surface layer is very weak and often spalls during exposure or cleaning. Consequently, the dissolution rates for austenitic steels show significant scatter since they represent the dissolution of major elements as well as the weight change due to the loss of the ferrite layer.

The solid lines in Fig. 3 represent the best fit for the dissolution rates for ferritic HT-9 and Fe-9Cr-1Mo steel and the austenitic Type 316 stainless steel. The results yield activation energies of 22.1 and 28.6 kcal/mole for the ferritic and austenitic steels, respectively.

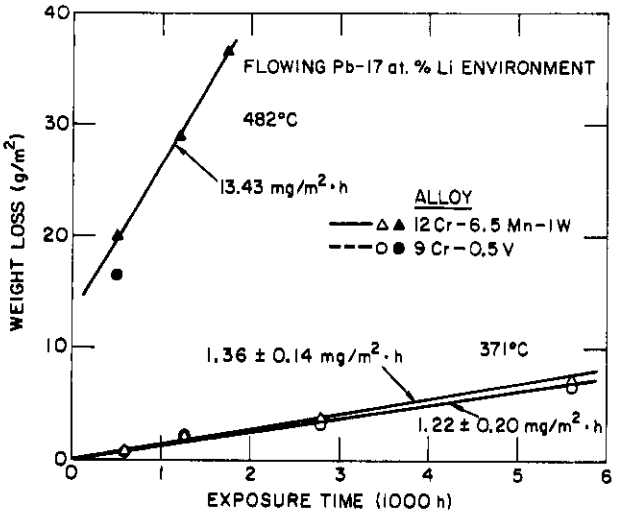

Fig. 2. Weight loss versus exposure time for low-activation ferritic steels exposed to flowing Pb-17Li at 482 and 371°C. Each symbol type represents weight loss for a single specimen after various exposure times.

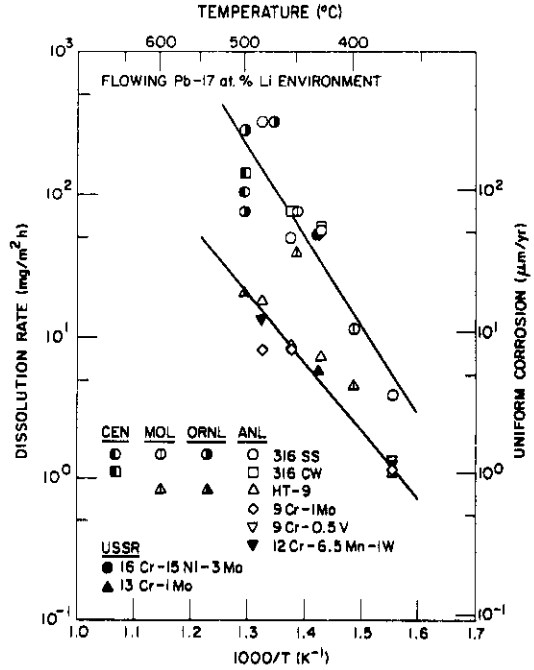

Fig. 3. Arrhenius plots of dissolution data for ferritic and austenitic steels exposed to flowing Pb-17Li. ANL: Argonne National Laboratory; ORNL: Oak Ridge National Laboratory; CEN: Centre D'Etudes Nucleaires, France; MOL: Studiecentrum Voor Kernenergie, MOL, Belgium; USSR: Soviet Union contribution to INTOR.

CONCLUSIONS

Corrosion data for low-activation ferritic steels in flowing Pb-17Li indicate that the dissolution behavior of these steels is similar to that for ferritic HT-9 or Fe-9Cr-1Mo steel. The temperature dependence of dissolution rates for Fe-9Cr-0.5V and Fe-12Cr-6.5Mn steel may be represented by an activation energy of 22.1 kcal/mole.

REFERENCES

1. O. K. Chopra and D. L. Smith, "Environmental Effects on Properties of Structural Alloys," pp. 216-200 in Alloy Development for Irradiation Performance: Semiannual Progress Report for Period Ending September 30, 1983, DOE/ER-0045/11, Oak Ridge National Laboratory, Oak Ridge, TN, March 1984.

2. O. K. Chopra and D. L. Smith, "Corrosion of Ferrous Alloys in Eutectic Lead-Lithium Environment," J. Nucl. Mater. 122-123, 1219-1224 (1984).

3. O. K. Chopra and D. L. Smith, "Corrosion of Structural Alloys in Flowing Pb-17Li Environment," pp. 183-189 in Alloy Development for Irradiation Performance: Semiannual Progress Report for Period Ending March 31, 1984, DOE/ER-0045/12, Oak Ridge National Laboratory, Oak Ridge, TN, July 1984.

4. O. K. Chopra and D. L. Smith, "Environmental Effects on Properties of Structural Alloys in Flowing Lithium," pp. 192-196 in Alloy Development for Irradiation Performance: Semiannual Progress Report for Period Ending March 31, 1985, DOE/ER-0045/14, Oak Ridge National Laboratory, Oak Ridge, TN, July 1985.

5. O. K. Chopra and D. L. Smith, "Environmental Effects on Properties of Structural Alloys in Flowing Lithium," pp. 167-170 in Alloy Development for Irradiation Performance: Semiannual Progress Report for Period Ending September 30, 1985, DOE/ER-0045/15, Oak Ridge National Laboratory, Oak Ridge, TN, February 1986.

6. O. K. Chopra and D. L. Smith, "Compatibility of Ferrous Alloys in a Forced Circulation Pb-17Li System," to be published in J. Nucl. Mater.

7. P. F. Tortorelli and J. H. DeVan, "Corrosion of Type 316 Stainless Steel and 12Cr-1MoVW in Thermally Convective 19-17 at. % Li," pp. 205-207 in Alloy Development for Irradiation Performance: Semiannual Progress Report for Period Ending March 31, 1985, DOE/ER-0045/14, Oak Ridge National Laboratory, Oak Ridge, TN, July 1985.

8. P. Fauvet, J. Sannier, and G. Santarini, "Corrosion of 316L Stainless Steel in Flowing 17Li83Pb Alloy," 13th Symposium on Fusion Technology, Varese, Italy, September 1984.

9. V. I. Nikitin et al., "Experimental Study of Selected Structural Materials Corrosion Resistivity in Pb-Li Eutectic," USSR Contribution to Phase IIA of the INTOR Workshop, October 1982.

10. H. Tas, Ja Dekeyser, and F. DeSchutter, "Corrosion of Structural Materials in a Li17Pb83 Natural Convection Stand," Contribution to Fourth International ENS/ANS Conference (ENC-4), Geneva, Switzerland, June 1986.

7. SOLID BREEDING MATERIALS

THE THERMAL CONDUCTIVITY OF MIXED BERYLLIA/LITHIUM CERAMIC IN SPHERE-PAC FORM - S. W. Tam and C. E. Johnson (Argonne National Laboratory)

OBJECTIVE

The objective of this program is to explore a novel concept to enhance the thermal conductivity of mixed Beryllia/Lithium ceramic in sphere-pace form.

SUMMARY

Lithium-containing ceramic tritium-breeder materials have been envisaged to be deployed within the blanket region of a fusion reactor in several possible configurations. One of these is the sphere-pac configuration. For this configuration an important material parameter is its thermal conductivity (K_{sp}). It is well known that K_{sp} demonstrates rather complex behavior as a function of temperature, gas pressure, gas composition, particle size, and packing fraction. The interrelationship of these parameters has been satisfactorily accounted for with a hierarchical effective media theory (HEMT). For tritium self sufficiency, most lithium ceramic breeder materials would require the presence of a neutron-multiplier (e.g., Be or BeO). Here, the influence of configuration on K_{sp} (i.e., how one put the different solid components together in the sphere-pac bed) becomes important. Using a generalized HEMT (i.e., a model with capability to describe systems with more than one solid material component), we have analyzed in detail the configurational dependence of K_{sp} for sphere-pac beds composed of lithium ceramic/BeO microspheres. Substantial improvements in K_{sp} can be achieved if a configuration of lithium ceramic spheres coated with BeO is chosen. Increases in K_{sp} would lead to enhanced mechanical and thermal performance of the breeder materials.

PROGRESS AND STATUS

Introduction

Lithium-containing ceramic breeder materials are among the leading candidates as tritium-breeder materials for fusion power reactors. One common form of these ceramic breeders is as sintered pellets or block format. A potential concern for ceramic materials in this form is the possible fracturing of these materials under relatively low stress levels. This fracturing would lead to a loss in mechanical integrity and possible degradation in thermal response. The sphere-pac (SP) configuration concept provides a possible solution to these problems.[1]

The sphere-pac concept involves the use of a bed of the ceramic breeder material in the form of microspheres of different sizes. The bed is usually permeated through with an inert gas such as helium. The need for a high packing fraction (of the order of 85 to 90%) for a more compact design requires microspheres of a fairly wide distribution of sizes. Such sphere-pac configurations would certainly minimize the potential for fracturing and loss of mechanical integrity. Much experience has been gained on the sphere-pac bed concept from fission technology research.[2] The nature of the sphere-pac configuration is such that its effective thermal conductivity (K_{sp}) can be significantly lower than the corresponding solid component. This is because of the limited contact between the spheres leading to the bulk thermal conductivity being dominated by the thermal conductivity (K_g) of the gas phase. Concepts that can lead to an enhancement of K_{sp} would provide definite benefits. This work describes a concept that can lead to an enhancement of thermal conductivity for materials of a sphere-pac configuration.

Consideration of the tritium breeding ratio (i.e., >1 for tritium self sufficiency) implies that for most solid breeder materials the addition of a neutron multiplier (e.g., Be or BeO) is a necessity.[1] Although the formalism presented in this work is in no way dependent on the specific material used for neutron multiplication, the following discussion is couched in terms of BeO. Exactly the same analysis could be employed should Be instead of BeO be chosen as the neutron multiplier, only the numerical results would be different. However, since Be has a higher thermal conductivity than that of BeO[3] one would expect our qualitative conclusions to be further reinforced.

The necessity for neutron multipliers leads to extra considerations for blanket designs that are generally less compact and more involved. However, the drawback of requiring neutron multipliers can, to some extent, be compensated by the enhancement of K_{sp} due to the presence of a highly thermally conductive component such as BeO (conductivity ~87 W/M-K compared to that of ~2.8 W/M-K for $LiAlO_2$ at T ~700 K).[3,4] The new notion introduced here is that there exists specific configurations (as compared to more conventional ones) through which the conductive component (BeO) can be introduced into the sphere-pac bed in such a manner so as to further enhance the effective thermal conductivity of the sphere-pac bed. By conventional configurations, one means those in which BeO is introduced in a random manner into sphere-pac beds in the form of spheres similar to that of the solid breeder component. We have found that by coating the solid breeder spheres (e.g., $LiAlO_2$) with the right amount of BeO one can achieve an optimized thermal conductivity for the coated-sphere configuration (CSC) that is greater than that of the conventional mixed-sphere configuration (MSC) of the same BeO/solid breeder composition. The basis for this conclusion is described in the following sections.

Theory

We have recently developed the hierarchical effective medium theory (HEMT) in order to estimate the thermal conductivity of finely divided materials.[5] For a sphere-pac bed composed of spheres of varying sizes HEMT is a particularly suitable tool. Sphere-pac beds prepared by successive mixing and vibratory compaction usually give rise to a heirarchical structure in which the interstices of the larger microspheres are occupied by that of the smaller ones. HEMT seeks to exploit this fact.

It starts with a two-phase medium with the smallest length scale in the system, namely the smallest microspheres immersed in an inert gas. The effective conductivity , $k_{eff}^{1,2}$, of this medium is calculated. Next we embed the particles of the next larger size into this effective medium, characterized by k_{eff}^{1}. The conductivity, k_{eff}^{2} of this new effective medium is then calculated. This scheme successively embeds the next larger sized particles into an effective medium of the smaller-sized spheres. The iterative procedure is carried out until it reaches the largest characteristic length scale of the problem, namely the size of the bed. Note that for each step of the iteration one only needs to due with a two-phase medium. This renders the problem much more tractable than otherwise. Since the basic iterative scheme of HEMT correctly mimics the complex heirarchical structure of actual sphere-pac beds, one expects that HEMT should be able to give a good account of K_{sp}. Comparison with literature data shows that this is indeed the case.[5] This generates confidence in HEMT and provides the motivation to generalize HEMT to take into account the presence of two materials components, namely Li ceramic and neutron multipliers.

These two components are considered to be arranged in two different configurations, namely, the coated-sphere configuration (CSC) and the mixed-sphere configuration (MSC). The CSC consists of a sphere-pac bed of touching spheres of $LiAlO_2$, each of which is coated with a layer of BeO of appropriate thickness, while the other configuration (MSC) is made up of randomly mixed similar-sized spheres of both $LiAlO_2$ and BeO. The relative volume fraction of BeO for the two beds is the same (20%). Both beds are assumed to be under a helium atmosphere. The spheres have diameters of 1200 μm, 300 μm and 35 μm, and they have, respectively, volume fractions of 0.511, 0.173, 0.182. These volume fractions are defined with respect to the total volume of the sphere-pac bed. They are typical of a fission-fuel sphere-pac system.[3] These system parameters can, of course, be varied without affecting the basic tenet of the theory.

Using these two generalizations to HEMT we have calculated the thermal conductivity of a sphere-pac bed in two configurations, i.e., the mixed-sphere and the coated-sphere configurations.

Results and Discussion

Figure 1 shows the calculated thermal conductivity of a sphere-pac bed in the mixed sphere (MSC) as well as the coated sphere (CSC) configuration. One notes immediately that K(CSC), the thermal conductivity of the coated-sphere configuration, is significantly above the corresponding conductivity for the mixed-sphere configuration K(MSC). To indicate in a quantitative manner the comparison between the two configurations we would introduce an enhancement factor, ε, defined as follows

$$\varepsilon = \frac{K(CSC) - K(MSC)}{K(MSC)} \times 100\%$$

where ε is a measure of the percentage enhancement achievable with CSC over that of MSC; it can also be considered a figure of merit for the CSC concept.

The results as shown in Fig. 1 indicate that ε varies from ~70% at 500 K to approximately 30% at 1500 K. The broad structure between 400 K and 600 K is a reflection of the different temperature dependance of the two configurations. In fact, K(CSC) decreases much more rapidly with temperature than does K(MSC). This can be easily understood since in the CSC concept there is a deliberate attempt to enhance the effective contribution of the more conductive component (in this case, BeO) to the overall thermal conductivity of the system. In turn, this leads to the result that over the temperature range considered K(CSC) decreases more rapidly with temperature since the thermal conductivity of BeO itself decreases much more rapidly with temperature than does that of $LiAlO_2$.[3,4]

The results shown in Fig. 1 have been obtained under a He pressure of 0.1 MPa (about 1 atmosphere). In powder-like systems such as the sphere-pac beds, the regions close to the points of contact between particles can have a linear dimension that is comparable or smaller than that of the mean free path of the gas (in our case, He). In that case, there could be significant pressure dependance of the thermal conductivity.[6] Again, the generalized HEMT was employed to estimate the pressure effect. The results are shown in Fig. 2.

The pressure range being considered is between P=0.1 to 0.9 MPa (approximately between one and nine atmospheres) at a temperature of 1000 K. Calculations also were carried out for a broad range of temperature. However, the results are qualitatively similar, and it is sufficient to center our discussion on the T=1000 K results.

Figure 2 indicates that for very moderate changes in gas pressure, significant enhancement in thermal conductivity can be achieved. In fact, for the CSC almost a factor of two was gained in thermal conductivity when the gas pressure was increased from 0.1 to 0.9 MPa. Although both K(CSC) and K(MSC) were affected by gas pressure, the CSC system is the more sensitive. This can be seen clearly in the enhancement factor ε, which increases rapidly with pressure initially and then tends towards a near-saturation value. Within the range of pressure considered, it is obvious that one has not yet reached saturation.

The results in Fig. 1 and Fig. 2 demonstrate the basic attractiveness of the CSC (i.e., coating) concept. It would be interesting to compare our present predictions when future experimental measurements become available. To proceed beyond this phase would require a detailed materials development program.

CONCLUSION

It is well understood that in order to characterize the properties of a complex heterogeneous medium one requires much more detailed microstructural information beyond simple averages. Differences in the details of the microstructural information, while retaining the same average as given by the volume fractions, can lead to substantial variations in the system properties. In fact, this point underlies one of the basic difficulties in constructing a satisfactory theory of the properties of heterogeneous media. However, our present concept of a coated-sphere configuration capitalizes on this system- dependance on microstructural details. The concept seeks to maximize the long-range connectivity of the better conductive component (namely, BeO).

Detailed considerations described in this work have demonstrated the qualitative performance expected of this concept as well as the quantitative enhancement achievable for the overall thermal conductivity of the composite system. It must be emphasized that although the present work concentrates on the $LiAlO_2$/BeO system, the coating concept is potentially applicable to other coating/substrate combination materials. For different coating/substrate combinations the detailed issues in a development program are likely to require different degrees of emphasis. However, a preliminary assessment of the potential attractiveness of any specific combination can be executed using the tool of a generalized version of HEMT, as described here and whose applicability has been demonstrated in this work.

FUTURE WORK

The sphere-pac configuration is receiving increasing attention in the international fusion community as an attractive option for tritium solid breeder deployment. The recent recognition that neutron multiplier materials are likely to be indispensible have prompted much increased activities. The present work provided a first step in addressing some of the critical issues that arises from consideration of solid breeder/neutron multiplier in sphere-pac configuration. It pointed to a number of crucial questions that needs to be answered if our coating concept in particular as well as the more generic consideration of multiplier/solid breeder combination is to be further developed. They include fabrication technique, coating integrity, alternative multiplier materials, and tritium behavior in multiplier materials. However, due to funding limitation, our ability to exploit and develop the lead that we have established in this area would be severely curtailed.

REFERENCES

1. "Blanket Comparison and Selection Study," D. L. Smith et al., ANL FPP 84-1, Argonne National Laboratory, 1984.

2. "Thermal Conductivity of Powders with LiO_2 or ThO_2 Microspheres in Various Gases from 300-1300K," J. P. Moore, R. J. Dippenaar, R. O. A. Hall, and D. L. McElroy, ORNL/TM-8196, June 1982.

3. "Thermophysical Properties of Matter, the TPRC Data Series," Vols. 2 and 3, Y. S. Touloukian, series editor; C. Y. Ho, series technical editor, IFI/Plenum, New York-Washington, 1970.

4. C. Denuzire and N. Roux, "Data and Properties of Lithium Aluminate $LiAlO_2$," C.E.N./Saclay Note 84/039, November 1984.

5. S. W. Tam and C. E. Johnson, accepted for presentation, Symposium on Fractal Aspects of Materials, Materials Research Society Fall Meeting, Boston, MA, Dec. 1-6, 1986.

6. R. O. A. Hall and D. G. Martin, J. of Nucl. Mat., 101, 172-83 (1981).

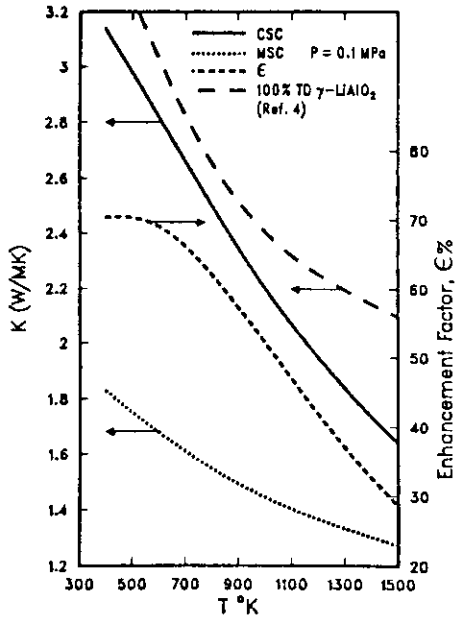

Fig. 1. Thermal conductivity of $LiAlO_2$ + BeO in different configurations (see text) versus temperature.

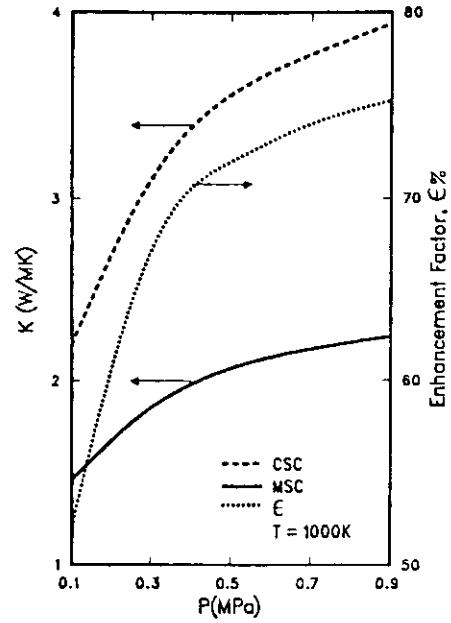

Fig. 2. Thermal conductivity of $LiAlO_2$ + BeO in different configurations (see text) versus gas pressure.

BEATRIX MATERIALS EXCHANGE IN THE INTERNATIONAL COMMUNITY - C. E. Johnson (Argonne National Laboratory) T. C. Reuther (U.S. Department of Energy) J. M. Dupouy (CEN/Saclay)

OBJECTIVE

A principal objective of this effort is to develop a collaborative program in which international partners will share data on irradiation behavior of ceramic breeder materials. This is being achieived thru the auspices of Annex II to the International Energy Agency Implementing Agreement for a Program of Reserach and Development on Radiation Damage in Fusion Materials.

SUMMARY

The BEATRIX experiment is an IEA-sponsored effort that involves the exchange of solid breeder materials and shared irradiation testing among research groups in several countries. The materials will be tested in both closed capsules (to evaluate material lifetime) and opened capsules (to evaluate purge-flow tritium recovery). Pre- and post-irradiation measurement of thermophysical and mechanical properties will also be carried out.

PROGRESS AND STATUS

Introduction

A critical element in development of fusion energy is the blanket for breeding tritium fuel. A program[1] is in progress to develop a data base for materials properties and irradiation behavior that can be used in evaluation and selection of a prime candidate breeder material. Lithium-containing ceramic materials (e.g., Li_2O, $LiAlO_2$, Li_4SiO_4, Li_2ZrO_3) are being given strong consideration because they offer the potential for tritium breeding, high-temperature stability, and ease of tritium recovery. Laboratory studies to measure the thermochemical, thermophysical, and mechanical properties of each material are underway. Irradiation experiments to test the response of each material to a neutron environment are being undertaken through a coordinated exchange of candidate breeder materials to ensure correlation among test environments and materials. The in-reactor experiments will give information on the response of the breeder material to a neutron environment and on the ease of tritium recovery.

Year-long capsule irradiation experiments (FUBR-1A)[2] have affirmed the attractiveness of ceramic breeder materials because of their chemical stability, resistance to radiation damage, and low tritium retention. These experiments also showed that swelling of Li_2O may be its least desirable property in comparison to the other ceramics. Since swelling is thought to be caused by defect and helium production, it is likely that swelling will be proportional to burnup and will increase at higher burnup levels. *In situ* tritium recovery experiments with $LiAlO_2$ (TRIO)[3] revealed low tritium solubility with this material, indicating that blanket tritium inventory is likely to be well below design guidelines. Complementary laboratory experiments on both irradiated and unirradiated materials are being undertaken to more rigorously define the tritium transport and release mechanisms. Such data are needed as input to models for analysis of breeder blanket designs.

Discussion

Because of the detailed technical knowledge required to understand the performance of a ceramic breeder blanket, an international collaborative effort has been established to conduct cooperative research on tritium breeding solids including Li_2O, $LiAlO_2$, Li_4SiO_4, Li_2SiO_3, and Li_2ZrO_3. This effort, which is under the auspices of Annex II to the International Energy Agency Implementing Agreement for a Program of Research and Development on Radiation Damage in Fusion Materials, involves the exchange of materials and shared irradiation testing. Participants in this program include Canada, the European Communities, Japan, and the United States. Contributing laboratories include CEA/Saclay, KfK/Karlsruhe, JAERI/Tokai, AERE/Springfield, CRE/Casaccia, and Argonne and Westinghouse-Hanford. This exchange program, named BEATRIX (Breeder Exchange mATRIX), will allow comparison of materials preparation and fabrication methods, irradiation techniques, and tritium extraction methods. Materials prepared by one partner will be irradiated in another partner's reactor. The irradiation experiments are of two types: closed-capsule tests to evaluate material lifetime, and open-capsule tests to evaluate *in situ* tritium recovery.

The in-reactor experiments are likely to impose thermal gradients upon the ceramic solid. Such temperature gradients may produce changes in the solid that could influence tritium transport and release. Thus, the in-reactor experiments are designed to more clearly define the relation between the thermal behavior of the solid and the mechanisms of tritium recovery.

Closed-capsule experiments will be done in mixed-spectrum reactors (HFR,[4] OSIRIS,[5a,b] and NRX[6a]) and in a hard-spectrum reactor (EBR-II[2]). These experiments are listed in Table I.

Probably the most detailed experiment, in the sense of variety of materials, is FUBR-1B because it involves five different materials, which are supplied by six different partners and are in three different configurations. This particular test will afford comparison of materials preparation and fabrication techniques for candidate breeder materials that will be irradiated under identical conditions. Experimental temeratures range from 500°C to 900°C (one casule at 1150°C). The experiment is also the only long-term (~2 yrs), high-burnup irradiation experiment in a hard-spectrum reactor. The data will significantly enlarge our understanding on the effects of temperature gradients and high fluence on the performance of solid breeder materials.

In the mixed-spectrum tests, a variety of materials will be tested using different irradiation vehicle designs in different reactors. The design of the EXOTIC[4] capsule allows for both open- and closed-capsule tests to be conducted simultaneously. In situ tritium extraction tests and detailed postirradiation tests (solubility and thermophysical and mechanical properties) will be carried out. The irradiation period is typically 25 days; temperatures of 400° and 600°C will be used. The materials being irradiated have been prepared by the USA, JAERI/Tokai, SCK/CEN-Mol, and SNL/Springfields. The EXOTIC experiment affords a direct comparison of Li_2O prepared by Argonne, Tokai, and Springfields. The ALICE[5a,b] and DELICE experiments are a continuing series of closed-capsule tests focused principally on the lithium aluminates and lithium silicates, which are irradiated in the OSIRIS reactor for 26-day cycles also at 400° and 600°C.

Postirradiation tritium release studies will focus on diffusion and desorption phenomenology. Irradiated materials from the ALICE experiments will also be used for measurement of fracture and tensile properties and compared with similar measurements made on unirradiated materials originating from the same lot. In the recently completed CREATE[6a] experiments, γ-$LiAlO_2$ and Li_2O were irradiated in sealed capsules, and the tritium release behavior was examined in postirradiation annealing experiments. Sweep gas composition, structural material, and ceramic characteristics were varied to determine their effect on release rate and the form of the released species.

Recent tritium release studies have shown that sintered materials of Li_2O[7] and Li_4SiO_4[8] exhibit high tritium diffusion even at temperatures as low as 400°C. The inclusion of solid breeder materials in the form of single crystals, high-density spheres, and sintered product (in experiments like ALICE and DELICE) will afford an excellent comparison of tritium diffusion in materials of different configuration. In the scope of this collaborative effort, diffusion coefficients from all tests will be compared to avoid a given experiment biasing the results.

The open-capsule tests (tritium recovery by purge-flow) provide complementary data on tritium release behavior for each solid under irradiation. Such data are extremely valuable in assessing steady-state tritium inventory and the influence of purge gas chemistry on tritium recovery. Several different purge-flow experiments are part of the BEATRIX materials exchange, and these are listed in Table II. These open-capsule tests will be performed in the HFR[6b], SILOE[7,9] and NRU[10] reactors. Each experimental system is equipped with an analytical train (gas station) for analysis of the tritium content of the purge gas and for characterization of the form of the released tritium, i.e., oxidized or reduced. Typically, the purge gas will contain small amounts of hydrogen to improve tritium desorption, through exchange, from the breeder surface.

The EXOTIC and LILA experiments will be the first purge-flow tests on Li_2ZrO_3, a material that exhibited excellent performance in the FUBR-1A irradiation. The CRITIC experiment test vehicle is quite similar to that of TRIO,[3] except for the fact that annular pellets of Li_2O, rather than $LiAlO_2$, are being irradiated. The LISA experiment will give attention to the silicates, with Li_4SiO_4 being present in the form of high-density spheres. The VOM-23H experiment will also contain high density spheres of Li_4SiO_4 (from Karlsruhe) in addition to rods of γ-$LiAlO_2$ (from Saclay).

TABLE I. BEATRIX; CLOSED-CAPSULE TESTS

Laboratory	Reactor	Experiment	Materials
Westinghouse/ Hanford	EBR-II	FUBR-1B	(Li_2O, γ-$LiAlO_2$, Li_2SiO_3 Li_4SiO_4, Li_2ZrO_3)
ECN/Petten	HFR	EXOTIC	(Li_2O, γ-$LiAlO_2$, Li_2SiO_3)
CEA/Saclay	OSIRIS	ALICE	(γ-$LiAlO_2$)
KFK/Karlsruhe	OSIRIS	DELICE	(Li_2SiO_3, Li_4SiO_4)
AECL/Chalk River	NRX	CREATE	(Li_2O, γ-$LiAlO_2$)

TABLE II. BEATRIX; PURGE-FLOW TESTS

Laboratory	Reactor	Experiment	Materials
ECN/Petten	HFR	EXOTIC	(Li_2SiO_3, $Li_2Si_2O_5$, Li_2ZrO_3, Li_4SiO_4)
CEA/Saclay	SILOE	LILA	(γ-$LiAlO_2$, Li_2ZrO_3)
KFK/Karlsruhe	SILOE	LISA	(Li_2SiO_3, Li_4SiO_4)
JAERI/Tokai	JRR2	VOM-23H	(Li_4SiO_4, γ-$LiAlO_2$)
AECL/Chalk River	NRU	CRITIC	(Li_2O)

CONCLUSION

Complementary irradiation experiments supported by detailed laboratory studies on materials preparation, fabrication, and properties will considerably enlarge the properties data base necessary for evaluation and selection of a prime candidate for the tritium breeder material. Data from several of the above experiments were reported at ICFRM-2, and other data will be forthcoming.

FUTURE WORK

Considerations are being given to further tests of candidate breeder materials to focus on a) basic material properties tests, and b) tritium recovery tests. Strong consideration is being given to using the fully instrumented FFTF/MOTA facility for conducting such tests.

REFERENCES

1. Johnson, C.E. and Hollenberg, G.W., J. Nucl. Mater. 122&123, 871-881 (1984).
2. Hollenberg, G.W. and Baldwen, D.L., J. Nucl. Mater. 133&134, 242-245 (1985).
3. Clemmer, R.G., et al., J. Nucl. Mater. 133&134, 171-175 (1985).
4. Kwast, H., Conrad, R., and Elen, J. D., J. Nucl. Mater. 133&134, 246-250 (1985).
5a. Rasneur, B., Proceedings Sixth Topical Meeting on the Technology of Fusion Energy, San Francisco CA, March 10-15 (1985) p. 1909.
5b. Benoit, R., et al., 13th Symposium on Fusion Technology SOFT, p. 1242 (1984).
6a. Miller, J. M., Bokwa, S. R., and Verral, R. A., Proceedings ICFRM-2, Chicago, IL, April 13-17, 1986.
6b. Kwast, H., et al., Proceedings ICFRM-2, Chicago, IL, April 13-17, 1986.
7. Werle, H., et al., Proceedings ICFRM-2, Chicago, IL, April 13-17, 1986.
8. Kurasawa, T., et al., Proceedings ICFRM-2, Chicago, IL, April 13-17, 1986.
9. Briec, M., et al., Proceedings ICFRM-2, Chicago, IL, April 13-17, 1986.
10. Hastings, I. J., Proceedings 7th Annual Conf. Canadian Nuclear Soc., Toronto, Canada, June 8-11, 1986.

ADSORPTION, DISSOLUTION, AND DESORPTION CHARACTERISTICS OF THE $LiAlO_2$-H_2O SYSTEM - A. K. Fischer and C. E. Johnson (Argonne National Laboratory)

OBJECTIVE

The objective of this work is to provide measured thermodynamic and kinetic data related to tritium retention and release from ceramic tritium breeders in fusion reactors. This information will (1) enable breeders to be compared and the most suitable one to be selected, and (2) enable operating conditions to be calculated. An additional objective is to elucidate the principles underlying the behavior of tritium in breeders as well as other interactions of breeders with reactor components.

SUMMARY

Experimental measurements are being made of surface adsorption of H_2O on $LiAlO_2$, the solubility of hydroxide in $LiAlO_2$, and the kinetics of release of H_2O from $LiAlO_2$. Up to about 500°C, evolution of H_2O is first order in dissolved protons (hydroxide). At higher temperatures, the reaction appears to shift to second order. Solubility of hydroxide appears to decrease with increasing temperature. A second condensed phase can appear at about 315°C for a partial pressure of H_2O of 550 vppm. The critical partial pressure of H_2O to form a LiOH--rich second phase can be similar for all breeders. Two different kinds of lattice sites appear to be involved in hydroxide dissolution. Surface adsorption of molecular oxygen or hydrogen can be understood to influence tritium release rates markedly; the thermodynamic and kinetic effects of these gases on the release rates operate in the same direction. "Tritium" diffusion is to be identified with triton diffusion.

PROGRESS AND STATUS

Introduction

Adsorption, dissolution, desorption and H_2O evolution are being measured for the $LiAlO_2$-H_2O-H_2 system to provide thermodynamic and kinetic information for the breeder, $LiAlO_2$. Earlier, extensive computational evaluations of these and other quantities were made on the basis of assumed ideal solution behavior in this system.[1] The present work will allow more realistic calculations to be made.

Frontal analysis gas chromatography (the breakthrough technique) is being used for the measurements of adsorption. Post-adsorption uptake of water vapor is being measured to determine the solubility of hydroxide in $LiAlO_2$. The data will yield adsorption isotherms to describe the thermodynamics of adsorption of water vapor and of hydroxide as a solute. The reverse processes, desorption and evolution of water vapor, are being measured to describe the kinetics of the release of water vapor. Determination of the dependence of these quantities on oxygen activity is included in the experimental program. Data have been obtained for a gas of 550 vppm H_2O in helium and in the temperature range of 213 to 618°C at relatively high oxygen activity (over 10^{-6}).

Adsorption-Dissolution Measurements

The overall comparison of the adsorption--dissolution processes at the different temperatures is presented in Fig. 1. The curves show the rate of water vapor flow issuing from the end of the chromatographic column as a function of time. (The ordinate is in units of "nominal ppm" which is related to moles/min by a calibration factor given in the caption.) The different behavior of the curves for 317 and 318°C compared to the others is believed to reflect the appearance of a second condensed phase, a LiOH--rich one in addition to the dominant $LiAlO_2$--rich one. This phenomenon can be understood in terms of the H_2O partial pressure in these measurements at 318°C being greater than that over the Li_2O--LiOH system at this temperature. It follows that the maximum partial pressure of HTO, T_2O, or H_2O to avoid formation of a second condensed phase that is LiOH--rich could be similar for all breeders. Differences would be due mainly to the extent that different breeders would show different degrees of solubility in LiOH to lower the activity of LiOH in the second phase to different degrees.

Heats of adsorption, solubilities, and activity coefficients have not been calculated yet because corrections for baseline differences and for non--adsorbed gas retention times still need to be determined. However, the qualitative indications are that the solubility of hydroxide for a fixed partial pressure of H_2O decreases with increasing temperature.

Kinetics of Evolution of Water Vapor

Isothermal evolution of water vapor into a stream of pure helium was measured. The early parts of the evolution curves in Fig. 2 show a short plateau before dropping off. This region reflects the process that is the converse of breakthrough and measures surface desorption, leading to information on surface desorption isotherms. The region of declining rate of water evolution reflects the dissolved hydroxide coming out of solution.

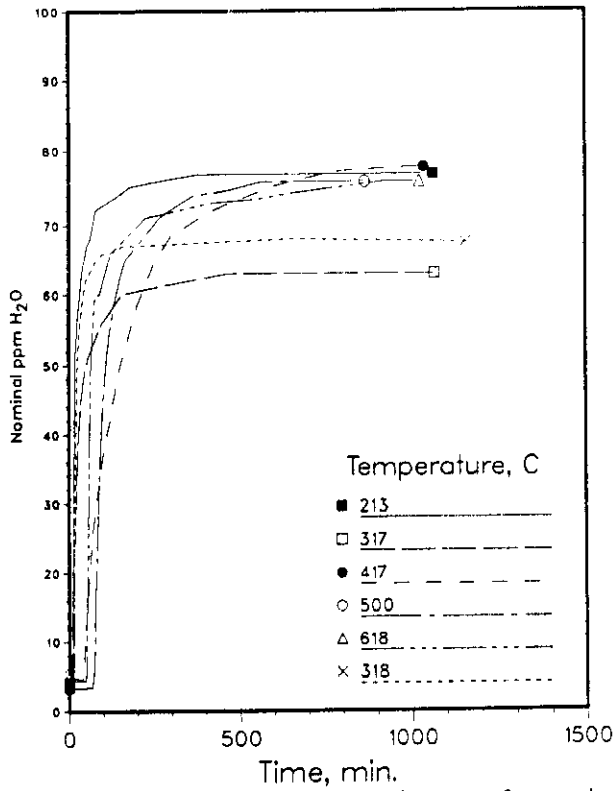

Fig. 1. Adsorption and dissolution of H_2O vapor from a helium stream containing 550 vppm H_2O. Flow rate is 13.8 std.cc/min. "Nominal ppm" x 4.145×10^{-9} = moles/min.

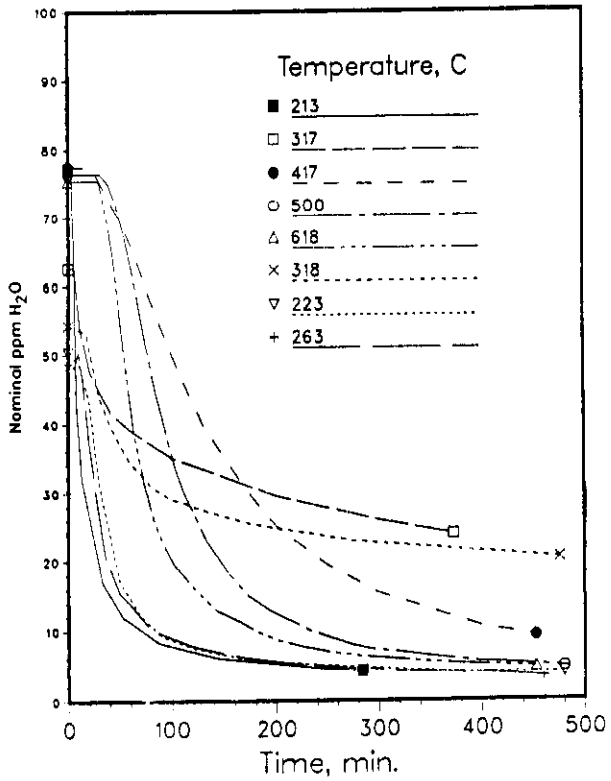

Fig. 2. Desorption and evolution of H_2O vapor from $LiAlO_2$. Same units as in Fig. 1.

First order and second order kinetics tests were applied to the water evolution data. For all temperatures considered so far with the exception of the 618°C case, the rate of evolution of water vapor during the first several hundred minutes reflects a rate--limiting process that is kinetically first order in dissolved hydroxide and suggests "hydroxide" diffusion to be the process. Since the diffusing species in solid solution (or on the surface, for that matter) is the proton, which effectively results in apparent hydroxide diffusion, these results actually indicate that the evolution of water is first order in the proton concentration. Combination of hydroxides on the surface to evolve water would be taken to be a second order process. A selected case, the one for 318°C shown in Fig. 3 shows the excellent fit of the fitted regression line to experimental points for a test of first order kinetics. However, for the 618°C case, which is not shown, the fit is better to second order kinetics than to first order kinetics, but not perfect. At higher temperatures, therefore, the rate limiting process may be shifting to a second order one, that is, a process of proton surface--diffusion and surface combination of hydroxides. Temperature alone might not be the only variable determining this; at lower temperatures, very low concentrations might also lead to surface--diffusion controlled rates of release.

Bakeout Measurements

For some cases, the furnace setpoint was raised to about 615°C after the measurements of water evolution at the temperature of the main measurement were finished. An example of these non--isothermal bakeouts is shown in Fig. 4. Two main peaks appear, and a small additional one appears on the early time side of the first large one. The interpretation of these observations is that the small peak (at about 20 min) reflects desorption of water from sites of surface adsorption and the two large peaks relate to protons, localized as hydroxide groups, at two different kinds of oxide sites in the $LiAlO_2$ lattice. The crystal structure of $LiAlO_2$ is known to have significantly different interoxide ion distances for oxides in tetrahedra around a lithium ion compared with the distances in tetrahedra around aluminum ions. Such different sites would be expected to allow protons to diffuse with different energetics and rate constants.

Kinetic Impact of Oxygen or Hydrogen Adsorption on Tritium Release Rates

It is known that the conductivity and carriers in a semiconductor can be influenced markedly by surface adsorption of either oxygen or hydrogen.[2,3] The adsorption of the molecular forms of these gases also has implications for ionic transport as well as for electronic or hole conductivity. It is now believed that adsorption of an electron--withdrawing material, such as oxygen, will induce in the solid surface region a boundary layer of positive charge.[2] Such a layer would present a repulsive barrier for penetration by protons moving to the surface so that evolution of proton--containing species would be inhibited. Conversely, adsorption of hydrogen, an electron--donating material, will enhance electron density in the near-surface oxides and present an attractive region into which proton diffusion will be enhanced. The magnitude of surface charge effects (at least the ones involving point defects) is substantial, both in depth (tenths of a micron) and in electric field gradient (thousands of volts/cm).[4]

These adsorptive effects can now be seen for the first time as a contributing kinetic cause for the greatly diminished release of tritium that was observed in the TRIO runs when oxygen was introduced into the sweep gas. It also rationalizes the common finding in release experiments that molecular hydrogen in the sweep gas enhances tritium release. These are kinetic effects related to oxygen activity. In addition, there is also the thermodynamic contribution by which high oxygen activity favors the more strongly adsorbed species, HTO or T_2O. Thus, oxygen activity now can be expected to affect tritium release kinetically in the same direction as thermodynamically. These concepts relate to any process involving proton diffusion through oxides, such as diffusion through oxide films, as well as to release from breeders.

Identification of "Tritium" Diffusion with Triton Diffusion

A considerable background of data and theory exists that provides strong analogical grounds for regarding "tritium" diffusion in ceramic breeders as triton diffusion. This earlier work was concerned, of course, with proton diffusion rather than triton diffusion and included both oxides and complex mixed oxides.[5] With the proton as the mobile species, diffusion involves the proton hopping from oxide ion to oxide ion so that the apparent motion is hydroxide diffusion. Due to the small ionic radius (about 10^{-4} A), the high polarizing power of a proton or triton leads to a strong tendency toward covalent bond formation with an oxide ion. As a result, it is reasonable to regard the proton or triton as remaining localized as hydroxide or tritoxide on the oxide sublattice and on which it moves about. Considerable physical evidence attests to the presence of the O--H bond in oxides. However, an especially relevant paper[6] reports infrared spectroscopic evidence for solute OH^- in alumina bombarded with protons.

It seems reasonable that on the basis of the concept of proton hopping, an initial understanding of tritium diffusion in ceramic breeders should center on the features of the oxide ion sublattice. The oxide sublattice approach would involve evaluating the diffusional pathways determined by the crystallographic O^{-2}-O^{-2} distances and of the lattice structures. Additional effects can be expected from modifications in the oxygen sublattice caused by vacancies in it, by polarization of oxide sites by the lithium ion or other

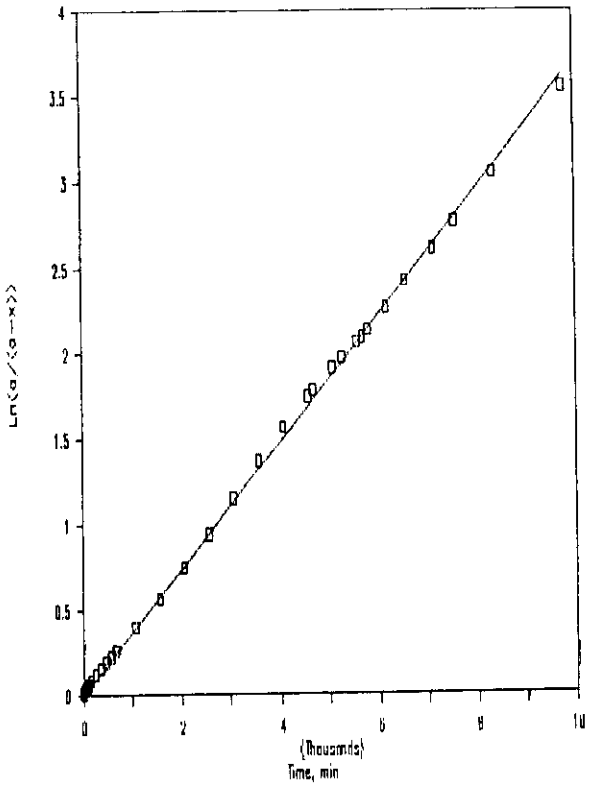

Fig. 3. Test for first order kinetics in evolution of H_2O at 318°C: regression line and experimental points. Order is first order in dissolved hydroxide.

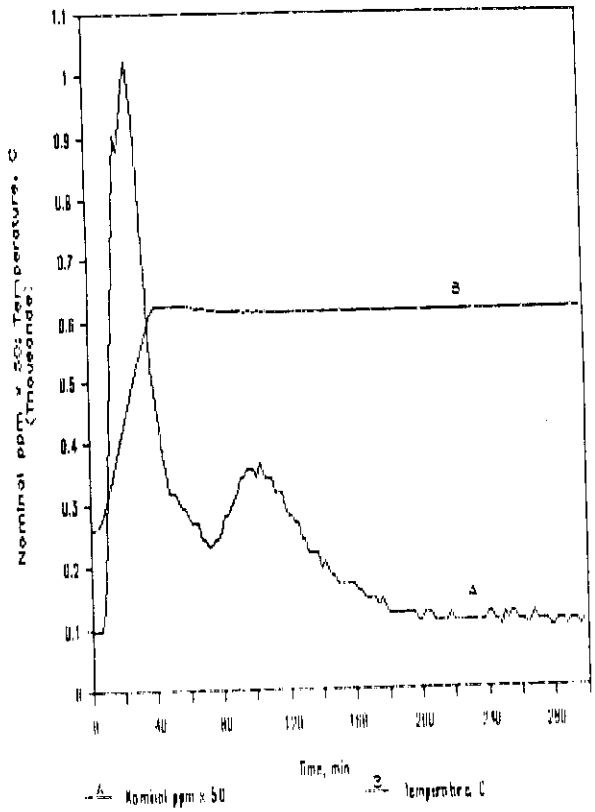

Fig. 4. Evolution of H_2O vapor during temperature ramp from 262 to 613°C and at 613°C.

cation sublattices and by vacancies in them, by impurities, and by orbital hybridization. From this viewpoint, it has been possible on the basis of only interionic oxide distance considerations to rationalize the differences in diffusion coefficients of tritium in $LiAlO_2$, Li_2O, and alumina.

CONCLUSIONS

Measurements of adsorption of H_2O, dissolution of hydroxide, and evolution of H_2O from $LiAlO_2$ are providing important data for the thermodynamics of adsorption, for hydroxide solubility, and for the kinetics of water vapor evolution. The triton has been indicated to be the diffusing species, and tritoxide to be the solute species.

FUTURE WORK

The present work will involve gathering sufficient additional data to construct adsorption isotherms, to determine solubility of hydroxide as a function of temperature and partial pressure of H_2O, and to determine activation energies of H_2O evolution. Subsequently, the breeder material, Li_4SiO_4, will be the probable candidate for study in the same way so that ultimate programmatic comparison of the two will be possible.

REFERENCES

1. A. K. Fischer, J. A. McDaniel, and C. E. Johnson, "Studies of Surface Adsorption on $LiAlO_2$," Proceedings of International Conference on Fusion Reactor Materials, II, Chicago, April 1986 and references therein.

2. E. G. Rochow, "Alternosorption," J. Inorg. Nucl. Chem., 29(1967)65.

3. S. E. Schwartz and E. G. Rochow, "Alternosorption--II. Inorganic Oxides at High Temperatures," J. Inorg. Nucl. Chem. 29(1967)1559.

4. L. Slifkin, "Subsurface Effects in Ionic Crystals," Mater. Sci. Forum 1(1984)75.

5. R. Gonzalez, Y. Chen, and K. L. Tsang, "Diffusion of Deuterium in Amorphous Cordierite," J. Am. Ceram. Soc. 67(1984)775.

6. D. M. Gruen, R. B. Wright, R. L. McBeth, and I. Sheft, "Hydroxyl Formation Accompanying Defect Center Production in Proton and Deuteron Bombarded Aluminum Oxide," J. Chem. Phys. 62(1975)1192.

SOLID BREEDER MATERIALS FABRICATION AND MECHANICAL PROPERTIES - R. B. Poeppel (Argonne National Laboratory)

OBJECTIVE

The objectives of this program are to synthesize ceramic powders and/or fabricate samples of candidate solid breeder materials for various international cooperative irradiation test programs and to characterize the mechanical properties of a number of lithium ceramics.

SUMMARY

The preliminary measurements of mechanical properties of lithium oxide were completed. Several batches of lithium zirconate (Li_2ZrO_3) powder were synthesized and sent to Hanford Engineering and Development Laboratory to be fabricated into FUBR-1B replacement capsules. Lithium oxide powder was prepared and the fabrication of ring-shaped Li_2O samples was initiated for the CRITIC experiment. Mechanical properties tests were initiated on $LiAlO_2$ and Li_2ZrO_3. Approximately 4000 kg of sintered lithium carbonate blocks were prepared and sent to Japan for neutronics cross-section tests.

PROGRESS AND STATUS

Constant-crosshead-speed compression of Li_2O polycrystals has been performed at temperatures of 700 to 950°C with strain rates ranging from about 10^{-6} to 10^{-4} s^{-1}. For temperatures greater than 850°C, data suggest deformation rates are controlled by recovery via dislocation climb. For lower temperatures, impurity effects may alter the deformation mechanism. At 950°C, viscous creep occurs at low strain rates. For porosities ranging from about 7 to 21%, deformation is strongly dependent on porosity, but is virtually independent of grain size.[1]

Fine-grained, sinterable lithium oxide powder was prepared by high-temperature, vacuum calcination of molten lithium carbonate. The product was ball milled, cold pressed, and fired in an oxygen atmosphere. The fired density, grain size, and surface roughness vary widely with firing schedule. Most variations can be attributed to moisture content. Rings of high-density, sintered lithium oxide will be sent to Chalk River to be used in the CRITIC in-reactor experiment to measure tritium release.[2]

The stress-strain behavior of $LiAlO_2$ and Li_2ZrO_3 polycrystals, with densities in the range from 0.70 to 0.95 of the theoretical, has been measured in constant-crosshead-speed compression tests at temperatures of 700 to 1000°C with strain rates ranging from about 10^{-6} to 10^{-4} s^{-1}. A steady-state stress, σ_s, for which the work-hardening rate vanishes, was achieved. These results, therefore, yield information equivalent to that obtained from creep experiments. Limited data on $LiAlO_2$ and Li_2ZrO_3 were obtained. Nevertheless, under comparable conditions, the lithium aluminate and zirconate were considerably stronger than lithium oxide. This finding may be related to differences in crystal structure. It is, however, likely that in operation as a fusion breeder blanket material, the oxide will swell whereas the aluminate and the zirconate will crack.[3]

Lithium carbonate is a stable, convenient, and inexpensive compound of lithium, especially suited to ambient-temperature neutronics experiments. The material was sintered at 390°C to provide a uniform and structurally stable lithium atom distribution. Lithium carbonate powder was blended with binder and sintering aid, spray dried, pressed into bricks, fired, machined, and coated with a tritium barrier. The bricks were sent to Japan to be used to provide the background to simulate the neutron energies and fluxes expected in a fusion solid breeder blanket.[4]

FUTURE WORK

The results obtained from the mechanical testing of Li_2O will be published. Additional Li_2ZrO_3 powder and Li_4SiO_4 powder will be synthesized for the FUBR-1B replacement capsules. The fabrication of lithium oxide rings for the CRITIC experiment will be completed. The initial mechanical properties tests on Li_2ZrO_3 will be completed. Mechanical properties tests will be initiated on Li_4SiO_4.

REFERENCES

1. K. C. Goretta, D. S. Applegate, R. B. Poeppel, M. C. Billone, and J. L. Routbort, "Deformation of Polycrystalline Li_2O," submitted to J. Nucl. Mater. (November 1986).

2. D. S. Applegate and R. B. Poeppel, "Microstructural Control of Sintered Lithium Oxide," submitted for presentation at Symp. on "Fabrication and Properties of Lithium Ceramics," 89th Ann. Mtg. of Am. Ceram. Soc., April 26-30, 1987, Pittsburgh, PA.

3. R. B. Poeppel, J. L. Routbort, E. Buchmann, B. Londschien, D. S. Applegate, and M. C. Billone," Steady-State Deformation of Some Lithium Ceramics," ibid.

4. R. B. Poeppel and R. F. Mattas, "Fabrication of Li_2CO_3 Bricks for Fusion Breeder Neutronics Experiments," ibid.

TRITIUM AND HELIUM RETAINED IN FAST NEUTRON IRRADIATED LITHIUM CERAMICS AS MEASURED BY HIGH TEMPERATURE VACUUM EXTRACTION - D. L. Baldwin and G. W. Hollenberg (Westinghouse Hanford Company)

OBJECTIVE

The objective of this effort is to develop a technique for measuring retained helium and tritium within lithium ceramics and to analyze materials irradiated in the FUBR-1A experiment.

SUMMARY

A vacuum apparatus was designed and constructed for the rapid measurement of retained helium and tritium in lithium ceramics. The apparatus eliminated the limitations and errors associated with the acid dissolution technique and the previous vacuum annealing technique (below the melting point) and allowed more accurate and less expensive analysis techniques.

Tritium retention in Li_2ZrO_3 was significantly less than in the other ceramics. Tritium retention appears to possess a proportional dependence to burnup. A review of available models reveals that none fully describe the absolute magnitude or the relationship of retention to temperature or burnup so that a model which considers irradiation effects is desired.

PROGRESS AND STATUS

Introduction

In the pursuit of a viable fusion energy source, tritium producing blanket materials are now under development internationally. Lithium ceramic solid breeder materials are prime candidates. Several design efforts, including STARFIRE[1] and DEMO[2], among others, have studied different candidate solid breeders. More recently, the Blanket Comparison Selection Study[3] reviewed many designs in search of future direction.

The FUBR-1A experiment and results, described here, differ from other tests[4-8] by the use of a fast neutron reactor, exposure to high neutron fluence levels, and the use of closed capsules for direct comparison of four ceramic tritium breeder materials. These candidate materials are Li_2O, $LiAlO_2$, Li_2ZrO_3, and Li_4SiO_4. The FUBR-1A experiment was primarily aimed at adding to the current data base for dimensional and chemical stability, tritium release, and other characteristics. This paper will provide the experimental results on tritium retention, helium retention, and burnup with some discussion on the mechanisms controlling tritium retention. The helium and tritium retention measurements reported here were obtained with a newly designed apparatus using a rapid, high temperature vacuum extraction method for all the ceramic materials. This new apparatus will be described along with supporting developmental data.

Irradiation experiment description

The four solid breeder materials making up the test matrix for the FUBR-1A experiment were irradiated at temperatures of 773, 973, and 1173 K to exposures of 105, 192, and 297 full power days (FPD), or approximately equivalent to 1, 2, and 3 at.% Li-6 burnup. In order to achieve more equivalent tritium generation and bulk heating rates, the Li-6 enrichment was highest in the $LiAlO_2$ and Li_2ZrO_3 materials and lowest in the case of Li_2O.

The fabrication and construction of the capsules and the characterization of the pellets was described previously.[9] The most notable feature of the hermetically sealed stainless steel tubes that contained the ceramics was the placement of cerium at the end opposite the pellets. The cerium is a strong oxygen getter and was predicted to chemically reduce any T_2O released from the ceramics so tritium could diffuse through the cladding material into the sodium coolant.

Approximately three weeks after the end of irradiation, the subassembly was removed from the reactor and the capsules were washed free of sodium and then laser punctured at the HFEF hot cells operated by ANL-W. The volume and composition of the plenum gas was then measured (i.e., analysis of both helium and tritium). After laser puncturing, each capsule was cut open with a rotary saw in an inert atmosphere shielded cell. The pellets were recovered and immediately placed in metal storage tubes until they were later opened in inert atmosphere glove boxes. After dimensional measurements, samples weighing one to two grams were removed for the retention measurements from a middle pellet in the column because axial thermal gradients were expected in these pellet columns. Because of radioactivity, the Li_2ZrO_3 pellets were dimensionally measured and fractured in an air-atmosphere shielded cell as rapidly as possible.

Analytical method description

The analytical approach taken for these measurements results from five objectives. These include: (1) the simultaneous measurement of tritium and helium on a single sample, (2) the complete melting of the sample to assure rapid release of both gases, (3) ^4He mass spectrometry measurement based upon the ^3He internal standard and resultant isotopic ratio $^4He/^3He$, (4) real-time oxidation of the tritium plus and added known hydrogen spike, followed by condensation and measurement by liquid scintillation counting, and (5) a measurement of hydrogen/tritium collection efficiency by gravimetric analysis of the oxidized and condensed hydrogen. The added diluent hydrogen enhances tritium release and collection while providing a carrier effect. After assessing the operational difficulties in the methods applied to the previously reported low burnup samples, the earlier methods (including acid dissolution,[10] molten salt fusion, and a simplified vacuum extraction) were discarded in favor of a greatly improved vacuum extraction method.

The tritium/helium extraction manifold is shown in Fig. 1. A 20 kW saturable-core induction generator, capable of heating a sample to 2275 K within 20 seconds, rapidly melts the sample inside a covered graphite crucible within a water-cooled quartz furnace chamber. The crucible is hung and positioned in place on a tantalum wire and basket. The manifold itself is a welded, stainless steel unit with Cajon O-Ring Ultra-Torr fittings for rapid connection of the quartz furnace chamber and pyrex cryogenic trap, Cajon VCR metal gasket fittings for connection of the pressure transducers, and Swagelok fittings for connection of all gas sample cylinders and vacuum line. This system is capable of 0.2 Pa vacuum with a rotary vane oil rough pump.

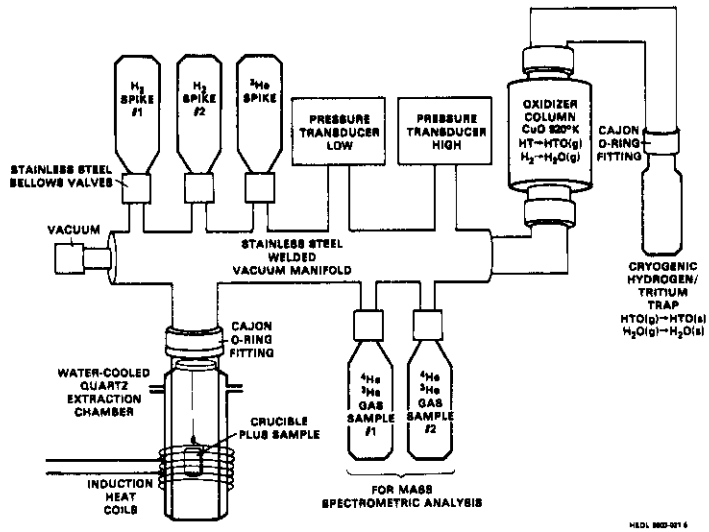

Fig. 1. Schematic diagram of the tritium/helium measurement system.

In preparation for a measurement, a 75 cm^3 ^3He cylinder and two 500 cm^3 hydrogen cylinders are filled to specified pressures, two 75 cm^3 mass spectrometry sample cylinders are evacuated and closed, and all are connected to the manifold. The graphite crucible and lid are outgassed at full temperature under vacuum. The sample is loaded, the system evacuated, and the cryogenic trap cooled with liquid nitrogen. During the initial phase of gradually increased heating, the first hydrogen spike is introduced to the system. Melting is accompanied by vigorous activity, spewing of molten material, and deposition of volatile material, probably predominantly elemental lithium, on the adjacent quartz wall. The heating phase is completed in 20 minutes, during which time the hydrogen and released tritium is oxidized to water vapor in the oxidizer column and condensed in the cryogenic trap, reducing the system pressure to a minimum within a few minutes. The ^3He spike is then introduced to the system, allowed to mix, and the second hydrogen spike added to carry any remaining tritium to the trap. When the system pressure again reaches minimum, two helium sample cylinders are opened, filled with the $^4He/^3He$ sample gas, and closed. The manifold is opened to the atmosphere, and the cryogenic trap removed, warmed to room temperature, and weighed. The condensate weight is a routine check for complete collection of hydrogen/tritium. the condensate is diluted and the tritium measured in duplicate by liquid scintillation. The helium samples are disconnected from the manifold and the $^4He/^3He$ ratio measured in duplicate by the mass spectrometer. The entire method takes less than three hours. The standard isotopic dilution technique, using a known ^3He spike followed by a measurement of the $^4He^3He$ ratio requires only a thorough mixing within the manifold of the two gases. This is advantageous since the manifold need not be isothermal nor the temperature or pressure even known. The instrument used for this work is a CEC 21-130 quantitative cycloidal mass spectrometer calibrated for these light gases.

All tritium and helium data reported here are not only the result of duplicate tritium and helium measurements from a single pellet, but also represent the average of replicate analyses from duplicate portions of pellets. The estimated uncertainty for both retained tritium and helium in the 200 and 300 FPD pellets analyzed by the current method is a maximum of ±5%. The estimated uncertainty in the retained tritium values of the 100 FPD pellets analyzed previously by several methods was about ±10-15%. The uncertainty in the retained helium values of the 100 FPD samples is ±10-20%.

In development of this vacuum extraction procedure, several tests were undertaken to check the apparatus and method. These tests include: (1) the addition, oxidation and collection of known quantities of hydrogen to determine accuracy and precision of the collection of hydrogen/tritium, (2) the determination of the rate of oxidation and condensation of hydrogen to determine the time necessary for >99% collection, (3) the addition of known quantities of ^3He and ^4He to determine accuracy of the mass spectrometric measurement, (4) a post-extraction acid dissolution on a few of the melted samples to determine any residual tritium, and (5) a post-extraction dissolution of a few of the quartz wall residues. A series of a dozen hydrogen recovery tests show an average recovery of 100.6 ± 1.1% within a 25-minute collection period. This is good evidence that following release of the tritium from the sample, the carrier effect of the added hydrogen provides >99% recovery of the tritium. The mass spectrometric isotopic ratio analysis of known quantities of ^3He and ^4He resulted in an average recovery factor of 98.2 + 1% of the ^4He. This reproducible recovery factor provides evidence of adequate mixing of the ^3He and ^4He within the manifold. This correction factor was applied to all helium results. An acid dissolution analysis of the post-extraction melted sample resulted in <1% tritium. An acid dissolution of the deposition on the quartz chamber resulted in a very consistent average residual 8.0% of the total tritium found. This same result was found regardless of the material being analyzed. This additional tritium may be due to formation of LiT on the quartz wall, which is then slow to exchange with the excess hydrogen. This correction factor was applied to all tritium results.

Retained helium results

In Figs. 2 and 3, the retained helium is presented in comparison with the amount of helium generated in the Li_2O and Li_2ZrO_3 pellets, respectively. As previously reported,[11] helium retention in the Li_2ZrO_3 and $LiAlO_2$ was significantly less than in the Li_2O pellets and thus will not be examined at length here. In Fig. 2, it can be seen that at 973 K the retained helium (about 23% retention) increases in a roughly proportional manner with respect to the helium that is generated. At both higher (1173 K) and lower (773 K) temperatures, much less helium is retained. At higher temperatures, an anticipated increased helium diffusivity can explain the enhanced release. But between 773 and 973 K, the relationship may be symptomatic of the bubble nucleation process.[12] Closer examination of the bubble morphology is necessary in order to confirm this postulation, but the swelling results also were greater at 973 K.[11] Swelling at 1173 K was also large, but this is expected to be the result of enhanced bubble growth in the more plastic matrix that would be present at that temperature.

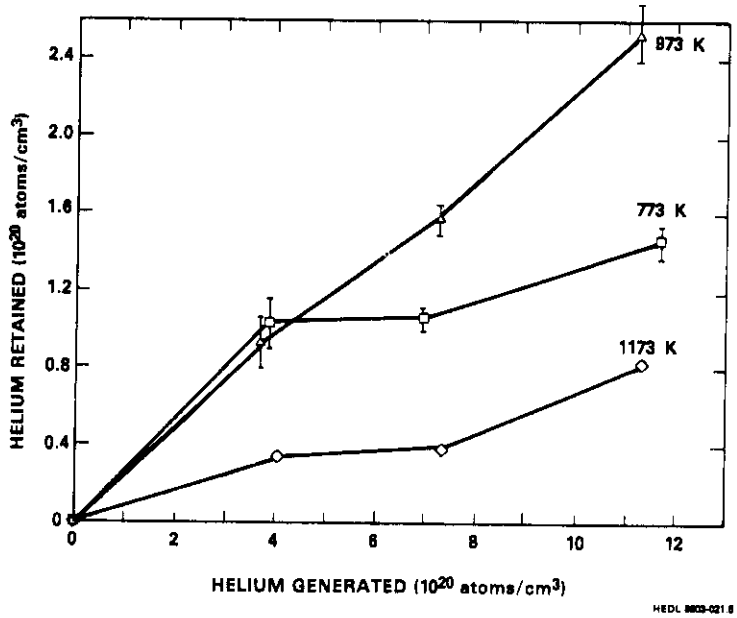

Fig. 2. Helium retained in Li_2O after irradiation.

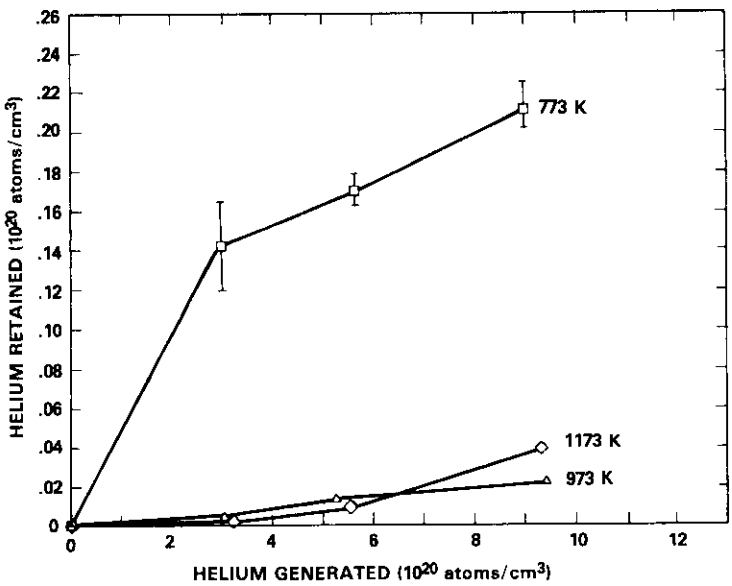

Fig. 3. Helium retained in Li_2ZrO_3 after irradiation.

The tritium generation rate as calculated by the combination of the measured retained and released helium components for Li_2O can be correlated against the position in the subassembly. The irradiation configuration consisted of a "center" pin surrounded by six other pins. Because the subassembly is at the edge of the EBR-II core, there is a gradient in flux and corresponding tritium generation across it. Always of concern in such an array of neutron absorbing materials is that there will be significant self-shielding, but it was observed that the center Li_2O pellets were within 7% of the average generation rate of the outer pellets. Considering the fact that some of the pellet columns were in the reactor with different core loadings than others, the agreement between these rates is indicative of a reasonably constant spectrum and flux in EBR-II and reproducibility in analysis of helium both in the plenum and in the pellets.

Retained tritium results

In Fig. 4, the tritium retention in Li_2O at the three temperatures and three exposures is presented. All tritium results are decay-corrected back to the end of irradiation. At 973 and 1173 K, the tritium level is approximately proportional to the tritium generated, with the 1173 K results being lower than that at 973, as would be expected from a thermally activated process such as diffusion. At 773 the data are consistent with this trend up to 7 x 10^{20} atoms/cm^3. No conclusive explanation is available for this behavior, but investigators have postulated that if Li_2O is operated below the melting point of LiOH (723 K) that the tritium inventory would rise rapidly. It is possible that because of the large swelling that occurs in these capsules that the temperature of this material was reduced to a temperature below 723 K, although it is difficult to compute this temperature redistribution accurately without better thermal conductivity data.

In Fig. 5, the tritium retention in $LiAlO_2$ at three temperatures and three exposure levels is presented. The tritium retention levels for $LiAlO_2$ are significantly higher than those of Li_2O. The expectation had been that the opposite would be true on the basis of higher T_2O solubility in the Li_2O,[1] but such does not appear to be the case. A maximum of 25% retention at 773 K and 192 FPD is much more than the 3.5 retention observed for Li_2O under those conditions. Again the tritium retention appears to be almost proportional with the tritium generation.

In Fig. 6, the tritium retention in Li_2ZrO_3 at the three temperatures and three exposure levels is presented. Retention in this material is also approximately proportional with tritium generation. About 2% retention is seen in the 773 K data, while the higher temperature data show 0.2-0.3% retention.

The tritium measured in the plenum of each capsule during postirradiation laser puncturing amounts to 0.01-0.1 appm of the plenum gas. There is no consistent trend with respect to the temperature or burnup of the material being irradiated. The very low tritium partial pressure levels observed in these capsules is indicative of the fact that high tritium diffusion in the cladding and high gettering rates were obtained in these pins, as was predicted before irradiation. It was predicted that tritium partial pressures in these capsules could be 300 appm during steady-state operation. The values measured are 3-4 decades less than that but they represent a plenum that had remained at the reactor inlet temperature of about 623 K for three weeks with no tritium generation before being allowed to cool to ambient.

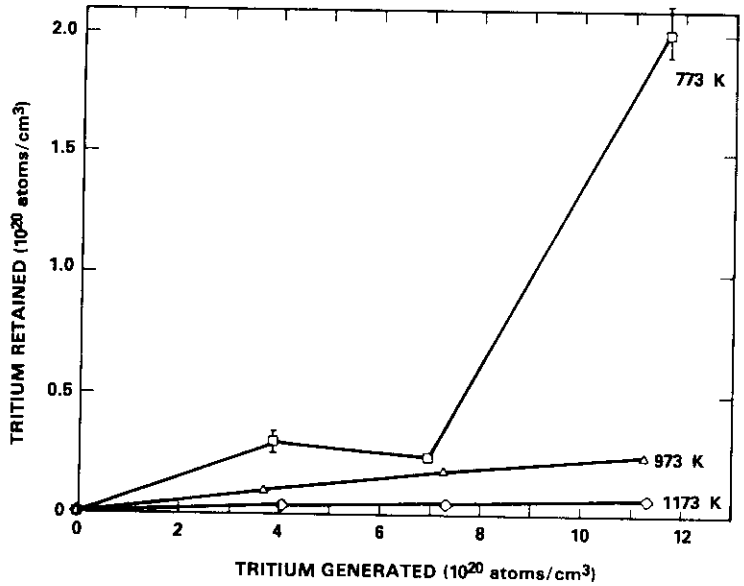

Fig. 4. Tritium retained in Li_2O after irradiation.

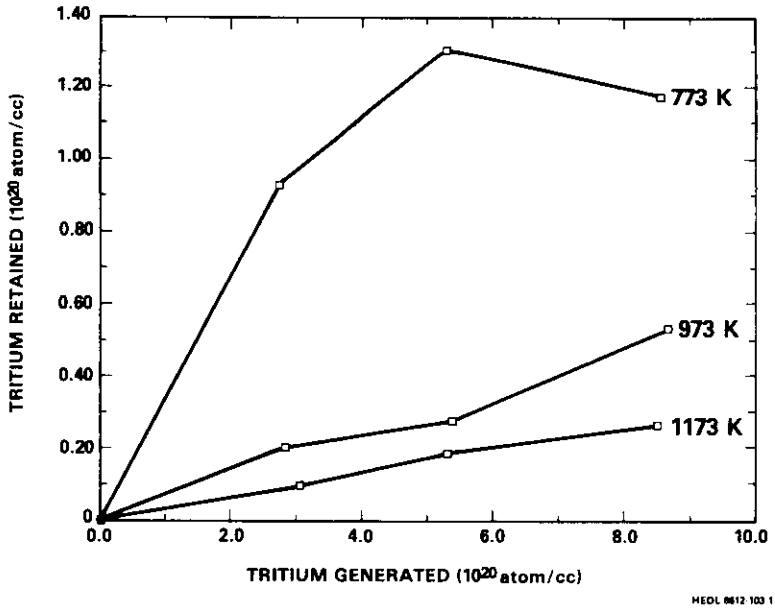

Fig. 5. Tritium retained in $LiAlO_2$ after irradiation.

Mechanism

Two major trends are apparent in the tritium retention data for all three materials. One, there is a rough proportionality with burnup (i.e., increasing retention with increasing Li-6 burnup). And two, there is an inverse relationship with temperature for all three materials (i.e., decreasing retention at the higher irradiation temperatures). In light of these two trends, some comments may be offered about the mechanism of tritium retention. The tritium retention mechanism in solid breeders is believed to consist possibly of several components, as shown in Table 1. The classical diffusion component provides the correct temperature dependence as a thermally activated mechanism, but in examining the data in Figs. 4-6 more closely, it appears inadequate to account for the increasing retention at the higher fluence levels. If classical diffusion from a sphere were controlling, then at 297 FPD and 973 K in Li_2O, a diffusion coefficient of approximately 5 x 10^{-15} cm^2/s would be obtained with a time constant of only 100 days. However, the data in Fig. 4 do not saturate at 100 days but continue to increase in a proportional manner with more tritium generation. A classical diffusional process would asymptotically approach a limiting value for the inventory (i.e., retained tritium) of $Gr^2/15D$ (where G = generation rate, r = grain size, and D = diffusion coefficient) in approximately one time constant. It is possible that grain growth in Li_2O could explain the proportional increase in retention, but this is not expected in $LiAlO_2$ or Li_2ZrO_3.

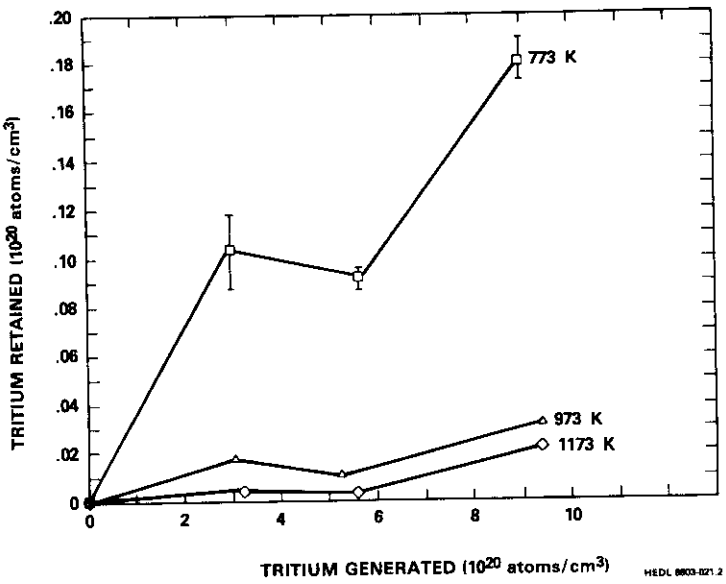

Fig. 6. Tritium retained in Li_2ZrO_3 after irradiation.

Table 1. Tritium retention mechanism components

Diffusion	This component can be modeled by the classical diffusion of tritium from a sphere of radius r as the inventory is equal to $Gr^2/15D$ at saturation where G is the generation rate and D is the tritium diffusion coefficient in the bulk.
Solubility	The inventory in Li_2O according to this model is equal approximately to $I_0 \exp(-\Delta G/RT)(P_{H_2O})^{\frac{1}{2}}$ where P_{H_2O} is the equilibrium partial pressure of moisture over a solid solution of LiOH in the material.
Surface Desorption	This component describes a physical or chemical desorption from the surface of the material. The inventory could be represented by $I_S A \exp(-\Delta G/RT)(P_{H_2O})^{\frac{1}{2}}$ where I_S is the surface area of the material.
Irradiation Trapping	This describes some physical or chemical bonding of tritium to lattice defects or helium bubbles. It might be dependent upon some as yet unknown function of fluence or more likely lithium burnup, where the inventory might be represented by $f(\phi t, \Phi, dpa...)$. There may be some unknown damage resulting from fast neutron irradiation. Other components such as grain boundary trapping might also influence the process.

From the standpoint of a possibly dominant solubility component, it is interesting to compare the present results with in situ experiments which provide a purge gas that can maintain the tritium partial pressure over the solid breeder to only a few ppm as compared to the closed capsule environment which leads to much higher partial pressures in the plenum. The solubility data on LiOH in Li_2O of Norman[13] and Tetenbaum[14] can be compared with the retained tritium from the VOM-15[4,5] experiment and these data. Assuming an operating T_2O partial pressure of about 300 appm in the capsules, the retained tritium values are in approximate agreement with the solubility results. However, the temperature dependence of the solubility model is totally inconsistent with these data since the Norman and Tetenbaum data show that solubility increases with temperature whereas the retained tritium in this experiment consistently decreased for all materials.

The surface desorption component is not well characterized, but the low temperature Li_2O data of Yoshida[15] is representative of the adsorption results that could be useful in evaluating this component. The Yoshida 773 K surface adsorption data are approximately two orders of magnitude less than the retained 773 K data, at the estimated 300 appm T_2O partial pressure in the capsules. But the surface adsorption model does possess an appropriate temperature dependence.

None of the above mechanisms fully explain the gradual but consistent increase in the tritium retention at higher fluence levels. The uncharacterized mechanism of tritium trapping by irradiation defects and the gradual accumulation of these defects at higher burnup and fluence levels could potentially explain the observed higher fluence retention. Additionally, the fast neutron environment might enhance direct displacement damage. In Li_2O the buildup of helium is roughly proportional to the increases in tritium retention, although the exact temperature dependence is not followed. From this observation, it is possible that irradiation damage can have a second order effect on the tritium retention. For example, irradiation damage and helium could impede the diffusion of tritium through the lattice and thus cause a decrease in D and a subsequent increase in the retention.

CONCLUSIONS

The conclusions stated here are based on the described method and the experimental conditions for this fast neutron closed capsule test, that is, irradiation temperatures of 773, 973, and 1173 K and Li-6 burnup levels of 1, 2, and 3 at.%.

1) A rapid and reliable analytical method meeting the outlined goals has been achieved. This high temperature vacuum extraction method measures both gases on a single sample and provides high reliability in both results due to the use of the isotopic dilution technique for helium and the hydrogen spike addition technique for tritium.

2) Of all the materials, Li_2O has the largest retention for helium. Helium retention in the oxide was greatest at the intermediate temperature (973 K) and less as expected at the higher temperature due to increased diffusivity. Decreased retention at 773 K may be due to the bubble nucleation process but requires further study.

3) Tritium retention was least under all conditions for Li_2ZrO_3, compared with Li_2O and $LiAlO_2$. All three materials show an approximately linear proportionality with burnup.

4) A simple mechanism of either classical diffusion, solubility or surface desorption appears inadequate to explain the increasing retention at the higher fluence levels. The inverse temperature dependence does appear to favor a strong diffusion term, modified perhaps by irradiation trapping or some irradiation damage phenomenon.

REFERENCES

1. C. Baker et al., "STARFIRE - A Commercial Tokamak Fusion Power Plant Study", ANL/FPP/80-1, Argonne National Laboratory, Argonne, IL (1980).

2. M. Abdou et al., "A Demonstration Tokamak Power Plant Study (DEMO)", ANL/FPP/82-1, Argonne National Laboratory, Argonne, IL (1982).

3. D. L. Smith et al., "Blanket Comparison and Selection Study Final Report", ANL/FPP/84-1, Argonne National Laboratory, Argonne, IL (1984).

4. T. Kurasawa et al., "In-Situ Tritium Recovery Experiment from Lithium Oxide Under High Neutron Fluence", J. Nucl. Mat. 122/123, 902 (1984).

5. T. Kurasawa et al., "In-Situ Tritium Recovery Experiment from Lithium Oxide Under High Neutron Fluence", J. Nucl. Mat. 133/134, 196-200 (1985).

6. R. Clemmer et al., "The TRIO-01 Experiment: In-Situ Tritium Recovery Results", J. Nucl. Mat. 122/123, 890 (1984).

7. E. Roth et al., "Irradiation of Lithium Aluminate and Tritium Extraction", J. Nucl. Mat. 133/134, 238-41 (1985).

8. H. Kwast et al., "EXOTIC, A Programme on Ceramic Tritium Breeding Materials", J. Nucl. Mat. 133/134, 246-50 (1985).

9. G. W. Hollenberg, D. C. King, and R. C. Knight, "A Fusion Solid Breeder Experiment in a Fast Neutron Fission Reactor", Conference on Fast, Thermal and Fusion Reactor Experiments, American Nuclear Society, Salt Lake City, UT (1981).

10. D. L. Baldwin, "Measurement of Retained Helium and Tritium in Irradiated Lithium Ceramics", J. Nucl. Mat. 122/123, 882 (1984).

11. G. W. Hollenberg and D. L. Baldwin, "The Effect of Irradiation on Four Solid Breeder Materials", J. Nucl. Mat. 133/134, 242-5 (1985).

12. Y. Y. Liu et al., "Microstructural Examination of Fast Neutron Irradiated Li_2O", J. Nucl. Mat. 133/134, 209-14 (1985).

13. J. H. Norman and G. R. Hightower, "Measurement of the Activity Coefficient of LiOH Dissolved in Li_2O(s) for an Evaluation of Li_2O as a Tritium Breeder Material", J. Nucl. Mat. 122/123, 913-20 (1984).

14. M. Tetenbaum, A. K. Fisher, and C. E. Johnson, "An Investigation of the Solubility of LiOH in Solid Li_2O", Fusion Tech. 7, 53-6 (1985).

15. H. Yoshida et al., "Water Adsorption on Lithium Oxide Pellets in Helium Sweep Gas Stream", J. Nucl. Mat. 122/123, 934 (1984).

TIME DEPENDENT ANALYSIS OF IN SITU TRITIUM RELEASE CURVES FROM THE VOM-22H EXPERIMENT - G. W. Hollenberg (Westinghouse Hanford Company) and T. Kurasawa, H. Watanabe, and Y. Ishii (JAERI)

OBJECTIVE

The objective of this effort was to assist JAERI in the analysis of the JRR-2 in situ tritium recovery experiment.

EXPERIMENT

An analysis method was developed which allows the transient response of in situ tritium recovery experiments after temperature change steps to be used in calculation of diffusion coefficients. The papers by Kurasawa et al. on the conclusions reached from this work are available in the open literature and will not be reproduced here.[1,2]

PROGRESS AND STATUS

Time dependent analysis

In situ tritium recovery experiments have become a common method for investigating the tritium release behavior of solid tritium breeder materials for use in fusion blankets. The VOM-22H experiment was conducted by JAERI as a part of their continuing series of VOM in situ recovery experiments in the JRR-2 reactor. As a part of the USDOE/Japan STA exchange agreements, development of an advanced analysis technique was to be a goal of the US participant.

Tritium recovery experiments have typically used the inventory technique to evaluate the apparent tritium diffusion coefficient, D, of a lithium ceramic:

$$D = G\, r^2/15I \qquad \text{Eq. [1]}$$

Billone and Clemmer[3] were the first to point out the practical limitations of using this expression during their analysis of the TRIO-1 experiment. The inventory, I, of tritium remaining in the solid breeder can be calculated very accurately at the end of the experiment since it is determined during postirradiation measurements; and at the beginning of the experiment, it is zero. In the middle of the experiment the errors associated with the integral of the quantity (R-G) become very large since there is a compounding of uncertainties from all the previous runs. The release rate, R, and the generation rate, G, are nearly the same and only small uncertainties are thus magnified in the calculation of (R-G), and anything but full power operation of the reactor is difficult to account for.

In addition, Billone and Clemmer noted that it is necessary to extrapolate when true steady-state release was not achieved; steady state can take a very long time. Consequently, a method was developed on the basis of the time dependence of the transient which occurs after a temperature change step from T_1 to T_2 as is pictured in Figure 1. The expression given by Billone and Clemmer for tritium release as expanded from the earlier work of Mulford and Mueller[4] after a temperature change step can be written as:

$$(R/G)-1 = [(D_1/D_2)-1]6/\pi^2 \sum_{n=1}^{\infty} (1/n^2)\exp(-n^2\pi^2 D_2 t/r^2) \qquad \text{Eq. [2]}$$

where D_1 is the diffusion coefficient before the temperature change, and D_2 is the diffusion coefficient after the temperature change; r is grain size and t is time after the temperature change. The quantity (R/G)-1 is called the normalized release rate since it removes the generation rate dependence of the diffusion curves.

It is possible to simplify Eq. 2 into the following form:

$$(R/G)-1 = A_1 \sum_{n=1}^{\infty} [1/n^2 \exp(A_2\, n^2 t)] \qquad \text{Eq. [3]}$$

where least square fitting can be used on tritium release data to provide the coefficients A_1 and A_2. The value of A_2 is most useful in the determination of D_2 since it does not require an assumption for the value of D_1. In addition, A_1 is highly dependent on the initial spike in the tritium release rate after the temperature change step. Even though the temperature changes were accomplished rapidly (<5 min.), the data taken in this short time period is the most unreliable. At t = 0 (Eq. 3), the second term reduces to 1 so that A_1 is easily determined, but errors at t = 0 are so large that this is not a reasonable technique for determination of D_2.

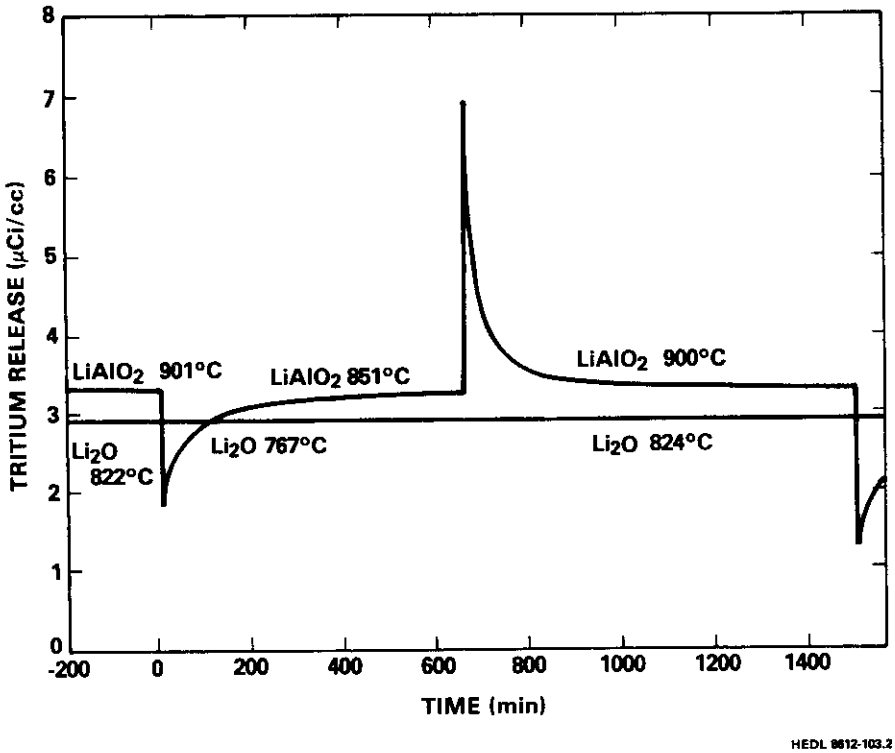

Fig. 1. Comparison of tritium release from $LiAlO_2$ and Li_2O ppm during temperature decreases from the reference temperature increases.

It should be noted here that the above time dependent analysis is advantageous to the simpler inventory technique when the data are very precise and the system is very stable. The VOM experiments have exceptional control of the operating parameters which is the only justification to using this technique. Temperature, for example, was in many cases measured to possess a standard deviation of less than 1°C, and the output of the self-powered neutron detectors provided standard deviations of 1%.

A procedure that was adopted during the testing program was to establish a reference temperature for most runs from which all lower temperature runs were initiated. The reference temperature was 900°C for the $LiAlO_2$ material and 825°C for Li_2O. A reference temperature not only allows more comparable data to be obtained, but it also allows more rapid equilibration to steady-state release. If a set of lower temperature runs are conducted without intermediate runs at high temperatures, long time intervals are required and steady state may never be obtained. As a rule, runs require tD_2/r^2 values of at least 1 to reach steady state, but only 0.3 for least square fitting.

The generation rate was obtained by time averaging the last hour of the release rate for the longer runs. It was found that after tD_2/r^2 values of 2 for temperature decrease runs (i.e., 900°C to a lower temperature and 5 for temperature increase runs (from a lower temperature to 900°C) that the steady-state release rates converged to the same value for the same purge gas composition, as snown in Fig. 2. At times shorter than these, the release rates were lower for temperature decrease runs and higher for temperature increase runs as would be predicted by theory.

Ionization chambers

Early in the experiment it was realized that the measurement system should have a minimum impact on the time dependence of the tritium release. The ionization chambers used for tritium measurement of the purge gas can be assumed for the inventory technique to have little impact on the data as in TRIO-1. But when using the time dependent technique, the ionization chamber's time constant can influence the results. In Fig. 3, the response of two different sizes of ion chambers after a rapid reactor shutdown is shown. The tritium release is expected to drop to zero within a few minutes of shutdown because the temperature decreases rapidly in the solid breeder. The identical lines for the large (1500 cc) and small (100 cc) ionization chambers represent the $LiAlO_2$ capsules during the first and second cycles of the VOM-22H experiment. The measured tritium concentration in the 200 cc ion chamber decreases rapidly while the 1500 cc ion chamber's response requires more than an hour for the same shutdown. If one assumes that the gas in an ion chamber is completely mixed at all times, then the solution to the differential expression becomes:

$$C_v = C_{in} + (C_o - C_{in})\exp(-Ft/V) \qquad \text{Eq. [4]}$$

where c_v is the measured tritium concentration; C_{in} is the tritium concentration of the incoming purge gas; C_o is the tritium concentration at time zero; F is flow rate (50 cc/min); t is time; and V is the volume of the ion chamber. Theoretically, the value of V/F for the 1500 cc ion chamber should be 30 min. while the lease square fit value from Fig. 2 is 24, which is indicative of channeling within the large chamber. For the 100 cc ion chamber, the theoretical value is 2 while the least square fit is 2.7. This is indicative of some mixing in the chamber. The data were modified by use of these ion chamber corrections.

Smaller ion chambers were purchased but there is some limit to their use. Because of their high surface to volume ratio they tend to be easily contaminated, especially in neutral or oxidizing atmosphere.

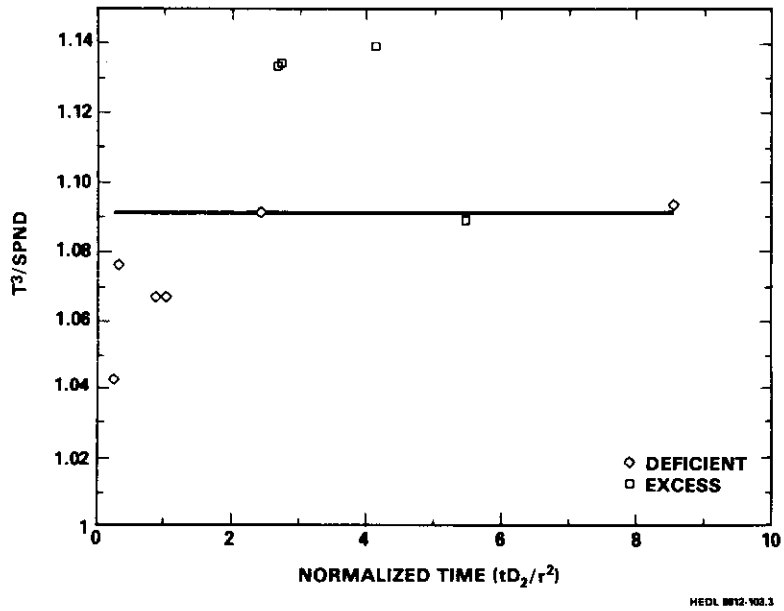

Fig. 2. Comparison of steady-state release rate over self-powered neutron detector signal to the normalized time for the last hour of VOM-22H runs of $LiAlO_2$ in 1000 ppm D2. Deficient means runs after temperature is decreased and excess indicates runs after temperature is increased.

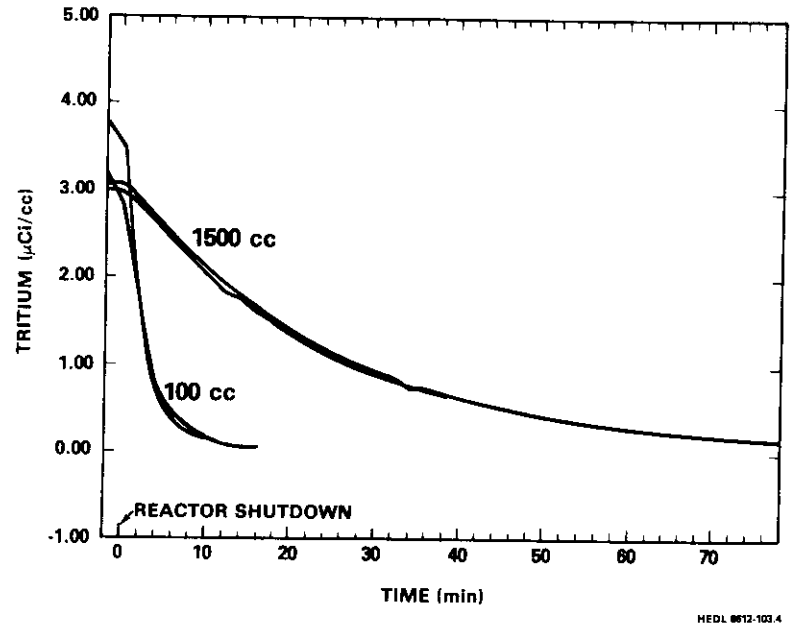

Fig. 3. Effect of ion chamber size on the time dependence of measured tritium release at shutdown for $LiAlO_2$ in 1000 ppm D2.

CONCLUSIONS

The use of a time dependent method of diffusional analysis for in situ tritium recovery data provides advantages over the inventory method, providing the measurements are sufficiently precise. The size of an ionization chamber directly affects the time dependence of its output with smaller chambers having less of an impact.

REFERENCES

1. T. Kurasawa et al., "The Time Dependence of In Situ Tritium Release from Lithium Oxide and Lithium Aluminate (VOM-22H Experiment)", J. Nucl. Mat. 141/143 (1986).

2. T. Kurasawa, G. W. Hollenberg, and H. Watanabe, "Tritium Recovery and Behavior of Li_2O and $LiAlO_2$ Spheres During the VOM-22H Experiment", in Proceedings of the International Symposium on Fusion Reactor Blanket and Fuel Cycle Technology, Tokyo University, Tokai-mura, Japan (October 1986).

3. M. C. Billone and R. G. Clemmer, "Modeling of Tritium Transport in Lithium Aluminate Fusion Solid Breeders", Fusion Tech. 8, 875-80 (1985).

4. R. N. R. Mulford and B. A. Mueller, "Measurements of Helium Release from Materials Containing $^{238}PuO_2$", LA-5215, Los Alamos National Laboratory, Los Alamos, NM (July 1973).

THE FUBR-1B EXPERIMENT AND BEATRIX-I - G. W. Hollenberg, R. C. Knight, and L. A. Pember (Westinghouse Hanford Company), C. E. Johnson and R. B. Poeppel (Argonne National Laboratory), and L. Yang (GA Technologies)

OBJECTIVE

The objective of this work is to irradiate lithium ceramics in a fast neutron environment to high burnup levels and with large temperature gradients. As a part of the BEATRIX-I, the object of the second part of this experiment is to irradiate materials from IEA participating countries in a similar manner.

SUMMARY

The first insertion of two subassemblies has completed its irradiation in December 1986. This irradiation exposed Li_2O and $LiAlO_2$ to not only high temperatures but also large temperature gradients which are expected in fusion blankets. In addition, it included other materials such as Li_2ZrO_3, Li_8ZrO_6, Li_4SiO_4, and $LiAlO_2$ (spheres and large grain size) some of which will go to high burnups.

The second insertion will contain lithium ceramics from Saclay, France; Casaccia, Italy; Karlsruhe, Federal Republic of Germany; Springfield Laboratories, England; and JAERI, Japan.

PROGRESS AND STATUS

Introduction

A high fluence irradiation experiment on solid breeder materials is being irradiated in the EBR-II reactor. The experiment is evaluating the performance of numerous materials which are presently viewed as candidates for use in a solid breeder blanket for tritium and sensible heat extraction. Accumulation of tritium and helium retention data, along with chemical and physical stability results, will aid not only in direct comparison of the materials themselves but also in the generation of better blanket designs. The experiment features large diameter pellets with large temperature gradients, thus providing a better simulation of actual component operating characteristics.

The objectives of solid breeder irradiation testing are long range in comparison with some other research areas but nevertheless important in the greater context of fusion power's eventual viability. Issues such as tritium self-sufficiency, blanket integrity, and component lifetime will only be further emphasized as an actual D-T fusion power plant nears reality.

At present, an international solid breeder test program has been initiated (BEATRIX) in which the FUBR-1B experiment complements irradiation testing conducted in thermal neutron reactors. In some respects, the FUBR-1B experiment is an extension of a previous experiment which had more limited test objectives (FUBR-1A).

The integrity and lifetime of the solid breeder may seem distant issues, but these issues force compromises of solid breeder design and neighboring structural material design which are basic to the economic credibility of a fusion power plant. Now prime issues related to the swelling (or lack thereof) and breeder integrity are of interest for specific solid breeder materials; but issues such as irradiation effects on tritium recovery and mass transport also require resolution.

Tests such as TRIO,[2] LILA, LISA, EXOTIC, VOM, and CRITIC[3] are devoted to in-situ recovery with the greatest emphasis being placed on temperature transients and purge gas effects in a thermal reactor environment under low exposure, essentially startup conditions. In contrast, the FUBR-1B experiment utilizes closed capsules in a fast neutron environment to achieve moderate burnup levels as shown by comparison to some early FINESSE design goals in Table 1.[5] The FUBR-1B experiment has an additional objective which differentiates it from other solid breeder tests in that temperature gradients have been made purposely large by using some large diameter solid breeder pellets in order to simulate the temperature gradients found in actual blankets. The low cross-section for Li-6 reaction, provided by the fast reactor neutrons, generates almost homogeneous heating throughout the pellets which is necessary for establishing the proper temperature distribution. Thermal stresses and swelling stresses associated with large temperature differences in solid breeder pellets can produce substantial cracking which would otherwise be unobserved. Additionally, temperature gradients and size are expected to influence the spatial dependence of tritium retention. Finally, the upper temperature limit of these solid breeder materials may be best evaluated under conditions of large temperature gradients rather than isothermally. For example, in the case of LiOH vapor transport under isothermal conditions, the high vapor pressure of LiOH at high temperatures leads to Li_2O deposition on the containment walls (metal). But in the case of temperature gradients, such depositions are expected to occur within Li_2O monoliths producing more realistic consequences. Also upper temperature limits for $LiAlO_2$ and the other ternary ceramics have been proposed with only the weakest of technical justification. Hence, irradiation testing under large temperature differences will provide a better definition of these limits.

Table 1. Comparison of design parameters

Test Parameter	FINESSE Blanket	FUBR-1A	FUBR-1B
Material	Li_2O	Li_2O	Li_2O
Peak Tritium Production (10^{20} at/cc)	19	11	33
Solid Breeder	850-510	500*	1000-524
Temperatures (°C)		700*	663-450
		900*	500, 700, 900*
Lithium Cross-Section (barns)	15	1	1
Material	$LiAlO_2$	$LiAlO_2$	$LiAlO_2$
Peak Tritium Production (10^{20} at/cc)	70	11	33
Solid Breeder	1000-350	500*	1127-600
Temperatures (°C)		700*	775-530
		900*	500, 700, 900*
Lithium Cross-Section (barns)	15	1	1

*Almost isothermal, $\Delta T < 50°C$.

Design

In Table 2, the test matrix for the first insertion of the FUBR-1B experiment is provided. Actually, two separate subassemblies are utilized at the same time for this testing. One subassembly contains seven pins for 1 cm diameter pellets that are very similar to those of the FUBR-1A experiment while the other subassembly contains three pins with 1.7 and 2.4 cm diameter pellets. The neutron fluence in Row 7 of the EBR-II reactor is approximately 6.2×10^{22} n/cm^2 (E > 0.1 MeV) at 900 FPD with a Li-6 spectrum-averaged cross-section of 0.5 to 2 barns. Because of the low cross-section for the Li-6 reaction, the self-shielding within the pellets is predicted to be less than 5%.

Table 2. FUBR-1B test matrix for first insertion

Material	Diameter (cm)	Density (% TD)	Grain Size (μm)	Temperature (°C)
Reference Materials				
Li_2O	2.4	80	4	1000-524
Li_2O	1.7	80	4	663-450
Li_2O	1.0	80	4	500, 700, 900*
$LiAlO_2$	2.3	80	1	1127-600
$LiAlO_2$	2.3	80	1	775-530
$LiAlO_2$	1.0	80	1	500, 700, 900*
Large Grained and Low Density Materials				
Li_2O	1.0	80	80	700*
$LiAlO_2$	1.0	80	35	500*
Other Materials				
Li_2ZrO_3	1.0	85	2	600*
Li_8ZrO_6	1.0	80	3	600*
Li_4SiO_4	1.0	80	2	500*
$LiAlO_2$ Spheres	1.0	60	30	700*

*Almost isothermal, $\Delta T < 50°C$

Materials

In Table 2, the materials contained within the FUBR-1B experiment's first insertion pins are described. The reference Li_2O and $LiAlO_2$ pellets were fabricated with a density of 80% by hot pressing and possessed less than 2000 μg/gm of metallic impurities. Chlorine and fluorine were maintained below 150 μg/gm. The moisture level was measured to be below 0.005 mol% with the carbonate as high as 0.34 mol% in the Li_2O. The grain size of the reference Li_2O was 4 μm; grain size of the reference $LiAlO_2$ was less than 1 μm. In order to evaluate the effect of grain size on the tritium and helium release and other

performance parameters, large grained samples of Li_2O (80 μm) and $LiAlO_2$ (35 μm) were included. Early in the development of solid breeder materials, it was thought that large grains would be detrimental to the release of tritium from the blanket; but more recently this has been reconsidered.

Since Li_2ZrO_3 was found to be a stable material which readily released tritium during the FUBR-1A experiment, continued evaluation in FUBR-1B was of interest. A new zirconium compound, Li_8ZrO_6, was initially enthusiastically included in the test matrix because of its potential neutronic advantages. However, Li_8ZrO_6 was found to be unstable during conventional vacuum outgassing, as it disassociated into Li_2O and Li_4ZrO_4. Thus, its role in the experiment diminished to only one capsule. Ultimately, it was determined that by very slow vacuum outgassing, Li_8ZrO_6 could be annealed successfully.

The use of sphere-packed $LiAlO_2$ has been proposed as a method for constructing the complex solid breeder blanket configuration. In an attempt to explore the feasibility of such a concept, stoichiometric $LiAlO_2$ spheres were fabricated by plasma spraying. In Figure 1, a SEM photograph of some of these spheres demonstrates their surface morphology as produced by quenching of the liquified $LiAlO_2$. The diameter of these spheres was approximately 35 μm.

10 μm

Fig. 1. $LiAlO_2$ spheres prepared by plasma spraying granulated $LiAlO_2$ that was hot pressed. Notice the dendritic surface texture.

FUTURE WORK

The schedule for FUBR-1B provides for a 900 FPD irradiation of three pins which will likely end in 1989. At the beginning of 1987 after 300 FPD of irradiation, selected pins will be removed and replaced by pins specifically dedicated to the BEATRIX exchange program of IEA. The designed materials and their source are shown in Table 3. Spheres or pellets of $LiAlO_2$, Li_2O, Li_2SiO_3, Li_4SiO_3, and Li_2ZrO_3 will be provided from Japanese and European sources which will yield a direct comparison between a variety of fabrication techniques.

CONCLUSIONS

The FUBR-1B experiment will significantly enlarge our understanding of the effects of temperature gradients and high fluence irradiation on the performance of solid breeder materials. This experiment provides a closer simulation of operating conditions in an actual fusion power plant's blanket with its higher burnup and larger dimensions. The spectrum of materials now being irradiated and those provided by the BEATRIX exchange program allows a direct comparison of the solid breeder materials that can be fabricated in the world today.

Table 3. BEATRIX/FUBR-1B test matrix second insertion

Capsule	Material	Source	Li-6 Enr. (%)	Diameter (cm)	Density (% TD)	Goal Temp. (C)
S4T	$LiAlO_2$	Saclay	95	2.320	73.5	1115
S4B	Li_4SiO_4	Karlsruhe	95	1.643	89.0	975
S5T	Li_2ZrO_3	HEDL	95	2.320	89.0	1150
S5B	Li_2O	JAERI	56	1.661	89.9	930
B8T	Li_2O	JAERI	56	0.952	88.8	700
B8C	Li_2O	JAERI	56	0.952	88.9	900
B8B	Li_2O	JAERI	56	0.952	89.3	500
B9T	Li_2O	Springfield	56	0.941	82.7	700
B9C	Li_2O	JAERI	56		90.0	700
B9B	Li_2O-sc	JAERI	7.5/0.07	0.800	100.0	500
B10T	$LiAlO_2$	Saclay	95	0.952	74.10	700
B10C	$LiAlO_2$	Saclay	95	0.952	73.02	900
B10B	$LiAlO_2$	Saclay	95	0.952	75.48	500
B11T	Li_2SiO_3	Karlsruhe	95	0.952	80.66	700
B11C	$LiAlO_2$	Casaccia	95	0.952	80.63	700
B11B	Li_4SiO_4	Karlsruhe	95	0.952	91.87	500
B12T	Li_2ZrO_3	Springfield	95	0.941	80.83	700
B12C	$LiAlO_2$	Casaccia	95	0.952	80.83	700
B12B	Li_4SiO_4	Karlsruhe	95		81.65	500

REFERENCES

1. G. W. Hollenberg, C. E. Johnson, and M. Abdou, "Tritium Breeding Materials", presented at Materials in Energy Systems Conference (May 1984).

2. R. G. Clemmer et al., "The TRIO Experiment", ANL-84-55, Argonne National Laboratory, Argonne, IL (September 1985).

3. J. M. Dupouy, "Report of Workshop on Solid Breeder Materials, Ispra, Italy, June 11-12, 1985" (July 1985).

4. G. W. Hollenberg and D. L. Baldwin, "The Effect of Irradiation on Four Solid Breeder Materials", J. Nucl. Mat. 133/134, 242-5 (1985).

5. M. Abdou, "FINESSE, A Study of the Issues, Experiments and Facilities for Fusion Nuclear Technology Research and Development, Interim Report", University of California, Los Angeles, CA (October 1984).

6. H. Kudo, C. W. Wu, and H. R. Ihle, "Mass-Spectrometric Study of Vaporization of Li_2O(s) and Thermochemistry of Gaseous LiO, Li_2O, Li_3O and Li_2O_2", J. Nucl. Mat., 380-9 (1978).

7. R. Stull and H. Prophets, Eds. JANAF Thermochemical Tables, 2nd Ed., U. S. Government Printing Office, Washington, DC (1971).

LITHIUM TRANSPORT WITHIN CLOSED IRRADIATION CAPSULES CONTAINING LITHIUM CERAMICS - G. W. Hollenberg and D. L. Baldwin (Westinghouse Hanford Company), R. Wisner and B. Carlson (Argonne National Laboratory)

OBJECTIVE

The objective of this work was to examine and explain the thermochemical stability of lithium oxide during irradiation to high burnup levels.

SUMMARY

Lithium was transported within the FUBR-1A capsules which contained Li_2O and Li_4SiO_4. The temperature and lithium burnup dependence, along with the absolute magnitude of this transport, suggest that it was caused by the formation of LiOT gas above the Li_2O pellet. Although transport in Li_2O blanket designs with high temperature purge channels can produce extensive material transport, the transport within the blanket may be limited by the localized burnup of the lithium.

PROGRESS AND STATUS

Introduction

Blanket designs utilizing oxide normally possess a neutronic advantage to those using ternary oxides since they are expected to achieve tritium breeding ratios significantly over 1.0 without a neutron multiplier. Tritium release from lithium oxide has been experimentally observed to be much better than anticipated from its hygroscopic character. The attractive features of lithium oxide for use in fusion blankets must be weighed against its lack of physical and chemical stability.

The Li_2O itself does not possess a significant vapor pressure ($>10^{-6}$ atm); but in the presence of moisture, the vapor pressure of LiOH is large at even moderate operating temperatures ($T > 750°C$).[1-4] The continual production of tritium provides a ready source of moisture to sustain LiOT formation and transport. From a design standpoint, LiOT gas formed at high temperature surfaces could travel to low temperature sites in the blanket where it could disassociate into $Li_2O(s)$ and $T_2O(g)$, hence, redepositing lithium oxide on this new site. Sufficient temperature gradients will exist to support this mass transport. There are basically three phenomena which could control the kinetics of this transport process:

(1) the high temperature vaporization process, $Li_2O(s) + T_2O(g) = 2LiOT(g)$

(2) the gas phase transport process, $LiOT(g)\ [HIGH\ T] = LiOT(g)\ [LOW\ T]$

(3) the low temperature condensation process, $LiOT(g) = Li_2O(s) + T_2O(g)$

The vaporization or transport process may be rate controlling while the condensation process is more important in considering where the Li_2O is deposited.

Tanaka et al.[5] conducted laboratory mass transport experiments on Li_2O pebbles at temperatures from 600 to 1000°C exposed to a flowing purge gas stream purposely doped with 1 to 1000 ppm H_2O. The resulting mass transport was then measured by deposition on downstream traps. Their measurements were in good agreement with the 1971 JANAF Tables and also the work of Berkowitz et al.[6] and Tetenbaum et al.[4] Laboratory experiments provide a simulation of the process which might occur in hot, flow stream channels in lithium oxide blankets. The amount of transport was proportional to flow rate and the square root of the water vapor pressure. Blankets which are intended to minimize lithium mass transport will attempt to channel flow into the lower temperature regions of the blanket.

Experimental

Pellets of lithium oxide, aluminate, zirconate, and orthosilicate were placed in stainless steel capsules for irradiation in the fast neutron flux of EBR-II for 105, 192, and 297 full power days (FPD) at predicted centerline temperatures of 500, 700, and 900°C.[7] A temperature difference existed in the helium filled gap between the pellet surface and the inner surface of the metal cladding (nickel lined); approximately 300°C difference at 900°C; 155°C at 700°C and less than 40°C at 500°C. Other cladding surfaces were at 400°C or lower. The T_2O released from the pellets was chemically reduced by cerium and constantly diffused through the cladding walls at a steady state.

After irradiation, the cladding adjacent to the pellet column was sectioned, mounted, polished, and examined in the hot cell. The remaining cladding material was rinsed in 0.5M HCl in order to remove lithium that had been deposited on the surface. The amount of lithium in the resulting solution was then determined by Inductively Couple Plasma emission spectrometry.

Results

After Li_2O pellet removal from the capsules, a layer of white deposit was observed on the inner surface of the cladding regions near the pellets. The longitudinally cut capsule after 297 FPD at 500°C allowed the coating to be directly photographed as shown in Fig. 1. The white deposit appears more dense at what was the center and the top of the pellet column. Near the cuts, areas of the coating appeared to be debonded and missing.

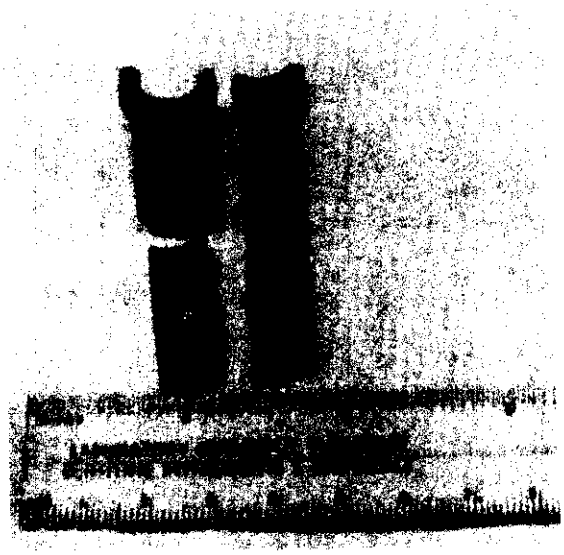

Fig. 1. Inside surface of capsule which contained Li_2O after 297 FPD at 500°C. Note white deposits on surface.

In Fig. 2, metallography of the thin deposit on the light-colored nickel lined cladding of irradiated Li_2O capsules are shown with the dark mounting media at the top of the photographs. Note that at 297 FPD (4 μm) the deposit is noticeably thicker than at 192 FPD (2 μm). It is interesting that the coating of lithium oxide did not appear to corrode the neighboring nickel during the test even though the nickel operated at over 500°C.

In Fig. 3, the lithium transfer is plotted against the lithium burnup for the 500, 700, and 900°C capsules containing Li_2O and for the $LiAlO_2$, Li_4SiO_4, and Li_2ZrO_3 capsules which operated at 900°C for 297 FPD. As seen in Fig. 3, the amount of lithium transported to the walls in the Li_2O capsules was strongly dependent on temperature. There is a rough proportionality between the burnup and the amount of lithium transported at 700 and 900°C. Least square analysis of these results reveal that the fractional lithium transport coefficient of lithium to the wall was 0.122 at 500°C, 0.255 at 700°C, and 0.651 at 900°C. At 500°C, however, there was very little burnup dependence. The fractional lithium transport coefficient (LTC) is the ratio of transported lithium (lithium transported/lithium total) to the burnup of lithium in the pellets (lithium burnup/lithium total, i.e., the tritium production in the sample). The fractional transport coefficient represents the ratio of tritium leaving the pellet as LiOT to the total tritium release rate, assuming that no H_2O was present and all the tritium left in the oxide form.

Lithium zirconate and lithium aluminate exhibited essentially no lithium transport after 297 FPD at 900°C, which confirms their anticipated stability. In the lithium orthosilicate capsule, however, there was 0.16% lithium transferred to the adjacent walls. Lithium orthosilicate's high lithium atom density is reflected in lithium transport properties closer to lithium oxide.

Analysis

The equilibrium constant, K, for LiOH vaporization is:

$$K = [P_{LiOT}]^2/P_{T_2O} \qquad \text{Eq. [1]}$$

where P_{T_2O} is the partial pressure of T_2O and P_{LiOT} is that LiOT. In the case of Li_2O under steady state irradiation during the FUBR-1A experiment, the total amount of tritium in the system was fixed by the release rate (RR > 90%) from the Li_2O which is assumed to be in the oxidized state. The steady state mass balance expression for tritium can be written as:

$$\text{Burnup rate} = 2\,F_{T_2O} + F_{LiOT} \qquad \text{Eq. [2]}$$

where F_{T_2O} is the T_2O total flux at the lithium oxide pellet surface and F_{LiOT} is the total flux of LiOT. With a single pass convection current, the flux of a species at steady state is proportional to the species partial pressure and the velocity at the surface. Mass balance then requires that:

$$2P_{eff} = P_{LiOT} + 2P_{T_2O} \qquad \text{Eq. [3]}$$

where P_{eff} is an effective total T_2O pressure. By substitution of Eq. 1 into Eq. 3, a quadratic expression is obtained with the following real solution:

$$P_{LiOT} = (K/4)[-1 + \sqrt{1 + 16\,P_{eff}/K}] \qquad \text{Eq. [4]}$$

In this simplified model, the lithium transfer coefficient becomes the ratio of P_{LiOT} to twice P_{eff}.

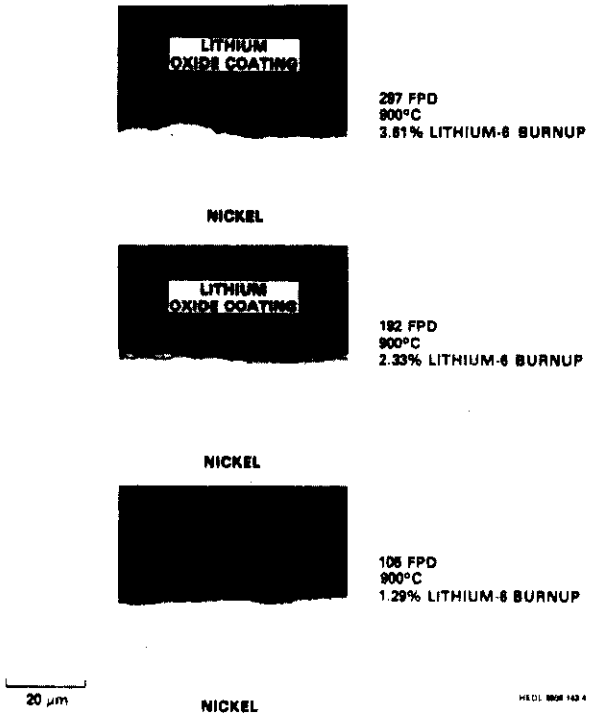

Fig. 2. Metallography of Li_2O surface coating buildup on inner surface of nickel after 105, 192 and 297 FPD of irradiation at 900°C pellet temperature. Notice no corrosive attack of nickel.

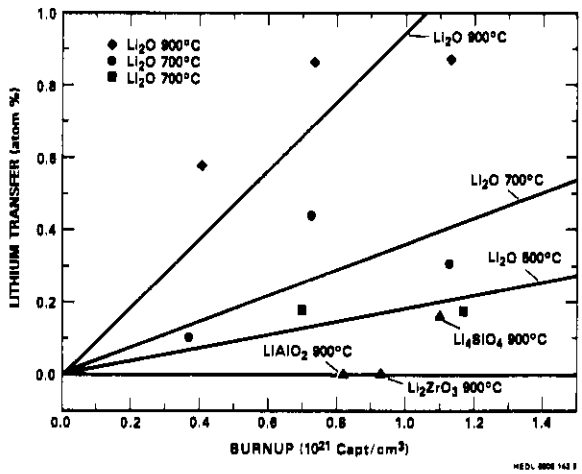

Fig. 3. Measured lithium transport after irradiation to cladding surface for Li_2ZrO_3, $LiAlO_2$, Li_4SiO_4 and Li_2O at 900°C and Li_2O at 500 and 700°C.

If gas diffusion plays a more important role than discussed here, a more complex solution is required; but for single pass steady-state diffusion, the maximum transfer rates would still be bounded by Eq. 3. A T_2O molecule can potentially make multiple paths from the high temperature to the low temperature regions of the blanket and thus enhance transport. If T_2O were much more mobile than LiOH or if T_2 was a significant release component, then transport is depressed.

In Fig. 4, the calculated lithium transfer coefficients based on JANF (1971) data are plotted against the pellet temperature for several P_{eff} values. The predicted lithium transfer rates vary from zero at low temperatures where all the tritium leaving is T_2O to 1 at high temperatures where essentially all the tritium is LiOT. In Fig. 4, the measured lithium transfer coefficients taken from Fig. 3 are also plotted. At 500°C the measured transfer coefficient could be from an initial transient in which the H_2O contamination present during reactor startup causes a deposition, which is consistent with the lack of burnup dependence at 500°C. At 700 and 900°C the lithium transport coefficients increase in a manner which qualitatively agrees with the predictions. The arrows in Fig. 4 represent the reduction which could be caused by the effect of initial moisture. The interesting feature of Figs. 3 and 4 is that there is approximate agreement with the absolute magnitude of the lithium transfer coefficient, i.e., a fraction of lithium burnup. This is far different than in laboratory situations where basically the amount of transfer is unbounded and only a function of temperature, flow rate, and the partial pressure of T_2O. Designs which can tolerate local lithium transfer rates equivalent to the local burnup can utilize Li_2O to very high temperatures (T > 900°C).

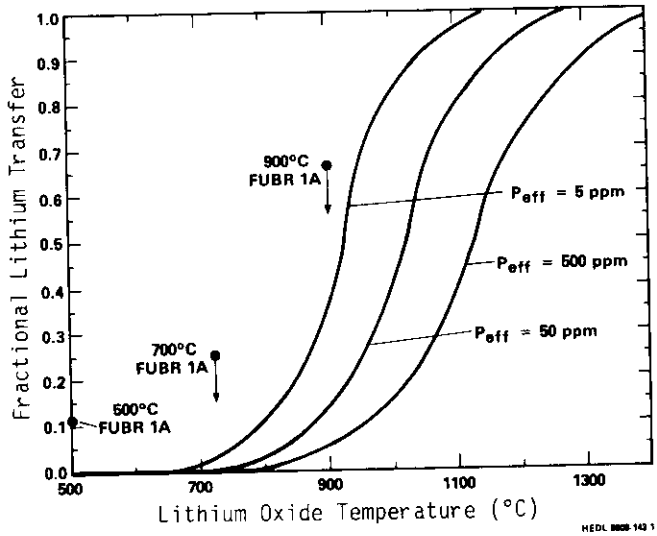

Fig. 4. Comparison of predicted fractional lithium transport at three values of the effective tritium pressure, P_{eff}, in the capsule with the measured values.

CONCLUSIONS

Lithium mass transfer at 900°C was not observed in $LiAlO_2$ and Li_2ZrO_3 after irradiation but measurable at 900°C from Li_4SiO_4 and significant from Li_2O. Lithium mass transport in Li_2O capsules appeared to increase with lithium burnup and with temperature. These results indicate that mass transport is not a significant problem with ternary oxides and may not even be significant in even Li_2O if purge flow channels are limited to low temperature regions of the blanket.

REFERENCES

1. H. Kudo, C. H. Wu, and H. R. Ihle, "Mass Spectrometric Study of the Vaporization of Li_2O and Thermochemistry of Gaseous LiO, Li_2O, Li_3O, and Li_2O_3", J. Nucl. Mat. 78, 380 (1978).

2. Y. Iketa, H. Ito, G. Matsumoto, and S. Nasu, "A Mass Spectrometric Study of Vaporization of Li_2O with Some Refractory Metal Cells", Mass Spectrosc. 27, 263 (1979).

3. H. Kimura, M. Asano, and K. Kubo, "Thermochemical Study of the Vaporization of Li_2O by Mass Spectrometric Knudsen Effusion Method", J. Nucl. Mat. 92, 221 (1980).

4. M. Tetenbaum and C. E. Johnson, "Vaporization Behavior of Lithium Oxide", J. Nucl. Mat. 120, 213 (1984).

5. Y. Tanaka, T. Suzuki, S. Mori et al., "Some Considerations on Li_2O Pebble-Type Breeding Blanket Design for Tokamak Fusion Reactors", Fusion Tech. 8, 947-52.

6. J. Berkowitz, D. J. Meshi, and W. A. Chupka, "Heterogeneous Reactions Studied by Mass Spectrometry, II Reaction of $Li_2O(s)$ with $Li_2(g)$", J. Chem. Phys. 33, 553 (1960).

7. D. E. Baldwin and G. W. Hollenberg, "Measurement of Tritium and Helium in Fast Neutron", to be published in J. Nucl. Mat.

PELLET INTEGRITY AND SWELLING OF LITHIUM CERAMICS - G. W. Hollenberg (Westinghouse Hanford Company)

OBJECTIVE

The objective of this effort is to determine the swelling and pellet integrity of Li_2O, Li_4SiO_4, Li_2ZrO_3, and $LiAlO_2$ after irradiation in a fast neutron fluence.

SUMMARY

Differences in the pellet integrity of lithium ceramics irradiated in the EBR-II reactor were observed to be related to the level of thermal strains within the ceramics which resulted from differences in thermal conductivity and thermal expansion of the solids. Swelling in Li_2O was found to be significantly greater than that of Li_2ZrO_3, $LiAlO_2$, and Li_4SiO_4 at high temperatures. At 500°C, Li_2O exhibited axial shrinkage which resulted in overall volumetric shrinkage of the pellets which is not presently understood. The high temperature swelling of Li_2O is thought to be caused by the high helium retention in this solid.

PROGRESS AND STATUS

Introduction

Lithium ceramics are being considered for the purpose of tritium production in D-T fusion power plants. One of the many issues which must be resolved before blankets containing lithium ceramics are brought into service is the degree of stability which can be expected from these new materials. Swelling of the solid breeder material can directly impact the design lifetime of the blanket. Accommodation of swelling in the design can correspondingly require compromises in the overall performance of the blanket.

Recently, an irradiation experiment was completed at moderate burnup levels in which swelling of solid breeder materials was observed. As will be discussed, the swelling of the Li_2O can be considerably more than that of the Li_4SiO_4, Li_2ZrO_3, and $LiAlO_2$. In addition, a degree of pellet cracking and fragmentation was observed which varied between the materials.

Experimental procedures

Pellets of Li_2O, Li_4SiO_4, Li_2ZrO_3, and $LiAlO_2$ were irradiated in the fast neutron spectrum of the EBR-II reactor at temperatures of 500, 700, and 900°C for periods of 105, 192 and 297 full power days (FPD).[1] The pellets were 85% of theoretical density except for two sets of 95% TD $LiAlO_2$ pellets at 700 and 900°C for 105 and 192 FPD.

After irradiation, the pins were neutron radiographed in order to examine the solid breeder's configuration within the cladding. Later the pellets were removed from their capsules by cutting through the vacant end of the cladding in an argon flooded box located in the HFEF hot cells. In some cases, it was necessary to longitudinally slit cladding in order to extract the pellets. The saw at times penetrated into the pellets and made surface cuts which are visible on the pellets. Finally, the lithium-6 burnup was determined by measurement of retained helium in the pellets and the released helium in the pin.[1]

Before irradiation, the dimensions of the pellets (approximately 1 cm OD x 1.4 cm L) were measured to the nearest 0.0005 cm with a micrometer in an inert gas glovebox prior to capsule loading. Diametral measurements were made at the top, center, and bottom of the pellet by making three individual measurements with a flat-faced micrometer 120 degrees apart. The lengths were measured by making three measurements near the circumference and one in the center with a ball-tipped micrometer. All measurements were then averaged to give the final values used for swelling computation.

After irradiation, the same mensuration method was attempted in an inert gas glovebox or, in the case of the more radioactive Li_2ZrO_3, in a hot cell. However, many pellets were fragmented into small pieces and thus sometimes measurements in the axial direction were not feasible as will be noted later. Most pellets were photographed after being transferred to inert gas gloveboxes; however, the radioactivity level of the Li_2ZrO_3 made it desirable to photograph and store these pellets in a hot cell until several half-lives (two months) had passed.

Pellet integrity discussion

Figure 1 is a mosaic of photographs of the Li_2ZrO_3 pellets after irradiation to 192 and 297 FPD. These pellets appeared to survive the irradiation better than any compositions. Only at an exposure of 297 FPD at 900°C did the pellets crack and fragment, and even then the cracking was limited to a separation of the pellets into shorter right cylinders. The origin of the surface spots on these pellets was not resolved. Ion microprobe analysis of the discolored areas did not reveal heavy metal contamination.

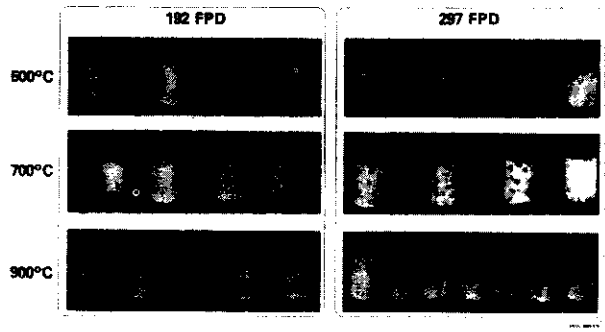

Fig. 1. Photographs of 85% TD Li_2ZrO_3 pellets after irradiation to 192 and 297 FPD at temperatures of 500, 700, and 900°C.

Figures 2a and 2b are of 85% and 95% TD $LiAlO_2$ pellets and 60% TD powder compacts after irradiation at temperatures from 500 to 900°C for exposures between 105 and 297 FPD. The 85% TD $LiAlO_2$ pellets irradiated at 500°C were not visibly cracked, but at 700 and 900°C the pellets appeared to not only be cracked but had also fragmented into many pieces. Cracking includes limited subcritical crack growth or extension which is contrasted with fragmentation which is indicative of crack propagation through the pellet, and thus two or more fragments were recovered in a fragmented pellet. Both transverse and radial cracks were observed in these pellets.

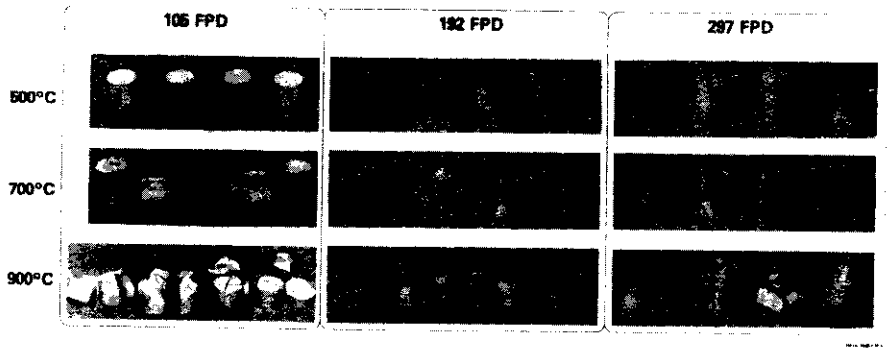

Fig. 2a. Photographs of 85% TD $LiAlO_2$ pellets after irradiation to 105, 192, and 297 FPD at temperatures of 500, 700, and 900°C.

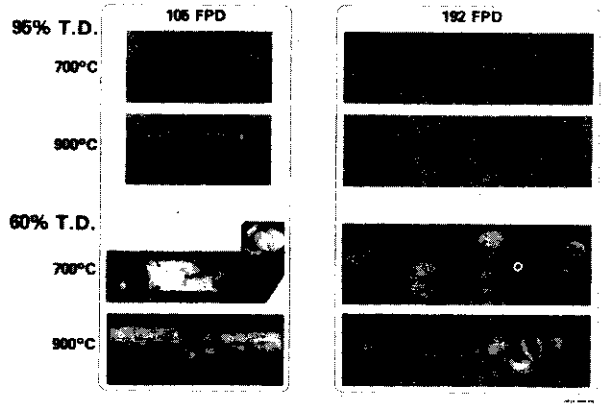

Fig. 2b. Photographs of 95% TD $LiAlO_2$ and 60% TD compacted $LiAlO_2$ powder after irradiation to 192 and 297 FPD to temperatures of 500, 700, and 900°C.

In Fig. 2b, the 95% TD $LiAlO_2$ pellets exhibited very little fragmentation or cracking at either 700 or 900°C. $LiAlO_2$ powder was simply compacted into the capsule in order to form the 60% TD $LiAlO_2$ material. This material was cut out of the surrounding cladding after irradiation and was amazingly tough considering it had never been sintered.

The lithium silicate in Fig. 3 fragmented more extensively than any other material. Even in the pellets which did not fragment, obvious radial cracks were observed. In the other materials, i.e., $LiAlO_2$, Li_2ZrO_3, and Li_2O, it was difficult to observe fragmented pieces in postirradiation neutron radiographs taken while the pellets were still in the capsule. This observation could be used as an argument that in these materials cracks were present during irradiation and that fragmentation occurred during the cutting and manipulator operations in the hot cells. But in the Li_4SiO_4 capsules, cracks could be easily distinguished in the neutron radiographs and material rearrangement of the fragmented pieces was observed.

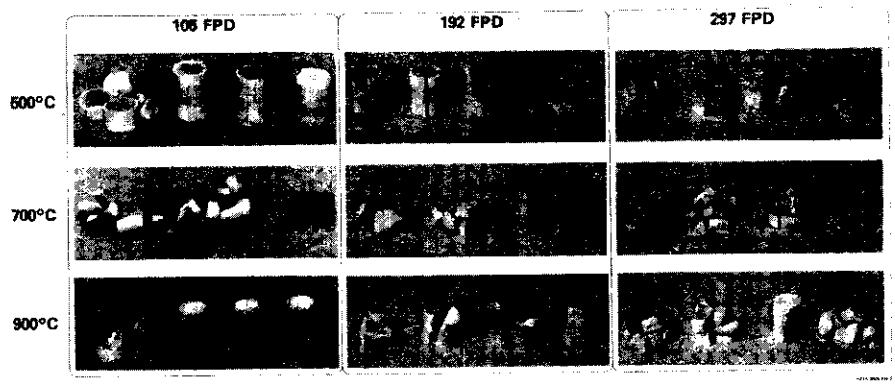

Fig. 3. Photographs of 85% TD Li_2O pellets after irradiation to 105, 192, and 297 FPD at temperatures of 500, 700, and 900°C.

The Li_2O pellets in Fig. 4 primarily have radial cracks with large crack opening displacements. There is also some transverse cracking and fragmentation. On some of the pellets, the longitudinal saw cuts are visible which were made during de-encapsulation.

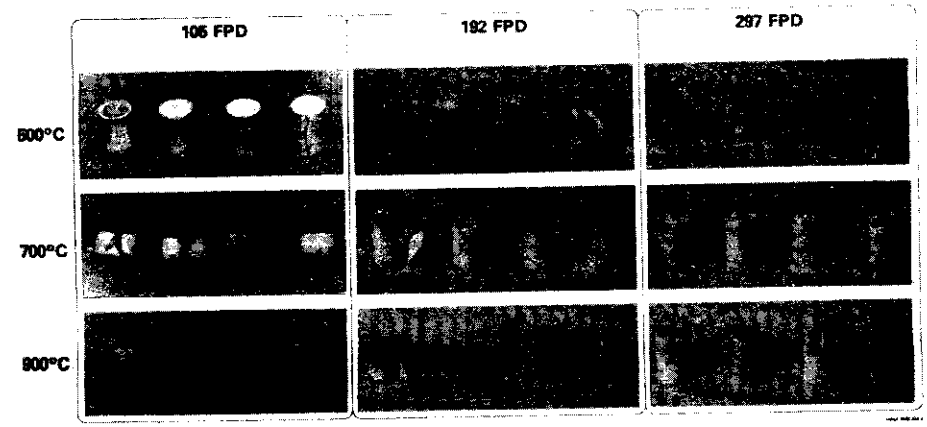

Fig. 4. Photographs of 85% TD Li_2O pellets after irradiation to 105, 192, and 297 FPD at temperatures of 500, 700, and 900°C.

Pellet cracking discussions

Although swelling gradients can contribute to pellet cracking, in these materials it is anticipated that thermal stresses are a more likely cause. It was recognized that the cracking did not appear to be burnup dependent and thus could have occurred at or shortly after the initial startup. Only limited thermal mechanical data are available on these particular materials. Hence, calculation of classical thermal stress parameters is not justified, but in Table 1, some of the information on these pellets has been compiled. Since heat generation rates are similar between the materials, their thermal conductivity dominates in the predicted temperature gradients that are calculated. Notice that the high thermal conductivity of Li_2O results in a lower temperature difference. Similarly, higher density materials, i.e., 95% TD $LiAlO_2$, possesses higher thermal conductivities and lower temperature gradients. Both Li_2O and Li_4SiO_4 possess the highest thermal expansion coefficients, almost twice as large as those for $LiAlO_2$ and Li_2ZrO_3.

Table 1. Thermal strains in irradiated lithium ceramic pellets

Material	Density	ΔT (°C)	Thermal Expansion Coefficient (10^{-6} cm/cm/C)	Maximum Strain Difference (%)*
Li_2O	85%	32 to 47	29.35	0.137
Li_2ZrO_3	85%	67 to 114	9.97	0.114
Li_4SiO_4	85%	54 to 105	27.1	0.285
$LiAlO_2$	60%	130 to 144	12.0	0.173
$LiAlO_2$	85%	54 to 102	12.0	0.122
$LiAlO_2$	95%	40 to 78	12.0	0.096

*Maximum thermal strain difference is calculated from the maximum temperature difference in the pellets and 500°C thermal expansion coefficient for the purpose of comparison.

The overall thermal strain difference has been calculated which is the driving force for thermal stress fracture. Notice that the Li_4SiO_4 material with its low thermal conductivity and high thermal expansion has the highest thermal strain difference. The Li_4SiO_4 exhibited the most cracking and fragmentation of these materials. Next highest is the Li_2O with its high thermal expansion coefficient. The Li_2O also exhibited extensive cracking but with less fragmentation. The Li_2O is known to exhibit plasticity at even very low temperatures (T < 500°C) so the fact that stable subcritical crack extension occurred is not surprising.

The higher thermal conductivity of the 95% TD $LiAlO_2$ (in comparison to the 85% TD reference material) results in the lower thermal strain difference. This, coupled with the anticipated higher strength of this material, explains the improved integrity of the 95% TD material. Hence, there is a qualitative agreement between the thermal strain differences and the extent of cracking in these pellets. The strong temperature dependence of the thermal conductivity of $LiAlO_2$ results in the lower predicted temperature differences (54°C) at 500°C and consequently lower strain differences which are thought to be the reason behind the good pellet integrity of the 85% TD pellets irradiated at 500°C.

Swelling measurements

Swelling had previously been reported but was only from measurements on neutron radiographs.[1,2] Volumetric swelling results from mensuration measurements are presented in Figs. 5-7 on $LiAlO_2$, Li_2ZrO_3, and Li_4SiO_4. Axial or length swelling and diametral radial swelling was nominally the same in these materials.

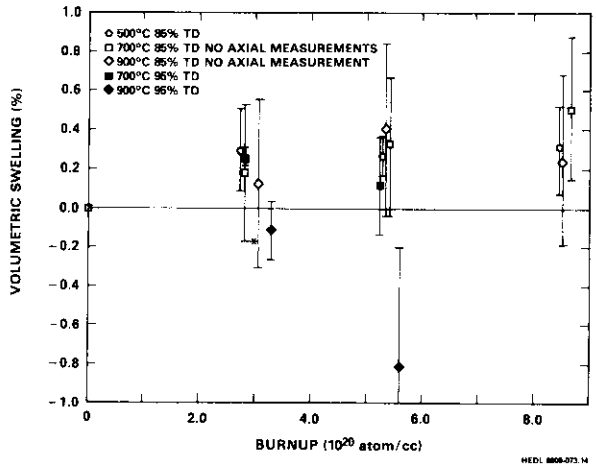

Fig. 5. The volumetric swelling of 85 and 95% TD $LiAlO_2$ at burnups up to 8.5 x 10^{20} captures/cc at temperatures from 500 to 900°C.

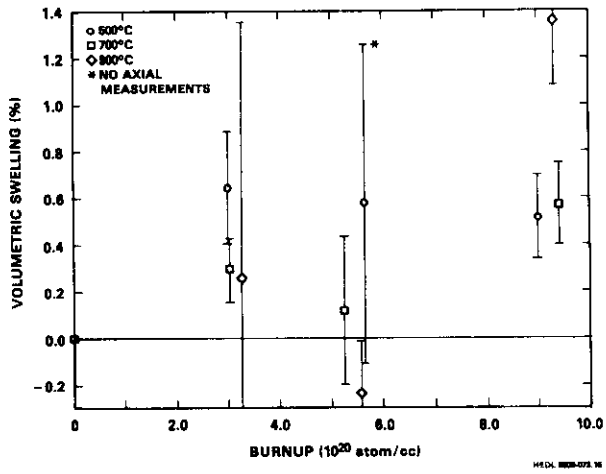

Fig. 6. The volumetric swelling of 85% TD Li_2ZrO_3 at burnups up to 9.5 x 10^{20} captures/cc at temperatures from 500 to 900°C.

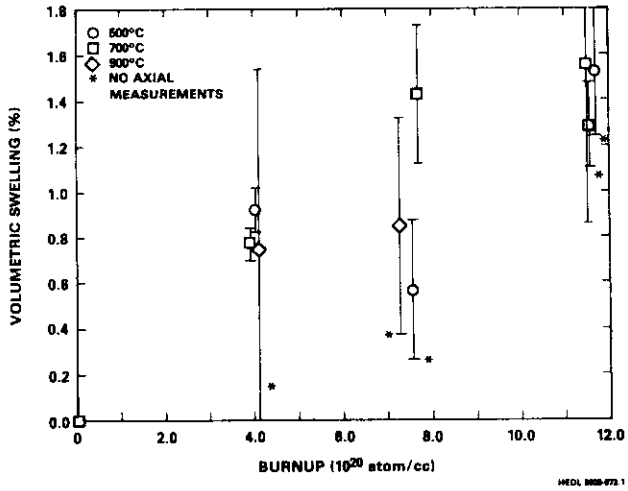

Fig. 7. The volumetric swelling of 85% TD Li_4SiO_4 at burnups up to 12 x 10^{20} captures/cc at temperatures from 500 to 900°C.

In Fig. 5, the swelling of 85% TD $LiAlO_2$ was observed to increase up to 8 x 10^{20} captures/cc, but was less than 0.5% for all data. The error bars which indicate the standard deviation for the measurements are quite large in comparison to the low swelling values in these pellets. Part of the error was thought to be associated with the internal cracks present in some of these pellets. In many cases, the measurement of swelling in the axial direction was not possible. At both 2.5 x 10^{20} and 5.6 x 10^{20} captures/cm^3, the higher density $LiAlO_2$ pellets actually exhibited shrinkage. In Fig. 6, the swelling of 85% TD Li_2ZrO_3 is almost as low ($\Delta V/V < 0.7\%$) as $LiAlO_2$ except for the 900°C data at the highest exposure. It should be pointed out that these 900°C pellets were the only Li_2ZrO_3 pellets that were fragmented (see Fig. 1).

In Fig. 7, the swelling of the Li_4SiO_4 pellets ($\Delta V/V < 1.6\%$) is almost twice that of the $LiAlO_2$ and Li_2ZrO_3. There appears to be an increasing trend of Li_4SiO_4 swelling with respect to burnup. In both Li_2ZrO_3 and Li_4SiO_4, the swelling at the intermediate burnup which corresponds to 192 FPD are on the average less than which might be interpolated from the lower and higher burnup data. In both cases the 192 FPD material was fabricated from a different batch of starting powder but was made to the same specification as the other two. In all these materials, swelling appears to be relatively independent of temperature.

In Fig. 8, the volumetric swelling of Li_2O at 700 and 900°C is much larger than in any of the other lithium ceramics, approximately 8% at 700°C. It appears that there is a nonlinear relationship between swelling and burnup at 700 and 900 °C. When higher burnup data (BU > 12 x 10^{20} captures/cm^3) becomes available, the apparent saturation of the volumetric swelling at a level of about 7% will be better described.

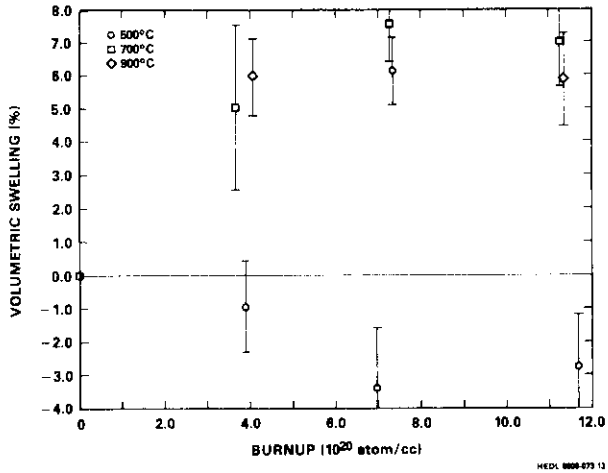

Fig. 8. The volumetric swelling of 85% TD Li_2O at burnups up to 12 x 10^{20} captures/cc at temperatures from 500 to 900°C.

At 500°C, the Li_2O pellets exhibited an overall volumetric contraction after irradiation. In Fig. 9, a comparison of the volumetric swelling to its two components, axial and diametral swelling, reveals that the diametral swelling of the Li_2O at 500°C is slightly smaller than, but highly consistent with, the higher temperature data. however, the axial swelling is very negative at 500°C and is thus the source of the overall volumetric shrinkage. At 700 and 900°C, the axial swelling is actually more than the diametral swelling values.

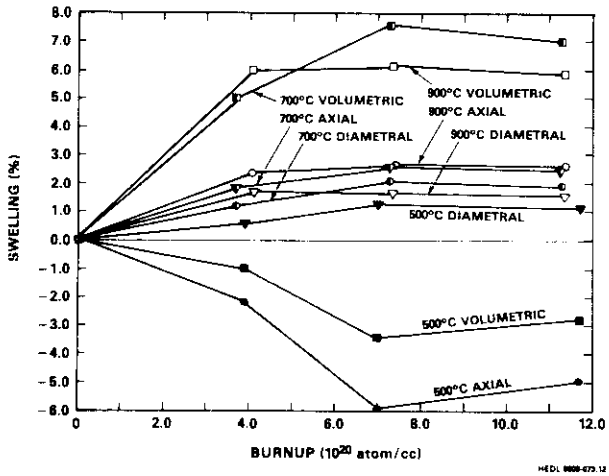

Fig. 9. A comparison of the volumetric swelling to the diametral and axial swelling of Li_2O after irradiation at burnups up to 12 x 10^{20} captures/cc at temperatures from 500 to 900°C.

Swelling discussions

Swelling in these ceramics is envisioned to have two components, a hard or high modulus component and a soft or low modulus component. The soft component is produced by internal macroscopic cracks as seen in Figs. 1-4 and microcracks present at grain boundaries. The soft component is of less consequence since very low stresses can be induced into neighboring structural material from this type of swelling. The hard component is, however, almost incompressible in comparison and originates from swelling internal in the individual crystallites. The data obtained cannot be quantitatively separated into these two component.

Swelling in irradiated materials is typically attributed to either Frenkel pair formation and vacancy agglomeration into voids or to gaseous transmutation product formation and agglomeration into bubbles. In this irradiation of lithium ceramics, it is anticipated that the gaseous transmutation products dominate because of the moderate lithium-6 neutron cross-section and the more permanent nature of these defects. Atomic displacements occur not only from the direct knock-on events with neutrons but also from the

transmutation products themselves. Displacement defects, i.e., vacancies and interstitials, need only annihilate while the helium and tritium must diffuse to a free surface in order to be eliminated from the crystals. Consequently, it is logical to correlate the retained helium and tritium to swelling. The low swelling of the $LiAlO_2$ and of the Li_2ZrO_3 were forecasted by the electron beam irradiations of Auvray-Gely et al.[3]

The helium and tritium are expected to take up different sites in the lattice. The inert helium atoms are expected to take up interstitial sites while the charged tritium ions can fill negatively charged lithium vacancies formed during the neutron capture process. Hence, the helium atoms are much more likely to introduce swelling as interstitials and have a higher driving force for bubble formation. Lui et al. have reported significant bubble formation in Li_2O irradiated under slightly different conditions.[4]

As reported earlier, the helium retention in 85% TD $LiAlO_2$ and Li_2ZrO_3 was much lower than in 85% TD Li_2O.[1] Of all the Li_2ZrO_3 pellets, the greatest amount of helium (0.21×10^{20} atoms/cc or 2.34%) was retained at 500°C and 297 FPD. The $LiAlO_2$ behaved in a similar manner with 0.23×10^{20} atoms/cc or 2.74% helium being retained at the lowest temperature (500°C) and at 297 FPD (8.5×10^{20} captures/cc). In contrast, the greatest amount of retained helium in the Li_2O pellets was reported to be 2.5×10^{20} atoms/cc or 22.5 at 700°C and at 297 FPD (11×10^{20} captures/cc). Thus, the helium retained in the Li_2O is approximately ten times greater than in either $LiAlO_2$ or Li_2ZrO_3. In order to appreciate how much helium induced swelling is possible, it is worthwhile to compute the retained helium volume per volume of solid breeder. For the maximum case discussed above, the volume of helium in Li_2O would be 30 cc/cc at 1 atm and 0.2 cc/cc at 300 atom of internal pressure at 700°C. Thus, the volumetric swelling ($\Delta V/V < 10\%$) in the Li_2O at 700°C ($\Delta V/V < 10\%$) disregarding the soft component of swelling. The radial swelling in Li_2O contains a soft swelling component as seen in Fig. 4. The lack of significant swelling in the Li_2ZrO_3 and $LiAlO_2$ is consistent with the low helium retention in those materials.

The shrinkage of Li_2O at 500°C is far more difficult to explain. In Fig. 9, the volumetric shrinkage is seen to result from axial shrinkage while radial swelling occurred in much the same manner as at the higher temperatures. Taken by itself, one simple explanation is that dilational creep occurred with a compressive creep force being applied axially to the pellet and shear creep resulting in the diametral strain. The predicted, but unmeasured, stress from the plenum spring was approximately 187 KPa. Normally creep is expected to be a thermally activated process such that even more creep would be expected at 700 and 900°C. However, in polycrystalline studies[5] and even more clearly in single crystal creep experiments,[6] it has been observed that Li_2O creep is not a simple thermally activated process at low temperatures. Perhaps the higher retention of tritium oxide or moisture at the lower temperatures provides for enhanced dilational creep rates at 500°C in comparison to the higher temperatures.

The shrinkage of the high density $LiAlO_2$ pellets is even more unusual. Although the error bands are proportionately large, there is measurable densification at both burnup levels. Sintering or creep could not be used to explain this densification since at 900°C $LiAlO_2$ does not normally sinter or creep. There was a net loss of lithium from the pellet of approximately 0.6% atomic, that is lithium burnup compared to total lithium, aluminum and oxygen atoms. It is possible that if complete defect annihilation and helium release occurred, this could lead to a reduced volume. The retained helium in the 95% TD $LiAlO_2$ was only 0.0179×10^{20} atoms/cc, which is less than either the 85% or even the 60% TD $LiAlO_2$ at 297 FPD. The growth of a $LiAl_5O_8$ second phase was reported by Auvray-Gely et al. after electron beam irradiation of $LiAlO_2$. Depending on where a second phase is deposited in the microstructure, it could lead to shrinkage.

CONCLUSIONS

The observed pellet integrity of the Li_2ZrO_3 pellets was best and could be explained by its moderate thermal conductivity and lower thermal expansion coefficient. The Li_4SiO_4 appeared to have the most pellet fragmentation which was explained by its low thermal conductivity and high thermal expansion. The higher density $LiAlO_2$ had better thermal integrity than the 85% dense $LiAlO_2$ in part because of its naturally higher thermal conductivity. The high plasticity of Li_2O provided it with limited crack growth.

Pellet swelling was very low in Li_2ZrO_3 and $LiAlO_2$. Pellet swelling was slightly higher for Li_4SiO_4. Pellet swelling of Li_2O was very high at 700 and 900°C and is thought to be caused by the retained helium in these samples. Pellet shrinkage occurred in Li_2O at 500°C and could be caused by enhanced dilational creep.

REFERENCES

1. D. L. Baldwin and G. W. Hollenberg, "Measurement of Tritium and Helium in Fast Neutron Irradiated Lithium Ceramics Using High Temperature Vacuum Extraction", presented at the Third International Conference on Fusion Reactor Materials, Chicago, IL (April 1986), to be published in J. Nucl. Mat.

2. G. W. Hollenberg and D. L. Baldwin, "The Effect of Irradiation on Four Solid Breeder Materials", J. Nucl. Mat. 133/134, 242-5 (1985).

3. M. H. Auvray-Gely, A. Dunlop, and L. W. Hobbs, "Irradiation Damage in Lithium Ceramics", J. Nucl. Mat. 133/134, 230-3 (1985).

4. Y. Y. Lui, R. F. Mattas, D. L. Smith, and D. L. Porter, "Microstructural Examination of Fast Neutron Irradiated Li_2O", J. Nucl. Mat. 133/134, 209-15 (1985).

5. G. W. Hollenberg, Y. Liu, and B. Arthur, "Creep of Li_2O", J. Nucl. Mat. 133/134, 216-20 (1984).

6. K. Noda et al., "Mechanical Properties of Lithium Oxide at High Temperatures", presented at the Third International Conference on Fusion Reactor Materials, Chicago, IL (April 1986), to be published in J. Nucl. Mat.

THE EFFECT OF IRRADIATION ON THE THERMAL CONDUCTIVITY OF LITHIUM CERAMICS

J. L. Ethridge and D. E. Baker (Westinghouse Hanford Company)

OBJECTIVE

The objective of this effort is to determine the extent to which irradiation in a fast neutron flux influences the thermal conductivity of Li_2O and $LiAlO_2$.

SUMMARY

An apparatus for measuring the thermal conductivity of irradiated lithium ceramics to 900°C was designed, fabricated, and tested. Special attention was necessary in order to accommodate tritium released during the high-temperature measurements.

PROGRESS AND STATUS

Introduction

The thermal conductivity of lithium ceramics is important in the design of fusion blankets and irradiation experiments. In blankets, thermal conductivity along with the projected operating temperature range of a specific solid dictates the optimum spacing of coolant passages that will be required. A high concentration of coolant passages in turn detracts from the tritium breeding ratio of the blanket.

The thermal conductivity of unirradiated Li_2O and $LiAlO_2$ have been measured[1-2] and appear to be controlled by phonon conduction according to their observed temperature dependence. At high temperatures, the conduction by the phonon process is interrupted by thermal vibrations in the lattice and a lower thermal conductivity results. In irradiated lithium ceramics, it is logical to propose that irradiation defects will also interrupt this process resulting in a shorter mean free path for phonons and thus a lower thermal conductivity. This has an obvious negative impact on the breeding ratio of blanket designs and thus must be evaluated. However, it is possible that only at low temperatures, where the unirradiated phonon mean free path is long, will the irradiation defects significantly contribute to the reduction of the mean free path and thus the thermal conductivity. Hence, it is important to measure the thermal conductivity of irradiated $LiAlO_2$ and Li_2O in order to assess how it might affect blanket designs and to also provide a basis for designing future irradiation experiments.

Experiment apparatus

Use of the thermal diffusivity technique on ceramics is common. The technique utilizes a laser pulse for heat deposition on one side of a thin cylindrical sample disc.[4] Besides the basic equipment necessary to measure thermal diffusivity, it was necessary to accommodate the tritium which is released during heating. Figure 1 shows a schematic of the apparatus fabricated for this investigation. A 9KJ ruby laser pulse is deposited on the front surface and the cryogenic indium-antimonide detector monitors the back surface temperature. The temperature transient is then stored in a Tektronix 7704A recording oscilloscope. From the least-square fit of the digitized waveform, the thermal diffusivity can be calculated.

The new contribution to this equipment is the self-contained furnace and sample chamber which is necessary for tritium containing materials. In a tritium glovebox, the sample chamber is loaded with a disc of irradiated lithium ceramic and hermetically sealed. Sapphire windows at the top and bottom of the chamber allow entrance of the beam and detection of the back surface temperature. The sample temperature is controlled by the internal furnace in the chamber. Tritium released during the measurements is contained within the chamber. After the measurements are completed, the chamber is returned to the glove box, and the tritium bearing chamber gas is circulated through a molecular sieve and getter (barium and cerium-nickel) gas cleanup system.

CONCLUSIONS

An apparatus has been developed which can be used to measure the thermal diffusivity of samples which contain tritium up to temperatures of 1000°C.

FUTURE WORK

The entire system has been made operational, and in the coming year it will be used to measure the thermal conductivity of irradiated Li_2O and $LiAlO_2$ from the FUBR-1A experiment.

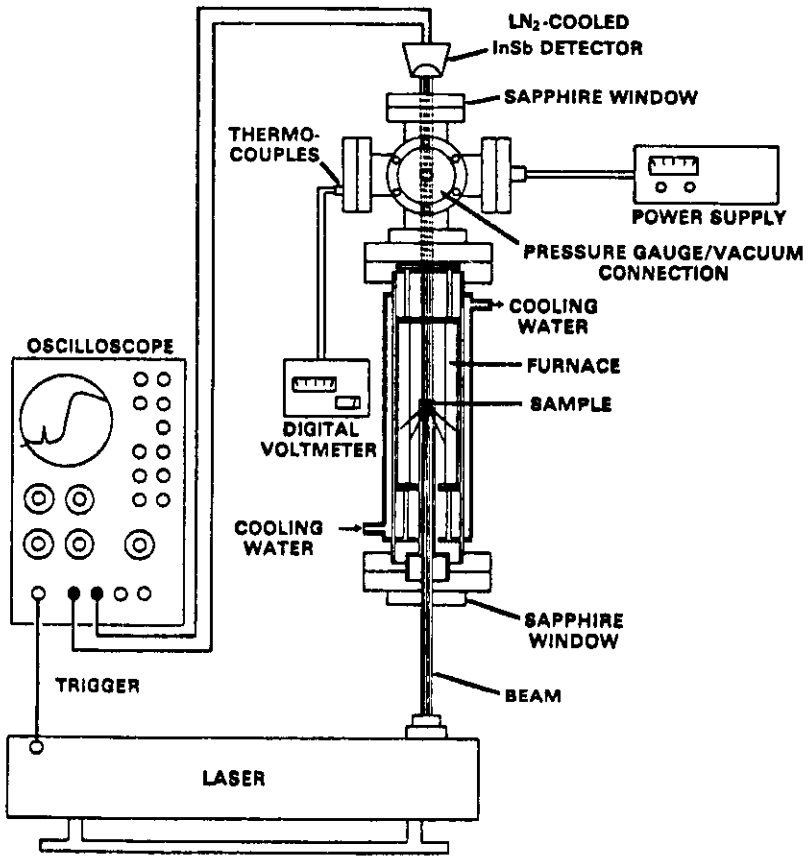

Fig. 1. Schematic drawing of the thermal diffusivity apparatus designed for use with tritium containing solids. The water cooled sample furnace chamber can be removed. Samples can be loaded in an inert gas/tritium glovebox (W701010-1).

REFERENCES

1. B. Schulz and H. Wedemeyer, "Preparation and Characterization and Thermal Diffusivity of Gamma-$LiAlO_2$", J. Nucl. Mat., 139, 35-41 (1986).

2. G. W. Hollenberg and D. E. Baker, "Thermal Properties of Lithium Ceramics for Fusion Applications", presented at the 84th Annual Meeting of the American Ceramic Society, Cincinnati, Ohio, May 2-5, 1982, HEDL-SA-2674, Westinghouse Hanford Company, Richland, WA.

3. T. Takahashi and T. Kikuchi, "Porosity Dependence of Thermal Diffusivity and Thermal Conductivity of Lithium Oxides", J. Nucl. Mat., 91 (1980).

4. W. J. Parker et al., "Flash Method of Determining Thermal Diffusivity Heat Capacity and Thermal Conductivity", J. Appl. Phys., 32, 1679-84 (1961).

8. CERAMICS

IN-WAVEGUIDE MEASUREMENTS OF MMW DIELECTRIC PROPERTIES OF CANDIDATE FUSION CERAMICS - H. M. Frost and C. D. Kise (Los Alamos National Laboratory)

OBJECTIVE

To measure dielectric constants "k" and loss tangents "tanδ" at room temperature and millimeter-wave (MMW) frequencies of ceramics within waveguide for their screening as rf-window materials, and to increase the corresponding precision and accuracy for this difficult measurement technique.

SUMMARY

The "rf window" in the first-wall structure of an MFE reactor is a crucial component for introducing powerful MMW beams into the plasma for electron cyclotron resonance heating (ECRH). As a follow-up to our prior findings of serious neutron-irradiation-induced damage to the MMW dielectric properties of polycrystalline alumina and beryllia for such windows, unirradiated specimens of silicon nitride and aluminum oxynitride ("ALON") from U.S. and Japanese sources were machined and inserted into WR-10 waveguide for computerized measurement of k and tanδ from 90 to 100GHz. The ALON was found to have a dielectric loss factor ktanδ of 0.0035--comparable to that for the alumina of last year's work. Its spinel-type structure is known to resist swelling and other mechanical property damage. A low-loss form of hot-pressed silicon nitride was also discovered.

Other progress includes computerized data reduction, and calculation of a correction factor yielding slightly smaller values of k and tanδ than reported in last years' SPM Progress Report on alumina and beryllia. Such steps are important: the in-waveguide approach at 100 GHz tolerates the small-sample requirements of fission-reactor irradiation studies (free-space techniques do not) and facilitates data collection over a wide frequency band.

PROGRESS AND STATUS

Introduction

Some background details on the importance and difficulty of measuring the MMW properties of candidate ceramic materials for rf windows are provided in the last two SPM progress reports.[1,2] (See Fig. 2.2.1 in Ref.2 for the rf window concept.) Briefly, dielectric heating in a thin disk increases with the factor f k tanδ, with "f" the (MMW) frequency, "k" the real part of the dielectric constant, and "tanδ" the loss tangent (tanδ<0.1). (Note: K, not k, was used in Ref. 2.) The increases in loss-factor (ktanδ) induced by fast-neutron irradiation were found to be unacceptable in the beryllia and alumina materials selected in a recent EBR-II experiment,[2] so it is especially important to continue the process of screening low-loss ceramics for eventually finding and/or developing one or more materials with the appropriate dielectric, thermal, and mechanical properties. Silicon nitride (polycrystalline) is an attractive candidate because it is a very strong insulating ceramic, is reasonably resistant to intense fast-neutron irradiation, especially at elevated temperatures like 815K,[3] and has a modest temperature coefficient at these temperatures for its MMW loss factor.[4] (There is a need , though, to find forms of Si_3N_4 with lower loss factors at room temperature than the value of 0.0016 reported.[4]) Further, the amount of transmuted carbon expected on an at% basis from 14MeV neutrons is one-half of that for Al_2O_3.[5] (Carbon is suspected of being dielectrically deleterious.) Aluminum oxynitride (ALON) is another low-loss ceramic but with the spinel-like structure known to be highly resistant to neutron irradiation.[6] Further, it is known that ALON, as polycrystalline $AlN(Al_2O_3)_{1.8}$, does not develop defect aggregates when irradiated by HVEM electrons.[7] Nitride ceramics generally have good thermal-shock resistance as well.

Relatively small changes in k and tanδ (and even window thickness) are potentially disastrous,[2] yet in-waveguide measurements are difficult to make so it is especially important to make accurate and precise measurements. Efforts in this area are thus described as well, against a back-drop of being constrained by fission reactor study requirements to use in-waveguide as opposed to the more conventional free-space or cavity-perturbation approaches[8].

Experimental procedures

Most of the experimental details are described elsewhere.[2] Basically, a rectangular parallelepiped ("matchstick") of 2.50 x 1.25mm cross section and 2-7cm length is precision-machined to fit snugly into rectangular WR-10 waveguide as part of a MMW reflectometer. These components as well as the directional couplers and detectors for measuring power reflected from and transmitted through the test specimen are shown in Fig. 1. Typical spectral data are shown in Fig. 2 for reflected (top) and transmitted (bottom) power for a 99.5% alumina. The frequency spacings δf between successive nulls in reflection or peaks in transmission lead via data reduction to k; the average 'drop' of the transmission peak heights relative to the zero reference line leads to tanδ.

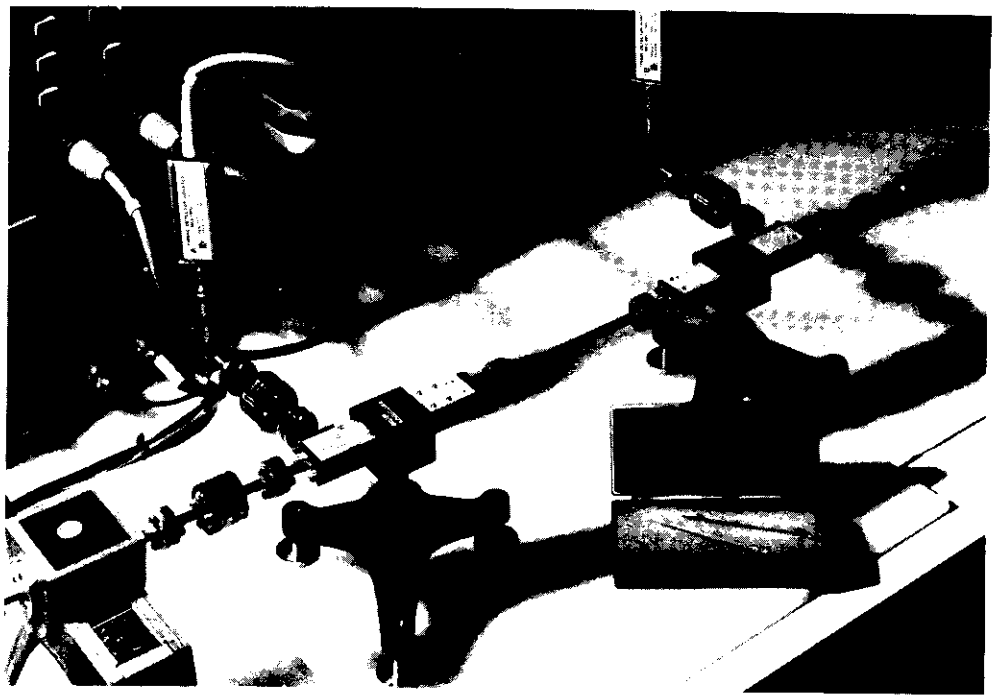

Fig. 1. Partial view of waveguide components and electronics for measuring MMW dielectric properties of ceramic specimens (lower right) inserted into a short waveguide section (center).

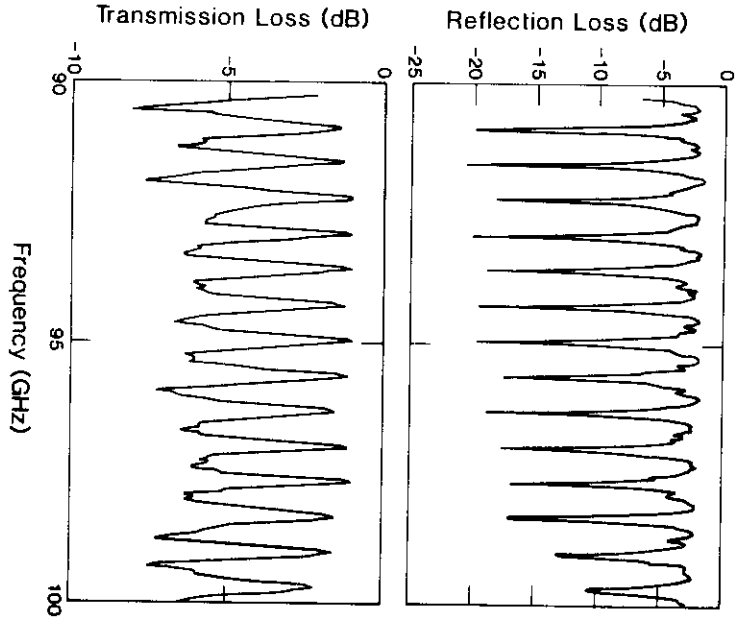

Fig. 2. Power spectra for reflection from and transmission through a 6.68 cm long specimen of 99.5% Al_2O_3 inserted into waveguide as per Fig. 1.

The three ceramics measured are described in Table 1, and the densities and dielectric properties are given in Table 2. For comparison, the lowest previously known value of ktanδ for HPSN in this frequency range was 49 x 10^{-3} for Ceradyne material (with yttria sintering aid).[8] No prior data on ALON are known;

its ktanδ value of 3.5×10^{-3} is comparable to the 3.8×10^{-3} subsequently given in this report for Coors AD995 alumina. Flexural strength is also comparable, but, based on vendor's values, the thermal conductivity of the alumina is three times that for the ALON. The ALON is more machinable, however, and because of its higher purity may have more consistent lot-to-lot characteristics. Further, ALON does not show the same defect-aggregation tendencies as does alumina under particle-radiation stress.[2,7]

Table 1. Low-loss ceramics

Ceramic	Abbreviation	Grade	Manufacturer	Remarks
Si_3N_4	HPSN	Toya Soda TS-7 powder	Union Carbide[a]	Hot-pressed; pressing axis unknown; Y_2O_3 and Al_2O_3 sintering aids
Si_3N_4	SN	"NS"	Sumitomo[b]	High purity
$Al_{23}O_{27}N_5$	ALON	99.95%	Raytheon[c]	Isotropic; 75 μm grains typical

[a] Supplied by M. Dowell, Union Carbide
[b] Supplied by N. Iwamoto, Osaka University
[c] Supplied by T. Hartnett, Raytheon

Table 2. Dielectric properties at room temperature and 90-100GHz for the ceramics represented in Table 1

Ceramic	Density (g/cm^3)	k[a]	$\tan\delta$[a] (10^{-4})	$k\tan\delta$[a] (10^{-3})	No. of specimens
HP Si_3N_4 (HPSN)	3.15	8.0	19	15	2
Si_3N_4 (SN)	3.11	7.7	24	18	3
ALON	3.59	9.5	3.7	3.5	3

[a] Rounded off to two significant figures; all measured in transmission.

The tanδ values found for ALON and alumina are also comparable to the maximum allowable values for 3-mm thick windows (face-cooled) of Al_2O_3 or $MgAl_2O_4$ subjected to a continuous power load of 200 kW over a 35 mm diameter disc.[9]

Precision and accuracy of data

Repeatability of the dielectric data depends on many factors, such as conformance of waveguide and specimens to rectangular shape, gaps between specimen surfaces and waveguide walls, stability and characterization of the (swept) frequency values of the IMPATT millimeter-wave source, nonlinearity of the diode detectors, repeatability of reflection characteristics of waveguide-to-waveguide connections, specimen conditioning, and lot-to-lot and spatial variations within the specimens' physical properties. As Table 2 indicates, large numbers of specimens were unavailable so that the measurement statistics cannot be fully determined. However, the typical total precision for same-day measurements can be good. For example, each average in Table 2 for the 'SN' Si_3N_4 is based on five determinations, with probable errors of ±0.25% for k and ±4% for tanδ (Gaussian distribution assumed).

Progress in increasing data precision and accuracy includes development of software programs for collection of data on frequency error (difference between indicated and true frequency values) and subsequent correction of the indicated values provided by the MMW 'sweeper' (Fig. 2.2.2., Ref. 2). That is why in Fig. 2 in this report the spectra do not start at the value of 90GHz preset in the sweeper. This

software also permits quick arithmetic averaging; a hundred 'sweeps' (90-100GHz) can be detected, digitized, and averaged in a fraction of a minute. Quality data also depend crucially on test specimens shaped as rectangular parallelepipeds which are easily inserted into and removed from precision waveguide holders, with minimal clearances of just a few microns between specimen side surfaces and waveguide walls. These clearances are not practicable with 'off-the-shelf' WR-10 waveguide sections and conventional slicing (diamond saw) and hand-grinding operations. In process now, however, are efforts to secure from specialty machining shops the needed precision fabrication of standard ceramic specimens of various lengths and the precision waveguide sections to hold them, with a view towards minimizing specimen-related systematic and random errors and quantifying errors from other sources.

A free-space version of the reflectometer now 'on line,' as described elsewhere in this progress report volume,[10] will provide a standard of comparison with the waveguide data as ceramic specimens of the same material become available in both matchstick (in-waveguide) and disc (free-space) form. It is easier to obtain quality data with the free-space approach (although this approach is not practicable for reactor studies), since, for example, specimen clearances are not critical, spurious standing waves can be preferentially suppressed, and the measured insertion losses correspond closely to the desired transmission losses. This latter point is not strictly true for in-waveguide measurements because of wall-related losses that cannot be completely subtracted out via the simple calibrations now performed for normalizing the measured data to the reference level for zero dielectric loss.

A more accurate expression has been determined for relating k to measured f than the one adopted from free-space measurements. In the free-space case,

$$k = (a/L)^2 \, (1/\delta f)^2 + p \qquad \text{Eq. (1)}$$

where "L" is specimen length, "a" is a constant, and "p" depends on angle of incidence of a MMW beam with the disc specimen. In waveguide, p still refers to an angle but one that now depends on frequency. The needed expression, correct to first order in p/k, has the different form

$$k = (a/L)^2 \, (1/\delta f)^2 \, G(f,\delta f,k), \qquad \text{Eq. (2)}$$

where the frequency-dependent correction factor G decreases with increasing frequency and with increasing dielectric constant. Equations (1) and (2) differ because the relationship between f and δf is linear (assuming a dispersion-free dielectric) over the frequency range 0 to f for free space measurements, but is nonlinear for the waveguide case and valid only over the range f_c to f, where f_c is the cut-off frequency for the waveguide. Our prior data on neutron-irradiated alumina[c] and beryllia[2] were corrected via Eq. (2), as shown in Table 3:

Table 3. MMW dielectric properties for neutron-irradiated ceramics, corrected for nonlinear f-vs.-δf relationship for waveguide case

Material and Type[a]	Density g/cm^3	k	tanδ (10^{-4})	k tanδ (10^{-3})
Al_2O_3:[b]				
C	3.78	9.86	3.9	3.8
I	3.67	9.68	8.3	8.1
BeO:				
C	2.71	6.23	6.5	4.0
I	2.48	5.42	15.0	8.3

[a] C ≡ control, I ≡ irradiated specimen.
[b] Coors AD-995.

Compared to the data in Table 2.2.1 of Ref.2, the k values are shifted down by about 0.4. The corrected tanδ values are also smaller because the expression for tanδ, calculated from the measured transmission (actually, insertion) loss of the specimen also depends on k. The doubling in loss factor k tanδ as induced by irradiation is preserved in Table 3, however.

Equation 2 applies to any waveguide type and band, not just to the 75-110GHz band applicable to WR-10 waveguide. A first-order approximation is adequate, as calculation of G correct to second order in p/k was found to affect k for alumina only by a fraction of one digit in the second decimal place. Because G is typically 0.95, the presence of k on both sides of Eq.(2) presents no problem in solving for k. That is,

the process of successive approximations, starting with the k value based on G ≡ 1, converges rapidly. Further, Eq.(2) actually represents a cubic equation in k, which can be solved analytically. (The G factor, however, does not correct for the effect of gaps, nor are the data in this report corrected for the small gaps that existed in the measurements.)

CONCLUSIONS

A ceramic-material system has been discovered for potential use as an rf window material at ECRH frequencies. This is $(Al_2O_3)_z$ AlN, or ALON for short. In this study, z =1.8, which provides the composition $Al_{23}O_{27}N_5$ which, according to one model, corresponds to a single cation vacancy per formula unit.[11] Another stable composition is $Al_{22}O_{30}N_2$, i.e., z =5 (2 cation vacancies). These predictions correspond closely to the phase-equilibrium diagram which indicates stability at about 35 mol% AlN (z = 1.8; gamma-Al_2O_3) and 15 mol% AlN (z = 5; zeta-Al_2O_3) for $Al_{23}O_{27}N_5$ and $Al_{22}O_{30}N_2$, respectively. Possibly, then, these or other compositions may be chosen to provide an optimum combination of material properties.

The relatively low dielectric losses found for the hot-pressed Si_3N_4 indicate that a chemical vapor deposition (CVD) form may have especially low losses. Specimens need to be tested.

Good precision and accuracy in measuring k and tanδ via the in-waveguide technique are essential for identifying ceramics with ktanδ values lower than the maximum allowed values (for disc windows) at the 0.001 level and below, corresponding to published estimates for maximum allowable tanδ of 0.0001 and below,[9] and for minimizing the potentially large uncertainties that can result from the power-law dependence of time-to-failure on ktanδ. To attain this, computerized operation of MMW equipment and reduction of data is a 'must,' along with development of measurement standards for quantifying systematic errors. The in-waveguide technique is preferred over the easier free-space approach because capsule-space limitations in fission reactors and health constraints on acceptable total radiation levels from activated specimens (assuming the measurements are not made by remote control) require small size and small mass. (Note: the diameter of the minicapsule used in the EBR-II experiment of Ref. 2 was about 15 mm.) Resonant-cavity techniques accommodate small specimens but tend to be limited to specific cavity resonances.

FUTURE WORK

We will continue to obtain, prepare, and measure specimens to identify ceramics with acceptably low losses in relation to the thermal-mechanical stress levels that can build up due to thermal gradients through the thickness of (surface cooled) windows. Of particular interest is CVD Si_3N_4, for example. Efforts will continue, too, to enhance measurement precision and accuracy, partly to obtain adequate sensitivity to tanδ values at the 0.0001 level.

REFERENCES

1. H. M. Frost, "Facility for Measuring Microwave Properties of Radiation-Damaged Ceramics for RF Windows and Other Fusion Applications," pp. 29-32 in SEVENTH ANNUAL PROGRESS REPORT ON SPECIAL PURPOSE MATERIALS FOR MAGNETICALLY CONFINED FUSION REACTORS, DOE/ER-0113/4, U. S. Department of Energy, Washington, D.C., May 1985.

2. H. M. Frost, "Millimeter-Wave Properties of Neutron-Irradiated Ceramics for RF-Window MFE Applications," pp. 11-16 in EIGHTH ANNUAL PROGRESS REPORT ON SPECIAL PURPOSE MATERIALS FOR MAGNETICALLY CONFINED FUSION REACTORS, DOE/ER-0113/5, U. S. Department of Energy, Washington, D.C., March 1986.

3. F. W. Clinard, Jr., et al., "Structural Performance of Ceramics in a High-Fluence Fusion Environment," J. NUCL. MATER. 122&123, 1386-1392 (1984).

4. W. W. Ho, "Millimeter Wave Dielectric Property Measurements of Gyrotron Window Materials," TECHNICAL REPORT FOR PERIOD January 1983 - February 1984, ORNL/SUB/83-51926/1, Rockwell International Science Center, Thousand Oaks, CA, April 1984.

5. G. R. Hopkins and R. J. Price, "Fusion Reactor Design with Ceramics," NUCL. ENG. DESIGN/FUSION 2, 111-143 (1985).

6. F. W. Clinard, Jr., "Ceramics for Fusion Devices," METALS/MATERIALS TECHNOLOGY SERIES, AMERICAN SOCIETY FOR METALS, paper 8403-005, pp. 1-8 (1985).

7. C. Parker, et al., "Damage Structures in Fast Neutron-Irradiated Magnesium Aluminate and Electron Irradiated Aluminum Oxynitride Spinels," J. NUCL. MATER. 133&134, 741-744 (1985).

8. W. W. Ho, "High Temperature Millimeter Wave Characterization of the Dielectric Properties of Advanced Window Materials," FINAL REPORT, AMMRC TR 82-28, Army Materials and Mechanics Research Center, Watertown, MA, May 1982.

9. W., Dienst and R. Heidinger, "Ceramic Insulator Materials for RF Windows," presented at the IAEA Consultants' Meeting on Insulators for Fusion Applications, Karlsruhe, Federal Republic of Germany, June 25-27, 1986.

10. H. M. Frost, "Capability for Measuring Millimeter-Wave Dielectric Properties in Free Space and at Elevated Temperatures," this PROGRESS REPORT.

11. J. W. McCauley, "A Simple Model for Aluminum Oxynitride Spinels," J. AM. CERAM. SOC. 61, 372-373 (1978).

PROPERTIES AND RADIATION RESISTANCE OF THE CANDIDATE RF WINDOW MATERIALS SiC AND Al_2O_3 - H. M. Frost and F. W. Clinard, Jr. (Los Alamos National Laboratory) and N. Iwamoto (Osaka University)

OBJECTIVE

The goal of this work is to assess changes in dielectric loss and other properties of Hitaceram SC-101 SiC and AD-995 Al_2O_3 before and after irradiation with 14 MeV neutrons in RTNS-II, as part of a study of candidate ceramics for RF window and related applications.

SUMMARY

RF windows must withstand transmission of an intense beam of electromagnetic energy. If absorption is excessive as a result either of intrinsic lossiness or degradation upon exposure to the operating environment, the resulting thermal stresses can cause structural failure. Samples of two candidate materials for this application, Hitaceram SC-101 SiC and AD-995 Al_2O_3, are currently being irradiated with 14 MeV neutrons at ambient temperature in RTNS-II; at this writing a fluence of $4x10^{22}$ n/m^2 has been attained. Work to date has shown that in unirradiated form the SiC exhibits low transmissivity but moderately high reflectivity at 10^{11} Hz, leading to consideration of its use as a mirror in RF heating systems. The alumina has enough transmissivity before irradiation to qualify this ceramic for further study as a window material under moderate irradiation conditions.

PROGRESS AND STATUS

Introduction

Dielectric windows are a potentially troublesome component of RF heating systems. At the high levels of power that will be transmitted, absorption of even a small fraction of the incident beam can lead to thermal stresses sufficient to cause fracture. Such a failure would be extremely serious, since escape of coolant from between the two layers of the laminated window would contaminate the plasma chamber and waveguide. The plasma chamber would be further contaminated by SF_6 dielectric gas from the pressurized waveguide. Thus a highly-transmissive, thermal stress-resistant dielectric material is required for window applications.

Prior work at relatively low frequencies ($\approx 10^5$-10^6 Hz) has shown[1] that even at doses as low as 10^{22} n/m^2, loss factor and therefore absorptivity of Al_2O_3 can be doubled. More recently, Frost[2] has found that both this material and BeO show a doubling of lossiness at higher doses ($9.5x10^{25}$ n/m^2) and frequencies (10^{11} Hz). In the latter case, it can be shown that the operating lifetime of a BeO window will be reduced from a year to less than a day by that magnitude of degradation.[2]

Conventional silicon carbide offers structural attributes that make it an attractive candidate material for this application, but its semiconducting properties imply unacceptable lossiness. Recently, however, Ogihara et al.[3] have described a new form of SiC with high thermal conductivity yet low dc electrical conductivity, the latter apparently resulting from depletion of charge carriers from regions near the grain boundaries. The present irradiation tests were initiated in part to determine the suitability of that material, Hitaceram SC-101, for RF window applications. Samples of AD-995 Al_2O_3 are also included in this study to allow assessment of lossiness at 10^{11} Hz after irradiation with 14 MeV neutrons.

Experimental procedure

Samples of SiC and Al_2O_3 have been submitted to RTNS-II for irradiation at ambient temperature to a maximum fluence equal to (or if possible, greater than) $5x10^{22}$ n/m^2. Test materials include Hitaceram SC-101 (from Hitachi, Ltd.) and AD-995 (from the Coors Porcelain Co., Inc.). Coupons of dimensions 21x21x1 mm (SiC) and 25x25x0.7 mm (Al_2O_3), are stacked alternately in the irradiation package to give each material a gradation of exposures. To date, a dose of $4x10^{22}$ n/m^2 has been attained.

Post-irradiation transmissivity will be characterized by carrying out dielectric measurements in waveguide[4] or in free space[5] via the millimeter-wave scalar network analyzer system at Los Alamos. Pre-irradiation measurements of properties of SiC and Al_2O_3 have been carried out using this facility in the waveguide mode.

Results and discussion

Hitaceram SC-101 SiC was found to be surprisingly lossy. A crude measurement indicated an upper limit on the room-temperature transmission loss of about 4 dB/mm, which is about 170 times the loss per unit length of Coors AD-995 alumina. Reflected power was estimated to be roughly one-third that of the incident beam, which according to the Hagen-Rubens approximation formula[6] corresponds to an electrical conductivity of roughly 20 $(\Omega\text{-m})^{-1}$. Thus while dc conductivity is $>10^{-11}$ $(\Omega\text{-m})^{-1}$ (ref. 3), this good insulating property is lost at ECRH frequencies, possibly as a result of displacement currents through the depleted near-

grain-boundary regions (e.g., from oscillating dipoles) that do not represent translation or migration of charge carriers and therefore do not contribute to dc conductivity. As a result of high ac conductivity and consequent lossiness, this material in its present form cannot be considered a candidate for RF window applications. The loss factor ktanδ for AD-995 Al_2O_3 was found to be 3.8×10^{-3}, a starting value that falls in the low range of that for dielectric ceramics.[4,2] Thus alumina is a viable candidate for window applications at ECRH frequencies.

It has been suggested[7] that RF windows be replaced or supplemented by mirrors, in which case high reflectivity is desirable. The relationship between electrical conductivity and relative reflected power R^2 is perturbational, e.g., $R^2 > 90\%$ for a wide range of reasonably high conductivities[6], so that even though one might think of a metallic mirror as most appropriate it is reasonable to consider for this application a ceramic such as Hitaceram SC-101 SiC. Potential benefits from use of a ceramic mirror include greater chemical stability (compared with a metal such as copper), superior dimensional stability (from a lower thermal expansion coefficient), better refractory qualities, and a usually lower sputtering yield.

Additional benefits accrue to a nonmetal such as SiC if, as expected, electrical conductivity and therefore reflectivity increase with increasing temperature and radiation flux (the latter effect due to radiation-induced conductivity). As an example, consider that the window is allowed to operate a few hundred degrees above room temperature to enhance defect recombination and reduce swelling.[8] If electrical resistivity of Hitaceram SC-101 SiC increases by an order of magnitude at this temperature, reflected power will increase from ≈33% to 77%. If absorption of ionizing radiation results in an additional order-of-magnitude increase in conductivity, reflective power will rise to 93%. By contrast, conductivity and reflectivity of metals decrease with increasing temperature and with displacement damage. These arguments indicate the potential value of semiconducting ceramics for use as mirrors and point to the desirability of engineering into the material a higher starting conductivity, perhaps by use of doping techniques.

CONCLUSIONS

Samples of the candidate RF window materials Hitaceram SC-101 SiC and AD-995 Al_2O_3 are presently being irradiated at RTNS-II, and have to date attained a fluence of 4×10^{22} n/m^2. Pre-irradiation lossiness of the alumina is low but lossiness and reflectivity for the SiC are high, leading to consideration of the use of this material as a mirror in ECRH heating systems. In its present form reflectivity of Hitaceram SiC is insufficient for that purpose, but enhancement by various means is possible. Other materials such as graphite can also be considered for mirror applications, and in this case can offer the possibility of serving the dual function of RF mirror and first wall armor.

FUTURE WORK

In a continuation of this work, the effect of irradiation at RTNS-II on dielectric properties of Al_2O_3 will be assessed and compared with earlier results obtained at lower frequencies. Measurements at 10^9 Hz are planned to be carried out at Osaka University, to determine the usefulness of this alumina ceramic at lower hybrid frequencies. The potential for using SiC as a mirror material will be further considered, and if results are favorable this information will be disseminated to the reactor design community. Both materials irradiated in this study will be examined by TEM to determine their characteristic defect content.

REFERENCES

1. J. D. Fowler, Jr., "Radiation-Induced RF Loss Measurements and Thermal Stress Calculations for Ceramic Windows," J. Nucl. Mater. 122&123, 1359-64 (1984).
2. H. M. Frost, "Millimeter Wave Properties of Neutron-Irradiated Ceramics for RF-Window MFE Applications," pp. 11-16 in Eighth Annual Progress Report on Special Purpose Materials for Magnetically Confined Fusion Reactors, DOE/ER-0113/5, U.S. Department of Energy, Washington, DC, March 1986.
3. S. Ogihara, K. Maeda, Y. Takeda and K. Nakamura, "Effect of Impurity and Carrier Concentrations on Electrical Resistivity and Thermal Conductivity of SiC Ceramics Containing BeO," J. Am. Ceram. Soc. 68, C-16-18 (1985).
4. H. M. Frost and C. D. Kise, "In-Waveguide Measurements of MMW Dielectric Properties of Candidate Fusion Ceramics," this Progress Report.
5. H. M. Frost, Capability for Measuring Millimeter-Wave Dielectric Properties in Free Space and at Elevated Temperatures," this Progress Report.
6. M. Born and E. Wolf, Principles of Optics, 2nd Edition, MacMillan, New York, 1964, p. 622.
7. L. J. Perkins, Lawrence Livermore National Laboratory, private communication (1986).
8. R. J. Price, "Effects of Fast-Neutron Irradiation on Pyrolytic Silicon Carbide," J. Nucl. Mater. 33, 17-22 (1969).

ON NEUTRON-INDUCED DAMAGE TO THE MILLIMETER-WAVE DIELECTRIC PROPERTIES OF ALUMINA - H. M. Frost, A. C. Lawson, and T. G. Zocco (Los Alamos National Laboratory) and L. W. Hobbs (Massachusetts Institute of Technology)

OBJECTIVE

Concerning the polycrystalline 99.5% alumina previously found to undergo a doubling of dielectric loss factor at 90-100GHz via fast-neutron irradiation, to correlate our prior and current results with the dielectric and neutronic literature on alumina, and identify possible mechanisms for the damage.

SUMMARY

We report the following findings concerning the previously reported doubling of the dielectric loss factor measured (post-radiation) at 90-100GHz and room temperature for Coors AD995 alumina irradiated to an averaged fluence of 0.95×10^{26} n/m²(E > 0.1MeV) at 385°C, in connection with the potential use of alumina as an rf-window material at ECRH frequencies:

*There is some evidence such a doubling may be relatively independent of frequency in frequency regions where strong dielectric dispersion is lacking.

*Associated with this doubling is a dense network of dislocation loops, apparently interstitial (as evidenced by TEM), and lattice strain in the basal planes (as evidenced by neutron diffraction).

*No evidence was found for colloidal aluminum formation.

*Possible mechanisms for the doubled dielectric loss include electromagnetically-induced vibration of dislocation entities, and interactions with point defects produced by displacement and transmutation events. Any future specification for a useable fusion ceramic at ECRH or lower frequencies (as for ICRH) will have to include more than a tabulation of desired property values, since compositional, microstructural, and processing variables are also important. These include the relative concentrations of major impurities, firing temperature, and cooling rates after firing.

PROGRESS AND STATUS

Neutron-induced doubling of dielectric losses

High fluences of fast neutrons ($F = 0.95 \times 10^{26}$ n/m², E > 0.1MeV, T = 385 ± 15°C) are known to increase the dielectric loss factor, ktanδ (dielectric constant x loss tangent) at 90-100GHz of Coors AD995 (99.5%) alumina by a factor of 2.1.[1,2] A similar post-radiation, room-temperature measurement result is known for 97.5% Deranox alumina irradiated by neutrons ($F \leq 1 \times 10^{24}$ n/m², E > 1 MeV, T = 60°C), then dielectrically measured at 0.1 to 65MHz.[3] In fact, the arithmetic mean of the ratios of the irradiated ktanδ values divided by their control values at the five frequencies in this range is 2.0 for the highest fluence of 1×10^{24} n/m², and 1.9 for the second highest fluence of 1×10^{23} n/m². Now, it can be shown from the data in Fig. 2 of Ref. 2 that strong dielectric dispersion (e.g., tanδ-vs.-frequency 'peaks') is absent, and the data of Ref. 3 lead to a similar conclusion. This evidence thus points toward at least some frequency independence in this doubling phenomenon in alumina, plus saturation with fluence at fluence levels of 10^{23} - 10^{24} n/m². This finding may be limited by the differences in irradiation temperatures (385 vs. 60°C) and in neutron energy spectrum (E > 0.1MeV vs. E > 1MeV) as well as the absence of data over the three decades of frequency between the preceding low and high frequency regions. However, data over the frequency range of about 0.02 to 2MHz on Coors AD995 alumina irradiated with fusion neutrons ($F \leq 1 \times 10^{22}$ n/m², E = 14MeV, T = 130°C) yielded a averaged value of 2.3 for the ratio of irradiated tanδ to control tanδ. Since k itself is not changed much by neutron irradiation,[2,3] the corresponding ratio for ktanδ is expected to be similar. The approach to saturation at fluences of 10^{22} n/m² is also suggested in Ref. 4.

The preceding findings are less valid for sapphire, as indicated by low-frequency dielectric data for fast[3] (E > 1MeV) and fusion[4] (E = 14MeV) neutrons, and for earlier formulations of the Coors AD995 alumina.[5] Concerning the latter point, a strong tanδ-vs.-fluence peak was observed at 1MHz and room temperature for the neutron-irradiated material ($F \leq 5 \times 10^{23}$ n/m², E = "fast," from the Sterling Forest reactor, T = 47°C). (A weak such peak was observed for Deranox alumina at f = 100KHz[3].)

Incidentally, we had also observed a neutron-irradiation-induced doubling in ktanδ for a BeO-based ceramic.[1] The irradiated beryllia 'matchstick' specimens were extremely fragile, however, in a manner consistent with the known abrupt decrease in rupture strength at $F < 10^{25}$ n/m² and E > 1 MeV that was reviewed by Wilks.[7] Beryllia also tends to be beam-sensitive in TEM, so it was not further investigated in this reporting period.

Selective review of the literature

In this section some of the published literature is reviewed on prior microscopy of fast-neutron-irradiated polycrystalline alumina including TEM, pertinent dielectric property measurements, and related matters.

Keilholtz et al. irradiated both solid cylinders and thin-walled cylindrical shells of three types of polycrystalline alumina in EBR-II ($F \leq 1.3 \times 10^{25}$ n/m², E > 1MeV, 670°C < T < 750°C).[8] The only type of alumina that fractured was the least pure, Coors AD995 alumina, and this occurred over the entire temperature range. Both this type and Wesgo AL-995 revealed, upon metallographic examination, separation at the grain boundaries at the highest fluence. Volume swelling at the highest fluences was greatest for the Wesgo AL-995 (e.g., 4.2% at 1.2×10^{25} n/m² and 740°C). At the highest fluence and temperature, the third type, GE opaque Lucalox, had the 'cleanest' appearing as-polished microstructure (at 100x magnification). The Lucalox also had the greatest density (3.91 g/cm³), smallest grain size (6 μm), and highest purity (99.94%).

Clinard et al. irradiated various types of alumina in EBR-II ($F \leq 6 \times 10^{25}$ n/m²; E > 0.1MeV; T = 650, 875, and 1025K): a GE Lucalox, two 99.9% Coors aluminas, an AVCO (99%), and sapphire.[9] Grain size for the Lucalox here was 20 μm. Only a fine dispersion of unresolved damage was observed in TEM at 650K in the various aluminas, but a high density of small 'pores' was present at 875 and 1025K with alignment along the c-axis. Subsequent instrumental analysis concluded these pores were voids.[10]

An early review of the TEM of the microstructure of neutron-irradiated alumina (E > 1MeV) indicates the formation of 50 - 75 Å dots and 50 - 600 Å loops at T ≤ 150°C and $F = 1$ to 4×10^{24} n/m².[7] The dots are not observed at T = 650°C and $F = 1 \times 10^{24}$ n/m², nor are the smaller loops at T = 1000°C and $F = 4 \times 10^{24}$ n/m². At this last temperature and fluence, "tangles" and 50 - 200 Å cavities were also seen. Most of the dislocation loops in alumina irradiated at 150°C (then annealed at 1500°C) lay on prismatic planes $\{10\bar{1}0\}$, while loops on basal planes {0001} were seen as well for irradiations at 650°C. Slight x-ray line broadening was seen for irradiations at about 80°C for fluences of 5×10^{24} n/m², with other broadening effects at 8×10^{24} n/m² and higher temperatures. The slight broadening that does occur at these fluences is said to indicate that the concentration of loops must be very low. Lattice parameter expansions for irradiations at 100°C were found to be isotropic for $F \leq 3 \times 10^{24}$ n/m², but for $F \geq 4 \times 10^{24}$ n/m² were anisotropic, with expanded c/a > 1. At relatively low fluences, the macroscopically determined density change equaled that calculated from the expanded lattice parameters (at 100°C irradiation). The macroscopic growths were greater than these calculated values for $F > 6 \times 10^{24}$ n/m² at T = 250°C and for $F > 4 \times 10^{24}$ n/m² at 475°C, possibly because of clustering of interstitials.

Quantitative TEM has been applied to single crystal and (Coors AD-995) polycrystalline alumina irradiated by fast neutrons ($F \leq 2.3 \times 10^{26}$ n/m²; E > 0.1MeV; T = 430, 925, 1015, and 1100K), in a study that also provides a review of earlier work.[11] Two types of dislocation loops are known, unfaulted interstitial prismatic loops $\{10\bar{1}0\}$ with Burgers vector $b = 1/3\langle 10\bar{1}1\rangle$ formed by neutron irradiation at T ≈ 400K, and analogous loops with the same Burgers vector formed on basal planes (0001) by HVEM electron irradiation at T ≈ 1100K. Both types of loop are known from weak-beam TEM to originate from nucleation of initially faulted four-layer loops. Either loop is faulted because only the cation sublattice is faulted. Both loops unfault by propagating across the loop plane of the appropriate partial shear. Continued irradiation at 700-1200K promotes unfaulted growth of loops until their intersection and formation of dislocation networks as observed in this study on neutron irradiation (next section). Such networking provides a basis for understanding the anisotropic expansion of the c- and a-lattice parameters in sapphire (which increases with increasing irradiation temperature) and the pronounced tendency for alumina to swell via the availability of networks as efficient interstitial sinks (to bias vacancy condensation into voids). These two effects in turn can lead to significant misfit strains and stresses in polycrystalline alumina. At 1100K and 1.2×10^{26} n/m², extensive grain boundary cracking (i.e., separation) was observed, for example.

Much less is known about the chemical segregation effects of fast-neutron-induced atomic displacements and transmutations. Estimated displacement levels for the preceding work go up to 23 dpa.[11] By use of calculated transmutation product levels for 14MeV neutrons in alumina,[12] and equating a fast-neutron fluence of 2×10^{26} n/m² to roughly ½ to 1 MW-yr/m² of fusion neutrons, then transmuted H, He, C, and Mg will be present at levels of hundreds of appm. The possibility of transmuted Si in alumina was mentioned in a recent review as well as the production of aluminum colloids.[13] In particular, Youngman suggests that Si produced from an EBR-II neutron spectrum may segregate on void surfaces and refers to other work on impurity concentration at these sites.[14] Also, Keilholtz et al. speculated that the tiny white areas they observed metallographically in neutron-irradiated alumina may be due to free silicon produced by transmutation.[8] Intergranular glassy phases containing silica and other impurity oxides exist in commercial polycrystalline aluminas,[15-17] including Coors AD-995 and Wesgo AL-995, and these provide potential sources of free Si, Ca, etc. upon occurrence of neutron-irradiation induced displacements and subsequent action of an appropriate segregation mechanism.

Next to be reviewed are prior dielectric property measurements and their bearing on material microstructure such as point defects, dislocations, and secondary phases.

Dielectric constants measured at room temperature and 9.368 GHz for some 22 commercial aluminas increase in approximately linear fashion with increase in density from about 3.5 to 4.0 g/cm^3 at the rate of about 4 cm^3/g.[18] Since only little or no dispersion in k is expected in alumina at microwave frequencies, this result is expected to apply at 100 GHz as well.

Room-temperature data from 100 to 400 GHz indicate averaged k values of about 9.60 for Wesgo 99.5% and 9.89 for Coors 99.9% alumina; corresponding tanδ values generally increase with frequency, roughly doubling at 400 GHz relative to the 100 GHz values of about 6 x 10^{-4} for the Wesgo and 15 x 10^{-4} for the Coors.[19] Data taken by an independent method at 30-100 GHz for the Wesgo aluminas gave nearly the same k and tanδ values at 100 GHz.[17] This and other data are summarized in Table 1:[19-21]

Table 1. Prior values of k and tanδ at 100GHz and room temperature for commercial high-purity aluminas

Mfr.	Purity or Grade	Density (g/cm^3)	k	tanδ (10^{-4})	Ref.
Wesgo	995	----	9.60	6.	19
Coors	999	----	9.89	15.	19
Crystal Systems	Sapphire	----	9.39	5.	19
Wesgo	AL-995	3.85	9.58	4.5	17
Coors	AD-999	3.88	9.71	13.	17
Coors	AD-995	3.89	9.72	4.3	17
Coors	AD-995	3.87	9.71	3.8	21
Ampex	99.5%	3.87	9.64	3.8	21
Ampex	99.9%	3.91	9.75	3.6	21

Comparison of our in-waveguide values[2] for Coors AD-995 alumina with the preceding ones indicates good agreement. The finding of two to three times higher loss in the 99.9% vs. the 99.5% version of the Wesgo and Coors aluminas seems odd, but evidence links this effect to differences in:

*The glassy intergranular phases known to exist in polycrystalline alumina containing major starting impurities such as MgO, CaO, and SiO_2, or

*Grain size,or

to a combination of these two.[3,15,17,21] (In the course of one of the preceding dielectric property studies, the grain sizes in the Coors AD-995 and AD-999 aluminas were 5-30 μm and 0.5-2.0 μm, respectively.[17]) Also, thermal-expansion mismatch between the alumina and the secondary phase are said to lead to dielectric loss.[15]

Magnesia is added to the starting powder of high-purity alumina as a sintering aid to retard grain growth and promote densification. Niwa et al. found that tanδ measured at 1 MHz and room temperature is an indication of the MgO content and also the firing temperature.[22] For example, for firing in an hydrogen atmosphere, tanδ plotted vs. MgO concentration shows shallow minima at about 0.25 wt% and 0.35 wt% for firing at 1600°C and 1650°C, respectively. For MgO concentrations of 0 to 0.35 wt%, tanδ plotted vs. firing temperature has a critical 'cross over' value of the firing temperature. Below this value of about 1670°C, zero magnesia gives the highest tanδ values, and above it zero magnesia gives the lowest ones. The tanδ values for zero MgO reach a minimum for firing at 1700°C, and increase at higher temperatures. Firing at 1700°C and above increases the likelihood of spinel forming from a solid state reaction between MgO and Al_2O_3, with which the tanδ increase seems to be associated. Since there is a tendency in the ($MgO;Al_2O_3$) system for the firing temperatures required to produce a given mass density to decrease as the (small) MgO concentrations are increased, there may be a tendency, competing against countervailing factors, for the various phases in the purer alumina to attain phase equilibrium during the sintering process and thus to be in solution in the fired product. To this end, XRD, SEM, and EDAX have revealed small amounts of spinel and calcium aluminate in both the Coors AD-995 and Wesgo AL-995 aluminas, but with more of the latter and none of the former in Coors AD-999 alumina.[17] More silica was present in Coors AD-999 rather than Coors AD-995. Evidence indicates there was probably no $MgAl_2O_4$ and $CaAl_2O_4$ in the starting powder.

The cooling history following firing is also important.[15] The metal oxides (such as MgO, SiO_2, and CaO) added as sintering aids form into a glass which, during cooling, may crystallize into other compounds (e.g., feldspars), solidify as a glass, or leave both types of material in the ceramic.

Since pure secondary phases such as silica and spinel are very low-loss materials themselves, the association of their presence with relatively high dielectric loss implies a more subtle cause for the loss, such as the levels and locations of other impurities, the relative composition and spatial distribution of the major impurities, the indirect effect of impurities on dislocation density and grain size achieved during sintering, and so on. A study on alumina compositions containing only silica/calcia fluxes indicates the presence of tanδ peaks (1 MHz, room temperature) at a "SiO_2/CaO ratio" of about 2.2, in plots of tanδ vs. this ratio for 92, 94, and 96% alumina levels.[15] The ratio for anorthite (calcium feldspar, $CaO{\cdot}Al_2O_3{\cdot}2SiO_2$) is 2.16. Similar behavior was observed for SiO_2/BaO and SiO_3/SrO flux systems in 90% alumina.

An example of how grain size may affect tanδ is potentially illustrated by the physics of scattering of long-wavelength electromagnetic waves from a collection of dielectric spheres of radius "a" and dielectric constant differing from that of the embedding medium.[23] Assuming an incoherent superposition of the contributions from each sphere and ignoring multiple scattering effects, then there will be a loss tangent contribution equal to ga^3f^4, where "f" is the frequency and "g" is a complicated function of dielectric constants. If an irregularly shaped grain is modeled by a dielectric sphere of equal volume, then energy will be extracted from the millimeter wave at a rate proportional to a^3f^4. This contribution may be relatively small compared to ones in which the MMW energy is directly converted instead into heat (i.e., small g), but subsequent examination of the grain-size and frequency dependence of published tanδ data[21] on Coors AD-995 and AD-999 alumina yields some notable observations summarized in Table 2.

Table 2. Tanδ and grain size for two high-purity Coors aluminas

Material Grade	Tanδ[a] (10^{-4}) at: 35 GHz	135 GHz[b]	Grain Size[c] (μm)	Tanδ ratio at constant: Grain Size	Frequency
AD-995	2.9	4.5	17	1.55 (17)	3.45 (35)
AD-999	10.0	15.0	3	1.50 (3)	3.33 (135)

The tanδ ratios were calculated to give values greater than unity, and the number in parentheses following each calculated ratio gives the appropriate value of grain size or measurement frequency held constant for the ratio calculation. The two tanδ-ratios showing the effect of frequency (fixed a) for either ceramic type are nearly equal, as is the case for the tanδ-ratios for the effect of material type, i.e., grain size (fixed f). These ratios are much smaller than the ones calculated from ga^3f^4, which are 220 (fixed a) and 180 (fixed f). Given the very simple assumptions here for modeling the ceramics, however, the averaged ratios of 3.4 (fixed f) and 1.5 (fixed a) do yield the roughly comparable effects suggested by the near-equality of 220 and 180. Further, the prediction from long-wavelength (i.e., Rayleigh) scattering that the effects of "a" and "f" are independent is borne out by Table 2. The picture is complicated, however, by the other differences in these two ceramics, such as impurity level (5:1 ratio) and firing temperature (180°C difference[25]). (However, the densities and k values are nearly the same; see Table 1.)

Preliminary Results from Advanced Characterization

Detailed TEM of the microstructures of the control and irradiated Coors AD-995 alumina specimens was performed. A JEOL 2000 EX TEM/STEM with high angle X-ray spectrometry was used to investigate defect structure and chemistry. Samples were prepared by ion thinning predimpled 3mm discs at 5kV and oriented approximately 10° with respect to the ion beams. Microstructural defects identified in alumina control samples included sintering voids, dislocations, and an intergranular glassy phase. Irradiated samples showed a similar structure, plus a high density of dislocation loops. These loops were imaged using the weak-beam dark-field technique, and are probably interstitial in nature. No microcracking or grain-boundary separation was observed. X-ray microanalysis provided no evidence of colloidal aluminum and showed no radiation-induced changes in composition of the glassy phase. These regions were analyzed by means of an electron beam (40nm probe size) and a high angle x-ray spectrometer. Both Si and Ca were resolved, but not the Mg expected from the $SiO_2{\cdot}CaO{\cdot}MgO$ flux used in sintering the ceramic. Selected TEM's for the control and neutron-irradiated alumina are given in Figs.1 and 2-3, respectively.

Preliminary neutron-diffraction experiments on the neutron-irradiated and unirradiated control alumina showed considerable irradiation-induced line-broadening and slight changes in crystallographic parameters. The neutron diffraction data were collected at the Los Alamos Neutron Scattering Center (LANSCE)[26] on the High Intensity Powder Diffractometer (HIPD). One 'matchstick' (MMW test specimen) of each was examined.

(X-ray analysis performed on the control specimen indicated the material was isotropic.) Data collection times were approximately 8 hours at an estimated average beam current of 10 μA. Rietveld analysis was used to analyze the data.[27]

Fig. 1. TEM's of unirradiated Coors AD-995 alumina. Calibration bars at bottom of each photo give scale (500 nm, top photos; 200 nm, bottom photos).

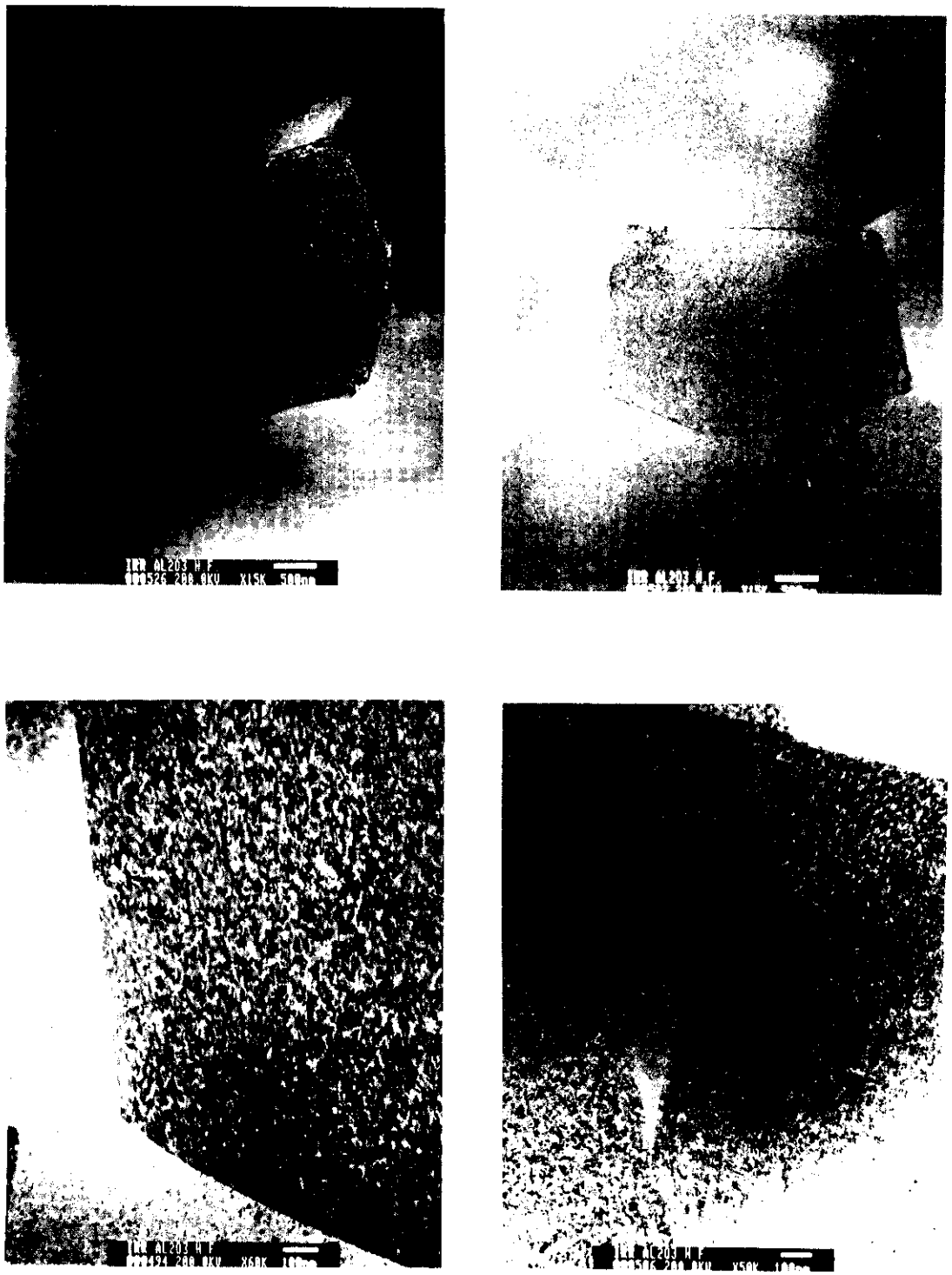

Fig. 2. Lower-magnification series for fast-neutron-irradiated Coors AD-995 alumina. Calibration bars: 500 nm, top photos; 100 nm, bottom photos.

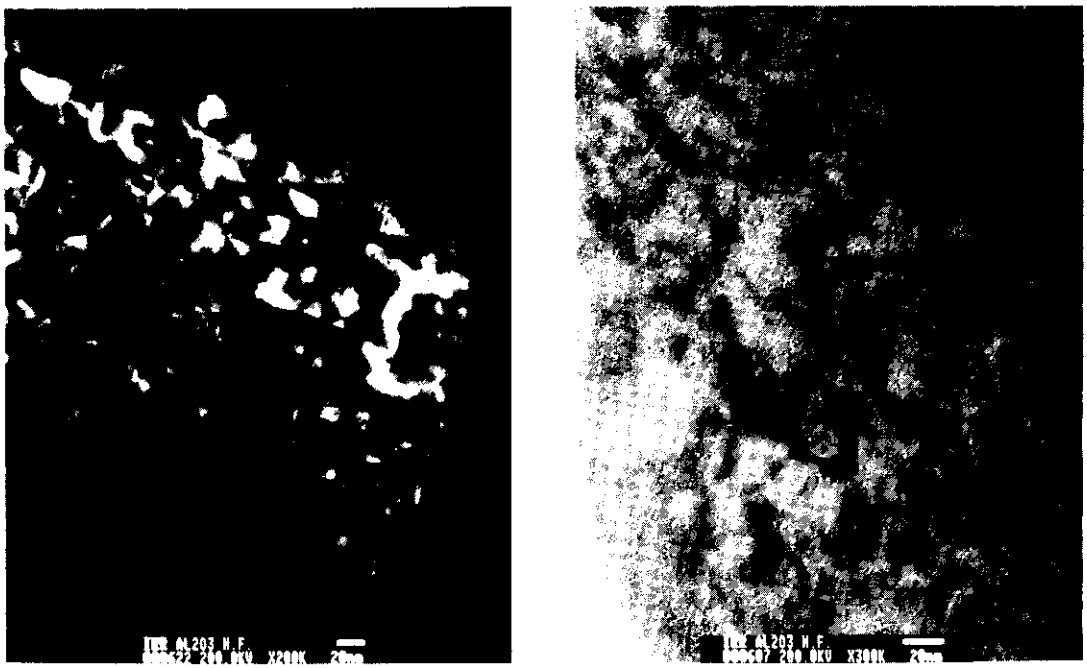

Fig. 3. Higher-magnification TEM's of fast-neutron-irradiated Coors AD-995 alumina. Calibration bars: 20 nm.

The Rietveld technique provides least-squares fits to crystallographic variables such as lattice constants, atomic positions and thermal factors, and morphological variables such as line-broadening by treating an entire powder diffraction set as a single entity. The background from the specimen holder can also be subtracted out. The specimen showed clear signs of radiation damage. A careful comparison of the refined crystallographic parameters indicates that the damage is probably confined to the atomic arrangement in the basal plane, leaving the stacking of planes relatively undisturbed. The observed line-broadening is modeled by a peak-width term which is linear in d-spacing. Such a term is usually associated with lattice strain. No line broadening associated with particle size or "paracrystallinity" was found. The observed lattice strain of 0.13% is of the same order of magnitude as the (low) resolution of HIPD.

Discussion and Conclusions

For copper specimens irradiated in EBR-II along with the ceramic specimens of this report, we have estimated the fission-neutron fluence was equivalent to about 20 to 40 weeks of 14MeV neutron first-wall loading of 1-MWyr/m^2. It is clear then that the doubling of dielectric loss factor ktanδ observed at 90-100GHz and room temperature for such an EBR-II exposure indicates that more progress is needed, especially since it is likely that the thermal conductivity was also degraded--a bad consequence for an rf window material subjected to fatigue cycles of thermo-mechanical stress.[1]

One needed step is the identification of critical issues before a realistic specification for a potential rf window material can be drawn up. Even specific materials, such as Coors AD-995 alumina, are not 'generic' because of uncontrolled compositional, microstructural, and processing variables which have a 'hidden' effect on the desired values and stability of k, tanδ, thermal conductivity, thermal expansion coefficient, fracture toughness, fracture strength, and so on. For alumina, some of these variables were described in a preceding section. For judgments to be made on whether and how an astute control of such variables can lead to acceptable modification of a given material system that satisfies in situ performance requirements, much more needs to be understood about the consequences of specific processing steps on MMW dielectric loss (and also on dielectric loss for other rf heating applications such as ICRH at lower frequencies). Furthermore, the stability of desired properties has to be considered in terms of the chemical and microstructural defects expected from neutron and other irradiation.

For example, atomically dispersed chemical impurities in ceramics can distort the local electronic structure from the symmetric non-dipolar case for a pure, ionic crystal (spherical valence-electron charge distribution) to an asymmetric dipolar case for an interstitial or substitutional point defect (ellipsoidal,

quadrupolar, or other charge distribution). This may occur, for example, for an anion-compensated Si atom or cation-compensated Ca atom substituted onto one of the Al sublattices in alumina. Furthermore, the covalent bonding tendencies of Si would differ from the anti-bonding tendencies of atoms in a pure ionic crystal. Some elemental impurities may be especially deleterous when their chemical properties 'clash' with those of the respective cation or anion host species. Electric dipoles can also result if locally uncompensated ionic impurities replace lattice ions of different valence.[28] Such chemically-dissimilar point defects can easily result from neutron-induced transmutation and displacement events.

Point defects are the starting point in a radiation-damage process that can lead to extended objects such as edge dislocations--and the dislocation loops observed in this study and in prior ones. To this end, it is well-known that dislocations in ionic crystals can carry an electrical charge; for example, edge dislocations can have unit-charged jogs surrounded by cation and anion vacancies as well as divalent impurities.[29] Such a charge tends to undergo periodic displacement in the presence of an electromagnetic wave, potentially leading to dielectric loss. Rotation of associated dipoles in such a field will also.

Charged dislocations have isoelectric points in temperature beyond which the charge changes sign; the isoelectric temperatures in NaCl crystals can vary from 400°C to 600°C, depending on free cation vacancy concentrations. Dislocations (charged or not) can be excited into vibration in ionic crystals by elastic waves at frequencies of up to 10^8 Hz at least, dissipating energy by either strain-field or re-radiation scattering.[31] Such excitation by MMW's seems plausible as well when the dislocations are charged.

These examples on microstructural-dielectric interactions indicate an apparent need to build into a fusion ceramic (for rf windows) a resistance to defect aggregation as well as swelling. Chemical additives to the pre-irradiation ceramic might be useful in this respect and for 'scavenging' or neutralizing the effect of deleterious point defects. Control of the nature of the interfaces between separate phases in multi-phase ceramics like polycrystalline alumina may also be important because of interfacial polarization (IPP) which increases tanδ, especially above room termperature.[20]

The sensitivity to radiation damage achieved with the preliminary use of high-intensity neutron diffraction on 'as-is' specimens indicates its potential as a useful complementary tool to TEM. Whether the basal-plane damage thus found is related to the unfaulted interstitial dislocation loops known to be produced by fast neutrons on the $\{10\bar{1}0\}$ prismatic planes[11] is a matter worth resolving, especially in light of the high density of loops revealed by TEM.

FUTURE WORK

The preceding mechanisms will be further explored, as will be the inter-relationship that may exist between the dislocation loops on the one hand and the lattice strain and basal-plane damage revealed by neutron diffraction on the other. (At room temperature and MMW frequencies, IFP may also become important if Si or Al segregation occurs.)

REFERENCES

1. H. M. Frost, "Millimeter-Wave Properties of Neutron-Irradiated Ceramics for RF-Window-MFE Applications," pp. 11-16 in Eighth Annual Progress Report on Special Purpose Materials for Magnetically Confined Fusion Reactors, DOE/ER-0113/5, U.S. Department of Energy, Washington, DC, March 1986.
2. H. M. Frost and C. D. Kise, "In-Waveguide Measurements of MMW Dielectric Properties of Candidate Fusion Ceramics," this Progress Report.
3. G. P. Pells, " Radiation Effects in Electrically Insulating Ceramics," Culham/EEC Fusion Technology Task MAT-13 (report), AERE R 11715, Harwell Laboratory, Oxforhire, England, November 1985.
4. J. D. Fowler, Jr., "Radiation-Induced RF Loss Measurements and Thermal Stress Calculations for Ceramic Windows," J. Nucl. Mater. 122&123, 1359-1364 (1984).
5. J. B. MacChesney and G. E. Johnson, "Room-Temperature Dielectric Properties of Fast-Neutron-Irradiated Fused Silica and Alumina," J. Appl. Phys. 35, 2784-2785 (1964).
6. H. M. Frost, "Facility for Measuring Microwave Properties of Radiation-Damaged Ceramics for RF Windows and Other Fusion Applications," pp. 29-32 in Seventh Annual Progress Report on Special Purpose Materials for Magnetically Confined Fusion Reactors, DOE/ER-0113/4, U. S. Department of Energy, Washington, D.C., May 1985.
7. R. S. Wilks, "Neutron-Induced Damage in BeO, Al_2O_3, and MgO -- A Review," J. Nucl. Mater. 26, 137-173 (1968).
8. G. W. Keilholtz, R. E. Moore, and H. E. Robertson, "Effects of Fast Neutrons on Polycrystalline Alumina and Other Electrical Insulators at Temperatures from 60° to 1230°C," Technical Report ORNL-4678-UC-4-Chemistry, Oak Ridge National Laboratory, Oak Ridge, TN, May 1971.
9. F. W. Clinard, Jr., J. M. Bunch, and W. A. Ranken, "Neutron Irradiation Damage in Al_2O_3 and Y_2O_3," pp. II-498 to II-516 in Proceedings of the International Conference on Radiation Effects and Tritium Technology for Fusion Reactors (October 1-3, 1975, Gatlinburg, TN), ed. by J. S. Watson and F. W. Wiffen, Oak Ridge National Laboratory, CONF-750989, Vol. II, March 1976.
10. J. M. Bunch, J. G. Hoffman, and A. H. Zeltmann, "On the Nature of Features Seen by TEM in Fast Neutron Irradiated Al_2O_3," J. Nucl. Mater. 73, 65-69 (1978).

11. F. W. Clinard, Jr., G. F. Hurley, and L. W. Hobbs, "Neutron Irradiation Damage in MgO, Al_2O_3 and $MgAl_2O_4$ Ceramics," J. Nucl. Mater. 108&109, 655-670 (1982).
12. G. R. Hopkins and R. J. Price, "Fusion Reactor Design with Ceramics," Nucl. Eng. Design/Fusion 2, 111-143 (1985).
13. G. P. Pells, "Ceramic Materials for Fusion Reactor Applications," J. Nucl. Mater. 122&123, 1338-1351 (1984).
14. R. A. Youngman, "Neutron-Irradiation Damage in Ceramic Solids," Doctoral thesis, Case Western Reserve University, August 1982.
15. J. R. Floyd, "Effect of Secondary Crystalline Phases on Dielectric Losses in High-Alumina Bodies," J. Am. Ceram. Soc. 47, 539-543 (1964).
16. S. C. Hansen, Y. R. Shiue, and D. S. Phillips, "Grain-Boundary Microstructures in a Commercial Alumina Ceramic," Adv. Ceram. 6, 163-170 (1983).
17. W. W. Ho, "Millimeter Wave Dielectric Property Measurement of Gyrotron Window Materials," Technical Report for Period January 1983 -- February 1984, ORNL/SUB/83-51926/1, Rockwell International Science Center, Thousand Oaks, CA, April 1984.
18. W. George and P. Popper, "The Dielectric Properties of Some Commercial Alumina Materials at 9368 MHz," Proc. Brit. Ceram. Soc. 10, 63-78 (1968).
19. M. N. Afsar and K. J. Button, Digest of Millimeter and Submillimeter Wave Materials Information and Measurements, Massachusetts Institute of Technology, Cambridge, MA, 1983.
20. G. Economos, "Effect of Microstructure on the Electrical and Magnetic Properties of Ceramics," pp. 201-213 in Ceramic Fabrication Processes, ed. by W. D. Kingery, The Technology Press of M.I.T. And John Wiley & Sons (jointly), Cambridge, MA and New York, NY, 1958.
21. W. W. Ho, "Millimeter Wave Dielectric Property Measurement of Gyrotron Window Materials," Technical Report for Period January 1983 --February 1984 [sic], ORNL/SUB/83-51926/2, Rockwell International Science Center, Thousand Oaks, Ca, April 1985.
22. K. Niwa, K. Hashimoto, and K. Murakawa, "Electrical Properties and Microstructure of Alumina Substrates," Fujitsu Sci. Tech. J. 9, 179-192 (1973).
23. J. D. Jackson, Classical Electrodynamics (2nd ed.), John Wiley & Sons, New York, 1975, pp. 411-427.
24. Technical data document, H 5M 5/85, Coors Porcelin Co., Golden, CO, 1985.
25. M. Dowell, private communication (1986).
26. R. N. Silver, "The Los Alamos Neutron Scattering Center," Physica 137B, 359-371 (1986).
27. A. C. Larson and R. B. Von Dreele, "Generalized Structure Analysis System," LA-UR-86-748, Los Alamos National Laboratory, Los Alamos, NM, February 1986.
28. G. Sarojini, "Dielectric Properties of Solids," J. Scient. Ind. Res. 27, 216-218 (1968).
29. W. H. Robinson, "Electrical-Mechanical Coupling Due to Charged Dislocations," Phil. Mag. 25, 355-369 (1972).
30. R. W. Whitworth, "Charged Dislocations in Ionic Crystals," Adv. Phys. 24, 203-304 (1975).
31. R. O. Schwenker and A. V. Granato, "The Frequency Dependence of Sound Radiation from Mobile Dislocation Walls," J. Phys. Chem. Solids 31, 1869-1875 (1970).

9. SUPERCONDUCTING MAGNET MATERIALS

IRRADIATION EFFECTS ON ORGANIC INSULATORS - M. B. Kasen (National Bureau of Standards)

OBJECTIVE

The overall objective of this work is to develop functional organic-matrix composite insulators for use in the superconducting magnets of magnetic fusion energy systems. The immediate objective is to develop a method for efficient screening of the significant parameters influencing degradation of such materials under neutron irradiation at 4 K.

SUMMARY

An integrated approach has been developed for rapid screening of the influence of component variables on the performance of electrical insulators required for superconducting magnets in magnetic fusion energy systems. It incorporates an efficient method of specimen production in the form of 3.2-mm (0.125-in) diameter rods. Test methods include short-beam shear, fracture strength (G_{Ic}), and strain-controlled torsion. The torsion test induces failure between the fiber and matrix, which is expected to be the dominant failure mode induced by cryogenic irradiation. In addition to providing quantitative data on the modulus of rupture and of rigidity, the strain control feature facilitates analysis of the stress-displacement curve in the region where damage is occurring, providing useful information on how the various component and irradiation parameters are influencing the failure mode. The torsional test facility is easily constructed, provides rapid specimen turnaround, and has a low consumption of cryogens. A specimen subjected to a torsion test may be subsequently tested by the short-beam and fracture strength methods, enabling five tests to be performed on the same specimen. Glass-fiber reinforced specimens having three types of epoxy matrix and one type of polyimide matrix have been produced and submitted to ORNL for irradiation in the NLTNIF facility, after which they will be returned to NBS for testing by these methods.

PROGRESS AND STATUS

Introduction

In developing organic-matrix composite insulators for use in the superconducting magnets of magnetic fusion energy systems, the resistance to degradation by neutron and gamma irradiation at 4 K must be maximized. As little is known of the performance of composite materials under these conditions, the significant parameters that are involved must be defined, and the results must be used to develop a data base that will permit optimization of the components from which the insulators are made. This will require screening of the influence of cryogenic neutron irradiation on a large number of parameters such as resin type, chemistry, and cure state as well as fiber type, finish, and chemistry.

Unfortunately, the cost of obtaining the large number of well characterized specimens required for such a study and of performing the required testing program would be prohibitive when normal approaches are used. The author has therefore undertaken development of a more efficient procedure for obtaining the required data. The specimen problem was addressed by developing procedures for rapid, in-house production of very highly characterized, 3.2-mm (0.125-in) diameter specimens as either uniaxially reinforced composites or as neat resin specimens.[1] These specimens need only be cut to length before testing, thereby reducing cost and eliminating surface defects. The specimen configuration eliminates edge effects and permits many specimens to be simultaneously exposed to the cryogenic radiation environment.

Procedures were developed for testing the specimens in conventional flexure or short-beam shear.[2] However, the non-symmetrical and changing stress state in these methods results in highly qualitative data that is difficult to interpret. The author therefore developed several novel test methods that could be used with the rod-shape specimens to produce more quantitative data. A simple method for determining the longitudinal mode I fracture energy, G_{Ic}, at temperatures to 4 K has been described elsewhere.[1] A torsional test method is described in this report.*

System Design and Operation

The system configuration is shown in Figs. 1(a) and 1(b). A 5-liter liquid helium dewar is added for testing at 4 K. The system was designed to apply strain-controlled torque loads of up to 3.53 N·m (500 in·oz) at temperatures from 295 K to 4 K. This is sufficient to test composite materials, unreinforced resins, and nonferrous alloys in the form of 3.2-mm (0.125-in) diameter rods. Materials such as stainless steel may be tested as rods of smaller diameter.

The torsional load is applied by a 186-W (0.25-hp) reversible, variable speed dc motor through a speed-reduction gear box. Output torque is delivered through a 90° miter gear box to a 3.53-N·m (500

*Also submitted for publication in Journal of Materials Science.

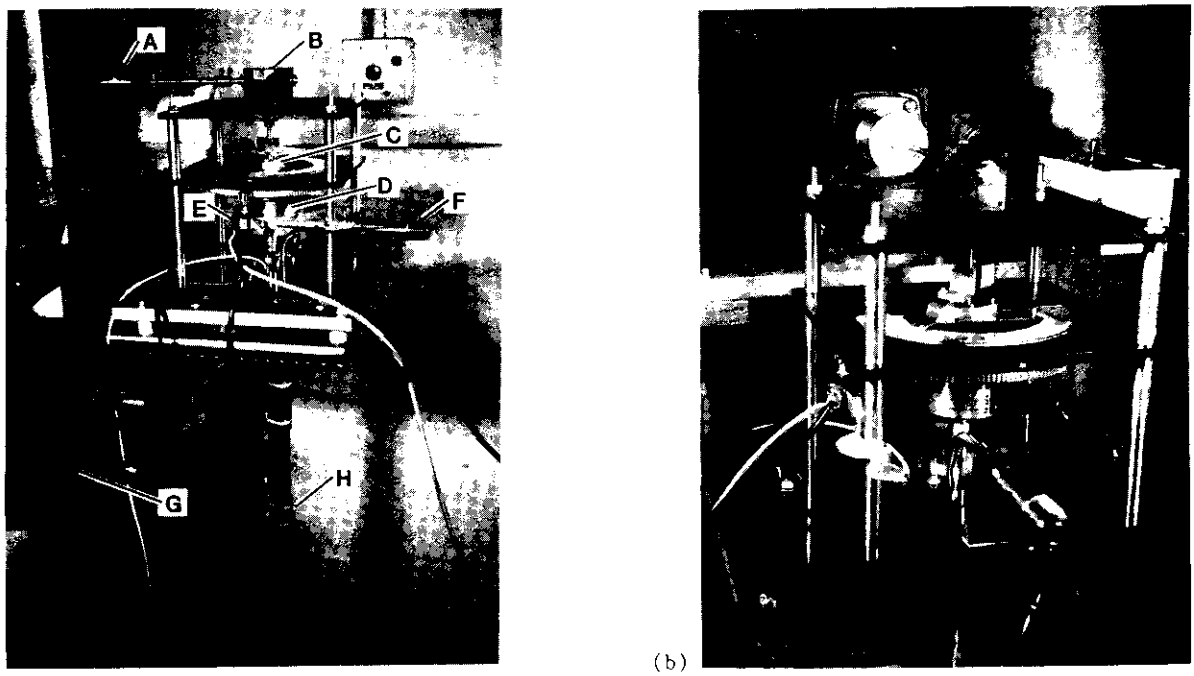

Fig. 1 (a) Overall view of the torsional test facility. A — drive motor and reduction gear box, B — 90° miter gear box, C — angular scale with indicator, D — torsion load cell, E — potentiometer, F — helium transfer line, G — power supplies, H — reaction tube, helium level indicator, and helium transfer line. (b) Detailed view of the torsional drive system and supporting framework.

in·oz) reaction torque sensor. The sensor is connected to a 6.35-mm (0.250-in) diameter stainless steel rod that transmits the torque to the specimen. Polytetrafluoroethylene (PTFE) bearings spaced about 28 cm (11 in) along the rod ensure centering of the rod within a 748-mm (19-in) long, 12.7-mm (0.5-in) o.d., 0.79-mm (0.03125-in) thick wall, stainless steel reaction tube. Roller bearings above and below the load cell minimize friction.

Angular displacement is determined by a geared 10-turn precision potentiometer driven by a large spur gear fastened to the load cell. The ratio between the driven and driving gears of 4.8 to 1.0 provides a total available angular displacement of about 720 deg. An excitation of 30 Vdc provides a good balance between sensitivity and noise. An indicator attatched to the drive shaft allows the angular rotation to be calibrated directly from an angular scale. The potentiometer is supported by a clamp fastened to one of the vertical support rods of the system, allowing it to be rotated away from the driving gear, and permitting the output of the potentiometer to be zeroed regardless of the position of the driving gear.

The torque sensor has an output of 5 $mV \cdot V^{-1}$ at rated capacity and is excited by 20 Vdc. It is calibrated by resistors simulating a known torque value. It may also be directly calibrated by dead-weight loading.

Specimens are typically 88.9-mm (3.5-in) long, although shorter specimens may be used. They are held in 9.5-mm (0.375-in) diameter 6061-T6 aluminum endcaps by a series of eight set screws arranged radially in two banks around each endcap as illustrated on Fig. 2(a). The endcaps are center drilled to a diameter closely matching that of the specimens, and to a depth of 34.9 mm (1.375 in), establishing a 25.4-mm (1.0-in) gage length between the first bank of retaining screws.

This gripping arrangement allows the endcaps to be reused, confines the failure zone to within the gage length, and allows the undamaged portions of the specimen to be recovered for further testing. For example, the undamaged 31.75-mm (1.25-in) ends of an 88.9-mm (3.5-in) long specimen may be subsequently tested in short-beam shear and for fracture strength, G_{Ic}.[1]

Close alignment of the endcaps is required to achieve free rotation within the reaction tube. The relatively long specimen aids in this alignment. Additionally, the endcap alignment may be fine tuned by adjusting the screws in the set nearest the gage length. As shown by Fig. 2, the i.d. of the endcaps has been enlarged in this region so as to allow this operation to slightly tilt the endcaps relative to the specimen.

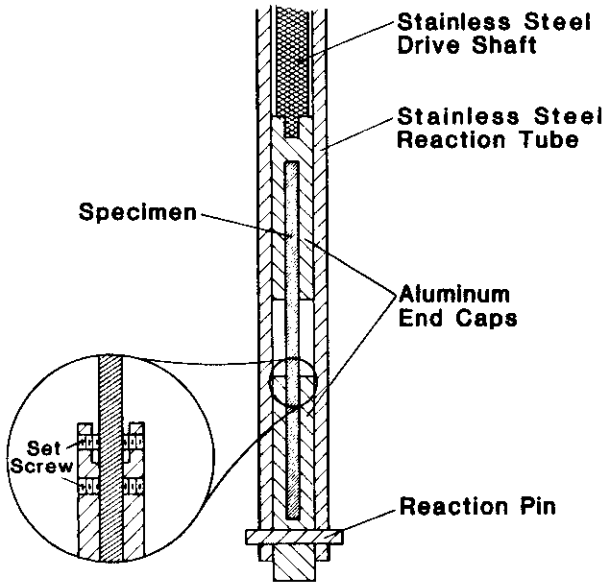

Fig. 2. Sketch of specimen installation in the reaction tube and details of the specimen gripping system. The specimen is held by eight set screws arranged radially around the endcaps in two banks of four screws each. Countersinking in the vicinity of the first bank of screws enables correcting the alignment of specimens that are not perfectly straight.

The drive shaft mates with a slot in the upper endcap; the bottom endcap is pinned to the stainless steel reaction tube. The bottom 114 mm (4.5 in) of the reaction tube is internally polished to reduce friction. The lower endcap protrudes slightly from the reaction tube to facilitate specimen insertion and removal. Compliance of the system is determined from a stress-vs.-angular rotation plot produced with a solid aluminum rod inserted into the specimen position.

Insertion of the specimen into the reaction tube is illustrated in Fig. 2(b). The drive shaft is rotated to a predetermined angular position that allows the blade of the shaft to mate with the slot in the upper endcap while simultaneously allowing the retaining pin to be inserted into the lower endcap. Proper alignment between the upper and lower endcaps is established by assembly in a fixture.

The system incorporates a helium-level indicator to ensure that only enough liquid helium is added to cover the specimen when working at 4 K. Precooling with liquid nitrogen and careful liquid helium transfer reduces helium consumption to approximately two liters per test. The cycle time for successive tests with specimens already assembled into the endcaps is on the order of 20-30 minutes.

The apparent shear strength in torsion (modulus of rupture) τ, at any given torsional load T, is given by the relationship

$$\tau = 16\ T/\pi d^3, \tag{1}$$

where d is the specimen diameter. When T is the torsional load at failure, τ is the apparent ultimate shear strength τ_{max}. These values are apparent because they are based on the assumption that the effective radius of the specimen remains unchanged during the fracture process. Although this is in error, the data are valid for comparative purposes.

The elastic shear stiffness (modulus of rigidity) G is given by the relationship

$$G = \tau L/\theta r, \tag{2}$$

where L is the gage length, θ is the angular displacement in radians, and r is the specimen radius. Alternatively, the modulus of rigidity may be calculated by the relationship

$$G = 10.18\ TL/\theta d^4, \tag{3}$$

which is derived by substituting eq. (1) into eq. (2).

Results and Discussion

Typical torsional stress-displacement curves produced to 90° rotation at 295 K, 77 K, and at 4 K with uniaxial glass-fiber reinforced composite specimens are presented on Fig. 3. The specimens contained 48 volume percent type E glass reinforcement in the resin system identified as System A in Table 1. This resin system simulates that used in fabricating the commercial G-11CR high-pressure industrial laminate materials that are widely used for cryogenic applications.[3]

At 295 K, the material deformed in a viscoelastic manner, without evidence of fracture. However, cooling to 77 K caused transition to a brittle behavior, with a substantial increase in modulus and strength. Further cooling to 4 K had little effect on the modulus but resulted in a further strength increase. Linearity of the curve up to the first indication of failure indicates negligible plastic deformation at cryogenic temperatures for this resin system.

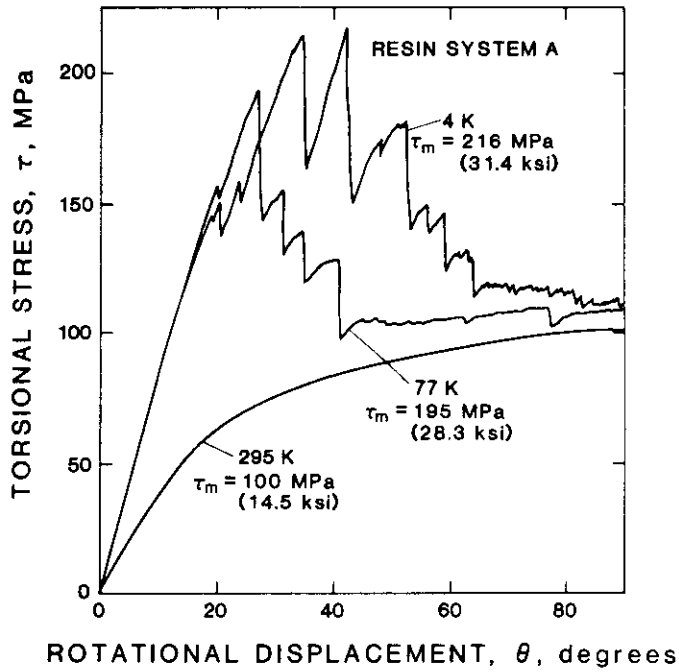

Fig. 3. Typical torsional stress-displacement curves obtained at 295 K, 77 K, and 4 K with epoxy matrix composite specimens uniaxially reinforced with 48 volume percent type E glass. Resin system A duplicates that of the G-11CR commercial product. Angular displacement is 0.3° s^{-1}.

Table 1. Resin systems used in preparation of materials for cryogenic irradiation testing

Designation	Type	Composition
A	Epoxy	DGEBA/DDS/BF_3MEA
B	Epoxy	DGEBA/DDS
C	Epoxy	DGEBA/AMD/POPA
D	Polyimide	4,4'-bismaleimidodiphenylmethane

DGEBA Diglycidyl ether of bisphenol A
DDS Diamino diphenyl sulphone
AMD Alkylated methylenedianilene
POPA Polyoxypropylenediamine
BF_3MEA Boron trifluoride monoethylamine

Because the specimen does not catastrophically fail, the strain-control torsional test method provides an opportunity for detailed study of the failure mode beyond the initial fracture event. As may be seen on Fig. 3, the onset of fracture events is evidenced by a series of small load drops. This may reflect minor cracking of the thin epoxy film that forms the specimen surface. This is followed by a series of very large load drops, between which the stress is observed to recover significantly. This implies that failure is occurring through development of several major cracks rather than by development and propagation of a single crack. The cross section of a failed specimen shown in Fig. 4 confirms that this is indeed the case.

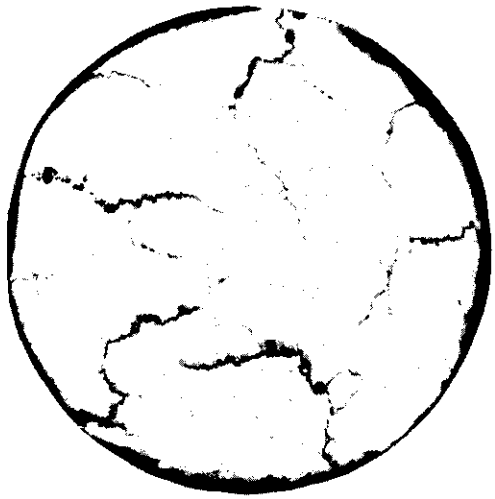

Fig. 4. Typical cross-section of a 3.2-mm-diameter, glass-reinforced specimen stressed in torsion at 4 K.

A consistent feature of torsional stress-displacement curves produced by the composite specimens at cryogenic temperatures is the eventual development of a region in which the average torsional stress remains fairly constant with additional torsional displacement. This region may be seen beyond 40° of rotational displacement at 77 K and beyond 60° displacement at 4 K on Fig. 3. An explanation for this phenomena may have been provided by Outwater[4] who has noted that the torque required to drive a diametral crack along a composite rod specimen that is uniaxially reinforced will remain essentially constant as the crack deepens. This suggests that the onset of the constant stress region reflects the coalescence of individual cracks to form a diametral crack, and that the load drops observed within this region reflect the extension of the crack along the specimen gage length. Cross sectioning specimens stressed into this region has confirmed the existence of such a diametral crack.

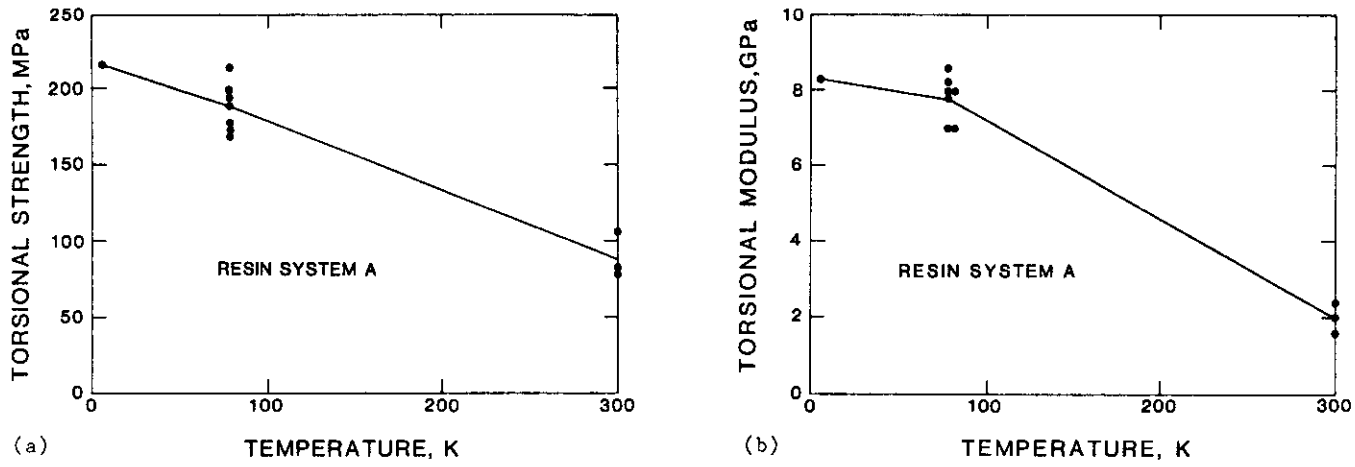

Fig. 5. Temperature dependence of the torsional properties of composite specimens made with resin system A and containing 48 volume percent glass-fiber reinforcement. (a) torsional strength (modulus of rupture); (b) torsional modulus (modulus of rigidity).

Plots of the temperature dependence of the torsional properties for a series of G-11CR specimens presented on Figs. 5(a) and 5(b) show that cooling to cryogenic temperatures increases the strength by about a factor of 2 and increases the modulus by about a factor of 4. These figures also show that the test procedure is capable of producing data having a acceptably low scatter.

Figure 3 shows that the load drops produced during deformation at 4 K are are much more prominent than those produced during deformation at 77 K. Since the test is performed under strain control, the magnitude of each stress drop is proportional to the newly cracked area. This indicates that the total cracked area generated by deformation at 4 K is much greater than that generated at 77 K, suggesting that cooling from 77 K to 4 K has decreased the fracture strength of the material.

The work per unit volume done during torsional deformation and fracture is proportional to the area under the stress-displacement curve. As this is a measure of material toughness, it is a parameter of interest in a materials performance screening program. Fig. 6 illustrates the temperature dependence of this parameter for two composite materials. Taking 90° as a standard rotational displacement, cooling from 295 K to 77 K increased the average work absorbed during deformation by about a factor of two for the System A material. However, this parameter increased by a factor of 4-5 for the system C material that is made with an epoxy resin formulated for impregnation of superconducting magnets. System C contains a flexibilizing agent that increases its toughness at cryogenic temperatures, while lowering its toughness at room temperature. Figure 6 also shows that the average work done during deformation of the unreinforced resins and that of the reinforced resins are the same at room temperature. This indicates that the visco-elastic behavior of the resins are controlling the room temperature deformation, with or without the glass reinforcement.

The influence of the fiber-matrix interface in controlling the fracture path during torsional deformation of composite specimens at cryogenic temperatures is illustrated in Fig. 7. The test method should therefore be of particular value in studies assessing the influence of various parameters on the integrity of this interface.

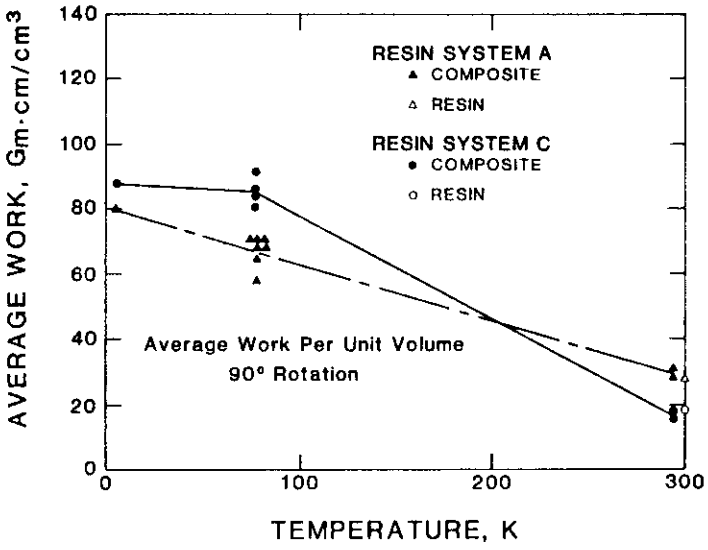

Fig. 6. Temperature dependence of the average work required per unit volume to deform composite specimens to a 90° rotational angle for epoxy resin systems A and C. Data for the unreinforced resins at 295 K are also shown.

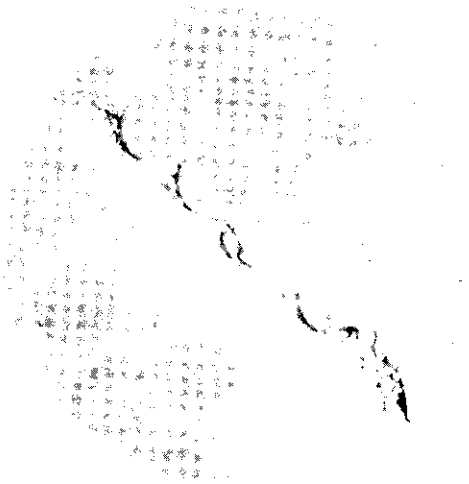

Fig. 7. Photomicrograph illustrating the influence of the fiber-matrix interface in controlling the fracture path during torsional deformation of the uniaxially reinforced composite specimens. Direction of crack propagation is lower right to upper left. Average fiber diameter is 12 μm.

CONCLUSIONS

The strain-controlled, torsional test method can provide an efficient and inexpensive method for screening the influence of component and irradiation parameters on the performance of fiber-reinforced composite materials at temperatures from 295 K to 4 K. A test facility using inexpensive rod-shaped specimens may be easily constructed. In addition to providing quantitative information on the torsional strength and modulus, analysis of the stress-deformation curve in the damage accumulation region provides valuable information on the failure mechanisms. The torsional test method therefore appears superior to the conventional flexure methods for screening composite materials performance.

FUTURE WORK

Specimens fabricated from the four resin systems listed on Table 1 have been submitted to ORNL for irradiation at 4 K in the National Low Temperature Neutron Irradiation Facility when that facility becomes operative. System A duplicates the resin formulation used in the G-11CR cryogenic-grade, high-pressure industrial laminate, and will therefore provide a baseline against which the performance of other systems may be compared. System B is similar to System A but does not have the boron-containing accelerator. A comparison between these two systems will therefore provide information on the significance of such catalysts or accelerators on degradation. System C represents an epoxy resin formulation that is widely used for magnet impregnation, and which is expected to have good radiation resistance. System D is a bismaleimide type of polyimide, and was included to determine how this advanced type of polymer system compares with the epoxies in radiation resistance.

These specimens will be exposed to three increasing radiation levels established in consultation with personnel at ORNL. Following irradiation, the specimens will be warmed up to room temperature and returned to NBS-Boulder for testing at 4 K in short-beam shear, torsion, and for fracture strength, G_{Ic}. An identical set of specimens will be tested in the unirradiated state.

This test series will provide the first systematic analysis of the influence of high levels of cryogenic neutron irradiation on highly characterized, organic-matrix composite materials. It will pave the way for future studies screening the influence of fiber type and chemistry (boron-free E glass, type S2 glass), the chemistry of the fiber finish (hydrogen content), and of advanced types of thermoplastic polymer matrices that may provide both improved radiation resistance and improved formability (poly-ether-etherketone (PEEK) and polyphenyl sulfide (PPS).

REFERENCES

1. M. B. Kasen, "High Quality Organic Matrix Composite Specimens for Research Purposes", J. Comp. Tech. Res., 8(3), 103-6 (1986).

2. M. B. Kasen, "Screening the Performance of Organic Insulators Under Cryogenic Neutron Irradiation", pp. 153-9 in Advances in Cryogenic Engineering, 32, edited by R. P. Reed and A. F. Clark, Plenum Press, New York, 1986.

3. M. B. Kasen et al., "Mechanical, Electrical, and Thermal Characterization of G-10CR and G-11CR Glass-Cloth/Epoxy Laminates Between Room Temperature and 4 K" in Advances in Cryogenic Engineering, 26, edited by R. P. Reed and A. F. Clark, Plenum Press, New York, 1980.

4. J. O. Outwater, "The Fracture Energy of Pultruded Rod", J. Comp. Mater., 20, 253-8 (1986).

DOE/ER-0313/1
Distribution
Categories
UC-20 and 20c

DISTRIBUTION

1–13. Argonne National Laboratory, 9700 South Cass Avenue, Argonne, IL 60439

M. C. Billone
O. K. Chopra
R. G. Clemmer
D. R. Diercks
P. A. Finn
A. K. Fischer
Y. Y. Liu
B. A. Loomis
R. F. Mattas
L. A. Niemark
S. W. Tam
E. R. Van Deventer
H. Wiedersich

14. Argonne National Laboratory, EBR-II Division, Reactor Materials Section, P.O. Box 2528, Idaho Falls, ID 83403-2528

D. L. Porter

15. Arizona State University, Department of Mechanical and Aerospace Engineering, Tempe, AZ 85281

W. A. Coghlan

16. Auburn University, Department of Mechanical Engineering, Auburn, AL 36849

B. A. Chin

17–30. Battelle-Pacific Northwest Laboratory, P.O. Box 999, Richland, WA 99352

J. L. Brimhall
D. G. Doran (5)
M. D. Freshley
F. A. Garner
D. S. Gelles
M. L. Hamilton
H. L. Heinisch
G. W. Hollenberg
B. D. Shipp
O. D. Slagle

31–32. Carnegie Institute of Technology, Carnegie-Mellon University, Schenley Park, Pittsburgh, PA 15213

W. M. Garrison, Jr.
J. C. Williams

33–36. GA Technologies, Inc., P.O. Box 85608, San Diego, CA 92138

J. Bauer
G. R. Hopkins
T. A. Lechtenberg
D. I. Roberts

37–38. General Dynamics Corporation, 5001 Kearny Villa Road, San Diego, CA 92138

T. L. Cookson
V. Stegar

39. General Electric, Advanced Nuclear Technology Operation, 310 Deguine Drive, Sunnyvale, CA 94088

S. Vaidyanathan

40. Georgia Institute of Technology, School of Textile Engineering, Atlanta, GA 30332

D. S. Tucker

41. Grumman Aerospace Corporation, c/o TFTR Project, Princeton Plasma Physics Laboratory, Princeton University, A. Site, Building 1-E, Princeton, NJ 08540

R. G. Micich

42–44. Lawrence Livermore National Laboratory, P.O. Box 808, Livermore, CA 94550

E.N.C. Dalder
M. Guinan
J. Perkins

45–53. Los Alamos National Laboratory, P.O. Box 1663, Los Alamos, NM 87545

J. L. Andersen
L. Caudel
D. J. Dudziak
H. M. Frost
G. Hurley
C. D. Kise
R. Liepens
R. J. Livak
T. Zocco

54. Manlabs, Inc., 231 Erie Street, Cambridge, MA 02139
D. Tognarelli

55. Massachusetts Institute of Technology, Department of Metallurgy and Materials Science, Cambridge, MA 02139
L. W. Hobbs

56. Massachusetts Institute of Technology, 138 Albany Street, Cambridge, MA 02139
O. K. Harling

57–58. Massachusetts Institute of Technology, 77 Massachusetts Avenue, Cambridge, MA 02139
I-Wei Chen
N. J. Grant

59–60. Massachusetts Institute of Technology, Plasma Fusion Center Headquarters, Cambridge, MA 02139
H. D. Becker
D. B. Montgomery

61. McDonnell-Douglas Astronautics Company, East, P.O. Box 516, Bldg. 92, St. Louis, MO 63166
J. W. Davis

62–63. National Bureau of Standards, Boulder, CO 80302
F. R. Fickett
M. B. Kasen

64. National Materials Advisory Board, 2101 Constitution Avenue, Washington, DC 20418
K. M. Zwilsky

65. Naval Research Laboratory, Washington, DC 20375
J. A. Sprague

66–131. Oak Ridge National Laboratory, P.O. Box X, Oak Ridge, TN 37831

Central Research Library
Document Reference Section
Laboratory Records Department (2)
Laboratory Records – RC
Patent Section
J. Bentley
L. A. Berry
E. E. Bloom
D. N. Braski
W. P. Eatherly
M. L. Grossbeck
S. Hamada
R. L. Klueh
R. A. Lillie
K. C. Liu
A. W. Longest
L. K. Mansur
P. J. Maziasz
T. K. Roche
A. F. Rowcliffe (35)
R. L. Senn
I. Siman-Tov
R. E. Stoller
M. S. Suzuki
K. R. Thoms
P. T. Thornton (3)
P. F. Tortorelli
F. W. Wiffen
S. J. Zinkle

132–134. Princeton Plasma Physics Laboratory, Princeton University, P.O. Box 451, Princeton, NJ 08540
J.P.F. Conrads
H. Furth
Long-Poe Ku

135. Rensselaer Polytechnic Institute, Troy, NY 12181
D. Steiner

136. Rockwell International Corporation, NA02, Rocketdyne Division, 6633 Canoga Avenue, Canoga Park, CA 91304
D. W. Kneff

137–138. Sandia National Laboratories, P.O. Box 5800, Albuquerque, NM 87185
M. J. Davis
W. B. Gauster

139–140. Sandia National Laboratories, Livermore Division 8316, Livermore, CA 94550
W. Bauer
W. G. Wolfer

141. University of California, Department of Chemical and Nuclear Engineering, Santa Barbara, CA 93106
G. R. Lucas

142–144. University of California, Department of Chemical, Nuclear and Thermal Engineering, Los Angeles, CA 90024
M. A. Abdou
R. W. Conn
N. M. Ghoniem

145. University of California, Los Alamos National Laboratory, P.O. Box 1663, Los Alamos, NM 87545
T. Zocco

146. University of Missouri, Department of Nuclear Engineering, Rolla, MO 65401
A. Kumar

147. University of Michigan, Department of Nuclear Engineering, Ann Arbor, MI 48109
T. Kammash

148–152. Westinghouse Hanford Company, P.O. Box 1970, Richland, WA 99352
A. M. Ermi
G. D. Johnson
F. M. Mann
R. J. Puigh
R. L. Simons

153. Department of Energy, Oak Ridge Operations Office, P.O. Box E, Oak Ridge, TN 37831
Assistant Manager for Energy Research and Development

154–157. Department of Energy, Department of Fusion Energy, Washington, DC 20545
S. E. Berk
J. F. Clarke
M. M. Cohen
T. C. Reuther

158–288. Department of Energy, Technical Information Center, Office of Information Services, P.O. Box 62, Oak Ridge, TN 37831
For distribution as shown in DOE/TIC-4500, Distribution Categories UC-20 (Magnetic Fusion Energy) and UC-20c (Reactor Materials)

☆ U.S. GOVERNMENT PRINTING OFFICE: 1987-548-118/60103